Universität
Rostock

Traditio et Innovatio

Study of Beauty Baryons Decaying to D^0pK and the Amplitudes of $\Lambda_b^0 \to D^0pK$ in the Dalitz Plane with the LHCb Experiment

Dissertation

for
obtaining the academic degree

doctor rerum naturalium (Dr. rer. nat.)

of the Faculty of Mathematics and Natural Sciences
of the University of Rostock, Germany

submitted by
Harald Viemann, born in Schweinfurt

Rostock, Juli 2020

https://doi.org/10.18453/rosdok_id00003026

Referees:

Privatdozent Dr. Roland Waldi
Universität Rostock
Institut für Physik
Albert-Einstein-Str. 23
D-18059 Rostock
roland.waldi@uni-rostock.de

Prof. Dr. Johannes Albrecht
Technische Universität Dortmund
Experimentelle Physik 5
Otto-Hahn-Strasse 4
D-44227 Dortmund
johannes.albrecht@tu-dortmund.de

Opening of the doctoral degree procedure:	9th Juli 2020
Date of scientific colloquium:	26th March 2021

Abstract

The decays $\Lambda_b^0 \to D^0 pK$ and $\Xi_b \to D^0 pK$ are studied with proton-proton collision data of an integrated luminosity of $9\,\mathrm{fb}^{-1}$ recorded by LHCb at center-of-mass energies of 7, 8 and $13\,\mathrm{TeV}$. Measurements of the signal yield ratios $R_{\Lambda_b^0}$ and R_{Ξ_b} with the normalising channel $\Lambda_b^0 \to D^0 p\pi$ are performed. They result in an update of the following branching fractions, that is about one and a half times more precise than the current worldwide best measurements:

$$\mathcal{B}(\Lambda_b^0 \to D^0 pK) = (4.93 \pm 0.18_{\mathrm{stat}} \pm 0.09_{\mathrm{syst}} \pm 0.55_{\mathrm{ext}}) \times 10^{-5}$$
$$f_{\Xi_b} \cdot \mathcal{B}(\Xi_b \to D^0 pK) = (2.23 \pm 0.08_{\mathrm{stat}} \pm 0.05_{\mathrm{syst}} \pm 0.40_{\mathrm{ext}}) \times 10^{-6}$$

The third uncertainty accounts for the branching fraction of the normalisation mode. The integrated CP asymmetries for $\Lambda_b^0 \to D^0 pK$ and $\Xi_b \to D^0 pK$ are calculated for the full phase space and the pK channel subregion of an squared invariant two-body mass $m^2_{D^0 p} > 14\,\mathrm{GeV}^2/c^4$. They are consistent with zero. We further measure the mass difference:

$$m_{\Xi_b} - m_{\Lambda_b^0} = 172.5 \pm 0.38_{\mathrm{stat}} \pm 0.17_{\mathrm{syst}}\,\mathrm{MeV}/c^2$$

Finally, an amplitude analysis of the $\Lambda_b^0 \to D^0 pK$ phase space with $D^0 \to K^- \pi^+$ is performed, yielding a large fraction of a $\Lambda_c^+(2950)$ resonance next to multiple Λ^* resonances. There are fractions for high spin resonances like $\Lambda(2100)$ and $\Lambda(2350)$ as well.

Zusammenfassung

Die Zerfälle $\Lambda_b^0 \to D^0 pK$ und $\Xi_b \to D^0 pK$ werden mit dem Proton-Proton Datensatz von einer integrierten Luminosität von $9\,\mathrm{fb}^{-1}$, aufgenommen mit dem LHCb Detektor bei den Schwerpunktsenergien von 7, 8 und 13 TeV, untersucht. Die Signalverhältnisse $R_{\Lambda_b^0}$ und R_{Ξ_b} werden normiert auf $\Lambda_b^0 \to D^0 p\pi$ gemessen und resultieren in rund eineinhalb mal genauere Verzweigungsverhältnisse, als die aktuell weltweit besten Messungen:

$$\begin{aligned}\mathcal{B}(\Lambda_b^0 \to D^0 pK) &= (4.93 \pm 0.18_{\mathrm{stat}} \pm 0.09_{\mathrm{syst}} \pm 0.55_{\mathrm{ext}}) \times 10^{-5}\\ f_{\Xi_b} \cdot \mathcal{B}(\Xi_b \to D^0 pK) &= (2.23 \pm 0.08_{\mathrm{stat}} \pm 0.05_{\mathrm{syst}} \pm 0.40_{\mathrm{ext}}) \times 10^{-6}\end{aligned}$$

Die dritte Messunsicherheit hat ihren Ursprung im Verzweigungsverhältnis des Normalisierungskanals. Die integrierten CP Asymmetrien von $\Lambda_b^0 \to D^0 pK$ und $\Xi_b \to D^0 pK$ werden sowohl für den kompletten Phasenraum als auch für die Region der pK Resonanzen mit einer quadrierten Zweikörpermasse von $m^2_{D^0 p} > 14\,\mathrm{GeV}^2/c^4$ bestimmt. Alle Asymmetrien sind konsistent mit Null. Weiterhin bestimmen wir die Massen Differnz:

$$m_{\Xi_b} - m_{\Lambda_b^0} = 172.5 \pm 0.38_{\mathrm{stat}} \pm 0.17_{\mathrm{syst}}\,\mathrm{MeV}/c^2$$

Eine Amplituden Analyse des $\Lambda_b^0 \to D^0 pK$ Phasenraumes mit $D^0 \to K^- \pi^+$ wird durchgeführt. Es wird ein großer Anteil einer $\Lambda_c^+(2950)$ Resonanz neben mehreren Λ^* Resonanzen gemessen. Zudem weist der Phasenraum Resonanzen mit hohem Spin, wie $\Lambda(2100)$ und $\Lambda(2350)$, auf.

Acknowledgement

The opportunity to explore such an interesting research domain and graduate in a familiar environment was only possible through **Priv.-Doz. Dr. Roland Waldi**. He always had a skilled advice at hand and enabled me to discuss various questions with physicists during my stays at CERN or at different conferences. Furthermore he left me the freedom for voluntary duties next to my work and kept accompanying whilst his well-earned free time after his retirement.

I also want to thank the **CERN** organisation, **LHCb** collaboration and **University of Rostock** for the trust in using their computing resources and making my research possible.

Further I will always bethink the refreshing coffee breaks with my former and most of the time only colleague **Nis Meinert**. The breaks extensive topics have lead to theories about a thesis on continuous paper. Not to mention, how this would have looked.

Next I want to thank my sports- and board-fellows from the rowing department of the **'HSG Uni Rostock'** for the mental balance, whether it has been during 'fat pulls' in the boat, debating about the future of the club or finishing off the day after training.

Then there have been people I could ask for distraction and help at any time. Special thanks should be given to **Jochen Zöllner** for always having an ear and running free our 'Sci-Fi' addiction, to **Armin Vinçon** for enhancing our photographing skills and mutually pining after unreachable gear, to **Kerstin Schiele** for supporting war wounded and **Franziska Strauer** for carrying in her positive smile.

I give the greatest and warmest thanks to my family. **Mum and Dad** I am more than grateful for the education you made possible, the support in any situation without questioning and for accepting whatever I have in my mind. Then there are two girls I cannot miss in my life. **Denise & Aurora** your love is my daily driver. Especially during the last part of this thesis you backed me up and listened to me whenever I thought to be stuck. Thank you for every smile and kiss that lightened things up.

Contents

Introduction

1

> *There's something that doesn't make sense.*
> *Let's go and poke it with a stick.*
>
> — **The Doctor**
> (from the British TV series 'Doctor Who')

One of, if not, the most important topic of cosmology is the formation of the universe we know. In contrast to the universe of matter, there is the Dirac equation, published by Pauli Dirac in 1928 [1]. The equation predicts the existence of an anti-particle next to every particle. As experiments have not been able to find sufficient amounts of anti-matter in the observable universe, yet, there are other approaches to this question.

A cosmological model, describing the expansion of the universe from an initial state of very high temperature and density, is the Big Bang theory. Within $1\,\mathrm{s}$ we find the evolution from presumably pure energy over a quark-gluon plasma to an admixture of photons, leptons and hadrons like protons and neutrons. From there we already do not find any anti-matter, but the creation of hydrogen and helium nuclei that then evolve over billion of years to the galaxies and gas nebula of our universe. At the point of recombination, the formation of hydrogen, electrons and protons start to be missing for the Thomson scattering of the photons. In consequence the universe became transparent and today we find the photons to shine through with a black body radiation of about $2.7\,\mathrm{K}$. We know this radiation as cosmic microwave background (CMB).

The most impressive number might be the ratio of baryons to the CMB photons of $\eta \approx 6 \cdot 10^{-10}$ [2]. This number hints for an explanation of the universe matter excess: Starting in a very early state of the universe we find the amount of quarks and anti-quarks at an equilibrium [3]. As the universe is expanding it cools down. At a critical temperature the quarks start to form hadrons of matter and anti-matter that then annihilate into photons. This left a fraction of matter in the order of η behind, which induces, that there must be asymmetries included. As matter is based on baryons and leptons, this process is called baryogenesis. Andrei Sakharov formulated in 1967 three conditions that have to be fulfilled for this baryogenesis to happen [4]. One of these is charge-parity (CP) violation, which is described later in section 2.2.

CP violation was first observed in 1964 as an irregularity in the kaon system [5]. Based on the quark mixing described by the Cabibbo matrix [6], Kobayashi and Maskawa introduced in 1973 the theory of CP violation into today's Standard Model (SM) [7]. The prediction of possible CP violation in beauty (b) meson decays [8] by Carter and Sanda in 1981 led to building B factories like SLAC [9] and KEK [10] and pinpoint testing of the CP violation in the Kobayashi-Maskawa model. Since then it became clear, that CP violation, as implemented in the SM, is far too suppressed [11] in order to explain baryogenesis. CP violation therefore could point to physics beyond the SM [12].

The measurement of CP violation such as SM parameters like the Cabibbo-Kobayashi-Maskawa (CKM) phase γ or the search for new physics has been dominated by experiments with b mesons for a long time. But since beauty baryons became accessible with the Large-Hadron-Collider beauty (LHCb) in 2011, they open up new opportunities. A candidate might be the decay $\Lambda_b^0 \to D^0 \Lambda$ [13, 14], which should allow the extraction of the CKM phase γ similar to the self tagging mesonic decay $B^0 \to D^0 K^{*0}$ [15]. There is no penguin pollution to expect and no need for a time dependent analysis. But the reconstruction efficiency of long living V^0 particles, like Λ, are low at LHCb [16]. A more suitable mode, which has already and only been seen at LHCb, is $\Lambda_b^0 \to D^0 pK$ [17]. It overcomes the Λ constrains, as its pK pair originates directly form the Λ_b^0 vertex. Another point for preferring a three-body decay, is the possibility to supersede the two-body with an amplitude analysis in sensitivity for the CKM phase γ, as it has been the case for $B^0 \to D^0 K\pi$ and $B^0 \to D^0 K^{*0}$ [18, 19]. With strangeness in the final states of $\Lambda_b^0 \to D^0 pK$ we can also expect the $\Xi_b \to D^0 pK$ mode with a similar magnitude [17, 20]. Both decays are further discussed in section 2.3 and we find the Ξ_b mode to promise sensitivity to γ as well.

Besides the prospect of measuring CP violation and studying the decays amplitudes in the Dalitz plot, there are further physical interests for these decays. The increased data set since their last analysis [17] should allow for higher sensitivity measurements of the branching fraction ratios of $\{\Lambda_b^0, \Xi_b\} \to D^0 pK$ to the more probable mode $\Lambda_b^0 \to D^0 p\pi$. The same is true for the mass difference between Λ_b^0 and Ξ_b. Apart from that the increase in statistics allows the study of the D^0 modes to $K^-\pi^+$, KK, $\pi\pi$ and $K^+\pi^-$.

Theory

2

2.1 The Standard Model

The Standard Model (SM) is the foundation of current particle physics, combining three basic forces by a renormalisable gauge field theory [21]: the electromagnetic, weak and strong force. The SM Lagrangian is gauge invariant for transformations of the $U(1) \times SU(2) \times SU(3)$ symmetry group. The SM results in predictions for elementary particles as well as their interactions represented by carrier particles of the forces. Both particle types are quantised excitations of fields.

2.1.1 Particles and Interactions

Elementary Particles: Fields of spin ${}^{1}\!/_{2}$ are called fermions and build up matter. Table 2.1 shows all elementary fermions. They are split up in leptons and quarks each with three generations of matter. Besides every lepton or quark having a different mass, they are characterised by specific flavour quantum numbers. Furthermore every fermion has an antiparticle behaving mostly like their counterpart. They have the same mass and spin, but inverse charges.

Tab. 2.1.: Elementary particles [20] of the SM: Leptons ℓ and quarks q are divided into their generations I - III as well as their electric charge Q and flavour quantum number F. Flavour quantum numbers being not mentioned for the respective particle are equal zero. As the masses for the lepton neutrinos ν_ℓ are defined to be zero in the SM, the shown ones are determined by the experiment.

	ℓ	Q (e)	m (MeV/c^2)	F	q	Q (e)	m (MeV/c^2)	F
I	e	-1	0.511	$\ell_e = 1$	u	$+{}^{2}\!/_{3}$	$2.55^{+0.75}_{-1.05}$	$I_3 = +{}^{1}\!/_{2}$
	ν_e	0	$< 2 \cdot 10^{-3}$	$\ell_e = 1$	d	$-{}^{1}\!/_{3}$	$5.04^{+0.96}_{-1.54}$	$I_3 = -{}^{1}\!/_{2}$
II	μ	-1	105.658	$\ell_\mu = 1$	c	$+{}^{2}\!/_{3}$	1270^{+70}_{-110}	$C = +1$
	ν_μ	0	$< 2 \cdot 10^{-3}$	$\ell_\mu = 1$	s	$-{}^{1}\!/_{3}$	104^{+26}_{-34}	$S = -1$
III	τ	-1	1776.84	$\ell_\tau = 1$	t	$+{}^{2}\!/_{3}$	$(171.2 \pm 2.1) \cdot 10^3$	$T = +1$
	ν_τ	0	$< 2 \cdot 10^{-3}$	$\ell_\tau = 1$	b	$-{}^{1}\!/_{3}$	4200^{+170}_{-70}	$B = -1$

Leptons carry an electric charge of $Q(e) = -1, 0$ and as quantum number a lepton number of $\ell = 1$. They are divided into electron e, muon μ, tauon τ and the respective uncharged neutrino ν_ℓ. Quarks on the other hand carry an electric charge of $Q(e) = -{}^{1}\!/_{3}, {}^{2}\!/_{3}$ and a colour charge. There are the three colours *red*, *green* and *blue* possible, as well as the respective anti-colours. The quarks are divided into up u and down quarks d with isospin $I_3 = {}^{1}\!/_{2}, -{}^{1}\!/_{2}$, charm quarks c with charm $C = 1$, strange quarks s with strangeness $S = -1$, top/truth quarks t with topness $T = 1$ and bottom/beauty quarks b with bottomness $B = -1$ as flavour quantum numbers. In addition to that every quark has got a baryon number $B' = {}^1\!/_3$.

Gauge Bosons: The quanta of bosonic fields with spin 1 are gauge bosons acting as carriers of the interaction forces. The electromagnetic force is carried by a photon. The latter couples to the electric charge and is massless, which leads to interactions over great distances. The electromagnetic matter-light interactions are described by Quantum Electrodynamics (QED). The weak force [21], which has superseded Fermi's interaction, gets mediated by massive carrier-particles, the $W^{\pm}$ and Z bosons, and couples to the weak charge. With the carriers having masses of

$$m_{W^{\pm}} = (80.40 \pm 0.025)\,\mathrm{GeV}/c^2, \qquad\qquad m_Z = (91.186 \pm 0.002)\,\mathrm{GeV}/c^2$$

their lifetime ($\tau < 10^{-24}\,\mathrm{s}$) is relatively short [20]. Additionally, due to its small coupling constant, the force has about the same magnitude as the electromagnetic force at a range of $r_0 \sim 10^{-18}\,\mathrm{m}$. This force decreases exponentially with a rising distance. Further it is the only one violating parity and charge-parity symmetries and is able to change the quark-flavour. Both the electromagnetic and weak force are unified in the electroweak Glashow-Weinberg-Salam model [22–24].

The strong force is mediated by eight massless gluons coupling to the colour charges *red*, *green*, *blue* and in case of an anti-particle to the respective anti-colour. The theory describing strong interactions is Quantum Chromodynamics (QCD). Only particles carrying colour, quarks and gluons, interact via the strong force, leptons not.

Hadrons: In comparison to leptons, colour charged particles (quarks) can not be observed in an unbound state. The colour field between quarks, that divert from each other, extends by gluon-gluon coupling and increases with distance. This results in more energy in the filed and thus, it would be more energy favourable for a $q\bar{q}$ pair (quark anti-quark pair) to form another pair at some point. These quark combinations are in a colour neutral state, called hadron. In the limit of extremely high energies and baryon density this colour confinement vanishes. The structure of hadrons consists of valence quarks and virtual $q\bar{q}$-pairs and gluons. The valence quarks define the hadron properties, like charge. There are two main types of hadrons: mesons with a $q\bar{q}$-pair as valence quarks, thus having $B' = 0$, and baryons with three quarks or anti-quarks as valence quarks, leading to $B' = \pm 1$.

However, the existence of so called exotic hadrons is being considered. There can be four-quark states $qq\overline{qq}$ (tetraquarks), five-quark states $qqqq\bar{q}$ (pentaquarks), pure gluon states (glue-balls) and mixed states of quarks and gluons.

The masses of the particles result from a Higgs-field spontaneously breaking the electroweak symmetry group $U(1) \times SU(2)$, leading to a massive Higgs boson with spin 0 [25].

2.1.2 The Standard Model Lagrangian

To describe any kind of processes, the SM uses equations of motion deduced from Lagrange-densities. Therefore, Lagrangians for the three field spin types have to be considered. First of all for a scalar (spin 0) field Φ

$$\mathcal{L}_{s=0} = \frac{1}{2} g^{\mu\nu} \partial_\mu \Phi \partial_\nu \Phi - \frac{1}{2} m^2 \Phi^2 \quad , \tag{2.1}$$

then for a spinor (spin $^1/_2$) field Ψ

$$\mathcal{L}_{s=1/2} = i\overline{\Psi}\gamma^\mu \partial_\mu \Psi - m\overline{\Psi}\Psi \tag{2.2}$$

and for a massless vector (spin 1) field

$$\mathcal{L}_{s=1} = -\frac{1}{4} F_{\mu\nu} F^{\mu\nu} \quad , \tag{2.3}$$

with the field-strength tensor $F_{\mu\nu}$ [26]. As mentioned before these Lagrangians have to be gauge invariant. We focus on Quantum Electrodynamics. In case of a free Dirac particle, one finds the Lagrangian of (2.2). However, as its derivative part is not invariant under the local gauge transformation $\Psi \rightarrow \exp[iq\Lambda(x)]\Psi(x)$, it has to be substituted by a gauge-covariant derivative and is found to be

$$\mathcal{L} = i\overline{\Psi}\gamma^\mu \partial_\mu \Psi - m\overline{\Psi}\Psi - j^\mu \mathbf{A}_\mu \quad , \tag{2.4}$$

where the additional term $-j^\mu \mathbf{A}_\mu$ represents the interaction between the Dirac particle and the electromagnetic field that is quantised into photons. $\mathbf{A}_\mu$ is the four-vector electromagnetic potential and $j^\mu = q\overline{\Psi}\gamma^\mu\Psi$ the conserved electromagnetic current. The QED Lagrangian is then given by adding a kinetic energy term $-\frac{1}{4}F_{\mu\nu}F^{\mu\nu}$, describing the propagation of free photons:

$$\mathcal{L}_{\text{QED}} = i\overline{\Psi}\gamma^\mu \partial_\mu \Psi - m\overline{\Psi}\Psi - j^\mu \mathbf{A}_\mu - \frac{1}{4} F_{\mu\nu} F^{\mu\nu} \quad . \tag{2.5}$$

The Lagrangian for the electroweak interactions evolves from splitting into a left-handed fermion doublet and a right-handed singlet. After taking gauge invariance into account and neglecting the fermion mass and the symmetry breaking by the Higgs field it reads [26, 27]

$$\begin{aligned}\mathcal{L}_{\text{e-weak}} = & -\frac{1}{4}\mathbf{W}_{\mu\nu}\mathbf{W}^{\mu\nu} - \frac{1}{4}B_{\mu\nu}B^{\mu\nu} \\ & + \overline{\Psi}_R \gamma^\mu \left[i\partial_\mu - \frac{1}{2} g' Y B_\mu \right] \Psi_R \\ & + \overline{\Psi}_L \gamma^\mu \left[i\partial_\mu - \frac{1}{2} g' Y B_\mu - g \mathbf{I} \mathbf{W}_\mu \right] \Psi_L \quad .\end{aligned} \tag{2.6}$$

The first part of the electroweak Lagrangian (2.6) describes the kinetic energies and self-interactions of the bosons. Followed by parts that describe the interactions to a right- and left-handed fermion-field. Right-handed fermions interact only with the Boson in the $U(1)$ symmetry group. Thus, we only find the scalar gauge field singlet B_μ paired with the generator of $U(1)$, the weak hypercharge Y, and the coupling g'. The Lagrangian part for left-handed fermions does have an additional term for $SU(2)$ group boson interactions. We find the isospin operator **I** containing the Pauli matrices paired with the massless gauge field triplet $\mathbf{W}_\mu$ of the $SU(2)$ and the coupling g. The Pauli matrices are the generators of the $SU(2)$ and have the weak isospin as their eigenvalues. The four electroweak bosons result from the linear combinations

$$\begin{pmatrix} |\gamma\rangle \\ |Z\rangle \end{pmatrix} = \begin{pmatrix} \cos\theta_W & \sin\theta_W \\ -\sin\theta_W & \cos\theta_W \end{pmatrix} \begin{pmatrix} |B_3\rangle \\ |W_3\rangle \end{pmatrix} \tag{2.7}$$

$$|W^\pm\rangle = \frac{1}{2}(|W_1\rangle \pm i|W_2\rangle) \quad , \tag{2.8}$$

where θ_W is the Weinberg angle that leads to γ and Z by rotating the W_3 and B_3 vector boson plane.

Electroweak Currents

The exchange of the gauge bosons Z and $W^\pm$ between two fermions mediates a current. In case of the Z boson, which couples to all fermions and does not carry electric charge, we speak of Neutral Current (NC). NC is flavour conserving and illustrated by the Feynman diagrams of lepton production in e^+e^- scattering in fig. 2.1.

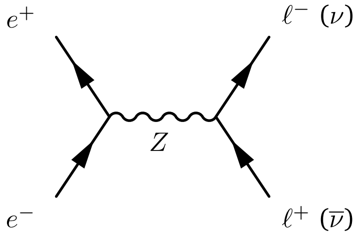

Fig. 2.1.: Neutral current of the Z shown for the charged (neutral) lepton pair production in e^+e^- scattering.

The other two bosons $W^\pm$ carry an electric charge and thus mediate a charged current (CC). CC change the particles flavour and since the W bosons couple to the left handed components of the fermion fields, the charged current violates parity. Examples for charge-raising current, where the W^- takes a charge of $-1e$ away, are given in fig. 2.2. The types of the Feynman diagrams are called tree-graphs.

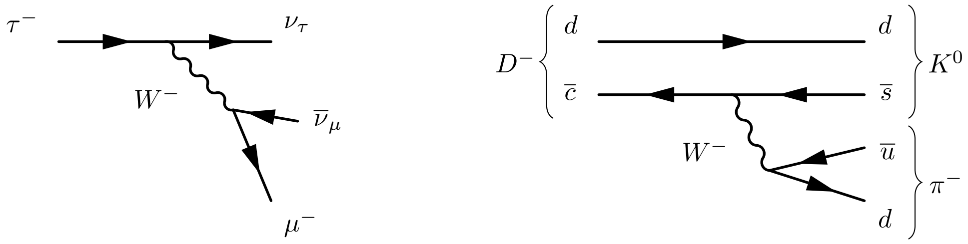

Fig. 2.2.: Charge-raising current of the W^- shown for the example of a lepton decay (left) and a quark transformation from s to s (right). An example for charge-lowering current would be the charge conjugated decays with a W^+.

Changing the flavour of a quark without altering its charge is called Flavour-Changing-Neutral-Current (FCNC). However, this is not allowed via the neutral Z boson, the photon, or any gluons. But there are processes involving loops, like box- and penguin-graphs, that achieve a ‘charge-even’ flavour transition via an intermediate quark state of altered charge. Fig. 2.3 shows such a process for the $B_s^0 \to \mu^+\mu^-$ decay.

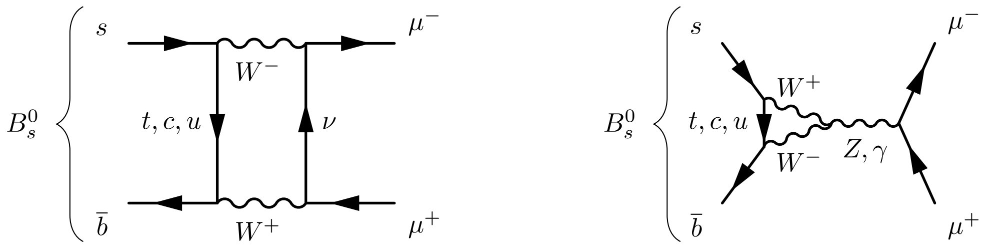

Fig. 2.3.: The Feynman diagrams show the FCNC'like s to $\bar{b}$ transition, using the example of the $B_s^0 \rightarrow \mu^+\mu^-$ decay via a box-graph (left) and a penguin-graph (right).

2.2 *CP* Violation

2.2.1 Symmetries and Violation

Leading to conserved quantities, as it is described by the Noether theorem [28], symmetries play an important role in particle physics. In the SM we find three discrete transformations. There are two space-time operations, parity (P) and time reversal (T). The parity operation basically mirrors the spatial coordinates of any positional vector. In case of the four-vector of a particle we would find $P(t, \mathbf{x}) = (t, -\mathbf{x})$, where its spatial vector gets flipped, but the angular momentum remains the same. Time reversal obviously flips the sign of the time component of a four-vector $\mathrm{T}(t, \mathbf{x}) = (-t, \mathbf{x})$. However in this case the momentum $\mathbf{p} = m\frac{\mathrm{d}\mathbf{x}}{\mathrm{d}t}$ changes as well. The third operation is the charge conjugation (C). This operator inverts all charges of the particle and converts a particle to its anti-particle or back.

In case of an invariance we speak of symmetry conservation, else breaking. Even though we might find P or T broken there is a 'higher order' operation that is invariant. For example in case of the weak $\tau^- \rightarrow \nu_\tau \pi^-$ decay we find C and P broken [29], but the combination CP conserved. The most fundamental symmetries known are the Lorentz[1] and the charge-parity-time reversal (CPT) invariance [30]. The latter states that any symmetry of the three operations or their combinations might be broken, but CPT is always conserved.

The observed symmetry breaking in the SM also has got a direct relation to the interaction force of the system we consider. Whereas we find all symmetries preserved in the strong interaction the weak interaction is broken for various quantum numbers, like the isospin, flavour (strangeness, etc.), parity and CP.

2.2.2 CKM Matrix

As already briefly mentioned in section 2.1.1 the Glashow-Weinberg-Salam model for electroweak interactions [22–24] introduces spontaneous symmetry breaking for the unified gauge-group $U(1) \times SU(2)$ to explain fermion masses and other effects [25, 31]. We find the fermion fields for the i^{th} quark family to be left-handed $SU(2)$ doublets of the form $\Psi_i = \binom{u_i}{d'_i}$ [20]. The quark mixing $d'_i = \sum_j V_{ij} d_j$ is generated by the matrix elements V_{ij} of

---

[1] continuous space-time symmetry

the CKM matrix [6, 7]. The unitary CKM matrix defines the weak eigenstates of the d-type quarks, that couple to the u-type quarks and reads

$$\begin{pmatrix} |d'\rangle \\ |s'\rangle \\ |b'\rangle \end{pmatrix} = \begin{pmatrix} V_{ud} & V_{us} & V_{ub} \\ V_{cd} & V_{cs} & V_{cb} \\ V_{td} & V_{ts} & V_{tb} \end{pmatrix} \begin{pmatrix} |d\rangle \\ |s\rangle \\ |b\rangle \end{pmatrix} \quad . \tag{2.9}$$

The matrix is described by four real parameters, with one being a phase and the rest rotation angles. There are several ways to parameterise the CKM matrix. The most common is the Wolfenstein parametrisation [32]

$$V_{\text{CKM}} = \begin{pmatrix} 1-\lambda^2/2 & \lambda & A\lambda^3(\rho - i\eta) \\ -\lambda & 1-\lambda^2/2 & A\lambda^2 \\ A\lambda^3(1-\rho-i\eta) & -A\lambda^2 & 1 \end{pmatrix} + \mathcal{O}(\lambda^4) \quad , \tag{2.10}$$

which is an approximation of the standard parametrisation [20, 33] and expresses the matrix elements in powers of $\lambda \approx |V_{us}|$. The approximation in (2.10) is up to order λ^3. Examples for higher orders can be found in [34]. A global fit to all measurements yields the unknown real parameters A, λ, ρ and η.

The probability for a quark changing its flavour to another one is given by $|V_{ij}|^2$. With charged current it is most likely for a quark to change flavour inside its generation. These are found on the diagonal where the matrix is close to unity. An example in-generation transition is shown in fig. 2.2 on the right for a c to s quark transition. However, it is also possible, but less probable, for the c quark to transform to a d or a b quark. The corresponding off-diagonal matrix elements show suppression by at least a factor of λ.

Unitarity Triangle: From the unitarity of the CKM matrix $V_{\text{CKM}}V_{\text{CKM}}^\dagger = I$, where I is the identity matrix, follows $\sum_i V_{ij}V_{ik}^* = \delta_{jk}$ [20]. This results into six triangles in the complex plane. With all elements being involved in B processes the most common unitarity triangle is represented by

$$V_{ud}V_{ub}^* + V_{cd}V_{cb}^* + V_{td}V_{tb}^* = 0 \quad . \tag{2.11}$$

The triangles are rescaled, so that the base is of unit length. Therefore (2.11) is divided by $V_{cd}V_{cb}^*$ resulting in three well defined vertices for the triangle, $(0,0)$, $(1,0)$ and $(\overline{\rho},\overline{\eta})$, where $\overline{\rho} = \rho(1-\lambda^2/2+...)$ and $\overline{\eta} = \eta(1-\lambda^2/2+...)$. A sketch of the unitarity triangle is in figure 2.4. The three angles α, β and γ, that are found in the unitarity triangle are defined as

$$\alpha = \arg\left(-\frac{V_{td}V_{tb}^*}{V_{ud}V_{ub}^*}\right), \quad \beta = \arg\left(-\frac{V_{cd}V_{cb}^*}{V_{td}V_{tb}^*}\right), \quad \gamma = \arg\left(-\frac{V_{ud}V_{ub}^*}{V_{cd}V_{cb}^*}\right) \quad . \tag{2.12}$$

Different measurements in the $\overline{\rho},\overline{\eta}$ plane enable us to over-constrain the triangle. Thus a global fit [35, 36] of the triangle, by combining all measurements as constraints is possible. The most current global fit to date can be seen in figure 2.5.

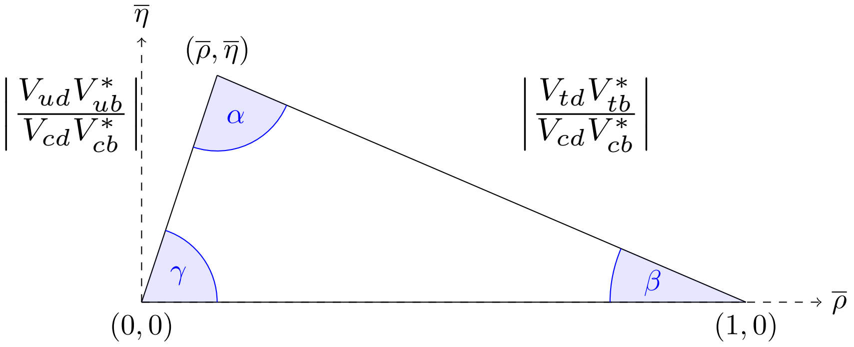

Fig. 2.4.: Sketch of the unitarity triangle of the CKM matrix elements of equation 2.11.

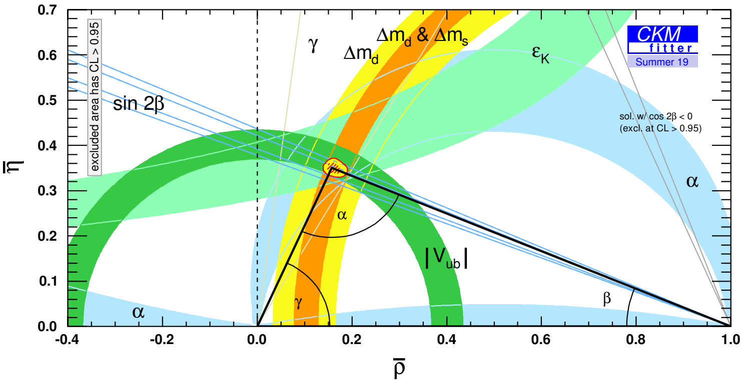

Fig. 2.5.: Recent result of the global fit in the $\overline{\rho}, \overline{\eta}$ plane by the CKMfitter group [35].

2.2.3 CP Violation and γ from $B^{\pm}$ Meson Decays

We distinguish between different kinds of CP violation that can be found in a decay. Direct CP violation occurs in the decay itself. In other words, the amplitude of the decay A differs from the one of the charge conjugated decay $\overline{A}$. Then there is mixing, where we have to have a neutral particle that can oscillate to its anti-particle state and back. And finally there is the mixing-induced CP violation, where the oscillating flavour eigenstates decay to the same final states.

Due to the context of this analysis we take a closer look at direct CP violation for a decaying B^- meson. We assume two contributing amplitudes of the form $|A_{1,2}| \exp i(\delta_{1,2} + \Phi_{1,2})$, with different strong phases δ and different CKM phases Φ. Now we can write down the decay amplitude of the B^+ meson to its final states f

$$A(B^+ \to f) = |A_1|e^{i(\delta_1+\Phi_1)} + |A_2|e^{i(\delta_2+\Phi_2)} \tag{2.13}$$

and apply the CP operation

$$\overline{A}(B^- \to \overline{f}) = |A_1|e^{i(\delta_1-\Phi_1)} + |A_2|e^{i(\delta_2-\Phi_2)} \quad , \tag{2.14}$$

while remembering that the strong phase δ is *CP* even and does not change. Comparing both amplitudes by calculating their difference

$$|A|^2 - |\overline{A}|^2 = -4|A_1||A_2|\sin(\delta_1 - \delta_2)\sin(\Phi_1 - \Phi_2) \quad , \tag{2.15}$$

it is easy to see, that measuring direct *CP* violation requires interfering decay amplitudes of different phases. From equation 2.12 we know that the angle γ does not depend on a t quark and thus can be measured in tree-level B decays like $B^\pm \to \{D^0, \overline{D}^0\}K^\pm$ [20, 37]. Figure 2.6 shows the Feynman diagrams for $B^- \to \{D^0, \overline{D}^0\}K^-$, where we easily spot the contributing CKM matrix elements per flavour changing vertex. There are two well established methods to extract γ from $B^\pm$ decays. On the one hand there is the Gronau-London-Wyler (GLW) method [38] and on the other hand there is the Atwood-Dunietz-Soni (ADS) method [39]. Both methods can be combined for a more sensitive extraction of γ. In the following a brief introduction in the strategy of both methods is given[2].

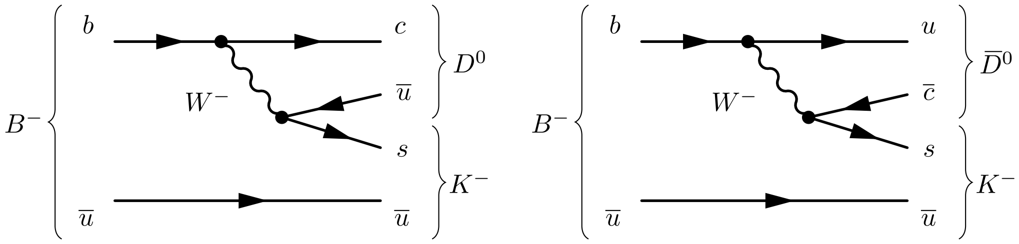

(a) $B^- \to D^0 K^-$ (b) $B^- \to \overline{D}^0 K^-$

Fig. 2.6.: Feynman diagrams of the decays $B^- \to \{D^0, \overline{D}^0\}K^-$.

GLW: The original GLW paper considers the decay $B^\pm \to D_{CP}K^\pm$, with $D_{CP,\text{even(odd)}} = [D^0 + (-)\overline{D}^0]/\sqrt{2}$, a *CP* eigenstate. We stick to $D_{CP} = D_{CP,\text{even}}$ for brevity. Starting from the amplitudes of equations 2.14 and 2.15 and we can rewrite them using the relative phase $\gamma = \Phi_2 - \Phi_1$ as

$$\begin{aligned}\sqrt{2}\cdot A(B^+ \to D_{CP}K^+) &= A(B^+ \to D^0K^+) + A(B^+ \to \overline{D}^0K^+)\\ &= |A|\cdot e^{i\gamma}e^{i\delta_1} + |\overline{A}|\cdot e^{i\delta_2}\end{aligned}$$

$$\begin{aligned}\sqrt{2}\cdot A(B^- \to D_{CP}K^-) &= A(B^- \to \overline{D}^0K^-) + A(B^- \to D^0K^-)\\ &= |A|\cdot e^{-i\gamma}e^{i\delta_1} + |\overline{A}|\cdot e^{i\delta_2} \quad .\end{aligned} \tag{2.16}$$

It is crucial to note here, that the different amplitudes need to be separable. The B flavour is easily tagged by the charge of the kaon. The D_{CP} eigenstate is given by the specific final states of its decay, that are KK or $\pi\pi$ in the *CP* even case[3]. Further the flavour of the D^0

---

[2] A more detailed explanation can be found in the papers of GLW [38] and ADS [39]

[3] $D_{CP,\text{odd}} \to K^0_S\{\pi^0, \rho^0, ...\}$

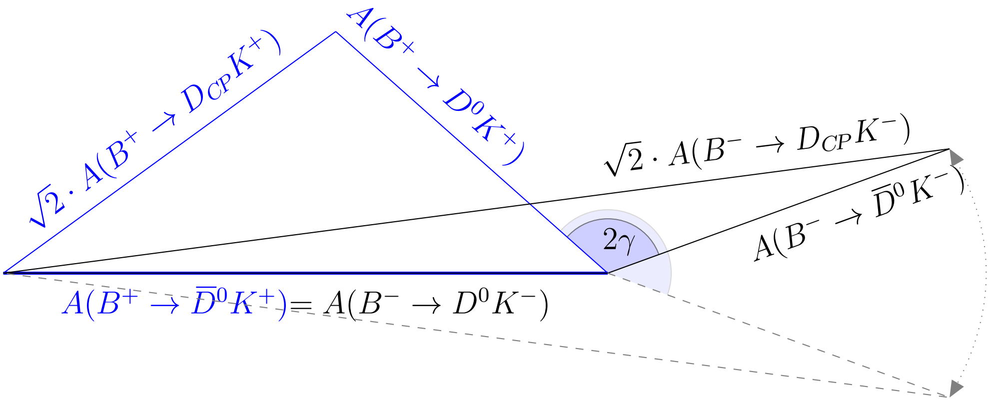

Fig. 2.7.: GLW Triangles of equations 2.17 and 2.16 in the complex plane. The dashed mirrored triangle shows a second solution for the angle γ.

could be found via a semileptonic decay of *e.g.* $D^0 \to K^-\mu^+\nu_\mu$. The amplitudes found in equation 2.16 can be expressed as triangles, see figure 2.7, where

$$\begin{aligned} A(B^+ \to \overline{D}^0K^+) &= A(B^- \to D^0K^-) \\ A(B^+ \to D^0K^+) &= A(B^- \to \overline{D}^0K^-)\cdot e^{2i\gamma} \\ |A(B^+ \to D_{CP}K^+)| &\neq |A(B^- \to D_{CP}K^-)| \quad . \end{aligned} \tag{2.17}$$

The relations in (2.17) assume that the amplitudes of the $B^\pm$ decay to the D^0 flavour states is CP conserving and violated by decaying over the CP eigenstates. The angle γ is then extractable by pure geometric relations. However, there are still four solutions for γ. Two solutions are introduced due to the unknown sign of γ and another two by the strong phase difference that is visualised in figure 2.7 by mirroring onto the dashed triangle. These ambiguities are eliminated by performing multiple measurements in different decay channels.

ADS: The GLW method does have some drawbacks. For example the decay amplitudes $B^- \to \{D^0, \overline{D}^0\}K^-$ come with different magnitudes and the interference is found in the decay of the D_{CP}, thus CP violating asymmetry effects are expected to be small. The ADS paper [39] promises to overcome the GLW drawbacks. They do not account for the decay via CP eigenstates of the D^0, but use $D^0 \to K^-\pi^+$ a Cabibbo-favoured decay and $D^0 \to K^+\pi^-$ a doubly-suppressed decay[4]. As a result the overall $B^\pm$ decay amplitudes level and can interfere. One possible approach, the paper mentions, would be to perform a GLW-like analysis with non-CP eigenstates, assuming the knowledge of the $\mathcal{B}(B^- \to \{D^0, \overline{D}^0\}K^-)$ branching fractions leading to an equation system solvable for γ.

---

[4] More to Cabibbo suppression in D^0 in appendix A.5.

2.3 Decay Phenomenology

In this section we picture the decay $\Lambda_b^0 \to D^0 pK$ within the SM. When speaking of $\Lambda_b^0 \to D^0 pK$ we also mean $\Lambda_b^0 \to \overline{D}^0 pK$ and their charge conjugates, unless stated otherwise or separated by the context.

We start with the classification of the involved particles. Properties, like their mass m, lifetime τ, quark content and quantum numbers I, J and P are summarised in table 2.2. The decay mother Λ_b^0 is the lightest baryon with one b-quark. The table list as well the slightly heavier Ξ_b, as it can decay to $D^0 pK$ as well and is expected to show up in the $m(D^0 pK)$ mass distribution. The listed quantum numbers in table 2.2 for Λ_b^0 and Ξ_b are only SM predictions. Considering *CP* violation only little is known for Λ_b^0 and almost nothing for Ξ_b. Onward to the final states, the proton is the most well known and stable particle. As a baryon it contributes to the baryon-number conservation. Finally there are three mesons the D^0, K^- and π^-. As the D^0 is considered to decay to combinations of kaons and pions, the table also lists the π^-. All three are the lightest mesons of their kind. The D^0 is the lightest meson with a charm quark, the K^- with a strange quark and the π^- without any flavour. The pion and kaon have been greatly explored since their discovery in cosmic rays in 1947. We find both to have a long lifetime compared to the other particles.

Tab. 2.2.: Properties of the involved particles. [20]

	quark content	m (MeV/c^2)	lifetime τ	$I(J^P)$
Λ_b^0	$\lvert udb\rangle$	5619.60 ± 0.17	$(1.464 \pm 0.011) \times 10^{-12}\,\mathrm{s}$	$0(^1/_2{}^+)$
Ξ_b	$\lvert usb\rangle$	5791.9 ± 0.5	$(1.480 \pm 0.030) \times 10^{-12}\,\mathrm{s}$	$^1/_2(^1/_2{}^+)$
p	$\lvert uud\rangle$	$938.2720813(58)$	$> 2.1 \times 10^{29}\,\mathrm{yr}$	$^1/_2(^1/_2{}^+)$
D^0	$\lvert c\overline{u}\rangle$	1864.83 ± 0.05	$(4.101 \pm 0.015) \times 10^{-13}\,\mathrm{s}$	$^1/_2(0^-)$
K^-	$\lvert s\overline{u}\rangle$	493.677 ± 0.016	$(1.2380 \pm 0.0020) \times 10^{-8}\,\mathrm{s}$	$^1/_2(0^-)$
π^-	$\lvert s\overline{u}\rangle$	139.57061 ± 0.00024	$(2.6033 \pm 0.0005) \times 10^{-8}\,\mathrm{s}$	$1(0^-)$

2.3.1 Feynman Diagrams

There are only few possible Feynman diagrams at lowest order showing how Λ_b^0 and Ξ_b can decay to $D^0 pK$ at quark level. Every higher order adds vertices to the Feynman diagram and is thus much less likely. For $\Lambda_b^0 \to D^0 pK$ we find a tree-level and W-exchange graph with $V_{cb}V_{us}^*$ contribution and for $\Lambda_b^0 \to \overline{D}^0 pK$ a tree-level graph with $V_{ub}V_{cs}^*$ contribution, as they are drawn in figure 2.8.

There is a similar structure for the possible lowest-order Feynman diagrams of the Ξ_b decays, see figure 2.8. For $\Xi_b \to D^0 pK$ we find again a tree-level and W-exchange graph, however this time with $V_{cb}V_{ud}^*$ contribution. And also $\Xi_b \to \overline{D}^0 pK$ is only possible at tree-level, with $V_{ub}V_{cd}^*$ contribution.

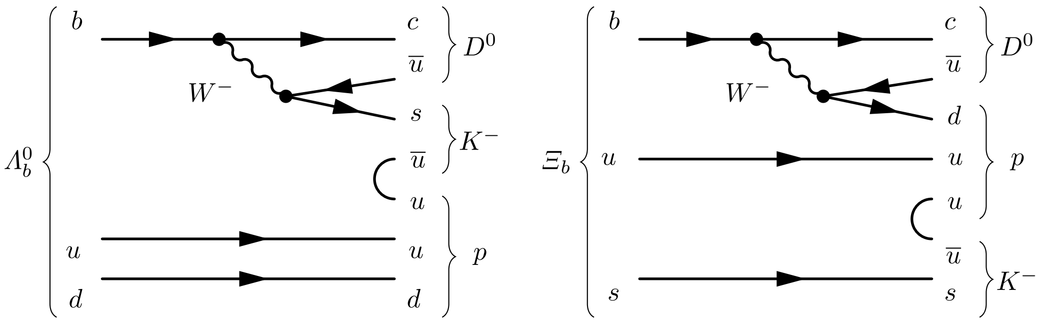

(a) $\Lambda_b^0 \rightarrow D^0 pK$, tree (b) $\Xi_b \rightarrow D^0 pK$, tree

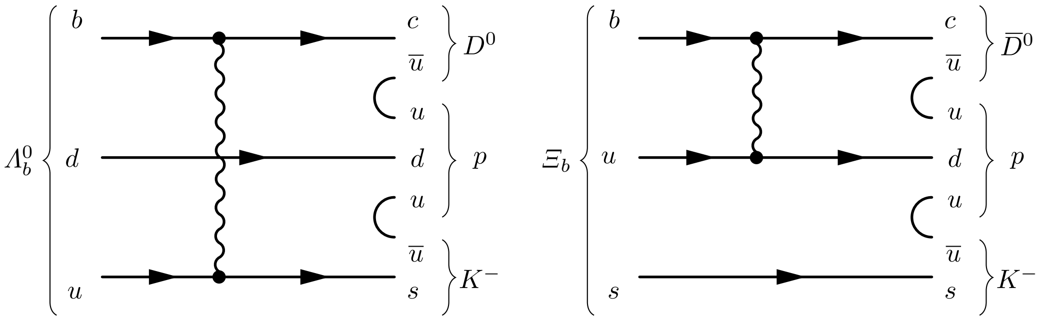

(c) $\Lambda_b^0 \rightarrow D^0 pK$, W exchange (d) $\Xi_b \rightarrow D^0 pK$, W exchange

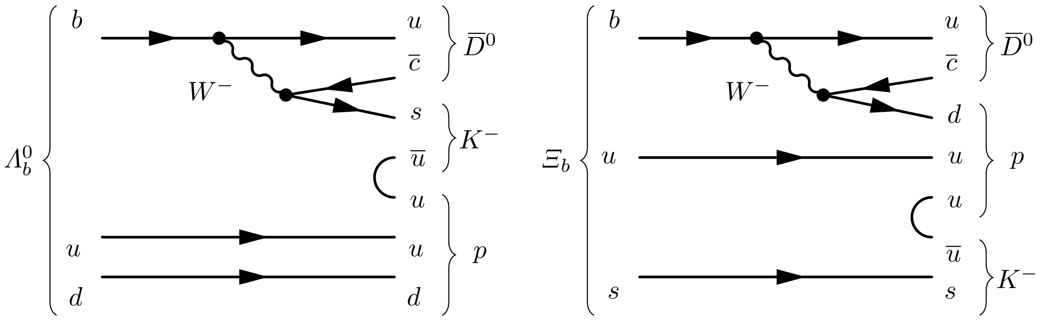

(e) $\Lambda_b^0 \rightarrow \overline{D}^0 pK$, tree (f) $\Xi_b \rightarrow \overline{D}^0 pK$, tree

Fig. 2.8.: Feynman diagrams of lowest order for the decays $\{\Lambda_b^0, \Xi_b\} \rightarrow \{D^0, \overline{D}^0\}pK^-$.

2.3.2 *CP* Observables

When comparing the tree-level Feynman diagrams for Λ_b^0 to the ones of B^- in section 2.2.3 we see, that they in principle just add a d as spectator and a $u\overline{u}$ pair from the vacuum. With the same matrix elements they should then have similar sensitivity to γ. Even the enhanced *CP* violation asymmetry due to the amplitude levelling effect of the ADS method (see section 2.2.3) can be expected. In case of the Ξ_b we can expect *CP* violation, but the amplitudes won't be of similar magnitude and asymmetry effects will be small for ADS and

GLW. We are most sensitive to γ in the context of the GLW (ADS) method, when the ratio r_b (r_{ADS}) equals 1. The ratios are calculated as

$$r_b(\mathit{\Lambda}_b^0) = \left|\frac{A(\mathit{\Lambda}_b^0 \to D^0 pK)}{A(\mathit{\Lambda}_b^0 \to \overline{D}{}^0 pK)}\right|^2 \approx \left|\frac{V_{cb}V_{us}^*}{V_{ub}V_{cs}^*}\right|^2 , \quad r_{\text{ADS}} = r_b r_D = r_b \cdot \frac{\mathcal{B}(D^0 \to K^+\pi^-)}{\mathcal{B}(\overline{D}{}^0 \to K^+\pi^-)} \quad . \tag{2.18}$$

Table 2.3 lists the CKM matrix element contributions to the amplitudes and an approximation for the ratios. We find the GLW method to be most promising for the $\mathit{\Lambda}_b^0$ decay and the ADS method for the $\mathit{\Xi}_b$ decay.

Tab. 2.3.: The sensitivity to γ for the different $\mathit{\Lambda}_b^0$ and $\mathit{\Xi}_b$ amplitudes according to the ratios in (2.18) is listed. The current measurements of the CKM matrix elements and D^0 ratios [20] are used. The CKM contributions and $\mathcal{B}$ ratios for the D^0 decay can be found in appendix A.5.

		CKM contribution $[10^{-6}]$	$r_b[\sim]$	$r_{\text{ADS}}[\sim]$
$\mathit{\Lambda}_b^0$	D^0	$\lvert V_{cb}V_{us}^*\rvert^2 = \lvert 9.46 \pm 0.17\rvert^2$	7.1	2.7×10^{-2}
	$\overline{D}{}^0$	$\lvert V_{ub}V_{cs}^*\rvert^2 = \lvert 3.93 \pm 0.12\rvert^2$		
$\mathit{\Xi}_b$	D^0	$\lvert V_{cb}V_{ud}^*\rvert^2 = \lvert 41.1 \pm 0.7\rvert^2$	2.5×10^3	9.5
	$\overline{D}{}^0$	$\lvert V_{ub}V_{cd}^*\rvert^2 = \lvert 0.819 \pm 0.027\rvert^2$		

With D denoting an admixture of D^0 and $\overline{D}{}^0$ we can define following CP observables [40]. As by the GLW method there is an asymmetry and charge-averaged rate

$$\begin{aligned}
\mathcal{A}_{CP} &= \frac{\Gamma(\mathit{\Lambda}_b^0 \to D_{CP}pK^-) - \Gamma(\overline{\mathit{\Lambda}}{}_b^0 \to D_{CP}pK^+)}{\Gamma(\mathit{\Lambda}_b^0 \to D_{CP}pK^-) + \Gamma(\overline{\mathit{\Lambda}}{}_b^0 \to D_{CP}pK^+)} \\
&\approx \frac{2r_b\kappa \sin\Delta\delta_b \sin\gamma}{\mathcal{R}_{CP}} && (2.19) \\
\mathcal{R}_{CP} &= 2\frac{\Gamma(\mathit{\Lambda}_b^0 \to D_{CP}pK^-) + \Gamma(\overline{\mathit{\Lambda}}{}_b^0 \to D_{CP}pK^+)}{\Gamma(\mathit{\Lambda}_b^0 \to D^0 pK^-) + \Gamma(\overline{\mathit{\Lambda}}{}_b^0 \to \overline{D}{}^0 pK^+)} \\
&\approx 1 + r_b^2 \pm 2r_b\kappa \cos\Delta\delta_b \cos\gamma \quad , && (2.20)
\end{aligned}$$

with the coherence factor κ. Further there is a partial-rate asymmetry and charge-averaged rate as by the ADS method

$$\begin{aligned}
\mathcal{A}_{\text{ADS}} &= \frac{\Gamma(\mathit{\Lambda}_b^0 \to [K^-\pi^+]_D pK^-) - \Gamma(\overline{\mathit{\Lambda}}{}_b^0 \to [K^+\pi^-]_D pK^+)}{\Gamma(\mathit{\Lambda}_b^0 \to [K^-\pi^+]_D pK^-) + \Gamma(\overline{\mathit{\Lambda}}{}_b^0 \to [K^+\pi^-]_D pK^+)} \\
&\approx \frac{2r_b r_D\kappa \sin(\Delta\delta_b + \Delta\delta_D) \sin\gamma}{\mathcal{R}_{\text{ADS}}} && (2.21) \\
\mathcal{R}_{\text{ADS}} &= \frac{\Gamma(\mathit{\Lambda}_b^0 \to [K^-\pi^+]_D pK^-) + \Gamma(\overline{\mathit{\Lambda}}{}_b^0 \to [K^+\pi^-]_D pK^+)}{\Gamma(\mathit{\Lambda}_b^0 \to [K^+\pi^-]_D pK^-) + \Gamma(\overline{\mathit{\Lambda}}{}_b^0 \to [K^-\pi^+]_D pK^+)} \\
&\approx r_b^2 + r_D^2 + 2r_b r_D\kappa \cos(\Delta\delta_b + \Delta\delta_D) \cos\gamma \quad . && (2.22)
\end{aligned}$$

We aim for calculating the asymmetries for $\mathit{\Lambda}_b^0$ and $\mathit{\Xi}_b$.

2.4 Dalitz Plot

With $\Lambda_b^0 \to D^0 pK$ being a three-body decay, it is crucial to study its dynamic behaviour. The mother Λ_b^0 can decay in multiple ways to its final states. Next to directly decaying into $D^0 pK$, there is the possibility of sequential two body decays via an intermediate resonance. In case of a resonance there might be only decays to a specific D^0 or $\overline{D}^0$ final state possible. In this case *CP* violation observation is impossible. Obviously this behaviour has to be understood, as the *CP* violation asymmetries in (2.19) and (2.21) heavily depend on these dynamics. A Dalitz plot, that allows to study the dynamics of a three-body decay, was first introduced by R.H. Dalitz [41]. Given two invariant two body masses squared m_{ij}^2 $(i \neq j)$ of the three final state particles, the partial decay width of $\Lambda_b^0 \to D^0 pK$ is expressed by [20]

$$\Gamma = \frac{1}{(2\pi)^3 32 \sqrt{m_{\Lambda_b^0}^3}} |\mathcal{M}|^2 dm_{D^0p}^2 dm_{pK}^2 \quad , \tag{2.23}$$

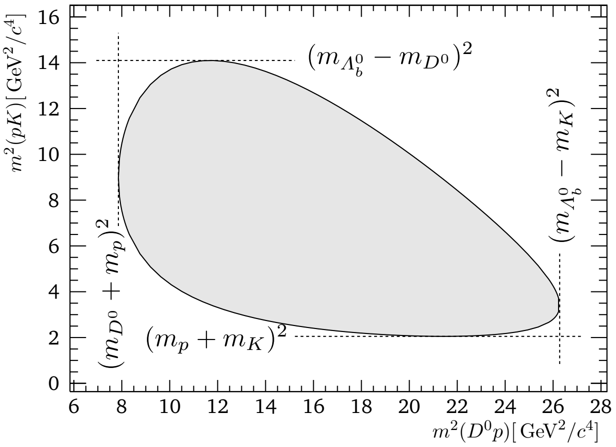

Fig. 2.9.: The contour of the kinematically allowed region for the $\Lambda_b^0 \to D^0 pK$ decay in the Dalitz plane is shown with the upper and lower mass limits for $m_{D^0p}^2$ and m_{pK}^2.

with the matrix element $|\mathcal{M}|^2$ containing the decay dynamics. A constant $|\mathcal{M}|^2$ would yield a uniform distribution and no dynamics across the Dalitz plot. Building the scatter plot of $m_{D^0p}^2$ and m_{pK}^2 is the Dalitz plot. Resonant states show up as bands of higher population with a varying distribution along the band due to the angular momentum of the resonance decay. A Dalitz plot based on massless particles causes a triangular shape of the plot. However as we use massive particles its shape is altered, as it can be seen in figure 2.9. Its kinematic boundary is found by four-momentum conservation. There are two separate contours for the maximum and minimum allowed values of m_{pK}^2 dependent on $m_{D^0p}^2$ [20]

$$\left(m_{pK}^2\right)^{\max}_{\min} = \left(E_p^* + E_K^*\right)^2 - \left(\sqrt{E_p^{*2} - m_p^2} \mp \sqrt{E_K^{*2} - m_K^2}\right)^2 \tag{2.24}$$

$$E_p^* = \frac{m_{D^0p}^2 - m_{D^0}^2 + m_p^2}{2m_{D^0p}}, \qquad E_K^* = \frac{m_{\Lambda_b^0}^2 - m_{D^0p}^2 - m_K^2}{2m_{D^0p}} \quad , \tag{2.25}$$

with E^* being the energy of the respective particle in the m_{D^0p} rest frame and $m_{D^0p} \in [m_{D^0p}^{\min}, m_{D^0p}^{\max}]$.

2.4.1 Resonances

As mentioned before, resonances show up as bands in the Dalitz plot. But they can also be examined by projecting the Dalitz plot onto its two body masses m_{ij}^2. A resonance in the D^0p channel will for example show up differently in these projections. The resonance band will show up as a peak, maybe with a tail, in the projection onto $m_{D^0p}^2$ and a reflection in the other two projections. The reflections might form more than one peak, which can be ascribed to the structure caused by the angular momentum.

In the D^0p channel we have a $|udc\rangle$ quark state, that basically can be a $\varLambda_c^{+*}$ or $\varSigma_c^*$. In the pK channel we find $|uds\rangle = \varLambda^*, \varSigma^*$ and in the D^0K^- channel $|cs\rangle = D_s^{-*}$. To determine all possible resonance isospin states, we evaluate the Feynman diagrams of the sequential decays in appendix M.1. All possible isospin states of the different resonances are listed in appendix M.2. There is isospin conservation in all possible tree-level Feynman diagrams of the $\varLambda_b^0$ with isospin $I_{\varLambda_b^0} = I_R = 0$. But the W-exchange graphs allows isospin $I_R = 1$ states for the resonances. However we do assume the contribution of the W-exchange graphs to be negligible and thus drop the possibility of $\varSigma^*$ and $\varSigma_c^*$ resonances.

Every resonance in the Dalitz plot is described by a specific amplitude. The general formalism to build up the decay specific matrix element $|\mathcal{M}|^2$ is to sum up all considered amplitudes and their possible helicity states λ. In this analysis the amplitude description is given by the helicity formalism. The details of building these amplitudes for all possible resonance channels is given in section 2.5 and summing them up to $|\mathcal{M}|^2$ in equation 2.57.

2.4.2 Square Dalitz Plot

One drawback of the Dalitz plot is the effective and correct calculation of the efficiency across it. Its kinematic boundary is not trivial to describe and resonances might tend to populate its edges. A rectangular Dalitz plot would be easier to handle especially if the efficiency calculation is based on a binned approach. The maybe first idea to transform the Dalitz Plot into a rectangular representation was to plot $\cos\theta_1$ against m_{12}, where θ_1 is helicity angle in the m_{12} rest frame. In this particular transformation we find for a specific m_{12} the phase space density to be uniform in $\cos\theta_1$ [42]. This method got picked up and is now known as the square Dalitz plot [43, 44]. The Dalitz plot variables are transformed to m'_{D^0p} and θ'_{D^0p}, that both range from 0 to 1. The transformation is given by

$$\begin{aligned}
m'_{D^0p} =& \frac{1}{\pi}\cos^{-1}\left[2\frac{m_{D^0p} - m_{D^0p}^{\text{min}}}{m_{D^0p}^{\text{max}} - m_{D^0p}^{\text{min}}} - 1\right] \\
\theta'_{D^0p} =& \frac{1}{\pi}\cos^{-1}\Bigg[\Big(m_{D^0p}^2(m_{pK}^2 - m_{D^0K}^2) - (m_p^2 - m_{D^0}^2)(m_{\varLambda_b^0}^2 - m_K^2)\Big) \,/ \\
& \sqrt{\left(m_{D^0p}^2 + m_{D^0}^2 - m_p^2\right)^2 - 4m_{D^0p}^2 m_{D^0}^2}\sqrt{\left(m_{\varLambda_b^0}^2 - m_{D^0p}^2 - m_{D^0}^2\right)^2 - 4m_{D^0p}^2 m_K^2}\Bigg] \\
=& \frac{1}{\pi}\theta_{D^0p} \\
m_{D^0K}^2 =& \sum_{\varLambda_b^0, D^0, p, K} m_i^2 - m_{D^0p}^2 - m_{pK}^2 \quad , \qquad (2.26)
\end{aligned}$$

with the helicity angle θ_{D^0p} of the D^0p system[5].

2.5 The Helicity Formalism

2.5.1 Helicity Amplitudes in General

There are different formalisms to account for particles with spin, like the covariant and the helicity formalism. The covariant approach directly expresses all properties with the respective tensors[6], vectors or scalars. The helicity formalism on the other hand describes how the spin states of the mother couple to the ones of the daughters [45–48]. In the following the general approach to calculate the helicity amplitudes of resonances R in a three body decay $\mathrm{D} \to \mathrm{ABC}$ is presented. This approach has already been used in various similar baryonic amplitude analyses like $\Lambda_b^0 \to D^0 p\pi$ [49, 50] and $\Lambda_b^0 \to J/\psi pK, \pi$ [51–54]. As these decays are very much comparable or similar the notation chosen strongly follows the one found in the previously mentioned analyses and some calculation might be found in more detail there.

A resonance can be seen in a sequential two-body decay of $\mathrm{D} \to \mathrm{AR}$ with $\mathrm{R} \to \mathrm{BC}$. So the basic principle of the helicity formalism is to follow down every possible sequential two-body decay till the final states are reached. The helicity formalism considers at each sequential step the transformations of the particle spin states or in other words the coupling of the particle's helicities.

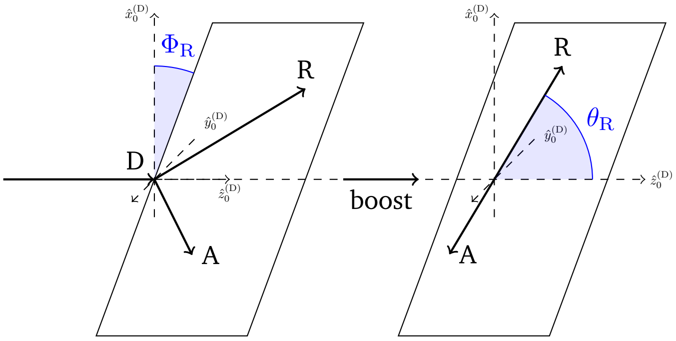

Fig. 2.10.: This plot visualises the general principle how to set up the reference frame and to find the helicity angles of a two-body decay.

$\mathrm{D} \to$ AR: Starting with the first two-body decay, a coordinate system, as seen in figure 2.10, has to be set up. This is in general arbitrary, but needs to be the same for every resonance chain. Here we align the unit vector of the z axis $\hat{z}_0^{(\mathrm{D})}$ to be in direction of spin quantisation

$$\hat{z}_0^{(\mathrm{D})} || \mathbf{p}_\mathrm{D}^{(LAB)}. \tag{2.27}$$

---

[5] $\theta_{D^0p} = \measuredangle(K^-D^0)$ in D^0p rest frame

[6] Dirac spinors and high-spin projection operators

Tab. 2.4.: Euler angles that define the rotation of the helicity carrying momentum in the reference frame of a two-body decay D → AR.

angle	rotation axis	type	definition	comment
α	$\hat{z}_0$	azimuth	$\Phi_{\mathrm{R}}^{(\mathrm{D})} \equiv \Phi_{\mathrm{R}}$	
β	$\hat{y}_1$	polar	$\theta_{\mathrm{R}}^{(\mathrm{D})} \equiv \theta_{\mathrm{R}}$	helicity angle
γ	$\hat{z}_2$		$\gamma \equiv 0$	rotation is arbitrary

The subscript indicates the order of transformation, where 0 are the initial coordinates and increments with every transformation. As the respective rest frame is crucial, the braced term (D) denotes the necessary rest frame. For the spin coupling we need to find the rotation of the mother's spin to the decaying resonance. As the particle spin states transform similar as their canonical states [47], we use the Euler angles in table 2.4 that rotate $\hat{z}_0^{(\mathrm{D})}$ in three increments (α, β and γ) to point into the direction of the coupling daughter $\mathbf{p}_{\text{daughter}}^{(\mathrm{D})}$ $\hat{z}_3^{(\mathrm{D})}$. In this case we rotate to the resonance R. The azimuth angle Φ_{R} and polar angle θ_{R}, as they are visualised in figure 2.10, are found by calculating

$$\cos\theta_{\mathrm{R}} = \hat{z}_0^{(\mathrm{D})} \cdot \mathbf{p}_{\mathrm{R}}^{(\mathrm{D})} \tag{2.28}$$

$$\begin{aligned} \Phi_{\mathrm{R}} &= \operatorname{atan2}\left(p_{\mathrm{R}\ y}^{(\mathrm{D})}, p_{\mathrm{R}\ x}^{(\mathrm{D})}\right) \\ &= \operatorname{atan2}\left(\hat{y}_0^{(\mathrm{D})} \cdot \mathbf{p}_{\mathrm{R}}^{(\mathrm{D})}, \hat{x}_0^{(\mathrm{D})} \cdot \mathbf{p}_{\mathrm{R}}^{(\mathrm{D})}\right) \\ &= \operatorname{atan2}\left(\left(\hat{z}_0^{(\mathrm{D})} \times \hat{x}_0^{(\mathrm{D})}\right) \cdot \mathbf{p}_{\mathrm{R}}^{(\mathrm{D})}, \hat{x}_0^{(\mathrm{D})} \cdot \mathbf{p}_{\mathrm{R}}^{(\mathrm{D})}\right) \quad . \end{aligned} \tag{2.29}$$

Knowing the angles to rotate the momentum, we can transfer the rotation of the canonical states directly onto the respective spin states [45]. The spin eigenstates $|J_{\mathrm{D}}, m_{\mathrm{D}}\rangle$ of the mother D in the initial coordinates are then expressed in the basis of the spin eigenstates of the rotated coordinates, $|J_{\mathrm{D}}, m'_{\mathrm{D}}\rangle$, via a Wigner's D-matrix

$$|J_{\mathrm{D}}, m_{\mathrm{D}}\rangle = \sum_{m'_{\mathrm{D}}} D^{J_{\mathrm{D}}}_{m_{\mathrm{D}}, m'_{\mathrm{D}}}(\alpha, \beta, \gamma) |J_{\mathrm{D}}, m'_{\mathrm{D}}\rangle \quad , \tag{2.30}$$

with the particles spin J and momentum m. Further the Wigner D matrix can be broken down into a Wigner small d matrix

$$D^{J}_{m,m'}(\alpha, \beta, \gamma) = \langle J, m | \mathcal{R}(\alpha, \beta, \gamma) | J, m' \rangle = e^{im\alpha} d^{J}_{m,m'}(\beta) e^{im'\gamma} \quad . \tag{2.31}$$

Finally every two-body decay adds a multiplicative term to the decay chain's matrix element, where one has to sum up over all possible helicities λ. Considering angular momentum conservation $m' = m'_{\mathrm{A}} + m'_{\mathrm{R}} = \lambda_{\mathrm{A}} - \lambda_{\mathrm{R}}$, as the momentum of A and R point into opposite directions, we find

$$\sum_{\lambda_{\mathrm{A}}, \lambda_{\mathrm{R}}} \mathcal{H}^{\mathrm{D}\to\mathrm{AR}}_{\lambda_{\mathrm{A}}, \lambda_{\mathrm{R}}} D^{J_{\mathrm{D}}}_{m_{\mathrm{D}}, \lambda_{\mathrm{A}} - \lambda_{\mathrm{R}}}(\Phi_{\mathrm{R}}, \theta_{\mathrm{R}}, 0) \quad . \tag{2.32}$$

The helicity couplings $\mathcal{H}$ are complex constants that have to be determined from a fit and that represent the decay dynamics.

Angular Momentum Conservation: There is the conservation of angular momentum that constrains the possible helicities we find in the helicity sum of equation 2.32. In case of the two-body decay $D \to AR$ these read

$$|\lambda_\mathrm{A}| \leq J_\mathrm{A}, \quad |\lambda_\mathrm{R}| \leq J_\mathrm{R}, \quad |\lambda_\mathrm{A} - \lambda_\mathrm{R}| \leq J_\mathrm{D} \quad . \tag{2.33}$$

R $\to$ BC (subsequent decay): The calculation for the subsequent decay of the resonance basically is the same, except that one has to boost into the resonances rest frame and find the new initial coordinates. The new rest frame is the one of the resonance R and is found by boosting the particles along $\mathbf{p}_\mathrm{R}^{(\mathrm{D})}$ (i.e. $\hat{z}_3^{(\mathrm{D})}$). The new initial coordinate system is not arbitrary anymore, as it is the rotated initial helicity frame $((\hat{x}, \hat{y}, \hat{z})_3^{(\mathrm{D})} \to (\hat{x}, \hat{y}, \hat{z})_0^{(\mathrm{R})})$.

To be able to calculate the new helicity angles we only need to know $\hat{z}_0^{(\mathrm{R})}$ and $\hat{x}_0^{(\mathrm{R})}$. As the new systems $\hat{z}_0^{(\mathrm{R})}$ is the previous ones $\hat{z}_3^{(\mathrm{D})}$ it points into the direction of the momentum of the resonance. Even though we have boosted into the resonances rest-frame, we know, that R and A go back to back. Thus this boost does not affect their direction and $\hat{z}_0^{(\mathrm{R})} = -\hat{p}_\mathrm{A}^{(\mathrm{B})}$. To extract the new $\hat{x}_0^{(\mathrm{R})}$, we have to follow both rotations of Φ_R and θ_R and find

$$\hat{x}_0^{(\mathrm{R})} = \hat{x}_3^{(\mathrm{D})} = -\hat{a}_{z_0\perp\mathrm{R}}^{(\mathrm{D})} \tag{2.34}$$
$$\mathbf{a}_{z_0\perp\mathrm{R}}^{(\mathrm{D})} = (\hat{z}_0^{(\mathrm{D})})_{\perp\mathbf{p}_\mathrm{R}^{(\mathrm{D})}} = \hat{z}_0^{(\mathrm{D})} - (\hat{z}_0^{(\mathrm{D})} \cdot \hat{p}_\mathrm{R}^{(\mathrm{D})})\hat{p}_\mathrm{R}^{(\mathrm{D})} \quad . \tag{2.35}$$

Again the rules angular momentum conservation apply if relevant.

Parity Conservation: In case of a strong or electromagnetic decay the rules of parity conservation apply and we find the helicity couplings $\mathcal{H}$ of different sign helicities to have a direct connection [47]. They have to fulfil the following dependence based on the particles intrinsic parities P, written down for a generic $D \to AR$.

$$\mathcal{H}_{-\lambda_\mathrm{A},-\lambda_\mathrm{R}}^{\mathrm{D}\to\mathrm{AR}} = P_\mathrm{D} P_\mathrm{A} P_\mathrm{R} (-1)^{J_\mathrm{A}+J_\mathrm{R}-J_\mathrm{D}} \mathcal{H}_{\lambda_\mathrm{A},\lambda_\mathrm{R}}^{\mathrm{D}\to\mathrm{AR}} \tag{2.36}$$

This reduces the number of different couplings.

2.5.2 Helicity Formalism in 2D

The $b\bar{b}$-jet axis of a LHCb-event is unknown and we thus have no relation with the lab momentum. This lets us expect an unpolarised Λ_b^0. Additionally the polarisation measured for Λ_b^0 production at the LHCb is consistent with zero [55, 56] for $\sqrt{s} = 7, 8, 13\,\mathrm{TeV}$, which upholds this claim.

We consider resonance states, that do have a width Γ in order of MeV. Thus, with the relation $\tau = \hbar/\Gamma$ we can expect the resonance states to have a maximum mean lifetime of about $\tau_\mathrm{max} < \hbar/1\,\mathrm{MeV} \approx \mathcal{O}(10^{-22}\,\mathrm{s})$. In comparison the lifetime of the shortest living final state particle D^0, as it can be found in table 2.2, is of order $\mathcal{O}(10^{-13}\,\mathrm{s})$. So, even though the final state D^0 is reconstructed as a decaying particle, we assume it to be ‘stable’ in this context and the Λ_b^0 decays into three true final states. Boosting into the Λ_b^0 rest-frame the decay of $\Lambda_b^0 \to D^0 pK$ becomes fully describable in a two dimensional plane, as it can be seen in figure 2.11. This makes the use of the azimuth angle Φ redundant. As our spin quantisation axis $\hat{z}$ can be chosen arbitrarily [48] we choose it to be along one possible resonance. From there we build up a basic cartesian coordinate system

$$\begin{aligned} \hat{z}_0^{(\Lambda_b^0)} &= \hat{p}_{\Lambda^*}^{(\Lambda_b^0)} \\ \hat{y}_0^{(\Lambda_b^0)} &= \hat{z}_0^{(\Lambda_b^0)} \times \hat{p}_p^{(\Lambda_b^0)} \\ \hat{x}_0^{(\Lambda_b^0)} &= \hat{y}_0^{(\Lambda_b^0)} \times \hat{z}_0^{(\Lambda_b^0)} \quad . \end{aligned} \tag{2.37}$$

There is an obvious benefit from the reduction into two dimensions. We only have to account for rotations about one axis, the initial $\hat{y}_0$. Except from $\theta \neq 0$ we can set the other Euler angles $\Phi = \gamma = 0$. Figure 2.11 shows the helicity angle definitions reduced two dimensions for the sequential decay of Λ_b^0.

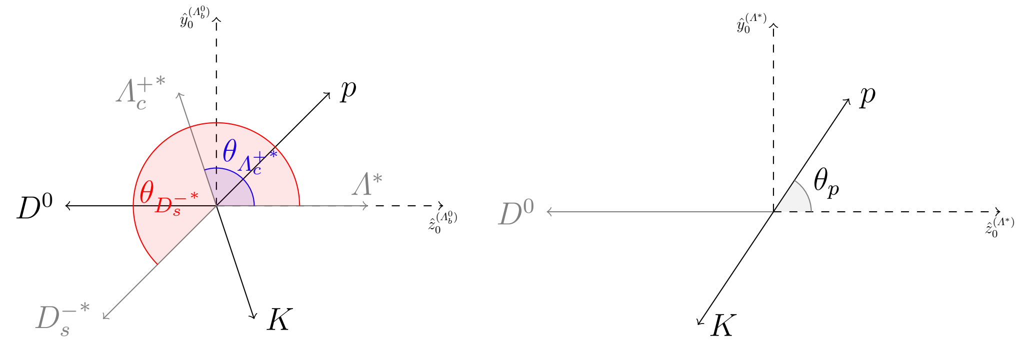

(a) Λ_b^0 rest frame (b) Λ^* rest frame

Fig. 2.11.: The two dimensional reduced helicity formalism. (a) shows the Λ_b^0 rest frame with the helicity angles $\theta_{\Lambda_c^{+*}}$ and $\theta_{D_s^{-*}}$. (b) shows the Λ^* rest frame with the helicity angle θ_p.

2.5.3 Amplitudes of the $\Lambda_n^* \to pK$ Resonances

We name the resonances to be Λ_n^*, where the index n denotes any of the possible excited Λ^*. The Feynman diagrams of this sequential decay can be found in figure M.1 (appendix). Following the terminology of section 2.5.1, we can write down the general helicity amplitude for a Λ_n^* resonance

$$\begin{aligned} A^{\Lambda_n^*}_{\lambda_{\Lambda_b^0},\lambda_{\Lambda_n^*},\lambda_p}(\Omega) =& \mathcal{H}^{\Lambda_b^0 \to \Lambda_n^* D^0}_{\lambda_{\Lambda_n^*}} D^{\frac{1}{2}}_{\lambda_{\Lambda_b^0},\lambda_{\Lambda_n^*}}(\Phi_{\Lambda_n^*}, \theta_{\Lambda_n^*}, 0) \\ & \mathcal{H}^{\Lambda_n^* \to pK}_{\lambda_p} D^{J_{\Lambda_n^*}}_{\lambda_{\Lambda_n^*},\lambda_p}(\Phi_p, \theta_p, 0) \cdot R_n(m_{pK}^2) \quad , \end{aligned} \tag{2.38}$$

with the lineshape R_n and Ω representing the invariant masses squared and angles. We now convert the amplitude to the two-dimensional representation introduced in section 2.5.2 and substitute with the Wigner small d representation. Additionally we shorten the subscriptions of the helicity coupling constants to Λ_n^* for more readability. Their relation to a specific two-body decay is distinct by the name of the helicities in their index.

$$\begin{aligned} A^{\Lambda_n^*}_{\lambda_{\Lambda_b^0},\lambda_{\Lambda_n^*},\lambda_p}(\Omega) =& \mathcal{H}^{\Lambda_n^*}_{\lambda_{\Lambda_n^*}} d^{\frac{1}{2}}_{\lambda_{\Lambda_b^0},\lambda_{\Lambda_n^*}}(\theta_{\Lambda_n^*}=0) \\ & \mathcal{H}^{\Lambda_n^*}_{\lambda_p} d^{J_{\Lambda_n^*}}_{\lambda_{\Lambda_n^*},\lambda_p}(\theta_p)\cdot R_n(m^2_{pK}) \end{aligned} \tag{2.39}$$

Parity Conservation: The sequential decay via a Λ_n^* resonance proceeds via the first weak $\Lambda_b^0 \to \Lambda_n^* K$ decay into the second strong $\Lambda_n^* \to pK$ decay. The latter is parity conserving and fulfils the relation between two couplings of opposite helicity in equation 2.36. In this case we look at the couplings of the decay of a Λ_n^*.

$$\begin{aligned} \mathcal{H}^{\Lambda_n^*}_{\lambda_p} &= P_{\Lambda_n^*} P_p P_K (-1)^{J_p+J_K-J_{\Lambda_n^*}} \mathcal{H}^{\Lambda_n^*}_{-\lambda_p} \\ &= -P_{\Lambda_n^*}(-1)^{\frac{1}{2}-J_{\Lambda_n^*}} \mathcal{H}^{\Lambda_n^*}_{-\lambda_p} \end{aligned} \tag{2.40}$$

The helicity couplings $\mathcal{H}^{\Lambda_n^*}_{\pm\lambda_p}$ are thus the same constants that can differ by a flipped sign. This enables us to rephrase $\mathcal{H}^{\Lambda_n^*}_{\lambda_{\Lambda_n^*}} \mathcal{H}^{\Lambda_n^*}_{\lambda_p}$ to $\eta^{\Lambda_n^*}_{\lambda_p} \mathcal{H}_{\lambda_{\Lambda_n^*}}$, with

$$\eta^{\Lambda_n^*}_{\lambda_p} = \begin{cases} -P_{\Lambda_n^*}(-1)^{\frac{1}{2}-J_{\Lambda_n^*}} & \text{if } \lambda_p = -1/2 \\ 1 & \text{if } \lambda_p = +1/2 \end{cases} \tag{2.41}$$

At this point the helicity amplitude reads

$$A^{\Lambda_n^*}_{\lambda_{\Lambda_b^0},\lambda_{\Lambda_n^*},\lambda_p}(\Omega) = \eta^{\Lambda_n^*}_{\lambda_p} \mathcal{H}_{\lambda_{\Lambda_n^*}} d^{\frac{1}{2}}_{\lambda_{\Lambda_b^0},\lambda_{\Lambda_n^*}}(0) d^{J_{\Lambda_n^*}}_{\lambda_{\Lambda_n^*},\lambda_p}(\theta_p)\cdot R_n(m^2_{pK}) \quad . \tag{2.42}$$

Summing up the Helicities: Taking a look at all spin contributions of the three-body decay of Λ_b^0, we only have to sum over the Λ_b^0 helicities $\lambda_{\Lambda_b^0} = \pm{}^1\!/_2$ and p helicities $\lambda_p = \pm{}^1\!/_2$. The Λ_n^* resonance on the other hand could have spin projections yielding from $-J_{\Lambda_n^*}$ to $+J_{\Lambda_n^*}$. However angular momentum conservation $|\lambda_{\Lambda_n^*}| \leq J_{\Lambda_b^0}$ shrinks the possibilities down to $\lambda_{\Lambda_n^*} = \pm{}^1\!/_2$. Finally we are left with two different complex helicity couplings, lets call them $\mathcal{H}^{\pm}_{\Lambda_n^*}$, for $\lambda_{\Lambda^*} = \pm{}^1\!/_2$. With $\lambda_{\Lambda_b^0} = \lambda_{\Lambda_n^*} = \lambda_p = \pm{}^1\!/_2$ we have to sum up and a total of $2\times2\times2=8$ helicity amplitudes for one Λ_n^* resonance. The final helicity amplitude for a Λ_n^* resonance, that is left to be summed up over 4 helicity combinations of $\lambda_{\Lambda_b^0}$ and λ_p, reads

$$\begin{aligned} A^{\Lambda_n^*}_{\lambda_{\Lambda_b^0},\lambda_p}(\Omega) = \eta^{\Lambda_n^*}_{\lambda_p} \big[& \mathcal{H}^{+}_{\Lambda_n^*} d^{\frac{1}{2}}_{\lambda_{\Lambda_b^0},+\frac{1}{2}}(0) d^{J_{\Lambda_n^*}}_{+\frac{1}{2},\lambda_p}(\theta_p)\cdot R_n(m^2_{pK}) + \\ & \mathcal{H}^{-}_{\Lambda_n^*} d^{\frac{1}{2}}_{\lambda_{\Lambda_b^0},-\frac{1}{2}}(0) d^{J_{\Lambda_n^*}}_{-\frac{1}{2},\lambda_p}(\theta_p)\cdot R_n(m^2_{pK}) \big] \quad . \end{aligned} \tag{2.43}$$

2.5.4 Amplitudes of the $\Lambda^{+*}_{c\ n} \to D^0 p$ Resonances

A $D^0 p$ final state will have had a Λ_c^{+*} as a mother. The Feynman diagrams of this sequential decay can be found in figure M.3 (appendix). Again we name the resonances to be $\Lambda^{+*}_{c\ n}$ and follow the terminology of section 2.5.1. The setup of the $\Lambda^{+*}_{c\ n}$ helicity amplitudes follows exactly the previous setup and is only described briefly.

- General matrix element for a $\Lambda_{c\;n}^{+*}$ resonance reduced into two dimensions, substituted with the Wigner small d functions and shortened subscript of the complex coefficients:

$$\begin{aligned} A^{\Lambda_{c\;n}^{+*}}_{\lambda_{\Lambda_b^0},\lambda_{\Lambda_{c\;n}^{+*}},\lambda_p'}(\Omega) =& \mathcal{H}^{\Lambda_{c\;n}^{+*}}_{\lambda_{\Lambda_{c\;n}^{+*}}} d^{\frac{1}{2}}_{\lambda_{\Lambda_b^0},\lambda_{\Lambda_{c\;n}^{+*}}}(\theta_{\Lambda_{c\;n}^{+*}}) \\ &\cdot \mathcal{H}^{\Lambda_{c\;n}^{+*}}_{\lambda_p'} d^{J_{\Lambda_{c\;n}^{+*}}}_{\lambda_{\Lambda_{c\;n}^{+*}},\lambda_p'}(\theta_{p'}) \cdot R_n(m^2_{D^0p}) \end{aligned} \tag{2.44}$$

- Parity conservation applies similarly to the decaying resonance and there are as well 8 helicity combinations to be summed up.

The final helicity amplitude for a $\Lambda_{c\;n}^{+*}$ resonance, that is left to be summed up over 4 helicity combinations of $\lambda_{\Lambda_b^0}$ and λ_p, reads

$$\begin{aligned} A^{\Lambda_{c\;n}^{+*}}_{\lambda_{\Lambda_b^0},\lambda_p'}(\Omega) = \eta^{\Lambda_{c\;n}^{+*}}_{\lambda_p'} \big[& \mathcal{H}^{+}_{\Lambda_{c\;n}^{+*}} d^{\frac{1}{2}}_{\lambda_{\Lambda_b^0},+\frac{1}{2}}(\theta_{\Lambda_c^{+*}}) d^{J_{\Lambda_{c\;n}^{+*}}}_{+\frac{1}{2},\lambda_p'}(\theta_{p'}) \cdot R_n(m^2_{D^0p}) \\ & + \mathcal{H}^{-}_{\Lambda_{c\;n}^{+*}} d^{\frac{1}{2}}_{\lambda_{\Lambda_b^0},-\frac{1}{2}}(\theta_{\Lambda_c^{+*}}) d^{J_{\Lambda_{c\;n}^{+*}}}_{-\frac{1}{2},\lambda_p'}(\theta_{p'}) \cdot R_n(m^2_{D^0p}) \big] \end{aligned} \tag{2.45}$$

2.5.5 Amplitudes of the $D_{s\;n}^{-*} \to \overline{D}^0 K$ Resonances

In case of the final states D^0K we can assume the presence of $D_{s\;n}^{-*}$ helicity amplitudes. These resonances are only possible for $\Lambda_b^0 \to \overline{D}^0 pK$, as it can be seen in the Feynman diagrams in figure M.2 (appendix). Again the setup follows the previous steps.

- General matrix element for a $D_{s\;n}^{-*}$ resonance:

$$\begin{aligned} A^{D_{s\;n}^{-*}}_{\lambda_{\Lambda_b^0},\lambda_{D_{s\;n}^{-*}},\lambda_p''}(\Omega) =& \mathcal{H}^{\Lambda_b^0 \to D_{s\;n}^{-*} p}_{\lambda_{D_{s\;n}^{-*}}} D^{\frac{1}{2}}_{\lambda_{\Lambda_b^0},\lambda_{D_{s\;n}^{-*}}-\lambda_p''}(\Phi_{D_{s\;n}^{-*}},\theta_{D_{s\;n}^{-*}},0)^* \\ &\cdot \mathcal{H}^{D_{s\;n}^{-*} \to D^0 K} D^{J_{D_{s\;n}^{-*}}}_{\lambda_{D_{s\;n}^{-*}},0}(\Phi_K,\theta_K,0)^* \cdot R_n(m^2_{D^0K}) \end{aligned} \tag{2.46}$$

- Reduction to two dimensions, substituting with the Wigner small d functions and shortening the subscripts of the complex coefficients:

$$\begin{aligned} A^{D_{s\;n}^{-*}}_{\lambda_{\Lambda_b^0},\lambda_{D_{s\;n}^{-*}},\lambda_p''}(\Omega) =& \mathcal{H}^{D_{s\;n}^{-*}}_{\lambda_{D_{s\;n}^{-*}}} d^{\frac{1}{2}}_{\lambda_{\Lambda_b^0},\lambda_{D_{s\;n}^{-*}}-\lambda_p''}(\theta_{D_{s\;n}^{-*}}) \\ &\cdot \mathcal{H}^{D_{s\;n}^{-*}} d^{J_{D_{s\;n}^{-*}}}_{\lambda_{D_{s\;n}^{-*}},0}(\theta_K) \cdot R_n(m^2_{D^0K}) \end{aligned} \tag{2.47}$$

The subsequent decay of the resonance is also strong and parity conserving in comparison to the decay of the Λ_b^0. Thus the helicity coupling $\mathcal{H}^{D_{s\;n}^{-*}}$ integrates, as before, into the one of the Λ_b^0. The relation between the helicity couplings of opposite helicity follows, as before, equation 2.36 and yields $\mathcal{H}^{D_{s\;n}^{-*}} = P_{D_{s\;n}^{-*}}(-1)^{J_{D_{s\;n}^{-*}}}\mathcal{H}^{D_{s\;n}^{-*}}$. In this case however, as $\eta_{D_{s\;n}^{-*}} = 1$, not all $J^P(D_{s\;m}^{-*})$ are possible and $J_{D_{s\;m}^{-*}}$ has to fulfil the following equation.

$$P(D_{s\;m}^{-*}) = (-1)^{J_{D_{s\;n}^{-*}}} \qquad \text{for } J \in \mathbb{N}_0 \tag{2.48}$$

We find, depending on the intrinsic parity, for $P_{D_{s\,n}^{-*}} = -1$ only uneven and in case of $+1$ only even $J_{D_{s\,m}^{-*}}$ including 0. Additionally there is angular momentum conservation. Taking into account the constraints from equation 2.33 we find $|\lambda_p'' - \lambda_{D_{s\,n}^{-*}}| \leq {}^1\!/_2$ and from the resonances $J_{D_{s\,n}^{-*}} \geq 0$. Thus there is only one helicity coupling for a $J_{D_{s\,n}^{-*}} = 0$ resonance and two otherwise. The possible helicities $\lambda_{D_{s\,n}^{-*}}$ are summarised in table 2.5. The corresponding helicity couplings are $\mathcal{H}_{D_{s\,0}^{-*}}$ and $\mathcal{H}^{\{0,\pm\}}_{D_{s\,n}^{-*}}$ respectively.

Tab. 2.5.: Possible helicities $\lambda_{D_{s\,n}^{-*}}$ for a $D_{s\,n}^{-*}$ resonance.

$J_{D_{s\,n}^{-*}}$	λ_p''	$\lambda_{D_{s\,n}^{-*}}$
0	$\pm{}^1\!/_2$	0
≥ 1	$+{}^1\!/_2$	$0, +1$
	$-{}^1\!/_2$	$-1, 0$

As a result we have 4 helicity amplitudes when $J_{D_{s\,m}^{-*}} = 0$ and 8 otherwise. The final helicity amplitude for a $D_{s\,n}^{-*}$ resonance, that is left to be summed up over the 4 helicity combinations of $\lambda_{\Lambda_b^0}$ and λ_p, reads in case of $J_{D_{s\,m}^{-*}} = 0$

$$A^{D_{s\,0}^{-*}}_{\lambda_{\Lambda_b^0},\lambda_p''}(\Omega) = d^{\frac{1}{2}}_{\lambda_{\Lambda_b^0},\lambda_p''}(\theta_{D_{s\,0}^{-*}}) d^{J_{D_{s\,0}^{-*}}}_{0,0}(\theta_K) \mathcal{H}_{D_{s\,0}^{-*}} \cdot R_0(m^2_{D^0K}) \tag{2.49}$$

and in case of $J_{D_{s\,m}^{-*}} > 0$

$$\begin{aligned} A^{D_{s\,n>0}^{-*}}_{\lambda_{\Lambda_b^0},\lambda_p''=\pm\frac{1}{2}}(\Omega) = \big[&\mathcal{H}^0_{D_{s\,n}^{-*}} d^{\frac{1}{2}}_{\lambda_{\Lambda_b^0},\lambda_p''}(\theta_{D_{s\,n}^{-*}}) d^{J_{D_{s\,n}^{-*}}}_{0,0}(\theta_K) \cdot R_n(m^2_{D^0K}) + \\ &\mathcal{H}^{\pm}_{D_{s\,n}^{-*}} d^{\frac{1}{2}}_{\lambda_{\Lambda_b^0},\pm1-\lambda_p''}(\theta_{D_{s\,n}^{-*}}) d^{J_{D_{s\,n}^{-*}}}_{\pm1,0}(\theta_K) \cdot R_n(m^2_{D^0K})\big] \quad . \end{aligned} \tag{2.50}$$

2.5.6 Definition of the Line Shapes

Breit-Wigner Lineshape: A well established parametrisation of a resonance lineshape is the Breit-Wigner lineshape, that consists of a relativistic Breit-Wigner (BW) distribution [57] that goes with a set of Blatt-Weisskopf form factors (B_L') [58] and angular barrier factors. The line shape

$$\mathcal{R}_{BW}(m^2_{\mathrm{R}}) = B'_{L_{\Lambda_b^0}}(p, p_0, d) \left[\frac{p}{p_0}\right]^{L_{\Lambda_b^0}} B'_{L_{\mathrm{R}}}(q, q_0, d) \left[\frac{q}{q_0}\right]^{L_{\mathrm{R}}} BW(m_{\mathrm{R}}, M_0, q, q_0, d), \tag{2.51}$$

describes the resonance R of the decay chain $\Lambda_b^0 \to \mathrm{AR}$ and $\mathrm{R} \to \mathrm{BC}$, where

$$BW(m_{\mathrm{R}}, M_0, q, q_0, d) = \frac{1}{M_0^2 - m^2_{\mathrm{R}} - iM_0\Gamma(m_{\mathrm{R}}, M_0, q, q_0, d)} \tag{2.52}$$

is the relativistic Breit-Wigner with

$$\Gamma(m_{\mathrm{R}}, M_0, q, q_0, d) = \Gamma_0 \left(\frac{q}{q_0}\right)^{2L_{\mathrm{R}}+1} \frac{M_0}{m_{\mathrm{R}}} B'_{L_{\mathrm{R}}}(q, q_0, d) \quad . \tag{2.53}$$

At first glance this looks like a huge set of parameters, that however are mostly well defined. Their definition can be found in table 2.6.

The Blatt-Weisskopf form factors B_L' try to describe effects on *e.g.* decay rates or cross sections correcting the assumption of point like particles in field theory. In practice particles

Tab. 2.6.: Parameters entering the relativistic Breit-Wigner with a set of Blatt-Weisskopf form factors. (equation 2.51)

p	break up momentum of A, R in D rest frame
q	break up momentum of B, C in R rest frame
p_0	p at resonance peak $M_\mathrm{R} = M_{0,R}$
q_0	q at resonance peak $M_\mathrm{R} = M_{0,R}$
d	radial parameter of D, R
m_R	invariant mass of the resonances two body decay
M_0	resonance peak mass
L_D	orbital angular momentum between A & R
L_R	orbital angular momentum between B & C
Γ_0	width of the resonance R

do have a definite radius. For a given particle decaying with an effective radius d, the model of Blatt and Weisskopf [58] considers a potential $U(d)$, where the decay products $(f_1 f_2)$ have to emerge from. The potential $U(d)$ is a potential well with its radius being the effective radius d. So $B'_l(p_{f_1})$ describes the probability of the final state f_1 to overcome the potential of the final state system $f_1 f_2$. Unfortunately the radial parameters d of the mother Λ_b^0 and the respective resonance are unknown. In general, as the radial parameters have got an effect on the resonances lineshapes, it would be desirable to leave these free in the fit [59]. This however would necessitate an appropriate number of events. As we do not have this freedom, we decide to set the values of the radial parameters to the same of the $\Lambda_b^0 \to D^0 p\pi$ analysis $d_{\Lambda_b^0} = 5\,\mathrm{GeV}/c^{-1}$ and $d_\mathrm{R} = 1.5\,\mathrm{GeV}/c^{-1}$ [49]. The Blatt-Weisskopf form factors are parameterised up to $L = 4$ as [58]

$$\begin{aligned}
B'_0(p, p_0, d) &= 1 \\
B'_1(p, p_0, d) &= \sqrt{\frac{1 + (p_0 d)^2}{1 + (pd)^2}} \\
B'_2(p, p_0, d) &= \sqrt{\frac{9 + 3(p_0 d)^2 + (p_0 d)^4}{9 + 3(pd)^2 + (pd)^4}} \\
B'_3(p, p_0, d) &= \sqrt{\frac{225 + 45(p_0 d)^2 + 6(p_0 d)^4 + (p_0 d)^6}{225 + 45(pd)^2 + 6(pd)^4 + (pd)^6}} \\
B'_4(p, p_0, d) &= \sqrt{\frac{11025 + 1575(p_0 d)^2 + 135(p_0 d)^4 + 10(p_0 d)^6 + (p_0 d)^8}{11025 + 1575(pd)^2 + 135(pd)^4 + 10(pd)^6 + (pd)^8}} \quad .
\end{aligned} \tag{2.54}$$

In the possible sequential decays, the resonance always decays strongly. Due to angular momentum conservation the Λ_n^* or $\Lambda_{c\ n}^{+\,*}$ resonance's decay angular momentum L_R is limited to $J_\mathrm{R} \pm {}^1\!/_2$. This is then clearly defined by parity conservation. To the weak Λ_b^0 decay also applies angular momentum conservation and we find $\max(J_\mathrm{R} - {}^1\!/_2, 0) \leq L_\mathrm{R} \leq J_\mathrm{R} + {}^1\!/_2$. Every possible angular momentum increases the total number of helicity couplings. As higher angular momenta are supressed, we only assume the minimal value $L_\mathrm{R} = J_\mathrm{R} - {}^1\!/_2$. This describes the data sufficiently, as we can see in the amplitude fit in chapter 6.

In case of the pK spectrum we have the $\Lambda(1405)$ resonance with a mass below the kinematically allowed threshold. We use a special Flatté lineshape [60], as it is done in the pentaquark analysis of $\Lambda_b^0 \to J/\psi pK$ [51]. A width for its decay to the dominant $\Lambda(1405) \to \Sigma\pi$ decay channel is added to the width of the pK channel yielding $\Gamma(m) = \Gamma_{pK}(m) + \Gamma_{\Sigma\pi}(m)$. A plot of the modified Flatté lineshape width can be found in the appendix M.4. The break up momentum q of the dominant decay and q_0 for both are calculated as if the resonance decays to $\Sigma\pi$. Under the assumption that both decay channels are equally likely and differ only by phase space factors, Γ_0 equals for both to the width of $\Lambda(1405)$.

Finally there is a description for a continuum distribution in the respective channel similar to a possible resonance like structure, whose tail is only visible in the kinematically allowed region. These distributions are modelled by an exponential function with Blatt-Weisskopf form factors [61]

$$\mathcal{R}_{BW}(m_{\mathrm{R}}^2) = B'_{L_{\Lambda_b^0}}(p, p_0, d) \left[\frac{p}{p_0}\right]^{L_{\Lambda_b^0}} B'_{L_{\mathrm{R}}}(q, q_0, d) \left[\frac{q}{q_0}\right]^{L_{\mathrm{R}}} e^{-\alpha M_{\mathrm{R}}} \quad . \tag{2.55}$$

2.5.7 Complete Matrix Element

The complete matrix element $|\mathcal{M}|^2$ can be found by summing up over all helicities and resonance states. The resonances, being intermediate states, sum up coherently, where the helicities $\lambda_{\Lambda_b^0}$ and λ_p sum up incoherently. We won't consider $D_{s\ n}^{-\ *}$ resonances in the following matrix element. But the general helicity amplitude given in section 2.5.5 is easily added.

Rotation of the p' Helicity States: The final state proton of the Λ_n^* ($\Lambda_{c\ n}^{+\ *}$) resonances recoils against the other final state particle K (D^0) in the resonances rest frame. So obviously the protons helicity axes are different for these two decay chains which is accentuated by a prime quotation (λ'_p) in the formulas of the helicity amplitudes. To be able to correctly add the amplitudes of different resonances coherently we need to rotate the proton helicities onto each other. As the protons are antiparallel to their recoiling partner the polar angle we have to rotate about is found by the angle between the K and D^0 in the proton's rest frame. Following the helicity amplitude of a $\Lambda_{c\ n}^{+\ *}$ resonance has to be preceded by

$$\sum_{\lambda'_p=\pm\frac{1}{2}} D^{\frac{1}{2}}_{\lambda_p,\lambda'_p}(0, \theta^{\mathrm{rot}}_{p'}, 0) \quad . \tag{2.56}$$

Final Sum: The Calculation of the necessary helicity angles can be found in appendix M.3. The complete matrix element then reads

$$\begin{aligned} |\mathcal{M}(\Omega)|^2 = \sum_{\lambda_{\Lambda_b^0}=\pm\frac{1}{2}} \sum_{\lambda_p=\pm\frac{1}{2}} \Big| \sum_n A^{\Lambda_n^*}_{\lambda_{\Lambda_b^0},\lambda_p}(\Omega) + \\ \sum_m \sum_{\lambda'_p=\pm\frac{1}{2}} d^{\frac{1}{2}}_{\lambda_p,\lambda'_p}(\theta^{\mathrm{rot}}_{p'}) \cdot A^{\Lambda_{c\ m}^{+\ *}}_{\lambda_{\Lambda_b^0},\lambda'_p}(\Omega) \Big|^2 \quad . \end{aligned} \tag{2.57}$$

LHCb Experiment

3

The Large-Hadron-Collider beauty (LHCb) is built by a worldwide collaboration of physicists and is one of six particle detectors located at the Large-Hadron-Collider (LHC) at CERN near Geneva in Switzerland. It is, as its name hints, mainly used to study b-decays and thus a good choice for the decay of this analysis $\Lambda_b^0 \to D^0 p K$. This chapter aims to give a brief overview over the LHC machine and the operating principle of the LHCb.

3.1 Large Hadron Collider

The LHC is built to accelerate and collide protons p and heavy ions. However, this analysis only utilises data taken from the pp collisions. By now the LHC is, with a circumference of about $27\,\mathrm{km}$, not only the largest, but also most powerful accelerator constructed by mankind. Subsequent to the construction period from 1994 until 2008, the first physics run started in 2011 at a center of mass energy of $\sqrt{s} = 7\,\mathrm{TeV}$. Proceeding in 2012 with $\sqrt{s} = 8\,\mathrm{TeV}$ the first run period, Run I, ended that same year. After a break, the LHC was ramped up again for Run II in 2015 to $\sqrt{s} = 13\,\mathrm{TeV}$. The Run II finished end of 2018.

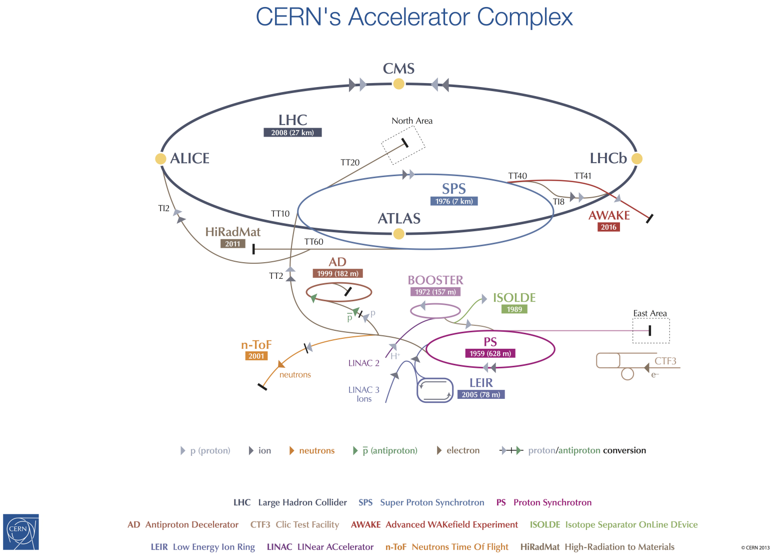

Fig. 3.1.: The scheme shows the principal layout of the CERN accelerator complex [62]. The black and largest ring symbolises the LHC with its four main experiments highlighted with yellow dots. Drawn in colour are smaller machines, that chain up to accelerate the particles or are separate experiments.

The scheme of the CERN accelerator complex in figure 3.1 gives an overview of the basic accelerator layout. It shows the LHC with its main experiments and the group of pre accelerators used to feed the LHC. Starting with stripping off electrons from hydrogen to generate protons, the linear accelerator LINAC 2 accelerates them to about $50\,\mathrm{MeV}$. Then their energy level is raised in stages up to $450\,\mathrm{GeV}$ via a chain of synchrotron (BOOSTER), proton synchotron PS and finally the super proton synchotron SPS. Bunches of accelerated protons are held in the SPS to be injected into the LHC during a fill. The LHC accelerates the proton bunches in opposite directions to their target energy. Superconducting magnets hold the bunches of about 1.15×10^{11} protons on track, ready to collide at any interaction point of the LHC's experiments. The bunch crossing delivered in Run I is about every $50\,\mathrm{ns}$ and cut down to $25\,\mathrm{ns}$ in Run II to deliver higher luminosity. An overview of the LHCb's recorded luminosity in Run I and II is given in figure 3.2.

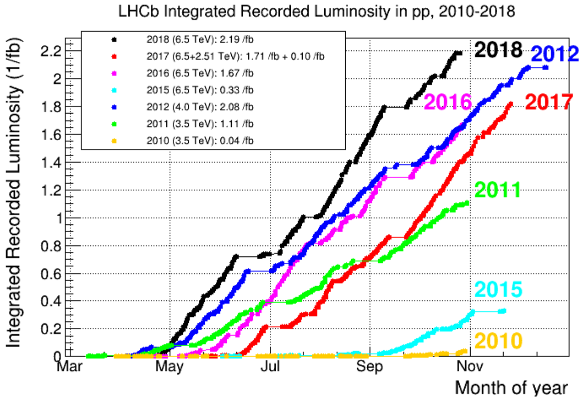

Fig. 3.2.: Summary of the by the LHCb recorded luminosity [63] delivered by the LHC.

A more detailed explanation of the LHC design and performance can be found in [64].

3.2 LHCb Detector

The LHCb experimental site sits at one of the four beam crossing points of the LHC, as visualised in figure 3.1. There are five more experiments found at the LHC: A Large Ion Collider Experiment (ALICE), A Toroidal LHC ApparatuS (ATLAS), Compact Muon Solenoid (CMS), Large Hadron Collider forward (LHCf) and Total Elastic and Diffractive Cross Section Measurement (TOTEM). TOTEM is installed near CMS and LHCf near ATLAS.

LHCb was developed to make precision CP measurements and to study decays involving b-quarks. With the $b\bar{b}$-pairs being dominantly generated along the beam pipe, the LHCb is build as a single-arm-spectrometer covering only a segment of the 4π space compared to other experiments like ATLAS or CMS, as it is shown in figure 3.3. The angular acceptance ranges from about $10\,\mathrm{mrad}$ to $300\,\mathrm{mrad}$ ($250\,\mathrm{mrad}$) in the bending (non-bending) plane of its magnet.

The LHCb detector combines different modules on a length of $21\,\mathrm{m}$, a width of $13\,\mathrm{m}$ and a height of $10\,\mathrm{m}$ to detect and identify particles. The origin of the LHCb coordinate system can be found at the interaction point of the pp collision. With its positive z-axis pointing

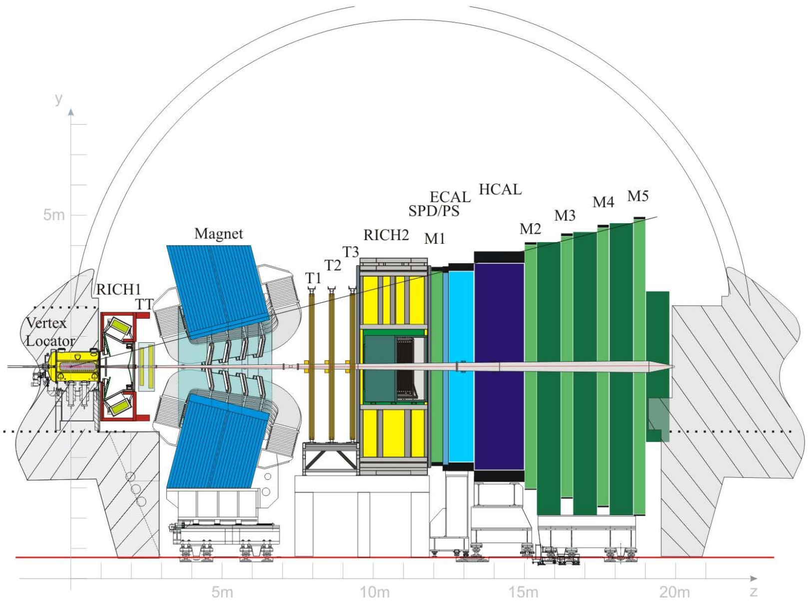

Fig. 3.3.: LHCb detector overview [65].

downstream along the beam pipe towards the detector. The y axis is perpendicular to the surface pointing upwards, thus the x axis follows the horizontal plane. Fig. 3.3 shows the layout of the LHCb, with the x-axis pointing into the drawing plane. Starting at the interaction point one finds the Vertex Locator (VELO), the Ring Imaging Cherenkov Detector (RICH), different kinds of tracking stations (T), two types of calorimeters and the muon system (M).

A more detailed description of the LHCb components can be found in [65] and its performance in [16].

3.2.1 Tracking System

In the presence of a magnetic field the trajectories of charged particles, so called tracks, are being measured by the VELO and the following tracking stations. With two crossing tracks being a vertex, the primary vertex denotes the interaction-point of the pp collision. The reconstruction and further definition of tracks and vertices can be found in section 3.2.4.

Dipole Magnet

The magnetic field is generated by a warm dipole magnet (see fig. 3.4 left). The magnet is designed to deliver a homogeneous field $\mathbf{B} = \pm B\mathbf{e}_y$, thus charged particles are only bent in the x-z plane. To minimise effects due to detector asymmetries the magnetic field gets inverted periodically and analyses are performed on both data sets. The different phases are named 'MagUp' ('MagDown') for the magnetic field pointing upwards (downwards). The magnetic field as a function of the z coordinate is shown in fig. 3.4 on the right. Along $10\,\mathrm{m}$ in z direction a particle will pass an integrated magnetic field of $\int B\,\mathrm{d}s = 4\,\mathrm{Tm}$.

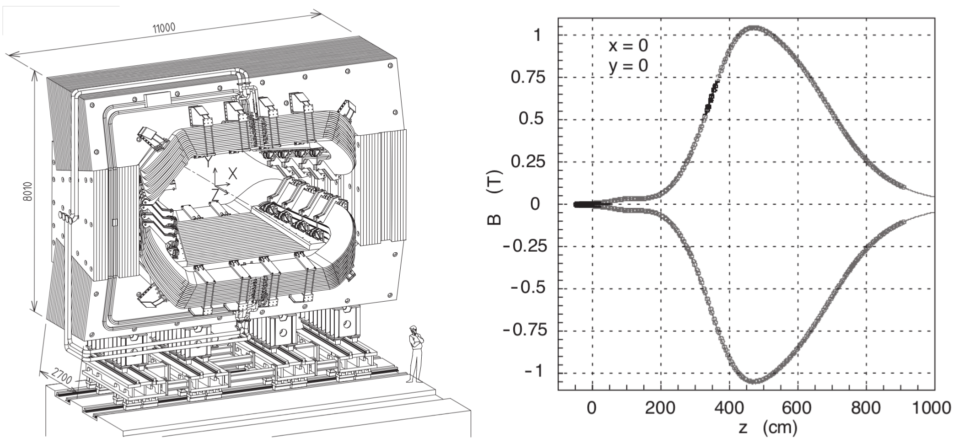

Fig. 3.4.: Scheme of dipole magnet design (left) and magnetic field in z-direction (right) [65].

Vertex Locator

The VELO is constructed to allow high resolution measurements near the interaction region. This is needed to differentiate between the primary vertices of the pp collision and secondary vertices of decaying long lived b- and c-hadrons. It is designed that particles with a pseudorapidity in the range $1.6 < \eta < 4.9$ and a distance to the primary vertex $|z| < 10.6\,\mathrm{cm}$ will have a minimum of three hits. The pseudorapidity $\eta = -\ln[\tan(\theta/2)]$ describes the angle between the moving direction of the particle and the beam pipe, with θ being the polar angle of the track. Fig. 3.5 shows the schematic layout of the 42 silicon modules of the VELO.

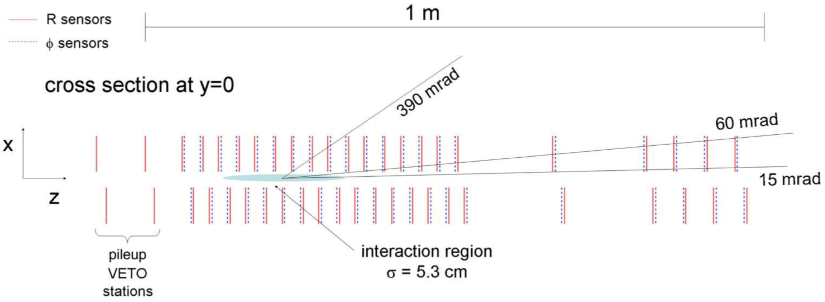

Fig. 3.5.: Schematic layout of the 42 silicon modules of the VELO [65].

For easy track reconstruction a cylindrical coordinate system is chosen. Thus every module consists of a grid of silicon rings and strips, to provide measurements of the R and Φ coordinates, when a charged particle passes through. Figure 3.6 shows the layout of these silicon strips. The b- and c-hadrons have a short life time and a decay length in the order of a millimetre [20]. To get a high acceptance, the modules are placed $8\,\mathrm{mm}$ from the proton beam axis, which is smaller than the diameter of the beam during injection. To prevent radiation damage due to an unstable beam, the modules form half shells, that can be retracted from the beam pipe. Further to preserve the needed high resolution near the beam pipe the pitch of the R measuring strips increases with distance to the beam pipe. The minimum distance of a track to the primary vertex can be measured with a spatial resolution of $(15 + \frac{29}{p_\mathrm{T}})\,\mathrm{\mu m}$, where p_T is the transverse momentum in GeV. In addition, there are two

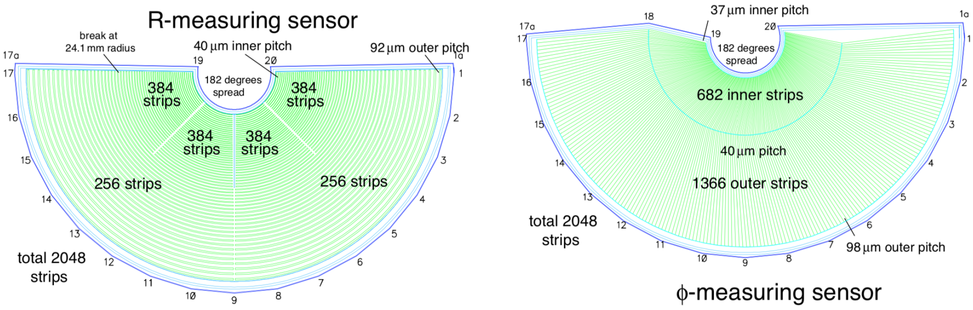

Fig. 3.6.: Schematic layout of the sensors silicon strips to measure R and Φ. [66]

modules placed upstream of the VELO which are called *pile-up veto system*, and used by the L0 trigger to veto events with multiple primary vertices.

The Tracking Stations

The tracking stations involve two detector types arranged in stations along the beam pipe. Upstream of the magnet there is the Tracker Turicensis (TT) and downstream the tracking stations T1-T3, as can be seen in figure 3.7.

Silicon Tracker The Silicon Tracker (ST) is divided into the TT and the Inner Tracker (IT). Both trackers use silicon microstrips with a $200\,\mu\mathrm{m}$ spacing and have a single-hit resolution of about $50\,\mu\mathrm{m}$. For three-dimensional measurements the tracking stations of the ST have pairs of silicon strip planes, where one plane is mounted perpendicular to the beam-axis and the second with a tilt of $5°$.

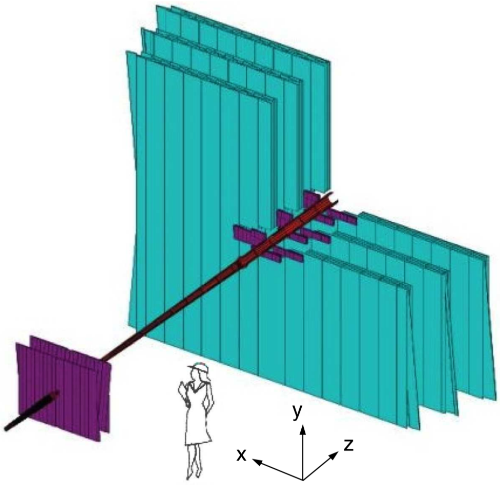

Fig. 3.7.: Tracking station arrangement, with the ST in violet and OT in cyan [65]. The magnet is located in the big gap.

The TT is placed at around $z = 2.5\,\mathrm{m}$, upstream of the dipole magnet and downstream of RICH1. Its two tracking-stations cover the LHCb acceptance with a height of $130\,\mathrm{cm}$ and width of $150\,\mathrm{cm}$. Its position is chosen to be able to detect low-momentum particles, which are bend by the magnetic field out of the acceptance of the following tracking stations, and to reconstruct long living V^0-particles, that decay mostly after the VELO.

The IT is part of the three tracking stations (T1-T3) downstream of the magnet and covers the area close to the beam pipe. Each IT-station covers a $40\,\mathrm{cm}$ high and $120\,\mathrm{cm}$ wide cross shaped region.

Outer Tracker The Outer Tracker (OT) is a drift-time detector consisting of straw-tubes and is located around the IT. Each of the three stations comprise four double-layer modules. The modules are *x*-*u*-*v*-*x* arranged, where *x* represents a vertically oriented layer whereas *u*- and *v*-layers are tilted by $\pm 5°$. The drift-tubes have a diameter of $4.9\,\mathrm{mm}$ and are filled with a gas-mixture of 70% Ar and 30% CO_2, to guarantee a drift time $< 50\,\mathrm{ns}$. The resulting drift-coordinate resolution of $200\,\mathrm{\mu m}$ is not as good as the ST one, but adequate, as the largest particle-flux being expected in the region of the IT.

The tracking stations upstream of the magnet and downstream provide two straight track-parts. The deflection angle of the track-parts gives some indication of the bend of the charged particle track in the magnetic field, thus one can calculate the resulting momentum of the respective particle. The achieved relative momentum resolution $\frac{\triangle p}{p}$ is about 0.4% for low momenta and 0.6% for momenta around $100\,\mathrm{GeV}$.

3.2.2 Particle Identification System

Particle Identification has different purposes. On the one hand the identification of the measured track's particle-type is needed for reconstructing b-decays and on the other hand it is used for b-flavour tagging. Two ring-imaging Cherenkov detectors (RICH1/2) are used to identify charged hadrons, a calorimeter for electrons and the energy measurement of photons and the muon system for muons.

Ring Imaging Cherenkov Detector

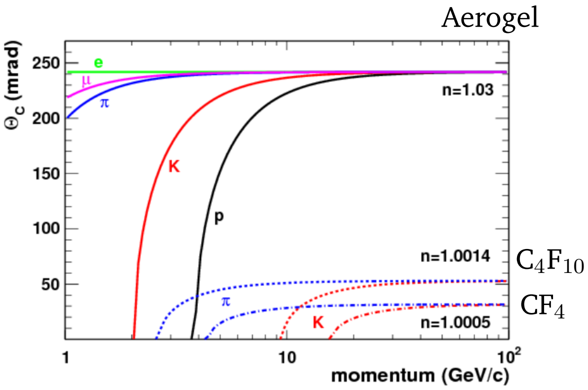

Fig. 3.8.: Separation of different hadrons for the radiators used [67]. Aerogel was removed from RICH1 after Run I.

The RICH-detectors make use of the Cherenkov effect to identify pions, kaons and protons. In case of a charged particle having a greater velocity in a dielectric medium than the speed of light has in this medium, these particles polarise the medium for a short time and thus emit photons. These photons form a Cherenkov cone, similar to the Mach cone, that is formed by the wave front of sound-waves of an object moving faster than the speed of sound. The opening angle θ_C of that cone depends on the medium specific refraction index n and the velocity of the particle β. The relation reads

$$\cos\theta_\mathrm{C} = \frac{1}{n\beta} \quad . \tag{3.1}$$

As the RICH detectors use permanent radiators as dielectric medium, n is constant. Thus measuring θ_C is analogous to measuring the particles' velocity. With this information and the resulting momentum measurements from the tracking, one is able to plot θ_C as function of p, which results due to the different particle masses in a curve for each particle. Fig. 3.8 shows these curves for the three different radiators used.

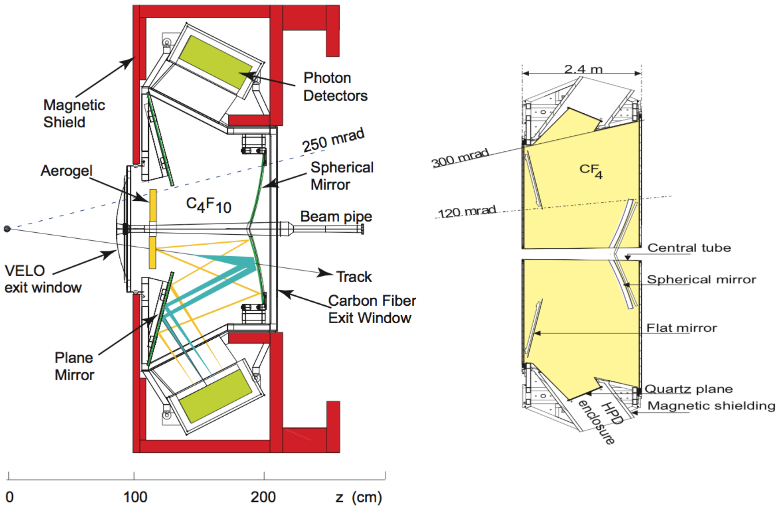

Fig. 3.9.: Side view of the RICH1 in the y-z-plane (left). The optical path of the Cherenkov light emitted by a passing track is illustrated in yellow and cyan. Top view of the RICH2 in the x-z-plane (right) [65].

RICH1 is located upstream of the magnet between the VELO and the TT and covers the full LHCb acceptance from $25\,\mathrm{mrad}$ to $300\,\mathrm{mrad}$ ($250\,\mathrm{mrad}$) in the bending (non-bending) plane. By using Aerogel[1] and C_4F_{10}-gas as radiator, it measures the low-momentum range 1-$60\,\mathrm{GeV}$ of the particles. The RICH2 location is further downstream right after the last tracking station T3. As CF_4-gas is used as radiator it is sensitive to the high-momentum range 15-$100\,\mathrm{GeV}$. Due to the fact that high-momentum particles move close along the beam pipe, there is no need to cover the whole LHCb acceptance. Thus the RICH2 covers from $15\,\mathrm{mrad}$ to $120\,\mathrm{mrad}$ ($100\,\mathrm{mrad}$) in the bending (non-bending) plane.

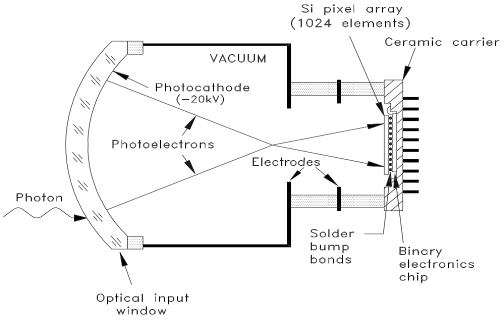

Fig. 3.10.: Schematic of a Hybrid-Photo-Detector [65].

Functionality of the RICH: Figure 3.9 shows the schematic of the RICH1 in the y-z-plane (side view) and the RICH2 in the x-z-plane (top view). The emitted photons of a charged particle moving through a radiator hit a set of spherical mirrors first. These mirrors focus photons of the same direction on one point away from the beam pipe, resulting in rings on the focal plane. A set of plane mirrors reflects these rings onto one of two arrays of Hybrid-Photo-Detectors (HPD), which detect photons from $200\,\mathrm{nm}$ to $600\,\mathrm{nm}$. Each array consists of 7 (9) rows with 14 (16) HPDs for the RICH1 (RICH2). The schematic of a HPD is shown in fig. 3.10. Photons hitting the optical input window emit a photoelectron that gets projected by an electric field onto a 32×32 silicon pixel array for detection. Due to the usage of electrons and the location of the RICH1 near the magnet, the HPD-array is surrounded by a magnetic shield.

---

[1] Aerogel is only used during Run I.

As there are multiple particles flying through the radiator at the same time, the Cherenkov rings detected by the HPD-array have to be separated. Therefore, the knowledge about track and momentum are used to calculate a theoretical $\theta_{\mathrm{C,theo}}$ and predict the location and size of a Cherenkov ring. The measured HPD hits are matched to the theoretical prediction of the Cherenkov ring and with the hits, that have found this way, the true Cherenkov angle θ_{C} is calculated.

The Calorimeter

The purpose of the LHCb calorimeter system [65, 68] is to trigger for electrons, photons and hadrons, further it measures their energy and direction. The system is located downstream of the RICH2 and is divided into the scintillating pad detector (SPD), the preshower detector (PS), the electromagnetic calorimeter (ECAL), and the hadronic calorimeter (HCAL). All detectors have a high granularity in the center region that decreases towards the outer regions. The basic functionality of the calorimeters does not differ: A particle or photon passing through an absorber material leads to particle-showers that cause light emissions in the following scintillator. The scintillating photons are transmitted to photomultipliers by glass fibres.

SPD and PS are basically two identical layers of scintillating pads separated by a $15\,\mathrm{mm}$ layer of lead, with a sensitive area of $7.6\,\mathrm{m}$ in width and $6.2\,\mathrm{m}$ in height. The inner region consists of 3072 cells of size $4 \times 4\,\mathrm{cm}$, the middle region out of 3584 cells of size $6 \times 6\,\mathrm{cm}$ and the outer region out of 5376 cells of size $12 \times 12\,\mathrm{cm}$, which makes a total of 12032 glass fibre readout channels. The SPD is used to distinguish between electrons and photons, with photons not leaving a signal in the scintillator.

Fig. 3.11.: **left:** ECAL-modules [65] for the outer (down-left), middle (down-right) and inner (upper) region. **- right:** Downstream view of the ECAL [69]; one can see the granularity changing from the inner to the outer region.

The ECAL and HCAL match the granularity of the SPD/PS. Both detectors have an alternating structure of absorber and scintillator. In order to detect particle showers of electrons and photons the ECAL is build out of tiles of alternating $2\,\mathrm{mm}$ lead- and $4\,\mathrm{mm}$ scintillator-layers. Fig. 3.11 shows the ECAL-modules for the three different regions and a downstream view of the ECAL itself. While the outer angular acceptance matches the one of the tracking system, the inner acceptance is limited to $25\,\mathrm{mrad}$ due to the radiation around the beam pipe. The design energy resolution of the ECAL modules is

$$\frac{\sigma_E}{E} = \frac{10\%}{\sqrt{E}} \oplus 1\% \quad , \tag{3.2}$$

with E in GeV and $\oplus$ standing for the quadratic sum.

For the HCAL iron is used as absorber material to induce hadronic showers. The layout of a HCAL module is shown in fig. 3.12. It consists of tiles in lateral direction of alternating $1\,\mathrm{mm}$ iron and scintillator layers, with a layer depth in longitudinal direction corresponding to the hadron interaction length of iron $\lambda_I \approx 17\,\mathrm{cm}$. The transverse segmentation of the HCAL is $131.3\,\mathrm{mm}$ in the inner section and $262.6\,\mathrm{mm}$ in the outer section. The readout is realised by wavelength shift fibres running along the longitudinal side to photomultipliers in the back. The design energy resolution of the HCAL modules is

$$\frac{\sigma_E}{E} = \frac{80\%}{\sqrt{E}} \oplus 1\% \quad , [E] = \mathrm{GeV}. \tag{3.3}$$

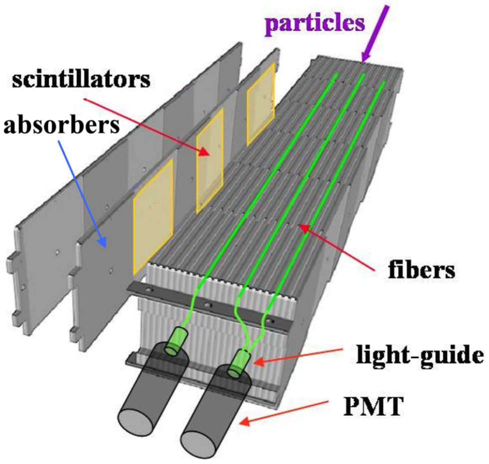

Fig. 3.12.: Schematic of a HCAL module. [65]. It is shown the alternating structure of iron and scintillator, as well as the glass fibre readout to the photomultipliers (PMT).

Muon System

Muons penetrate all detector systems of the LHCb, including the calorimeter. With all particles except from muons being stopped by the calorimeter, the muon system is located at the end of the detector. Fig. 3.13 shows the setup of the system. It consists of five stations, where the first station M1 is located upstream and the stations M2 - M5 downstream of the calorimeters. Each one of the stations (M2 - M5) is followed by a $80\,\mathrm{cm}$ thick iron absorber to select passing muons and absorb non-muons.

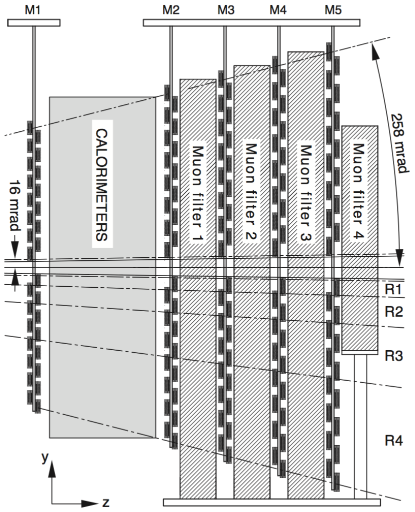

Fig. 3.13.: Side view of the muon system [65].

The system has a total number of 1368 multi-wire proportional chambers holding four anode wired sections filled with a gas-mixture of Ar, CO_2 and CF_4. The granularity of the chambers changes similar to the other subdetectors from the inner to the outer region. Each station is divided into four sections (R1 -

R4) with a linear scale-ratio of $1:2:4:8$, to assure almost the same particle flux in each quadrant.

Besides the identification of muons, the muon system measures their transverse momentum p_T. These information play a further role in the Trigger (see section 3.2.3).

3.2.3 Trigger

At the interaction point of the LHCb, proton bunches collide with a frequency of $20\,\mathrm{MHz}$ ($40\,\mathrm{MHz}$) in Run I (II). A trigger [70] decides for every collision if the event is interesting for further inspection, leading to a shrinkage of the rate. There are two main trigger stages, the Level 0 (L0) and the High Level Trigger (HLT), that reduce the rate of writing to storage to about $5\,\mathrm{kHz}$ ($12.5\,\mathrm{kHz}$) for Run I (Run II).

The L0 is a hardware trigger with a fixed latency of $4\,\mu\mathrm{s}$ splitting into $2\,\mu\mathrm{s}$ for data readout and data processing to make a decision. As there is no time for a complex reconstruction the trigger considers only basic calculations. The pile up veto stations in the VELO are used to calculate the number of primary vertices. The highest transverse energy of hadrons, electrons and photons gets calculated by the calorimeter data, as well as the highest p_T for muons with the muon system data. Further the calorimeter information indicates the number of tracks and total energy being observed. At the end the L0 provides an output frequency of $1\,\mathrm{MHz}$.

The second trigger stage, the HLT, is a software based trigger that is divided into two sub-stages, the HLT1 and HLT2. The HLT1 follows after a positive L0 decision and consults the measurements of the tracking system shrinking the frequency to $50\,\mathrm{kHz}$. Therefore the HLT1 checks for secondary vertices by a basic track reconstruction of the event that is considered. After passing the HLT1 the HLT2 performs a complete reconstruction of the event with less CPU consuming algorithms than in the offline analysis, by taking less detail into account. Since Run II the HLT already performs a full reconstruction of the event.

3.2.4 Reconstruction Software

In the following the reconstruction of tracks and vertices, as well as the identification of particles is covered.

Track Reconstruction

The track reconstruction software [65] takes the measurements of the VELO and the other tracking stations to form particle trajectories. There are different kind of tracks that can be divided into the following track types that are illustrated in fig. 3.15:

Long tracks have hits in all tracking stations from the VELO to T3 resulting in a precise momentum measurement. Thus, they are mostly used to reconstruct b-hadrons. **Upstream tracks** are only measured in the VELO and the TT. They must have a small momentum to be bent out of the LHCb acceptance region by the magnetic field. If their velocity is high enough they may be measured in the RICH1 and are used for RICH Particle Identification background.

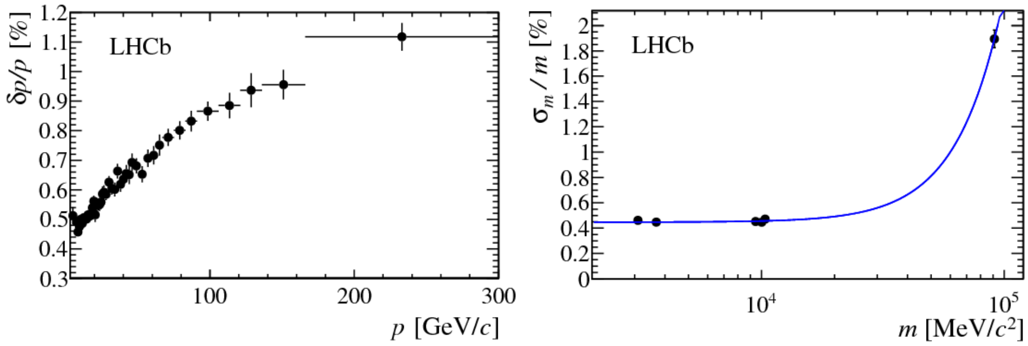

Fig. 3.14.: The relative momentum resolution for long tracks in data obtained using J/ψ decays are shown on the left. The right side shows the relative mass resolution, that is obtained from a fit to the mass distributions [16].

Downstream tracks leave only hits in the TT and T1 to T3. They are mostly decay products of V^0 particles (K^0_S and Λ), as they have long decay times and thus rather decay outside of the VELO acceptance. **VELO tracks** rather have large angles or run backwards. They are used for primary vertex reconstruction. **T tracks** can only be seen in the tracking stations T1 to T3 and are mostly produced by products of secondary interactions.

To form the trajectories the software starts with finding hits in regions of low magnetic field, that could initiate a track. The whole trajectory is found by a Kalman fitter [71]. This fitter uses a recursive filter, the Kalman filter [72], to associate measured hits to the tracks. The evolution of a trajectory in time is understood as a linear transformation of the system state vector. A Kalman filter calculates the optimum solution in terms of squared error (χ^2) for this state vector by taking three operations in account: *Filtering* estimates the present state vector based on all past events, *prediction* estimates the state vector at a future time and *smoothing* estimates a state vector of the past by using all already added hits. A new hit, measured by the tracking system, is iteratively added to the trajectory starting from the seed. In the end the Kalman fitter leads to the track parameters and aims to give significant accuracy of the track parameters close to the vertex. Thus a fit is always performed towards the interaction region.

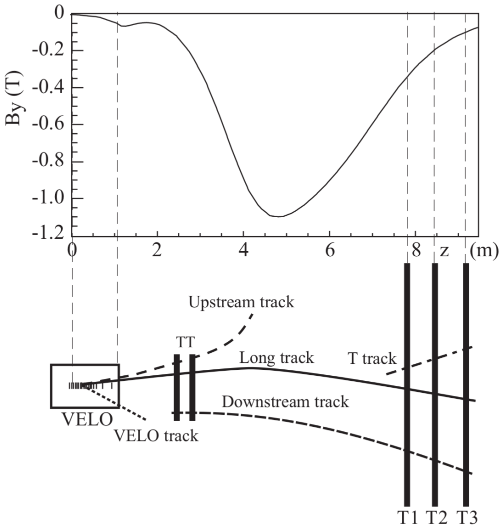

Fig. 3.15.: The figure shows the different track types that can be found at the LHCb [65]. Further the y component of the magnetic field is shown with respect to the different tracking stations.

The relative momentum and mass resolutions that are achieved with the reconstruction software are extracted from $J/\psi \to \mu\mu$ decays and shown in fig. 3.14 [16].

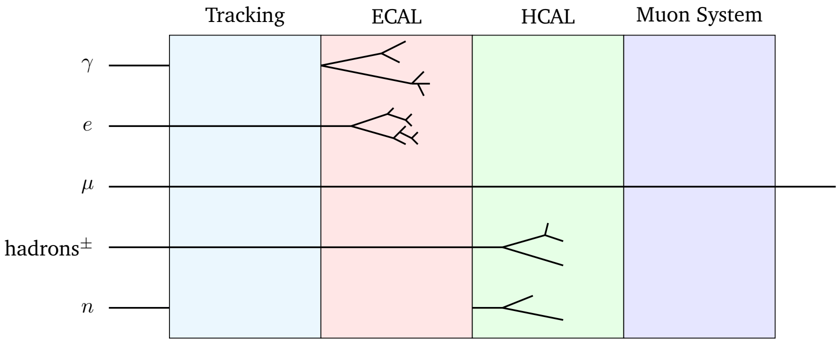

Fig. 3.16.: Identification scheme for different particles, depending on which sub-detectors measure the specific particle types [74].

Vertex Reconstruction

A vertex is a point, where two or more tracks cross. One can distinguish two main types: primary and secondary vertices. All particle trajectories that emerge from one pp interaction point combine to a primary vertex (PV). There can be events with multiple PVs if there happen to be more than one pp interaction. However, as mentioned in section 3.2.3 events with too many PV get rejected. Secondary vertices are vertices formed by tracks of particles being the decay products of a particle from the PV.

The reconstruction of vertices is done by a vertex fit [73]. This results in an estimation of the interaction point and the momentum vector of emerging tracks. With the vertex fit being a special case of a nonlinear Kalman filter [72] the vertex fit results, like the track fit, into a χ^2 minimisation. Further, this gives information about a track truly originating from the specific vertex.

Only a few tracks are assumed to originate from a secondary vertex. Thus, at first all tracks are associated to the primary vertex. They get removed or moved to a secondary vertex by a Kalman filter if it is more likely.

Particle Identification

The particle identification (PID) distinguishes between charged and uncharged particles. Charged particles (e, μ, p, π, K) are identified by the combined measured data of the RICH detectors, the calorimeters and the muon system. Uncharged particles (γ, π^0) are identified by the ECAL.

Figure 3.16 illustrates how to discern photons γ, electrons e, muons μ, neutrons n and hadrons (π, p and K). On the one hand, uncharged particles do not leave a trace in the tracking system. Thus a photon is only being measured in the ECAL and a neutron only in the HCAL. On the other hand, charged particles do leave a trace in the tracking system, so their charge is determined by the bend of the trajectory in the magnetic field. As muons are not stopped in the calorimeter, they are identified by being measured in the muon system. Electrons are stopped and measured in the ECAL and hadrons in the HCAL.

The discrimination of hadrons is done with the RICH system. An algorithm matches the observed pixel hit pattern to expected hits calculated from the reconstructed trajectories. The logarithmic likelihood (LL) is maximised by variation of the particle hypothesis for the trajectories. The output of this *global pattern-recognition* is a best hypothesis for each measured track. There are two different variables accessible to discriminate between e, μ, K, π and p. The delta-log-likelihood $\Delta\mathrm{LL}_{x\pi}$ is the LL difference to a π, giving information how likely it is to be particle x in comparison to a pion. Further the output of a PID trained neural net is accessible, a classification variable that gives some kind of probability $P_{NN,x} \in [0.0, 1.0]$, how likely the particle is to be of kind x.

To test performance and calibrate the PID-system pure samples of e, μ, K, π and p have to be isolated. They are build by purely kinematic selections of exclusive decays such as $\gamma \to e^+e^-$, $J/\psi \to \mu^+\mu^-$, $K^0_\mathrm{S} \to \pi\pi$, $\Lambda \to p\pi^-$ and $\phi \to KK$ [75]. The performance is studied by calculating the efficiencies in the identification of known particle tracks. The average efficiency achieved for kaon identification for momenta from 2 to $100\,\mathrm{GeV}$ is $\epsilon(K \to K) \sim 95\%$ and for pion mis-identification (mis-ID) $\epsilon(\pi \to K) \sim 5\%$ [65]. This is quite essential to be able to discriminate between the K and π in the final states of the analysed decay. The notation $\epsilon(X \to Y)$ has to be understood as the efficiency of particle X to be identified as particle Y. In general, particle-identification efficiencies and purities in the region of 90% to 100% are achieved [76].

3.2.5 Data Recording

The LHC provides pp-collisions every $50\,\mathrm{ns}$ $(25\,\mathrm{ns})$ in Run I (Run II). In 2011 the data was taken with a luminosity of $3.5 \times 10^{32}\,\mathrm{cm}^{-2}\,\mathrm{s}^{-1}$ with $\sqrt{s} = 7\,\mathrm{TeV}$, in 2012 with a luminosity of $4 \times 10^{32}\,\mathrm{cm}^{-2}\,\mathrm{s}^{-1}$ with $\sqrt{s} = 8\,\mathrm{TeV}$ and during Run II $6.5 \times 10^{32}\,\mathrm{cm}^{-2}\,\mathrm{s}^{-1}$ with $\sqrt{s} = 13\,\mathrm{TeV}$.

Data Samples

As luminosity or other machine specific conditions, changed during both runs, the recorded data are found in different data sets that will be analysed separately. An overview over the available data sets is listed in table 3.1 including the corresponding recorded integrated luminosities $\mathcal{L}$. The samples of different magnet polarities will be merged. It is to note here, that this analysis does not use raw data but stripped data sets (compare with section 4.2.1). We use the identifier DATA if we refer to the truly recorded data.

Tab. 3.1.: Integrated luminosity $\mathcal{L}$ and proton energy E_p of the available pp samples.

	Run I		Run II			
Year	2011	2012	2015	2016	2017	2018
$\mathcal{L}/\,\mathrm{fb}^{-1}$	1.107	2.082	0.328	1.665	1.609	2.186
$E_p/\,\mathrm{TeV}$	3.5	4	6.5			

3.2.6 Monte Carlo Simulation

The understanding of the behaviour of signal events under certain conditions is necessary. This might be the effect of the detector, that measures only a projection of the decays with its sensitive areas, the efficiency of specific decisions, or to investigate the distortion of measured rates and physics. Therefore, we simulate signal events and process them to DATA-like samples. As these simulations are based on Monte Carlo (MC) calculations [77], we use the identifier MC to refer to a simulation.

There are three stages involved: the simulation of the underlying pp interaction, the decay of the b-hadron and the detector response. The pp interaction is simulated with PYTHIA8 [78]. It simulates their parton-parton interaction based on the latest parton-distribution for a proton within a LHCb-configuration [79]. There it handles the b-quark production in these interactions and their hadronisations. The second step involves the decay of the b hadron, which is done by EVTGEN [80]. Their final state radiation is generated by PHOTOS [81]. Finally in the last step a detector simulation is carried out with the LHCb package GAUSS [82] based on the GEANT4 detector simulation tool kit [83, 84]. The basic simulation includes the complete 4π angle, but the LHCb measures only on one side of the pp interaction along the beam pipe ($z > 0$). So the simulation mirrors the generated event on purpose to ensure the signal to be in the positive z direction and double the generation efficiency.

User configured decay files (DecFiles [85, 86]) give the basic conditions for EVTGEN and GAUSS. For example in case of $\Lambda_b^0 \to D^0 pK$ the decay file specifies the decay of the mother Λ_b^0 to its three final states and the secondary decay of the D^0. One can specify if the decays follow, like here, the general phase space or *e.g.* a specific polarisation. Further multiple decays with different branching fractions $\mathcal{B}$ are possible. At this point, one can force a three-body decay to be uniform across a dedicated Dalitz plot representation. For this analysis, a square Dalitz plot is chosen. As disc space is limited, selections are also available. The most common and useful one is called `DecProdCut`. It ensures that only events are saved, when all daughters of the signal particle are present within the detector volume.

To increase the MC production efficiency there is also the possibility of a filtered production, where only events are saved that fulfil the conditions of a specific stripping line. More details on the definition of stripping are given in section 4.2.1.

4

Candidate Selection - $\Lambda_b^0 \to D^0 pK$

In this chapter we present our selection process for $\Lambda_b^0 \to D^0 pK$ candidates. The chosen control channel is $\Lambda_b^0 \to D^0 p\pi$, so most of the selection criteria will apply as well.

4.1 Reconstruction of $\Lambda_b^0 \to D^0 pK$ Candidates

The reconstruction of Λ_b^0 candidates uses the already preprocessed stripping lines (see section 4.2.1). The utilised line already offers candidates of the structure $\Lambda_b^0 \to D^0 ph$, where the h stands for a generic hadron. We use the DAVINCI framework to select $\Lambda_b^0 \to D^0 pK$ candidates with the D^0 to decay into $K\pi$, KK, $\pi\pi$. The reconstruction of the decay is performed by the framework-tool `DecayTreeFit` (DTF) [87]. It performs a trajectory fit based on the Kalman fitter [71] mentioned in section 3.2.4. The tool takes all particle information of the mother-particle, the specific daughters and their momentum vectors as well as their covariance matrix. If the DTF fails or diverges the event is discarded, else the events are stored in ROOT files [88, 89]. Further a set of constraints can be used to reduce the degrees of freedom for the fit. A constraint to the origin vertex is used and the daughter D^0 is constrained to its known mass. Further a second DTF is performed with an additional constraint on the mass of the mother Λ_b^0. This ensures the boundary of the dalitz plot not to be smeared, by using the variables of the second fit.

4.2 Preselections

We apply some preliminary selections that on the one hand aim to reject background candidates and on the other hand serve to reduce the size of the data sample. These selections include trigger flags, stripping and kinematic decisions.

4.2.1 Stripping Line

The first selections applied to the raw data are the stripping selections. In general there are multiple stripping lines that are optimised for different decay channels. Thus these stripping lines provide a set of preselected data. In our case we chose the *Lb2D0PHD02HH-Beauty2CharmLine* [90]. This line selects $\Lambda_b^0 \to D^0 ph$ candidates, with a two-body decay $D^0 \to hh$, where h represents a K or π. Starting from charged particles the line builds up the decay chain to the mother particle Λ_b^0. As the line uses two-body decays as building kit it selects a $\Lambda_b^0 \to D^0$'Λ', where 'Λ' $\to ph$. This might distort physical variables in the DTF of section 4.1. Therefore the Λ is substituted to be a $\Lambda(1405)$, that has got a reasonable short lifetime. Table 4.1 lists the selections the stripping line applies to the data sets.

Tab. 4.1.: Stripping Selections of the *Lb2D0PHD02HHBeauty2CharmLine* [90]. The PID selections apply only to the direct Λ_b^0 daughters, except for the 2018 data sets.

Tracks	min p_t	$0.1\,\mathrm{GeV}/c$
	min p	$1.0\,\mathrm{GeV}/c$
	max $\chi^2_{\text{track}}/n_{\text{DoF}}$	3
	min ${\chi^2}_{\text{IP}}(\text{PV})$	4
D^0	min $\sum_{\text{daughters}} p_t$	$1.8\,\mathrm{GeV}/c$
	min ${\chi^2}_{\text{IP}}(\text{best PV})$	36
	max DOCA(tracks)	$0.5\,\mathrm{mm}$
	max $\chi^2_{\text{vertex}}/n_{\text{DoF}}$	10
	max $\lvert m_{D^0} - m_{\text{PDG}}\rvert$	$0.1\,\mathrm{GeV}/c^2$
Λ_b^0	min $\sum_{\text{daughters}} p_t$	$5.0\,\mathrm{GeV}/c$
	min $\tau(\text{best PV})$	$0.2\,\mathrm{ps}$
	min ${\chi^2}_{\text{IP}}(\text{best PV})$	25
	max $\chi^2_{\text{vertex}}/n_{\text{DoF}}$	10
	min $\cos\theta_{\text{dira}}(\text{best PV})$	0.999
	$m_{\Lambda_b^0}$	$[5.2, 7.0]\,\mathrm{GeV}/c^2$
p	min $\Delta\mathrm{LL}_{p\pi}$	-10
K	min $\Delta\mathrm{LL}_{K\pi}$	-10
π	max $\Delta\mathrm{LL}_{K\pi}$	20

The PID selections apply only to the direct Λ_b^0 daughters, except for the 2018 data sets, where they apply to the D^0 daughters as well. To ensure equality between the different data sets the 2018 PID cuts are reapplied to all samples. There are different stripping versions in existence, this analysis utilises versions *21r1*, *21*, *24r1*, *28r1*, *29r2* and *34*.

The cuts of a stripping line are loose cuts, where the impact on the signal decay is expected to be negligible in comparison to the background reduction[1]. They ensure to have kinematically sensible tracks and strengthen their decision with a cut on χ^2/n_{DoF}, the goodness of fit, χ^2 reduced by its degrees of freedom. Further a cut on ${\chi^2}_{\text{IP}}(\text{PV})$, the significance of the impact parameter, is applied. The latter calculates $\Delta\chi^2_{\text{fit}}$ for the primary-vertex (PV) fit with and without the track, which is small for prompt tracks.

The D^0 particle track is worked out by similar decisions, additionally the vertex of its daughters is of interest. Therefore a maximum distance of closest approach (DOCA) of its daughter tracks selects a possible vertex, which is ensured by a cut on the goodness of the vertex fit via $\chi^2_{\text{vertex}}/n_{\text{DoF}}$. A symmetric mass window around the true D^0 mass filters for sensible D^0 candidates. The Λ_b^0 filter works likewise. A minimum lifetime τ in respect to the best PV, lets the Λ_b^0 become a particle that must have travelled. To ensure that the Λ_b^0 originates from the best PV, its direction angle θ_{dira}, which is the angle between the Λ_b^0 momentum and the vector between the Λ_b^0 vertex and the best PV, is required to be almost zero.

---

[1] This statement might not be true for every stripping line.

4.2.2 Trigger

The amount of background events can be significantly reduced, by maintaining mostly all signal, when using trigger flags. However it is not reasonable to use all available flags, but only the ones, that are sensitive to the decay studied. Apart from the different trigger levels presented in section 3.2.3, thereare different trigger categories, that are associated to the signal candidate [91]:

TOS	Trigger On Signal: The signal of the event is sufficient to lead to a positive decision.
TIS	Trigger Independent Signal: The non-signal part of the event creates a positive decision.
TOB	Trigger On Both: Neither TIS nor TOS alone are sufficient, but both together lead to a positive decision.

This analysis does not use TOB decisions, but TIS and TOS can have triggered simultaneously. The trigger decision, that has to be true is

$$\texttt{L0Global\_TIS} \quad \vee \quad \texttt{L0HadronDecision\_TOS} \quad . \tag{4.1}$$

The `L0Hadron` trigger scans the calorimeter HCAL for a minimum transversal energy E_T deposit and requires the SPD hits to be less than 600 at the same time. This hints for an hadron and can be induced by the p or K from the Λ_b^0 or any of the D^0 daughters. The `L0Global` trigger is the general trigger decision, so equation 4.1 requires, that any of the decay products must have triggered or the event was triggered independently of the signal. As the trigger is not simulated adequately enough, the efficiencies we get from MC samples are only a rough estimate. We find an efficiency of $\epsilon_{\text{trigger}} \approx 98\%$.

4.2.3 Clean Final States (PID)

Tab. 4.2.: Cuts on hadronic final states to ensure valid PID information.

	η		$p\,[\,\text{GeV}/c]$	
	min	max	min	max
p	2.0	4.5	9.0	200.0
K	2.0	4.5	3.0	200.0
π	2.0	4.5	3.0	200.0

Using PID information comes with some limitations. We have to ensure that we use tracks with valid and useful PID information. Therefore we require that all hadrons of the decay have been registered in the RICH detectors. Additionally there are some kinematic constraints. First of all, due to the detector acceptance, pseudorapidities η outside of the interval $[2.0, 4.5]$ lead to unreasonable tracks. Secondly PID calculations heavily depend on the particles momentum. There has to be a minimum momentum p_{min}, as the particles need to have sufficient energy to radiate Cherenkov light. Lastly a maximum momentum p can be useful, as hadrons above a specific momentum are basically indistinguishable. In case of a two-body decay this cut might not be necessary, due to superior kinematic cuts. However in case of a three-body discriminability is necessary. The cuts to ensure valid PID information are listed in table 4.2.

4.2.4 Additional Preselections

The preselections till now are based on rather loose kinematic cuts. We now apply some further cuts that aim to reduce background. In figure 4.1 we compare the DATA and MC distributions for the fit probability P_{fit} of the `DeacyTreeFit` and the Λ_b^0 decay-length significance $S_{\text{decay length}}(\Lambda_b^0)$, which is the decay length divided by its error.

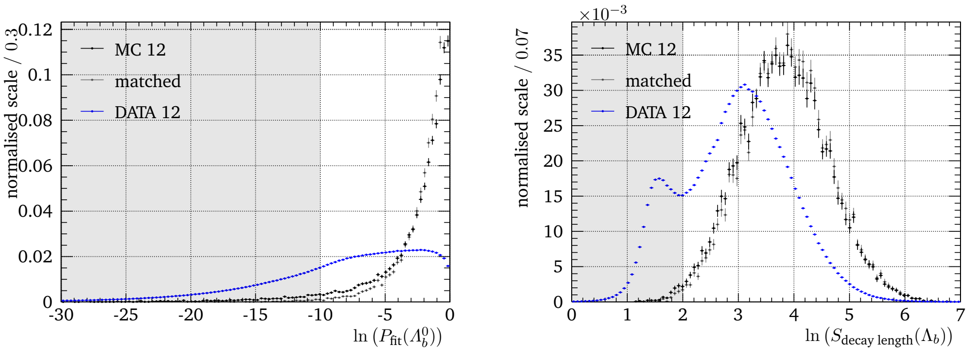

Fig. 4.1.: Comparison of DATA and MC distributions for the fit probability (a) and Λ_b^0 decay length (b). Trigger, $m(D^0)$ filter and the respective other cut are applied to the $\Lambda_b^0 \to D^0 pK$ samples. The chosen cut is visualised by a grey exclusion area.

The fit probability is expected to be a uniform distribution in the range $[0.0, 1.0]$ for true decays, where background events tend to peak at zero. This background peak is very narrow, so it is stretched by applying the natural logarithm. A cut of $\ln(P_{\text{fit}}(\Lambda_b^0)) > -10$ is chosen. For similar reasons the logarithm is also applied to the Λ_b^0 decay-length significance. We chose a cut of $\ln(S_{\text{decay length}}(\Lambda_b^0)) > 2.0$. The mass window around the D^0 is tightened with $|m(D^0) - m(D^0)_{\text{PDG}}| < 25.0\,\text{MeV}/c^2$ and all daughter tracks must not have tracks in the muon chambers. The resulting invariant mass distributions for Λ_b^0 and D^0 are in appendix B for all Run I DATA samples[2].

4.3 Simulation

The simulation described in section 3.2.6has got different purposes in this analysis. First of all the MC samples are used as signal samples in the training in section 4.4.1. Then efficiencies are extracted from MC for the $\Lambda_b^0 \to D^0 pK$ signal and $\Lambda_b^0 \to D^0 p\pi$ normalisation samples. These are used as constraints in the fit to the DATA in chapter 5, reducing its free parameters and thus increasing its stability. Additionally the mass distributions of MC samples are used to determine the fit functions, that are used in the global fit. Another purpose of the MC samples is to study charmless or mis-ID background in section 4.5. Table C.1 in the appendix lists all generated samples.

The reconstruction of the MC samples follows the same steps as the DATA samples, except for an additional smearing of the track momentum by the `TrackSmearState` tool of DaVinci. This matches the track reconstruction resolution of simulation and data. A general tool to

---

[2] Run II is not expected to behave much differently.

Tab. 4.3.: Relative scaling factors to compare the expected amount of a decay relative to a reference decay. Used branching fractions are in appendix A.

sample \ reference	$\varLambda_b^0 \to D^0pK$			$\varLambda_b^0 \to D^0p\pi$		
$\varLambda_b^0 \to D^0pK$	1			$\frac{\mathcal{B}(\varLambda_b^0\to D^0pK)}{\mathcal{B}(\varLambda_b^0\to D^0p\pi)}$	$\approx$	0.07
$\varLambda_b^0 \to D^0p\pi$	$\frac{\mathcal{B}(\varLambda_b^0\to D^0p\pi)}{\mathcal{B}(\varLambda_b^0\to D^0pK)}$	$\approx$	13.7	1		
$B^0 \to \overline{D}^0KK$	$\frac{f_d}{f_{\varLambda_b^0}} \frac{\mathcal{B}(B^0\to\overline{D}^0KK)}{\mathcal{B}(\varLambda_b^0\to D^0pK)}$	$\approx$	2.43	$\frac{f_d}{f_{\varLambda_b^0}} \frac{\mathcal{B}(B^0\to\overline{D}^0KK))}{\mathcal{B}(\varLambda_b^0\to D^0p\pi))}$	$\approx$	0.18
$B^0 \to \overline{D}^0\pi\pi$	$\frac{f_d}{f_{\varLambda_b^0}} \frac{\mathcal{B}(B^0\to\overline{D}^0\pi\pi)}{\mathcal{B}(\varLambda_b^0\to D^0pK)}$	$\approx$	35.25	$\frac{f_d}{f_{\varLambda_b^0}} \frac{\mathcal{B}(B^0\to\overline{D}^0\pi\pi))}{\mathcal{B}(\varLambda_b^0\to D^0p\pi))}$	$\approx$	2.57
$B_s^0 \to \overline{D}^0KK$	$\frac{f_s}{f_{\varLambda_b^0}} \frac{\mathcal{B}(B_s^0\to D^0KK)}{\mathcal{B}(\varLambda_b^0\to D^0pK)}$	$\approx$	0.58	$\frac{f_s}{f_{\varLambda_b^0}} \frac{\mathcal{B}(\overline{B}\to\overline{D}^0KK))}{\mathcal{B}(\varLambda_b^0\to D^0p\pi))}$	$\approx$	0.04
$\varLambda_b^0 \to D^*pK$	$R'_{D^*,K}$	$\approx$	1.09	$R'_{D^*,K}R_{\varLambda_b^0\to D^0pK}$	$\approx$	1.05
$\varLambda_b^0 \to D^*p\pi$	$R'_{D^*,\pi}R_{\varLambda_b^0\to D^0pK}$	$\approx$	14.3	$R'_{D^*,\pi}$	$\approx$	0.08
$\varLambda_b^0 \to p\pi^-\pi^+\pi^-$	$\frac{\mathcal{B}(\varLambda_b^0\to p\pi^-\pi^+\pi^-)}{\mathcal{B}(\varLambda_b^0\to D^0pK)\mathcal{B}(D^0)}$	$\approx$	$0.46/\mathcal{B}(D^0)$	$\frac{\mathcal{B}(\varLambda_b^0\to p\pi^-\pi^+\pi^-)}{\mathcal{B}(\varLambda_b^0\to D^0p\pi)\mathcal{B}(D^0)}$	$\approx$	$0.03/\mathcal{B}(D^0)$
$\varLambda_b^0 \to pK^-K^+\pi^-$	$\frac{\mathcal{B}(\varLambda_b^0\to pK^-K^+\pi^-)}{\mathcal{B}(\varLambda_b^0\to D^0pK)\mathcal{B}(D^0)}$	$\approx$	$0.09/\mathcal{B}(D^0)$	$\frac{\mathcal{B}(\varLambda_b^0\to pK^-K^+\pi^-)}{\mathcal{B}(\varLambda_b^0\to D^0p\pi)\mathcal{B}(D^0)}$	$<$	$0.01/\mathcal{B}(D^0)$
$\varLambda_b^0 \to pK^-\pi^+\pi^-$	$\frac{\mathcal{B}(\varLambda_b^0\to pK^-\pi^+\pi^-)}{\mathcal{B}(\varLambda_b^0\to D^0pK)\mathcal{B}(D^0)}$	$\approx$	$1.11/\mathcal{B}(D^0)$	$\frac{\mathcal{B}(\varLambda_b^0\to pK^-\pi^+\pi^-)}{\mathcal{B}(\varLambda_b^0\to D^0p\pi)\mathcal{B}(D^0)}$	$\approx$	$0.08/\mathcal{B}(D^0)$
$\varLambda_b^0 \to pK^-K^+K^-$	$\frac{\mathcal{B}(\varLambda_b^0\to pK^-K^+K^-)}{\mathcal{B}(\varLambda_b^0\to D^0pK)\mathcal{B}(D^0)}$	$\approx$	$0.28/\mathcal{B}(D^0)$	$\frac{\mathcal{B}(\varLambda_b^0\to pK^-K^+K^-)}{\mathcal{B}(\varLambda_b^0\to D^0p\pi)\mathcal{B}(D^0)}$	$\approx$	$0.02/\mathcal{B}(D^0)$
$\varXi_b \to pK^-K^-\pi^+$	$\frac{\mathcal{B}(\varXi_b\to pK^-K^-\pi^+)}{\mathcal{B}(\varXi_b\to D^0pK)\mathcal{B}(D^0)}$	$\approx$	$0.09/\mathcal{B}(D^0)$			
$\varXi_b \to pK^-\pi^+\pi^-$	$\frac{\mathcal{B}(\varXi_b\to pK^-\pi^+\pi^-)}{\mathcal{B}(\varXi_b\to D^0pK)\mathcal{B}(D^0)}$	$\approx$	$0.09/\mathcal{B}(D^0)$			
$\varXi_b \to pK^-K^+K^-$	$\frac{\mathcal{B}(\varXi_b\to pK^-K^+K^-)}{\mathcal{B}(\varXi_b\to D^0pK)\mathcal{B}(D^0)}$	$<$	$0.01/\mathcal{B}(D^0)$			

measure the efficiency of PID selection is `PIDCalib` [92]. This tool however has got the drawback that PID variables have to be handled differently from the other variables. An unbinned approach to correct the PID response can be done with kernel density estimation. A transformation, that preserves all correlations of the PID variables, is performed, as it is proposed in [93].

4.3.1 Relative Scaling Factors

Every simulated decay was generated with a differing number of candidates. To compare a MC sample to a reference MC sample its integral has to be rescaled by a factor f_s

$$f_s = r_s \cdot \frac{N^{\text{gen}}_{\text{reference}}}{N^{\text{gen}}_{\text{sample}}} \quad , \tag{4.2}$$

that includes the respective branching fraction ratio r_s (table 4.3) and the amount of generated events (table C.1). A list of all used branching fractions and their estimations, if necessary, can be found in appendix A.

4.3.2 MC Matching

MC samples are reconstructed as DATA, which can distort the distributions of the bare signal. At some point it is interesting to study the true signal distributions. Therefore it is necessary to match the reconstructed particle objects to their underlying true simulated particle. An in

LHCb analyses commonly used tool for this task is the `TupleToolMCBackgroundInfo` [94] of the DaVinci framework. It enables us to store flag-based information about different physics cases and thus filter for true signal candidates. The tool therefore compares the user required decay sequence (decay descriptor) with the decay sequence information of the stripping line. Next to various background categories there are two signal categories (BKGCAT), as described in [94]:

0 **Signal:** $\Lambda_b^0 \to D^0 pK$ and its subsequent D^0 decay are fully reconstructed as described in the decay descriptor and all final state particles are matched to their true simulation partner.

10 **Quasi-Signal:** The decay fulfils the BKGCAT-0 conditions but must not have the decay topology, as defined in the decay descriptor. Therefore intermediate states must not match, allowing the pseudo Λ of the stripping line.

Although this tool classifies efficiently it fails with the mismatching $\Lambda_b^0 \to D^0[pK]_\Lambda$ decay structure of the stripping line (see section 4.2.1) and mixes BKGCAT-0 into BKGCAT-10. Thus this analysis uses its own algorithm, where the particle types of the particles themselves, their mother and grandmother, if existent, are matched.

4.3.3 MC *vs.* DATA

There are differences in the kinematical distributions of the Λ_b^0 and Ξ_b candidates, when comparing MC and DATA. The kinematical distributions cannot be perfectly simulated, as they involve perturbative QCD calculations due to the nature of pp collisions. Additionally the simulation of the detector does not cover a full-featured LHCb model with no difference to the reality. This distorts the kinematic distributions as well.

In this section we aim to overcome these issues to improve the efficiency of the supervised training in section 4.4.1 with a set of kinematically more accurate signal samples. Therefore we compare the DATA extracted signal kinematics (p, p_{T}, η) of the Λ_b^0 mother with the ones of the MC samples. In principle it would be best to compare the MC samples in DATA with the same decay they are based on and with the least, but same selections applied to both samples. After the application of the preselection $\Lambda_b^0 \to D^0 pK$ is not visible in the $m(D^0 pK)$ invariant mass distribution. As the normalising channel $\Lambda_b^0 \to D^0 p\pi$ is kinematically similar and visible in the respective DATA samples, it will be the source of the true signal kinematics.

Extracting Signal Kinematics

In order to extract the signal kinematics from DATA, we use the statistical tool *sPlot* [95]. Based on an unbinned likelihood fit, the contribution of different sources can be unfolded leading to an event wise *sWeight* calculation. The application of these weights allows to study variable distribution of the fit contributions. We calculate *sWeights* for the Λ_b^0 signal from a fit to the invariant mass distribution $m(D^0 p\pi)$ of the preselected DATA in appendix D.1. The resulting signal-like distributions of the weighted DATA samples are then compared to the truth-matched MC distributions in figs. 4.2 to 4.4 for p, p_T and η of the decay mother Λ_b^0.

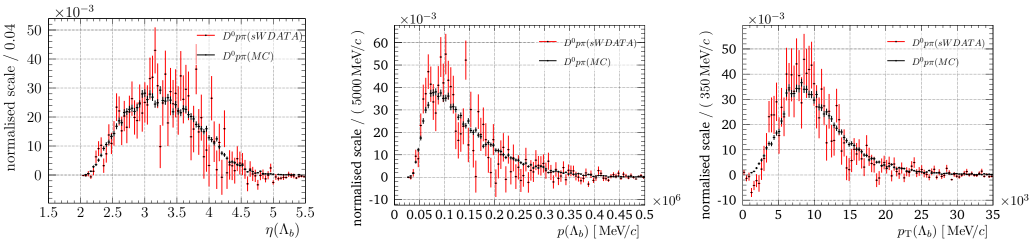

(a) $\eta(\Lambda_b^0)$ (b) $p(\Lambda_b^0)$ (c) $p_\mathrm{T}(\Lambda_b^0)$

Fig. 4.2.: Compared kinematics of *sWeight*'ed $\Lambda_b^0 \to D^0 p\pi$ DATA to truth-matched MC - 2011

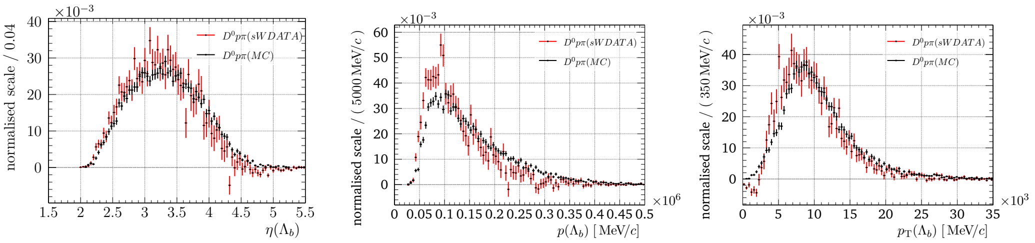

(a) $\eta(\Lambda_b^0)$ (b) $p(\Lambda_b^0)$ (c) $p_\mathrm{T}(\Lambda_b^0)$

Fig. 4.3.: Compared kinematics of *sWeight*'ed $\Lambda_b^0 \to D^0 p\pi$ DATA to truth-matched MC - 2012

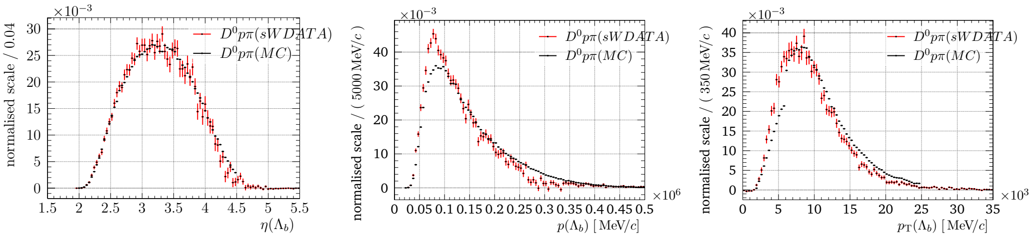

(a) $\eta(\Lambda_b^0)$ (b) $p(\Lambda_b^0)$ (c) $p_\mathrm{T}(\Lambda_b^0)$

Fig. 4.4.: Compared kinematics of *sWeight*'ed $\Lambda_b^0 \to D^0 p\pi$ DATA to truth-matched MC - Run II

MC Weights

There is a visible discrepancy between the MC distributions and signal-like DATA in figs. 4.2 to 4.4. To correct for this discrepancy each MC candidate will be weighted according to the fraction $f_\mathrm{DATA/MC}$, which is calculated by dividing the bins of normalised DATA and MC histograms. The weights are generally found by fitting a two-dimensional weight function $w(a, b)$. However a two-dimensional fit is challenging and we assume the weights to factorise $w(p_\mathrm{T}, \eta) = w_{p_\mathrm{T}}(p_\mathrm{T}) \cdot w_\eta(\eta)$. Thus we only need to fit in the projections of $f_\mathrm{DATA/MC}$ onto p_T and η. The weight functions $w_{p_\mathrm{T}}(p_\mathrm{T})$ and $w_\eta(\eta)$ are splines with four equidistant sampling points in p_T (η). The fit is implemented as a binned χ^2-fit [96] using `MINUIT` [97] as minimiser. The p_T model is fit and applied first. The fit result is listed in tables 4.4 and 4.5. Figures 4.5 to 4.7 show the fitted weight functions. The found MC weights lead to an improved agreement between MC and DATA, as shown in appendix D.1.

Tab. 4.4.: Fitted sampling points of the spline for the p_T projections of $f_{\mathrm{DATA/MC}}$.

$p_\mathrm{T}\,[\mathrm{GeV}/c]$	$w_{p_\mathrm{T},i}$		
	2011	2012	Run II
0.0	1.16 ± 0.23	1.50 ± 0.14	1.42 ± 0.05
$9.\overline{6}$	1.05 ± 0.08	0.98 ± 0.04	0.992 ± 0.014
$17.\overline{3}$	0.62 ± 0.11	0.71 ± 0.06	0.731 ± 0.020
25.0	1.0 ± 0.4	0.52 ± 0.17	0.45 ± 0.07

Tab. 4.5.: Fitted sampling points of the spline for the η projections of $f_{\mathrm{DATA/MC}}$.

η	$w_{\eta,i}$		
	2011	2012	Run II
2.0	0.68 ± 0.22	1.11 ± 0.16	0.62 ± 0.04
$2.8\overline{3}$	0.99 ± 0.07	1.13 ± 0.05	1.100 ± 0.014
$3.\overline{6}$	1.08 ± 0.10	1.02 ± 0.05	1.010 ± 0.018
4.5	0.72 ± 0.34	0.10 ± 0.15	0.59 ± 0.06

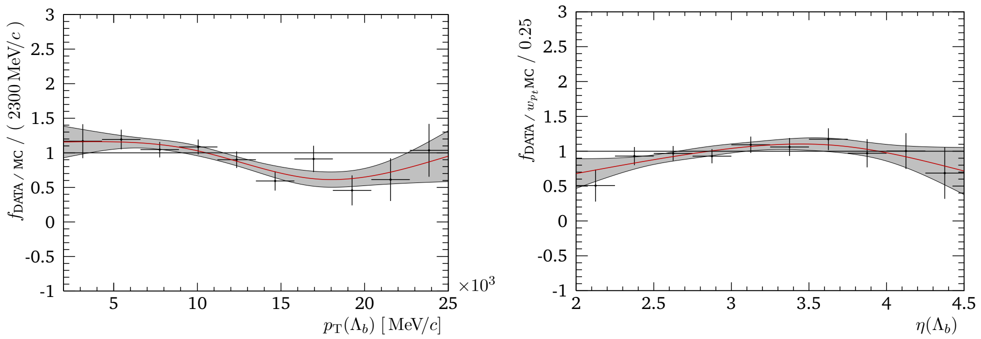

(a) $w_{p_\mathrm{T}}(p_\mathrm{T})$

(b) $w_\eta(\eta)$

Fig. 4.5.: Spline fit to the p_T (a) and η (b) projections of $f_{\mathrm{DATA/MC}}$. - 2011

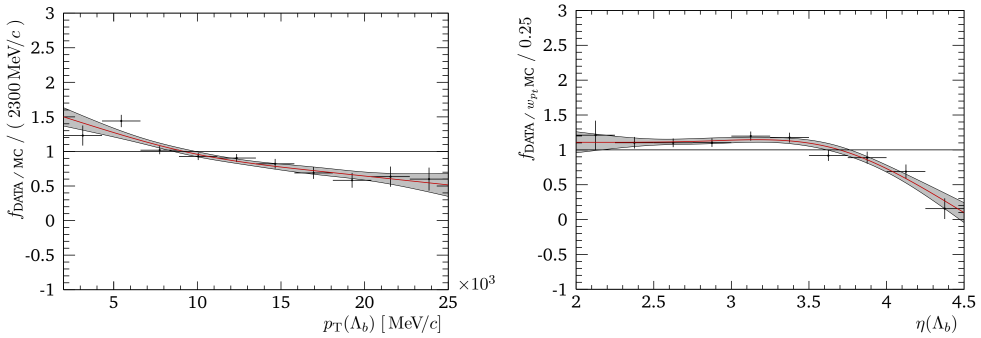

(a) $w_{p_\mathrm{T}}(p_\mathrm{T})$

(b) $w_\eta(\eta)$

Fig. 4.6.: Spline fit to the p_T (a) and η (b) projections of $f_{\mathrm{DATA/MC}}$. - 2012

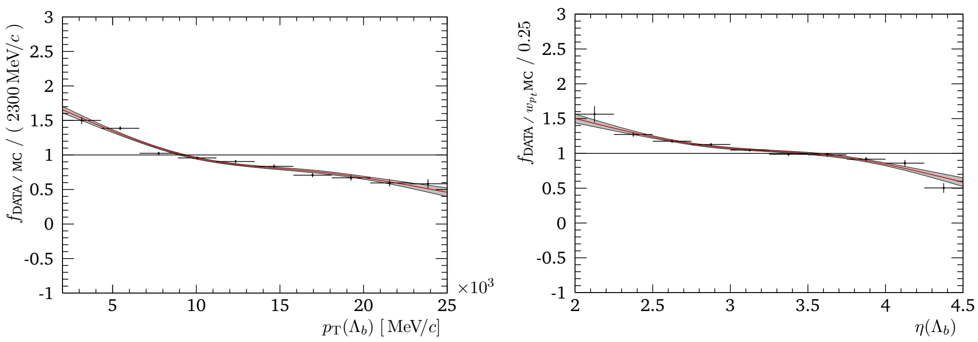

(a) $w_{p_{\mathrm{T}}}(p_{\mathrm{T}})$ (b) $w_{\eta}(\eta)$

Fig. 4.7.: Spline fit to the p_{T} (a) and η (b) projections of $f_{\mathrm{DATA/MC}}$. - Run II

4.4 Reducing Combinatoric

4.4.1 Multivariate Analysis

In classical rectangular-cut based analyses, the signal-candidate selection strongly depends on the discrimination power of the variables used or available. Finding optimal cuts in a high dimensional variable set is challenging and basic rectangular cuts may fail to separate signal from background. A powerful tool to efficiently remove combinatorial background is artificial intelligence [98]. The `TMVA` toolkit [99] of ROOT offers multiple multivariate methods. Given a signal and background sample, these methods learn to transform a set of variables to one variable with strong discrimination power. The classification method chosen is a gradient boosted decision-tree (BDTG), as described the following.

Training Setup

Input Variables: In principle every variable is valid to train the BDTG. However, since we intend an unbiased study of the $\Lambda_b^0 \to D^0 pK$ Dalitz plot, the chosen variables must not be sensitive to the Λ_b^0 mass and Dalitz variables. Therefore we chose topological and basic kinematical variables as listed in table 4.6. Additionally the χ^2 of the DTF improves the training, as the fit of true signal events tends to converge to smaller χ^2. The comparison between the signal and background distributions of all classification variables can be found in the appendix E.1 and their correlation in E.2. To eliminate linear correlations for Gaussian distributed variables, the classifier performs a principal component analysis (PCA) [100] prior to the training.

Tab. 4.6.: Variables used for training the classifier.

	Λ_b^0	D^0	p	h^-	$h^-_{D^0}$	$h^+_{D^0}$
$\chi^2_{\mathtt{DecayTreeFit}}$	x					
$\theta_{\mathrm{dira}}(\mathrm{PV})$	x					
$\ln \chi^2_{\mathrm{IP}}(\mathrm{rel.V})$	x	x	x	x	x	x
p_{T}	x	x		x	x	x
η	x					
$S_{c\tau} = \frac{c\tau}{\mathrm{error}}$	x	x				

Training Candidates: Our training is based on learning features from labelled samples, known as supervised training [98]. We use truth-matched $\Lambda_b^0 \to D^0pK$ MC as signal and extract a sample of combinatorial background from DATA. The preselections are applied to both samples and they are split randomly to sets of equal size for training and testing. MC of different D^0 modes is merged and corrected according to section 4.3.3.

Tab. 4.7.: Training and testing candidates.

	Signal (MC)	Background (DATA)
2011	$41,995$	$315,802$
2012	$59,815$	$781,714$
Run II	$4,572,722$	$3,073,206$

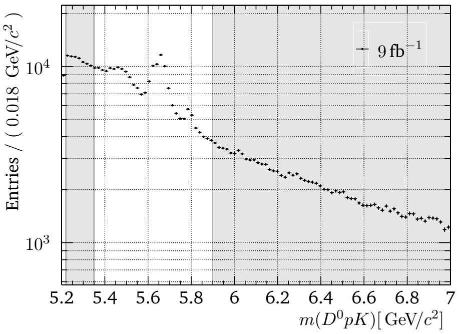

Fig. 4.8.: Visualisation of sideband boundaries used for training. A temporary cut of $P_{NN,p}(p) > 0.8$ is applied besides the general preselections.

The Λ_b^0-signal sideband in DATA is used as the background sample. Even though it is possible to use impure samples to train a classifier [101], we aim to select a sideband region with almost no signal contribution. As the Λ_b^0 signal is not clearly visible at this point we apply a temporary high cut on the proton PID. We find a lower sideband $m(D^0pK) \in [5.22, 5.35]$ GeV/c^2 and an upper sideband $[5.9, 7.0]$ GeV/c^2, as visualised in figure 4.8. As we use momentum dependent input variables choosing only one sideband could limit the performance of the training. In appendix E.4 we tested trainings with exclusive left (right) or both sidebands and chose to use both. Table 4.7 lists the number of available signal and background candidates. The samples are randomly split to an equal size to train and test the classifier.

Boosted Decision Tree

A decision tree, as in figure 4.9, splits a data sample at each node based on its features. The final nodes result into a label or probability. Each decision aims to gain most information possible, where the information gain is defined as entropy difference caused by the split. The entropy is maximal for an equal split and minimal for a full acceptation or rejection. During training the condition of a split-node is found by minimising the entropy. Split-nodes are added till a termination criterion, like a maximum tree depth or minimal information gain, is reached.

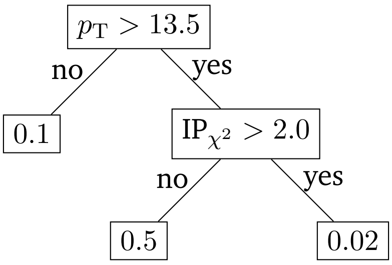

Fig. 4.9.: Schematic of a decision tree.

To reduce bias and error [102] one can utilise multiple 'weak learners' and combine these into a 'strong' classifier [103], called boosting. The output more specifically label prediction of the boosted decision-tree (BDT) is $\hat{y} = \sum_i w_i t_i(x)$, with the output of a single tree $t_i(x)$

and a weight w_i based on its accuracy. Each tree is generated iteratively and data samples are weighted according to their importance after each iteration step. During training the BDT minimises the objective function $O(x) = \sum_j L(\hat{y}_j, y_j) + \sum_i R(f_i)$. The loss function $L(\hat{y}, y)$ calculates for every sample the distance of its label prediction $\hat{y}$ to the true label y. Additionally a regularisation term $R(f_i)$ penalises the complexity f_i of every tree, which should prevent overfitting [104].

There are multiple approaches to add a 'weak learner' to the training ensemble. To name a few next to the chosen gradient descent boosting [105], there are adaptive boosting [106] or randomised trees [99] similar to random forests [107]. The benefit of a BDTG over adaptive boosting is its modified exponential loss to a binomial log-likelihood loss $L(\hat{y}, y) = \ln(1 + \exp(-2\hat{y}y))$. It is therefore more robust in presence of noise as the basic exponential.

A BDTG is defined by a set of tuning parameters that change its learning behaviour and are optimised in preliminary studies. The number of trees is set to 400 (800) for Run I (II), with 20 cuts and a maximum tree-depth of five. The learning rate (shrinkage) of the gradient boost is set to 0.1. The separation criterion for node splitting is calculated from the information gain $p \cdot (1 - p)$ (GiniIndex), where p is the probability of a specific class found in a feature. An improvement was also found during the optimisation by training on re-sampled data (bagging), where the sample fraction is 60% (40%) for Run I (II). All other options are the default values of a `TMVA` BDT. More extensive descriptions are found in [99].

The Training Result is visualised by the distribution of the classification variable c_{BDTG} in figure 4.10. The c_{BDTG} distributions show good agreement between training and testing for signal and background samples. The Kolmogorow-Smirnow test [96] indicates no failure. The receiver operating characteristic (ROC) in figure 4.10 plots the classifiers background suppression $(1 - \epsilon_{\text{bkg}})$ against its signal efficiency ϵ_{sig}. It is an intuitive way to visualise the classifier performance [108]. Where a diagonal from $(\epsilon_{\text{sig}}, 1 - \epsilon_{\text{bkg}}) = (0, 1)$ to $(1, 0)$ would represent 'pure luck' in the classification, the ROC of the present training can be considered as sufficient. Evaluation-results including overtraining tests are in appendix E.3.

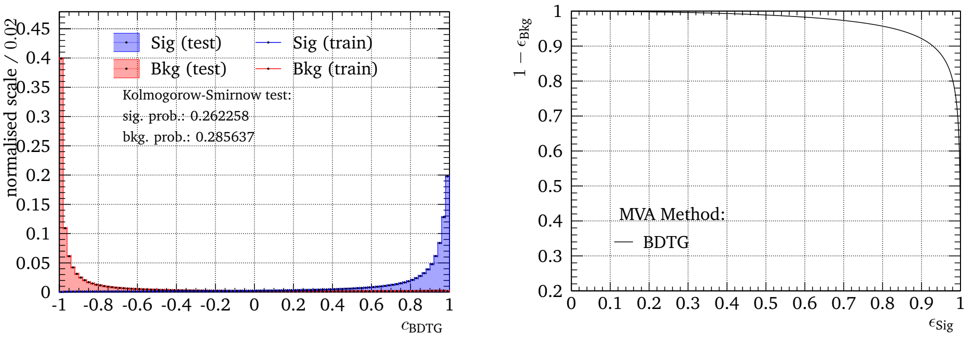

(a) c_{BDTG}

(b) ROC

Fig. 4.10.: Distribution of c_{BDTG} (a) and ROC (b) for Run II. (Run I result in appendix E.3)

4.4.2 Optimisation of Classifier & PID Selection

We use PID cuts on the hadron final states to filter for particle mis-ID in combination with the trained classifier of section 4.4.1 to reduce combinatorial background (B). The optimisation of the selections is found by comparing the signal count (S) with the respective Poisson uncertainty of the candidates in the signal region. This Figure of Merit (FoM) is calculated as

$$S_{\mathrm{FoM}} = \frac{S}{\sqrt{S+B}} = \frac{\epsilon_S S_0}{\sqrt{\epsilon_S S_0 + \epsilon_B B_0}} \quad , \tag{4.3}$$

where the subscript 0 indicates S or B before the cut to be optimised. The signal efficiencies ϵ_S are determined from weighted signal MC and the background efficiencies ϵ_B from DATA sidebands. We extract S_0 and B_0 only from DATA. Therefore the sum of a background and signal model is fit to the Λ_b^0 candidates mass distribution, yielding S_0, the signal width σ_S and peak value μ_S. Then the background model is fit to the lower and upper sidebands.

By extrapolating the latter exponential into the signal region $|m(D^0 p h^-) - \mu_S| < 3\sigma_S$ we can calculate B_0. Cuts for Run I and II are optimised separately. Each optimisation uses data samples with the previously optimised cuts applied. The fit models and results can be found in appendix F.

We find $P_{NN,p}(p) > 0.46$ (0.86) for Run I (II), as visualised in fig. 4.11a. As the D^0 daughters are K and π particles, the PID cuts on the respective particle types are scanned simultaneously and are visualised as contour plot in fig. 4.11b. We chose $P_{NN,K}(K_{D^0}) > 0.1$ and $P_{NN,\pi}(\pi_{D^0}) > 0.1$. The optimal cut on the classification variable is $c_{\mathrm{BDTG}} > 0.43$ (0.5) for Run I (II), as visualised in fig. 4.12a. Due to the high branching fraction of $\Lambda_b^0 \to D^0 p\pi$ compared to $\Lambda_b^0 \to D^0 pK$ [20], we test to not only filter with a cut on $P_{NN,K}(K^-)$ but to also cut against a π with $P_{NN,\pi}(K^-)$. Again the significance by the FoM is visualised as a contour plot in fig. 4.12b. We find $P_{NN,K}(K^-) > 0.34$ (0.54) for Run I (II). An additional cut on $P_{NN,\pi}(K^-)$ is not sufficient, which is to expect, as the $P_{NN,x}$ PID variables are trained to filter for a specific particle type.

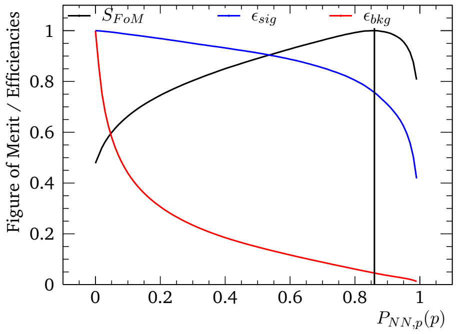

(a) Proton PID (Run II)

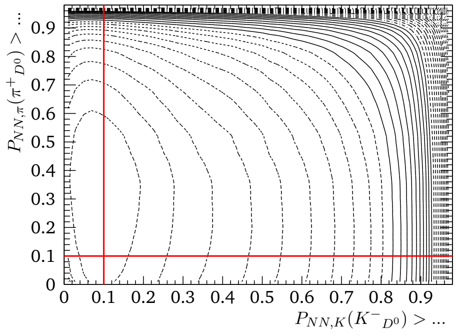

(b) D^0 daughter PID (FoM, Run II)

Fig. 4.11.: FoM and Efficiencies for the PID selection of the proton and the D^0 daughters. The chosen cuts values are shown as lines. (Run I in fig. F.5)

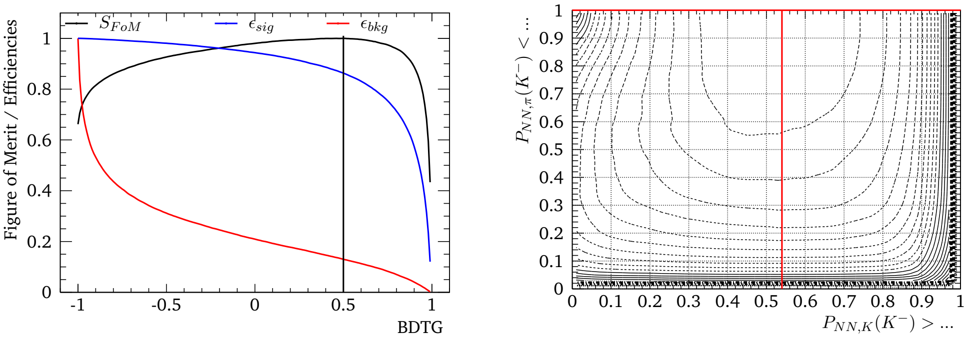

(a) Classifier (Run II)

(b) Kaon PID (FoM, Run II)

Fig. 4.12.: FoM and Efficiencies for the classifier and kaon PID selection. The chosen cuts values are shown as lines. (Run I in app. F.5)

4.5 Background Studies

After the preliminary preselections and the optimised PID and Classifier selections of sections 4.2 and 4.4.2 we still expect various contributions in the distribution of the $m(D^0pK)$ candidates. This can be seen in figure 4.13. Next to the signal peak of the Λ_b^0 (Ξ_b) at about $5.62\,\mathrm{GeV}/c^2$ ($5.8\,\mathrm{GeV}/c^2$) there is a clear contribution of $\Lambda_b^0 \to D^0 p\pi$ mis-ID right to the Λ_b^0 signal shoulder and partially reconstructed decays to masses below $5.5\,\mathrm{GeV}/c^2$. In this section we investigate in the identification and further suppression of such backgrounds.

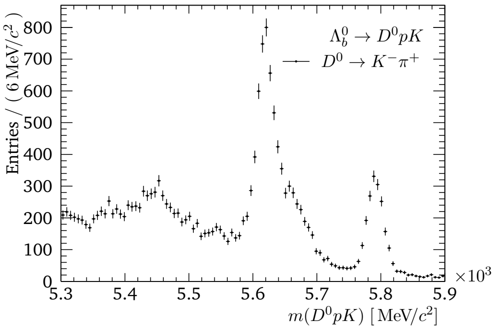

Fig. 4.13.: Interim $m(D^0pK)$ distribution of the $D^0 \to K^-\pi^+$ DATA samples, with the preselection and optimised cuts applied.

4.5.1 Mis-Identification of Particle Types

The determination of the particle types is not perfect and selections via the PID variables only filter for particles with a higher probability to be the specific particle type. Therefore we have to consider similar decays where the mis-ID of a particle results into the signal decay. During reconstruction the mass of a 'particle object' is based on the knowledge of the particle type, therefore a misidentified particle results in a peak-shifted and distorted mass distribution of the original decay.

First of all we account for a cross-feed of the Cabibbo favoured mode to the other D^0 modes. In section 4.4.2 we already enforced the particle type of the D^0 daughters with $P_{\mathrm{NN},\{K,\pi\}} > 0.1$. In figure 4.14 we compare the mass distributions for $m(KK)$ and $m(\pi\pi)$, reconstructed from $D^0 \to K\pi$ MC, to the selection area of the D^0 mass. The MC candidates are signal matched for their D^0 sub-decay. We expect the cross-feed of $D^0 \to K^-\pi^+$ to the $D^0 \to \{KK, \pi\pi\}$ modes to be negligible.

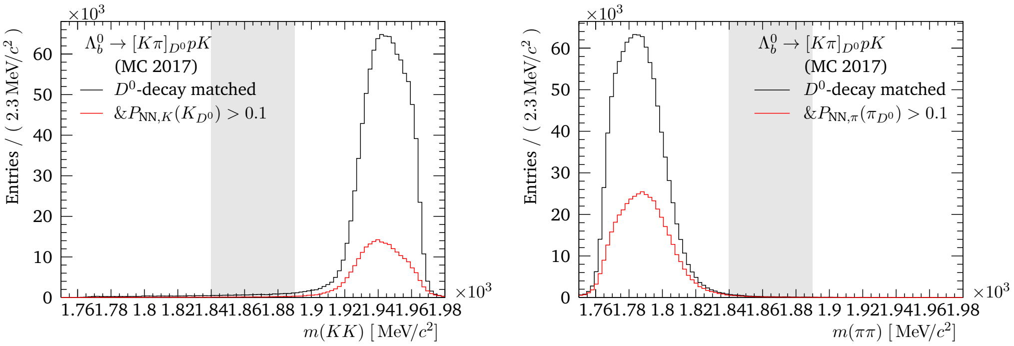

Fig. 4.14.: Distribution of $m(KK)$ and $m(\pi\pi)$ from $D^0 \to K\pi$ simulation. The D^0 candidates are matched to the simulated D^0 decay. The candidates are shown with (red) and without (black) their PID selection of $P_{\mathrm{NN},\{K,\pi\}} > 0.1$. The required $m(D^0)$ window of the preselections is highlighted in grey. - MC 2017

A further mis-ID distribution in $m(D^0pK)$ emerges form the normalisation channel $\varLambda_b^0 \to D^0p\pi$. As the misidentified π is lighter than the assumed K we expect a shift to higher masses. We can see its distribution in figure 4.13 right on the $\varLambda_b^0$ signal shoulder. The PID selections have already been optimised in section 4.4.2 for an optimal signal to background ratio. Furthermore there is the possibility of a contribution of the signal $\varLambda_b^0 \to D^0pK$ in the $m(D^0p\pi)$ distribution. However as $\mathcal{B}(\varLambda_b^0 \to D^0p\pi)$ is about a factor ten greater than $\mathcal{B}(\varLambda_b^0 \to D^0pK)$ [20] this contribution is small. We chose to cut against the K hypothesis of $P_{\mathrm{NN},K}(\pi) < 0.5$ and for the π hypothesis $P_{\mathrm{NN},\pi}(\pi) > 0.5$. For more detail see appendix G.1.

Finally there could be mis-ID background from $\{B_s^0/B^0\} \to D^0KK$, where a K is misidentified as a p. However these contributions are negligible, which conveys, when considering the comparison of the rescaled MC with all selections applied in section 4.5.5.

4.5.2 Partially Reconstructed Decays

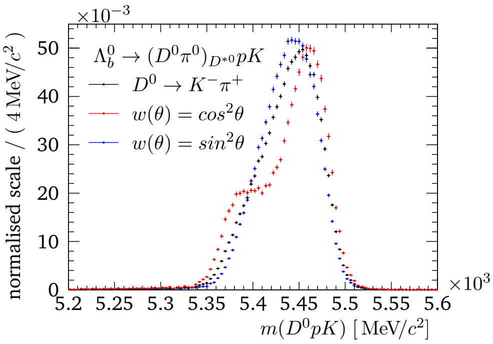

Fig. 4.15.: $m(D^0pK)$ for (un)polarised D^{*0}, by weighting in θ_{π^0} of $\varLambda_b^0 \to [D^0\pi^0]_{D^{*0}}pK$. - MC 2018

The already mentioned enhancement below the $\varLambda_b^0$ signal in fig. 4.13 is associated to partially reconstructed decays, where the neutral particle is not reconstructed. We account for $\{\varLambda_b^0, \varXi_b\} \to D^{*0}p\{K/\pi\}$. The available simulation considers the most probable $D^{*0} \to \{\pi^0, \gamma\}D^0$ modes.

The mass distribution has got a dependence on the polarisation of the D^{*0} [109, 110] the MC does not account for. We overcome this issue by weighting the helicity angle $\theta_{\pi^0} = \hat{p}_{\pi^0}^{(D^{*0})} \cdot \hat{p}_{D^{*0}}^{(\varLambda_b^0)}$ of the missing π^0. We use the weight function $w(\theta_{\pi^0}) = \cos^2\theta_{\pi^0}$

for $J_{m,D^{*0}} = 0$ and $w(\theta_{\pi^0}) = 1 - \cos^2\theta_{\pi^0} = \sin^2\theta_{\pi^0}$ for $J_{m,D^{*0}} = \pm1$. The polarisations $J_{m,D^{*0}} = \pm1$ are indistinguishable and in case of equal distribution of the events and no preference in polarisation the D^{*0} would be unpolarised.

The D^{*0} polarisation has got a visible effect on distorting the mass distribution of Λ_b^0 candidates, as it is shown for $\Lambda_b^0 \to [D^0\pi^0]_{D^{*0}}pK$ in figure 4.15. The double peak structure, as it forms for $J_{m,D^{*0}} = 0$, is easily explained, when considering the correlation plot of $\cos\theta_{\pi^0}$ and the Λ_b^0 mass distribution in appendix G.6. $\Lambda_b^0 \to D^*p\pi$ in $m(D^0p\pi)$ behaves similar, but the mis-ID distributions of both show no significant effect, as shown in appendix G.2.

Tab. 4.8.: Reduced stripping sel. for `RapidSim`.

p_T(track)	$>$	$0.1\,\mathrm{GeV}/c$
p(track)	$>$	$1.0\,\mathrm{GeV}/c$
$\sum_{D^0,\mathrm{dau.}} p_\mathrm{T}$	$>$	$1.8\,\mathrm{GeV}/c$
$\lvert m(D^0) - m_\mathrm{PDG}\rvert$	$<$	$0.1\,\mathrm{GeV}/c^2$
$m(\Lambda_b^0)$		$5.2 \to 7.0\,\mathrm{GeV}/c^2$
$\sum_{\Lambda_b^0,\mathrm{dau.}} p_\mathrm{T}$	$>$	$5.0\,\mathrm{GeV}/c$
$\tau_{\Lambda_b^0}$	$>$	$0.2\,\mathrm{ps}$

As we do not have simulation for the $\Xi_b \to D^{*0}ph$ modes available we use `RapidSim` [111], a lightweight application for fast phase space simulation, to compare the expected shapes of the Ξ_b modes to the ones of Λ_b^0. `RapidSim` already offers to apply a `DecProdCut`-like LHCb acceptance cut, similar to the full simulation in section 3.2.6, but not all variables are available. We can only apply kinematic- and lifetime-cuts, as listed in table 4.8, of the stripping selections in section 4.2.1.

We generate 10^5 candidates of $\Xi_b \to D^{*0}pK$ for each mode. The Λ_b^0 candidate mass distributions for the missing neutral particle are compared in figure 4.16, with the D^{*0} modes weighted according to their branching fraction and the Λ_b^0 mode shifted by the measured difference $|m_{\Xi_b} - m_{\Lambda_b^0}| = 172.5 \pm 0.4$ [20]. With all mentioned cuts applied we find a sufficient agreement between the mass distributions. Further the partially reconstructed mode shows the same mass difference as the nominal Λ_b^0 and Ξ_b masses, with the caveat, that the partially reconstructed Ξ_b mode shares its maximum peak value with the nominal Λ_b^0 mass. We assume the Ξ_b shapes to be representable by the shifted Λ_b^0 shapes, but they may show different D^{*0} polarisations.

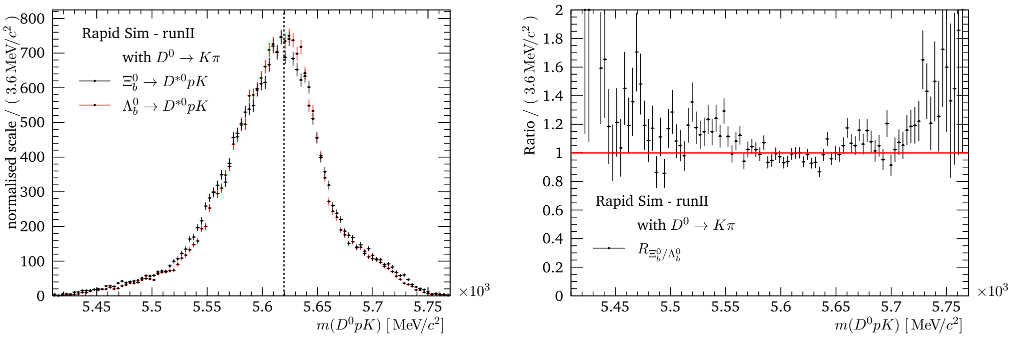

Fig. 4.16.: Distribution of $m(D^0pK)$ (left) for $\Xi_b \to D^{*0}pK$ and $\Lambda_b^0 \to D^{*0}pK$ shifted by $|m_{\Xi_b} - m_{\Lambda_b^0}| = 172.5 \pm 0.4$ [20]. The nominal Λ_b^0 mass is highlighted via a dashed line (left) and the ratio of the histograms is shown (right). - `RapidSim` Run II

4.5.3 $\varLambda_c^+$ Veto

The branching fractions of three-body $\varLambda_c^+$ decays like $\varLambda_c^+ \to ph^-h^+$ are about 10^2 to 10^3 times greater than $\mathcal{B}(\varLambda_b^0 \to D^0pK)$ [20]. Therefore we check for $\varLambda_c^+$ peaks in $m(ph^-_{D^0}h^+_{D^0})$ and $m(ph^-_{\varLambda_b^0}h^+_{D^0})$ in appendix G.3. We apply a $\varLambda_c^+$ veto against $m(ph^-_{\varLambda_b^0}h^+_{D^0}) \in [2.26, 2.30]\ \mathrm{GeV}/c^2$ for $\varLambda_b^0 \to D^0pK$ except the $D^0 \to KK$ mode and for $D^0 \to \pi\pi$ for $\varLambda_b^0 \to D^0p\pi$. The $\varLambda_c^+$ vetoed regions are shown in figure G.7.

4.5.4 Charmless Background

Another background to consider emerges from $\{\varLambda_b^0, \varXi_b\} \to ph^-h^+h^-$ decays, a charmless background, where the mother does not decay to the intermediate D^0. The risk of this background type is it's location almost at the nominal $\varLambda_b^0$ or $\varXi_b$ mass and no possibility to veto. When considering all possible D^0 modes for $\varLambda_b^0 \to D^0ph$ and $\varXi_b \to D^0pK$, we find by skipping the D^0 the matching combinations of table 4.9. The $\varXi_b$ branchin fractions are estimated by

$$\frac{\mathcal{B}(\varXi_b \to ph^-h^+h^-)}{\mathcal{B}(\varXi_b \to D^0pK)\mathcal{B}(D^0)} = \frac{f_{\varXi_b}}{f_{\varLambda_b^0}}\mathcal{B}(\varXi_b \to ph^-h^+h^-) \times \frac{f_{\varLambda_b^0}}{f_{\varXi_b}}\frac{\mathcal{B}(\varLambda_b^0 \to D^0pK)}{\mathcal{B}(\varXi_b \to D^0pK)} \times \frac{1}{\mathcal{B}(\varLambda_b^0 \to D^0pK)} \times \frac{1}{\mathcal{B}(D^0)} \quad . \tag{4.4}$$

The charmless decays get enhanced up to 10^2 when considering the D^0 branching fraction.

Tab. 4.9.: Possible combinations of the charmless four-body $\varLambda_b^0$ and $\varXi_b$ decays with $\varLambda_b^0 \to [h^-h^+]_{D^0}ph$ are listed with their approximated $\mathcal{B}$ ratio. The used branching fractions can be found in appendices A.1 and A.3.

Charmless Mode	DATA Sample	$\frac{\mathcal{B}(\varLambda_b^0 \to ph^-h^+h^-)}{\mathcal{B}(\varLambda_b^0 \to D^0ph)\mathcal{B}(D^0)}$	$\frac{\mathcal{B}(\varXi_b \to ph^-h^+h^-)}{\mathcal{B}(\varXi_b \to D^0pK)\mathcal{B}(D^0)}$
$\{\varLambda_b^0, \varXi_b\} \to pK^-K^+K^-$	$[K^-K^+]_{D^0}pK^-$	$\sim 6.8 \times 10^1$	$\sim 2.2 \times 10^0$
$\varXi_b \to pK^-K^-\pi^+$	$[K^-\pi^+]_{D^0}pK^-$		$\sim 2.2 \times 10^0$
$\varLambda_b^0 \to pK^-K^+\pi^-$	$[K^+\pi^-]_{D^0}pK^-$	$\sim 5.9 \times 10^2$	
	$[K^-K^+]_{D^0}p\pi^-$	$\sim 1.6 \times 10^0$	
$\{\varLambda_b^0, \varXi_b\} \to pK^-\pi^+\pi^-$	$[\pi^-\pi^+]_{D^0}pK^-$	$\sim 7.6 \times 10^2$	$\sim 6.5 \times 10^1$
	$[K^-\pi^+]_{D^0}p\pi^-$	$\sim 2.1 \times 10^0$	
$\varLambda_b^0 \to p\pi^-\pi^+\pi^-$	$[\pi^-\pi^+]_{D^0}p\pi^-$	$\sim 5.6 \times 10^1$	

In DATA, when all previous selections are applied, the $\varLambda_b^0 \to ph^-h^+h^-$ decays are very much present in $\varLambda_b^0 \to D^0pK$, with $D^0 \to \{KK, \pi\pi\}$ and $\varLambda_b^0 \to [KK]_{D^0}p\pi$. As shown in appendix G.4.1 we are not able to remove the charmless background in $m([\pi\pi]_{D^0}pK)$, while maintaining sufficiently enough $\varLambda_b^0$ signal for an amplitude analysis. The $D^0 \to KK$ channel on the other hand seems manageable, as appendix G.4.2 shows. The charmless $\varXi_b$ decays are expected to be negligible and will contribute as systematic uncertainty for $\varXi_b$ related measurements.

In appendix G.4.3 we study the D^0 lifetime distribution from signal candidates in the Λ_b^0 signal window, to get an impression of the $\Lambda_b^0 \to D^0 ph$ signal peak purity. Therefore the $c\tau_{D^0}$ distributions of $\Lambda_b^0 \to D^0 pK$ and $\Lambda_b^0 \to D^0 p\pi$ signal candidates, with $D^0 \to KK$, are fit with an unbinned simultaneous likelihood fit sharing the detector resolution σ_{res} as a parameter. From the fitted functions we calculate for cuts on $c\tau_{D^0}$ the fractions of charm $f(D^0 ph)$ in the signal-region of $\Lambda_b^0 \to D^0 ph$. The result can be seen in fig. 4.17. We chose to cut $c\tau_{D^0} > 0.01$, where we expect to suppress the charmless background to a fraction of $\sim 33\%$ ($\sim 1\%$) in $m([KK]_{D^0} pK)$ ($m([KK]_{D^0} p\pi)$), while retaining about 91% of matched signal MC. We use these fractions as start values in the global $m(D^0 ph)$ fit in section 5.

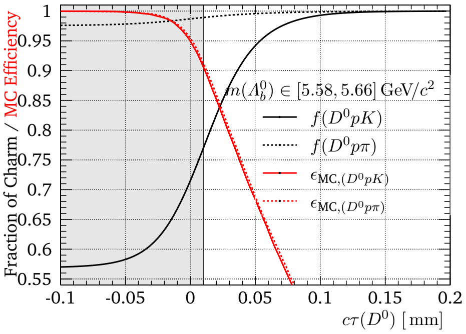

Fig. 4.17.: Fractions of $m([KK]_{D^0} ph)$ charm candidates in approximately 2σ from the nominal Λ_b^0 mass and efficiencies from matched signal MC for various cuts on $c\tau_{D^0}$. The chosen cut is visualised by a grey overlay. The fractions are extracted from a fit to the $c\tau_{D^0}$ distribution in appendix G.4.3.

4.5.5 Summary of Background Contributions & Final DATA Samples

We use the relative scaling factors of section 4.3.1 to scale the background simulations and re-normalise them by the number of generated events from table C.1 to match the $\Lambda_b^0 \to D^0 ph$ reference samples. This can be seen for all charm contributions of this chapter in fig. 4.18 and in appendix G.4.4 for all charmless MC, which is mostly a first approximation. We find the contributions of $\{B_s^0/B^0\} \to D^0 KK$ in $m(D^0 ph)$ to be negligible for the global fit in chapter 5. Further we do not consider $\Lambda_b^0 \to D^0 pK$ mis-ID in $m(D^0 p\pi)$. The $m(D^0 pK)$ samples will have an additional Ξ_b contribution as signal and partially reconstructed decays. Finally we will also have charmless background from $\Lambda_b^0 \to pKKK$ in the $D^0 \to KK$ samples.

Figures 4.19 and 4.20 show the mass distribution for the final selection of the $\Lambda_b^0 \to D^0 ph$ candidates from DATA split into the four D^0 modes. The comparison to the scaled MC in fig. 4.18 shows a good agreement of the considered backgrounds.

As already stated in section 4.5.4 we won't use the $D^0 \to \pi\pi$ samples for the further analysis. After the suppression of the charmless background, their number of events won't be sufficient for the amplitude analysis in chapter 6. Additionally we will also leave the $D^0 \to K^+\pi^-$ samples untouched. This is mostly due to the same reason, as the charmless signal in $m([K^+\pi^-]_{D^0} pK)$ is expected to have an enhancement of about 10^2 according to table 4.9. Further we see an enhancement of the partially reconstructed peak in $m([K^+\pi^-]_{D^0} pK)$ compared to the other samples. This enhancement could be due to partially reconstructed $\Lambda_b^0 \to [\overline{D}^{*0} K^-]_{D_s^{*-}} p$, where $\overline{D}^{*0} \to \overline{D}^0 x^0$. However, this would require an excited D_s^{*-} favouring a decay to D^* over D^0, like $D_{s1}(2536)^+ \to D(2007)^0 K^+$. In addition to that we would have a $\overline{D}^0$ and therefore see the charge-conjugated Cabibbo favoured mode, which could also explain the enhancement.

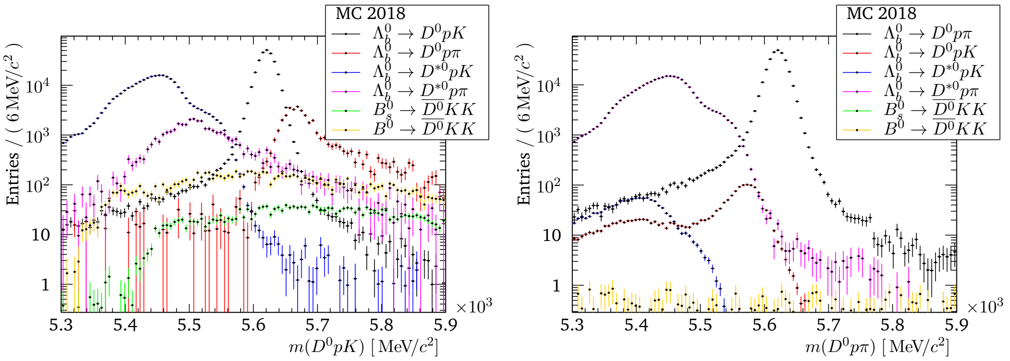

Fig. 4.18.: Comparison of different charm background contributions in $m([K^-\pi^+]_{D^0}ph)$ with all selections applied and re-normalised to match the $\Lambda_b^0 \to D^0ph$ reference signal MC. The background MC has been scaled according to their relative scaling factors in table 4.3 - MC 2018

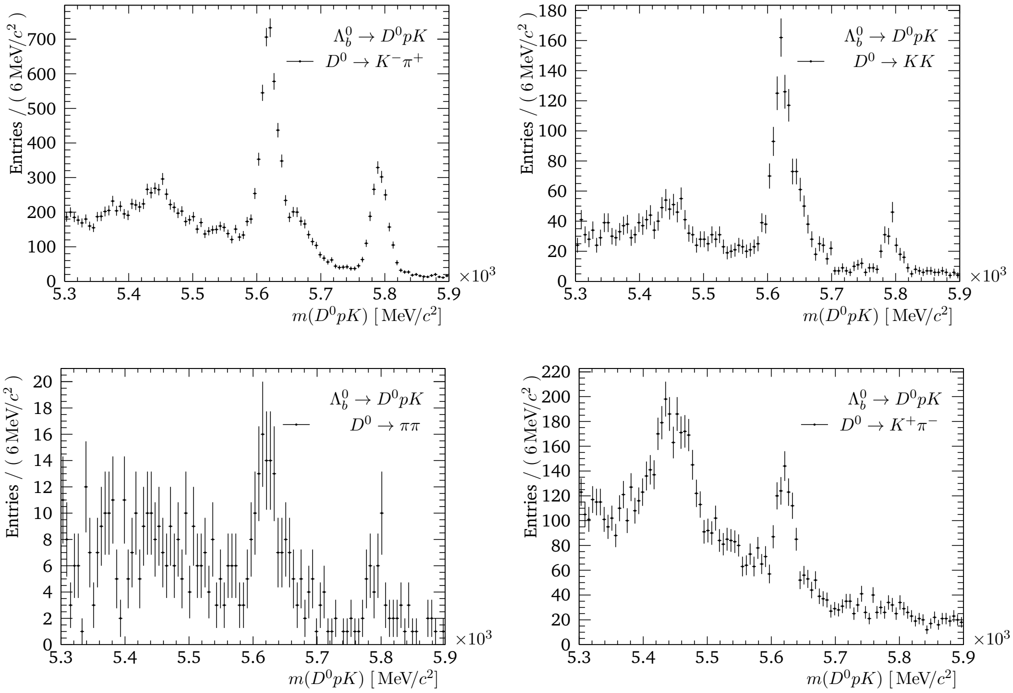

Fig. 4.19.: Distributions of $m(D^0pK)$ candidates with all cuts applied - DATA

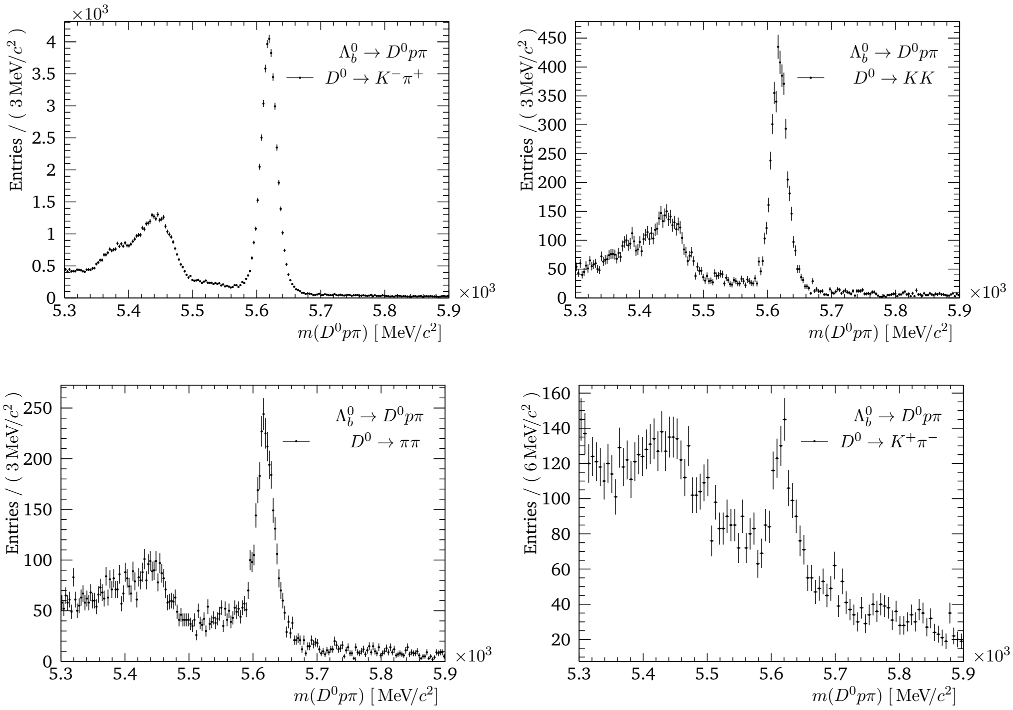

Fig. 4.20.: Distributions of $m(D^0 p\pi)$ candidates with all cuts applied - DATA

4.6 Efficiencies

To normalise $\Lambda_b^0 \to D^0 pK$ to $\Lambda_b^0 \to D^0 p\pi$ in the global fit in chapter 5, we need to know the total efficiency ϵ_{tot} of the Λ_b^0 candidate selection. The efficiency is calculated by dividing the number of signal events after all selections N_{sig} by the number of all signal events N_0. For simplicity we will determine the efficiency factorised for the different selection steps.

Each efficiency is extracted from signal MC. The number of signal candidates before and after a specific selection is determined from an extended maximum likelihood fit to their $m(D^0 ph)$ distribution. Again we use RooFit [112] to fit a double Gaussian function to the Λ_b^0 signal. The combinatorial background visible in unmatched MC is described by an exponential function. For convenience we only show a fit-example of the general idea in fig. 4.21. As we use signal MC to calculate the efficiency N_0 equals with the number of generated events. The number of events after a selection is N_{sel}. To compare efficiencies from different samples, they have to be determined in the same order, which is

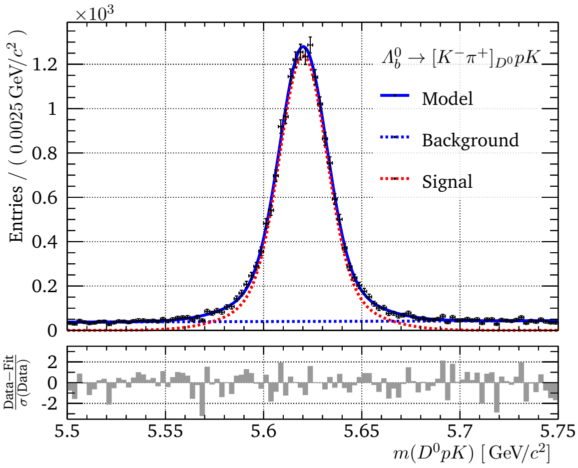

Fig. 4.21.: Fit-example for the efficiency calculation to all $m(D^0pK)$ candidates with $D^0 \to K^-\pi^+$ we find after the `DecayTreeFit`. - MC 2012

$$\epsilon_{\text{tot}} = \epsilon_{\text{Acc}} \cdot \epsilon_{\text{Strip}} \cdot \epsilon_{\text{DTF}} \cdot \epsilon'_{\text{PreSel}} \cdot \epsilon_{p-\text{PID}} \cdot \epsilon_{h^{\pm}_{D^0}-\text{PID}} \cdot \epsilon^{\text{L0}} \cdot \epsilon_{\text{BDTG}} \cdot \epsilon_{h^-_{\Lambda_b^0}-\text{PID}} \cdot \epsilon_{c\tau_{D^0}} \cdot \epsilon_{\Lambda_c^+-\text{Veto}} \cdot \tag{4.5}$$

The following visualisation must not follow this order. For simplicity an error weighted average is calculated, when possible. All values can be found in appendix H.

The Detector Acceptance is already measured during the generation phase of the simulation by counting the amount of signal events N_{Acc}, where all daughter particles are in the detector acceptance. Thus the previously mentioned fit is not needed. The detector acceptance efficiency is calculated as $\epsilon_{\text{Acc}} = N_{\text{Acc}}/N_0$, where N_0 is the number of generated events. Figure 4.22 shows ϵ_{Acc} for different years and samples.

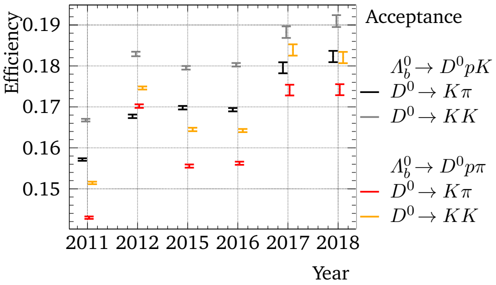

Fig. 4.22.: Detector acceptance efficiencies.

Tab. 4.10.: Preselection Efficiencies (no stripping and DTF).

	$\Lambda_b^0 \to D^0pK$	$\Lambda_b^0 \to D^0p\pi$
$D^0 \to K\pi$	$(72.254 \pm 0.029)\,\%$	$(71.136 \pm 0.030)\,\%$
$D^0 \to KK$	$(74.495 \pm 0.029)\,\%$	$(73.419 \pm 0.030)\,\%$

The Preselection Efficiencies, as shown in fig. 4.23, have the stripping and the DTF efficiency $\epsilon_{\text{Strip}}\epsilon_{\text{DTF}} = N_{\text{DTF}}/N_{\text{Acc}}$ separated. This is due to the fact, that the datasets used for the efficiency fit are available after the reconstruction by the DTF and stripping is already applied by the LHCb software chain. We use the error weighted average over all years for the remaining preselection efficiencies $\epsilon'_{\mathrm{PreSel}} = N_{\mathrm{PreSel}}/N_{\mathrm{DTF}}$, as listed in table 4.10.

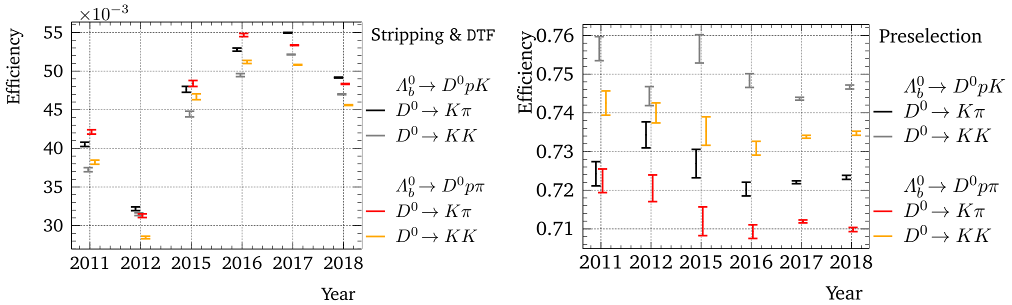

Fig. 4.23.: Preselection efficiencies (right), with stripping and DTF (left) separated.

PID Efficiencies are determined directly from the MC samples, as we use PID corrected MC, which is mentioned in section 4.3. We calculate the efficiency of the proton PID cut $\epsilon_{p-\mathrm{PID}} = N_{p-\mathrm{PID}}/N_{\mathrm{PreSel}}$, of the D^0 daughter PID cuts $\epsilon_{h^\pm_{D^0}-\mathrm{PID}} = N_{h^\pm_{D^0}-\mathrm{PID}}/N_{p-\mathrm{PID}}$ and of the cut on the kaon or pion from the Λ_b^0 as $\epsilon_{h^-_{\Lambda_b^0}-\mathrm{PID}} = N_{h^-_{\Lambda_b^0}-\mathrm{PID}}/N_{\mathrm{BDTG}}$. The efficiencies are visualised in figs. 4.24 and 4.25. Again we find error weighted averages, as listed in table 4.11. Further $\epsilon_{p-\mathrm{PID}}$ and $\epsilon_{h^\pm_{D^0}-\mathrm{PID}}$ will cancel in the ratio $\epsilon_{\Lambda_b^0\to D^0pK}/\epsilon_{\Lambda_b^0\to D^0p\pi}$.

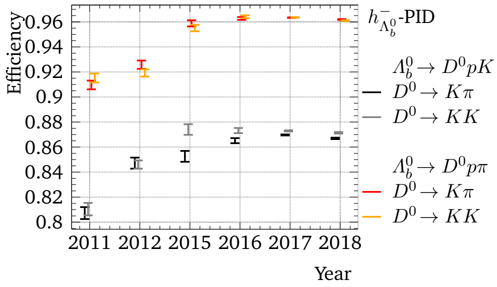

Fig. 4.24.: $h^-_{\Lambda_b^0}$ − PID efficiency.

Tab. 4.11.: Uncertainty weighted average of the PID efficiencies in %.

	$p-\mathrm{PID}$	$h^\pm_{D^0}-\mathrm{PID}$		$h^-_{\Lambda_b^0}-\mathrm{PID}$	
		$D^0 \to K\pi$	$D^0 \to KK$	$\Lambda_b^0 \to D^0pK$	$\Lambda_b^0 \to D^0p\pi$
2011	57.78 ± 0.20	94.58 ± 0.17	91.61 ± 0.22	80.88 ± 0.34	91.23 ± 0.25
2012	63.70 ± 0.18	96.59 ± 0.14	93.50 ± 0.15	84.64 ± 0.26	92.20 ± 0.22
Run II	74.913 ± 0.017	97.034 ± 0.011	94.506 ± 0.015	87.048 ± 0.024	96.282 ± 0.014

BDTG Cut Efficiencies are calculated from $\epsilon_{\mathrm{BDTG}} = N_{\mathrm{BDTG}}/N_{\mathrm{Trigger}}$. The efficiencies are visualised in fig. 4.26. Again we find error weighted averages, as listed in table 4.12.

Tab. 4.12.: Error weighted average of $\epsilon_{\mathrm{BDTG}}/\,\%$.

	$\Lambda_b^0 \to D^0pK$	$\Lambda_b^0 \to D^0p\pi$
Run I	84.21 ± 0.19	82.04 ± 0.21
Run II	85.916 ± 0.023	84.786 ± 0.024

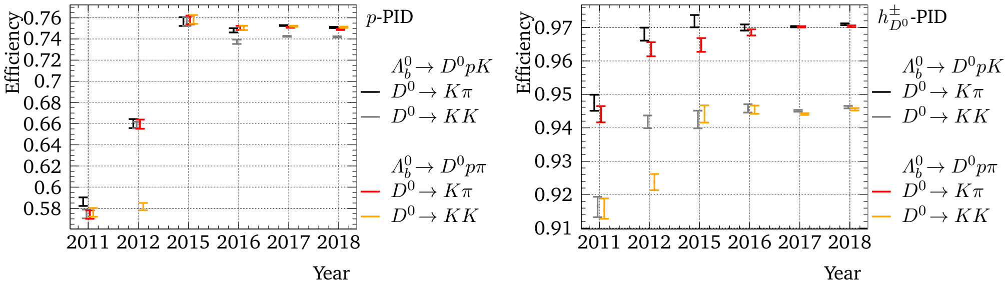

Fig. 4.25.: p and $h^\pm_{D^0}$ PID efficiencies. They cancel in the ratio of $\Lambda_b^0 \to D^0 pK$ to $\Lambda_b^0 \to D^0 p\pi$.

$c\tau_{D^0}$ and Λ_c^+ Veto Efficiencies are calculated by $\epsilon_{c\tau_{D^0}} = N_{c\tau_{D^0}}/N_{h^-_{\Lambda_b^0}-\text{PID}}$ and $\epsilon_{\Lambda_c^+\text{-veto}} = N_{\Lambda_c^+\text{-veto}}/N_{c\tau_{D^0}}$. Figure 4.27 shows the efficiencies, which both cancel in the ratio $\epsilon_{\Lambda_b^0 \to D^0 pK}/\epsilon_{\Lambda_b^0 \to D^0 p\pi}$. We find their error weighted average to be

$$\begin{aligned} \epsilon_{c\tau_{D^0}} &= (95.111 \pm 0.016)\,\% \\ \epsilon_{\Lambda_c^+\text{-veto}} &= (99.754 \pm 0.004)\,\% \quad . \end{aligned} \tag{4.6}$$

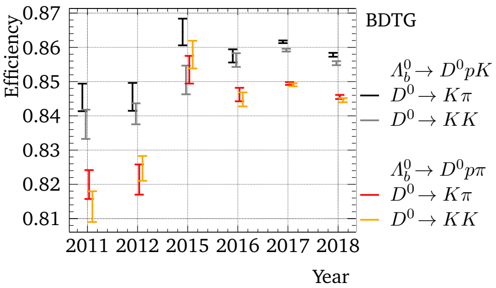

Fig. 4.26.: Efficiencies for applying the classifier.

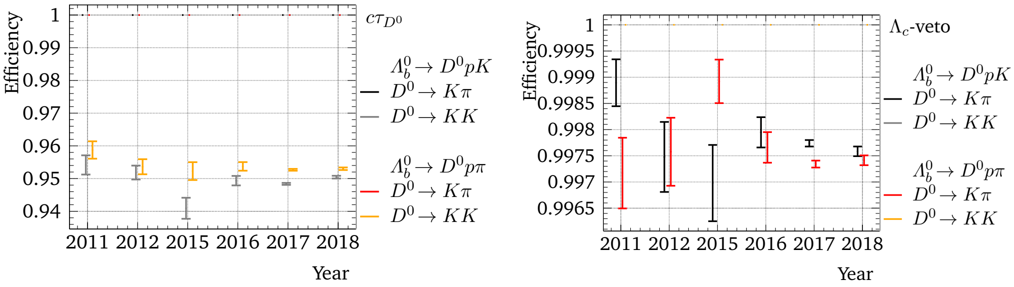

Fig. 4.27.: Efficiencies for applying the $c\tau_{D^0}$ cut on the $D^0 \to KK$ samples (left) and the Λ_c^+ veto on the $\Lambda_b^0 \to D^0 pK$ samples (right).

4.6.1 L0 Trigger Efficiencies

We cannot calculate these efficiencies from MC, as the simulation does not emulate L0 decisions very well. We evaluate the trigger decision at the earliest possible moment in the analysis with a significant signal. We use DATA with the preselection (without trigger), p PID and D^0 daughters PID cuts applied. With the different trigger categories introduced in section 4.2.2, we find the trigger efficiency to be

$$\epsilon_{\texttt{L0}} = \epsilon_{\texttt{TIS}} + \epsilon_{\texttt{TOS}} - \epsilon_{\texttt{TIS}}\epsilon_{\texttt{TOS}} \quad . \tag{4.7}$$

As only events are written to disc, when either TIS or TOS have triggered, we can only determine efficiency fractions that survive the chosen L0 trigger decision via a fit to the DATA distributions. Following the approach of the TISTOS method [91], we assume that the TIS and TOS efficiencies factorise and define them to be

$$\epsilon_{\mathrm{TIS}} = \frac{N_{\mathrm{TISTOS}}}{\epsilon_{\mathrm{TIS}}} \qquad\qquad \epsilon_{\mathrm{TOS}} = \frac{N_{\mathrm{TISTOS}}}{\epsilon_{\mathrm{TOS}}} \quad , \tag{4.8}$$

where N_{TISTOS} is the number of events that have triggered for TIS and TOS. With eqs. (4.7) and (4.8), we find

$$\epsilon_{\mathrm{L0}} = \frac{N_{\mathrm{TISTOS}}(N_{\mathrm{TIS}} + N_{\mathrm{TOS}} - N_{\mathrm{TISTOS}})}{N_{\mathrm{TIS}}N_{\mathrm{TOS}}} \quad . \tag{4.9}$$

The L0 efficiencies determined by the TISTOS method can be found along their ratios in appendix H.1. Figure 4.28 shows the resulting L0 efficiency ratios for the Λ_b^0 decay channels. Even though the different L0 trigger thresholds vary yearly [113–115], we find a luminosity weighted mean efficiency ratio of about one, highlighted as a red line in fig. 4.28. With the same strategy we extract the L0 efficiency ratios for $\Xi_b \to D^0pK$ to $\Lambda_b^0 \to D^0p\pi$ from DATA, summarised in appendix H.1. Considering the extracted L0 efficiency ratios and the simiarity of the decay channels, we set ratios to one and assign a systematic uncertainty in section 5.4.6.

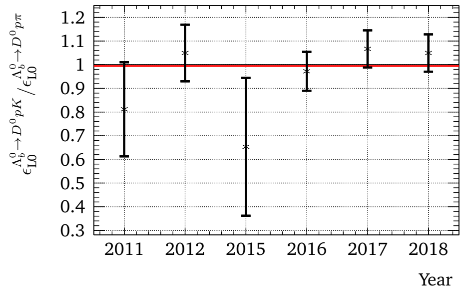

Fig. 4.28.: L0 efficiency ratios for the Λ_b^0 decay channels in the $D^0 \to K^-\pi^+$ samples. The red line highlights the luminosity weighted mean ratio. - DATA

4.6.2 Total Efficiency

When combining all efficiencies, we find the total efficiencies without the L0 trigger, as listed in table 4.13. In the global fit in chapter 5 we will use the year dependent efficiency ratios

$$r_\epsilon = \frac{\epsilon^{D^0\to hh}_{\Lambda_b^0\to D^0p\pi}}{\epsilon^{D^0\to hh}_{\Lambda_b^0\to D^0pK}} \times \frac{\epsilon^{\mathrm{L0}}_{\Lambda_b^0\to D^0p\pi}}{\epsilon^{\mathrm{L0}}_{\Lambda_b^0\to D^0pK}}, \tag{4.10}$$

where $\epsilon^{D^0\to hh}_{\Lambda_b^0\to D^0ph}\epsilon^{\mathrm{L0}}_{\Lambda_b^0\to D^0ph}$ is the product of the above determined efficiencies according to eq. (4.5).

As already stated, the efficiencies $\epsilon_{p-\mathrm{PID}}$, $\epsilon_{h^\pm_{D^0}-\mathrm{PID}}$, $\epsilon_{c\tau_{D^0}}$ and $\epsilon_{\Lambda_c^+-\mathrm{Veto}}$ cancel in the ratio of eq. (4.10). A combined Run II efficiency ratio can be calculated by weighting the efficiencies according to the integrated luminosities $\mathcal{L}$ of the years 2015 to 2018

$$r_\epsilon^{\text{Run II}} = \frac{\sum_{a=15}^{18}\mathcal{L}_a r_\epsilon^a}{\sum_{a=15}^{18}\mathcal{L}_a}. \tag{4.11}$$

Tab. 4.13.: Total efficiencies in %. The `L0` trigger efficiency is being left out, as it is determined as a ratio from the DATA samples.

yr.	$\Lambda_b^0 \to D^0 pK$		$\Lambda_b^0 \to D^0 p\pi$	
	$D^0 \to K\pi$	$D^0 \to KK$	$D^0 \to K\pi$	$D^0 \to KK$
11	0.1708 ± 0.0016	0.1586 ± 0.0015	0.1748 ± 0.0015	0.1601 ± 0.0015
12	0.1706 ± 0.0016	0.1732 ± 0.0014	0.1759 ± 0.0016	0.1564 ± 0.0012
15	0.3170 ± 0.0027	0.2994 ± 0.0026	0.3170 ± 0.0027	0.3099 ± 0.0027
16	0.3502 ± 0.0016	0.3347 ± 0.0016	0.3597 ± 0.0016	0.3392 ± 0.0016
17	0.3867 ± 0.0029	0.3683 ± 0.0028	0.3912 ± 0.0030	0.3772 ± 0.0029
18	0.3512 ± 0.0027	0.3367 ± 0.0026	0.3546 ± 0.0028	0.3351 ± 0.0026

4.6.3 Dalitz Acceptance

The efficiency however, is not constant and does vary across the Dalitz plane. This acceptance is calculated in the square Dalitz plot for every sample in appendix H.3. From there we find a luminosity weighted mean acceptance for the examined decay modes as shown in the Dalitz plane in fig. 4.29.

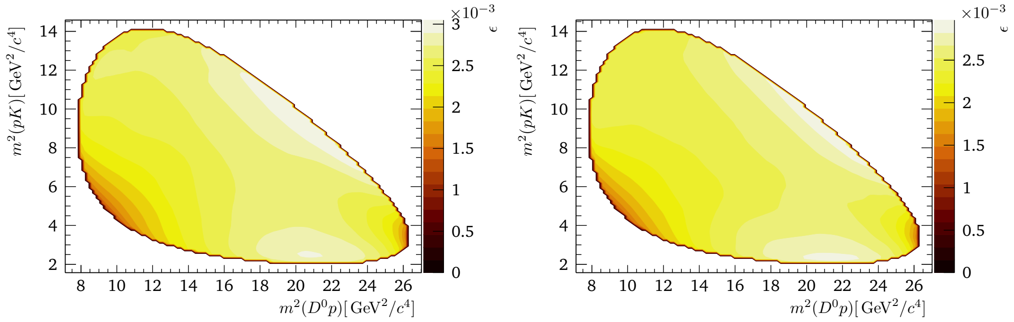

(a) $\Lambda_b^0 \to D^0 pK$, $D^0 \to K\pi$

(b) $\Lambda_b^0 \to D^0 pK$, $D^0 \to KK$

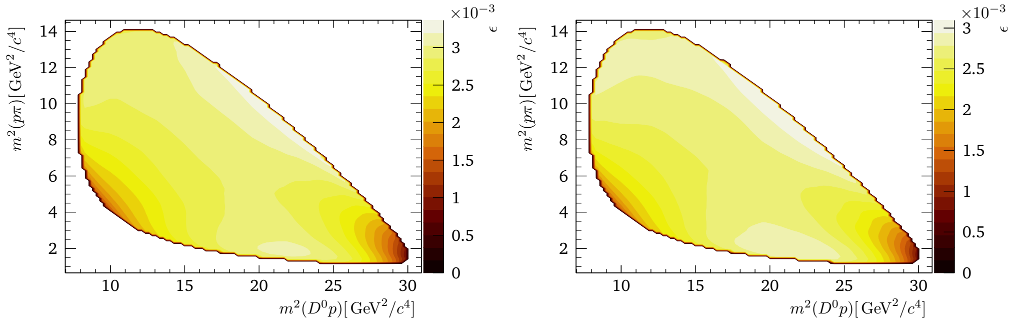

(c) $\Lambda_b^0 \to D^0 p\pi$, $D^0 \to K\pi$

(d) $\Lambda_b^0 \to D^0 p\pi$, $D^0 \to KK$

Fig. 4.29.: Acceptance across the Dalitz Plot for the $\Lambda_b^0 \to D^0 pK$ and $\Lambda_b^0 \to D^0 p\pi$ modes as a luminosity weighted mean value from the year specific acceptances.

Fit to $m(D^0ph)$

5

In this chapter we use RooFit [112] to fit the mass distributions $m(D^0pK)$ of the Λ_b^0 candidates to extract signal yields, ratios and integrated *CP* asymmetries for $\Lambda_b^0 \to D^0pK$ and $\Xi_b \to D^0pK$. Our fit strategy is to apply a preliminary fit to the full DATA, enabling us to constrain different dynamics in the subsequent fits to the datasets split for Λ_b^0 and $\overline{\Lambda}_b^0$. All fits are performed as simultaneous maximum likelihood fits to unbinned data. The shape models of the different contributions are determined from fits to the MC samples and fixed in the fits to the DATA. These models and fits can be found in appendix I.

We perform four main types of fits in total. The first fit type in section 5.1 to the unweighted DATA is based on the efficiency ratios calculated in section 4.6. The fit is used as proof of concept, *sWeight* calculation and fit validation with pseudo experiments. Next, in section 5.2, a fit variation is carried out that uses the acceptance of appendix H.3 as event weights instead of the efficiency ratios. The physics parameters are extracted from this fit type. A second set of these two fit types in section 5.3 is applied to the phase space region of Λ^* resonances.

5.1 Likelihood Fit to Unweighted Dataset- Full Dalitz Plot

5.1.1 Preliminary Fit to Full Dataset

Fit Setup: As already mentioned, the fit performed is a simultaneous fit to multiple DATA subsets. We separate the DATA according to the time periods 2011, 2012 and Run II. They are further split for the D^0 channels $D^0 \to K^-\pi^+$ and $D^0 \to KK$ and for the signal decay mode $\Lambda_b^0 \to D^0pK$ and normalisation mode $\Lambda_b^0 \to D^0p\pi$. We chose a fit window of $m(D^0ph) \in [5.42, 6.00]\,\mathrm{GeV}/c^2$ for all samples. The lower cutoff at $5.42\,\mathrm{GeV}/c^2$ is due to the unknown polarisation of the $\Lambda_b^0 \to D^*ph$ modes, visible in their double peak structure in figs. 4.19 and 4.20. This reduces the number of fit parameters.

We use the contributions stated in section 4.5.5 with their shapes determined in appendix I. The $\Xi_b \to D^0pK$ signal shape reuses the parameters of the $\Lambda_b^0 \to D^0pK$ shape and is shifted by the mass difference $\Delta m_{\Xi_b} = m(\Xi_b) - m(\Lambda_b^0)$, that we measure as a free parameter in the fit. As the momentum calibration of the LHCb software chain must not be perfect we apply a shift Δm_{MC} as free parameter in the fit to the mean values of the simulation shapes. The D^* shapes will have another free shift parameter $\Delta m_{\mathrm{MC},D^*}$ to compensate for the unknown polarisation that can cause a shift of the peak value, seen in section 4.5.2. We account for further discrepancies between MC and DATA by adding a Gaussian model of width σ_{add} with the same fraction f_{add} to each signal peak. Due to the lack of simulation for $\Xi_b \to D^0pK$

and $\varXi_b \to D^* pK$ we will reuse the shapes determined for the respective $\varLambda_b^0$ modes. The shapes are shifted by the known mass difference $\Delta m_{\varXi_b,\mathrm{PDG}} = 172.5 \pm 0.4\,\mathrm{MeV}/c^2$ [20]. The effect of a possible polarisation in $\varXi_b \to D^* pK$ is studied as a systematic in section 5.4. The combinatorial background of every sample will be described by an exponential function $N \cdot \exp(\lambda x)$ with a normalisation factor N and the exponential decay constant λ.

Measured Parameters: The signal yields can be set into context as

$$\begin{aligned}
N^{a,D^0\to hh}_{\varLambda_b^0\to D^0pK} &= \mathcal{L}^a \times \sigma^a(pp \to b\bar{b}) \times f^a_{\varLambda_b^0} \times \epsilon^{a,D^0\to hh}_{\varLambda_b^0\to D^0pK} \times \mathcal{B}_s(\varLambda_b^0 \to D^0pK) \times \mathcal{B}(D^0 \to hh) \\
N^{a,D^0\to hh}_{\varXi_b\to D^0pK} &= \mathcal{L}^a \times \sigma^a(pp \to b\bar{b}) \times f^a_{\varXi_b} \times \epsilon^{a,D^0\to hh}_{\varXi_b\to D^0pK} \times \mathcal{B}_s(\varXi_b \to D^0pK) \times \mathcal{B}(D^0 \to hh) \\
N^{a,D^0\to hh}_{\varLambda_b^0\to D^0p\pi} &= \mathcal{L}^a \times \sigma^a(pp \to b\bar{b}) \times f^a_{\varLambda_b^0} \times \epsilon^{a,D^0\to hh}_{\varLambda_b^0\to D^0p\pi} \times \mathcal{B}_s(\varLambda_b^0 \to D^0p\pi) \times \mathcal{B}(D^0 \to hh) \\
N^{a}_{\varLambda_b^0\to pKKK} &= \mathcal{L}^a \times \sigma^a(pp \to b\bar{b}) \times f^a_{\varLambda_b^0} \times \epsilon^{a}_{\varLambda_b^0\to pKKK} \times \mathcal{B}(\varLambda_b^0 \to pKKK), \qquad (5.1)
\end{aligned}$$

with the integrated luminosity $\mathcal{L}$, b production cross section in pp collisions $\sigma(pp \to b\bar{b})$, hadron production fraction f_h, total selection efficiency ϵ and the decay specific branching fraction $\mathcal{B}$. The superscript a denotes, when a specific value is dependent on the year of data taking.

As we cannot distinguish between D^0 and $\overline{D}^0$, we find a sum of D^0ph and $\overline{D}^0ph$ in the selected tuples. This circumstance is indicated by the subscript s in $\mathcal{B}_s$. In case of the $D^0 \to K^-\pi^+$ tuples, we can approximate $\mathcal{B}_s(X \to D^0ph) \approx \mathcal{B}(X \to D^0ph)$, as we assume the doubly Cabibbo suppressed contribution to be negligible. Further we can approximate $\mathcal{B}_s(\varLambda_b^0 \to D^0p\pi) \approx \mathcal{B}(\varLambda_b^0 \to D^0p\pi)$. This is due to the strong λ^4 suppression of $\varLambda_b^0 \to \overline{D}^0p\pi$ in comparison to λ^2 of $\varLambda_b^0 \to D^0p\pi$, when considering the Wolfenstein metric of the CKM matrix presented in section 2.2.2.

The strength of a simultaneous fit is the ability to share parameters between the different datasets and to increase the number of events while reducing free parameters. This enables us to formulate physical dependencies shared between the fit-samples. Next to the mass difference $\Delta m_{\varXi_b}$ we measure

$$\begin{aligned}
R^{K\pi}_{\varLambda_b^0} &= \frac{\mathcal{B}(\varLambda_b^0 \to D^0pK)}{\mathcal{B}(\varLambda_b^0 \to D^0p\pi)} = \frac{N^{a,D^0\to K\pi}_{\varLambda_b^0\to D^0pK}}{N^{a,D^0\to K\pi}_{\varLambda_b^0\to D^0p\pi}} \times \frac{\epsilon^{a,D^0\to K\pi}_{\varLambda_b^0\to D^0p\pi}}{\epsilon^{a,D^0\to K\pi}_{\varLambda_b^0\to D^0pK}} \times \frac{\epsilon^{a,\mathrm{L0}}_{\varLambda_b^0\to D^0p\pi}}{\epsilon^{a,\mathrm{L0}}_{\varLambda_b^0\to D^0pK}} \\
R^{KK}_{\varLambda_b^0} &= \frac{\mathcal{B}_s(\varLambda_b^0 \to D^0pK)}{\mathcal{B}(\varLambda_b^0 \to D^0p\pi)} = \frac{N^{a,D^0\to KK}_{\varLambda_b^0\to D^0pK}}{N^{a,D^0\to KK}_{\varLambda_b^0\to D^0p\pi}} \times \frac{\epsilon^{a,D^0\to KK}_{\varLambda_b^0\to D^0p\pi}}{\epsilon^{a,D^0\to KK}_{\varLambda_b^0\to D^0pK}} \times \frac{\epsilon^{a,\mathrm{L0}}_{\varLambda_b^0\to D^0p\pi}}{\epsilon^{a,\mathrm{L0}}_{\varLambda_b^0\to D^0pK}} \\
R^{K\pi}_{\varXi_b} &= \frac{f_{\varXi_b}}{f_{\varLambda_b^0}} \cdot \frac{\mathcal{B}(\varXi_b \to D^0pK)}{\mathcal{B}(\varLambda_b^0 \to D^0p\pi)} = \frac{N^{a,D^0\to K\pi}_{\varXi_b\to D^0pK}}{N^{a,D^0\to K\pi}_{\varLambda_b^0\to D^0p\pi}} \times \frac{\epsilon^{a,D^0\to K\pi}_{\varLambda_b^0\to D^0p\pi}}{\epsilon^{a,D^0\to K\pi}_{\varLambda_b^0\to D^0pK}} \times \frac{\epsilon^{a,\mathrm{L0}}_{\varLambda_b^0\to D^0p\pi}}{\epsilon^{a,\mathrm{L0}}_{\varXi_b\to D^0pK}} \\
R^{KK}_{\varXi_b} &= \frac{f_{\varXi_b}}{f_{\varLambda_b^0}} \cdot \frac{\mathcal{B}_s(\varXi_b \to D^0pK)}{\mathcal{B}(\varLambda_b^0 \to D^0p\pi)} = \frac{N^{a,D^0\to KK}_{\varXi_b\to D^0pK}}{N^{a,D^0\to KK}_{\varLambda_b^0\to D^0p\pi}} \times \frac{\epsilon^{a,D^0\to KK}_{\varLambda_b^0\to D^0p\pi}}{\epsilon^{a,D^0\to KK}_{\varLambda_b^0\to D^0pK}} \times \frac{\epsilon^{a,\mathrm{L0}}_{\varLambda_b^0\to D^0p\pi}}{\epsilon^{a,\mathrm{L0}}_{\varXi_b\to D^0pK}}. \qquad (5.2)
\end{aligned}$$

These ratios are free parameters in the fit and are calculated under consideration of the efficiency ratios found in section 4.6. As we don't have $\varXi_b \to D^0pK$ MC available, we assume the $\varXi_b$ and $\varLambda_b^0$ selection efficiencies to be the same. We conclude this from the fact, that both mothers have similar mass and we reconstruct the same final states. The ratios R are equal across all datasets and reduce the total amount of free parameters. To prevent a distortion of the CP effects in the $\Xi_b \to D^0 pK$ mode, the ratios $R^{hh}_{\Xi_b}$ also normalise to $\Lambda_b^0 \to D^0 p\pi$.

Constraints & Miscellaneous: The CP asymmetry of the charmless decay $\Lambda_b^0 \to pKKK$ has been measured to be $\Delta A^{CP}(\Lambda_b^0 \to pKKK) = (+0.2 \pm 1.8 \pm 0.6)\%$ [116]. Therefore we assume this asymmetry to be negligible in our case. The ratio

$$R_{\Lambda_b^0 \to pKKK} = \frac{\mathcal{B}(\Lambda_b^0 \to pKKK)}{\mathcal{B}(\Lambda_b^0 \to D^0 p\pi)\mathcal{B}(D^0 \to KK)} = \frac{N^a_{\Lambda_b^0 \to pKKK}}{N^{a,D^0 \to KK}_{\Lambda_b^0 \to D^0 p\pi}} \times \frac{\epsilon^{a,D^0 \to KK}_{\Lambda_b^0 \to D^0 p\pi}}{\epsilon^{a}_{\Lambda_b^0 \to pKKK}} \times \frac{\epsilon^{a,\mathrm{L0}}_{\Lambda_b^0 \to D^0 p\pi}}{\epsilon^{a,\mathrm{L0}}_{\Lambda_b^0 \to D^0 pK}} \tag{5.3}$$

normalises $\Lambda_b^0 \to pKKK$ to $\Lambda_b^0 \to D^0 p\pi$. This prevents an influence on the CP effects we aim to measure. $R_{\Lambda_b^0 \to pKKK}$ is constrained by applying a soft Gaussian constrain on $\mathcal{B}(\Lambda_b^0 \to pKKK) = (1.27 \pm 0.14) \times 10^{-5}$ [20]. The efficiency ratios are implemented as constraints as well. The exact ratio is in listing J.1. We require the ratios of D^0 to D^* modes to be the same across all samples. The ratios are defined as

$$r^{\Lambda_b^0,K}_{D^*} = \frac{N(\Lambda_b^0 \to D^0 pK)}{N(\Lambda_b^0 \to D^* pK)}, \quad r^{\Xi_b,K}_{D^*} = \frac{N(\Xi_b \to D^0 pK)}{N(\Xi_b \to D^* pK)}, \quad r^{\Lambda_b^0,\pi}_{D^*} = \frac{N(\Lambda_b^0 \to D^0 p\pi)}{N(\Lambda_b^0 \to D^* p\pi)} \tag{5.4}$$

and left free in the fit. Finally we formulate the measured yields of the different data taking years as

$$N^{(11)}, \quad N^{(12)} = s^{(12)} \cdot N^{(11)}, \quad N^{(\text{Run II})} = s^{(\text{Run II})} \cdot N^{(11)}, \tag{5.5}$$

where the scaling factors s^a are decay specific. This will enable us, when fixed, to calculate *sWeights* for the fitted decay species in appendix J.1.3.

The Fit Result is visualised in fig. 5.1. Table 5.1 lists the overall yields for the Λ_b^0 and Ξ_b signals in the fitted dataset. The complete list of all parameters and the plots for all sub-samples are shown in appendix J.1.1. We find a good visual agreement between the fitted model and the data. Even though this fit is mainly used to determine constraints for the following fits, we find the interesting result of $|m_{\Xi_b} - m_{\Lambda_b^0}| = 172.5 \pm 0.4\,\mathrm{MeV}/c^2$.

Tab. 5.1.: Overall yields for $\Lambda_b^0 \to D^0 ph$ and $\Xi_b \to D^0 pK$ found by the fits to the full unweighted dataset and split for the D^0 channels and Λ_b^0 and $\overline{\Lambda}_b^0$-type.

		$\Lambda_b^0 \to D^0 pK$	$\Xi_b \to D^0 pK$	$\Lambda_b^0 \to D^0 p\pi$
	$D^0 \to K\pi$	2912.7 ± 77.0	1667.5 ± 38.5	42850.5 ± 230.9
	$D^0 \to KK$	444.1 ± 31.4	148.2 ± 12.0	4370.4 ± 58.7
Λ_b^0	$D^0 \to K\pi$	1442.0 ± 51.5	842.6 ± 27.2	21671.8 ± 122.3
	$D^0 \to KK$	249.6 ± 22.9	90.6 ± 9.9	2215.0 ± 39.9
$\overline{\Lambda}_b^0$	$D^0 \to K\pi$	1482.7 ± 52.7	819.5 ± 26.6	21173.9 ± 121.0
	$D^0 \to KK$	191.8 ± 21.5	63.8 ± 8.2	2160.2 ± 40.0

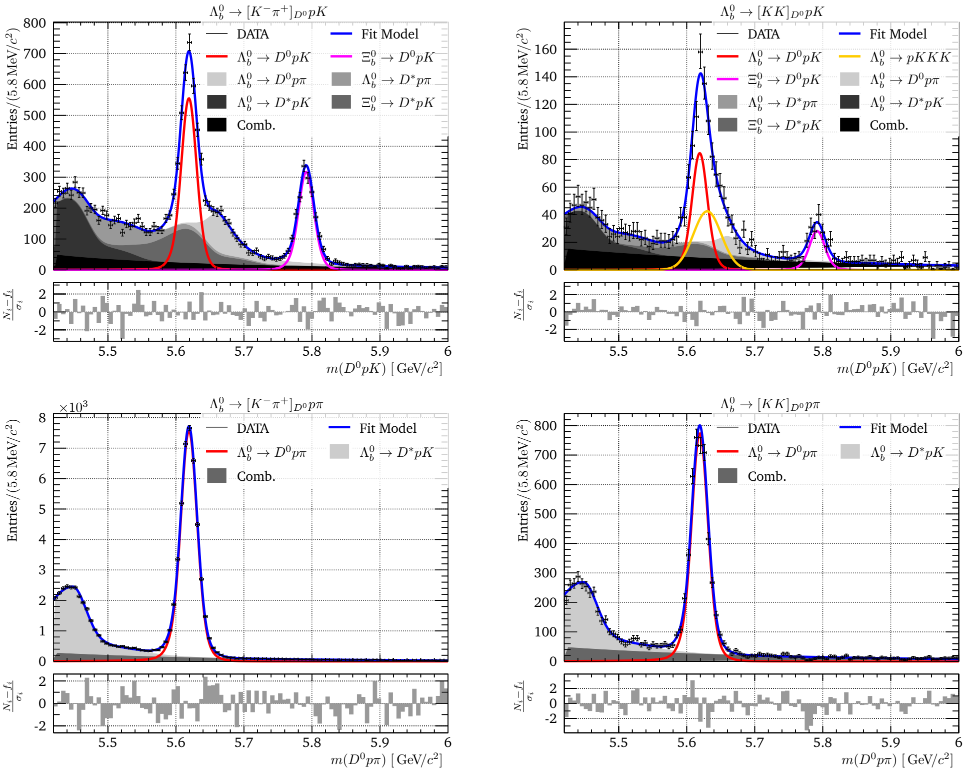

Fig. 5.1.: Preliminary fit to $m(D^0pK)$ and $m(D^0p\pi)$ of unweighted DATA. The models for 2011, 2012 and Run II are summed together and background models are stacked and visualised as shaded area.

5.1.2 Fit to Split Dataset

The dataset of the preliminary fit in section 5.1.1 is split into the two D^0 modes and separated for the Λ_b^0 and charge conjugated $\overline{\Lambda}_b^0$ decay. The charge conjugated decays are separable by the charge of the K or π in the direct final states of the Λ_b^0 decay. We refer to a Λ_b^0-type in case of a K^- (π^-) and to a $\overline{\Lambda}_b^0$-type in case of a K^+ (π^+). The full model, as introduced in section 5.1.1, is reapplied. In the four separate fits we constrain parameters of the previous fit that will not affect the *CP* effects in $\Lambda_b^0 \to D^0pK$ and $\Xi_b \to D^0pK$. We fix the overall MC shift Δm_{MC}, the mass difference Δm_{Ξ_b}, the shape parameters of the additional Gaussian model and of the $\Lambda_b^0 \to D^*p\pi$ mode in $m(D^0p\pi)$. Further we set the decay specific scaling parameters s^a of the yields constant. Finally we fix the ratio $r_{D^*}^{\Lambda_b^0,\pi}$, as it does not depend on the $\Lambda_b^0 \to D^0pK$ and $\Xi_b \to D^0pK$ yields. The fit result is visualised as sum of the 2011, 2012 and Run II data in fig. 5.2. We find the signal yields, listed in table 5.1. The split plots and all parameters are found in appendix J.1.2.

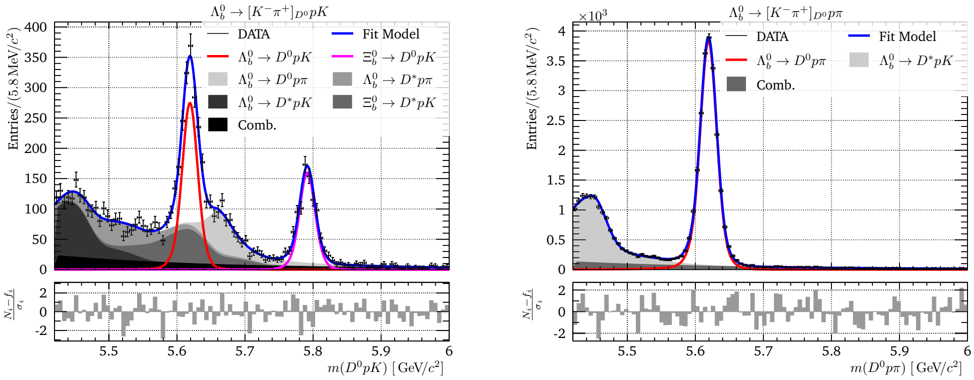

(a) Λ_b^0-type - $m(D^0ph^-)$, with $D^0 \to K^-\pi^+$

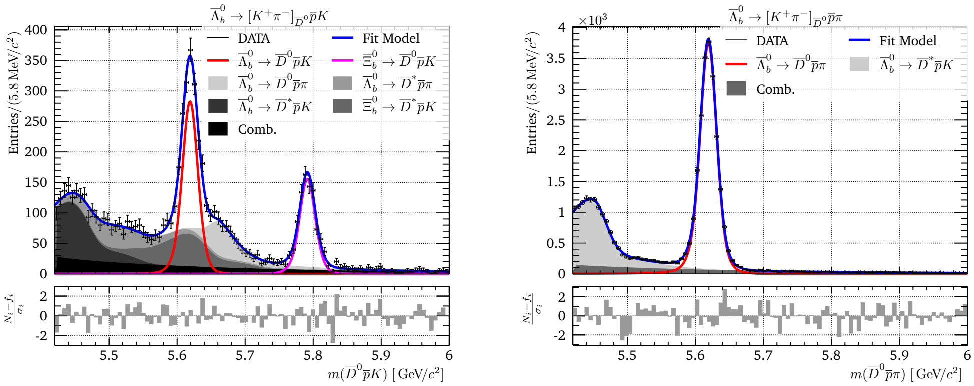

(b) $\overline{\Lambda}_b^0$-type - $m(D^0\overline{p}h^+)$, with $D^0 \to K^-\pi^+$

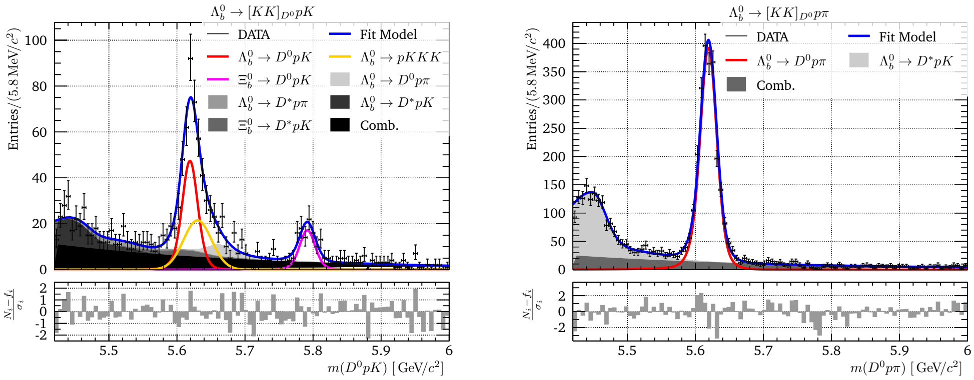

(c) Λ_b^0-type - $m(D^0ph^-)$, with $D^0 \to KK$

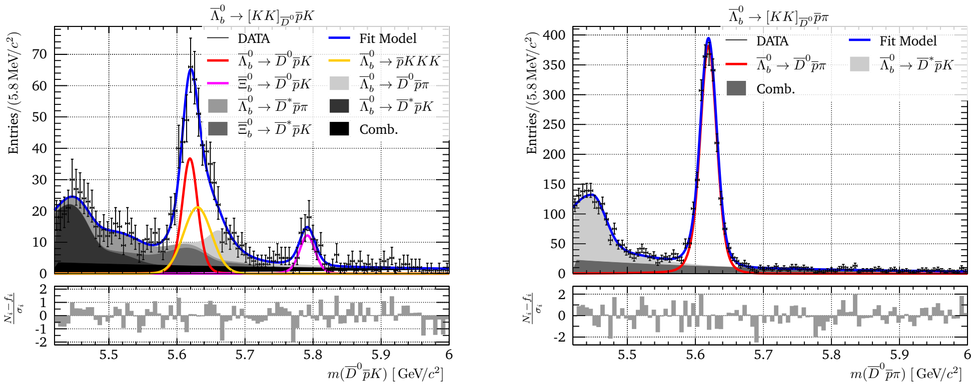

(d) $\overline{\Lambda}_b^0$-type - $m(D^0\overline{p}h^+)$, with $D^0 \to KK$

Fig. 5.2.: Fits to $m(D^0pK)$ and $m(D^0p\pi)$ of unweighted DATA and split for the D^0 modes and Λ_b^0-types.

5.2 Acceptance Weighted Likelihood Fit - Full Dalitz

We cannot use the fit, based on the phase space integrated efficiency ratios, to extract the signal ratios used to calculate CP asymmetries and branching fractions. As the Λ_b^0 signal prefers different phase space regions we have to consider the varying acceptance across the Dalitz plot. Therefore we reuse the previous fit model of section 5.1.1 with some minor tweaks. We account for the acceptance calculated in appendix H.3 by weighting each candidate with its inverse phase space efficiency value. This shifts all efficiencies except for the `L0` trigger efficiencies from the ratios in eq. (5.2) into the candidate weights and therefore the likelihood of the unbinned maximum likelihood fit. The `L0` trigger efficiency ratios used in $R^{hh}_{\Xi_b}$ are calculated from DATA and therefore already account for a varying phase space efficiency. As the acceptance of the Λ_b^0 signal must not match the one of the charmless background, the meaning of the branching fraction $\mathcal{B}(\Lambda_b^0 \to pKKK)$ in the ratio of eq. (5.3) changes to the general fraction $F(\Lambda_b^0 \to pKKK)$ and its Gaussian constrain must be removed. The signal and background shapes show no distortion, when applying the acceptance correction, as it can be seen in appendix I.

The $m(D^0pK)$ distributions of the preliminary fit can be seen in fig. 5.3 and all plots and outputs can be found in appendix J.2. We fit the split dataset, as described in section 5.1.2 and find the acceptance corrected ratios listed in table 5.3 and all yields in table 5.2.

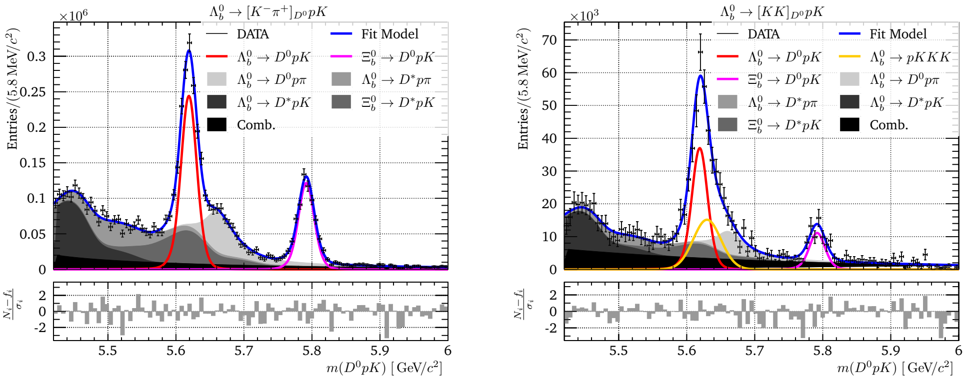

Fig. 5.3.: Fit to $m(D^0pK)$ and $m(D^0p\pi)$ with acceptance weights. Only the $m(D^0pK)$ distributions of the preliminary fit are shown. All Plots are in appendix J.2.

Tab. 5.2.: Overall yields for $\Lambda_b^0 \to D^0ph$ and $\Xi_b \to D^0pK$ found by the fits to the full acceptance corrected dataset and split for the D^0 channels and Λ_b^0 and $\overline{\Lambda}_b^0$-type.

$N/10^4$		$\Lambda_b^0 \to D^0pK$	$\Xi_b \to D^0pK$	$\Lambda_b^0 \to D^0p\pi$
	$D^0 \to K\pi$	129.32 ± 3.19	64.67 ± 1.55	1646.71 ± 13.70
	$D^0 \to KK$	19.56 ± 1.91	5.90 ± 0.51	174.60 ± 2.58
Λ_b^0	$D^0 \to K\pi$	65.93 ± 2.15	32.53 ± 1.05	835.34 ± 4.13
	$D^0 \to KK$	10.79 ± 0.82	3.40 ± 0.39	89.60 ± 1.55
$\overline{\Lambda}_b^0$	$D^0 \to K\pi$	64.47 ± 2.02	31.87 ± 0.99	811.17 ± 3.71
	$D^0 \to KK$	8.13 ± 0.80	2.48 ± 0.31	84.93 ± 1.52

Tab. 5.3.: Phase-space integrated ratios found by the fits to the acceptance corrected dataset split for the D^0 channels and Λ_b^0 and $\overline{\Lambda}_b^0$-type.

		$R^{hh}_{\Lambda_b^0}$ / 10^{-2}	$R^{hh}_{\Xi_b}$ / 10^{-2}
	$D^0 \to K\pi$	7.85 ± 0.28	4.02 ± 0.14
	$D^0 \to KK$	11.20 ± 1.52	3.45 ± 0.41
Λ_b^0	$D^0 \to K\pi$	7.89 ± 0.37	3.98 ± 0.18
	$D^0 \to KK$	12.04 ± 1.30	3.88 ± 0.61
$\overline{\Lambda}_b^0$	$D^0 \to K\pi$	7.94 ± 0.35	4.02 ± 0.17
	$D^0 \to KK$	9.56 ± 1.33	2.99 ± 0.50

5.3 Likelihood Fit in the Λ^* Resonance Region

In the previous fits we determined all interesting parameters in the whole phase space region of the $\Lambda_b^0 \to D^0 pK$ and $\Lambda_b^0 \to D^0 p\pi$ decays. As we aim to measure *CP* relevant parameters of the $\Lambda_b^0 \to D^0 pK$ decay, it is also interesting to select subregions of the $\Lambda_b^0 \to D^0 pK$ phase space. The amplitude fit in chapter 6 shows only Λ^* and Λ_c^{+*} resonances. The latter are found in the $m(D^0 p)$ invariant mass and fix, depending on the actual decay, the D^0 candidate to its (anti-)particle state. They therefore cannot contribute to the *CP* violation. The Λ^* in the $m(pK)$ mass, however, allow for *CP* violation effects. We further learn from the amplitude fit, that there is no significant contribution of Λ_c^{+*} resonances in a Dalitz region of $m^2(D^0 p) > 14\,\mathrm{GeV}^2/c^4$. We name this the Λ^* resonance region.

The previous fits to the unweighted and acceptance weighted data are applied to the dataset of the Λ^* resonance region. This time the Gaussian constrain on $\mathcal{B}(\Lambda_b^0 \to pKKK)$ also has to be removed for the model of the unweighted DATA, as it looses its physical meaning. In appendix I we show that the cut of $m^2(D^0 p) > 14\,\mathrm{GeV}^2/c^4$ causes significant distortions of most non signal shapes determined from MC. We re-determine all mis-ID shapes and all shapes of the partially reconstructed decays. The effect of D^{*0} polarisation seems to be more prominent in this phase space region. We find a clear double peak structure in $\Lambda_b^0 \to D^* pK$ for a missing π^0 and $J_{m,D^*} = 0$. A respective plot is supplied in fig. I.19. In DATA we also find an enhancement at about $5.54\,\mathrm{GeV}/c^2$ in $m(D^0 pK)$, clearly visible in fig. 5.4 on the left. This enhancement would match the peak to lower masses of the polarisation caused double peak, when considering $\Xi_b \to D^* pK$.

With the partially reconstructed $\Xi_b \to D^* pK$ peaking directly in the Λ_b^0 signal region, we have to cover this polarisation effect in the fit. We use the normalised shapes in appendix I.4 for the channels $D^* \to D^0\gamma$ and the polarised $D^* \to D^0\pi^0$ to build a probability denstity function (PDF) $\mathrm{PDF}_{\Lambda_b^0 \to D^* pK}$ that allows for a polarisation of the D^*.

$$\mathrm{PDF}_{\Lambda_b^0 \to D^* pK} = \mathcal{B}(D^* \to D^0\gamma) \cdot \mathrm{PDF}_{D^* \to D^0\gamma} + \mathcal{B}(D^* \to D^0\pi^0) \cdot \mathrm{PDF}_{D^* \to D^0\pi^0}(f_{\mathrm{pol}}) \quad (5.6)$$

The D^* polarisation factor f_{pol} in

$$\mathrm{PDF}_{D^* \to D^0\pi^0}(f_{\mathrm{pol}}) = 2f_{\mathrm{pol}} \cdot \mathrm{PDF}^{J_{m,D^*}=\pm 1}_{D^* \to D^0\pi^0} + (1 - 2f_{\mathrm{pol}}) \cdot \mathrm{PDF}^{J_{m,D^*}=0}_{D^* \to D^0\pi^0} \quad (5.7)$$

realises this polarisation. The additional factor 2 is based on the fact, that we cannot distinguish between $J_{m,D^*} = \pm 1$. We would find no polarisation, if there is no preferred angular momentum and thus $f_{\mathrm{pol}} = {}^1/_3$. We assume f_{pol} to be the same in the $\Lambda_b^0 \to D^*pK$ and $\Xi_b \to D^*pK$ models, as both contributions are implemented to share the same shape. The overall model however, should only reflect the D^* polarisation of $\Xi_b \to D^*pK$, as the lower boundary of the fit region does not include the low mass peak of $\Lambda_b^0 \to D^*pK$.

The $m(D^0pK)$ distributions of the preliminary fit with acceptance weights can be seen in fig. 5.4. All plots and outputs of the fit to the unweighted DATA can be found in appendix J.3 and for the acceptance weighted fit in appendix J.4. We find the acceptance corrected ratios from the split dataset, listed in table 5.3. The signal yields are summarised in table 5.4 and acceptance corrected in table 5.2. We measure the polarisation factor in the acceptance corrected Λ^* resonance region to be

$$f_{\mathrm{pol}} = 0.2 \pm 0.6 \quad . \tag{5.8}$$

Thus no assumption concerning a polarised or unpolarised D^* of the $\Xi_b \to D^*pK$ decay is possible. There is a noticeably enhanced Ξ_b signal for the $D^0 \to K\pi$ data in comparison to the full phase space. We ascribe this to a charmless background of $\Xi_b \to pKK\pi$, that has already been mentioned in section 4.5.4. Charmless decays seem to prefer the Dalitz region of Λ^* resonances, as a Λ_c^{+*} resonance requires a true D^0. This assumption is braced by the also visibly enhanced $\Lambda_b^0 \to pKKK$ background in the $D^0 \to KK$ samples. We will assign the Ξ_b ratios a systematic uncertainty in section 5.4.5.

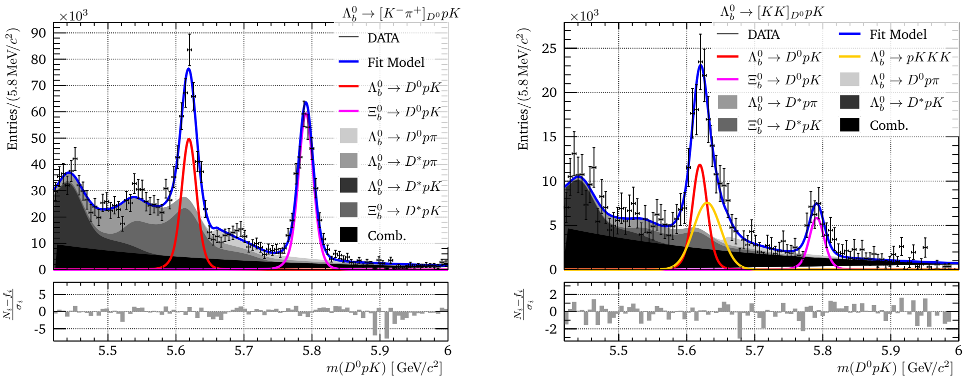

Fig. 5.4.: Fit to $m(D^0pK)$ and $m(D^0p\pi)$ with acceptance weights in the Λ^* Dalitz subregion ($m^2(D^0p) > 14\,\mathrm{GeV}^2/c^4$). Only the $m(D^0pK)$ distributions of the preliminary fit are shown. All plots are in appendix J.4.

Tab. 5.4.: Overall yields for $\Lambda_b^0 \to D^0ph$ and $\Xi_b \to D^0pK$ found by the fits to the full uncorrected dataset in the Λ^* resonance region and split for the D^0 channels and Λ_b^0 and $\overline{\Lambda}_b^0$-type.

		$\Lambda_b^0 \to D^0pK$	$\Xi_b \to D^0pK$	$\Lambda_b^0 \to D^0p\pi$
	$D^0 \to K\pi$	657.0 ± 48.8	841.9 ± 27.5	15778.9 ± 146.2
	$D^0 \to KK$	177.4 ± 19.6	81.9 ± 9.3	1544.0 ± 35.7
Λ_b^0	$D^0 \to K\pi$	288.5 ± 26.9	426.2 ± 19.1	7939.1 ± 73.6
	$D^0 \to KK$	92.8 ± 12.0	49.0 ± 7.3	781.9 ± 24.2
$\overline{\Lambda}_b^0$	$D^0 \to K\pi$	362.9 ± 28.3	412.3 ± 18.9	7835.6 ± 74.4
	$D^0 \to KK$	94.9 ± 15.5	34.5 ± 6.2	762.9 ± 24.1

Tab. 5.5.: Phase-space integrated ratios found by the fits to the dataset in the acceptance corrected Λ^* resonance region. The fits are split for the D^0 channels and Λ_b^0 and $\overline{\Lambda}_b^0$-type.

		$R^{hh}_{\Lambda_b^0}$ / 10^{-2}	$R^{hh}_{\Xi_b}$ / 10^{-2}
Λ_b^0	$D^0 \to K\pi$	4.16 ± 0.50	5.44 ± 0.32
	$D^0 \to KK$	10.01 ± 2.00	5.85 ± 1.18
$\overline{\Lambda}_b^0$	$D^0 \to K\pi$	4.96 ± 1.48	5.34 ± 0.51
	$D^0 \to KK$	11.41 ± 2.37	4.78 ± 1.14

Tab. 5.6.: Overall yields for $\Lambda_b^0 \to D^0 ph$ and $\Xi_b \to D^0 pK$ found by the fits to the full dataset in the acceptance corrected Λ^* resonance region and split for the D^0 channels and Λ_b^0 and $\overline{\Lambda}_b^0$-type.

$N/10^4$		$\Lambda_b^0 \to D^0 pK$	$\Xi_b \to D^0 pK$	$\Lambda_b^0 \to D^0 p\pi$
	$D^0 \to K\pi$	25.13 ± 14.06	30.16 ± 4.47	552.42 ± 11.27
	$D^0 \to KK$	5.98 ± 2.37	2.97 ± 0.81	56.99 ± 1.52
Λ_b^0	$D^0 \to K\pi$	11.56 ± 1.00	15.27 ± 0.64	278.39 ± 2.45
	$D^0 \to KK$	2.93 ± 0.41	1.73 ± 0.25	29.30 ± 0.88
$\overline{\Lambda}_b^0$	$D^0 \to K\pi$	13.58 ± 2.94	14.75 ± 1.03	273.92 ± 2.65
	$D^0 \to KK$	3.15 ± 0.45	1.33 ± 0.23	27.67 ± 0.88

5.4 Systematic Uncertainties

The uncertainties determined from the mass fits are of statistical nature only. There are several sources of systematic uncertainties that can vary the result of the fit and therefore all following calculations. As we perform a relative measurement of the branching fractions and are calculating asymmetries, many systematic sources cancel in the normalisation. With the fit model being relatively complex for the $m(D^0pK)$ distributions we will address it next to a possible polarisation of the D^* modes and a systematic due to the momentum calibration. Tables 5.7 to 5.11 list the systematic uncertainties which are introduced in the following.

5.4.1 Fit Validation

With the simultaneous fits being relatively complex and having a variety of parameters it is necessary to validate the results of the fits. Every likelihood fit yields a set of measured parameters $\xi_m \pm \sigma_m$. Even though the fit models are not Gaussian, we expect ξ_m to follow a Gaussian distribution. Thus for a sufficient amount of iterations the pull

$$\text{pull} = \frac{\xi_m - \xi_t}{\sigma_m} \tag{5.9}$$

is expected to be a standard Gaussian distribution with $\mu = 0$ and $\sigma = 1$. We use the fitted models of the fits to the unweighted DATA for the full phase space and the Λ^* resonance region in sections 5.1 and 5.3 to generate and then fit a set of one thousand pseudo experiments (toys). Each toy is generated with the same number of events as the respective DATA sample and yields a set of parameters ξ_t. When fitting the parameter pull distributions with a Gaussian model we are able to determine the correctness of the statistical error σ_m

and a possible bias of the measurement. The fitted pull distributions of the most relevant fit parameters can be found in appendix K. They show no major deviation from a standard Gaussian distribution.

5.4.2 Fit Model

The lower mass region of the Λ_b^0 signal is composed of several partially reconstructed distributions. The visualisation of the fits in *e.g.* fig. 5.1 show the necessity of $\Lambda_b^0 \to D^* pK$, $\Xi_b \to D^* pK$ and mis-ID of $\Lambda_b^0 \to D^* p\pi$ in the $m(D^0 pK)$ distributions. In section 4.5.5 we already mentioned that we additionally might have to expect a partially reconstructed $\Lambda_b^0 \to D_s^{*-} p$, where the D_s^{*-} will decay via a $\overline{D}^{*0}$. Even though the fit describes DATA well in this region, we test the general influence of these partially reconstructed contributions with a simplified model by removing the $\Lambda_b^0 \to D^* ph$ models and repeating the fit in a cropped range of $m(D^0 ph) \in [5.55, 6.00]\,\mathrm{GeV}/c^2$. This is, however not possible for the fit in the Λ^* resonance region. In this case we have to describe the peak at $5.54\,\mathrm{GeV}/c^2$ in $m(D^0 pK)$, we find due to the polarisation of the partially reconstructed $\Xi_b \to D^* pK$ mode.

We further consider varying shapes for the signal and combinatorial background. The signal models are changed to a double Gaussian distribution with parameters determined by prior fits to the MC distributions. For the combinatorial background we test an additional quadratic term in the Exponential $\exp \lambda x \to \exp \lambda(x + ax^2)$.

5.4.3 Polarisation of D^{*0}

A possible polarisation of the D^{*0} from partially reconstructed background has already been allowed in the fit models for $m(D^0 ph)$ in the Λ^* resonance region in section 5.3. Fits to events of the full Dalitz plane in sections 5.1 and 5.2 assume no polarisation. However, polarisation is especially necessary for the partially reconstructed $\Xi_b \to D^* pK$, which peaks directly in the Λ_b^0 signal region. We address the polarisation as a systematic uncertainty by allowing the polarisation in the fits to the full phase space and neglecting it for the Λ^* resonance region. We use the previously defined model $\mathrm{PDF}_{\Lambda_b^0 \to D^* pK}(f_{\mathrm{pol}})$ in eqs. (5.6) and (5.7) to realise the polarisation. We find a polarisation factor of $f_{\mathrm{pol}} = 0.22 \pm 0.13$ for the acceptance corrected full phase space region, which is in agreement to the one for the Λ^* resonance region in eq. (5.8).

5.4.4 Momentum Calibration

With the LHCb being able to spectroscopy as well, momentum scaling is applied, to calibrate its mass measurements. This scaling is not perfect. This however is only relevant for the measurement of the mass difference $\Delta m_{\Xi_b} = m_{\Xi_b} - m_{\Lambda_b^0}$. Under the premise, that the masses found in the reconstructed simulation are correct, we make a rough estimate of the systematic uncertainty using the shift Δm_{MC}. The deviation between the peak values from MC to DATA is a free parameter of the preliminary fit in section 5.1.1. It is

Tab. 5.7.: Summary of the systematic uncertainties for the ratios fitted in the preliminary fit with acceptance correction in section 5.2.

	$R_{\Lambda_b^0}$ / 10^{-2}		R_{Ξ_b} / 10^{-2}		
	$D^0 \to K^-\pi^+$	$D^0 \to KK$	$D^0 \to K^-\pi^+$	$D^0 \to KK$	χ^2/DoF
Fit value	$7.849 \pm 0.271_{\mathrm{stat}}$	$11.196 \pm 1.520_{\mathrm{stat}}$	$4.017 \pm 0.132_{\mathrm{stat}}$	$3.454 \pm 0.402_{\mathrm{stat}}$	$1168.2/850$
Bias corr.	-0.016	-0.132	$+0.000$	$+0.023$	
Error scale	1.045	1.070	1.060	1.032	
Corrected	$7.833 \pm 0.283_{\mathrm{stat}}$	$11.063 \pm 1.626_{\mathrm{stat}}$	$4.017 \pm 0.140_{\mathrm{stat}}$	$3.478 \pm 0.415_{\mathrm{stat}}$	
$2\times$ Gauss Signal	0.077	0.157	0.022	0.019	$1171.5/850$
$m(\Lambda_b^0) > 5.55\,\mathrm{GeV}/c^2$	0.024	0.575	0.047	0.016	$1289.0/866$
D^{*0}-pol	0.060	0.002	0.010	0.004	$1164.9/849$
Bkg $= \exp\lambda(x + ax^2)$	0.062	0.276	0.056	0.041	$1336.7/838$
Charmless Λ_b^0	0.045	1.502	0.021	0.151	$1164.3/849$
Charmless Ξ_b			0.011		
L0 Trigger	0.039	0.055	0.020	0.017	
Total syst. uncert.	0.132	1.640	0.083	0.159	

Tab. 5.8.: Summary of the systematic uncertainties for the ratios found with the fits with acceptance correction in section 5.2 to the Λ_b^0- and $\overline{\Lambda}_b^0$-type separated $D^0 \to K^-\pi^+$ DATA samples.

$D^0 \to K^-\pi^+$-samples

	$R_{\Lambda_b^0}$ / 10^{-2}	R_{Ξ_b} / 10^{-2}	χ^2/DoF	$R_{\overline{\Lambda}_b^0}$ / 10^{-2}	$R_{\overline{\Xi}_b}$ / 10^{-2}	χ^2/DoF
Fit value	$7.887 \pm 0.365_{\mathrm{stat}}$	$3.983 \pm 0.177_{\mathrm{stat}}$	$642.2/531$	$7.943 \pm 0.350_{\mathrm{stat}}$	$4.019 \pm 0.170_{\mathrm{stat}}$	$622.9/531$
Bias corr.	$+0.005$	$+0.006$		-0.007	$+0.008$	
Error scale	1.035	0.992		0.984	1.009	
Corrected	$7.892 \pm 0.377_{\mathrm{stat}}$	$3.989 \pm 0.175_{\mathrm{stat}}$		$7.936 \pm 0.345_{\mathrm{stat}}$	$4.027 \pm 0.172_{\mathrm{stat}}$	
$2\times$ Gauss Signal	0.171	0.028	$655.5/531$	0.098	0.019	$622.9/531$
$m(\Lambda_b^0) > 5.55\,\mathrm{GeV}/c^2$	0.001	0.024	$648.0/533$	0.064	0.031	$611.8/533$
D^{*0}-pol	0.020	0.011	$641.1/531$	0.077	0.007	$621.1/531$
Bkg $= \exp\lambda(x + ax^2)$	0.047	0.065	$720.5/525$	0.015	0.068	$709.1/525$
Charmless Λ_b^0	0.007	0.002	$642.4/531$	0.003	0.003	$624.0/531$
Charmless Ξ_b		0.011			0.011	
L0 Trigger	0.039	0.020		0.040	0.020	
Total syst. uncert.	0.183	0.079		0.146	0.081	

Tab. 5.9.: Summary of the systematic uncertainties for the ratios found with the fits with acceptance correction in section 5.2 to the Λ_b^0- and $\overline{\Lambda}_b^0$-type separated $D^0 \to KK$ DATA samples.

$D^0 \to KK$-samples

	$R_{\Lambda_b^0}$ / 10^{-2}	R_{Ξ_b} / 10^{-2}	χ^2/DoF	$R_{\overline{\Lambda}_b^0}$ / 10^{-2}	$R_{\overline{\Xi}_b}$ / 10^{-2}	χ^2/DoF
Fit value	$12.036 \pm 1.299_{\mathrm{stat}}$	$3.881 \pm 0.602_{\mathrm{stat}}$	$382.8/339$	$9.563 \pm 1.322_{\mathrm{stat}}$	$2.988 \pm 0.499_{\mathrm{stat}}$	$458.0/339$
Bias corr.	$+0.075$	$+0.036$		-0.023	$+0.057$	
Error scale	1.007	0.989		1.016	0.986	
Corrected	$12.111 \pm 1.308_{\mathrm{stat}}$	$3.917 \pm 0.596_{\mathrm{stat}}$		$9.540 \pm 1.343_{\mathrm{stat}}$	$3.045 \pm 0.492_{\mathrm{stat}}$	
$2\times$ Gauss Signal	0.194	0.018	$365.3/339$	0.102	0.022	$456.9/339$
$m(\Lambda_b^0) > 5.55\,\mathrm{GeV}/c^2$	0.643	0.026	$355.8/343$	0.700	0.009	$388.0/343$
D^{*0}-pol	0.064	0.001	$382.5/339$	0.084	0.003	$456.5/339$
Bkg $= \exp\lambda(x + ax^2)$	0.120	0.015	$379.8/333$	0.302	0.009	$466.1/333$
Charmless Λ_b^0	1.584	0.006	$379.5/339$	1.565	0.002	$455.3/339$
L0 Trigger	0.061	0.020		0.048	0.015	
Total syst. uncert.	1.727	0.040		1.747	0.030	

Tab. 5.10.: Summary of the systematic uncertainties for the ratios found with the fits with acceptance correction in section 5.3 to the Λ_b^0- and $\overline{\Lambda}_b^0$-type separated $D^0 \to K^-\pi^+$ DATA samples in the Λ^* resonance region. There is an additional unknown systematic due to charmless Ξ_b (section 5.4.5).

$D^0 \to K^-\pi^+$-samples

	$R_{\Lambda_b^0}$ / 10^{-2}	R_{Ξ_b} / 10^{-2}	χ^2/DoF	$R_{\overline{\Lambda}_b^0}$ / 10^{-2}	$R_{\overline{\Xi}_b}$ / 10^{-2}	χ^2/DoF
Fit value	$4.160 \pm 0.496_{\text{stat}}$	$5.443 \pm 0.318_{\text{stat}}$	$459.0/410$	$4.964 \pm 1.472_{\text{stat}}$	$5.343 \pm 0.505_{\text{stat}}$	$471.0/410$
Bias corr.	$+0.007$	$+0.012$		-0.028	$+0.024$	
Error scale	1.035	0.992		0.984	1.009	
Corrected	$4.167 \pm 0.513_{\text{stat}}$	$5.454 \pm 0.316_{\text{stat}}$		$4.936 \pm 1.448_{\text{stat}}$	$5.368 \pm 0.510_{\text{stat}}$	
$2\times$ Gauss Signal	0.041	0.282	$461.4/410$	0.067	0.232	$465.1/410$
D^{*0}-pol	0.449	0.297	$461.9/410$	0.503	0.271	$467.5/410$
Bkg = $\exp\lambda(x + ax^2)$	0.073	0.268	$455.5/404$	0.077	0.254	$463.6/404$
Charmless Λ_b^0	0.092	0.268	$460.8/410$	0.084	0.263	$469.4/410$
Charmless Ξ_b		?			?	
L0 Trigger	0.083	0.109		0.099	0.107	
Total syst. uncert.	0.473	0.569		0.529	0.522	

Tab. 5.11.: Summary of the systematic uncertainties for the ratios found with the fits with acceptance correction in section 5.3 to the Λ_b^0- and $\overline{\Lambda}_b^0$-type separated $D^0 \to KK$ DATA samples in the Λ^* resonance region.

$D^0 \to KK$-samples

	$R_{\Lambda_b^0}$ / 10^{-2}	R_{Ξ_b} / 10^{-2}	χ^2/DoF	$R_{\overline{\Lambda}_b^0}$ / 10^{-2}	$R_{\overline{\Xi}_b}$ / 10^{-2}	χ^2/DoF
Fit value	$10.005 \pm 1.996_{\text{stat}}$	$5.848 \pm 1.173_{\text{stat}}$	$267.8/268$	$11.414 \pm 2.364_{\text{stat}}$	$4.775 \pm 1.136_{\text{stat}}$	$419.6/268$
Bias corr.	$+0.116$	$+0.070$		-0.041	$+0.130$	
Error scale	1.007	0.989		1.016	0.986	
Corrected	$10.121 \pm 2.011_{\text{stat}}$	$5.919 \pm 1.161_{\text{stat}}$		$11.374 \pm 2.401_{\text{stat}}$	$4.905 \pm 1.120_{\text{stat}}$	
$2\times$ Gauss Signal	0.230	0.284	$262.9/268$	0.731	0.172	$424.6/268$
D^{*0}-pol	-0.106	0.390	$267.5/268$	1.087	0.107	$419.1/268$
Bkg = $\exp\lambda(x + ax^2)$	0.563	0.385	$267.1/262$	1.258	0.366	$427.5/262$
Charmless Λ_b^0	2.689	0.363	$264.9/268$	2.830	0.242	$415.5/268$
L0 Trigger	0.202	0.118		0.227	0.098	
Total syst. uncert.	2.767	0.726		3.371	0.494	

Tab. 5.12.: Summary of the systematic uncertainties for the mass difference $m_{\Xi_b} - m_{\Lambda_b^0}$ fitted in the fit of section 5.1.1.

	$m_{\Xi_b} - m_{\Lambda_b^0}$/ MeV/$c^2$	χ^2/DoF
Fit value	$172.516 \pm 0.361_{\text{stat}}$	787.0/850
Bias corr.	-0.001	
Error scale	1.028	
Corrected	$172.515 \pm 0.371_{\text{stat}}$	
2× Gauss Signal	0.085	800.7/850
$m(\Lambda_b^0) > 5.55\,\text{GeV}/c^2$	0.137	755.4/866
D^{*0}-pol	0.033	783.8/849
Bkg $= \exp\lambda(x + ax^2)$	0.001	787.2/838
Charmless Λ_b^0	0.002	784.3/849
Momentum Scaling	0.036	
Total syst. uncert.	0.169	

found to be $\Delta m_{\text{MC}} = -1.18 \pm 0.07$. We estimate the systematic uncertainty on Δm_{Ξ_b} as $u_{\Delta m_{\Xi_b}} = \frac{|\Delta m_{\text{MC}}|}{m_{\Lambda_b^0}} = 0.04$.

5.4.5 Charmless Background

We further consider the $\Lambda_b^0 \to pKKK$ background. The mass constrain of the DTF on the D^0 mass causes a shift to lower masses of the $m(D^0)$ peak value, as it can be seen in appendix G.4. This translates into a shift to higher masses of the charmless Λ_b^0 candidate mass. These kinematics are also based on the momentum calibration and thus might have a different true shift from the nominal Λ_b^0 mass. This would have an impact on the measurements, as the charmless background also peaks in the signal region. We therefore consider an additional shift $\Delta m_{\text{charmless}}$ on the peak value of the charmless background in the fit-models to determine the systematic.

Apart from the previously mentioned systematic of the $\Lambda_b^0 \to pKKK$ peak value we have to consider a systematic due to $\Xi_b \to pKK\pi$, as we have seen in the fit to the Λ^* resonance region in section 5.3. A common method would be to estimate the charmless contribution in the signal peak from the D^0 mass sidebands. Due to the preselection cut on the D^0 mass we take another approach. We assume $\Lambda_b^0 \to pKKK$ and $\Xi_b \to pKK\pi$ to behave similarly in the candidate selection. We justify this, as Λ_b^0 and Ξ_b have similar nominal masses, their decays analogos topologies and thus presumably likewise kinematics. We estimate the $\Xi_b \to pKK\pi$ fraction $f_{\Xi_b}^{\text{charmless}}$ in the Ξ_b signal peak of the $D^0 \to K\pi$ samples to be

$$f_{\Xi_b}^{\text{charmless}} = \frac{\mathcal{B}(\Xi_b \to pKK\pi)\epsilon_{\Xi_b \to pKK\pi}}{\mathcal{B}(\Xi_b \to D^0 pK)\mathcal{B}(D^0 \to K^-\pi^+)\epsilon_{\Xi_b \to D^0 pK} + \mathcal{B}(\Xi_b \to pKK\pi)\epsilon_{\Xi_b \to pKK\pi}} \tag{5.10}$$

$$= \frac{r_{\mathcal{B}(\Xi_b \to pKK\pi)} \frac{\epsilon_{\Xi_b \to pKK\pi}}{\epsilon_{\Xi_b \to D^0 pK}}}{1 + r_{\mathcal{B}(\Xi_b \to pKK\pi)} \frac{\epsilon_{\Xi_b \to pKK\pi}}{\epsilon_{\Xi_b \to D^0 pK}}} \tag{5.11}$$

where $r_{\mathcal{B}(\Xi_b \to pKK\pi)}$ is the branching fraction ratio to $\Lambda_b^0 \to D^0 pK$ from table 4.9. We assume the no-charm to charm efficiency ratios to be the same for Λ_b^0 and Ξ_b and evaluate the systematic on $R_{\Xi_b}^{K\pi}$ due to the charmless Ξ_b contribution as

$$u_{\Xi_b}^{\text{charmless}} = f_{\Xi_b}^{\text{charmless}} \cdot R_{\Xi_b}^{K\pi} . \tag{5.12}$$

These assumptions cannot be used for the Λ^* resonance region, as the phase space distributions of the charmless background may not be the same. Therefore we won't use $R_{\Xi_b}^{K\pi}$ from these fits in further calculations.

5.4.6 Trigger Efficiency

As we have set the the `L0` efficiency ratios to one in section 4.6.1, we have to assign an systematic uncertainty. The efficiencies are determined via a fit to DATA. Due to peaking background in the $m(D^0 pK)$ distribution and the low number of events in the 2011 and 2015 samples the efficiencies partly show a large uncertainty. The uncertainties can be seen in appendix H.1. We additionally determine the trigger efficiencies from MC. The MC samples have a higher event count without background and therefore reflect the trend of the ratio better. Under consideration of the MC efficiencies in tables H.4 and H.5 we assign a systematic uncertainty of 0.5% to the branchin ratios of the likelihood fit to the full phase space and 2% for the likelihood fit in the Λ^* resonance region.

5.5 Results

5.5.1 Ratios and Branching Fractions

We report the final branching fraction ratios from eq. (5.2) for the Λ_b^0 and Ξ_b modes as they are listed in tables 5.13 and 5.14. As expected, the systematic uncertainty due to the possible shift of the $\Lambda_b^0 \to pKKK$ peak value dominates all $R_{\Lambda_b^0}^{KK}$ measurements. The effect can be seen in appendix L.1. In the Λ^* resonance region we find the D^{*0} polarisation to have a significant contribution, leading to a systematic dominated measurement of $R_{\Lambda_b^0}^{K\pi}$ for the $\overline{\Lambda}_b^0$-type decays, which is discussed in more detail in appendix L.2. We further do not list the $R_{\Xi_b}^{K\pi}$ measurement for the Λ^* resonance region, due to an unknown contribution of $\Xi_b \to pKK\pi$ to the Ξ_b signal.

The Branching Fractions for $\Lambda_b^0 \to D^0 pK$ and $\Xi_b \to D^0 pK$ are determined from the ratios extracted from the $D^0 \to K\pi$ samples, where we expect the admixture of D^0 and $\overline{D}^0$ to be

Tab. 5.13.: Phase-space integrated ratios for the different D^0 channels. The second part of the table lists the ratios split for the Λ_b^0-type fit to $m(D^0pK)$ and $\overline{\Lambda}_b^0$-type fit to $m(D^0\overline{p}K^+)$.

	D^0	$R^{hh}_{\Lambda_b^0}$ / 10^{-2}	$R^{hh}_{\Xi_b}$ / 10^{-2}
	$K\pi$	$7.83 \pm 0.29_{\text{stat}} \pm 0.14_{\text{syst}}$	$4.02 \pm 0.14_{\text{stat}} \pm 0.09_{\text{syst}}$
	KK	$11.1 \pm 1.7_{\text{stat}} \pm 1.7_{\text{syst}}$	$3.48 \pm 0.42_{\text{stat}} \pm 0.16_{\text{syst}}$
Λ_b^0	$K\pi$	$7.89 \pm 0.38_{\text{stat}} \pm 0.19_{\text{syst}}$	$3.99 \pm 0.18_{\text{stat}} \pm 0.08_{\text{syst}}$
	KK	$12.1 \pm 1.4_{\text{stat}} \pm 1.8_{\text{syst}}$	$3.92 \pm 0.60_{\text{stat}} \pm 0.05_{\text{syst}}$
$\overline{\Lambda}_b^0$	$K\pi$	$7.94 \pm 0.35_{\text{stat}} \pm 0.15_{\text{syst}}$	$4.03 \pm 0.18_{\text{stat}} \pm 0.09_{\text{syst}}$
	KK	$9.5 \pm 1.4_{\text{stat}} \pm 1.8_{\text{syst}}$	$3.04 \pm 0.50_{\text{stat}} \pm 0.03_{\text{syst}}$

Tab. 5.14.: Λ^* resonance region integrated ratios split for the Λ_b^0-type fit to $m(D^0pK)$ and $\overline{\Lambda}_b^0$-type fit to $m(D^0\overline{p}K^+)$.

	D^0	$R^{hh}_{\Lambda_b^0}$ / 10^{-2}	$R^{hh}_{\Xi_b}$ / 10^{-2}
Λ_b^0	$K\pi$	$4.2 \pm 0.6_{\text{stat}} \pm 0.5_{\text{syst}}$	
	KK	$10.1 \pm 2.1_{\text{stat}} \pm 2.8_{\text{syst}}$	$5.9 \pm 1.2_{\text{stat}} \pm 0.8_{\text{syst}}$
$\overline{\Lambda}_b^0$	$K\pi$	$4.9 \pm 1.5_{\text{stat}} \pm 0.6_{\text{syst}}$	
	KK	$11.4 \pm 2.4_{\text{stat}} \pm 3.4_{\text{syst}}$	$4.9 \pm 1.2_{\text{stat}} \pm 0.5_{\text{syst}}$

negligible. We use the ratios from the acceptance corrected fit to the full phase space. With $\mathcal{B}(\Lambda_b^0 \to D^0 p\pi) = (6.3 \pm 0.7) \times 10^{-4}$ [20] we find

$$\begin{aligned}\mathcal{B}(\Lambda_b^0 \to D^0pK) &= R^{K\pi}_{\Lambda_b^0} \cdot \mathcal{B}(\Lambda_b^0 \to D^0p\pi) \\ &= (4.93 \pm 0.18_{\text{stat}} \pm 0.09_{\text{syst}} \pm 0.55_{\text{ext}}) \times 10^{-5} \qquad (5.13)\\ \frac{f_{\Xi_b}}{f_{\Lambda_b^0}} \cdot \mathcal{B}(\Xi_b \to D^0pK) &= R^{K\pi}_{\Xi_b} \cdot \mathcal{B}(\Lambda_b^0 \to D^0p\pi) \\ &= (2.53 \pm 0.09_{\text{stat}} \pm 0.06_{\text{syst}} \pm 0.29_{\text{ext}}) \times 10^{-5} \quad , \qquad (5.14)\end{aligned}$$

where the uncertainty of $\mathcal{B}(\Lambda_b^0 \to D^0p\pi)$ is propagated as an external contribution u_{ext}. We further find for $\Xi_b \to D^0pK$ under consideration of the b-baryon production fraction $\mathcal{B}(b \to b\text{−baryon}) = 0.088 \pm 0.012$ [20], which contributes to the external uncertainty as well,

$$\begin{aligned}f_{\Xi_b} \cdot \mathcal{B}(\Xi_b \to D^0pK) &= R^{K\pi}_{\Xi_b} \cdot \mathcal{B}(\Lambda_b^0 \to D^0p\pi) \cdot \mathcal{B}(b \to b\text{−baryon}) \\ &= (2.23 \pm 0.08_{\text{stat}} \pm 0.05_{\text{syst}} \pm 0.40_{\text{ext}}) \times 10^{-6} \quad . \qquad (5.15)\end{aligned}$$

The branching fraction measurements are in agreement with the current particle data group (PDG) values [20] and about one and a half times more precise.

5.5.2 Integrated *CP* Asymmetry

The asymmetries from eqs. (2.19) and (2.21) can be evaluated using the ratios $R_{\varLambda_b^0}$ and $R_{\varXi_b}$, presented in section 5.5.1. The branching fraction of the $\varLambda_b^0 \to D^0 p\pi$ mode cancels and we calculate

$$\begin{aligned}
\mathcal{A}_{CP}^{\varLambda_b^0} &= \frac{\Gamma(\varLambda_b^0 \to D_{CP}pK^-) - \Gamma(\overline{\varLambda}_b^0 \to D_{CP}pK^+)}{\Gamma(\varLambda_b^0 \to D_{CP}pK^-) + \Gamma(\overline{\varLambda}_b^0 \to D_{CP}pK^+)} = \frac{R_{\varLambda_b^0 \to D_{CP}pK^-} - R_{\overline{\varLambda}_b^0 \to D_{CP}pK^+}}{R_{\varLambda_b^0 \to D_{CP}pK^-} + R_{\overline{\varLambda}_b^0 \to D_{CP}pK^+}} \\
\mathcal{A}_{\text{ADS}}^{\varLambda_b^0} &= \frac{\Gamma(\varLambda_b^0 \to [K^-\pi^+]_D pK^-) - \Gamma(\overline{\varLambda}_b^0 \to [K^+\pi^-]_D pK^+)}{\Gamma(\varLambda_b^0 \to [K^-\pi^+]_D pK^-) + \Gamma(\overline{\varLambda}_b^0 \to [K^+\pi^-]_D pK^+)} \\
&= \frac{R_{\varLambda_b^0 \to [K^-\pi^+]_D pK^-} - R_{\overline{\varLambda}_b^0 \to [K^+\pi^-]_D pK^+}}{R_{\varLambda_b^0 \to [K^+\pi^-]_D pK^-} + R_{\overline{\varLambda}_b^0 \to [K^-\pi^+]_D pK^+}} \quad . \qquad (5.16)
\end{aligned}$$

The same is performed for $\varXi_b \to D^0 pK$ and we find the *CP* asymmetries listed in table 5.15. One has to keep in mind that these asymmetries are integrated over the phase space. This means that the *CP* asymmetries integrated over the full phase space do not exclude effects that arise from resonances like $\varLambda_c^{*+} \to D^0 p$. Further the *CP* asymmetries from the $\varLambda^*$ resonance region might not be affected by $\varLambda_c^{*+}$ resonances, however they do include interference effects. All asymmetries are in agreement with zero.

Tab. 5.15.: *CP* asymmetries calculated from the ratios found by the acceptance corrected fits to the $\varLambda_b^0$- and $\overline{\varLambda}_b^0$-type split DATA.

	Full Phase Space	$\varLambda^*$ Resonance Region
$\mathcal{A}_{CP}^{\varLambda_b^0}$	$0.12 \pm 0.09_{\text{stat}} \pm 0.11_{\text{syst}}$	$-0.06 \pm 0.15_{\text{stat}} \pm 0.20_{\text{syst}}$
$\mathcal{A}_{\text{ADS}}^{\varLambda_b^0}$	$-0.003 \pm 0.032_{\text{stat}} \pm 0.015_{\text{syst}}$	$-0.09 \pm 0.16_{\text{stat}} \pm 0.08_{\text{syst}}$
$\mathcal{A}_{CP}^{\varXi_b}$	$0.13 \pm 0.11_{\text{stat}} \pm 0.01_{\text{syst}}$	$0.09 \pm 0.15_{\text{stat}} \pm 0.08_{\text{syst}}$
$\mathcal{A}_{\text{ADS}}^{\varXi_b}$	$-0.005 \pm 0.031_{\text{stat}} \pm 0.014_{\text{syst}}$	

5.5.3 Mass Difference of $\varXi_b$ to $\varLambda_b^0$

We measure the mass difference between $\varXi_b$ and $\varLambda_b^0$ to be

$$m_{\varXi_b} - m_{\varLambda_b^0} = 172.5 \pm 0.38_{\text{stat}} \pm 0.17_{\text{syst}}\,\text{MeV}/c^2 \quad . \qquad (5.17)$$

This is on par with the latest LHCb (Run I) precision mass measurement of $m_{\varXi_b}$ [117]. With the latest LHCb measurement of $m_{\varLambda_b^0} = 5619.62 \pm 0.16 \pm 0.13\,\text{MeV}/c^2$ [118] we find $m_{\varXi_b} = 5792.1 \pm 0.41_{\text{stat}} \pm 0.21_{\text{syst}}\,\text{MeV}/c^2$.

6 Amplitude Analysis

In this chapter we perform two types of unbinned fits to the Dalitz plot. The first type is for data within a mass window of $2\sigma_{\Lambda_b^0}$ around the Λ_b^0 mass peak. The likelihood is described in section 6.1. The standard deviation of the Λ_b^0 signal has been determined from MC to be $\sigma_{\Lambda_b^0} = 13.66\,\mathrm{MeV}/c^2$. With the Λ_b^0 mass peak value, taken from the fit of the previous chapter, this results into a mass window of $m(\Lambda_b^0) \in [5591.90, 5646.53]\,\mathrm{MeV}/c^2$. The second type of fit is a background subtracting fit, called *sFit* [119].

The phase space variables are extracted from a DTF with an additional mass constrain on the Λ_b^0 mass (section 4.1) to ensure sharp phase space borders. The distribution of the Λ_b^0 candidates for the $D^0 \to K^-\pi^+$ and $D^0 \to KK$ samples in fig. 6.1 show enhancements to the lower m_{ph}^2 masses, we identify as Λ_c^{+*} and Λ^* resonances. The Λ_c^{+*} resonance region already shows strong con- and destructive interference effects of the resonances, where we find a distinct resonance line in the Λ^*resonance region. We further see possible interferences of Λ_c^{+*} and Λ^* resonances in their overlap region. There is also a light enhancement visible at the border of the $D^0 \to KK$ sample phase space, where we would expect resonances in the m_{D^0K} spectrum. This is especially interesting, as these could be $D_s^{-*} \to \overline{D}^0K$ resonances, which fix the D^0 to its anti particle state. The enhancement is also visible in the *sWeight*ed projections, that can be found in the appendix in fig. M.6. The Ξ_b Dalitz plots including all *sWeight*ed Dalitz plots and projections are discussed in appendix M.5.

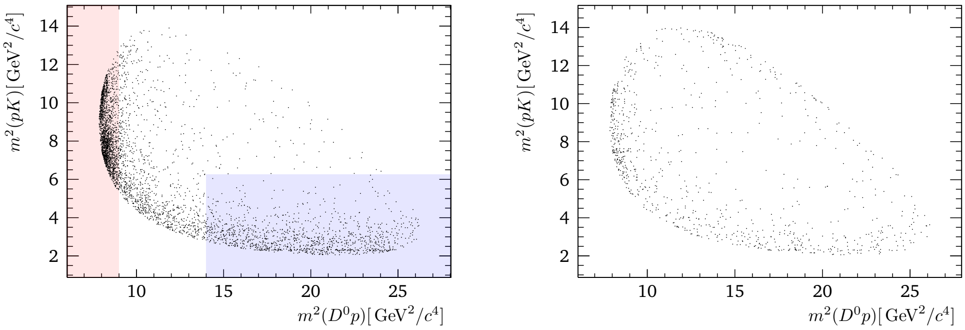

(a) $D^0 \to K^-\pi^+$ (b) $D^0 \to KK$

Fig. 6.1.: Dalitz plot of the selected $\Lambda_b^0 \to D^0pK$ candidates within a $2\sigma_{\Lambda_b^0}$ mass window of $m(\Lambda_b^0) \in [5591.90, 5646.53]\,\mathrm{MeV}/c^2$. The left plot additionally highlights the Dalitz subregions used to determine the Λ_c^{+*} (red) and Λ^* (blue) amplitude contributions.

The PDF used for both amplitude fit types contains only a parametrisation of signal components. Whereas a background model is not necessary for the *sFit*, we justify this for the fit in the $2\sigma_{\Lambda_b^0}$ signal mass window with the unknown distribution of the remaining underlying background. We expect a relatively high amount of $\Xi_b \to D^*pK$ candidates in the $2\sigma_{\Lambda_b^0}$ window (table 6.1). In general one would approach this by a global fit including the m_{D^0} sidebands. Due to the tight preselection of $|m(D^0) - m(D^0)_{\text{PDG}}| < 25.0\,\text{MeV}/c^2$ (section 4.2.4) this is not possible. There is only $\sim 66\,\%$ ($\sim 47\,\%$) Λ_b^0 signal expected in the selected candidates of the $D^0 \to K^-\pi^+$ (KK) samples in fig. 6.1. This amounts to about 2747 (419) true signal candidates in the shown $D^0 \to K^-\pi^+$ (KK) sample. The fractions of all contributions in the selected Λ_b^0 candidates is shown in table 6.1. Due to the limited number of events we will fit only the Dalitz plot of the $\Lambda_b^0 \to D^0 pK$ candidates with $D^0 \to K^-\pi^+$. This decision is also strengthened by the additional D_s^{-*} resonances that add to the complexity of the PDF.

Tab. 6.1.: Fractions in $\%$ of all contributions in a 2σ window from the fitted Λ_b^0 mass peak value.

	D^0	Signal	$\Lambda_b^0 \to pKKK$	$\Xi_b \to D^* pK$	Comb.	$\Lambda_b^0 \to D^0 p\pi$	$\Lambda_b^0 \to D^* p\pi$
Λ_b^0	$K\pi$	66		22	5	4	3
	KK	47	32	9	9	2	2

6.1 Likelihood Fit

Under consideration of the partial decay width of a Dalitz plot from eq. (2.23) we can formulate the general PDF, that describes the amplitudes in the Dalitz plot to be

$$\mathcal{P}(\Omega) = \frac{|\mathcal{M}(\Omega)|^2 \epsilon(m_{pK}^2, m_{D^0 p}^2)}{\int_{\text{DP}} |\mathcal{M}(\Omega)|^2 \epsilon(m_{pK}^2, m_{D^0 p}^2) d\Omega} \quad . \tag{6.1}$$

The matrix element $|\mathcal{M}|^2$ is the sum of the helicity amplitudes from eq. (2.57) and $\epsilon(m_{pK}^2, m_{D^0 p}^2)$ accounts for the efficiency (see section 4.6.3) in a specific phase space region. The integral over the full Dalitz plot $\int_{\text{DP}}$ in the denominator ensures the normalisation of the PDF and is calculated numerically by the method of finite elements in a 1000×1000 grid. We find the negative logarithmic likelihood (NLL)

$$\text{NLL} = -2 \log \mathcal{L} = -2 \sum_{i=1}^{N} \log \mathcal{P}(\Omega_i) \quad , \tag{6.2}$$

we need to minimise. The minimisation is carried out with TensorFlowAnalysis (TFA) [120], an amplitude analysis toolkit utilising Google's TensorFlow [121]. TFA minimises the NLL with `MINUIT` [97] and uses TensorFlow for its calculation. This enables us to utilise GPU units that prove beneficial in the highly parallelised NLL calculation of the unbinned fit.

The fit implements two free parameters per complex helicity coupling $\mathcal{H}$. For more stability, the couplings are realised with cartesian coordinates, $\text{Re}\,\mathcal{H}$ and $\text{Im}\,\mathcal{H}$, and transformed to their polar representation $\mathcal{H} = r \exp \Phi$ afterwards. The overall normalisation of $\mathcal{P}(\Omega)$ is arbitrary, which gives us the freedom to set the magnitude r and phase Φ of one helicity coupling to a fixed value. We chose to set $\mathcal{H}^+[\Lambda_c^+(2880)] = 1 + i0$.

The helicity couplings $\mathcal{H}$ are no observables. Therefore we use the spin-averaged fit fraction [20, 49]

$$\mathcal{F}_i = \frac{\sum_{\lambda_{\Lambda_b^0},\lambda_p} \int_{\text{DP}} \left| A^i_{\lambda_{\Lambda_b^0},\lambda_p}(\Omega) \right|^2 d\Omega}{\sum_{\lambda_{\Lambda_b^0},\lambda_p} \int_{\text{DP}} \left|\mathcal{M}(\Omega)\right|^2 d\Omega} \tag{6.3}$$

to present the relative magnitude of an amplitude as an observable. If the sum $\sum_i \mathcal{F}_i$ differs from unity, this indicates the presence of interference effects between the amplitudes. The interference between two amplitudes is calculated with the interference fit fraction

$$\mathcal{F}_{ij} = \frac{\sum_{\lambda_{\Lambda_b^0},\lambda_p} \int_{\text{DP}} 2\,\text{Re}\left[A^i_{\lambda_{\Lambda_b^0},\lambda_p}(\Omega) A^{j*}_{\lambda_{\Lambda_b^0},\lambda_p}(\Omega) \right] d\Omega}{\sum_{\lambda_{\Lambda_b^0},\lambda_p} \int_{\text{DP}} \left|\mathcal{M}(\Omega)\right|^2 d\Omega} \quad \text{, for } i < j. \tag{6.4}$$

The statistical uncertainty of the fit fractions is determined from pseudo experiments.

6.2 Correction of the $P_{\text{NN},p}(p)$ Efficiency

The efficiencies in section 4.6 are determined from corrected MC. As there is a known issue for the PID response of protons due to long living Λ in the calibration sample [122], we use a $\Lambda_b^0 \to \Lambda_c^+ \pi$ sample for calibration. As we assume the effects of the low event count of the alternative calibration sample to cancel in the ratios of the $m(D^0 ph)$ fit in chapter 5 we need to validate the proton PID efficiency for the amplitude fit. It is to expect, that the efficiency is a function of the proton momentum $P(p)$. We find an adaptive binning in $P(p)$ that yields an even distribution of simulated $\Lambda_b^0 \to D^0 p\pi$ candidates without the proton PID selection applied. We calculate the proton PID selection efficiency from sideband subtraction for each bin. The resulting efficiency ratio from simulation to DATA is shown in fig. 6.2.

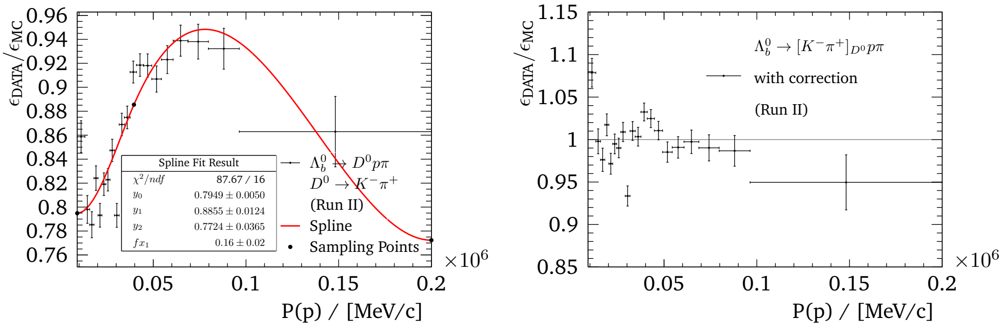

(a) Spline Fit

(b) $P_{\text{NN},p}(p)$ Correction

Fig. 6.2.: Spline fit to the $P_{\text{NN},p}(p)$ cut efficiency ratios $\epsilon_{\text{DATA}}/\epsilon_{\text{MC}}$ in bins of the proton momentum (left) and the effect of the applied correction (right). Determined from Run II samples of $\Lambda_b^0 \to D^0 p\pi$ with $D^0 \to K^-\pi^+$.

The function to correct the efficiency deviations is found by fitting a spline with three sampling points. The y_i values of the sampling points are free, the x_0 and x_2 values are fixed to the histogram boundaries and x_1 is free but defined via a fraction f_{x_1}, such that: $x_1 = x_0 + f_{x_1} \cdot (x_2 - x_0)$. The fitted spline, its parameters and the correction effect is shown in fig. 6.2. Due to the available number of events, the correction is extracted from Run II samples only and in addition contributes to the acceptance as momentum dependent correction to the efficiency in eq. (6.1).

6.3 Preliminary Dalitz Plot Fit

The general strategy is to precede the fit to the full Dalitz plot with fits to subregions to extract sets of significant amplitude contributions. In fig. 6.1 resonances in the $m^2_{D^0p}$ and m^2_{pK} are clearly visible and the respective subregions are highlighted. The selected regions and their selection boundaries are listed in table 6.2. We expect interference effects of the different resonance channels in the region where both channels overlap. To exclude these effects there is a gap ($m^2_{D^0p} \in [9, 14]\,\mathrm{GeV}^2/c^4$) left between the two subregions.

Tab. 6.2.: Amplitude fit regions. The colour matches the highlighted areas of the Dalitz plot in fig. 6.1.

	Region	Selection
red	Λ_c^{+*} resonances	$m^2_{D^0p} < 9\,\mathrm{GeV}^2/c^4$
blue	Λ^* resonances	$m^2_{D^0p} > 14\,\mathrm{GeV}^2/c^4$, $m^2_{pK} < 2.5^2\,\mathrm{GeV}^2/c^4$
	full dalitz	

6.3.1 Fit Full Dalitz Plot

First an amplitude fit to the low $m^2_{D^0p}$ region is performed in appendix N.3.1 to find the necessary Λ_c^{+*} amplitudes. This fit is then followed up by a fit to the low m^2_{pK} region in appendix N.3.2 to find the Λ^* amplitudes. Both fits start with a full set of possible resonances and then insignificant amplitudes are iteratively removed. An overview of all amplitudes considered is given in the appendix in tables N.1 and N.4. We combine the resonances of the reduced fits to both subregions to find the full amplitude model. The exponential decay constants of the continuum contributions are fixed to the values found in the low $m^2_{D^0p}$ region.

By using only amplitudes of the reduced models, we could reduce the amount of 78 free parameters of the full fit (see appendix N.3.3) to 50. The distribution of the fitted reduced amplitude model, as shown for the full Dalitz plot in fig. 6.3, follows the scatter plot of Λ_b^0 candidates in fig. 6.1. We find the Λ_c^{+*} and Λ^* amplitudes pushed towards their low mass borders of the Dalitz plot. These regions are described well according to the pull, which is described by the difference of model and DATA divided by uncertainty. A collection of the fitted partial amplitudes squared plotted in the Dalitz plane can be found in appendix N.3.4.

It is interesting to observe, that the fit gains significantly in stability, when including both, the pK- and D^0p-resonance channels. This is obvious from the statistical uncertainties of the resulting fit parameters in table 6.3 and from the shrinkage of the covariance ellipses of the

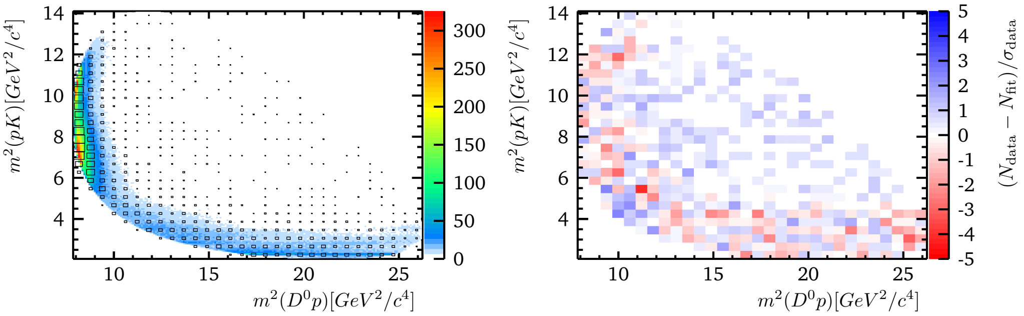

Fig. 6.3.: Reduced amplitude fit to the full Dalitz plot, shown with a resolution of 200 × 200 bins overlayed by DATA in 30 × 30 bins (left) and the pull distribution (right).

Tab. 6.3.: Fit fractions and fitted parameters of the reduced fit in the full Dalitz plot region.

	$\mathcal{F}_i$	$\mathrm{Re}\,\mathcal{H}^+$	$\mathrm{Im}\,\mathcal{H}^+$	$\mathrm{Re}\,\mathcal{H}^-$	$\mathrm{Im}\,\mathcal{H}^-$
$\Lambda_c^+(2850)$	34.45%	-120 ± 35	-176 ± 30	-131 ± 22	$(9 \pm 4) \times 10^1$
$\Lambda_c^+(2880)$	2.92%	1.0	0.0	20.3 ± 1.3	-7 ± 4
$\Lambda_c^+(2940)$	2.89%	18.6 ± 2.5	9 ± 5	-15 ± 4	-25 ± 5
$C_{1/2^+}(D^0p)$	8.42%	-55 ± 32	140 ± 11	106 ± 18	-41 ± 20
$C_{1/2^-}(D^0p)$	17.63%	186 ± 18	$(0 \pm 4) \times 10^1$	89 ± 12	-40 ± 18
$C_{3/2^+}(D^0p)$	7.83%	$(-0 \pm 4) \times 10^1$	143 ± 22	$(2.3 \pm 0.6) \times 10^2$	$(2 \pm 5) \times 10^1$
$\Lambda(1405)$	3.32%	-28 ± 13	56 ± 6	-19 ± 14	8 ± 8
$\Lambda(1520)$	3.98%	-11.3 ± 1.2	-8 ± 4	9.7 ± 2.8	-11.3 ± 2.0
$\Lambda(1600)$	8.76%	39 ± 9	-40 ± 10	-35 ± 12	10 ± 12
$\Lambda(1690)$	4.63%	-30 ± 7	-16 ± 4	-10 ± 7	-25 ± 9
$\Lambda(1810)$	3.53%	-3 ± 9	-21 ± 7	-8 ± 5	-24.6 ± 2.2
$\Lambda(1890)$	3.78%	-12 ± 8	36 ± 4	-15 ± 17	-34 ± 8
$\Lambda(2110)$	5.01%	26 ± 14	-90 ± 14	67 ± 11	36 ± 13

helicity couplings in fig. N.5, when compared to the results of the fits in the Dalitz subregions (tables N.3 and N.6). Consequently there is a strong dependence of the amplitudes, which interfere in the overlap region of both resonance channels. The $\mathcal{H}^\pm$ interference test in appendix N.2 supports this claim, as we see strong deviations of the amplitude model, when shifting the phase of one coupling. We further calculate, that the broad resonance $\Lambda_c^+(2850)$, which also has the highest fit fraction, and $C_{1/2^\pm}(D^0p)$ have relatively large interference fit fractions with the Λ^* resonances. This is observed in the fit fraction values determined from pseudo experiments in fig. 6.5.

The projections on the $m^2_{D^0p}$ and m^2_{pK} are in fig. 6.4 and show an agreement between the amplitude model and DATA. This is also true for the model slices of the previously fitted Dalitz subregions in the same figure. We further notice a contribution of the $\Lambda_c^+(2850)$ in the Λ^* resonance region, visible in its slice's projection on $m^2_{D^0p}$. This contribution also adds to the fit stability, as it further links the Λ_c^{+*} region with high event count and small number of amplitudes to the amplitude dense Λ^* region with less events. It can be also seen in fig. 6.4a, that the $\Lambda_c^+(2850)$ resonance ranges across the full phase space.

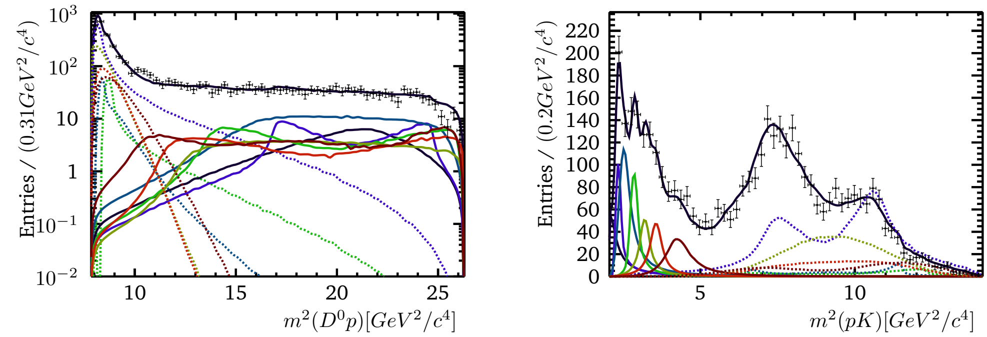

(a) Full Region

(b) Full Region

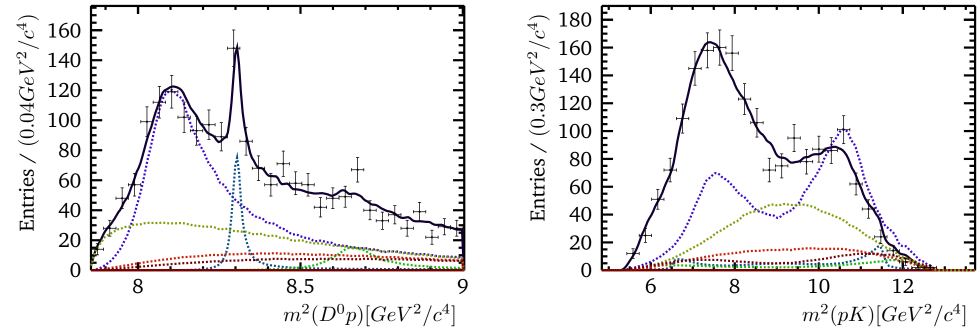

(c) Λ_c^{+*} Region Slice

(d) Λ_c^{+*} Region Slice

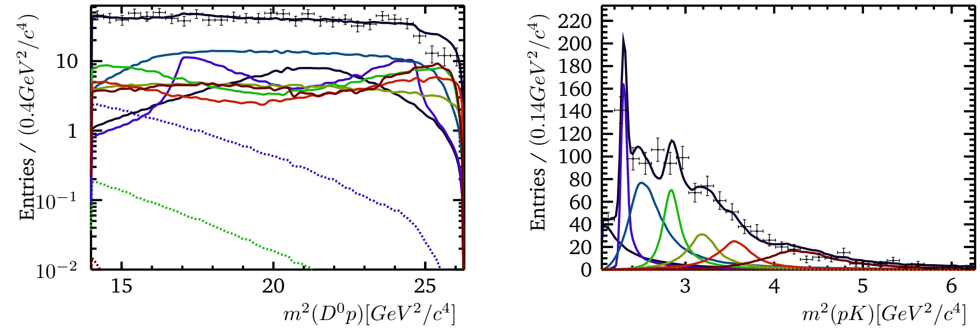

(e) Λ^* Region Slice

(f) Λ^* Region Slice

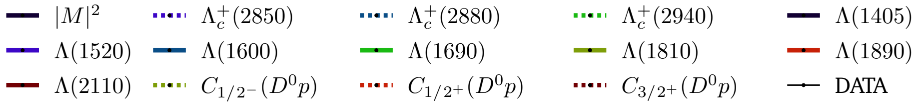

Fig. 6.4.: Reduced amplitude fit to the full Dalitz plot. Shown as projection on $m^2_{D^0p}$ in (a) and on m^2_{pK} in (b). The partial amplitudes are shown as their amplitudes squared.

6.3.2 Fit Validation

Due to the circumstance, that we expect only a fraction of about 46% to be signal candidates and that there is no background model considered we have an unknown large systematic. Thus, there is no point in the investigation of other systematics and we focus on the validation of the amplitude model. We generate and fit a set of one thousand pseudo experiments from the reduced amplitude model of the full Dalitz plot fit from section 6.3.1.

Similar to the validation of the fit for the $m(D^0ph)$ distribution in section 5.4.1, we use the pull, as defined in eq. (5.9) to calculate the bias and a correction factor for the statistical uncertainty. Some distributions show an asymmetric shape. We therefore calculate the asymmetric limits of the confidence interval numerically by finding the respective integral of the model, that fulfils the 1σ condition of $\sim 68.27\%$ from the distributions peak value.

Calculating the pull is only possible for model parameters that have a valid uncertainty. We are able to calculate and fit the pull distributions for $\mathrm{Re}\,\mathcal{H}^{\pm}$, $\mathrm{Im}\,\mathcal{H}^{\pm}$ and the magnitude $r^{\pm}$ of the helicity coupling polar representation. In case of the phase $\Phi^{\pm}$, we cannot ensure a valid propagation of the uncertainties, as the transformation is no continuous function to differentiate. Thus, we use the residuals $\xi_m - \xi_t$ to extract their bias and uncertainty correction. We further evaluate the (interference) fit fractions of fig. 6.5 directly from their distributions. A summary of all fits and fit fraction values can be found in appendix N.3.5.

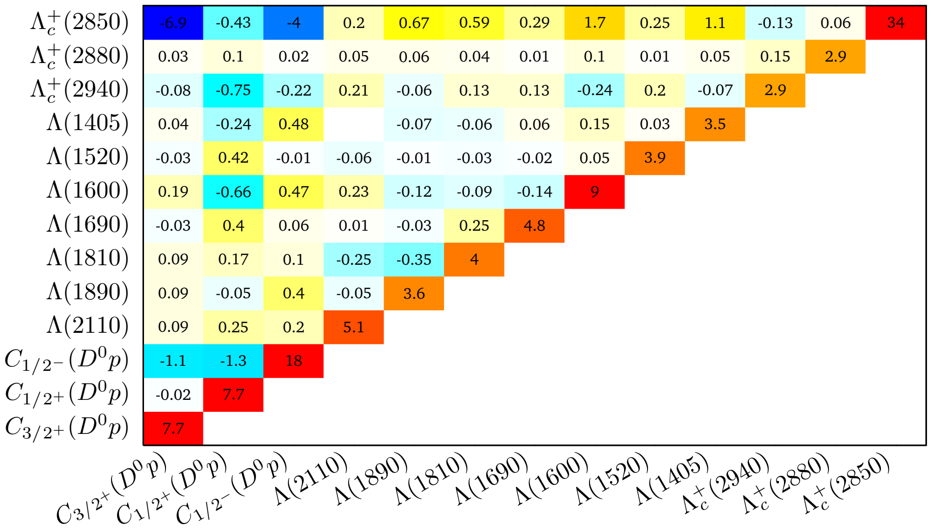

	$C_{3/2^+}(D^0p)$	$C_{1/2^+}(D^0p)$	$C_{1/2^-}(D^0p)$	$\Lambda(2110)$	$\Lambda(1890)$	$\Lambda(1810)$	$\Lambda(1690)$	$\Lambda(1600)$	$\Lambda(1520)$	$\Lambda(1405)$	$\Lambda_c^+(2940)$	$\Lambda_c^+(2880)$	$\Lambda_c^+(2850)$
$\Lambda_c^+(2850)$	-6.9	-0.43	-4	0.2	0.67	0.59	0.29	1.7	0.25	1.1	-0.13	0.06	34
$\Lambda_c^+(2880)$	0.03	0.1	0.02	0.05	0.06	0.04	0.01	0.1	0.01	0.05	0.15	2.9	
$\Lambda_c^+(2940)$	-0.08	-0.75	-0.22	0.21	-0.06	0.13	0.13	-0.24	0.2	-0.07	2.9		
$\Lambda(1405)$	0.04	-0.24	0.48		-0.07	-0.06	0.06	0.15	0.03	3.5			
$\Lambda(1520)$	-0.03	0.42	-0.01	-0.06	-0.01	-0.03	-0.02	0.05	3.9				
$\Lambda(1600)$	0.19	-0.66	0.47	0.23	-0.12	-0.09	-0.14	9					
$\Lambda(1690)$	-0.03	0.4	0.06	0.01	-0.03	0.25	4.8						
$\Lambda(1810)$	0.09	0.17	0.1	-0.25	-0.35	4							
$\Lambda(1890)$	0.09	-0.05	0.4	-0.05	3.6								
$\Lambda(2110)$	0.09	0.25	0.2	5.1									
$C_{1/2^-}(D^0p)$	-1.1	-1.3	18										
$C_{1/2^+}(D^0p)$	-0.02	7.7											
$C_{3/2^+}(D^0p)$	7.7												

Fig. 6.5.: Summary of the (interference) fit fractions evaluated with pseudo experiments in section 6.3.2. Only the top half of the matrix is shown and empty bins fall below the shown precision. All numbers are listed including their uncertainties in table N.9.

The correction of all coupling polar parameters in table 6.4 shows no bias larger than one standard deviation of the corrected result. We find the magnitude r^- of $\Lambda(2110)$ and r^+ of the continuum contribution with spin $+^3/_2$ to deviate the most. Both magnitudes are corrected towards larger values and are therefore necessary. There is a noticeable underestimation of the statistical uncertainty. Further, we list and calculate the parameters significance in standard deviations as x/σ_x. In case of an asymmetric uncertainty we use the mean uncertainty as standard deviation. The significance of the phase is calculated as $2\pi/\sigma_\Phi$. The corrections of $\mathrm{Re}\,\mathcal{H}^{\pm}$ and $\mathrm{Im}\,\mathcal{H}^{\pm}$ are listed in table N.8.

Tab. 6.4.: Bias and scale of the systematic uncertainties for the helicity couplings magnitude and phase. The last row shows the corrected parameters' significance in standard deviations. The uncertainty on the phases u_Φ is partly underestimated, when compared to the covariance ellipses in appendix N.1.

		Fit value	Bias corr.	Error scale		Corrected	$n \cdot \sigma$
				lo	hi		
$\Lambda_c^+(2850)$	r^+	213 ± 19	$+20.7$	-2.3	2.53	$(2.3^{+0.5}_{-0.4}) \times 10^2$	$5.07 \cdot \sigma$
	ϕ^+	4.113	-0.0282			$4.08^{+0.34}_{-0.38}$	$17.44 \cdot \sigma$
	r^-	160 ± 28	$+6.16$	-1.79	1.99	$(1.7^{+0.6}_{-0.5}) \times 10^2$	$3.12 \cdot \sigma$
	ϕ^-	2.528	$+0.046$			2.6 ± 0.4	$14.86 \cdot \sigma$
$\Lambda_c^+(2880)$	r^-	21.3 ± 2.1	$+2.19$	-1.04	1.62	$23.5^{+3.4}_{-2.2}$	$8.33 \cdot \sigma$
	ϕ^-	5.969	-0.118			$5.85^{+0.40}_{-0.31}$	$17.70 \cdot \sigma$
$\Lambda_c^+(2940)$	r^+	21 ± 4	$+4.78$	-2.18	2.27	26 ± 9	$2.83 \cdot \sigma$
	ϕ^+	0.468	$+0.13$			$0.6^{+0.4}_{-0.5}$	$12.79 \cdot \sigma$
	r^-	29 ± 4	$+0.206$	-1.72	1.96	29^{+9}_{-8}	$3.60 \cdot \sigma$
	ϕ^-	4.152	-0.126			$4.0^{+0.5}_{-0.4}$	$13.58 \cdot \sigma$
$\Lambda(1405)$	r^+	63 ± 4	$+5.51$	-2.77	2.61	68^{+10}_{-11}	$6.59 \cdot \sigma$
	ϕ^+	2.028	-0.0496			2.0 ± 0.4	$16.98 \cdot \sigma$
	r^-	21 ± 12	$+2.89$	-0.912	1.91	24^{+23}_{-11}	$1.40 \cdot \sigma$
	ϕ^-	2.755	$+0.281$			$3.0^{+1.4}_{-1.6}$	$4.24 \cdot \sigma$
$\Lambda(1520)$	r^+	14.1 ± 3.5	$+0.865$	-1.31	1.55	15 ± 5	$2.96 \cdot \sigma$
	ϕ^+	3.782	-0.0903			3.7 ± 0.5	$13.70 \cdot \sigma$
	r^-	14.9 ± 2.3	$+1.95$	-2.27	1.79	17^{+4}_{-5}	$3.61 \cdot \sigma$
	ϕ^-	5.424	$+0.0884$			$5.5^{+0.5}_{-0.6}$	$11.26 \cdot \sigma$
$\Lambda(1600)$	r^+	56 ± 5	$+7.32$	-2.1	2.42	64^{+12}_{-11}	$5.53 \cdot \sigma$
	ϕ^+	5.486	$+0.0102$			5.5 ± 0.4	$16.35 \cdot \sigma$
	r^-	36 ± 13	-2.11	-1.2	2.1	34^{+26}_{-15}	$1.65 \cdot \sigma$
	ϕ^-	2.874	$+0.129$			3.0 ± 0.9	$7.14 \cdot \sigma$
$\Lambda(1690)$	r^+	34 ± 7	$+0.605$	-1.64	1.84	35^{+13}_{-11}	$2.91 \cdot \sigma$
	ϕ^+	3.628	-0.0641			$3.6^{+0.6}_{-0.4}$	$13.04 \cdot \sigma$
	r^-	27 ± 6	$+6.29$	-2.05	2.15	33^{+12}_{-11}	$2.88 \cdot \sigma$
	ϕ^-	4.326	$+0.244$			$4.6^{+0.5}_{-0.6}$	$10.81 \cdot \sigma$
$\Lambda(1810)$	r^+	21 ± 8	$+5.6$	-1.41	2.44	27^{+19}_{-11}	$1.79 \cdot \sigma$
	ϕ^+	4.554	-0.204			$4.3^{+0.7}_{-0.5}$	$11.16 \cdot \sigma$
	r^-	25.7 ± 2.8	$+1.97$	-3.18	3.41	28^{+10}_{-9}	$2.97 \cdot \sigma$
	ϕ^-	4.415	$+0.0893$			$4.5^{+0.9}_{-0.7}$	$7.53 \cdot \sigma$
$\Lambda(1890)$	r^+	38 ± 4	$+4.89$	-2.8	2.77	43 ± 12	$3.65 \cdot \sigma$
	ϕ^+	1.890	$+0.075$			2.0 ± 0.4	$14.97 \cdot \sigma$
	r^-	37 ± 7	$+0.0542$	-1.91	2.07	37^{+14}_{-13}	$2.68 \cdot \sigma$
	ϕ^-	4.292	-0.000693			4.3 ± 0.6	$10.88 \cdot \sigma$
$\Lambda(2110)$	r^+	93 ± 16	-3.97	-1.83	1.94	89^{+31}_{-29}	$2.99 \cdot \sigma$
	ϕ^+	4.996	-0.113			$4.88^{+0.35}_{-0.34}$	$18.09 \cdot \sigma$
	r^-	76 ± 9	$+24.6$	-2.78	2.29	100^{+22}_{-26}	$4.21 \cdot \sigma$
	ϕ^-	0.499	$+0.00399$			0.5 ± 0.4	$14.78 \cdot \sigma$
$C_{1/2^-}(D^0p)$	r^+	186 ± 18	$+15.4$	-1.89	2.14	$(2.0^{+0.4}_{-0.3}) \times 10^2$	$5.54 \cdot \sigma$
	ϕ^+	0.019	$+0.0434$			$0.06^{+0.35}_{-0.39}$	$17.14 \cdot \sigma$
	r^-	98 ± 10	$+19.1$	-3.43	3.97	$(1.2 \pm 0.4) \times 10^2$	$3.07 \cdot \sigma$
	ϕ^-	5.861	-0.149			5.7 ± 0.4	$15.47 \cdot \sigma$
$C_{1/2^+}(D^0p)$	r^+	150 ± 16	-3.38	-2.12	2.69	$(1.5^{+0.4}_{-0.3}) \times 10^2$	$3.79 \cdot \sigma$
	ϕ^+	1.943	$+0.109$			$2.05^{+0.35}_{-0.46}$	$15.60 \cdot \sigma$
	r^-	114 ± 16	$+12.3$	-2.7	3.06	$(1.3^{+0.5}_{-0.4}) \times 10^2$	$2.69 \cdot \sigma$
	ϕ^-	5.912	-0.0171			$5.9^{+0.5}_{-0.4}$	$14.16 \cdot \sigma$
$C_{3/2^+}(D^0p)$	r^+	143 ± 22	$+36.4$	-2.84	3.33	$(1.8^{+0.7}_{-0.6}) \times 10^2$	$2.68 \cdot \sigma$
	ϕ^+	1.605	$+0.0519$			$1.7^{+0.5}_{-0.6}$	$11.45 \cdot \sigma$
	r^-	$(2.3 \pm 0.6) \times 10^2$	$+11.9$	-1.21	1.23	$(2.4 \pm 0.8) \times 10^2$	$3.07 \cdot \sigma$
	ϕ^-	0.109	-0.0508			$0.1^{+0.4}_{-0.7}$	$11.25 \cdot \sigma$

6.4 *sFit* of the $\Lambda_b^0 \to D^0pK$ Amplitudes

The advantage of the *sFit* [119] approach is, that there is no need in correctly describing an underlying background contribution. A *sFit* [119] weights each likelihood term with the event specific *sWeight*. The *sWeights* for the $\Lambda_b^0 \to D^0pK$ candidates are extracted from the fit in appendix J.1.3. However, due to the small signal to background ratio in the fitted mass distribution, this *sFit* is highly unstable and we optimise the logarithmic likelihood function to gain in stability. As the acceptance only affects the normalisation of the PDF [96] we can reformulate eq. (6.1) to

$$\mathcal{P}(\Omega)' = \frac{|\mathcal{M}(\Omega)|^2}{\int_{\text{DP}} |\mathcal{M}(\Omega)|^2 \epsilon(m_{pK}^2, m_{D^0p}^2) d\Omega} = \frac{|\mathcal{M}(\Omega, \xi)|^2}{N(\xi)} \quad , \tag{6.5}$$

where ξ represents the set of amplitude parameters. We then expand the resulting NLL function as followed:

$$\begin{aligned} \text{NLL}' &= -2s_{\text{corr}} \sum_{i=1}^{N} w_i \log \mathcal{P}(\Omega_i, \xi)' \\ &= -2s_{\text{corr}} \sum_{i=1}^{N} w_i |\mathcal{M}(\Omega, \xi)|^2 + 2s_{\text{corr}} \log N(\xi) \sum_{i=1}^{N} w_i - 2s_{\text{corr}} \sum_{i=1}^{N} w_i \log \epsilon(m_{pK}^2, m_{D^0p}^2) \end{aligned} \tag{6.6}$$

The factor $s_{\text{corr}} = \sum_i \frac{w_i}{\sum_i w_i^2}$ is a constant scaling of the likelihood to account for uncertainties by the background subtraction. This factor, however, does not sufficiently correct the uncertainty estimation [123]. The error estimation is evaluated and corrected later in section 6.4.3. The last term is independent of ξ and thus a constant offset, which can be neglected in the likelihood calculation.

The fit is developed similar to the preliminary amplitude fit in section 6.3. We start with a fit of the Λ_c^{+*} resonances in the low $m_{D^0p}^2$ region, but skip the Λ^* resonance fit in the low m_{pK}^2 region to directly fit the full phase space.

6.4.1 *sFit* of Λ_c^{+*} in Low $m_{D^0p}^2$ Region

As in the previous fit to the low $m_{D^0p}^2$ region in appendix N.3.1 we develop an Λ_c^{+*} amplitude model from all possible resonances (table N.1) and reduce the fit parameters by removing insignificant amplitudes. Both $C_{3/2^\pm}(D^0p)$ amplitudes are removed and we find the fitted parameters and fit fractions in table 6.5. The Dalitz plane and the projections of the model and *sWeight*ed data on m_{D^0p} and m_{pK}^2 are shown in fig. 6.6. The pull distribution in the same figure proves a sufficient agreement of the model with the DATA across the fitted phase space. In comparison to the fit in the $2\sigma_{\Lambda_b^0}$ mass window (fig. N.11) the resonances found by the *sFit* are distributed the same way in the Dalitz plane, but show more distinct structures.

Tab. 6.5.: Fit fractions and fitted parameters of the *sFit* to the low $m^2_{D^0p}$ region.

	$\mathcal{F}_i$	$\mathrm{Re}\,\mathcal{H}^+$	$\mathrm{Im}\,\mathcal{H}^+$	$\mathrm{Re}\,\mathcal{H}^-$	$\mathrm{Im}\,\mathcal{H}^-$	α
$\varLambda_c^+(2850)$	37.09%	21.0 ± 2.0	-6.8 ± 2.6	-7.9 ± 2.1	-14 ± 4	
$\varLambda_c^+(2880)$	5.64%	1.0	0.0	2.09 ± 0.26	1.285 ± 0.026	
$\varLambda_c^+(2940)$	4.15%	-3.6 ± 0.9	-0.2 ± 0.8	-1.6 ± 0.9	-1.6 ± 0.5	
$C_{1/2^+}(D^0p)$	11.23%	-3.1 ± 2.4	-10.1 ± 2.0	15 ± 6	12 ± 5	1.31 ± 0.33
$C_{1/2^-}(D^0p)$	41.89%	-9.5 ± 3.0	23 ± 5	16 ± 5	18 ± 5	0.89 ± 0.13

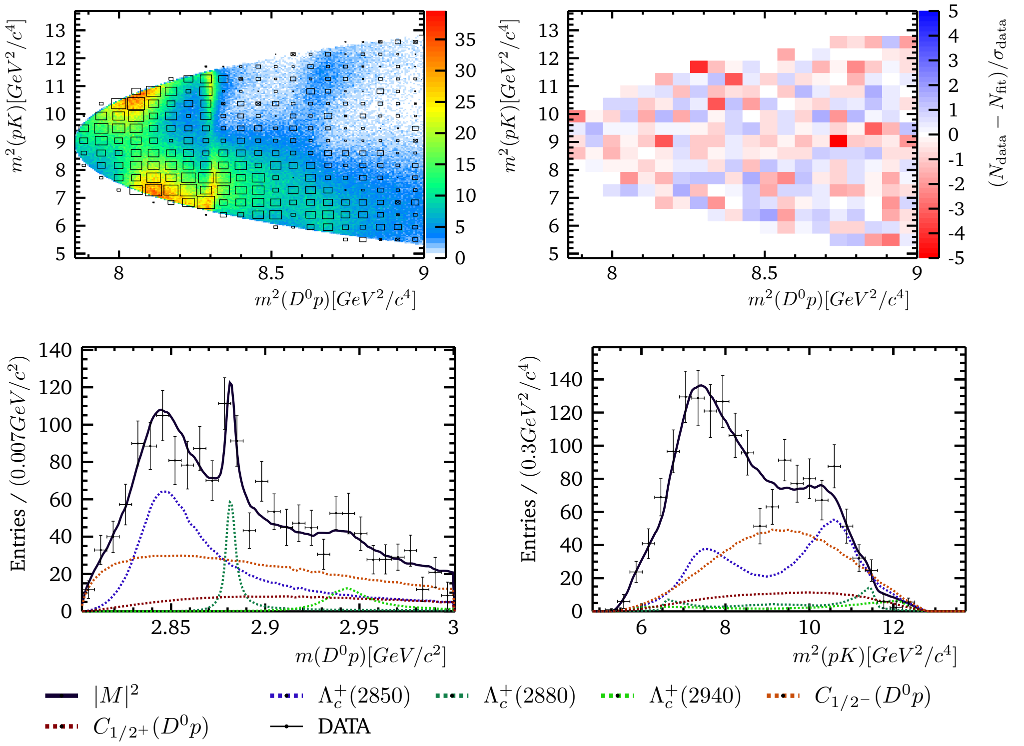

Fig. 6.6.: Amplitude *sFit* to the low $m^2_{D^0p}$ region. The projections on m_{D^0p} (bottom left) and on m^2_{pK} (bottom right) are shown. The partial components are their amplitudes squared.

6.4.2 *sFit* of Full Dalitz Plot

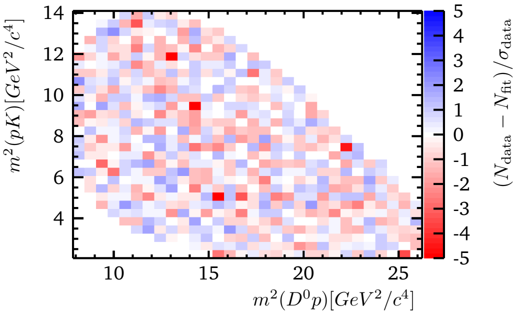

Fig. 6.7.: Pull distribution of the amplitude *sFit* in fig. 6.8.

We use the D^0p amplitude model of section 6.4.1 with fixed exponential decay constants α and start with the full set of possible $\varLambda^*$ resonances in table N.4. Again we remove insignificant amplitudes from the model. We reduce the amplitude model to the contributions listed in the fit result of the reduced *sFit* in table 6.6. In comparison to the fit in the $2\sigma_{\varLambda_b^0}$ mass region in section 6.3.1 we have to add the high spin resonances $\Lambda(2100)$ with spin parity $7/2^-$

and $\Lambda(2350)$ with spin parity $9/2^+$. The model without one of these high spin resonances would result into an underestimation of the data in the overlap region of the pK and D^0p resonance channels. The fitted model could be reduced from 78 to 54 free fit parameters.

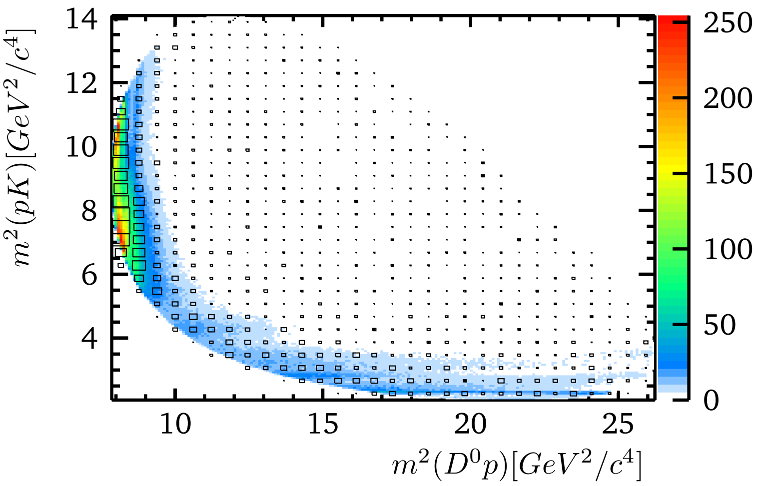

Fig. 6.8.: Amplitude *sFit* of Λ_c^{+*} and Λ^* resonances to the full phase space, shown in the Dalitz plot with a resolution of 200×200 bins overlayed by DATA in 30×30 bins.

The amplitude fit result in the Dalitz plot is visualised in fig. 6.8 and its pull in fig. 6.7 proves the agreement of model and *sWeight*ed DATA. In comparison to the fit in the $2\sigma_{\Lambda_b^0}$ mass window (fig. 6.3) there is a distinct structure of multiple Λ^* resonances visible in the pK channel. It is also noticeable from fig. 6.8, that both resonance channels tend to interfere in a way, that they primarily populate the phase space towards lower $m^2_{D^0p}$ and m^2_{pK} masses. This interference effect is also visible in the fit to the $2\sigma_{\Lambda_b^0}$ mass window (fig. 6.3), but more prominent by the distinctly separated Λ^* resonances. The distribution of all partial amplitudes' squared in the Dalitz plane can be found in appendix N.4.2. The projections in fig. 6.9 of the amplitude model on $m^2_{D^0p}$ and m^2_{pK} agree with the *sWeight*ed DATA for the full Dalitz plot and both subregions of the Λ_c^{+*} and Λ^* resonances.

Tab. 6.6.: Fit fractions and fitted parameters of the *sFit* in the full Dalitz plot region.

	$\mathcal{F}_i$	$\mathrm{Re}\,\mathcal{H}^+$	$\mathrm{Im}\,\mathcal{H}^+$	$\mathrm{Re}\,\mathcal{H}^-$	$\mathrm{Im}\,\mathcal{H}^-$
$\Lambda_c^+(2850)$	22.71%	-64.7 ± 1.0	-67.0 ± 1.0	-76.3 ± 1.1	-93.8 ± 1.0
$\Lambda_c^+(2880)$	3.46%	1.0	0.0	14.2 ± 1.0	8.1 ± 1.0
$\Lambda_c^+(2940)$	3.82%	8.9 ± 1.0	19.4 ± 1.1	-16.6 ± 1.0	-10.2 ± 1.2
$C_{1/2^+}(D^0p)$	14.37%	-92.4 ± 1.1	110.1 ± 1.2	85.7 ± 1.1	45.2 ± 1.0
$C_{1/2^-}(D^0p)$	30.54%	113.4 ± 1.3	-37.6 ± 1.2	113.7 ± 1.2	103.9 ± 1.0
$\Lambda(1405)$	2.35%	6.0 ± 1.5	9.8 ± 0.9	-20.9 ± 1.2	-31.1 ± 2.2
$\Lambda(1520)$	2.77%	-7.0 ± 0.8	7.9 ± 0.9	3.0 ± 0.9	4.9 ± 0.8
$\Lambda(1600)$	7.40%	-8.7 ± 1.3	-37.3 ± 1.0	-0.6 ± 1.0	-20.4 ± 0.9
$\Lambda(1690)$	4.70%	-7.6 ± 1.0	-4.8 ± 1.0	7.8 ± 1.1	-28.8 ± 1.0
$\Lambda(1810)$	7.52%	-23.4 ± 1.1	14.2 ± 0.9	16.9 ± 1.0	-11.6 ± 1.0
$\Lambda(1890)$	4.45%	7.2 ± 1.2	26.2 ± 1.3	-11.5 ± 1.1	-27.8 ± 1.8
$\Lambda(2100)$	2.86%	-28.0 ± 0.9	-5.3 ± 1.1	36.7 ± 1.1	48.2 ± 1.2
$\Lambda(2110)$	3.82%	-10.5 ± 1.1	-32.1 ± 1.0	46.1 ± 1.0	47.1 ± 1.0
$\Lambda(2350)$	0.63%	6.4 ± 0.8	-11.3 ± 0.8	3.5 ± 0.9	27.7 ± 1.3

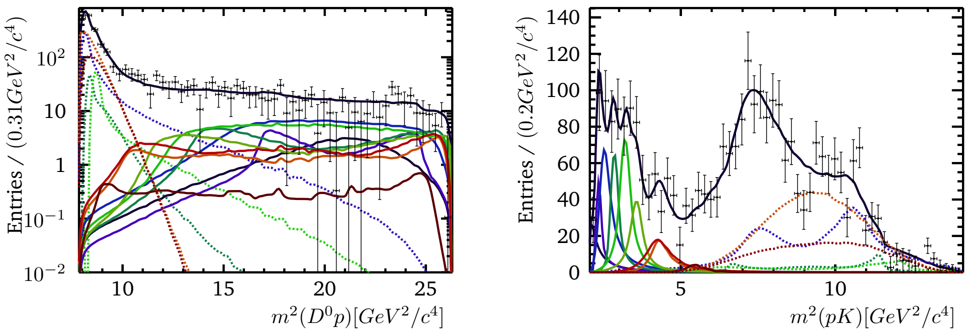

(a) Full Dalitz (b) Full Dalitz

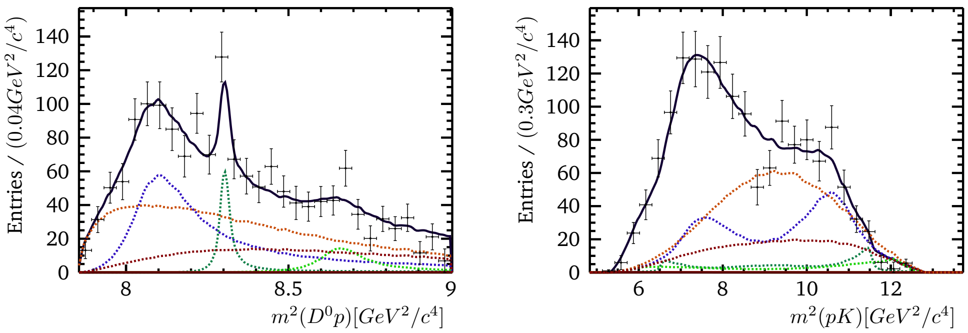

(c) Λ_c^{+*} Region Slice (d) Λ_c^{+*} Region Slice

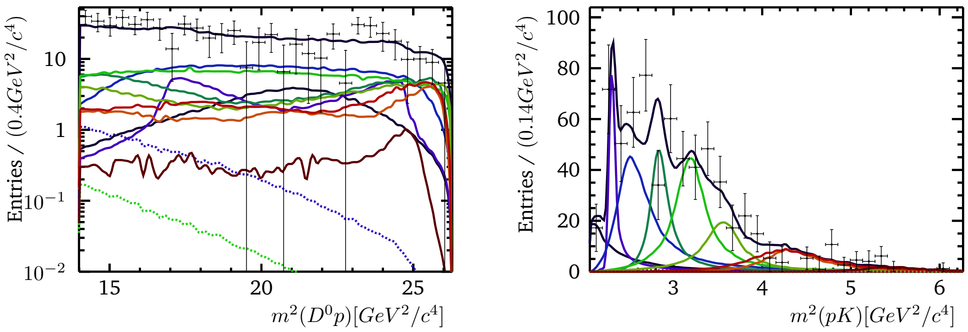

(e) Λ^* Region Slice (f) Λ^* Region Slice

$|M|^2$ · $\Lambda_c^+(2850)$ · $\Lambda_c^+(2880)$ · $\Lambda_c^+(2940)$ · $\Lambda(1405)$
$\Lambda(1520)$ · $\Lambda(1600)$ · $\Lambda(1690)$ · $\Lambda(1810)$ · $\Lambda(1890)$
$\Lambda(2100)$ · $\Lambda(2110)$ · $\Lambda(2350)$ · $C_{1/2^-}(D^0p)$ · $C_{1/2^+}(D^0p)$
DATA

Fig. 6.9.: Amplitude *sFit* of all possible Λ_c^{+*} and Λ^* resonances to the full Dalitz plot. Shown as projection on $m^2_{D^0p}$ (left) and on m^2_{pK} (right). The partial components are shown as their amplitudes squared.

6.4.3 *sFit* Validation

The fit validation follows the one in section 6.3.2. The *sFit* (interference) fit fractions are evaluated from their distributions resulting out of 800 pseudo experiments and visualised in fig. 6.10. All pull, residual and fit fraction distributions and a table of the (interference) with their uncertainty are in appendix N.4.1.

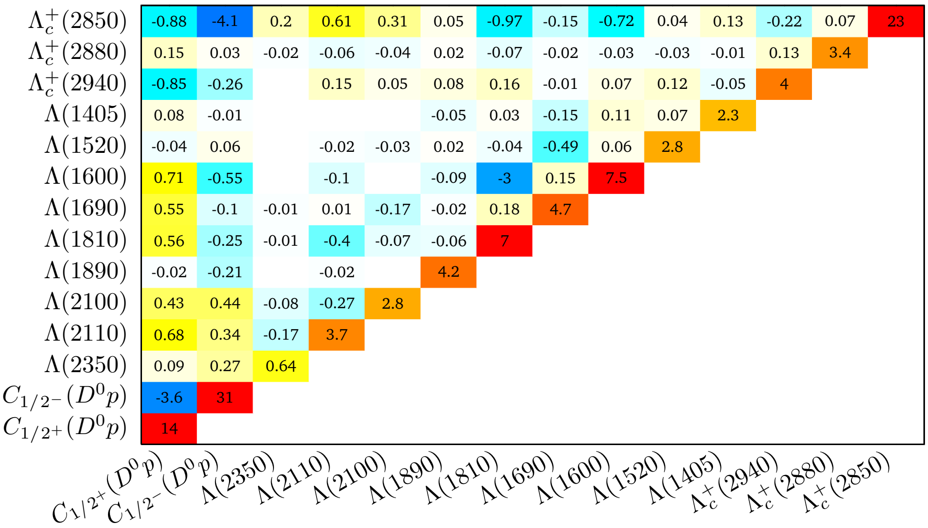

	$C_{1/2^+}(D^0p)$	$C_{1/2^-}(D^0p)$	$\Lambda(2350)$	$\Lambda(2110)$	$\Lambda(2100)$	$\Lambda(1890)$	$\Lambda(1810)$	$\Lambda(1690)$	$\Lambda(1600)$	$\Lambda(1520)$	$\Lambda(1405)$	$\Lambda_c^+(2940)$	$\Lambda_c^+(2880)$	$\Lambda_c^+(2850)$
$\Lambda_c^+(2850)$	-0.88	-4.1	0.2	0.61	0.31	0.05	-0.97	-0.15	-0.72	0.04	0.13	-0.22	0.07	23
$\Lambda_c^+(2880)$	0.15	0.03	-0.02	-0.06	-0.04	0.02	-0.07	-0.02	-0.03	-0.03	-0.01	0.13	3.4	
$\Lambda_c^+(2940)$	-0.85	-0.26		0.15	0.05	0.08	0.16	-0.01	0.07	0.12	-0.05	4		
$\Lambda(1405)$	0.08	-0.01				-0.05	0.03	-0.15	0.11	0.07	2.3			
$\Lambda(1520)$	-0.04	0.06		-0.02	-0.03	0.02	-0.04	-0.49	0.06	2.8				
$\Lambda(1600)$	0.71	-0.55		-0.1		-0.09	-3	0.15	7.5					
$\Lambda(1690)$	0.55	-0.1	-0.01	0.01	-0.17	-0.02	0.18	4.7						
$\Lambda(1810)$	0.56	-0.25	-0.01	-0.4	-0.07	-0.06	7							
$\Lambda(1890)$	-0.02	-0.21		-0.02		4.2								
$\Lambda(2100)$	0.43	0.44	-0.08	-0.27	2.8									
$\Lambda(2110)$	0.68	0.34	-0.17	3.7										
$\Lambda(2350)$	0.09	0.27	0.64											
$C_{1/2^-}(D^0p)$	-3.6	31												
$C_{1/2^+}(D^0p)$	14													

Fig. 6.10.: Summary of the *sFit* (interference) fit fractions evaluated with pseudo experiments. Only the top half of the matrix is shown and empty bins fall below the shown precision. All numbers are listed including their uncertainties in table N.10.

The corrected helicity couplings magnitude and phase are listed in table 6.7. We find similar biases of the helicity couplings, when compared to the amplitude fit in the $2\sigma_{\Lambda_b^0}$ mass window (table 6.4). The largest biases are found for the helicity coupling magnitudes. They are, however, not larger than one standard deviation of the corrected result. The phases have negligible deviations. Further, we find the statistical uncertainty to be clearly underestimated. The scaling of the uncertainty ranges from four standard deviations to about 25. This underestimation is also apparent from the helicity couplings' negligible covariance ellipses in fig. N.6 compared to the ones of the fit in the $2\sigma_{\Lambda_b^0}$ region in fig. N.5. Even though we have expected an incorrect estimation of the uncertainty (section 6.4), scalings up to 25 standard deviations are surprising.

Tab. 6.7.: Bias and scale of the systematic uncertainties of the *sFit* for the helicity couplings magnitude and phase. The last row shows the corrected parameters' significance in standard deviations. The uncertainty on the phases u_Φ is partly underestimated, when compared to the covariance ellipses in appendix N.1.

		Fit value	Bias corr.	Error scale		Corrected	$n \cdot \sigma$
				lo	hi		
$\Lambda_c^+(2850)$	r^+	93.1 ± 1.0	$+17.6$	-30.9	23.2	111^{+24}_{-32}	$3.98 \cdot \sigma$
	ϕ^+	3.945	-0.0538			$3.89^{+0.29}_{-0.22}$	$24.43 \cdot \sigma$
	r^-	120.9 ± 1.0	$+3.6$	-22.8	24.5	125^{+25}_{-23}	$5.20 \cdot \sigma$
	ϕ^-	4.029	$+0.0245$			$4.05^{+0.18}_{-0.25}$	$29.06 \cdot \sigma$
$\Lambda_c^+(2880)$	r^-	16.3 ± 1.0	$+1.36$	-1.93	2.55	$17.7^{+2.5}_{-1.9}$	$8.13 \cdot \sigma$
	ϕ^-	0.518	-0.00799			$0.51^{+0.28}_{-0.35}$	$19.87 \cdot \sigma$
$\Lambda_c^+(2940)$	r^+	21.3 ± 1.1	$+3.12$	-7.27	7.36	24 ± 8	$2.98 \cdot \sigma$
	ϕ^+	1.142	-0.164			$0.98^{+0.42}_{-0.32}$	$17.04 \cdot \sigma$
	r^-	19.5 ± 1.1	-1.73	-7.15	7.67	18 ± 8	$2.26 \cdot \sigma$
	ϕ^-	3.694	$+0.00438$			$3.7^{+0.5}_{-0.6}$	$11.58 \cdot \sigma$
$\Lambda(1405)$	r^+	11.4 ± 1.1	$+8.71$	-8.33	11.4	20^{+13}_{-10}	$1.78 \cdot \sigma$
	ϕ^+	1.021	-0.284			0.7 ± 1.4	$4.44 \cdot \sigma$
	r^-	37.5 ± 1.8	-2.41	-5.09	4.84	35 ± 9	$3.94 \cdot \sigma$
	ϕ^-	4.121	$+0.0133$			$4.1^{+0.7}_{-0.5}$	$10.80 \cdot \sigma$
$\Lambda(1520)$	r^+	10.6 ± 0.9	$+0.457$	-4.18	2.5	$11.0^{+2.2}_{-3.7}$	$3.73 \cdot \sigma$
	ϕ^+	2.293	-0.385			$1.9^{+1.0}_{-0.8}$	$6.71 \cdot \sigma$
	r^-	5.8 ± 0.8	$+0.286$	-3.25	5.55	$6.0^{+4.5}_{-2.6}$	$1.69 \cdot \sigma$
	ϕ^-	1.029	$+0.025$			1.1 ± 1.2	$5.23 \cdot \sigma$
$\Lambda(1600)$	r^+	38.3 ± 1.0	$+3.15$	-12.6	6.71	41^{+7}_{-13}	$4.13 \cdot \sigma$
	ϕ^+	4.482	-0.538			$3.9^{+0.8}_{-0.6}$	$8.77 \cdot \sigma$
	r^-	20.4 ± 0.9	$+1.18$	-11.0	16.1	22^{+14}_{-10}	$1.77 \cdot \sigma$
	ϕ^-	4.681	$+0.488$			$5.2^{+1.0}_{-1.2}$	$5.74 \cdot \sigma$
$\Lambda(1690)$	r^+	9.0 ± 1.0	$+7.14$	-7.67	8.13	16 ± 8	$1.97 \cdot \sigma$
	ϕ^+	3.700	-0.447			$3.3^{+1.3}_{-1.4}$	$4.68 \cdot \sigma$
	r^-	29.9 ± 1.0	$+1.56$	-9.51	4.44	31^{+4}_{-10}	$4.49 \cdot \sigma$
	ϕ^-	4.977	$+0.221$			5.2 ± 0.5	$12.20 \cdot \sigma$
$\Lambda(1810)$	r^+	27.4 ± 1.0	-1.47	-10.7	10.7	26 ± 10	$2.48 \cdot \sigma$
	ϕ^+	2.597	-0.13			$2.5^{+0.7}_{-0.6}$	$9.58 \cdot \sigma$
	r^-	20.4 ± 1.1	$+0.76$	-8.77	8.85	21 ± 9	$2.29 \cdot \sigma$
	ϕ^-	5.683	$+0.0277$			$5.7^{+0.7}_{-0.6}$	$9.11 \cdot \sigma$
$\Lambda(1890)$	r^+	27.2 ± 1.2	$+1.1$	-8.29	8.41	28 ± 10	$2.77 \cdot \sigma$
	ϕ^+	1.304	-0.208			1.1 ± 1.2	$5.35 \cdot \sigma$
	r^-	30.1 ± 1.7	-1.14	-6.26	6.38	29^{+11}_{-10}	$2.76 \cdot \sigma$
	ϕ^-	4.319	$+0.0011$			4.3 ± 0.7	$8.70 \cdot \sigma$
$\Lambda(2100)$	r^+	28.5 ± 0.9	-1.56	-13.2	24.1	27^{+23}_{-13}	$1.52 \cdot \sigma$
	ϕ^+	3.329	$+0.239$			$3.6^{+0.9}_{-0.7}$	$7.96 \cdot \sigma$
	r^-	60.6 ± 1.0	$+4.46$	-16.3	10.1	65^{+10}_{-17}	$4.79 \cdot \sigma$
	ϕ^-	0.920	$+0.0545$			$0.97^{+0.38}_{-0.31}$	$18.40 \cdot \sigma$
$\Lambda(2110)$	r^+	33.8 ± 0.9	$+5.55$	-19.1	21.0	39^{+20}_{-18}	$2.08 \cdot \sigma$
	ϕ^+	4.395	-0.16			$4.2^{+0.6}_{-0.7}$	$9.34 \cdot \sigma$
	r^-	65.9 ± 1.0	$+0.832$	-15.3	13.3	67^{+13}_{-15}	$4.67 \cdot \sigma$
	ϕ^-	0.796	$+0.0584$			$0.85^{+0.35}_{-0.32}$	$18.84 \cdot \sigma$
$\Lambda(2350)$	r^+	13.0 ± 0.8	$+2.9$	-8.63	14.0	16^{+12}_{-7}	$1.69 \cdot \sigma$
	ϕ^+	5.226	-0.225			$5.0^{+0.7}_{-0.8}$	$8.22 \cdot \sigma$
	r^-	28.0 ± 1.3	-0.847	-7.53	7.62	27^{+10}_{-9}	$2.86 \cdot \sigma$
	ϕ^-	1.447	$+0.272$			$1.7^{+0.5}_{-0.4}$	$13.88 \cdot \sigma$
$C_{1/2^-}(D^0p)$	r^+	119.5 ± 1.1	$+21.1$	-33.5	26.9	$(1.4^{+0.3}_{-0.4}) \times 10^2$	$4.10 \cdot \sigma$
	ϕ^+	5.963	$+0.0937$			$6.06^{+0.30}_{-0.27}$	$21.88 \cdot \sigma$
	r^-	154.0 ± 1.2	$+3.73$	-23.8	24.7	158^{+30}_{-29}	$5.35 \cdot \sigma$
	ϕ^-	0.740	-0.0512			$0.69^{+0.17}_{-0.24}$	$30.75 \cdot \sigma$
$C_{1/2^+}(D^0p)$	r^+	143.7 ± 1.1	$+3.98$	-26.3	23.6	148^{+25}_{-28}	$5.61 \cdot \sigma$
	ϕ^+	2.269	$+0.0103$			$2.28^{+0.31}_{-0.22}$	$23.68 \cdot \sigma$
	r^-	96.9 ± 1.2	$+14.6$	-34.3	28.1	$(1.1^{+0.3}_{-0.4}) \times 10^2$	$3.11 \cdot \sigma$
	ϕ^-	0.485	-0.0467			0.4 ± 0.4	$16.18 \cdot \sigma$

6.5 Results

As we have not considered a background model for the fit in the $2\sigma_{\Lambda_b^0}$ signal window, there is a large deviation to be expected (section 6.3.2). Further there are no systematic uncertainties evaluated for the result of the *sFit*. Thus the following results give a first approximation of the $\Lambda_b^0 \to D^0 pK$ resonance structure. We report the fit fractions listed in table 6.8. Both fit types show a similar distribution of the amplitudes. The largest contributions are $\Lambda_c^+(2850)$ and $C_{1/2^-}(D^0p)$ in the D^0p channel and $\Lambda(1600)$ in the pK channel. The *sFit* result has an additional large $\Lambda(1810)$ fraction. The $\Lambda_c^+(2850)$ amplitude is less dominant in the *sFit* result and the continuum contribution $C_{1/2^\pm}(D^0p)$ is increased. As the fit in the $2\sigma_{\Lambda_b^0}$ signal window implements no background models, the relative fit fractions also reflect the underlying background contributions (table 6.1). An explanation for the increased fraction of $C_{1/2^\pm}(D^0p)$ in the *sFit* result could be resonances below the threshold of $m_{D^0p}^{\text{min}} \approx 2.803\,\text{GeV}/c^2$. There is $\Lambda_c^{++}(2765)$ next to few lower mass Λ_c^{+*} possibilities [20]. In case of the lightest Λ_c^{+*} this might be the Λ_c^+ formfactor, which is visible.

Tab. 6.8.: Summary of the evaluated fit fractions with statistical uncertainty only.

	sFit		$2\sigma_{\Lambda_b^0}$ Region	
	$\mathcal{F}_i/\%$	$n \cdot \sigma$	$\mathcal{F}_i/\%$	$n \cdot \sigma$
$\Lambda_c^+(2850)$	$22.9^{+2.0}_{-1.9}$	$11.57 \cdot \sigma$	$33.8^{+3.4}_{-3.5}$	$9.81 \cdot \sigma$
$\Lambda_c^+(2880)$	$3.4^{+0.7}_{-0.5}$	$5.68 \cdot \sigma$	2.9 ± 0.5	$5.97 \cdot \sigma$
$\Lambda_c^+(2940)$	$4.0^{+1.0}_{-0.8}$	$4.42 \cdot \sigma$	$2.9^{+0.8}_{-0.7}$	$3.98 \cdot \sigma$
$C_{1/2^-}(D^0p)$	$30.7^{+2.3}_{-2.5}$	$12.74 \cdot \sigma$	$17.8^{+1.9}_{-1.5}$	$10.37 \cdot \sigma$
$C_{1/2^+}(D^0p)$	$13.8^{+2.5}_{-2.3}$	$5.79 \cdot \sigma$	$7.7^{+2.6}_{-2.1}$	$3.27 \cdot \sigma$
$C_{3/2^+}(D^0p)$			$7.7^{+3.4}_{-2.4}$	$2.66 \cdot \sigma$
$\Lambda(1405)$	$2.3^{+0.6}_{-0.5}$	$4.34 \cdot \sigma$	$3.5^{+0.6}_{-0.5}$	$6.38 \cdot \sigma$
$\Lambda(1520)$	2.8 ± 0.5	$5.85 \cdot \sigma$	3.9 ± 0.5	$8.14 \cdot \sigma$
$\Lambda(1600)$	7.5 ± 1.6	$4.82 \cdot \sigma$	$9.0^{+2.2}_{-1.3}$	$5.05 \cdot \sigma$
$\Lambda(1690)$	$4.7^{+1.0}_{-0.9}$	$5.00 \cdot \sigma$	$4.8^{+1.3}_{-1.0}$	$4.14 \cdot \sigma$
$\Lambda(1810)$	$7.0^{+2.4}_{-2.1}$	$3.15 \cdot \sigma$	$4.0^{+3.1}_{-1.1}$	$1.90 \cdot \sigma$
$\Lambda(1890)$	4.2 ± 0.9	$4.52 \cdot \sigma$	$3.6^{+0.9}_{-0.8}$	$4.32 \cdot \sigma$
$\Lambda(2100)$	$2.8^{+0.8}_{-0.6}$	$4.00 \cdot \sigma$		
$\Lambda(2110)$	$3.7^{+0.9}_{-0.8}$	$4.33 \cdot \sigma$	5.1 ± 0.7	$7.27 \cdot \sigma$
$\Lambda(2350)$	$0.64^{+0.29}_{-0.20}$	$2.65 \cdot \sigma$		
$\sum_i \mathcal{F}_i$	111 ± 4		110^{+8}_{-6}	

The sum of the fit fractions is for both fits larger than one (table 6.8). Both sums are one with the interference fit fractions, which sum up to $\sum_{ij} \mathcal{F}_{ij} = (-10^{+6}_{-8})\,\%$ for the fit in the $2\sigma_{\Lambda_b^0}$ region (see fig. N.20) and to $(-11 \pm 4)\,\%$ for the *sFit* (see fig. N.27). These interferences are necessary for the fit stability of the Λ^* resonances, which densely populate, in comparison to the Λ_c^{+*} amplitudes, a region with lower event counts. The fit to the full Dalitz plot improved the statistical uncertainty of every Λ^* helicity coupling in comparison to the fit in the low m_{pK}^2 region (tables 6.3 and N.6). In both fits, most interferences are found for the largest resonance contribution $\Lambda_c^+(2850)$ ranging across the whole phase space, and the continuum contributions $C(D^0p)$ (figs. 6.5 and 6.10).

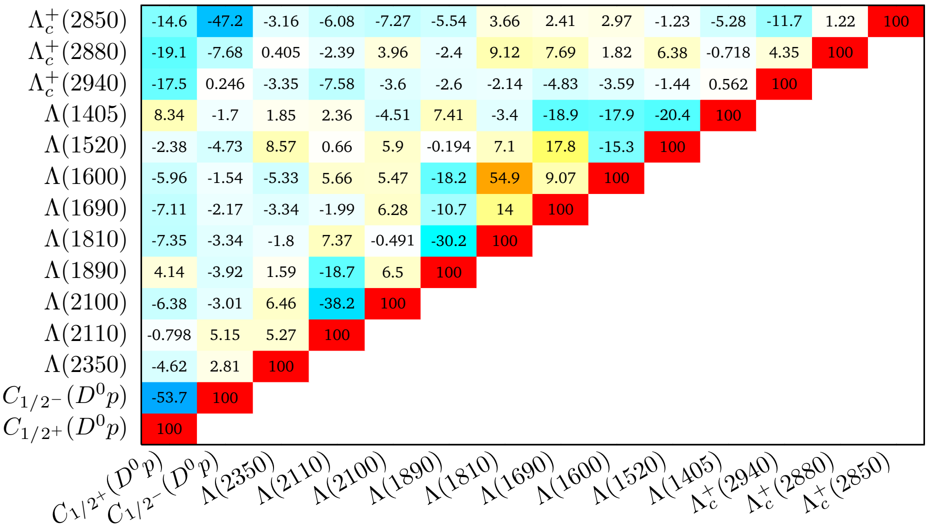

	$C_{1/2^+}(D^0p)$	$C_{1/2^-}(D^0p)$	$\Lambda(2350)$	$\Lambda(2110)$	$\Lambda(2100)$	$\Lambda(1890)$	$\Lambda(1810)$	$\Lambda(1690)$	$\Lambda(1600)$	$\Lambda(1520)$	$\Lambda(1405)$	$\Lambda_c^+(2940)$	$\Lambda_c^+(2880)$	$\Lambda_c^+(2850)$
$\Lambda_c^+(2850)$	-14.6	-47.2	-3.16	-6.08	-7.27	-5.54	3.66	2.41	2.97	-1.23	-5.28	-11.7	1.22	100
$\Lambda_c^+(2880)$	-19.1	-7.68	0.405	-2.39	3.96	-2.4	9.12	7.69	1.82	6.38	-0.718	4.35	100	
$\Lambda_c^+(2940)$	-17.5	0.246	-3.35	-7.58	-3.6	-2.6	-2.14	-4.83	-3.59	-1.44	0.562	100		
$\Lambda(1405)$	8.34	-1.7	1.85	2.36	-4.51	7.41	-3.4	-18.9	-17.9	-20.4	100			
$\Lambda(1520)$	-2.38	-4.73	8.57	0.66	5.9	-0.194	7.1	17.8	-15.3	100				
$\Lambda(1600)$	-5.96	-1.54	-5.33	5.66	5.47	-18.2	54.9	9.07	100					
$\Lambda(1690)$	-7.11	-2.17	-3.34	-1.99	6.28	-10.7	14	100						
$\Lambda(1810)$	-7.35	-3.34	-1.8	7.37	-0.491	-30.2	100							
$\Lambda(1890)$	4.14	-3.92	1.59	-18.7	6.5	100								
$\Lambda(2100)$	-6.38	-3.01	6.46	-38.2	100									
$\Lambda(2110)$	-0.798	5.15	5.27	100										
$\Lambda(2350)$	-4.62	2.81	100											
$C_{1/2^-}(D^0p)$	-53.7	100												
$C_{1/2^+}(D^0p)$	100													

Fig. 6.11.: Correlation $\rho(\mathcal{F}_i, \mathcal{F}_j)$ of the *sFit* fit fractions in %. Only the top half of the matrix is shown.

The interferences of $\Lambda_c^+(2850)$ are also reflected in the fit fraction correlations of both fits in figs. 6.11 and N.21. The largest correlations are either between fit fractions of amplitudes within the pK or D^0p channel. In the fit to the $2\sigma_{\Lambda_b^0}$ region, further correlations of similar magnitude are found between both channels for fit fractions of resonances in the overlap region, like $\Lambda(2110)$ and $\Lambda(1890)$ (fig. N.21). The fit fractions of the *sFit*, on the other hand, have throughout higher correlations (fig. 6.11) compared to the fit in the $2\sigma_{\Lambda_b^0}$ region.

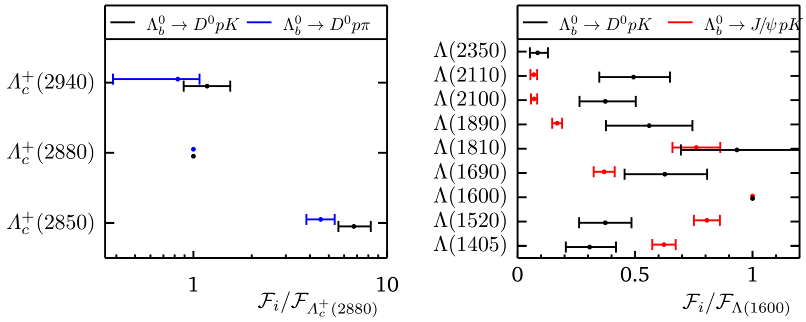

(a) (b)

Fig. 6.12.: Comparison of the *sFit* fit fractions ratios of eq. (6.7) to LHCb results. The D^0p-channel is compared to $\Lambda_b^0 \to D^0p\pi$ [49] and the pK-channel to $\Lambda_b^0 \to J/\psi pK$ [51].

The amplitude model of $\Lambda_b^0 \to D^0pK$ includes the same D^0p channel amplitudes as in $\Lambda_b^0 \to D^0p\pi$ [49]. Their subregions with $m^2_{D^0p} < 9\,\mathrm{GeV}^2/c^4$ show a similar distribution of the Λ_b^0 candidates in the Dalitz plot. This is not surprising as the decays differ only by the K or π. We compare the Λ_c^{+*} fit fractions of the *sFit* to the $\Lambda_b^0 \to D^0p\pi$ analysis in fig. 6.12a by normalising all to $\Lambda_c^+(2880)$. The $\Lambda_c^+(2850)$ fit fraction is enhanced in the $\Lambda_b^0 \to D^0pK$ phase space compared to the $\Lambda_b^0 \to D^0p\pi$ analysis. The ratios for $\Lambda_c^+(2940)$ match within their uncertainty. The *sFit* fit fractions of the pK channel are compared in fig. 6.12b with the ones of the $\Lambda_b^0 \to J/\psi pK$ LHCb analysis [51] by normalisation to $\Lambda(1600)$. The pK channel ratios of $\Lambda_b^0 \to D^0 pK$ show no similarity to the ones of the $\Lambda_b^0 \to J/\psi pK$ analysis. In contrast to $\Lambda_b^0 \to J/\psi pK$ the pK channel ratios of $\Lambda_b^0 \to D^0 pK$ show mostly uniform values within the scope of their larger statistical uncertainty. We observe an enhanced fraction of $\Lambda(1600)$ and $\Lambda(1810)$ resonances. Additionally, the fraction of the high spin resonance $\Lambda(2100)$ ($J = 7/2$) is larger in the $\Lambda_b^0 \to D^0 pK$ phase space. We take the ratios of the *sFit* fit fractions as branching fraction ratios and find

$$\frac{\mathcal{B}(\Lambda_b^0 \to \Lambda_c^+(2850)K^-) \cdot \mathcal{B}(\Lambda_c^+(2850) \to D^0 p)}{\mathcal{B}(\Lambda_b^0 \to \Lambda_c^+(2880)K^-) \cdot \mathcal{B}(\Lambda_c^+(2880) \to D^0 p)} = 6.7^{+1.5}_{-1.2}$$

$$\frac{\mathcal{B}(\Lambda_b^0 \to \Lambda_c^+(2240)K^-) \cdot \mathcal{B}(\Lambda_c^+(2240) \to D^0 p)}{\mathcal{B}(\Lambda_b^0 \to \Lambda_c^+(2880)K^-) \cdot \mathcal{B}(\Lambda_c^+(2880) \to D^0 p)} = 1.2^{+0.38}_{-0.29}$$

$$\begin{aligned}
\frac{\mathcal{B}(\Lambda_b^0 \to D^0 \Lambda(1405)) \cdot \mathcal{B}(\Lambda(1405) \to pK^-)}{\mathcal{B}(\Lambda_b^0 \to D^0 \Lambda(1600)) \cdot \mathcal{B}(\Lambda(1600) \to pK^-)} &= 0.31^{+0.12}_{-0.11} \\
\frac{\mathcal{B}(\Lambda_b^0 \to D^0 \Lambda(1520)) \cdot \mathcal{B}(\Lambda(1520) \to pK^-)}{\mathcal{B}(\Lambda_b^0 \to D^0 \Lambda(1600)) \cdot \mathcal{B}(\Lambda(1600) \to pK^-)} &= 0.37^{+0.12}_{-0.12} \\
\frac{\mathcal{B}(\Lambda_b^0 \to D^0 \Lambda(1690)) \cdot \mathcal{B}(\Lambda(1690) \to pK^-)}{\mathcal{B}(\Lambda_b^0 \to D^0 \Lambda(1600)) \cdot \mathcal{B}(\Lambda(1600) \to pK^-)} &= 0.63^{+0.19}_{-0.18} \\
\frac{\mathcal{B}(\Lambda_b^0 \to D^0 \Lambda(1810)) \cdot \mathcal{B}(\Lambda(1810) \to pK^-)}{\mathcal{B}(\Lambda_b^0 \to D^0 \Lambda(1600)) \cdot \mathcal{B}(\Lambda(1600) \to pK^-)} &= 0.93^{+0.27}_{-0.24} \\
\frac{\mathcal{B}(\Lambda_b^0 \to D^0 \Lambda(1890)) \cdot \mathcal{B}(\Lambda(1890) \to pK^-)}{\mathcal{B}(\Lambda_b^0 \to D^0 \Lambda(1600)) \cdot \mathcal{B}(\Lambda(1600) \to pK^-)} &= 0.56^{+0.19}_{-0.19} \\
\frac{\mathcal{B}(\Lambda_b^0 \to D^0 \Lambda(2100)) \cdot \mathcal{B}(\Lambda(2100) \to pK^-)}{\mathcal{B}(\Lambda_b^0 \to D^0 \Lambda(1600)) \cdot \mathcal{B}(\Lambda(1600) \to pK^-)} &= 0.37^{+0.13}_{-0.11} \\
\frac{\mathcal{B}(\Lambda_b^0 \to D^0 \Lambda(2110)) \cdot \mathcal{B}(\Lambda(2110) \to pK^-)}{\mathcal{B}(\Lambda_b^0 \to D^0 \Lambda(1600)) \cdot \mathcal{B}(\Lambda(1600) \to pK^-)} &= 0.49^{+0.16}_{-0.15} \\
\frac{\mathcal{B}(\Lambda_b^0 \to D^0 \Lambda(2350)) \cdot \mathcal{B}(\Lambda(2350) \to pK^-)}{\mathcal{B}(\Lambda_b^0 \to D^0 \Lambda(1600)) \cdot \mathcal{B}(\Lambda(1600) \to pK^-)} &= 0.09^{+0.05}_{-0.04} \quad ,
\end{aligned} \tag{6.7}$$

with statistical uncertainty only.

Conclusion & Outlook

7

> *Much to learn, you still have.*
>
> — **Master Yoda**
> (from the movie 'Star Wars: Episode II')

We have been able to reconstruct $\Lambda_b^0 \to D^0 pK$ with the D^0 modes to $K^-\pi^+$, KK, $\pi\pi$ and $K^+\pi^-$, as shown in fig. 4.19. During the selection we noticed that there is a dominant amount of charmless decays from Λ_b^0 in the D^0 modes KK and $\pi\pi$. The charmless contribution of $\Lambda_b^0 \to pKKK$ and $\Lambda_b^0 \to pK\pi\pi$ could be significantly reduced by requiring a large lifetime of the D^0 candidate. This reduces the $D^0 pK$ sample size for $D^0 \to \pi\pi$ to an amount below the one of the doubly Cabibbo suppressed D^0 mode. The primary focus is, therefore, on the $D^0 \to K^+\pi^-$ and $D^0 \to KK$ samples.

We measured the ratios $R_{\Lambda_b^0}$ and R_{Ξ_b} defined in eq. (5.2). These have been presented in the results of the $m(D^0 ph)$ likelihood fit in section 5.5. In recapitulation of eqs. (5.13) and (5.15) the consequential branching fractions

$$\begin{aligned} \mathcal{B}(\Lambda_b^0 \to D^0 pK) &= (4.93 \pm 0.18_{\text{stat}} \pm 0.09_{\text{syst}} \pm 0.55_{\text{ext}}) \times 10^{-5} \\ f_{\Xi_b} \cdot \mathcal{B}(\Xi_b \to D^0 pK) &= (2.23 \pm 0.08_{\text{stat}} \pm 0.05_{\text{syst}} \pm 0.40_{\text{ext}}) \times 10^{-6} \end{aligned} \tag{7.1}$$

are found to be about one and a half times more precise than the current PDG value [20], which is only based on the previous LHCb measurement [17]. The branching fractions external and largest uncertainty contribution originates from $\mathcal{B}(\Lambda_b^0 \to D^0 p\pi)$. As the values of this thesis and from the PDG are only based on the previous LHCb measurement [17], an update of this measurement will significantly improve the determined branching fractions. The measurement of the Λ_b^0 and Ξ_b mass difference

$$m_{\Xi_b} - m_{\Lambda_b^0} = 172.5 \pm 0.38_{\text{stat}} \pm 0.17_{\text{syst}}\ \text{MeV}/c^2 \tag{7.2}$$

is on par with the LHCb (Run I) precision measurement [117].

We have been able to establish and fit two amplitude models for $\Lambda_b^0 \to D^0 pK$, with the Cabibbo favoured $D^0 \to K\pi$ mode. This first model is able to describe the $D^0 p$ and pK channel resonances with a reduced set of amplitudes in a 2σ region from the Λ_b^0 mass peak value (section 6.3). Further, an amplitude model based on background subtraction (*sFit*) is found (section 6.4) with contributions of the high spin resonances $\Lambda(2100)$ and $\Lambda(2350)$. A set of branching fraction ratios calculated from the fit fractions of the *sFit* is given in eq. (6.7). These ratios are normalised within the $D^0 p$ and pK channel. The results of both fit approaches are discussed in more detail in section 6.5. As the $D^0 p$ channel has a strong enhancement over the pK channel, it leaves a challenging number of events for the big variety of Λ^* resonances. With an approximately halved event-count of the Λ_b^0- and $\overline{\Lambda}_b^0$-type samples, the *CP* asymmetries are therefore calculated as integrated asymmetries $\mathcal{A}$ from the ratios $R_{\Lambda_b^0}$ and R_{Ξ_b} of the fit to the $m(D^0ph)$ distributions. The integrated CP asymmetries $\mathcal{A}$ in section 5.5.2 are consistent with zero for the full phase space and the Λ^* resonance region. The correlations of the helicity couplings and interferences among the D^0p and pK channel, that are found by the amplitude analysis, have shown to lead to more precise measurements of the Λ^* amplitude parameters. Especially the broad $\Lambda_c^+(2850)$ resonance populates a large fraction of the full phase space. As the CP observables of interest will be calculated from the pK channel amplitudes, they will definitely benefit from an amplitude analysis of the full Dalitz plot.

We propose for follow up analyses of the decays $\{\Lambda_b^0, \Xi_b\} \to D^0pK$ to additionally reconstruct their excited D^{*0} modes. These appear as partially reconstructed background in the D^0pK samples. This will help to constrain the partially reconstructed $\Xi_b \to D^*pK$ contribution under the Λ_b^0 signal peak of all D^0 modes. Another improvement should be found for the amplitude analysis by the description of the $\Xi_b \to D^*pK$ amplitudes in the phase space of the Λ_b^0 decay. This is due to the D^{*0} polarisation to have a major effect in the Λ^* resonance region (section 5.3). We further suggest for a particular analysis of $\Xi_b \to D^0pK$ to include charmless Ξ_b modes, as the $\Xi_b \to pKK\pi$ is found to populate the Λ^* resonance region of the Ξ_b phase space.

The Upgrade I of LHCb is announced to result into a potential factor of 20 increase for the hadron channels [124] in the continuing Run III till 2030. The subsequent Upgrade II will coincide with the implementation of the High Luminosity LHC [125] that promises to further boost the expected luminosity of $50\,\text{fb}^{-1}$ (Run I-III) to $> 300\,\text{fb}^{-1}$. This lets expect another factor of 6 for the hadron channels. The gain on data will elevate the potential of this analysis, as it will make the amplitude analysis of Λ_b^0- and $\overline{\Lambda}_b^0$-type separated samples possible for $D^0 \to K^-\pi^+$. The suppressed D^0 modes will become more accessible in general. This is especially interesting, as the $\Lambda_b^0 \to D^0pK$ phase space with $D^0 \to KK$ indicates D_s^{-*} resonances in the D^0K channel. Whether the $D^0 \to KK$ and $D^0 \to \pi\pi$ modes can contribute as an GLW based measurement of the CP observables strongly depends on the charmless decays. We propose to constrain these from the D^0 mass sidebands, which have been rejected during the preselections of this analysis. Further, an analysis of the $\Xi_b \to D^0pK$ mode, with its lower expected CKM phase γ significance, might outweigh the background complexity of the $\Lambda_b^0 \to D^0pK$ mode. As there have to be Σ^* (Σ_c^*) resonances considered in the pK (D^0p) channel, they are adding up in the amplitude model. The Ξ_b phase space, however, looks promising. It can be found in appendix M.5 and shows that the pK and D^0p channels are similarly populated.

Branching Fractions

A

A.1 Known Branching Fractions

Tab. A.1.: Branching Fractions used in Analysis. [20]

$\mathcal{B}(\Lambda_b^0 \to D^0 p\pi)$	$(6.3 \pm 0.7) \times 10^{-4}$	
$\mathcal{B}(\Lambda_b^0 \to D^0 pK)$	$(4.6 \pm 0.8) \times 10^{-5}$	
$\mathcal{B}(B^0 \to \overline{D}^0 KK)$	$(5.9 \pm 0.5) \times 10^{-5}$	
$\mathcal{B}(B_s^0 \to \overline{D}^0 KK)$	$(5.5 \pm 0.8) \times 10^{-5}$	
$f_{\Xi_b} \cdot \mathcal{B}(\Xi_b \to D^0 pK)$	$(1.7 \pm 0.6) \times 10^{-6}$	
$\mathcal{B}(\Lambda_b^0 \to p\pi^-\pi^+\pi^-)$	$(2.11 \pm 0.23) \times 10^{-5}$	
$\mathcal{B}(\Lambda_b^0 \to pK^-K^+\pi^-)$	$(4.1 \pm 0.6) \times 10^{-6}$	
$\mathcal{B}(\Lambda_b^0 \to pK^-\pi^+\pi^-)$	$(5.1 \pm 0.5) \times 10^{-5}$	
$\mathcal{B}(\Lambda_b^0 \to pK^-K^+K^-)$	$(1.27 \pm 0.14) \times 10^{-5}$	
$\frac{f_{\Xi_b}}{f_{\Lambda_b^0}} \cdot \mathcal{B}(\Xi_b \to pK^-K^-\pi^+)$	$(1.73 \pm 0.32) \times 10^{-6}$	
$\frac{f_{\Xi_b}}{f_{\Lambda_b^0}} \cdot \mathcal{B}(\Xi_b \to pK^-\pi^+\pi^-)$	$(1.9 \pm 0.4) \times 10^{-6}$	
$\frac{f_{\Xi_b}}{f_{\Lambda_b^0}} \cdot \mathcal{B}(\Xi_b \to pK^-K^+K^-)$	$(1.8 \pm 1.0) \times 10^{-7}$	
$\mathcal{B}(\Lambda_b^0 \to D^* p\pi)$	unknown	estimation in A.4
$\mathcal{B}(\Lambda_b^0 \to D^* pK)$	unknown	estimation in A.4
$\mathcal{B}(B^+ \to \overline{D}^0 K^+)$	$(3.63 \pm 0.12) \times 10^{-4}$	used in A.4
$\mathcal{B}(B^+ \to \overline{D}^* K^+)$	$(3.97^{+0.31}_{-0.28}) \times 10^{-4}$	used in A.4
$\mathcal{B}(B^+ \to \overline{D}^0 \pi^+)$	$(4.68 \pm 0.13) \times 10^{-3}$	used in A.4
$\mathcal{B}(B^+ \to \overline{D}^* \pi^+)$	$(4.90 \pm 0.17) \times 10^{-3}$	used in A.4
$\mathcal{B}(D^0 \to K^-\pi^+)$	$(3.950 \pm 0.031) \times 10^{-2}$	
$\mathcal{B}(D^0 \to KK)$	$(4.08 \pm 0.06) \times 10^{-3}$	
$\mathcal{B}(D^0 \to \pi\pi)$	$(1.455 \pm 0.024) \times 10^{-3}$	
$\mathcal{B}(D^0 \to K^+\pi^-)$	$(1.50 \pm 0.07) \times 10^{-4}$	

A.2 Production Fractions

Tab. A.2.: Production fractions in pp collisions at the LHCb.

	avg.	2011 7 TeV	2012 8 TeV	Run II 13 TeV	
$f_{\Lambda_b^0}/(f_u+f_d)$	0.259		0.259 ± 0.018		[126]
$f_s/(f_u+f_d)$	0.126	0.1295 ± 0.0075		0.122 ± 0.006	[126]
f_s/f_d	0.256	0.256 ± 0.020			[127]
$f_s/f_{\Lambda_b^0}$	0.486				
$f_d/f_{\Lambda_b^0}$	1.897				

A.3 Known Ratios

$$
\begin{aligned}
\frac{\mathcal{B}(B_s^0 \to \overline{D}{}^0 KK)}{\mathcal{B}(B^0 \to \overline{D}{}^0 KK)} &= 0.930 \pm 0.089 \pm 0.069 && [128] \\
\frac{\mathcal{B}(B^0 \to \overline{D}{}^0 KK)}{\mathcal{B}(B^0 \to \overline{D}{}^0 \pi\pi)} &= 0.069 \pm 0.004 \pm 0.003 && [128] \\
R_{\Lambda_b^0 \to D^0 pK} = \frac{\mathcal{B}(\Lambda_b^0 \to D^0 pK)}{\mathcal{B}(\Lambda_b^0 \to D^0 p\pi)} &= 0.073 \pm 0.008^{+0.005}_{-0.006} && [17] \\
\frac{f_{\Xi_b}}{f_{\Lambda_b^0}} \times \frac{\mathcal{B}(\Xi_b \to D^0 pK)}{\mathcal{B}(\Lambda_b^0 \to D^0 pK)} &= 0.44 \pm 0.09 \pm 0.06 && [17]
\end{aligned}
\tag{A.1}
$$

A.4 Estimation of $\mathcal{B}(\Lambda_b^0 \to D^* ph)$

The branching fractions $\mathcal{B}(\Lambda_b^0 \to D^* ph)$ have not been measured jet. An estimation might be found by comparison with a similar decay where a D^0 can replace a D^*. As there is also no measurement for a baryonic branching fraction $\mathcal{B}(\Lambda_b^0 \to D^* X)$ we fall back to $B \to D^* h$. The decay $B \to D^* K$ ($B \to D^* \pi$) is the most obvious guess.

When considering the Feynman diagrams in figs. 2.6 and 2.8, itis basically just replacing the ud with an $\overline{u}$. In addition to the resulting internal graph, there is also the possibility of an external graph, where the K (π) is directly produced by a W-boson. This graph might not have a negligible effect on the branching fraction ratio. The B meson is lighter than the Λ_b^0, thus resulting in a smaller phase space. This could result in a relatively lesser $B \to D^* h$ production than $\Lambda_b^0 \to D^* ph$ or even an enhancement of $B \to D^* h$, which is common for decays at the edge of the phase space. We neglect these effects as we aim for a rough estimate and no precise number to be used as a fit constraint. We assume

$$
\mathcal{B}(\Lambda_b^0 \to D^* X) : \mathcal{B}(\Lambda_b^0 \to D^0 X) \simeq \mathcal{B}(B^+ \to \overline{D}{}^* h^+) : \mathcal{B}(B^+ \to \overline{D}{}^0 h^+) \quad , \tag{A.2}
$$

Tab. A.3.: CKM matrix element contributions to different D^0 decay amplitudes, by using their current measurements [20], and their potential Cabibbo suppression factors.

	CKM contribution	suppression	note
$D^0 \to K^-\pi^+$	$\|V_{cs}V_{ud}^*\|^2 = \|0.94872 \pm 0.00014\|^2$	$\|1 \cdot 1\|^2$	Cabibbo-favoured
$D^0 \to KK$	$\|V_{cs}V_{us}^*\|^2 = \|0.2186 \pm 0.0004\|^2$	$\|1 \cdot \lambda\|^2$	suppressed
$D^0 \to \pi\pi$	$\|V_{cd}V_{ud}^*\|^2 = \|0.2186 \pm 0.0004\|^2$	$\|1 \cdot \lambda\|^2$	suppressed
$D^0 \to K^+\pi^-$	$\|V_{cd}V_{us}^*\|^2 = \|0.05038 \pm 0.00014\|^2$	$\|\lambda \cdot \lambda\|^2$	doubly-suppressed

which leads us to

$$\begin{aligned} R'_{D^*,K} &= \frac{\mathcal{B}(\Lambda_b^0 \to D^* pK)}{\mathcal{B}(\Lambda_b^0 \to D^0 pK)} \simeq \frac{\mathcal{B}(B^+ \to \bar{D}^* K^+)}{\mathcal{B}(B^+ \to D^0 K^+)} = 1.09 \\ R'_{D^*,\pi} &= \frac{\mathcal{B}(\Lambda_b^0 \to D^* p\pi)}{\mathcal{B}(\Lambda_b^0 \to D^0 p\pi)} \simeq \frac{\mathcal{B}(B^+ \to \bar{D}^* \pi^+)}{\mathcal{B}(B^+ \to D^0 \pi^+)} = 1.05 \quad . \end{aligned} \tag{A.3}$$

A.5 D^0 Decay

- Feynman diagrams of lowest order for the decays $D^0 \to \{K^-\pi^+, KK, \pi\pi, K^+\pi^-\}$ are given in figure A.1.
- Table A.3 shows the connection to CKM matrix elements and their potential suppression according to the Wolfenstein parametrisation of the CKM matrix in equation 2.10.
- Ratio of the Cabibbo-favoured to doubly-suppressed D^0 mode [20]:

$$\frac{\mathcal{B}(D^0 \to K^+\pi^-)}{\mathcal{B}(\bar{D}^0 \to K^+\pi^-)} = (3.79 \pm 0.18) \times 10^{-3} \tag{A.4}$$

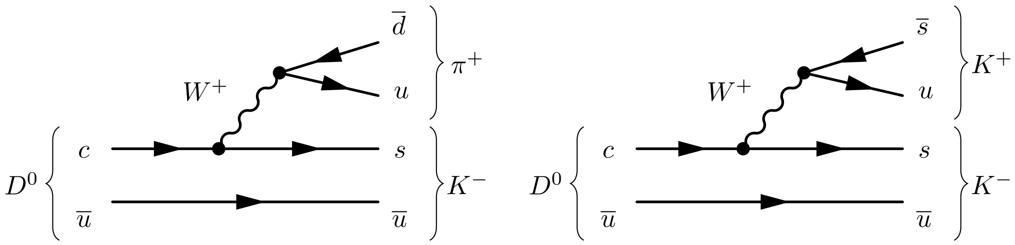

(a) $D^0 \to K^-\pi^+$ (b) $D^0 \to KK$

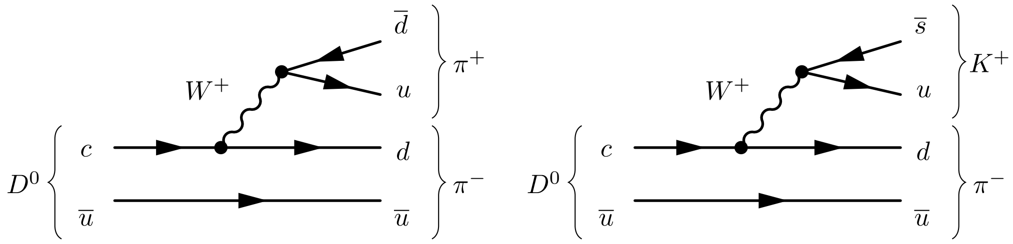

(c) $D^0 \to \pi\pi$ (d) $D^0 \to K^+\pi^-$

Fig. A.1.: Feynman diagrams of lowest order for the decays $D^0 \to \{K^-\pi^+, KK, \pi\pi, K^+\pi^-\}$.

B

Combined Preselection

This appendix lists invariant mass distributions of the Run I DATA samples, after application of the preselections in section 4.2. The MC samples are shown before and after the preselections.

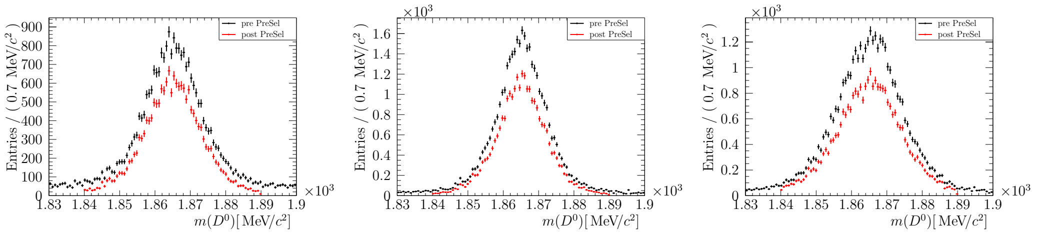

(a) MC - $D^0 \to K^-\pi^+$ (b) MC - $D^0 \to KK$ (c) MC - $D^0 \to \pi\pi$

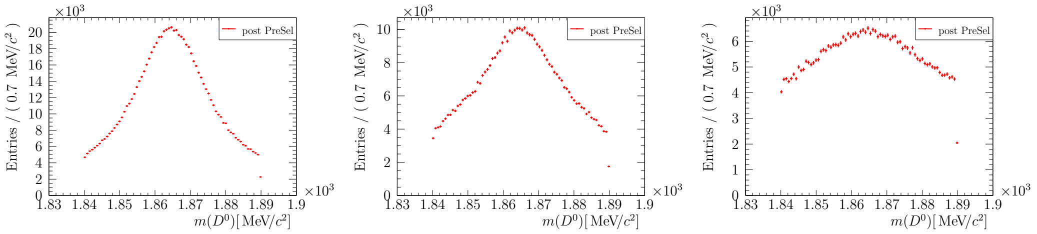

(d) DATA - $D^0 \to K^-\pi^+$ (e) DATA - $D^0 \to KK$ (f) DATA - $D^0 \to \pi\pi$

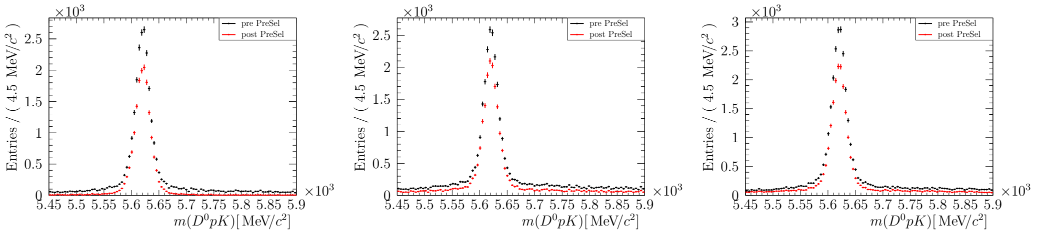

(g) MC - $D^0 \to K^-\pi^+$ (h) MC - $D^0 \to KK$ (i) MC - $D^0 \to \pi\pi$

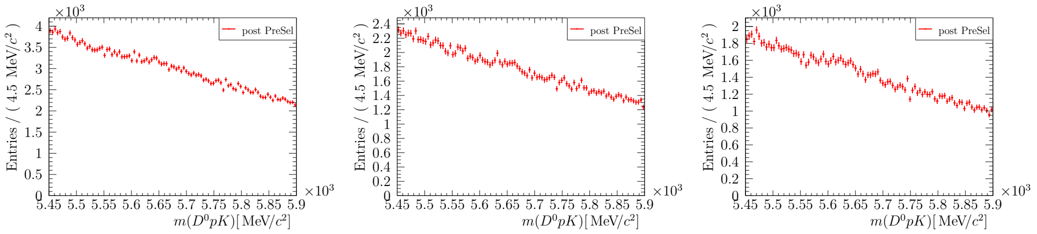

(j) DATA - $D^0 \to K^-\pi^+$ (k) DATA - $D^0 \to KK$ (l) DATA - $D^0 \to \pi\pi$

Fig. B.1.: Preselections on DATA and MC ($\Lambda_b^0 \to D^0pK$) - 2011

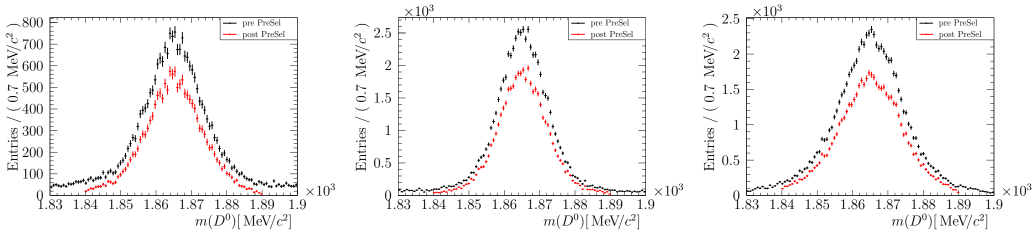

(a) MC - $D^0 \to K^-\pi^+$ (b) MC - $D^0 \to KK$ (c) MC - $D^0 \to \pi\pi$

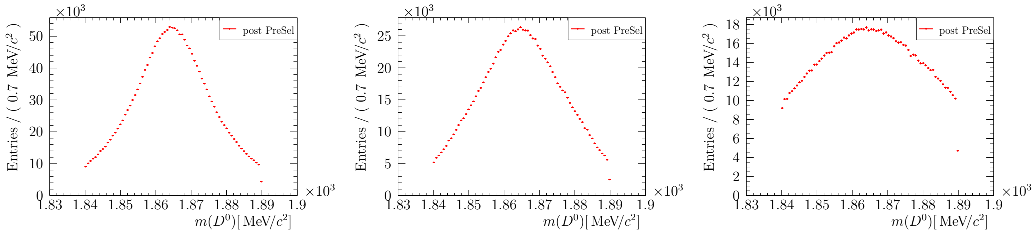

(d) DATA - $D^0 \to K^-\pi^+$ (e) DATA - $D^0 \to KK$ (f) DATA - $D^0 \to \pi\pi$

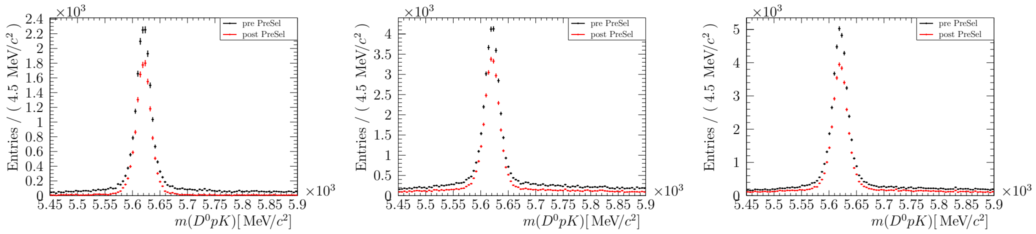

(g) MC - $D^0 \to K^-\pi^+$ (h) MC - $D^0 \to KK$ (i) MC - $D^0 \to \pi\pi$

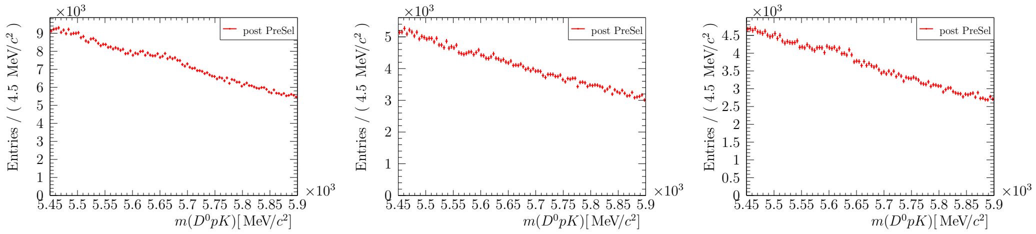

(j) DATA - $D^0 \to K^-\pi^+$ (k) DATA - $D^0 \to KK$ (l) DATA - $D^0 \to \pi\pi$

Fig. B.2.: Preselections on DATA and MC ($\Lambda_b^0 \to D^0pK$) - 2012

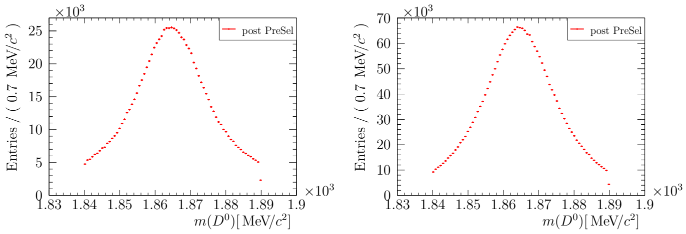

(a) DATA11 - $D^0 \to K^- \pi^+$ (b) DATA12 - $D^0 \to K^- \pi^+$

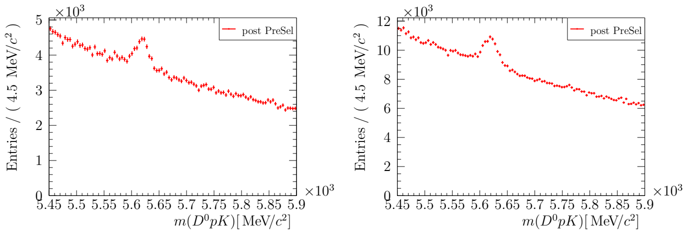

(c) DATA11 - $D^0 \to K^- \pi^+$ (d) DATA12 - $D^0 \to K^- \pi^+$

Fig. B.3.: Preselections on DATA ($\Lambda_b^0 \to D^0 p\pi$) - DATA 2011/12

C

Simulation Samples & Conditions

Tab. C.1.: Available Simulation - * marks a filtered production and $D^0 \to K\pi$ is the Cabibbo favoured mode. The simulation conditions are listed in table C.2.

	Generated Events					
	2011	2012	2015	2016	2017	2018
$\Lambda_b^0 \to D^0 pK$						
$D^0 \to K\pi$	502,324	535,000	309,108	1,212,702	2,054,004*	1,058,662*
$D^0 \to KK$	513,262	1,003,060	309,785	1,208,421	1,873,881*	1,009,633*
$D^0 \to \pi\pi$	500,844	1,138,374	303,757	1,200,540	2,088,856*	1,103,984*
$\Lambda_b^0 \to D^0 p\pi$						
$D^0 \to K\pi$	511,369	542,499	307,519	1,210,904	2,051,575*	1,064294*
$D^0 \to KK$	509,818	1,008,373	307,852	1,206,629	1,948,193*	1,061016*
$D^0 \to \pi\pi$	507,780	1,092,824	307,965	1,2131,00	2,129,242*	1,108883*
$B_s^0 \to D^0 KK$						
$D^0 \to K\pi$	0	771,498	0	0	2,178,772*	1,110,131*
$D^0 \to KK$	0	1,053,668	0	0	0	0
$D^0 \to \pi\pi$	0	1,053,056	0	0	0	0
$B^0 \to D^0 KK$						
$D^0 \to K\pi$	0	778,489	0	0	2,022,459*	1,024,483*
$D^0 \to KK$	0	1,017,701	0	0	0	0
$D^0 \to \pi\pi$	0	1,047,842	0	0	0	0
$\Lambda_b^0 \to D^* pK$						
$D^0 \to K\pi$	0	0	0	0	1,903,870*	1,018,057*
$\Lambda_b^0 \to D^* p\pi$						
$D^0 \to K\pi$	0	0	0	0	2,019,514*	1,024,366*
$\Lambda_b^0 \to ph^-h^+h^-$						
$\Lambda_b^0 \to pKKK$	1,032,138	2,019,736	0	4,270,082	0	0
$\Lambda_b^0 \to pKK\pi$	1,025,976	2,011,991	0	4,324,859	0	0
$\Lambda_b^0 \to pK\pi\pi$	1,046,073	2,017,682	0	4,137,806	0	0
$\Lambda_b^0 \to p\pi\pi\pi$	1,033,876	2,025,489	0	4,264,938	0	0

EventType is a unique eight-digit number for every DecFile. It specifies its basic decay and simulation conditions [129]. A list for every decay file by its EventType is found in [85].

ReDecay is an option to speed up the detector simulation [130]. The underlying event is being reused for 100 event generations resulting into a significant speedup by maintaining the quality of the nominal simulation.

Tab. C.2.: Simulation conditions of the used MC samples. The amount of generated events is found in table C.1. ’Pol’ represents the magnet polarity ’MagUp’ (MU) and ’MagDown’ (MD).

Decay	Year	Pol	EventType	Sim	Reco	Filter	ReDecay	Trigger
$\Lambda_b^0 \to D^0 pK$								
$D^0 \to K\pi$	2011	MD	15164024	09d	14c			0x40760037
$D^0 \to K\pi$	2011	MU	15164024	09d	14c			0x40760037
$D^0 \to KK$	2011	MD	15164081	09d	14c			0x40760037
$D^0 \to KK$	2011	MU	15164081	09d	14c			0x40760037
$D^0 \to \pi\pi$	2011	MD	15164071	09d	14c			0x40760037
$D^0 \to \pi\pi$	2011	MU	15164071	09d	14c			0x40760037
$D^0 \to K\pi$	2012	MD	15164022	08a	14a			0x409f0045
$D^0 \to K\pi$	2012	MU	15164022	08a	14a			0x409f0045
$D^0 \to KK$	2012	MD	15164080	08g	14c			0x409f0045
$D^0 \to KK$	2012	MU	15164080	08g	14c			0x409f0045
$D^0 \to \pi\pi$	2012	MD	15164070	08g	14c			0x409f0045
$D^0 \to \pi\pi$	2012	MU	15164070	08g	14c			0x409f0045
$D^0 \to K\pi$	2015	MD	15164024	09d	15a			0x411400a2
$D^0 \to K\pi$	2015	MU	15164024	09d	15a			0x411400a2
$D^0 \to KK$	2015	MD	15164081	09d	15a			0x411400a2
$D^0 \to KK$	2015	MU	15164081	09d	15a			0x411400a2
$D^0 \to \pi\pi$	2015	MD	15164071	09d	15a			0x411400a2
$D^0 \to \pi\pi$	2015	MU	15164071	09d	15a			0x411400a2
$D^0 \to K\pi$	2016	MD	15164024	09d	16			0x6139160F
$D^0 \to K\pi$	2016	MU	15164024	09d	16			0x6139160F
$D^0 \to KK$	2016	MD	15164081	09d	16			0x6139160F
$D^0 \to KK$	2016	MU	15164081	09d	16			0x6139160F
$D^0 \to \pi\pi$	2016	MD	15164071	09d	16			0x6139160F
$D^0 \to \pi\pi$	2016	MU	15164071	09d	16			0x6139160F
$D^0 \to K\pi$	2017	MD	15164022	09f	17	x	v01	0x62661709
$D^0 \to K\pi$	2017	MU	15164022	09f	17	x	v01	0x62661709
$D^0 \to KK$	2017	MD	15164080	09f	17	x	v01	0x62661709
$D^0 \to KK$	2017	MU	15164080	09f	17	x	v01	0x62661709
$D^0 \to \pi\pi$	2017	MD	15164070	09f	17	x	v01	0x62661709
$D^0 \to \pi\pi$	2017	MU	15164070	09f	17	x	v01	0x62661709
$D^0 \to K\pi$	2018	MD	15164022	09f	18	x	v01	0x617d18a4
$D^0 \to K\pi$	2018	MU	15164022	09f	18	x	v01	0x617d18a4
$D^0 \to KK$	2018	MD	15164080	09f	18	x	v01	0x617d18a4
$D^0 \to KK$	2018	MU	15164080	09f	18	x	v01	0x617d18a4
$D^0 \to \pi\pi$	2018	MD	15164070	09f	18	x	v01	0x617d18a4
$D^0 \to \pi\pi$	2018	MU	15164070	09f	18	x	v01	0x617d18a4
$\Lambda_b^0 \to D^0 p\pi$								
$D^0 \to K\pi$	2011	MD	15164090	09d	14c			0x40760037
$D^0 \to K\pi$	2011	MU	15164090	09d	14c			0x40760037
$D^0 \to KK$	2011	MD	15164062	09d	14c			0x40760037
$D^0 \to KK$	2011	MU	15164062	09d	14c			0x40760037
$D^0 \to \pi\pi$	2011	MD	15164052	09d	14c			0x40760037
$D^0 \to \pi\pi$	2011	MU	15164052	09d	14c			0x40760037
$D^0 \to K\pi$	2012	MD	15164012	08a	14a			0x409f0045
$D^0 \to K\pi$	2012	MU	15164012	08a	14a			0x409f0045

Continued on the next page.

Tab. C.2.: Simulation Conditions (Main decay might be continued from previous page.)

Decay	Year	Pol	EventType	Sim	Reco	Filter	ReDecay	Trigger
$D^0 \to KK$	2012	MD	15164061	09c	14c			0x409f0045
$D^0 \to KK$	2012	MU	15164061	09c	14c			0x409f0045
$D^0 \to \pi\pi$	2012	MD	15164051	08g	14c			0x409f0045
$D^0 \to \pi\pi$	2012	MU	15164051	08g	14c			0x409f0045
$D^0 \to K\pi$	2015	MD	15164090	09d	15a			0x411400a2
$D^0 \to K\pi$	2015	MU	15164090	09d	15a			0x411400a2
$D^0 \to KK$	2015	MD	15164062	09d	15a			0x411400a2
$D^0 \to KK$	2015	MU	15164062	09d	15a			0x411400a2
$D^0 \to \pi\pi$	2015	MD	15164052	09d	15a			0x411400a2
$D^0 \to \pi\pi$	2015	MU	15164052	09d	15a			0x411400a2
$D^0 \to K\pi$	2016	MD	15164090	09d	16			0x6139160F
$D^0 \to K\pi$	2016	MU	15164090	09d	16			0x6139160F
$D^0 \to KK$	2016	MD	15164062	09d	16			0x6139160F
$D^0 \to KK$	2016	MU	15164062	09d	16			0x6139160F
$D^0 \to \pi\pi$	2016	MD	15164052	09d	16			0x6139160F
$D^0 \to \pi\pi$	2016	MU	15164052	09d	16			0x6139160F
$D^0 \to \pi\pi$	2016	MD	15164012	09c	16	x		0x6138160F
$D^0 \to \pi\pi$	2016	MU	15164012	09c	16	x		0x6138160F
$D^0 \to K\pi$	2017	MD	15164012	09f	17	x	01	0x62661709
$D^0 \to K\pi$	2017	MU	15164012	09f	17	x	01	0x62661709
$D^0 \to KK$	2017	MD	15164061	09f	17	x	01	0x62661709
$D^0 \to KK$	2017	MU	15164061	09f	17	x	01	0x62661709
$D^0 \to \pi\pi$	2017	MD	15164051	09f	17	x	01	0x62661709
$D^0 \to \pi\pi$	2017	MU	15164051	09f	17	x	01	0x62661709
$D^0 \to K\pi$	2018	MD	15164012	09f	18	x	01	0x617d18a4
$D^0 \to K\pi$	2018	MU	15164012	09f	18	x	01	0x617d18a4
$D^0 \to KK$	2018	MD	15164061	09f	18	x	01	0x617d18a4
$D^0 \to KK$	2018	MU	15164061	09f	18	x	01	0x617d18a4
$D^0 \to \pi\pi$	2018	MD	15164051	09f	18	x	01	0x617d18a4
$D^0 \to \pi\pi$	2018	MU	15164051	09f	18	x	01	0x617d18a4
$B_s^0 \to D^0 KK$								
$D^0 \to K\pi$	2012	MD	13164076	08a	14a			0x409f0045
$D^0 \to K\pi$	2012	MU	13164076	08a	14a			0x409f0045
$D^0 \to KK$	2012	MD	13164079	08g	14c			0x409f0045
$D^0 \to KK$	2012	MU	13164079	08g	14c			0x409f0045
$D^0 \to \pi\pi$	2012	MD	13164078	08g	14c			0x409f0045
$D^0 \to \pi\pi$	2012	MU	13164078	08g	14c			0x409f0045
$D^0 \to K\pi$	2017	MD	13164076	09f	17	x	01	0x62661709
$D^0 \to K\pi$	2017	MU	13164076	09f	17	x	01	0x62661709
$D^0 \to K\pi$	2018	MD	13164076	09f	18	x	01	0x617d18a4
$D^0 \to K\pi$	2018	MU	13164076	09f	18	x	01	0x617d18a4
$B^0 \to D^0 KK$								
$D^0 \to K\pi$	2012	MD	11164086	08a	14a			0x409f0045
$D^0 \to K\pi$	2012	MU	11164086	08a	14a			0x409f0045
$D^0 \to KK$	2012	MD	11164089	08g	14c			0x409f0045
$D^0 \to KK$	2012	MU	11164089	08g	14c			0x409f0045
$D^0 \to \pi\pi$	2012	MD	11164088	08g	14c			0x409f0045

Continued on the next page.

Tab. C.2.: Simulation Conditions (Main decay might be continued from previous page.)

Decay	Year	Pol	EventType	Sim	Reco	Filter	ReDecay	Trigger
$D^0 \to \pi\pi$	2012	MU	11164088	08g	14c			0x409f0045
$D^0 \to K\pi$	2017	MD	11164086	09f	17	x	01	0x62661709
$D^0 \to K\pi$	2017	MU	11164086	09f	17	x	01	0x62661709
$D^0 \to K\pi$	2018	MD	11164086	09f	18	x	01	0x617d18a4
$D^0 \to K\pi$	2018	MU	11164086	09f	18	x	01	0x617d18a4
$\Lambda_b^0 \to D^* pK$								
$D^0 \to K\pi$	2017	MD	15164611	09f	17	x	01	0x62661709
$D^0 \to K\pi$	2017	MU	15164611	09f	17	x	01	0x62661709
$D^0 \to K\pi$	2018	MD	15164611	09f	18	x	01	0x617d18a4
$D^0 \to K\pi$	2018	MU	15164611	09f	18	x	01	0x617d18a4
$\Lambda_b^0 \to D^* p\pi$								
$D^0 \to K\pi$	2017	MD	15164601	09f	17	x	01	0x62661709
$D^0 \to K\pi$	2017	MU	15164601	09f	17	x	01	0x62661709
$D^0 \to K\pi$	2018	MD	15164601	09f	18	x	01	0x617d18a4
$D^0 \to K\pi$	2018	MU	15164601	09f	18	x	01	0x617d18a4
$\Lambda_b^0 \to ph^-h^+h^-$								
$\Lambda_b^0 \to pKKK$	2011	MD	15204013	08e	14a			0x40760037
$\Lambda_b^0 \to pKKK$	2011	MU	15204013	08e	14a			0x40760037
$\Lambda_b^0 \to pKKK$	2012	MD	15204013	08e	14a			0x409f0045
$\Lambda_b^0 \to pKKK$	2012	MU	15204013	08e	14a			0x409f0045
$\Lambda_b^0 \to pKKK$	2016	MD	15204013	09b	16			0x6138160F
$\Lambda_b^0 \to pKKK$	2016	MU	15204013	09b	16			0x6138160F
$\Lambda_b^0 \to pKK\pi$	2011	MD	15204012	08e	14a			0x40760037
$\Lambda_b^0 \to pKK\pi$	2011	MU	15204012	08e	14a			0x40760037
$\Lambda_b^0 \to pKK\pi$	2012	MD	15204012	08e	14a			0x409f0045
$\Lambda_b^0 \to pKK\pi$	2012	MU	15204012	08e	14a			0x409f0045
$\Lambda_b^0 \to pKK\pi$	2016	MD	15204012	09b	16			0x6138160F
$\Lambda_b^0 \to pKK\pi$	2016	MU	15204012	09b	16			0x6138160F
$\Lambda_b^0 \to pK\pi\pi$	2011	MD	15204011	08e	14a			0x40760037
$\Lambda_b^0 \to pK\pi\pi$	2011	MU	15204011	08e	14a			0x40760037
$\Lambda_b^0 \to pK\pi\pi$	2012	MD	15204011	08e	14a			0x409f0045
$\Lambda_b^0 \to pK\pi\pi$	2012	MU	15204011	08e	14a			0x409f0045
$\Lambda_b^0 \to pK\pi\pi$	2016	MD	15204011	09b	16			0x6138160F
$\Lambda_b^0 \to pK\pi\pi$	2016	MU	15204011	09b	16			0x6138160F
$\Lambda_b^0 \to p\pi\pi\pi$	2011	MD	15204010	08e	14a			0x40760037
$\Lambda_b^0 \to p\pi\pi\pi$	2011	MU	15204010	08e	14a			0x40760037
$\Lambda_b^0 \to p\pi\pi\pi$	2012	MD	15204010	08e	14a			0x409f0045
$\Lambda_b^0 \to p\pi\pi\pi$	2012	MU	15204010	08e	14a			0x409f0045
$\Lambda_b^0 \to p\pi\pi\pi$	2016	MD	15204010	09b	16			0x6138160F
$\Lambda_b^0 \to p\pi\pi\pi$	2016	MU	15204010	09b	16			0x6138160F

End of table.

D

Simulation compared to DATA

D.1 Fit to Preselected $\Lambda_b^0 \to D^0 p\pi$

A Gaussian signal and exponential background function are fitted to the DATA to extract *sWeights* via the *sPlot* [95] tool. The fit is shown in fig. D.1 and the result in tab. D.1.

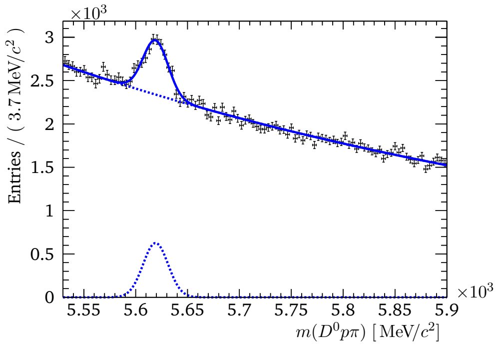

(a) 2011

(b) 2012

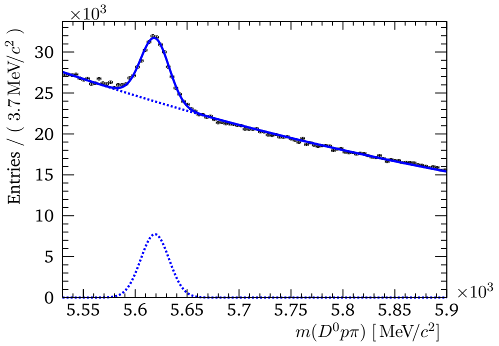

(c) Run II

Fig. D.1.: Extended maximum likelihood fit to mass distribution of $\Lambda_b^0 \to D^0 p\pi$ - DATA

Test MC Weights

Here we test the effect of weighting the truth-matched MC samples. The comparison of the Λ_b^0 kinematics of *sWeight*'ed $\Lambda_b^0 \to D^0 p\pi$ candidates of DATA to MC is shown in figs. D.2 to D.4.

Tab. D.1.: Results of fit to mass distribution of preselected $\Lambda_b^0 \to D^0 p\pi$ candidates.

	2011	2012	Run II
N_{Sig}	5126.1^{+257}_{-258}	13410^{+446}_{-439}	71510^{+870}_{-976}
μ_{Sig}	$5619.2^{+0.594}_{-0.594}$	$5619.5^{+0.423}_{-0.423}$	$5619.0^{+0.163}_{-0.166}$
σ_{Sig}	$12.088^{+0.640}_{-0.630}$	$13.682^{+0.481}_{-0.464}$	$13.626^{+0.175}_{-0.197}$
$N_{\text{Bkg}}/10^3$	204740^{+521}_{-510}	500930^{+826}_{-827}	2090000^{+1740}_{-1660}
$d = \lambda_{\text{exp}} \cdot 10^5$	$-152.70^{+2.25}_{-2.26}$	$-143.09^{+1.47}_{-1.47}$	$-157.37^{+0.698}_{-0.743}$

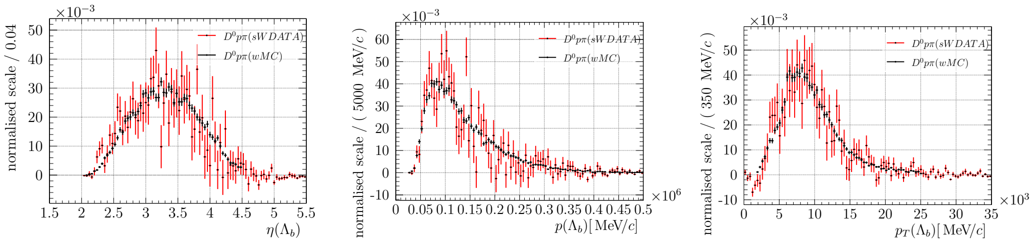

(a) $\eta(\Lambda_b^0)$ (b) $p(\Lambda_b^0)$ (c) $p_{\text{T}}(\Lambda_b^0)$

Fig. D.2.: Compared kinematics of *sWeight*'ed $\Lambda_b^0 \to D^0 p\pi$ candidates of DATA to truth-matched weighted MC - 2011

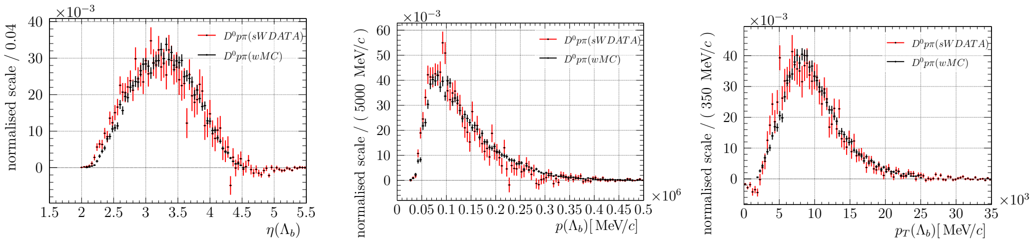

(a) $\eta(\Lambda_b^0)$ (b) $p(\Lambda_b^0)$ (c) $p_{\text{T}}(\Lambda_b^0)$

Fig. D.3.: Compared kinematics of *sWeight*'ed $\Lambda_b^0 \to D^0 p\pi$ candidates of DATA to truth-matched weighted MC - 2012

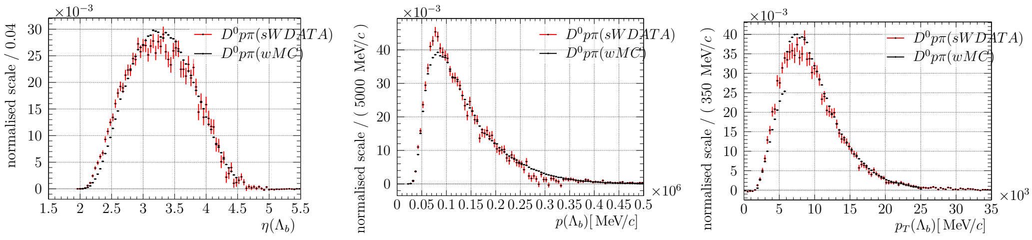

(a) $\eta(\Lambda_b^0)$ (b) $p(\Lambda_b^0)$ (c) $p_{\text{T}}(\Lambda_b^0)$

Fig. D.4.: Compared kinematics of *sWeight*'ed $\Lambda_b^0 \to D^0 p\pi$ candidates of DATA to truth-matched weighted MC - Run II

E

Multivariate Analysis

E.1 Classification Variables

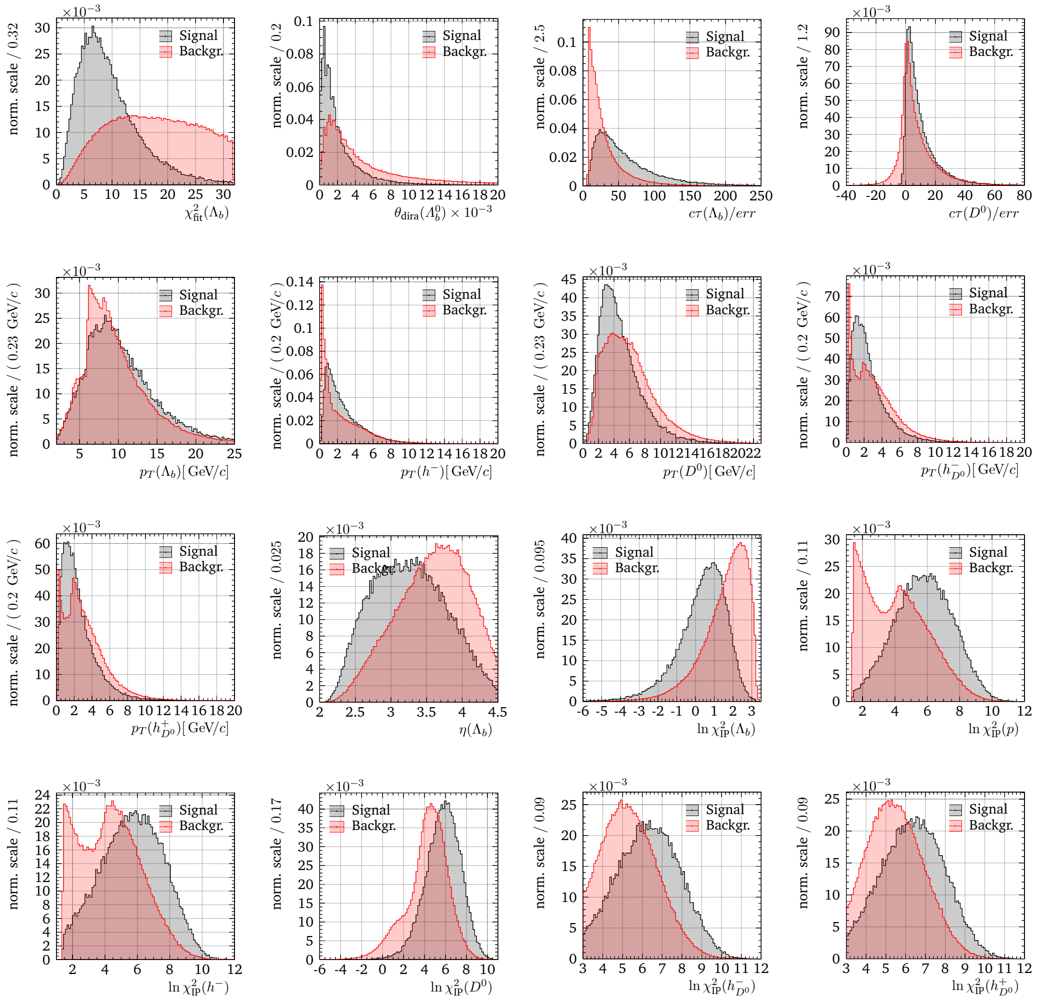

Fig. E.1.: Variables that are used for training the classifier in section 4.4.1. - 2011

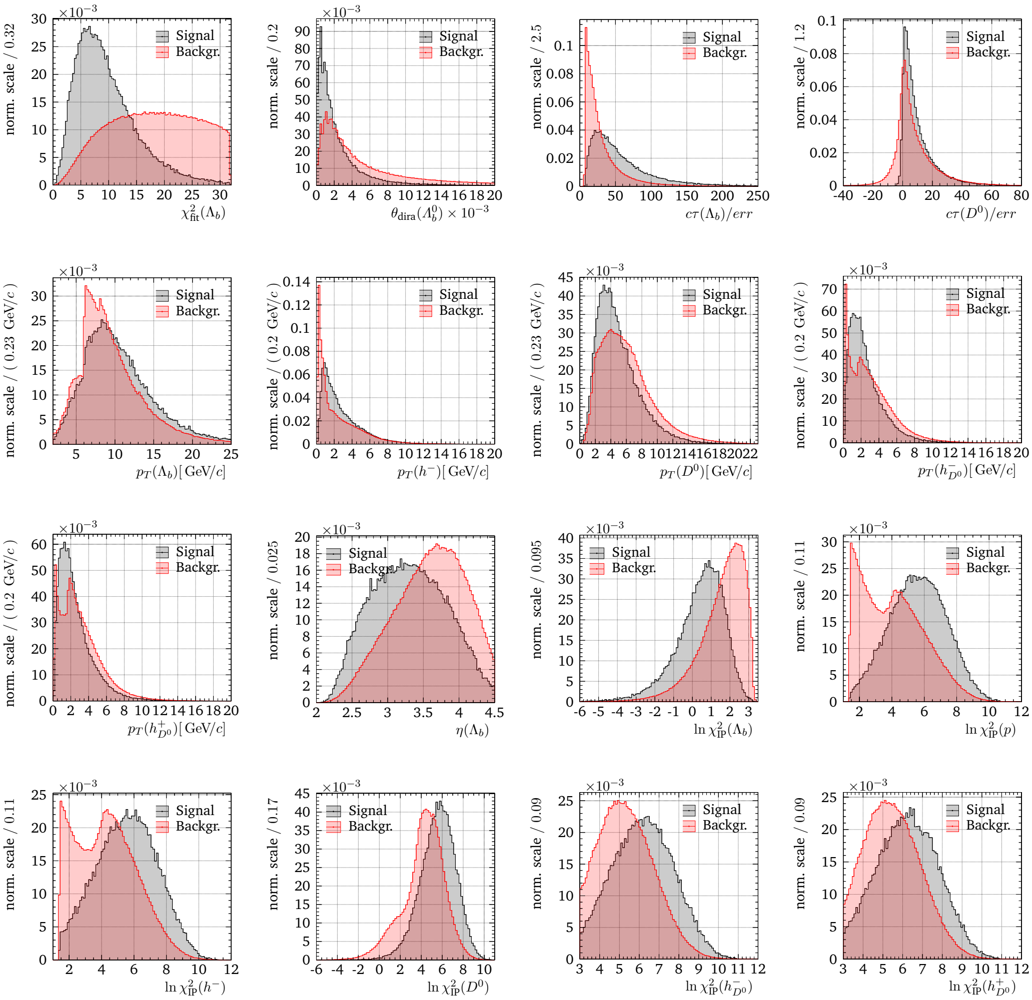

Fig. E.2.: Variables that are used for training the classifier in section 4.4.1. - 2012

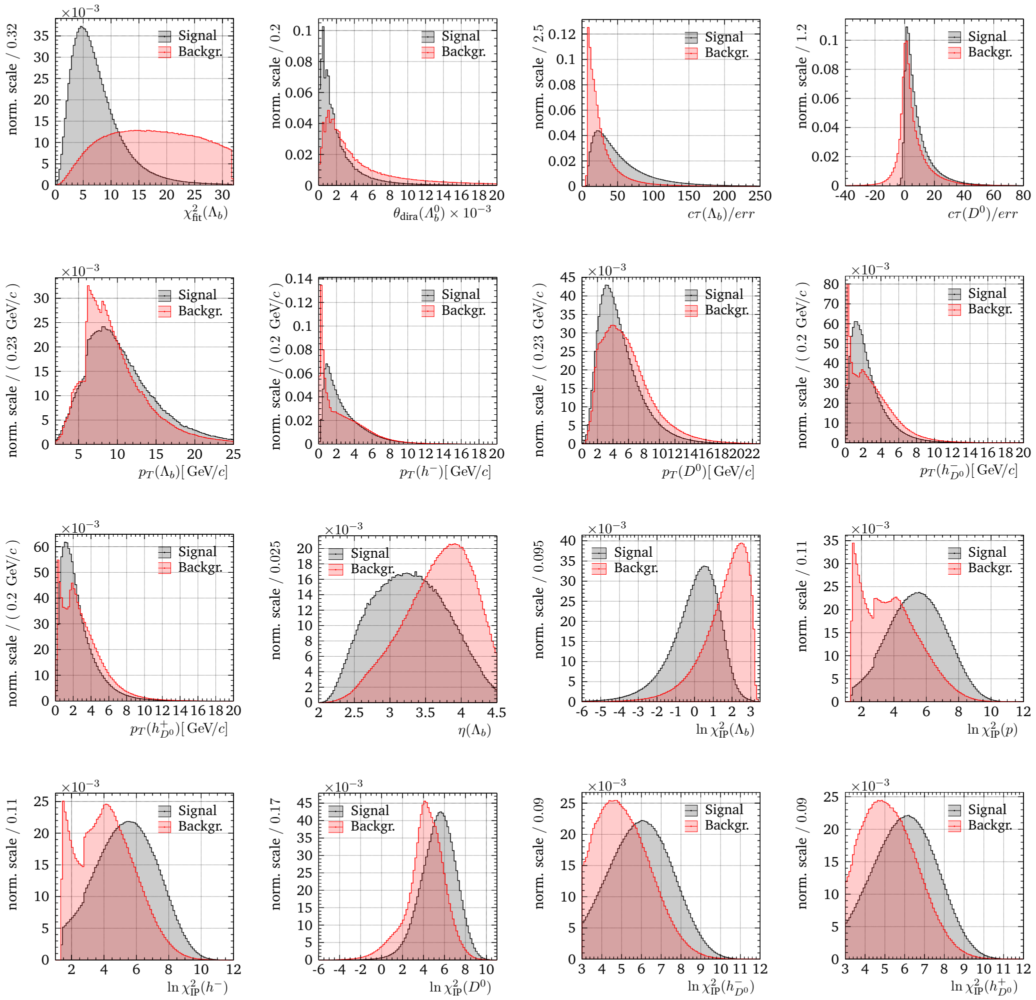

Fig. E.3.: Variables that are used for training the classifier in section 4.4.1. - Run II

E.2 Variable Correlations

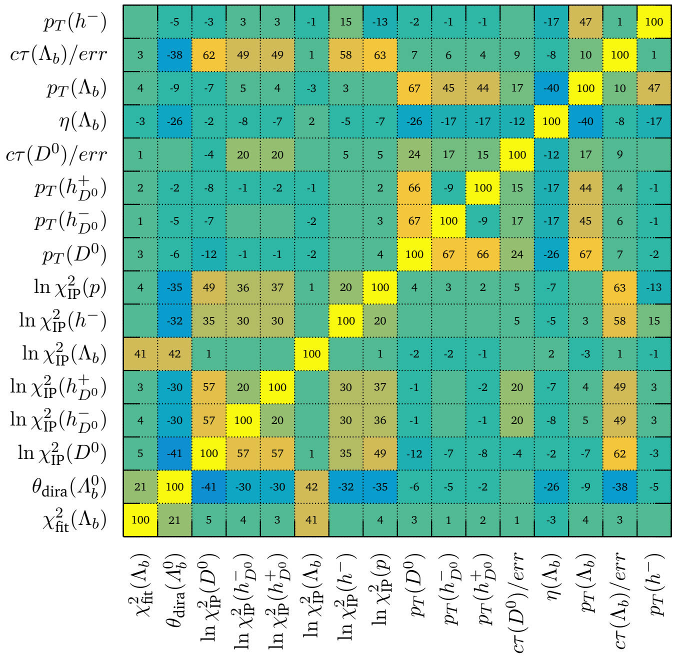

	$\chi^2_{\text{fit}}(\Lambda_b)$	$\theta_{\text{dira}}(\Lambda_b^0)$	$\ln\chi^2_{\text{IP}}(D^0)$	$\ln\chi^2_{\text{IP}}(h^-_{D^0})$	$\ln\chi^2_{\text{IP}}(h^+_{D^0})$	$\ln\chi^2_{\text{IP}}(\Lambda_b)$	$\ln\chi^2_{\text{IP}}(h^-)$	$\ln\chi^2_{\text{IP}}(p)$	$p_T(D^0)$	$p_T(h^-_{D^0})$	$p_T(h^+_{D^0})$	$c\tau(D^0)/err$	$\eta(\Lambda_b)$	$p_T(\Lambda_b)$	$c\tau(\Lambda_b)/err$	$p_T(h^-)$
$p_T(h^-)$		-5	-3	3	3	-1	15	-13	-2	-1	-1		-17	47	1	100
$c\tau(\Lambda_b)/err$	3	-38	62	49	49	1	58	63	7	6	4	9	-8	10	100	1
$p_T(\Lambda_b)$	4	-9	-7	5	4	-3	3		67	45	44	17	-40	100	10	47
$\eta(\Lambda_b)$	-3	-26	-2	-8	-7	2	-5	-7	-26	-17	-17	-12	100	-40	-8	-17
$c\tau(D^0)/err$	1		-4	20	20		5	5	24	17	15	100	-12	17	9	
$p_T(h^+_{D^0})$	2	-2	-8	-1	-2	-1		2	66	-9	100	15	-17	44	4	-1
$p_T(h^-_{D^0})$	1	-5	-7			-2		3	67	100	-9	17	-17	45	6	-1
$p_T(D^0)$	3	-6	-12	-1	-1	-2		4	100	67	66	24	-26	67	7	-2
$\ln\chi^2_{\text{IP}}(p)$	4	-35	49	36	37	1	20	100	4	3	2	5	-7		63	-13
$\ln\chi^2_{\text{IP}}(h^-)$		-32	35	30	30		100	20				5	-5	3	58	15
$\ln\chi^2_{\text{IP}}(\Lambda_b)$	41	42	1			100		1	-2	-2	-1		2	-3	1	-1
$\ln\chi^2_{\text{IP}}(h^+_{D^0})$	3	-30	57	20	100		30	37	-1		-2	20	-7	4	49	3
$\ln\chi^2_{\text{IP}}(h^-_{D^0})$	4	-30	57	100	20		30	36	-1		-1	20	-8	5	49	3
$\ln\chi^2_{\text{IP}}(D^0)$	5	-41	100	57	57	1	35	49	-12	-7	-8	-4	-2	-7	62	-3
$\theta_{\text{dira}}(\Lambda_b^0)$	21	100	-41	-30	-30	42	-32	-35	-6	-5	-2		-26	-9	-38	-5
$\chi^2_{\text{fit}}(\Lambda_b)$	100	21	5	4	3	41		4	3	1	2	1	-3	4	3	

(a) Signal

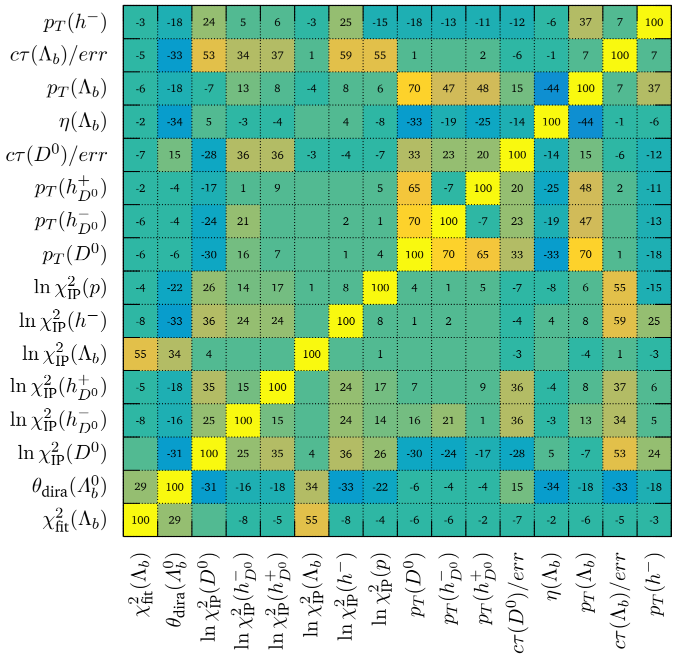

	$\chi^2_{\text{fit}}(\Lambda_b)$	$\theta_{\text{dira}}(\Lambda_b^0)$	$\ln\chi^2_{\text{IP}}(D^0)$	$\ln\chi^2_{\text{IP}}(h^-_{D^0})$	$\ln\chi^2_{\text{IP}}(h^+_{D^0})$	$\ln\chi^2_{\text{IP}}(\Lambda_b)$	$\ln\chi^2_{\text{IP}}(h^-)$	$\ln\chi^2_{\text{IP}}(p)$	$p_T(D^0)$	$p_T(h^-_{D^0})$	$p_T(h^+_{D^0})$	$c\tau(D^0)/err$	$\eta(\Lambda_b)$	$p_T(\Lambda_b)$	$c\tau(\Lambda_b)/err$	$p_T(h^-)$
$p_T(h^-)$	-3	-18	24	5	6	-3	25	-15	-18	-13	-11	-12	-6	37	7	100
$c\tau(\Lambda_b)/err$	-5	-33	53	34	37	1	59	55	1		2	-6	-1	7	100	7
$p_T(\Lambda_b)$	-6	-18	-7	13	8	-4	8	6	70	47	48	15	-44	100	7	37
$\eta(\Lambda_b)$	-2	-34	5	-3	-4		4	-8	-33	-19	-25	-14	100	-44	-1	-6
$c\tau(D^0)/err$	-7	15	-28	36	36	-3	-4	-7	33	23	20	100	-14	15	-6	-12
$p_T(h^+_{D^0})$	-2	-4	-17	1	9			5	65	-7	100	20	-25	48	2	-11
$p_T(h^-_{D^0})$	-6	-4	-24	21			2	1	70	100	-7	23	-19	47		-13
$p_T(D^0)$	-6	-6	-30	16	7		1	4	100	70	65	33	-33	70	1	-18
$\ln\chi^2_{\text{IP}}(p)$	-4	-22	26	14	17	1	8	100	4	1	5	-7	-8	6	55	-15
$\ln\chi^2_{\text{IP}}(h^-)$	-8	-33	36	24	24		100	8	1	2		-4	4	8	59	25
$\ln\chi^2_{\text{IP}}(\Lambda_b)$	55	34	4			100		1				-3		-4	1	-3
$\ln\chi^2_{\text{IP}}(h^+_{D^0})$	-5	-18	35	15	100		24	17	7		9	36	-4	8	37	6
$\ln\chi^2_{\text{IP}}(h^-_{D^0})$	-8	-16	25	100	15		24	14	16	21	1	36	-3	13	34	5
$\ln\chi^2_{\text{IP}}(D^0)$		-31	100	25	35	4	36	26	-30	-24	-17	-28	5	-7	53	24
$\theta_{\text{dira}}(\Lambda_b^0)$	29	100	-31	-16	-18	34	-33	-22	-6	-4	-4	15	-34	-18	-33	-18
$\chi^2_{\text{fit}}(\Lambda_b)$	100	29		-8	-5	55	-8	-4	-6	-6	-2	-7	-2	-6	-5	-3

(b) Background

Fig. E.4.: Correlation of the classification variables in % used in section 4.4.1. - 2011

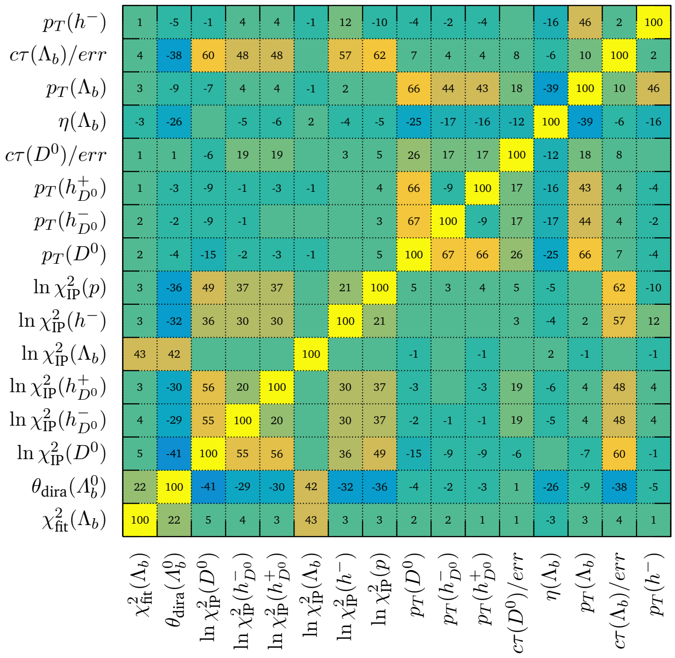

	$\chi^2_{\text{fit}}(\Lambda_b)$	$\theta_{\text{dira}}(\mathit{\Lambda}_b^0)$	$\ln\chi^2_{\text{IP}}(D^0)$	$\ln\chi^2_{\text{IP}}(h^-_{D^0})$	$\ln\chi^2_{\text{IP}}(h^+_{D^0})$	$\ln\chi^2_{\text{IP}}(\Lambda_b)$	$\ln\chi^2_{\text{IP}}(h^-)$	$\ln\chi^2_{\text{IP}}(p)$	$p_T(D^0)$	$p_T(h^-_{D^0})$	$p_T(h^+_{D^0})$	$c\tau(D^0)/err$	$\eta(\Lambda_b)$	$p_T(\Lambda_b)$	$c\tau(\Lambda_b)/err$	$p_T(h^-)$
$p_T(h^-)$	1	-5	-1	4	4	-1	12	-10	-4	-2	-4		-16	46	2	100
$c\tau(\Lambda_b)/err$	4	-38	60	48	48		57	62	7	4	4	8	-6	10	100	2
$p_T(\Lambda_b)$	3	-9	-7	4	4	-1	2		66	44	43	18	-39	100	10	46
$\eta(\Lambda_b)$	-3	-26		-5	-6	2	-4	-5	-25	-17	-16	-12	100	-39	-6	-16
$c\tau(D^0)/err$	1	1	-6	19	19		3	5	26	17	17	100	-12	18	8	
$p_T(h^+_{D^0})$	1	-3	-9	-1	-3	-1		4	66	-9	100	17	-16	43	4	-4
$p_T(h^-_{D^0})$	2	-2	-9	-1				3	67	100	-9	17	-17	44	4	-2
$p_T(D^0)$	2	-4	-15	-2	-3	-1		5	100	67	66	26	-25	66	7	-4
$\ln\chi^2_{\text{IP}}(p)$	3	-36	49	37	37		21	100	5	3	4	5	-5		62	-10
$\ln\chi^2_{\text{IP}}(h^-)$	3	-32	36	30	30		100	21				3	-4	2	57	12
$\ln\chi^2_{\text{IP}}(\Lambda_b)$	43	42				100			-1		-1		2	-1		-1
$\ln\chi^2_{\text{IP}}(h^+_{D^0})$	3	-30	56	20	100		30	37	-3		-3	19	-6	4	48	4
$\ln\chi^2_{\text{IP}}(h^-_{D^0})$	4	-29	55	100	20		30	37	-2	-1	-1	19	-5	4	48	4
$\ln\chi^2_{\text{IP}}(D^0)$	5	-41	100	55	56		36	49	-15	-9	-9	-6		-7	60	-1
$\theta_{\text{dira}}(\mathit{\Lambda}_b^0)$	22	100	-41	-29	-30	42	-32	-36	-4	-2	-3	1	-26	-9	-38	-5
$\chi^2_{\text{fit}}(\Lambda_b)$	100	22	5	4	3	43	3	3	2	2	1	1	-3	3	4	1

(a) Signal

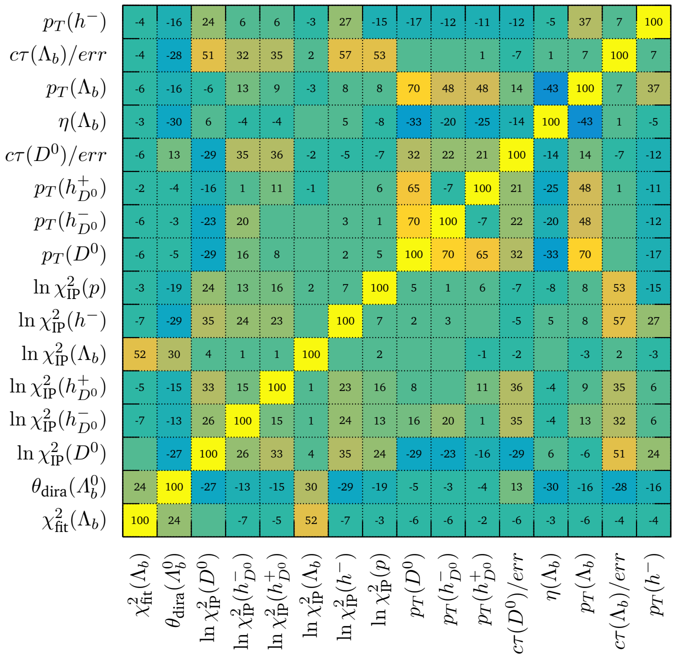

	$\chi^2_{\text{fit}}(\Lambda_b)$	$\theta_{\text{dira}}(\mathit{\Lambda}_b^0)$	$\ln\chi^2_{\text{IP}}(D^0)$	$\ln\chi^2_{\text{IP}}(h^-_{D^0})$	$\ln\chi^2_{\text{IP}}(h^+_{D^0})$	$\ln\chi^2_{\text{IP}}(\Lambda_b)$	$\ln\chi^2_{\text{IP}}(h^-)$	$\ln\chi^2_{\text{IP}}(p)$	$p_T(D^0)$	$p_T(h^-_{D^0})$	$p_T(h^+_{D^0})$	$c\tau(D^0)/err$	$\eta(\Lambda_b)$	$p_T(\Lambda_b)$	$c\tau(\Lambda_b)/err$	$p_T(h^-)$
$p_T(h^-)$	-4	-16	24	6	6	-3	27	-15	-17	-12	-11	-12	-5	37	7	100
$c\tau(\Lambda_b)/err$	-4	-28	51	32	35	2	57	53			1	-7	1	7	100	7
$p_T(\Lambda_b)$	-6	-16	-6	13	9	-3	8	8	70	48	48	14	-43	100	7	37
$\eta(\Lambda_b)$	-3	-30	6	-4	-4		5	-8	-33	-20	-25	-14	100	-43	1	-5
$c\tau(D^0)/err$	-6	13	-29	35	36	-2	-5	-7	32	22	21	100	-14	14	-7	-12
$p_T(h^+_{D^0})$	-2	-4	-16	1	11	-1		6	65	-7	100	21	-25	48	1	-11
$p_T(h^-_{D^0})$	-6	-3	-23	20			3	1	70	100	-7	22	-20	48		-12
$p_T(D^0)$	-6	-5	-29	16	8		2	5	100	70	65	32	-33	70		-17
$\ln\chi^2_{\text{IP}}(p)$	-3	-19	24	13	16	2	7	100	5	1	6	-7	-8	8	53	-15
$\ln\chi^2_{\text{IP}}(h^-)$	-7	-29	35	24	23		100	7	2	3		-5	5	8	57	27
$\ln\chi^2_{\text{IP}}(\Lambda_b)$	52	30	4	1	1	100		2			-1	-2		-3	2	-3
$\ln\chi^2_{\text{IP}}(h^+_{D^0})$	-5	-15	33	15	100	1	23	16	8		11	36	-4	9	35	6
$\ln\chi^2_{\text{IP}}(h^-_{D^0})$	-7	-13	26	100	15	1	24	13	16	20	1	35	-4	13	32	6
$\ln\chi^2_{\text{IP}}(D^0)$		-27	100	26	33	4	35	24	-29	-23	-16	-29	6	-6	51	24
$\theta_{\text{dira}}(\mathit{\Lambda}_b^0)$	24	100	-27	-13	-15	30	-29	-19	-5	-3	-4	13	-30	-16	-28	-16
$\chi^2_{\text{fit}}(\Lambda_b)$	100	24		-7	-5	52	-7	-3	-6	-6	-2	-6	-3	-6	-4	-4

(b) Background

Fig. E.5.: Correlation of the classification variables in % used in section 4.4.1. - 2012

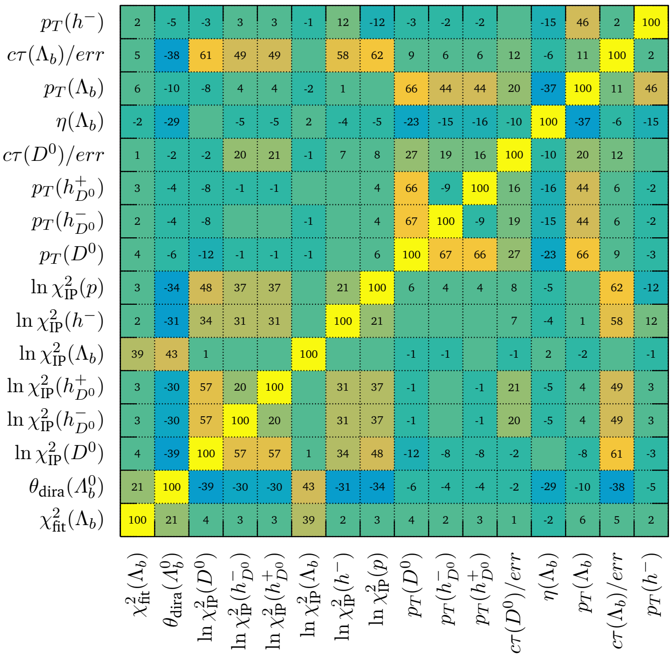

	$\chi^2_{\text{fit}}(\Lambda_b)$	$\theta_{\text{dira}}(\mathit{\Lambda}_b^0)$	$\ln\chi^2_{\text{IP}}(D^0)$	$\ln\chi^2_{\text{IP}}(h^-_{D^0})$	$\ln\chi^2_{\text{IP}}(h^+_{D^0})$	$\ln\chi^2_{\text{IP}}(\Lambda_b)$	$\ln\chi^2_{\text{IP}}(h^-)$	$\ln\chi^2_{\text{IP}}(p)$	$p_T(D^0)$	$p_T(h^-_{D^0})$	$p_T(h^+_{D^0})$	$c\tau(D^0)/err$	$\eta(\Lambda_b)$	$p_T(\Lambda_b)$	$c\tau(\Lambda_b)/err$	$p_T(h^-)$
$p_T(h^-)$	2	-5	-3	3	3	-1	12	-12	-3	-2	-2		-15	46	2	100
$c\tau(\Lambda_b)/err$	5	-38	61	49	49		58	62	9	6	6	12	-6	11	100	2
$p_T(\Lambda_b)$	6	-10	-8	4	4	-2	1		66	44	44	20	-37	100	11	46
$\eta(\Lambda_b)$	-2	-29		-5	-5	2	-4	-5	-23	-15	-16	-10	100	-37	-6	-15
$c\tau(D^0)/err$	1	-2	-2	20	21	-1	7	8	27	19	16	100	-10	20	12	
$p_T(h^+_{D^0})$	3	-4	-8	-1	-1			4	66	-9	100	16	-16	44	6	-2
$p_T(h^-_{D^0})$	2	-4	-8			-1		4	67	100	-9	19	-15	44	6	-2
$p_T(D^0)$	4	-6	-12	-1	-1	-1		6	100	67	66	27	-23	66	9	-3
$\ln\chi^2_{\text{IP}}(p)$	3	-34	48	37	37		21	100	6	4	4	8	-5		62	-12
$\ln\chi^2_{\text{IP}}(h^-)$	2	-31	34	31	31		100	21				7	-4	1	58	12
$\ln\chi^2_{\text{IP}}(\Lambda_b)$	39	43	1			100			-1	-1		-1	2	-2		-1
$\ln\chi^2_{\text{IP}}(h^+_{D^0})$	3	-30	57	20	100		31	37	-1		-1	21	-5	4	49	3
$\ln\chi^2_{\text{IP}}(h^-_{D^0})$	3	-30	57	100	20		31	37	-1		-1	20	-5	4	49	3
$\ln\chi^2_{\text{IP}}(D^0)$	4	-39	100	57	57	1	34	48	-12	-8	-8	-2		-8	61	-3
$\theta_{\text{dira}}(\mathit{\Lambda}_b^0)$	21	100	-39	-30	-30	43	-31	-34	-6	-4	-4	-2	-29	-10	-38	-5
$\chi^2_{\text{fit}}(\Lambda_b)$	100	21	4	3	3	39	2	3	4	2	3	1	-2	6	5	2

(a) Signal

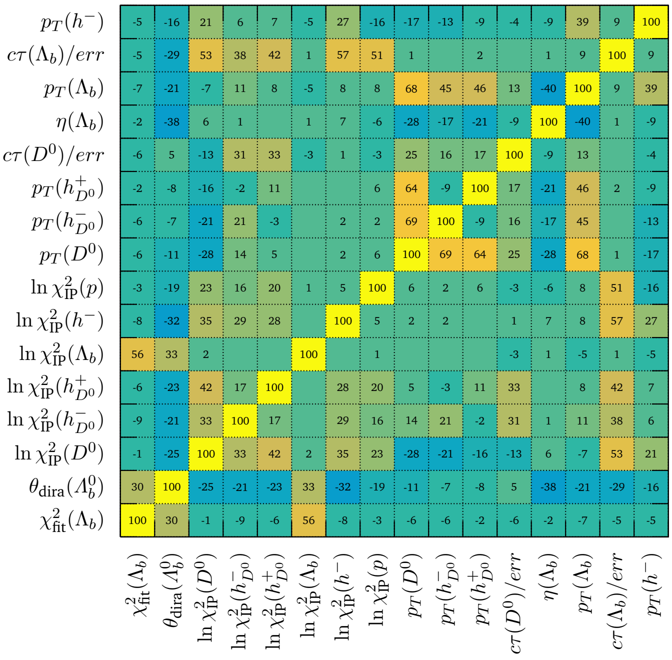

	$\chi^2_{\text{fit}}(\Lambda_b)$	$\theta_{\text{dira}}(\mathit{\Lambda}_b^0)$	$\ln\chi^2_{\text{IP}}(D^0)$	$\ln\chi^2_{\text{IP}}(h^-_{D^0})$	$\ln\chi^2_{\text{IP}}(h^+_{D^0})$	$\ln\chi^2_{\text{IP}}(\Lambda_b)$	$\ln\chi^2_{\text{IP}}(h^-)$	$\ln\chi^2_{\text{IP}}(p)$	$p_T(D^0)$	$p_T(h^-_{D^0})$	$p_T(h^+_{D^0})$	$c\tau(D^0)/err$	$\eta(\Lambda_b)$	$p_T(\Lambda_b)$	$c\tau(\Lambda_b)/err$	$p_T(h^-)$
$p_T(h^-)$	-5	-16	21	6	7	-5	27	-16	-17	-13	-9	-4	-9	39	9	100
$c\tau(\Lambda_b)/err$	-5	-29	53	38	42	1	57	51	1		2		1	9	100	9
$p_T(\Lambda_b)$	-7	-21	-7	11	8	-5	8	8	68	45	46	13	-40	100	9	39
$\eta(\Lambda_b)$	-2	-38	6	1		1	7	-6	-28	-17	-21	-9	100	-40	1	-9
$c\tau(D^0)/err$	-6	5	-13	31	33	-3	1	-3	25	16	17	100	-9	13		-4
$p_T(h^+_{D^0})$	-2	-8	-16	-2	11			6	64	-9	100	17	-21	46	2	-9
$p_T(h^-_{D^0})$	-6	-7	-21	21	-3		2	2	69	100	-9	16	-17	45		-13
$p_T(D^0)$	-6	-11	-28	14	5		2	6	100	69	64	25	-28	68	1	-17
$\ln\chi^2_{\text{IP}}(p)$	-3	-19	23	16	20	1	5	100	6	2	6	-3	-6	8	51	-16
$\ln\chi^2_{\text{IP}}(h^-)$	-8	-32	35	29	28		100	5	2	2		1	7	8	57	27
$\ln\chi^2_{\text{IP}}(\Lambda_b)$	56	33	2			100		1				-3	1	-5	1	-5
$\ln\chi^2_{\text{IP}}(h^+_{D^0})$	-6	-23	42	17	100		28	20	5	-3	11	33		8	42	7
$\ln\chi^2_{\text{IP}}(h^-_{D^0})$	-9	-21	33	100	17		29	16	14	21	-2	31	1	11	38	6
$\ln\chi^2_{\text{IP}}(D^0)$	-1	-25	100	33	42	2	35	23	-28	-21	-16	-13	6	-7	53	21
$\theta_{\text{dira}}(\mathit{\Lambda}_b^0)$	30	100	-25	-21	-23	33	-32	-19	-11	-7	-8	5	-38	-21	-29	-16
$\chi^2_{\text{fit}}(\Lambda_b)$	100	30	-1	-9	-6	56	-8	-3	-6	-6	-2	-6	-2	-7	-5	-5

(b) Background

Fig. E.6.: Correlation of the classification variables in % used in section 4.4.1. - Run II

E.3 Training Result

The result of the training in section 4.4.1 can be found in figs. 4.10, E.7 and E.8. The evaluation of the different trainings is listed in table E.1. The ROC integrals above 0.95 indicate a good performance. Signal efficiencies of the training and test samples for increasing background suppression show no deviation for Run II and only a small one for Run I. The numbers hint for overtraining of the 2011 classifier. As the 2011 sample is small in comparison to Run II and the deviation is only in order of a few percent, we accept the expected drop of the true signal efficiency.

Tab. E.1.: Evaluation results as from the `TMVA` output.

	ROC	ϵ_{sig} from test sample (from training sample)		
	integral	$\epsilon_{\text{bkg}} = 1\%$	$\epsilon_{\text{bkg}} = 10\%$	$\epsilon_{\text{bkg}} = 30\%$
2011	0.955	0.360 (0.372)	0.873 (0.875)	0.983 (0.983)
2012	0.958	0.381 (0.383)	0.887 (0.888)	0.986 (0.986)
Run II	0.972	0.497 (0.497)	0.936 (0.936)	0.993 (0.993)

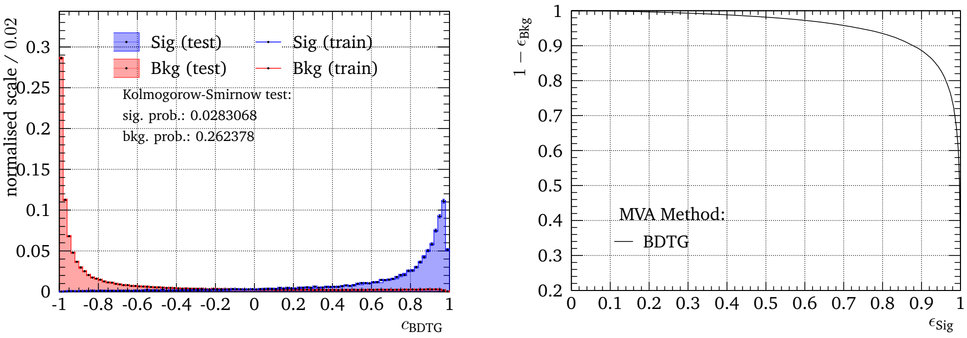

(a) c_{BDTG} (b) ROC

Fig. E.7.: Distribution of c_{BDTG} (a) and ROC (b) for 2011. (Run II result in fig. 4.10)

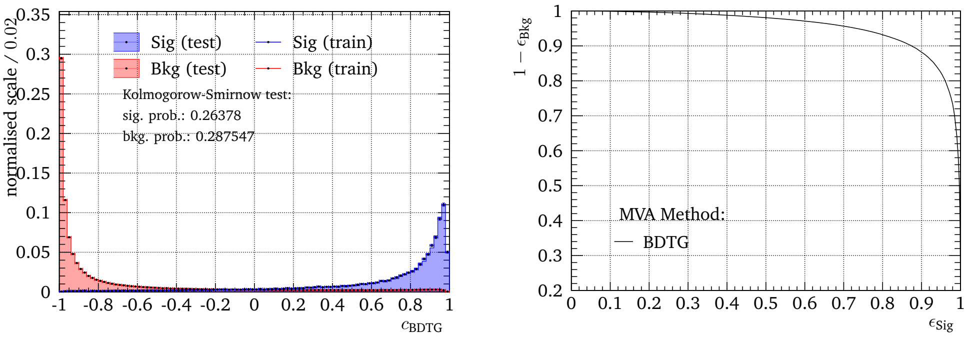

(a) c_{BDTG} (b) ROC

Fig. E.8.: Distribution of c_{BDTG} (a) and ROC (b) for 2012. (Run II result in fig. 4.10)

E.4 Comparing Sidebands

The combinatorial background is removed with the classifier trained in section 4.4.1. We use the left and right sideband to eliminate effects of energy and momentum dependencies, that might arise in the far upper sideband. This section studies the effects of training exclusively on the left or right sideband. We compare their performance on removing combinatorial background to the training with both sidebands. The left sideband still might include a significant amount of partially reconstructed D^{*0} decays, additionally the D^0 is kinematically not far from a D^{*0}, so a smaller signal efficiency is possible. This is reflected in the ROC of the training in fig. E.9. In principle the ROC of the exclusive right sideband training has the best performance, but the Λ_b^0 candidates mass distributions in fig. E.10 states a significant drop in combinatorial background for the combined sidebands. Figure E.10 shows the Λ_b^0 candidates mass distributions $m(D^0ph)$ for $D^0 \to K^-\pi^+$ with the same cuts on the different classifiers. We chose to use the training from both sidebands, as it has sufficient background suppression without the full risk of neglecting D^0 as the exclusive left sideband training or learning high energy or momentum effects as the exclusive right sideband training.

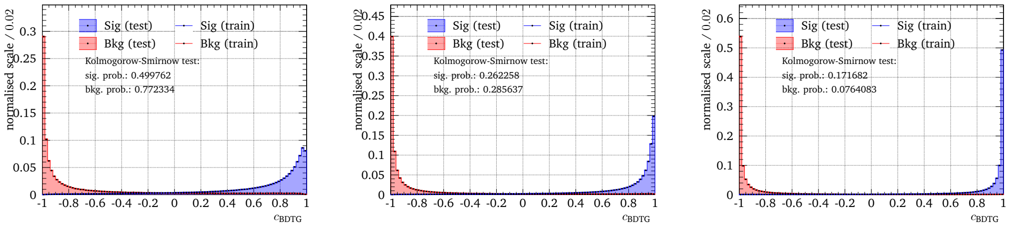

(a) exclusively left sideb. (b) both sideb. (c) exclusively right sideb.

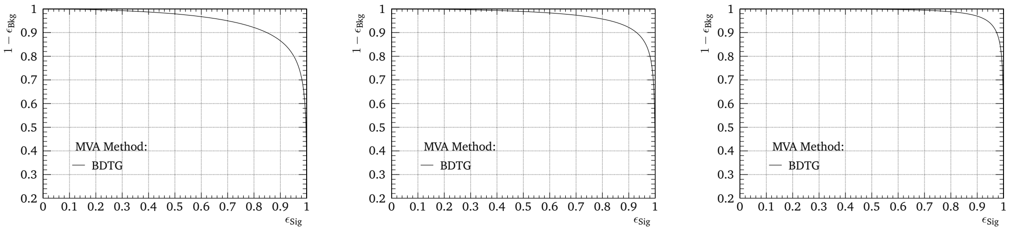

(d) exclusively left sideb. (e) both sideb. (f) exclusively right sideb.

Fig. E.9.: Comparison of the classification variable distributions for the training samples based on different sidebands (a-c) and their ROC (d-f) for the Run II datasets.

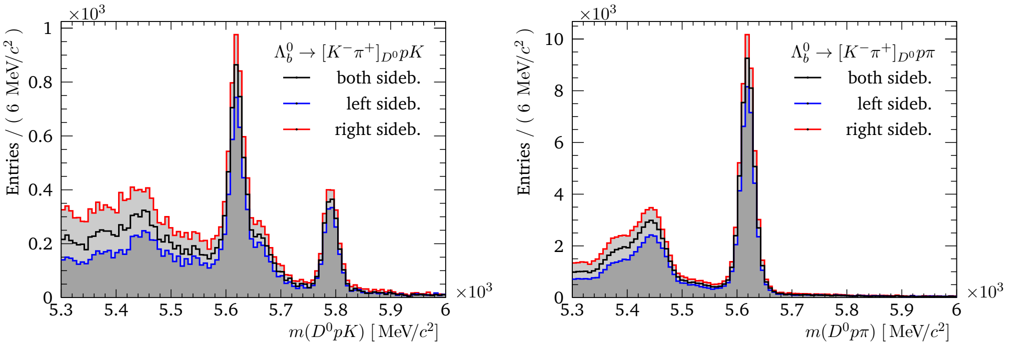

Fig. E.10.: Comparison of training classification performance in the $m(D^0ph)$ mass distributions. The DATA samples have all cuts applied and differ only in the use of the classification variable.

F

Figure of Merit Cut-Optimisation

The cut optimisation of section 4.4.2 uses fits to determine the counts of signal and background candidates (S_0 and B_0), which are used in the FoM. This appendix describes the fit models and results. We use RooFit [112] to perform extended unbinned maximum likelihood fits [96]. The extraction of S_0 and B_0 for the proton and D^0 daughters PID optimisation is done as described in section 4.4.2.

The optimisation of the p and D^0 daughter PID is done with the normalisation channel $\Lambda_b^0 \to D^0 p\pi$, where $D^0 \to K\pi$. The fit-model for the background is an exponential and for the signal a Gaussian. Their RooFit result is listed in table F.1. The fits for the proton PID are shown in fig. F.1 and for the D^0 daughters PID in fig. F.2.

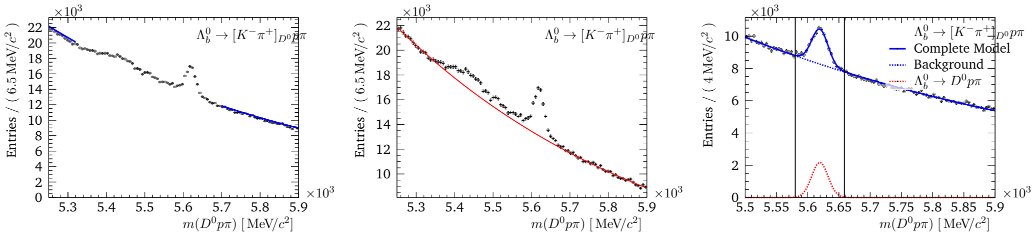

(a) sideband fit (Run I) (b) sideband extrapol. (Run I) (c) signal fit (Run I)

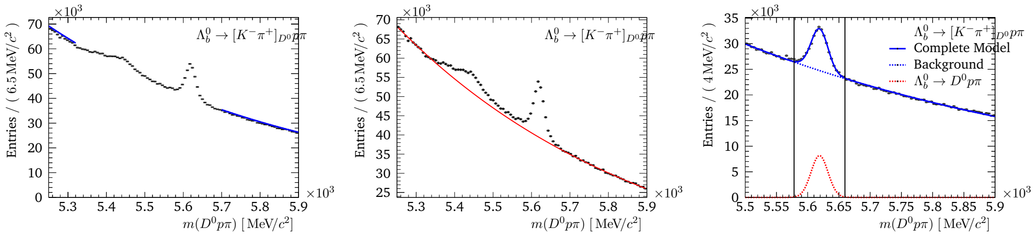

(d) sideband fit (Run II) (e) sideband extrapol. (Run II) (f) signal fit (Run II)

Fig. F.1.: Fits of the sideband extrapolation and signal extraction for the p PID optimisation.

The optimisation of the cut on the trained classifier and the K PID is done with the signal mode $\Lambda_b^0 \to D^0 pK$, where $D^0 \to K\pi$. Here we have to consider two more contributions to describe the signal mass distribution. There is the $\Lambda_b^0 \to D^0 p\pi$ mis-ID, which is modelled by the `RooNovosibirsk` function of the RooFit package, and a $\Xi_b \to D^0 pK$ signal modelled with a Gaussian. The Ξ_b model uses the same width as the Λ_b^0 signal. The RooFit result is listed in table F.2. The fits for the classifier are shown in fig. F.3 and for the K^- PID in

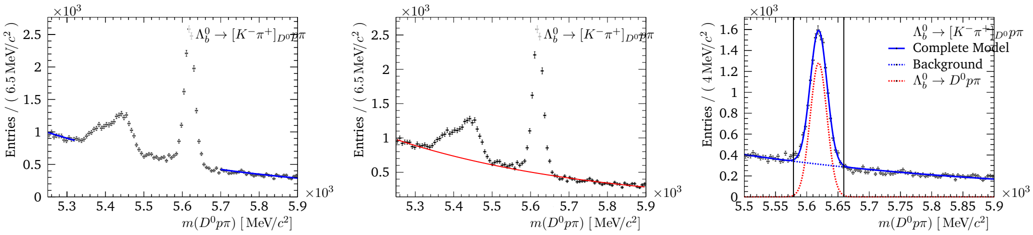

(a) sideband fit (Run I) (b) sideband extrapol. (Run I) (c) signal fit (Run I)

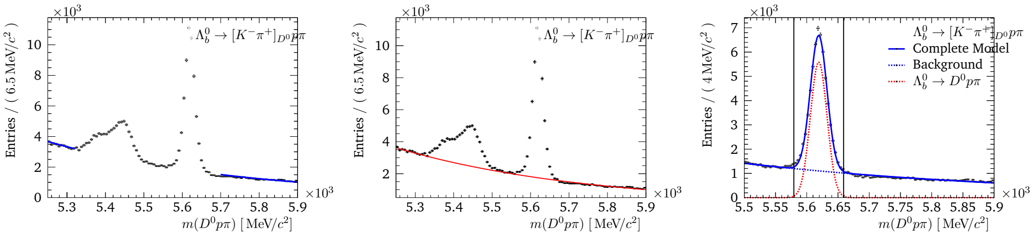

(d) sideband fit (Run II) (e) sideband extrapol. (Run II) (f) signal fit (Run II)

Fig. F.2.: Fits of the sideband extrapolation and signal extraction for the D^0 daughter PID optimisation.

Tab. F.1.: Fit Result to $m(D^0p\pi)$ for the FoM calculation of the p and D^0 daughter PID cuts.

	Proton PID		D^0 Daughter PID	
	Run I	Run II	Run I	Run II
Full Mass				
$\lambda_B/10^{-3}$	-1.536 ± 0.010	-1.600 ± 0.006	-2.17 ± 0.06	-2.110 ± 0.030
$N_B/10^4$	149.98 ± 0.33	451.3 ± 0.6	6.05 ± 0.08	21.25 ± 0.14
$\sigma_S/\,\mathrm{MeV}/c^2$	13.1 ± 0.4	13.57 ± 0.18	13.43 ± 0.18	13.28 ± 0.08
$\mu_S/\,\mathrm{MeV}/c^2$	5619.40 ± 0.35	5618.90 ± 0.16	5619.00 ± 0.18	5619.10 ± 0.08
$N_S/10^4$	1.78 ± 0.05	6.93 ± 0.08	1.077 ± 0.014	4.642 ± 0.028
Sidebands				
$\lambda_B/10^{-3}$	-1.390 ± 0.005	-1.4891 ± 0.0030	-1.904 ± 0.027	-1.978 ± 0.014
$N_B/10^4$	144.03 ± 0.20	437.41 ± 0.35	5.61 ± 0.04	20.40 ± 0.08

fig. F.4. The mis-ID contribution of $\Lambda_b^0 \to D^0 p\pi$ reaches into the 3σ signal-window, thus the background number B of the FoM calculates as

$$B = \epsilon_B B_0 + \epsilon_{\text{mis-ID}} B_0^{\text{mis-ID}} \quad , \tag{F.1}$$

where the mis-ID efficiency $\epsilon_{\text{mis-ID}}$ is determined from $\Lambda_b^0 \to D^0 p\pi$ mis-ID MC and the mis-ID background $B_0^{\text{mis-ID}}$ is calculated from the integral within the 3σ signal-window of the mid-ID shape.

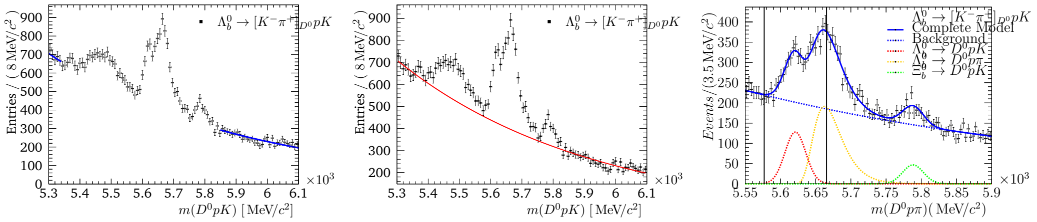

(a) sideband fit (Run I) (b) sideband extrapol. (Run I) (c) signal fit (Run I)

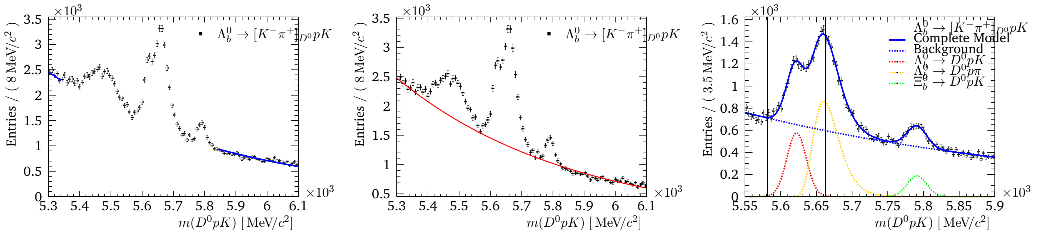

(d) sideband fit (Run II) (e) sideband extrapol. (Run II) (f) signal fit (Run II)

Fig. F.3.: Fits of the sideband extrapolation and signal extraction for the optimisation of the trained classifier.

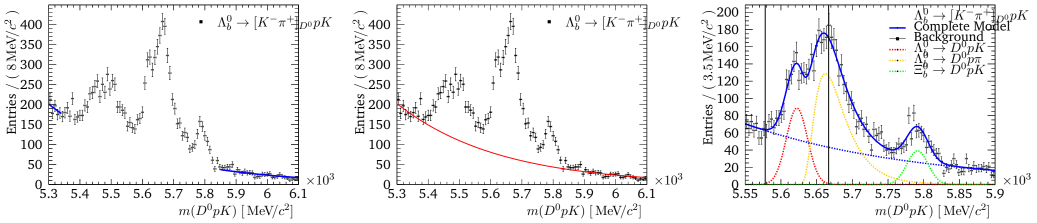

(a) sideband fit (Run I) (b) sideband extrapol. (Run I) (c) signal fit (Run I)

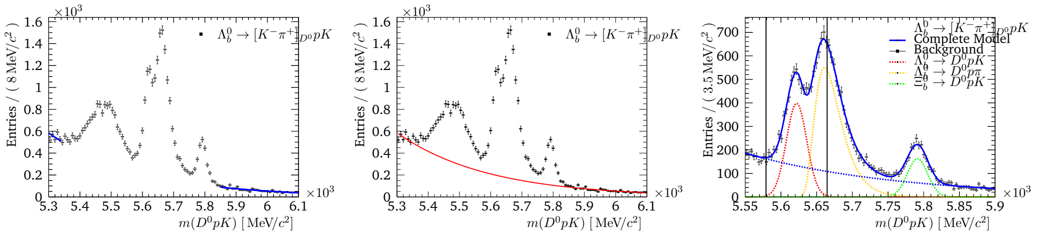

(d) sideband fit (Run II) (e) sideband extrapol. (Run II) (f) signal fit (Run II)

Fig. F.4.: Fits of the sideband extrapolation and signal extraction for the K PID optimisation.

Tab. F.2.: Fit Result to $m(D^0pK)$ for the FoM calculation of the classifier and K PID cuts.

	TMVA		Kaon PID	
	Run I	Run II	Run I	Run II
Full Mass				
$\lambda_B/10^{-3}$	-1.93 ± 0.09	-2.16 ± 0.05	-4.18 ± 0.22	-4.72 ± 0.14
$N_B/10^4$	4.36 ± 0.08	14.19 ± 0.15	1.32 ± 0.06	3.58 ± 0.11
$\sigma_S/\,\text{MeV}/c^2$	14.8 ± 1.5	13.6 ± 0.7	14.8 ± 1.2	14.3 ± 0.5
$\mu_S/\,\text{MeV}/c^2$	5621.2 ± 2.0	5622.3 ± 1.1	5622.4 ± 1.7	5621.9 ± 0.7
$N_S/10^2$	13.5 ± 1.7	56 ± 4	9.4 ± 0.9	40.6 ± 1.7
$\mu_{\Xi_b}/\,\text{MeV}/c^2$	5788.2 ± 2.2	5790.9 ± 0.9	5791.3 ± 1.4	5791.3 ± 0.6
$N_{\Xi_b}/10^2$	4.9 ± 0.7	18.3 ± 1.2	4.2 ± 0.4	16.6 ± 0.6
$\alpha_{\text{mis-ID}}/10^{-1}$	-3.5 ± 0.8	-2.8 ± 0.4	-5.3 ± 0.7	-4.08 ± 0.32
$\sigma_{\text{mis-ID}}/\,\text{MeV}/c^2$	20.1 ± 1.1	18.0 ± 0.6	22.1 ± 1.0	18.5 ± 0.4
$\mu_{\text{mis-ID}}/\,\text{MeV}/c^2$	5662.7 ± 1.6	5660.7 ± 0.7	5662.4 ± 1.6	5661.2 ± 0.6
$N_{\text{mis-ID}}/10^3$	2.85 ± 0.16	11.31 ± 0.35	2.18 ± 0.11	7.59 ± 0.16
Sidebands				
$\lambda_B/10^{-3}$	-1.605 ± 0.031	-1.777 ± 0.017	-3.07 ± 0.07	-3.42 ± 0.05
$N_B/10^3$	40.0 ± 0.4	132.2 ± 0.8	7.55 ± 0.18	20.01 ± 0.30

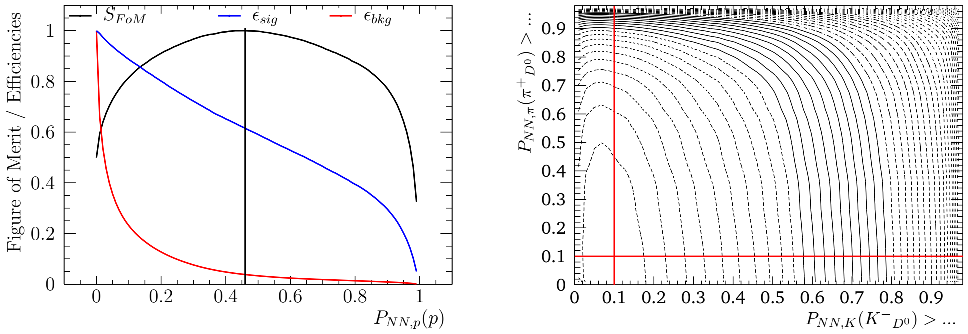

(a) Proton PID (Run I)

(b) D^0 daughter PID (FoM, Run I)

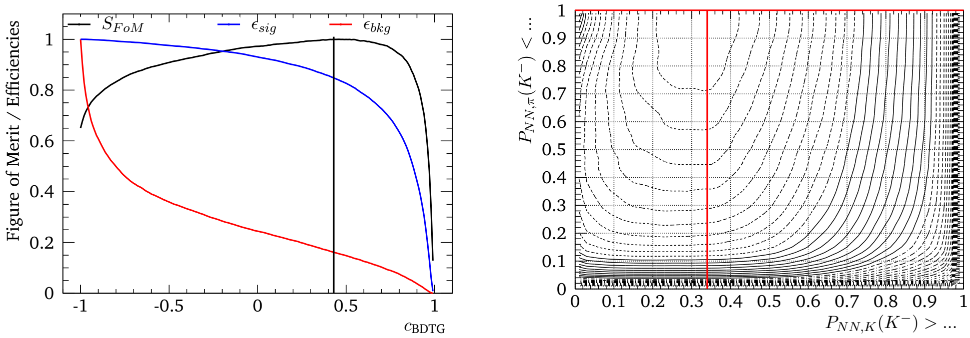

(c) Classifier (Run I)

(d) Kaon PID (FoM, Run I)

Fig. F.5.: FoM and Efficiencies for the PID selection of the proton, the D^0 daughters and kaon. Further the plot for the classifier selection is shown. The chosen cuts values are indicated as lines. (Run II in figs. 4.11 and 4.12)

G

Miscellaneous Background Studies for $m(D^0ph)$

G.1 $\Lambda_b^0 \to D^0pK$ mis-ID in $m(D^0p\pi)$

We expect a small contribution of $\Lambda_b^0 \to D^0pK$ mis-ID in $\Lambda_b^0 \to D^0p\pi$ due to their branching fractions. However the mass distribution of Λ_b^0 candidates in $m(D^0p\pi)$ shows a varying enhancement of the low-mass Λ_b^0 signal shoulder for the different D^0 modes in DATA, as can be seen in fig. G.1. To get a hold on the PID variables distribution of the $\Lambda_b^0 \to D^0pK$ mis-ID and $\Lambda_b^0 \to D^0p\pi$ we consider the correlation plot of $P_{NN,K}(\pi)$ and $P_{NN,\pi}(\pi)$ in the extended Λ_b^0 signal window $m(D^0p\pi) \in [5.5, 5.7\,\mathrm{GeV}/c^2]$. The PID correlations in fig. G.1 show a clear separation for K and π. The PID correlation plots lead to an obvious decision for a cut against the K hypothesis of $P_{\mathrm{NN},K}(\pi) < 0.5$, for the π hypothesis $P_{\mathrm{NN},\pi}(\pi) > 0.5$, which are also shown in fig. G.1. There is a visible suppression of the $\Lambda_b^0 \to D^0pK$ mis-ID and a reduction of the combinatoric. Both cuts are used in the mis-ID background studies in section 4.5.1.

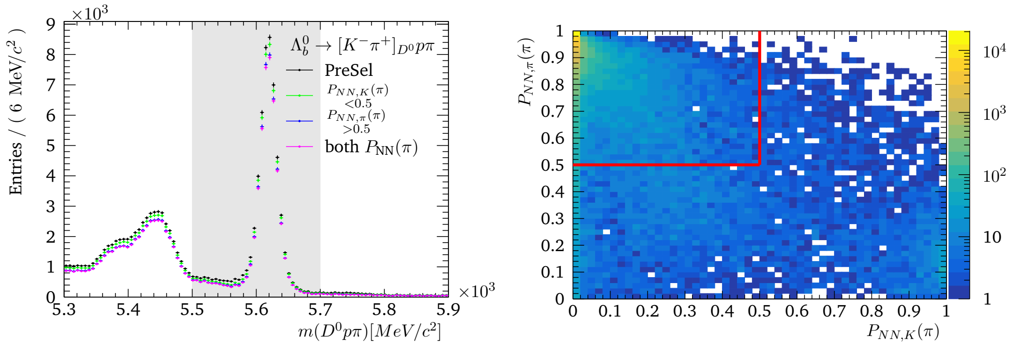

(a) $D^0 \to K^-\pi^+$- mass (b) $D^0 \to K^-\pi^+$- PID

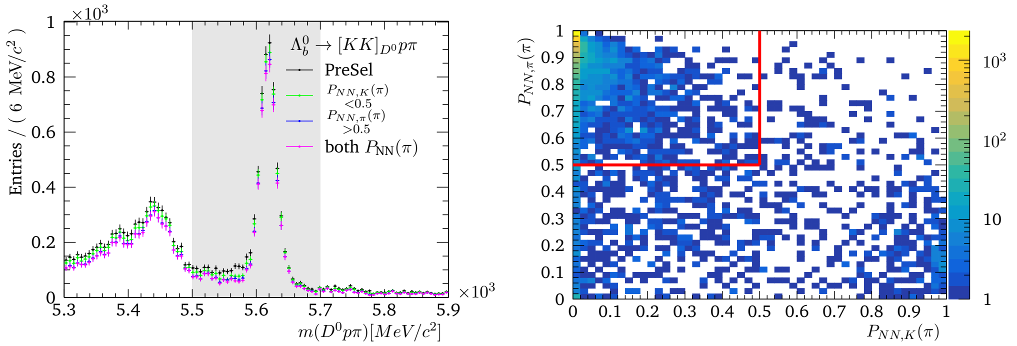

(c) $D^0 \to KK$- mass (d) $D^0 \to KK$- PID

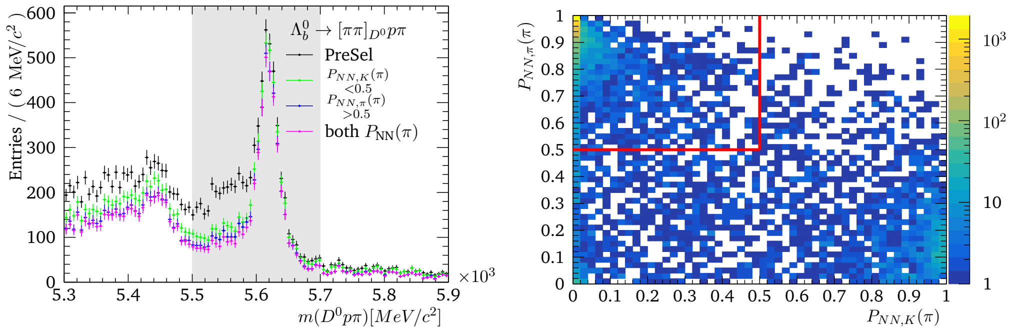

(e) $D^0 \to \pi\pi$- mass (f) $D^0 \to \pi\pi$- PID

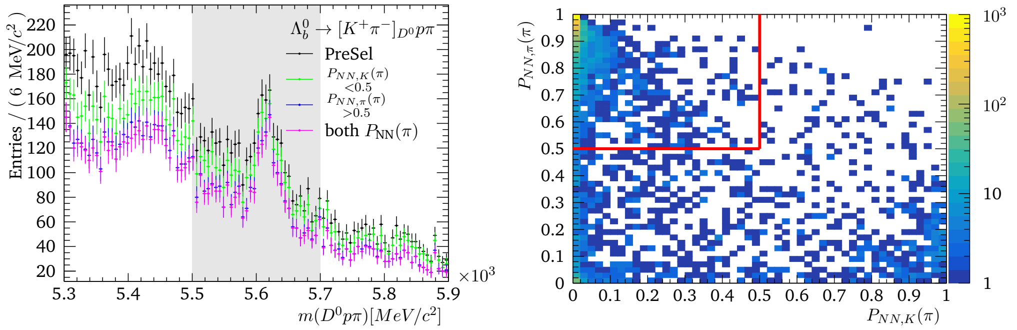

(g) $D^0 \to K^+\pi^-$- mass (h) $D^0 \to K^+\pi^-$- PID

Fig. G.1.: Distributions of $m(D^0p\pi)$ (left) and the correlation between $P_{\mathrm{NN},K/\pi}(\pi)$ (right) for Λ_b^0 candidates in the grey highlighted mass region (left). The chosen $P_{\mathrm{NN},K/\pi}$ values are visualised as red lines (right). - DATA

G.2 D^{*0} Polarisation in Partially Reconstructed Background

As mentioned in section 4.5.2 one can find polarised D^{*0} in the partially reconstructed decays $\{\Lambda_b^0, \Xi_b\} \to D^{*0}p\{K/\pi\}$. The effects on $m(D^0ph)$ are modelled by weighting the MC samples based on the helicity θ_{π^0} of the missing π^0. We use the weight function $w(\theta_{\pi^0}) = \cos^2\theta_{\pi^0}$ for $J_{m,D^{*0}} = 0$ and $w(\theta_{\pi^0}) = 1 - \cos^2\theta_{\pi^0} = \sin^2\theta_{\pi^0}$ for $J_{m,D^{*0}} = \pm 1$. We find negligible polarisation effects on the mass distributions of mis-ID MC (compare figs. G.3 and G.5). Further a double-peak like structure in 'true-ID' MC for $J = 0$ analogous to the one found in $B^0 \to DK^{*0}$ [109, 110] and a slight peak-value shift to lower masses in 'true-ID' MC for $J = \pm 1$ (compare figs. G.2 and G.4). The correlation between the helicity angle θ_{π^0} and the Λ_b^0 mass distribution, as shown in fig. G.6, can explain the different behaviour of the D^{*0} polarisation generated by weighting in the π^0 helicity distribution.

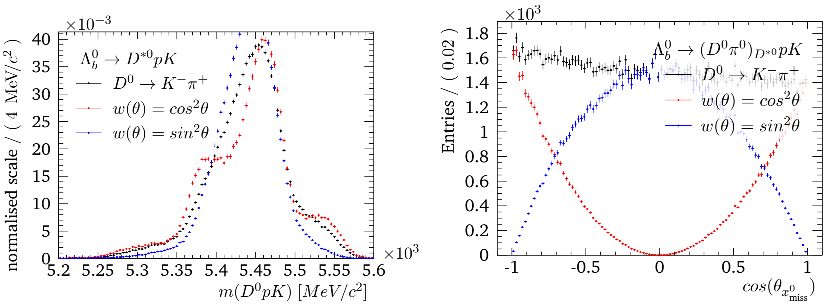

(a) $D^* \to D^0\{\pi^0, \gamma\}$ (b) π^0 helicity distribution

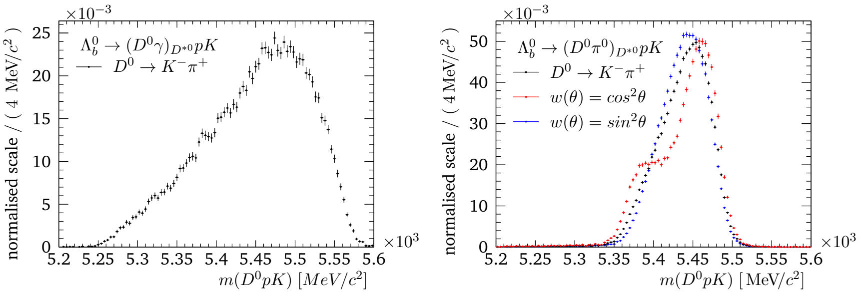

(c) $D^* \to D^0\gamma$ (d) $D^* \to D^0\pi^0$

Fig. G.2.: Comparison of $m(D^0pK)$ distributions for (un)polarised D^{*0} of $\Lambda_b^0 \to D^{*0}pK$. They are shown for the channels $D^{*0} \to D^0\gamma$ (c), $D^{*0} \to D^0\pi^0$ (d) and both (a). Polarisation is simulated by weighting in the π^0 helicity distribution (b). - MC 2018

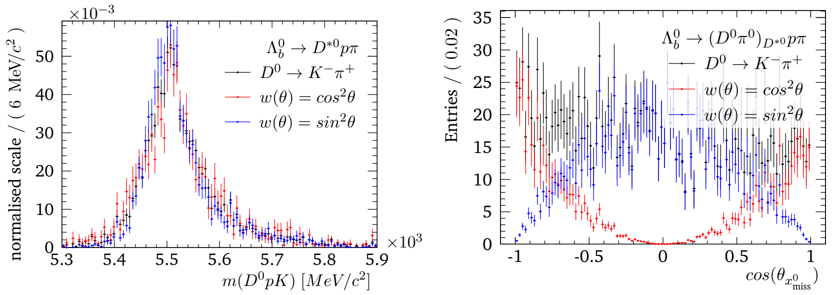

(a) $D^* \to D^0\{\pi^0, \gamma\}$ (b) π^0 helicity distribution

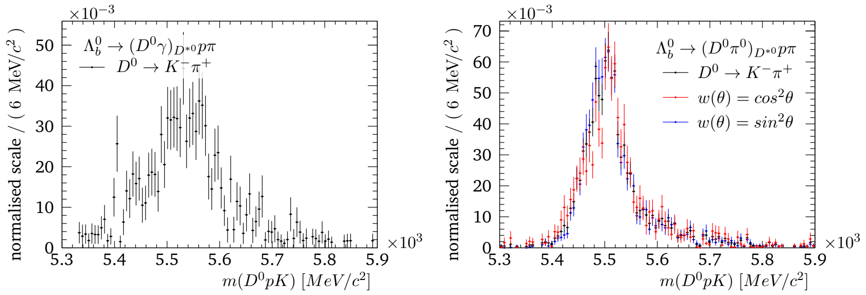

(c) $D^* \to D^0\gamma$ (d) $D^* \to D^0\pi^0$

Fig. G.3.: Comparison of $m(D^0pK)$ distributions for (un)polarised D^{*0} of $\Lambda_b^0 \to D^{*0}p\pi$. They are shown for the channels $D^{*0} \to D^0\gamma$ (c), $D^{*0} \to D^0\pi^0$ (d) and both (a). Polarisation is simulated by weighting in the π^0 helicity distribution (b). - MC 2018

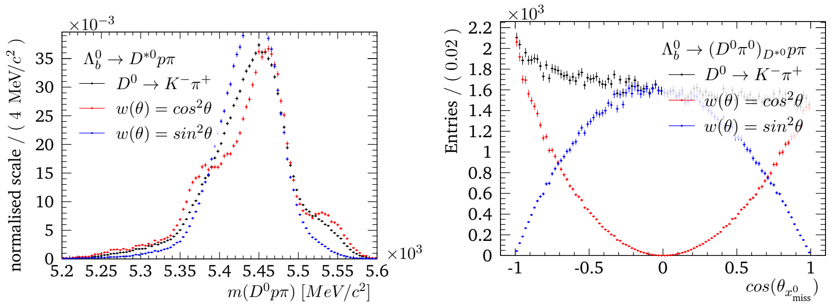

(a) $D^* \to D^0\{\pi^0, \gamma\}$ (b) π^0 helicity distribution

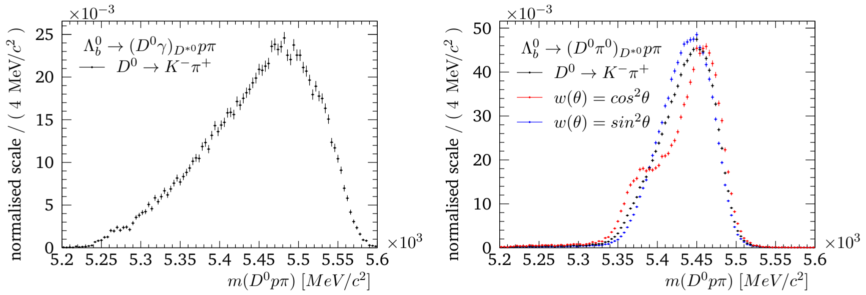

(c) $D^* \to D^0\gamma$ (d) $D^* \to D^0\pi^0$

Fig. G.4.: Comparison of $m(D^0p\pi)$ distributions for (un)polarised D^{*0} of $\Lambda_b^0 \to D^{*0}p\pi$. They are shown for the channels $D^{*0} \to D^0\gamma$ (c), $D^{*0} \to D^0\pi^0$ (d) and both (a). Polarisation is simulated by weighting in the π^0 helicity distribution (b). - MC 2018

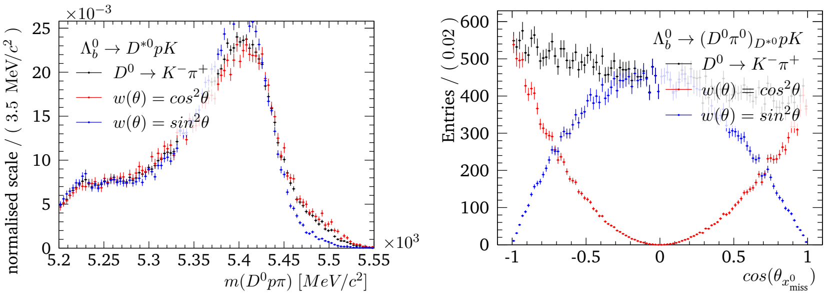

(a) $D^* \to D^0\{\pi^0, \gamma\}$ (b) π^0 helicity distribution

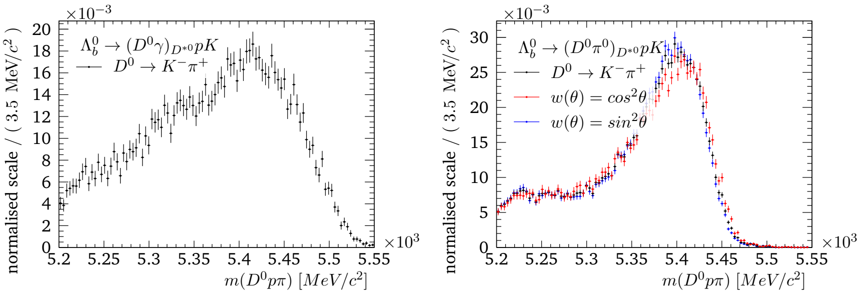

(c) $D^* \to D^0\gamma$ (d) $D^* \to D^0\pi^0$

Fig. G.5.: Comparison of $m(D^0p\pi)$ distributions for (un)polarised D^{*0} of $\Lambda_b^0 \to D^{*0}pK$. They are shown for the channels $D^{*0} \to D^0\gamma$ (c), $D^{*0} \to D^0\pi^0$ (d) and both (a). Polarisation is simulated by weighting in the π^0 helicity distribution (b). - MC 2018

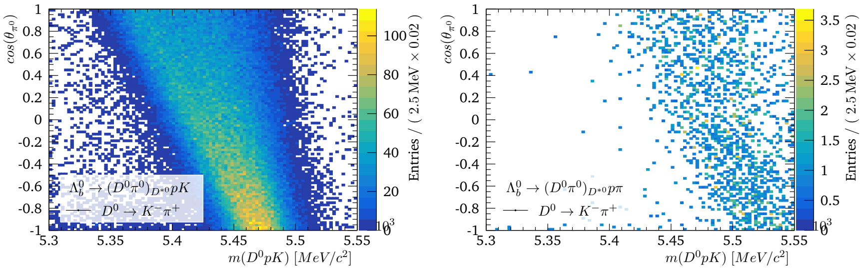

(a) $\Lambda_b^0 \to D^{*0}pK$ in $m(D^0pK)$ (b) $\Lambda_b^0 \to D^{*0}p\pi$ in $m(D^0pK)$

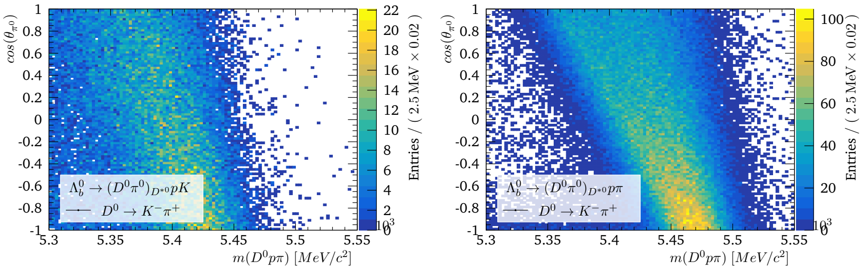

(c) $\Lambda_b^0 \to D^{*0}pK$ in $m(D^0p\pi)$ (d) $\Lambda_b^0 \to D^{*0}p\pi$ in $m(D^0p\pi)$

Fig. G.6.: Correlation between the helicity angle θ_{π^0} and $m(D^0ph)$ is shown for ‘true-ID’ and mis-ID of $\Lambda_b^0 \to D^{*0}ph$. The effect of simulating D^{*0} polarisation by weighting in θ_{π^0} is easily understood; *e.g.* in case of $J_m = \pm 1$ ($w(\theta_{\pi^0}) = \cos^2\theta_{\pi^0}$) we find a broad peak for lower masses and a sharp peak for higher. - MC 2018

G.3 Λ_c^+ in $m(ph^-{}_{D^0}h^+{}_{D^0})$ and $m(ph^-{}_{\Lambda_b^0}h^+{}_{D^0})$

Checking for $\Lambda_c^+ \to ph^-h^+$ in $m(ph^-_{D^0}h^+_{D^0})$ and $m(ph^-_{\Lambda_b^0}h^+_{D^0})$ to veto Λ_c^+ as proposed in section 4.5.3. The mass distributions for the $\Lambda_b^0 \to D^0pK$ samples are shown in fig. G.8 and for $\Lambda_b^0 \to D^0p\pi$ in G.9. The Λ_c^+ vetoed regions are shown in fig. G.7. We observe that in case of using both D^0 daughters we find $m(ph^-_{D^0}h^+_{D^0})$ to be always above the nominal Λ_c^+ mass, therefore a Λ_c^+ decay is only possible for an admixture of the mesons kaon and pion from Λ_b^0 and D^0.

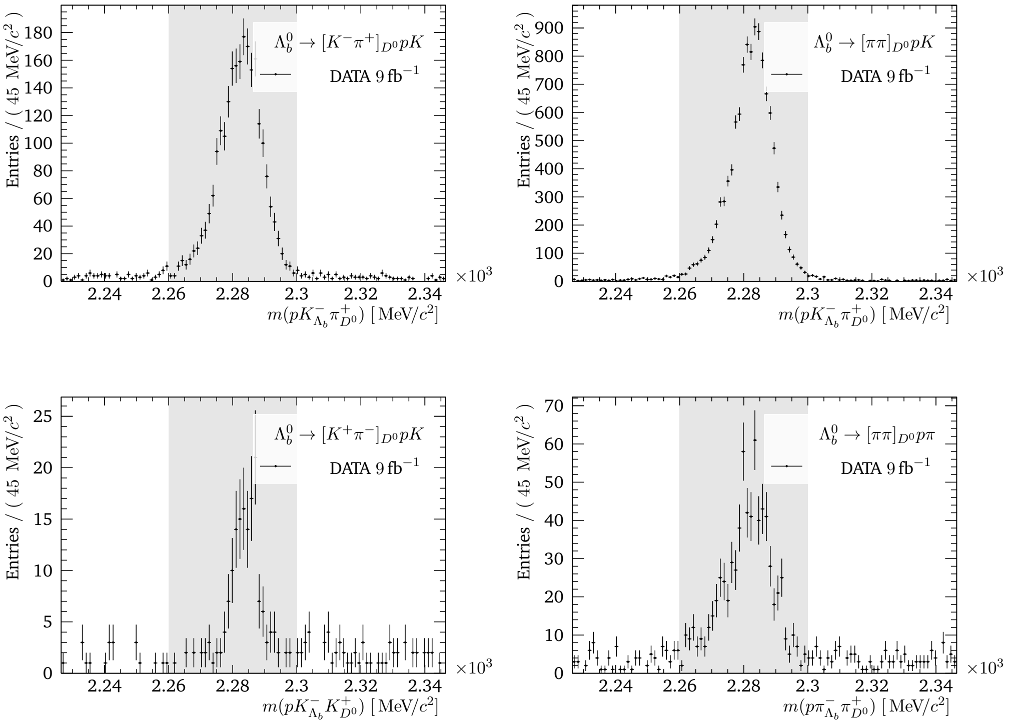

Fig. G.7.: Λ_c^+ veto regions highlighted as grey area.

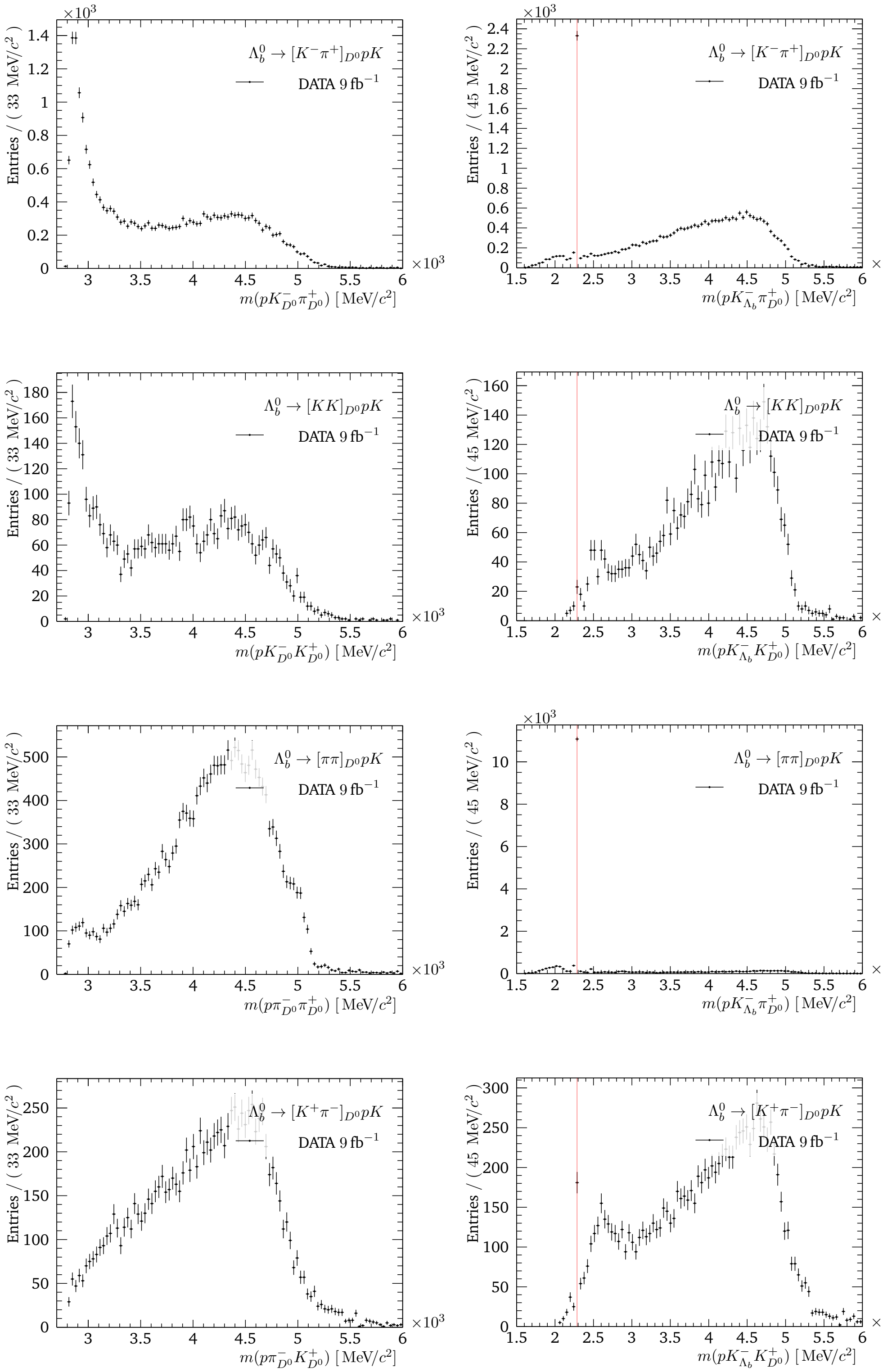

Fig. G.8.: $m(ph^-_{\Lambda_b^0}h^+_{D^0})$ (left) and $m(ph^-_{D^0}h^+_{D^0})$ (right) for the $m(D^0pK)$ tuples to check for a possible Λ_c^+. A red line indicates the nominal Λ_c^+ mass.

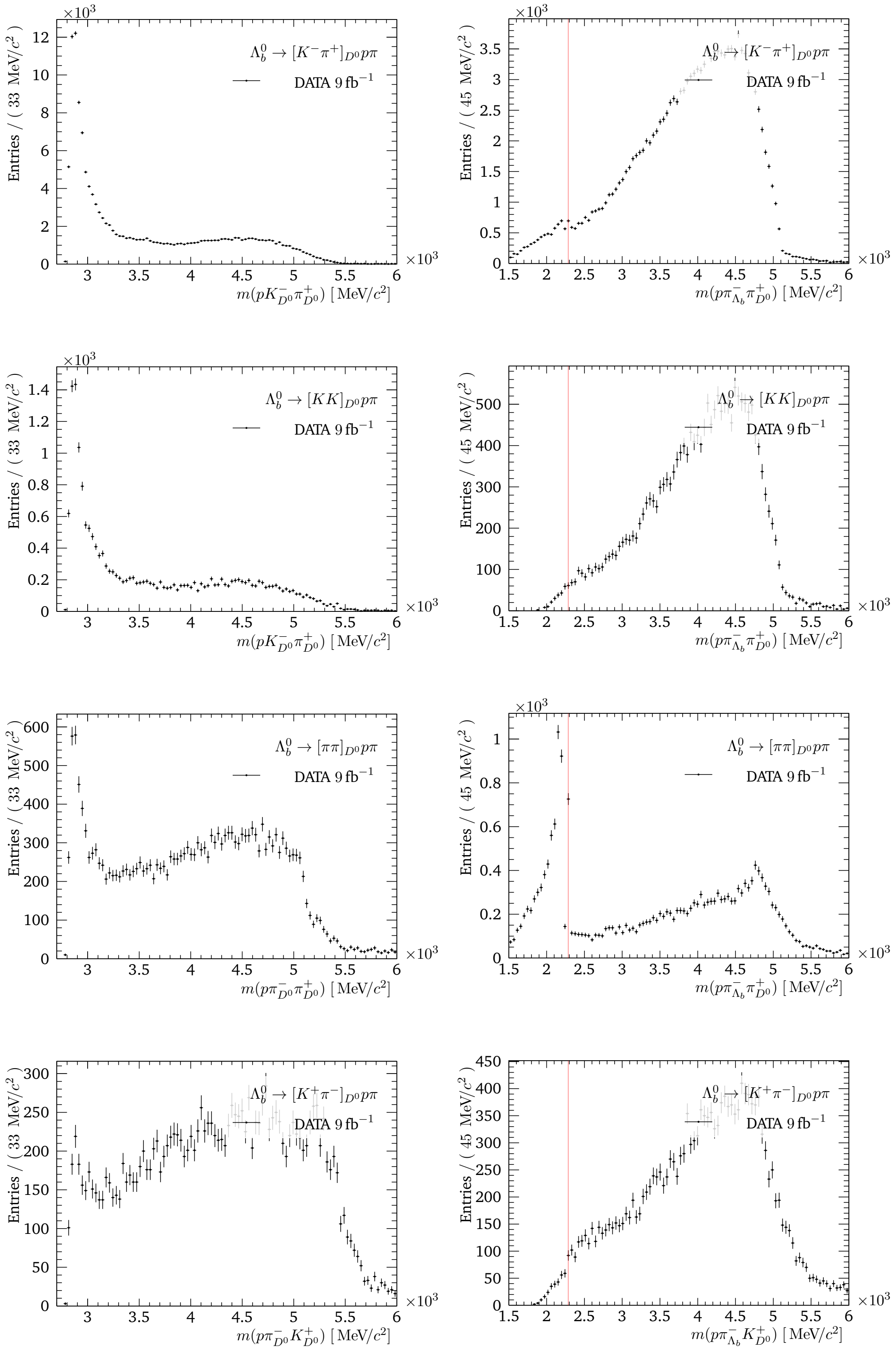

Fig. G.9.: $m(ph^-_{\Lambda_b^0}h^+_{D^0})$ (left) and $m(ph^-_{D^0}h^+_{D^0})$ (right) for the $m(D^0p\pi)$ tuples to check for a possible Λ_c^+. A red line indicates the nominal Λ_c^+ mass.

G.4 Charmless Background

As presented in section 4.5.4 we expect charmless background of $\Lambda_b^0 \to ph^-h^+h^-$ decays. In general a reconstructed D^0-mass is expected to be show a uniform distribution, however due to the D^0 mass constraint in the DTF we see a broadened $m(D^0)$ distribution with a peak value shifted away from the nominal D^0 mass. This effect is shown for $m(KK)$ in fig. G.10. Further the Λ_b^0 signal peak will be broadened and the charmless background distribution will be shifted slightly in $m(D^0ph)$.

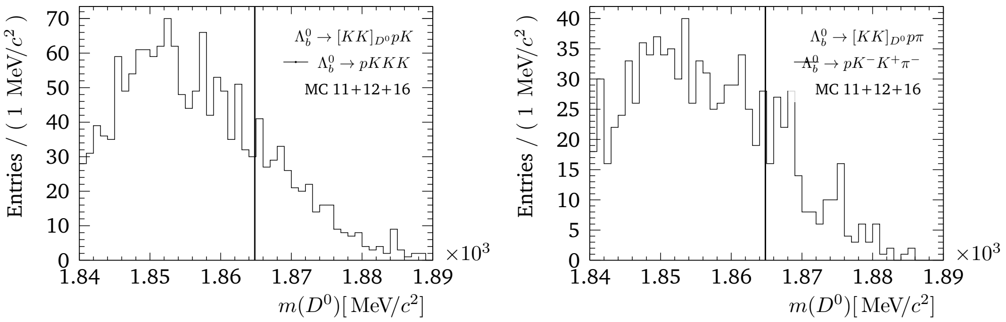

Fig. G.10.: $m(D^0)$ for $\Lambda_b^0 \to pK^-KK$ (left) in $m([KK]_{D^0}pK)$ and $\Lambda_b^0 \to pKK\pi^-$ (right) in $m([KK]_{D^0}p\pi)$. Both distributions show a shift from the nominal D^0-mass (vertical line) due to the D^0-mass constrain of the DTF.

G.4.1 $\Lambda_b^0 \to pK^-\pi^+\pi^-$ in $m([\pi^-\pi^+]_{D^0}pK^-)$

The Λ_b^0 signal broadening is clearly visible in $m([\pi\pi]_{D^0}pK)$ in fig. G.11, when compared to $m([KK]_{D^0}pK)$ in fig. G.13. Additionally we see a significant enhancement to lower D^0 masses in $m(\pi\pi)$ of fig. G.11.

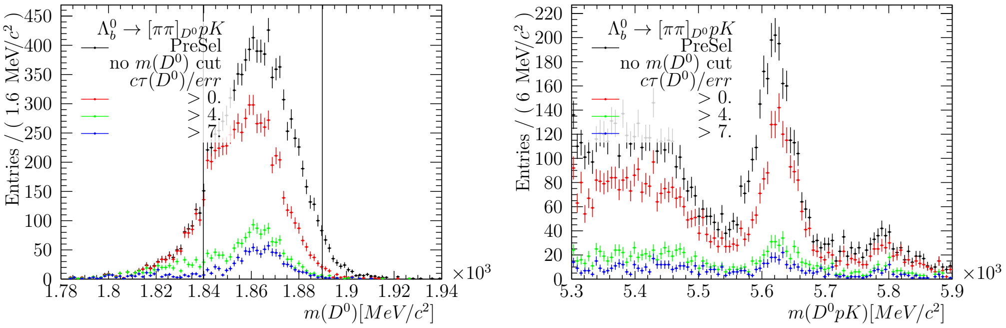

Fig. G.11.: D^0 (left) and Λ_b^0 (right) mass comparison for $\Lambda_b^0 \to [\pi\pi]_{D^0}pK$ candidates with strengthened cuts on $c\tau$/err. The charmless contribution (enhancement to lower D^0 masses) remains in the D^0 mass preselection window. - DATA

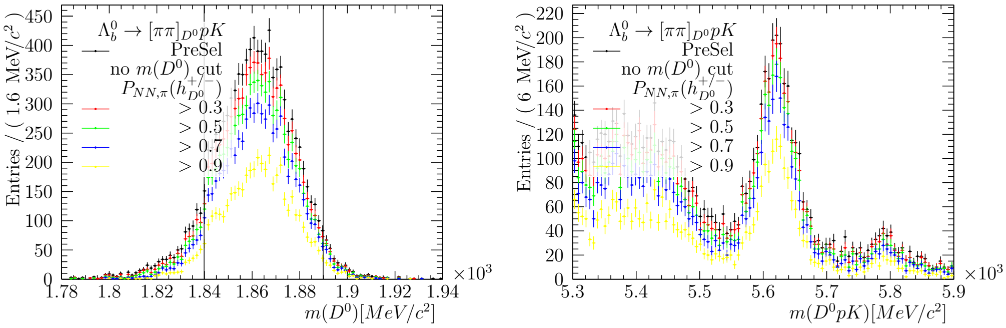

Fig. G.12.: Charmless background - Check of $P_{NN,\pi}(\pi_{D^0})$ for clean D^0 daughters. No altering of general D^0 (left) and Λ_b^0 (right) shapes visible in DATA, thus no mis-ID effect.

We fist test the particle type of the D^0 daughters by applying a strong cut on $P_{NN,\pi}(\pi_{D^0})$. As shown in fig. G.12 the shape of the Λ_b^0 and D^0 mass distributions is not effected, thus we assume to see no mis-ID effect. In fig. G.11 we test a rather loose, medium and strong cut on the D^0 lifetime via $c\tau$/err to enforce a detached Λ_b^0 and D^0 vertex. However, even a strong cut of $c\tau/\mathrm{err} > 7$, which comes with a great cost in remaining candidates, does not sufficiently suppress the enhancement in the D^0 mass.

G.4.2 $\Lambda_b^0 \to pK^-K^+K^-$ in $m([K^-K^+]_{D^0}pK^-)$

In $m([KK]_{D^0}pK)$, which is shown in fig. G.13 we do not see the eye-catching broadening in the Λ_b^0 mass. However a slight enhancement to lower masses in the D^0 mass is present. The suppression of the charmless contribution via a cut on the D^0 lifetime, is visibly better than for $D^0 \to \pi\pi$. In the following section we study the D^0 lifetime distribution, to get an impression of the $\Lambda_b^0 \to D^0 ph$ signal peak purity.

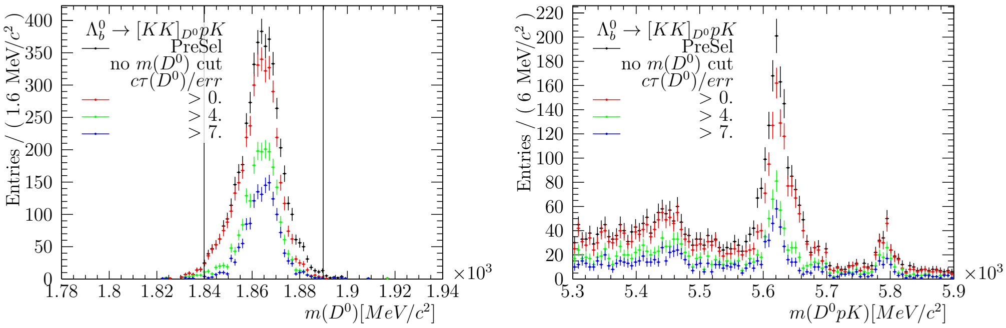

Fig. G.13.: D^0 (left) and Λ_b^0 (right) mass comparison for $\Lambda_b^0 \to [KK]_{D^0}pK$ candidates with strengthened cuts on $c\tau$/err. - DATA

G.4.3 D^0 Lifetime Fit

We aim to extract the following fractions f and ratios R for the charm and charmless contributions of the Λ_b^0 signal peak in $m([KK]_{D^0}ph)$.

$$\begin{aligned} f(pKKK) &= \frac{N(pKKK)}{N_\text{all}} & f(pKK\pi) &= \frac{N(pKK\pi)}{N_\text{all}} \\ f(D^0pK) &= \frac{N(D^0pK)}{N_\text{all}} & f(D^0p\pi) &= \frac{N(D^0p\pi)}{N_\text{all}} \\ R(pKKK) &= \frac{N(pKKK)}{N(D^0pK)} & R(pKK\pi) &= \frac{N(pKK\pi)}{N(D^0p\pi)} \end{aligned} \tag{G.1}$$

We use reconstructed Λ_b^0 candidates from the signal region $m(\Lambda_b^0) \in [5.58, 5.66]\,\text{GeV}/c^2$ in an unbinned simultaneous likelihood fit to the $c\tau_{D^0}$ distributions of the two DATA samples. The fit is performed with the RooFit toolkit [112]. The $\Lambda_b^0 \to D^0pK$ decay does have a 'normal' decaying D^0, thus we can model this decay with a basic exponential decay $\exp\left(-\frac{t}{\tau_{D^0}}\right)$. Without the DTF during reconstruction we would expect an additional single peak at zero caused by the charmless decay. But due to the DTF we have a fake D^0 causing a double-sided exponential decay slightly shifted from zero, we model as $\exp\left(-\frac{|t|}{\tau_{\text{no-}D^0}}\right)$. Both decay models are convolved with a Gaussian distribution of width σ_res to account for the detector resolution and interrelated by their ratio $R(pKKh)$. In the simultaneous fit the models for $\Lambda_b^0 \to D^0pK$ and $\Lambda_b^0 \to D^0p\pi$ share the resolution width σ_res and the fixed D^0 lifetime $\tau_{D^0} = 410.1 \pm 1.5\,\text{fs}$ [20]. Figure G.14 shows the fitted function and table G.1 lists the fitted parameters.

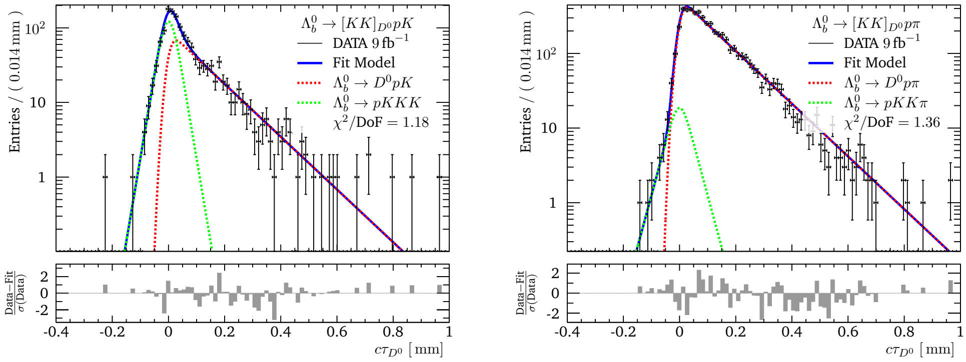

Fig. G.14.: Simultaneous likelihood fit to $c\tau_{D^0}$ distributions of $\Lambda_b^0 \to [KK]_{D^0}pK$ (left) and $\Lambda_b^0 \to [KK]_{D^0}p\pi$ (right) candidates in the Λ_b^0 signal-region $m(\Lambda_b^0) \in [5.58, 5.66]\,\text{GeV}/c^2$.

Tab. G.1.: Result of the simultaneous fit to the $c\tau$ distribution of the $D^0 \to KK$ DATA in fig. G.14.

	$[KK]_{D^0}pK$	$[KK]_{D^0}p\pi$
σ_res / mm	0.0164 ± 0.0011	
$\tau_{\text{no-}D^0}$ / fs	65.0 ± 4.7	104 ± 18
N	781 ± 34	4772 ± 75
$R(pKKh)$	0.757 ± 0.060	0.0252 ± 0.0065

From the result of the fit we are now able to calculate the total amounts, charm (charmless) fractions and the charm to charmless ratios for a specific cut on $c\tau_{D^0}$. The evolution of these parameters can be seen in fig. G.15 for cuts on $c\tau$ in the range $[-0.1, 0.2]\,\mathrm{mm}$. It is not possible to completely suppress the charmless background without loosing too much signal. We chose an additional cut of $c\tau_{D^0} > 0.01mm$ on the $D^0 \to KK$ tuples resulting in the approximated ratios, fractions and efficiencies (from matched MC), listed in table G.2.

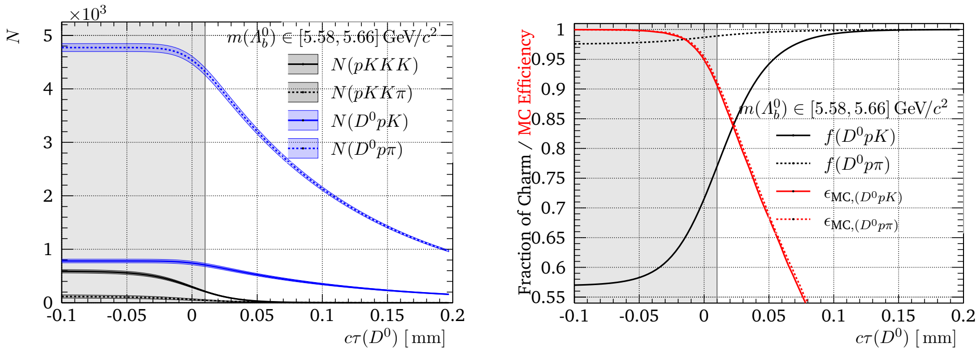

(a) Amounts

(b) Charm Fractions *vs.* Efficiencies

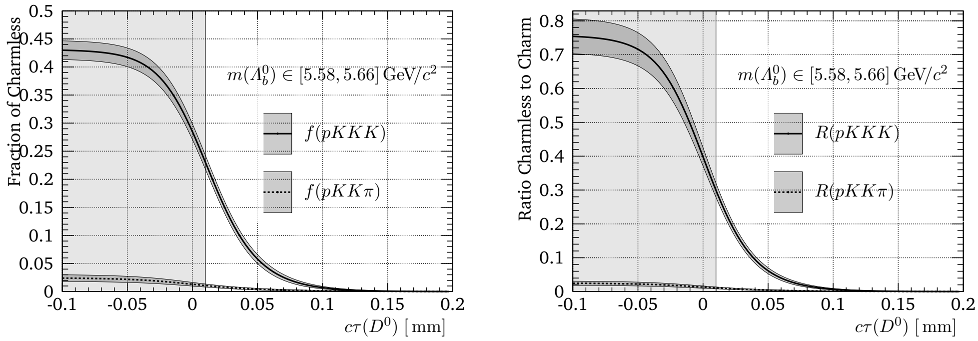

(c) Charmless Fractions

(d) Charm to Charmless Ratios

Fig. G.15.: Remaining amounts of charm and charmless signal in $m([KK]_{D^0}ph)$ for various cuts on $c\tau_{D^0}$ (a). Resulting charm fractions (b), charmless fractions (c) and ratios (d) are shown. Additionally the cut efficiencies from matched signal MC are drawn (b). The chosen cut of $c\tau_{D^0} > 0.01$ is visualised by a transparent grey overlay.

Tab. G.2.: Expected ratios, efficiencies (MC truth matched) and charmless fractions for $c\tau > 0.01mm$ in $m([KK]_{D^0}pK)$ and $m([KK]_{D^0}p\pi)$ DATA samples.

	$[KK]_{D^0}pK$	$[KK]_{D^0}p\pi$
$R(pKKh)$	0.299 ± 0.021	0.011 ± 0.003
$f(D^0ph)$	$\sim 77\%$	$\sim 99\%$
$\epsilon_{\text{MC truth}}$	$\sim 91\%$	$\sim 91\%$

G.4.4 Comparing Charmless to Signal MC

The charmless MC samples in fig. G.16 are normalised to the reference signal and scaled, as described in section 4.5.5.

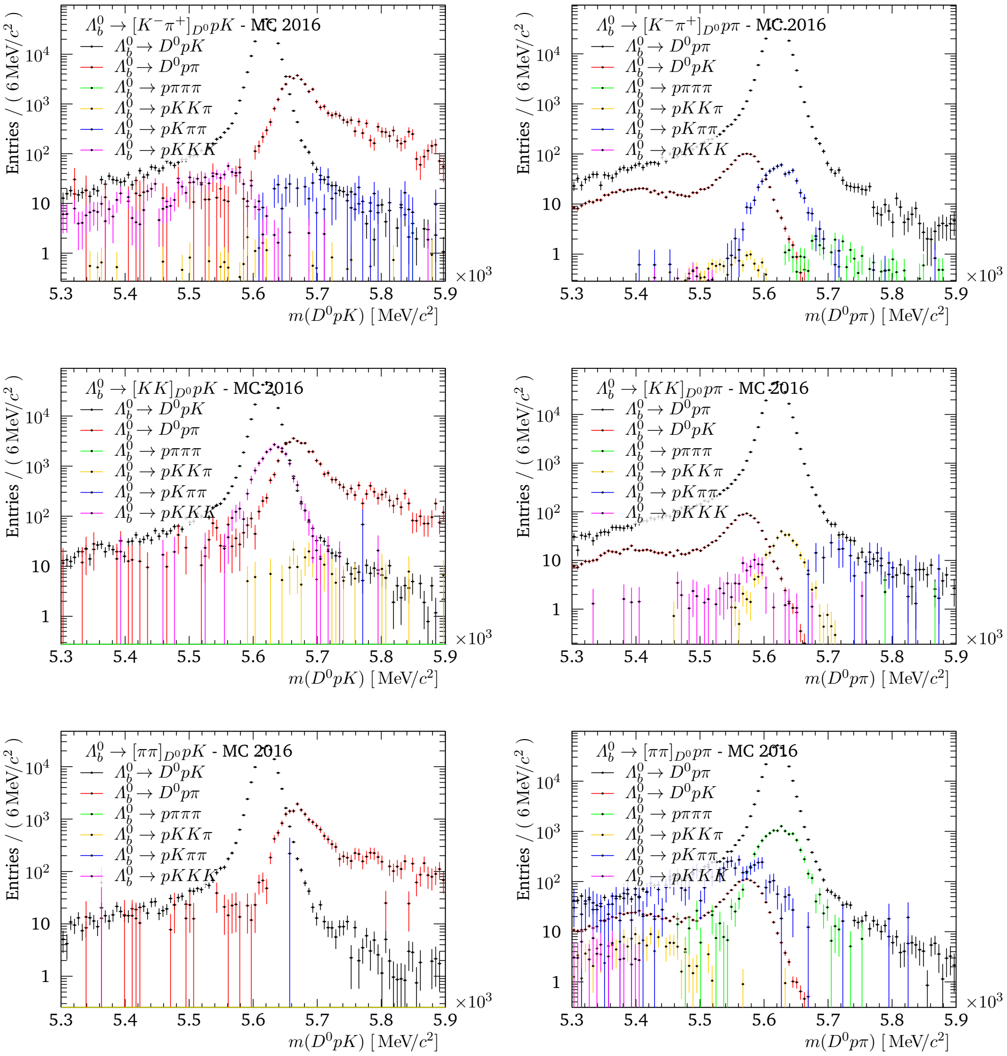

Fig. G.16.: Comparison of different charmless background contributions in $m(D^0ph)$ with all selections applied and re-normalised to match the $\Lambda_b^0 \to D^0ph$ reference signal MC. The background MC has been scaled according to their relative scaling factors in table 4.3 - MC 2016

H

Efficiencies by Selection and Sample

Table H.1 shows the determined efficiencies for all signal channels. The efficiencies are calculated from MC samples, as proposed in section 4.6. Therefore the determined trigger efficiency can't be used, but as introduced in section 4.6.1 the efficiencies in appendix H.1 are calculated.

H.1 `L0` Trigger

According to section 4.6.1 we calculate the efficiency ratios of the `L0` trigger efficiencies, following the `TISTOS` method [91]. In the fits in chapter 5 we measure the Λ_b^0 and $\Xi_b \to D^0pK$ decay channels normalised to $\Lambda_b^0 \to D^0p\pi$ for the full Dalitz phase space and the Λ^* resonance region. Therefore we need to determine different ratios. The $\Lambda_b^0 \to D^0pK$ and $\Xi_b \to D^0pK$ to $\Lambda_b^0 \to D^0p\pi$ ratios and all efficiencies extracted from DATA are listed in table H.2 for the full phase space and in table H.3 for the Λ^* resonance region. All `L0` efficiency ratios are visualised in fig. H.1.

The `L0` efficiencies and ratios determined from MC can be found in tables H.4 and H.5

H.2 Charmless Decays

The efficiencies are background reconstruction efficiencies, that are calculated from fits to MC samples as proposed for signal MC in section 4.6. They are used in the global fit in chapter 5 to normalise $\Lambda_b^0 \to pKKh$ to $\Lambda_b^0 \to D^0p\pi$. Table H.7 lists the found efficiencies and table H.6 the total background selection efficiency for the charmless modes without the trigger efficiencies.

As for signal MC we cannot calculate the trigger efficiencies from MC. Charmless decays, like $\Lambda_b^0 \to pKKK$, have the same final states as the $\Lambda_b^0 \to D^0ph^-$ modes. But due to kinematics, the 'fake' D^0 of a charmless decay has got a broad $m(D^0)$ distribution in comparison to a true D^0. With the `L0` trigger being sensitive for specific transversal energy deposits in the calorimeter and thus being linked to the particles momentum, one could expect to have different `L0` trigger efficiencies. As the D^0ph^- samples clearly show charmless background for $D^0 \to \{KK, \pi\pi\}$, the `L0` trigger seems to be unaffected for charmless decays by the rather tight cut around the D^0 mass in the studied samples. Hence it is stated that the `L0` trigger efficiencies for charmless background don't differ from the respective charmed signal and cancel in normalisation.

Tab. H.1.: Efficiencies in % for all cuts of the years 2011 to 2018. The efficiencies of stripping and DTT-acceptance are combined for unfiltered MC due to the software situation. See appendix H.1 for the calculation of `TISTOS` trigger efficiencies [91].

yr.	$h^-_{\Lambda_b^0}$	D^0	Acc	Strip	DTT	PreSel	p-PID	$h^\pm_{D^0}$-PID	Trigger	BDTG	$h^-_{\Lambda_b^0}$-PID	$c\tau_{D^0}$	Λ_c^+-veto	totEff
11	K	$K\pi$	15.715 ± 0.031		4.052 ± 0.028	72.42 ± 0.31	58.6 ± 0.4	94.75 ± 0.24	98.62 ± 0.13	84.5 ± 0.4	80.7 ± 0.5		99.89 ± 0.04	0.1722 ± 0.0015
11	K	KK	16.676 ± 0.033		3.724 ± 0.026	75.66 ± 0.31	57.5 ± 0.4	91.63 ± 0.31	98.85 ± 0.12	83.8 ± 0.4	81.0 ± 0.5	95.42 ± 0.29		0.1584 ± 0.0015
11	K	$\pi\pi$	14.884 ± 0.030		4.342 ± 0.029	71.79 ± 0.31	57.5 ± 0.4	97.76 ± 0.16	98.72 ± 0.12	87.1 ± 0.4	78.4 ± 0.5	51.4 ± 0.6	99.70 ± 0.10	0.0901 ± 0.0009
11	π	$K\pi$	14.295 ± 0.030		4.213 ± 0.028	72.24 ± 0.31	57.4 ± 0.4	94.41 ± 0.24	98.62 ± 0.13	82.0 ± 0.4	90.96 ± 0.35		99.72 ± 0.07	0.1729 ± 0.0014
11	π	KK	15.144 ± 0.031		3.821 ± 0.027	74.25 ± 0.31	57.6 ± 0.4	91.59 ± 0.30	98.74 ± 0.13	81.3 ± 0.4	91.5 ± 0.4	95.87 ± 0.27		0.1598 ± 0.0014
11	π	$\pi\pi$	13.598 ± 0.029		4.433 ± 0.029	70.01 ± 0.31	57.8 ± 0.4	97.27 ± 0.17	98.31 ± 0.14	85.7 ± 0.4	91.81 ± 0.32		99.88 ± 0.04	0.1831 ± 0.0013
12	K	$K\pi$	16.77 ± 0.04		3.218 ± 0.024	73.43 ± 0.34	66.0 ± 0.4	96.80 ± 0.19	99.20 ± 0.10	84.6 ± 0.4	84.7 ± 0.4		99.75 ± 0.07	0.1795 ± 0.0015
12	K	KK	18.29 ± 0.06		3.148 ± 0.017	74.43 ± 0.25	65.86 ± 0.31	94.18 ± 0.19	99.17 ± 0.08	84.06 ± 0.31	84.60 ± 0.33	95.18 ± 0.21		0.1785 ± 0.0012
12	K	$\pi\pi$	16.66 ± 0.05		3.340 ± 0.017	72.37 ± 0.23	65.74 ± 0.29	98.71 ± 0.08	98.96 ± 0.08	87.10 ± 0.25	83.85 ± 0.30	51.9 ± 0.4	99.85 ± 0.05	0.0979 ± 0.0007
12	π	$K\pi$	17.02 ± 0.04		3.128 ± 0.024	72.05 ± 0.34	66.0 ± 0.4	96.35 ± 0.21	99.11 ± 0.11	82.1 ± 0.4	92.58 ± 0.33		99.76 ± 0.06	0.1833 ± 0.0015
12	π	KK	17.46 ± 0.04		2.846 ± 0.017	74.00 ± 0.26	58.16 ± 0.34	92.38 ± 0.24	98.71 ± 0.11	82.5 ± 0.4	91.92 ± 0.29	95.36 ± 0.23		0.1410 ± 0.0010
12	π	$\pi\pi$	16.23 ± 0.05		3.276 ± 0.017	70.07 ± 0.24	65.64 ± 0.30	98.66 ± 0.09	99.08 ± 0.08	84.81 ± 0.29	93.48 ± 0.21		99.72 ± 0.05	0.1889 ± 0.0010
15	K	$K\pi$	16.98 ± 0.04		4.76 ± 0.04	72.7 ± 0.4	75.6 ± 0.4	97.19 ± 0.18	98.04 ± 0.16	86.4 ± 0.4	85.3 ± 0.4		99.70 ± 0.07	0.3114 ± 0.0026
15	K	KK	17.95 ± 0.04		4.44 ± 0.04	75.7 ± 0.4	75.7 ± 0.4	94.25 ± 0.26	98.15 ± 0.16	85.0 ± 0.4	87.4 ± 0.4	94.09 ± 0.32		0.2955 ± 0.0028
15	K	$\pi\pi$	16.14 ± 0.04		4.89 ± 0.04	71.9 ± 0.4	74.4 ± 0.4	99.57 ± 0.07	98.02 ± 0.16	88.99 ± 0.35	85.8 ± 0.4	45.6 ± 0.6	99.77 ± 0.09	0.1433 ± 0.0015
15	π	$K\pi$	15.55 ± 0.04		4.84 ± 0.04	71.2 ± 0.4	75.8 ± 0.4	96.48 ± 0.21	98.38 ± 0.14	85.3 ± 0.4	95.88 ± 0.25		99.89 ± 0.04	0.3152 ± 0.0024
15	π	KK	16.45 ± 0.04		4.67 ± 0.04	73.5 ± 0.4	75.8 ± 0.4	94.42 ± 0.26	98.67 ± 0.13	85.8 ± 0.4	95.51 ± 0.26	95.23 ± 0.27		0.3113 ± 0.0026
15	π	$\pi\pi$	14.93 ± 0.04		5.30 ± 0.04	68.8 ± 0.4	74.8 ± 0.4	99.57 ± 0.07	98.62 ± 0.13	87.3 ± 0.4	96.06 ± 0.23		99.68 ± 0.07	0.3347 ± 0.0024
16	K	$K\pi$	16.93 ± 0.04		5.279 ± 0.020	72.03 ± 0.18	74.82 ± 0.20	97.00 ± 0.09	97.75 ± 0.08	85.75 ± 0.19	86.51 ± 0.20		99.795 ± 0.029	0.3381 ± 0.0014
16	K	KK	18.03 ± 0.04		4.948 ± 0.020	74.83 ± 0.18	73.73 ± 0.21	94.58 ± 0.12	97.75 ± 0.08	85.63 ± 0.20	87.32 ± 0.21	94.94 ± 0.14		0.3231 ± 0.0015
16	K	$\pi\pi$	16.16 ± 0.04		5.551 ± 0.021	70.69 ± 0.18	73.99 ± 0.20	99.625 ± 0.032	97.78 ± 0.08	88.24 ± 0.17	86.39 ± 0.20	46.48 ± 0.31	99.73 ± 0.05	0.1614 ± 0.0008
16	π	$K\pi$	15.62 ± 0.04		5.467 ± 0.021	70.93 ± 0.18	75.04 ± 0.20	96.86 ± 0.09	97.71 ± 0.08	84.62 ± 0.20	96.27 ± 0.11		99.766 ± 0.029	0.3497 ± 0.0013
16	π	KK	16.42 ± 0.04		5.119 ± 0.020	73.09 ± 0.18	75.04 ± 0.20	94.54 ± 0.12	97.81 ± 0.08	84.48 ± 0.20	96.41 ± 0.11	95.37 ± 0.13		0.3312 ± 0.0014
16	π	$\pi\pi$	14.86 ± 0.04		5.809 ± 0.021	68.86 ± 0.17	74.83 ± 0.20	99.636 ± 0.031	97.71 ± 0.08	86.65 ± 0.18	96.28 ± 0.11		99.682 ± 0.033	0.3601 ± 0.0013
17	K	$K\pi$	17.95 ± 0.13	7.559 ± 0.005	72.719 ± 0.031	72.21 ± 0.04	75.27 ± 0.04	97.024 ± 0.019	97.960 ± 0.016	86.16 ± 0.04	86.97 ± 0.04		99.774 ± 0.006	0.3811 ± 0.0006
17	K	KK	18.82 ± 0.14	7.034 ± 0.005	74.135 ± 0.032	74.36 ± 0.04	74.25 ± 0.04	94.510 ± 0.026	98.054 ± 0.016	85.92 ± 0.04	87.29 ± 0.04	94.837 ± 0.030		0.3573 ± 0.0006
17	K	$\pi\pi$	17.41 ± 0.13	8.035 ± 0.005	71.894 ± 0.031	71.24 ± 0.04	73.94 ± 0.04	99.671 ± 0.006	97.916 ± 0.016	88.43 ± 0.04	86.48 ± 0.04	46.05 ± 0.06	99.775 ± 0.009	0.18160 ± 0.00031
17	π	$K\pi$	17.41 ± 0.13	7.676 ± 0.005	69.512 ± 0.032	71.19 ± 0.04	75.10 ± 0.04	97.022 ± 0.019	97.909 ± 0.017	84.94 ± 0.04	96.341 ± 0.024		99.734 ± 0.007	0.3851 ± 0.0006
17	π	KK	18.39 ± 0.14	7.285 ± 0.005	69.760 ± 0.033	73.38 ± 0.04	75.20 ± 0.04	94.412 ± 0.026	97.955 ± 0.017	84.91 ± 0.04	96.357 ± 0.024	95.268 ± 0.028		0.3718 ± 0.0006
17	π	$\pi\pi$	17.18 ± 0.13	8.127 ± 0.005	70.121 ± 0.031	68.93 ± 0.04	74.95 ± 0.04	99.642 ± 0.007	97.822 ± 0.017	87.05 ± 0.04	96.329 ± 0.023		99.755 ± 0.006	0.4124 ± 0.0006
18	K	$K\pi$	18.23 ± 0.14	7.119 ± 0.007	69.06 ± 0.04	72.33 ± 0.05	75.08 ± 0.06	97.098 ± 0.027	97.769 ± 0.024	85.78 ± 0.06	86.69 ± 0.06		99.759 ± 0.009	0.3428 ± 0.0006
18	K	KK	19.10 ± 0.14	6.717 ± 0.006	69.97 ± 0.05	74.67 ± 0.05	74.19 ± 0.06	94.62 ± 0.04	97.859 ± 0.024	85.54 ± 0.06	87.14 ± 0.06	95.04 ± 0.04		0.3261 ± 0.0007
18	K	$\pi\pi$	17.36 ± 0.13	7.569 ± 0.007	68.68 ± 0.04	70.75 ± 0.05	73.67 ± 0.06	99.684 ± 0.009	97.789 ± 0.023	87.93 ± 0.05	86.25 ± 0.06	46.68 ± 0.09	99.774 ± 0.013	0.16192 ± 0.00033
18	π	$K\pi$	17.42 ± 0.13	7.229 ± 0.007	66.87 ± 0.05	70.98 ± 0.05	74.90 ± 0.06	97.036 ± 0.027	97.867 ± 0.024	84.55 ± 0.06	96.190 ± 0.035		99.741 ± 0.009	0.3449 ± 0.0006
18	π	KK	18.20 ± 0.14	6.842 ± 0.006	66.66 ± 0.05	73.47 ± 0.05	75.11 ± 0.06	94.56 ± 0.04	97.763 ± 0.024	84.46 ± 0.06	96.100 ± 0.035	95.30 ± 0.04		0.3276 ± 0.0006
18	π	$\pi\pi$	16.89 ± 0.13	7.634 ± 0.007	67.74 ± 0.04	68.56 ± 0.05	74.71 ± 0.06	99.669 ± 0.009	97.560 ± 0.025	86.51 ± 0.06	96.112 ± 0.034		99.732 ± 0.009	0.3606 ± 0.0006

Tab. H.2.: Efficienceis of `L0` triggered events for the specific DATA tuples as well as the resulting ratio of `L0` trigger efficiencies.

yr.	D^0	$\epsilon^{\mathrm{L0}}_{\Lambda_b^0\to D^0pK}$	$\epsilon^{\mathrm{L0}}_{\Xi_b\to D^0pK}$	$\epsilon^{\mathrm{L0}}_{\Lambda_b^0\to D^0p\pi}$	$\frac{\epsilon^{\mathrm{L0}}_{\Lambda_b^0\to D^0pK}}{\epsilon^{\mathrm{L0}}_{\Lambda_b^0\to D^0p\pi}}$	$\frac{\epsilon^{\mathrm{L0}}_{\Xi_b\to D^0pK}}{\epsilon^{\mathrm{L0}}_{\Lambda_b^0\to D^0p\pi}}$
11	$K\pi$	0.46 ± 0.11	0.42 ± 0.26	0.569 ± 0.019	0.81 ± 0.20	0.7 ± 0.5
12	$K\pi$	0.57 ± 0.06	0.73 ± 0.07	0.540 ± 0.013	1.05 ± 0.12	1.35 ± 0.14
15	$K\pi$	0.34 ± 0.15	0.69 ± 0.13	0.526 ± 0.023	0.65 ± 0.29	1.32 ± 0.25
16	$K\pi$	0.53 ± 0.04	0.44 ± 0.09	0.548 ± 0.009	0.97 ± 0.08	0.80 ± 0.17
17	$K\pi$	0.61 ± 0.04	0.36 ± 0.11	0.568 ± 0.009	1.07 ± 0.08	0.63 ± 0.19
18	$K\pi$	0.55 ± 0.04	0.44 ± 0.10	0.527 ± 0.009	1.05 ± 0.08	0.83 ± 0.18
All	$K\pi$	0.548 ± 0.022	0.46 ± 0.05	0.546 ± 0.005	1.00 ± 0.04	0.85 ± 0.09

Tab. H.3.: Efficienceis of `L0` triggered events for the DATA specific tuples as well as the resulting ratio of `L0` trigger efficiencies in the Λ^* resonance region ($m^2(D^0p) > 14\,\mathrm{GeV}^2/c^4$).

yr.	D^0	$\epsilon^{\mathrm{L0}}_{\Lambda_b^0\to D^0pK}$	$\epsilon^{\mathrm{L0}}_{\Xi_b\to D^0pK}$	$\epsilon^{\mathrm{L0}}_{\Lambda_b^0\to D^0p\pi}$	$\frac{\epsilon^{\mathrm{L0}}_{\Lambda_b^0\to D^0pK}}{\epsilon^{\mathrm{L0}}_{\Lambda_b^0\to D^0p\pi}}$	$\frac{\epsilon^{\mathrm{L0}}_{\Xi_b\to D^0pK}}{\epsilon^{\mathrm{L0}}_{\Lambda_b^0\to D^0p\pi}}$
11	$K\pi$	0.32 ± 0.21	0.00 ± 0.33	0.53 ± 0.04	0.6 ± 0.4	0.0 ± 0.6
12	$K\pi$	0.66 ± 0.10	0.77 ± 0.09	0.526 ± 0.027	1.26 ± 0.21	1.47 ± 0.19
15	$K\pi$	0.09 ± 0.26	0.71 ± 0.19	0.52 ± 0.04	0.2 ± 0.5	1.4 ± 0.4
16	$K\pi$	0.60 ± 0.06	0.40 ± 0.16	0.517 ± 0.018	1.16 ± 0.13	0.77 ± 0.30
17	$K\pi$	0.73 ± 0.07	0.15 ± 0.15	0.534 ± 0.018	1.37 ± 0.13	0.28 ± 0.27
18	$K\pi$	0.61 ± 0.09	0.42 ± 0.14	0.474 ± 0.018	1.29 ± 0.20	0.88 ± 0.30
All	$K\pi$	0.59 ± 0.04	0.42 ± 0.08	0.511 ± 0.009	1.16 ± 0.08	0.82 ± 0.15

Tab. H.4.: Efficienceis of `L0` triggered events for the specific MC tuples as well as the resulting ratio of `L0` trigger efficiencies.

yr.	D^0	$\epsilon^{\mathrm{L0}}_{\Lambda_b^0\to D^0pK}$	$\epsilon^{\mathrm{L0}}_{\Lambda_b^0\to D^0p\pi}$	$\frac{\epsilon^{\mathrm{L0}}_{\Lambda_b^0\to D^0pK}}{\epsilon^{\mathrm{L0}}_{\Lambda_b^0\to D^0p\pi}}$
11	$K\pi$	0.685 ± 0.007	0.703 ± 0.006	0.975 ± 0.013
12	$K\pi$	0.672 ± 0.007	0.654 ± 0.007	1.027 ± 0.015
15	$K\pi$	0.681 ± 0.007	0.688 ± 0.007	0.989 ± 0.014
16	$K\pi$	0.7155 ± 0.0031	0.7227 ± 0.0029	0.990 ± 0.006
17	$K\pi$	0.7789 ± 0.0005	0.7887 ± 0.0005	0.9875 ± 0.0009
18	$K\pi$	0.7112 ± 0.0009	0.7135 ± 0.0009	0.9968 ± 0.0018

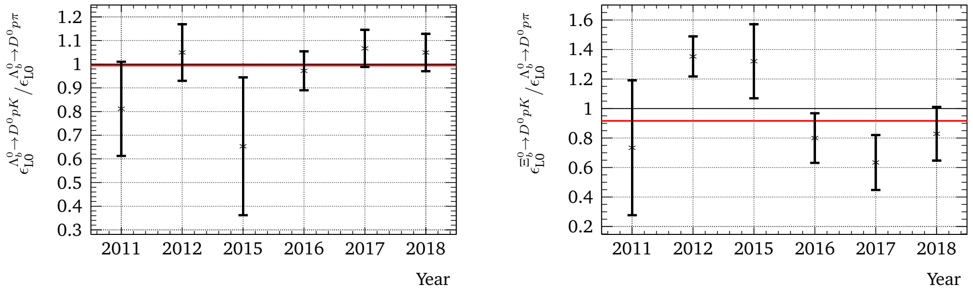

(a) $\Lambda_b^0 \to D^0pK$ to $\Lambda_b^0 \to D^0p\pi$　(b) $\Lambda_b^0 \to D^0pK$ to $\Lambda_b^0 \to D^0p\pi$

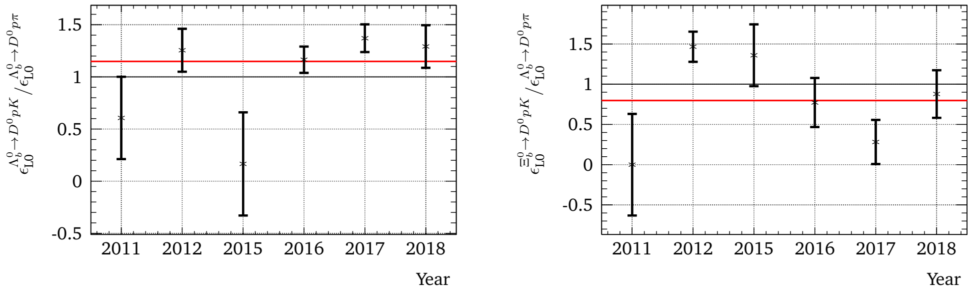

(c) $\Lambda_b^0 \to D^0pK$ to $\Lambda_b^0 \to D^0p\pi$- Dalitz Subregion　(d) $\Xi_b \to D^0pK$ to $\Lambda_b^0 \to D^0p\pi$- Dalitz Subregion

Fig. H.1.: `L0` efficiency ratios in the $D^0 \to K^-\pi^+$ samples. The red line highlights the luminosity weighted mean ratio. - DATA

Tab. H.5.: Efficienceis of `L0` triggered events for the specific MC tuples as well as the resulting ratio of `L0` trigger efficiencies in the Λ^* resonance region ($m^2(D^0p) > 14\,\mathrm{GeV}^2/c^4$).

yr.	D^0	$\epsilon^{\rm L0}_{\Lambda_b^0\to D^0pK}$	$\epsilon^{\rm L0}_{\Lambda_b^0\to D^0p\pi}$	$\frac{\epsilon^{\rm L0}_{\Lambda_b^0\to D^0pK}}{\epsilon^{\rm L0}_{\Lambda_b^0\to D^0p\pi}}$
11	$K\pi$	0.665 ± 0.011	0.685 ± 0.010	0.972 ± 0.021
12	$K\pi$	0.651 ± 0.011	0.642 ± 0.011	1.014 ± 0.025
15	$K\pi$	0.668 ± 0.012	0.683 ± 0.011	0.978 ± 0.023
16	$K\pi$	0.716 ± 0.005	0.717 ± 0.005	0.999 ± 0.010
17	$K\pi$	0.7716 ± 0.0009	0.7839 ± 0.0008	0.9843 ± 0.0015
18	$K\pi$	0.7016 ± 0.0015	0.7094 ± 0.0014	0.9890 ± 0.0029

Tab. H.6.: Total selection efficiencies in % for the charmless background determined via fits to MC. The `L0` trigger efficiency is being left out, as it is determined as a ratio from the DATA samples.

yr.	$\Lambda_b^0 \to pKKK$	$\Lambda_b^0 \to pKK\pi$
11	$(0.00381 \pm 0.00027)\%$	$(0.00168 \pm 0.00017)\%$
12	$(0.00326 \pm 0.00018)\%$	$(0.00202 \pm 0.00014)\%$
16	$(0.00555 \pm 0.00017)\%$	$(0.00314 \pm 0.00012)\%$

Tab. H.7.: Efficiencies in % for all cuts applied to the charmless MC. See appendix H.1 for the calculation of `TISTOS` trigger efficiencies [91].

yr.	$h^-_{\Lambda_b^0}$	D^0	Acc	Strip	DTT	PreSel	p-PID	$h^\pm_{D^0}$-PID	Trigger	BDTG	$h^-_{\Lambda_b^0}$-PID	$c\tau_{D^0}$	Λ_c^+-veto	totEff
11	K	KK	18.706 ± 0.035		0.645 ± 0.008	15.3 ± 0.4	65.3 ± 1.6	92.1 ± 1.1	98.8 ± 0.4	64.0 ± 2.0	87.8 ± 1.7	61.3 ± 2.7		0.00377 ± 0.00016
11	π	KK	17.742 ± 0.034		0.376 ± 0.006	15.6 ± 0.6	65.4 ± 2.0	91.1 ± 1.5	98.6 ± 0.6	63.3 ± 2.6	84.0 ± 2.5	51 ± 4		0.00166 ± 0.00010
12	K	KK	19.02 ± 0.04		0.591 ± 0.005	15.77 ± 0.33	64.2 ± 1.1	94.5 ± 0.7	98.98 ± 0.31	64.1 ± 1.5	88.1 ± 1.2	53.7 ± 2.1		0.00323 ± 0.00010
12	π	KK	17.99 ± 0.04		0.348 ± 0.004	15.1 ± 0.4	67.9 ± 1.5	92.9 ± 1.0	99.24 ± 0.34	62.0 ± 1.9	91.2 ± 1.4	60.1 ± 2.6		0.00200 ± 0.00008
16	K	KK	19.51 ± 0.05		0.755 ± 0.004	15.64 ± 0.20	74.8 ± 0.6	93.6 ± 0.4	97.87 ± 0.25	65.3 ± 0.8	90.6 ± 0.6	58.2 ± 1.1		0.00543 ± 0.00010
16	π	KK	18.62 ± 0.05		0.4501 ± 0.0032	16.63 ± 0.27	73.9 ± 0.8	92.8 ± 0.5	98.42 ± 0.27	60.7 ± 1.1	94.9 ± 0.6	57.0 ± 1.4		0.00309 ± 0.00007

H.3 Square Dalitz Plot Acceptance

With the decays $\Lambda_b^0 \to D^0 pK$ and $\Lambda_b^0 \to D^0 p\pi$ being three body decays we do not have a point like phase space and have to consider a varying reconstruction efficiency across the Dalitz plane. Therefore the efficiency is determined from the simulations in $n \times n$ bins of the square Dalitz plot representation introduced in section 2.4.2. As each simulation is generated flat in the square Dalitz plot the initial amount of events can be calculated from tables C.1 and H.1. The number of reconstructed events after all selections is found by filling the remaining candidates in a histogram of the same square Dalitz plot binning. The resulting efficiency histogram is smoothed with the standard ROOT algorithm. The algorithm preserves the histogram boundaries by convoluting the histogram with a 5×5-kernel, where the kernel bins extending the histogram are set to zero and are not used when calculating the kernel normalisation. The phase space specific acceptance is then found by bilinear interpolation, as ROOT implements it for two-dimensional histograms [131]. This interpolation method is sufficient, as the bins are well defined in a $n \times n$ grid of the square Dalitz plot. We found, due to the remaining number of events of the simulation, $n = 10$ (30) to be sufficient for 2011 to 2016 (2017 and 2018). The found acceptance functions across the square Dalitz plot for each sample can be found for $\Lambda_b^0 \to D^0 pK$ in fig. H.2 and for the normalisation channel in fig. H.3. For a luminosity weighted mean of the year specific acceptance functions across the general Dalitz plot see fig. 4.29.

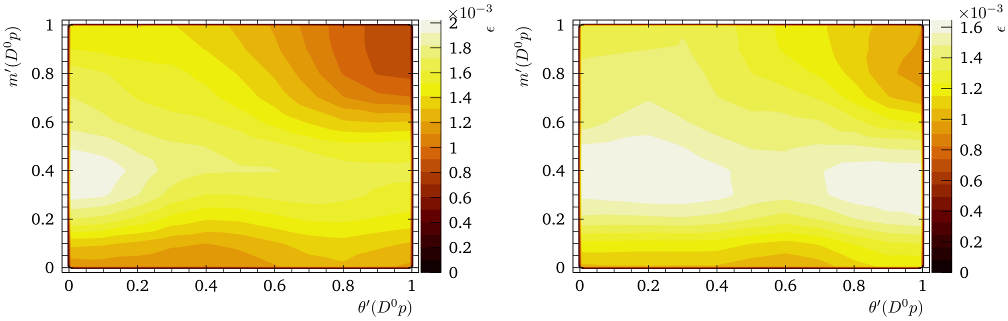

(a) 2011, $D^0 \to K\pi$

(b) 2011, $D^0 \to KK$

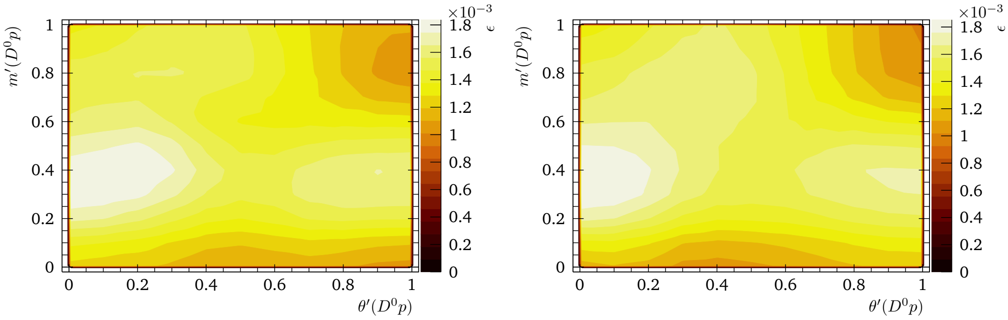

(c) 2012, $D^0 \to K\pi$

(d) 2012, $D^0 \to KK$

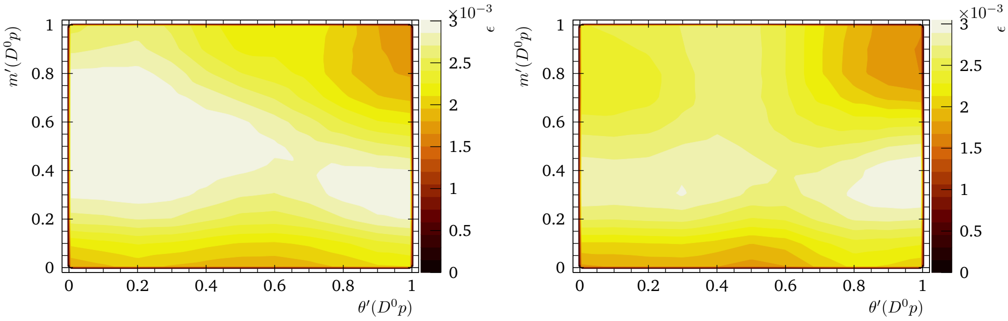

(e) 2015, $D^0 \to K\pi$

(f) 2015, $D^0 \to KK$

Fig. H.2.: Acceptance across the square Dalitz Plot for the $\Lambda_b^0 \to D^0pK$ signal. (1/2)

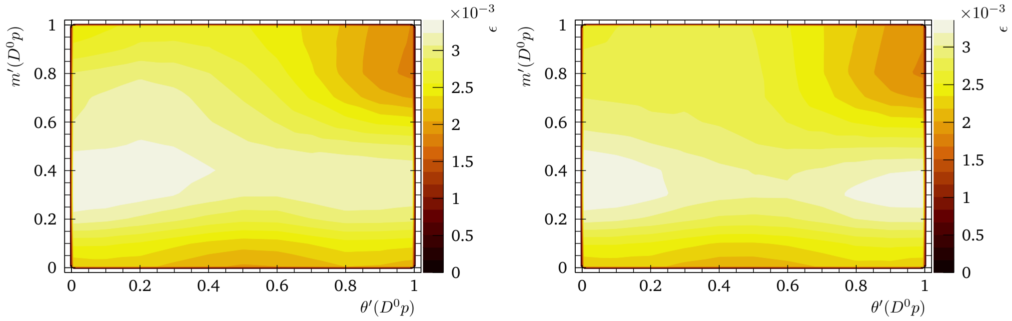

(g) 2016, $D^0 \to K\pi$

(h) 2016, $D^0 \to KK$

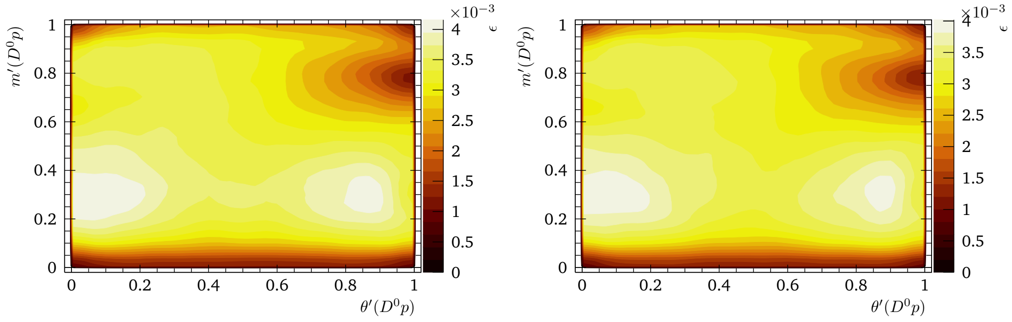

(i) 2017, $D^0 \to K\pi$

(j) 2017, $D^0 \to KK$

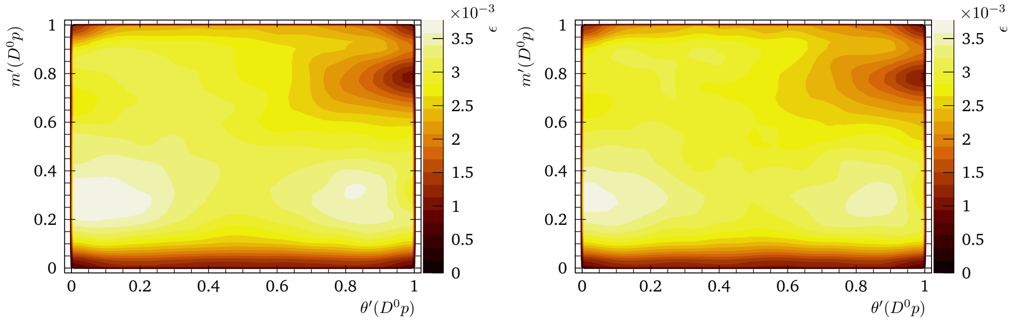

(k) 2018, $D^0 \to K\pi$

(l) 2018, $D^0 \to KK$

Fig. H.2.: Acceptance across the square Dalitz Plot for the $\Lambda_b^0 \to D^0pK$ signal. (2/2)

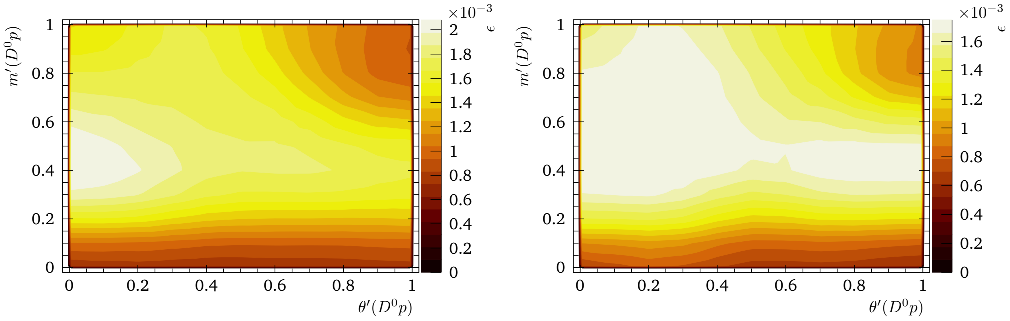

(a) 2011, $D^0 \to K\pi$ (b) 2011, $D^0 \to KK$

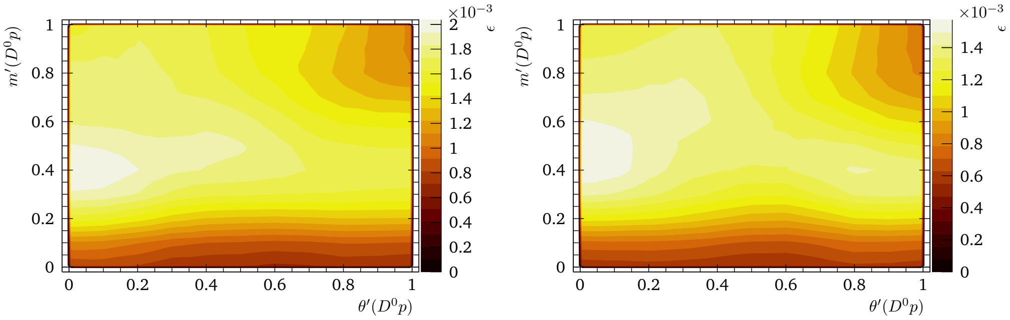

(c) 2012, $D^0 \to K\pi$ (d) 2012, $D^0 \to KK$

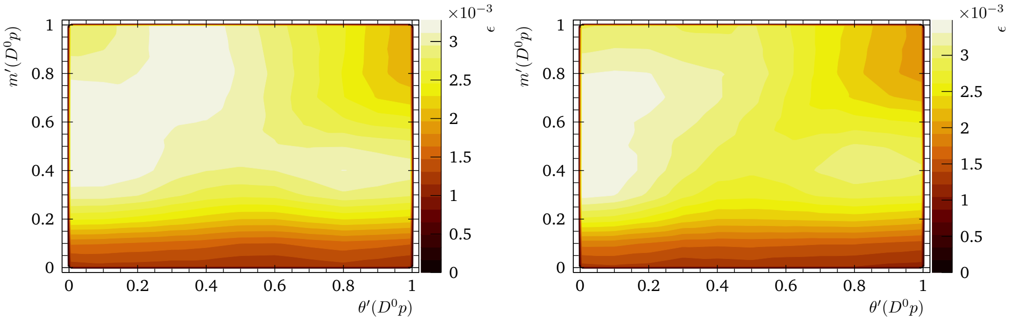

(e) 2015, $D^0 \to K\pi$ (f) 2015, $D^0 \to KK$

Fig. H.3.: Acceptance across the square Dalitz Plot for the $\Lambda_b^0 \to D^0 p\pi$ signal. (1/2)

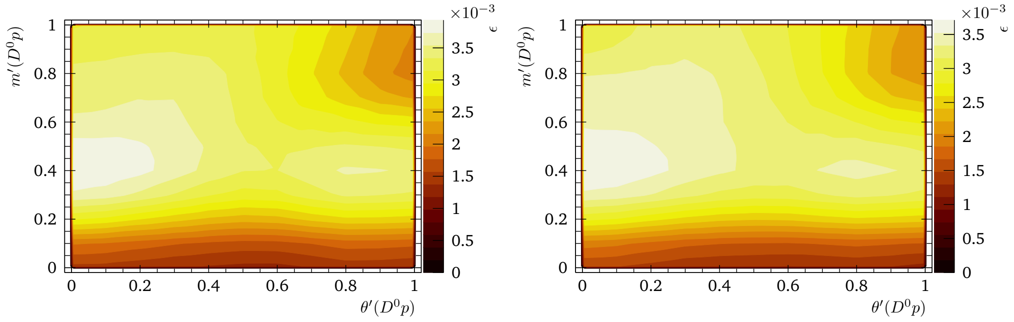

(g) 2016, $D^0 \to K\pi$

(h) 2016, $D^0 \to KK$

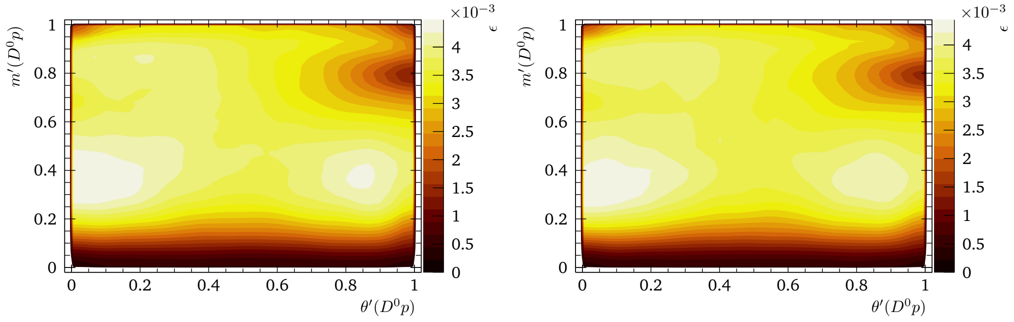

(i) 2017, $D^0 \to K\pi$

(j) 2017, $D^0 \to KK$

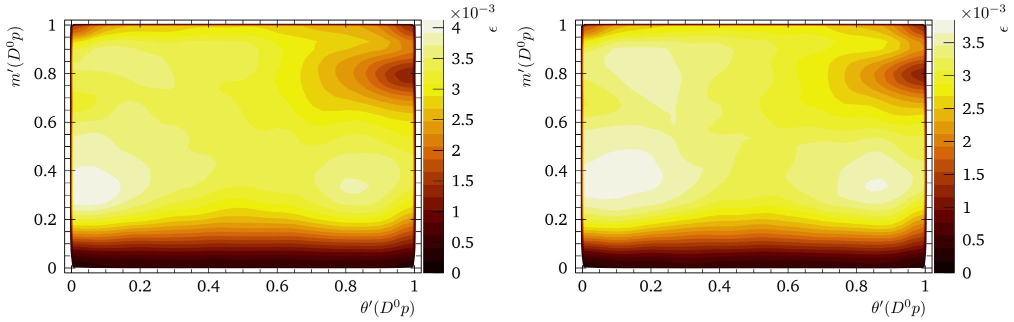

(k) 2018, $D^0 \to K\pi$

(l) 2018, $D^0 \to KK$

Fig. H.3.: Acceptance across the square Dalitz Plot for the $\Lambda_b^0 \to D^0 p\pi$ signal. (2/2)

Simulation Shapes in $m(D^0ph)$

In this appendix we determine the shapes for the decay contributions in $m(D^0ph)$ from MC. The shape parameters are fixed in the fit to DATA in section 5. The Λ_b^0 candidate mass is based on the DTF constraining the D^0 mass. Therefore we model all $D^0 \to hh$ modes with the same shape and fit combined MC sets of all D^0 modes. As trigger and machine conditions are the same within the years 2011 and 2012 of Run I and the complete Run II, the MC samples are split for these three categories.

We further test the effect of correcting for the acceptance found in appendix H.3 by weighting the MC with the inverse acceptance and comparing it normalised to the unweighted MC. Additionally we check for a shape distortion by selecting only the Λ^* resonance region ($m^2(D^0p) > 14\,\mathrm{GeV}^2/c^4$) in the Dalitz plot. If necessary an alternative shape is determined and used in the corresponding fit type of 5.

I.1 Signal Shapes

The signal shapes of $\Lambda_b^0 \to D^0ph$ are modelled as a sum of two Crystal-Ball functions $p = f \cdot p_{\mathrm{CB},1} + (1-f) \cdot p_{\mathrm{CB},2}$, with the fraction f. The Crystal-Ball function $p_{\mathrm{CB}}(x|\mu,\sigma,\alpha,n)$ was developed in the Crystal Ball Collaboration [132, 133] and consists out of a Gaussian function with a power law tail attached. It is defined as

$$
\begin{aligned}
p_{\mathrm{CB}}(x|\mu,\sigma,\alpha,n) &= N \cdot \begin{cases} e^{-\frac{1}{2}A^2} & \text{for } A > -\alpha \\ \left(\frac{n}{|\alpha|}\right)^n \left(\frac{n}{|\alpha|} - |\alpha| - A\right)^{-n} e^{-\frac{|\alpha|^2}{2}} & \text{for } A \leq -\alpha \end{cases} \\
A(x|\mu,\sigma) &= \frac{x-\mu}{\sigma} \quad ,
\end{aligned}
\tag{I.1}
$$

with its normalisation factor N, Gaussian mean value μ and width σ. The parameters n and α control the slope of the exponent of the power and where it is attached. The function itself and its first derivative are continuous. We use the RooFit implementation `RooCBShape` of the Crystal-Ball function. The fitted MC shapes can be seen in figs. I.1 and I.4 and their parameters in tables I.1 and I.2.

We find no distortion of the MC distributions by applying the acceptance correction, as it is shown in figs. I.2 and I.5. The same is true for selecting only the Λ^* resonance region in the Dalitz plot, as it can be seen in figs. I.3 and I.6.

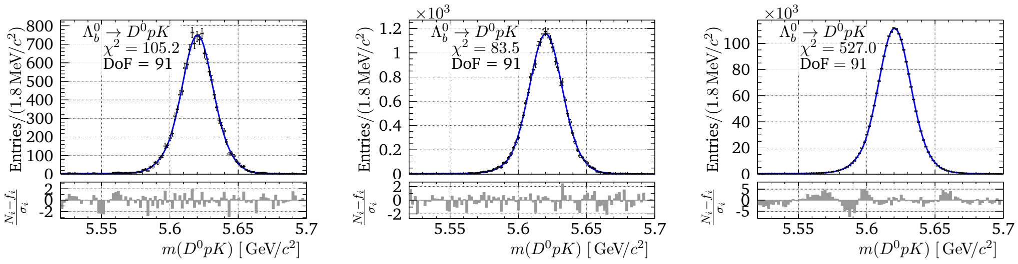

(a) 2011 (b) 2012 (c) Run II

Fig. I.1.: Fit to $\Lambda_b^0 \to D^0pK$ signal MC in $m(D^0pK)$.

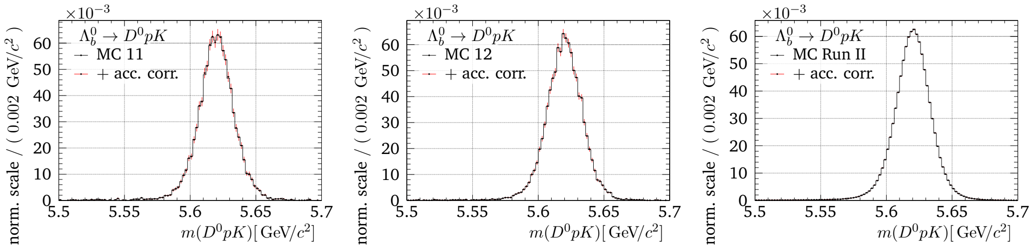

(a) 2011 (b) 2012 (c) Run II

Fig. I.2.: Test of the acceptance correction for $\Lambda_b^0 \to D^0pK$ signal MC in $m(D^0pK)$.

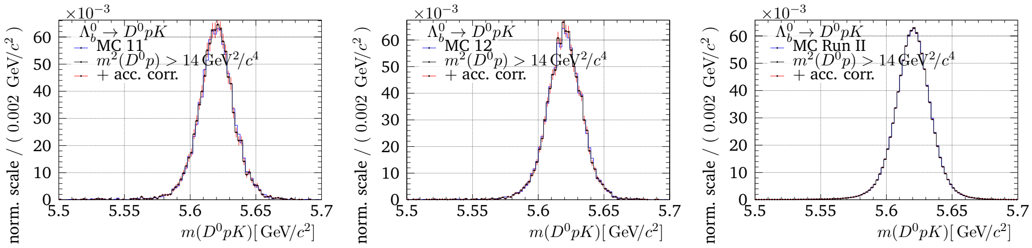

(a) 2011 (b) 2012 (c) Run II

Fig. I.3.: Test of selecting only the Λ^* Dalitz subregion and additional acceptance correction for $\Lambda_b^0 \to D^0pK$ signal MC in $m(D^0pK)$.

Tab. I.1.: Fitted shape parameters for $\Lambda_b^0 \to D^0pK$ signal in $m(D^0pK)$.

	2011	2012	Run II
N	13098 ± 114	20665 ± 144	1982010 ± 1414
f	0.63 ± 0.10	0.44 ± 0.10	0.497 ± 0.020
$\mu/\,\text{MeV}/c^2$	5620.18 ± 0.14	5620.08 ± 0.10	5620.356 ± 0.015
$\sigma_1/\,\text{MeV}/c^2$	14.99 ± 0.62	15.92 ± 0.70	15.71 ± 0.21
$\sigma_2/\,\text{MeV}/c^2$	9.31 ± 0.73	10.89 ± 0.42	10.36 ± 0.08
α_1	-2.43 ± 0.21	-2.44 ± 0.17	-2.146 ± 0.029
α_2	2.33 ± 0.30	2.42 ± 0.17	2.137 ± 0.060
n_1	2.9 ± 1.7	2.8 ± 1.4	3.98 ± 0.27
n_2	0.66 ± 0.30	0.92 ± 0.27	1.18 ± 0.08

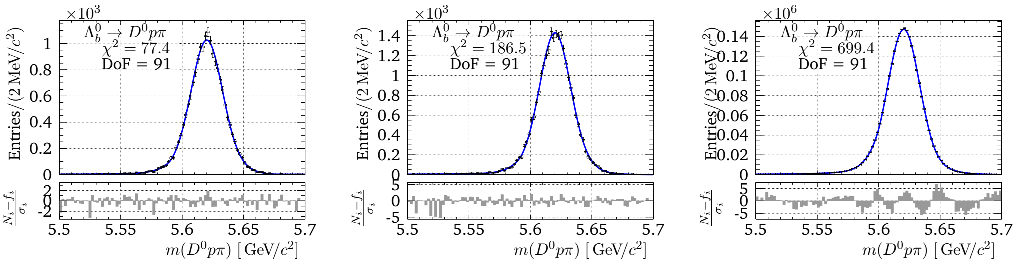

(a) 2011 (b) 2012 (c) Run II

Fig. I.4.: Fit to $\Lambda_b^0 \to D^0 p\pi$ signal MC in $m(D^0 p\pi)$.

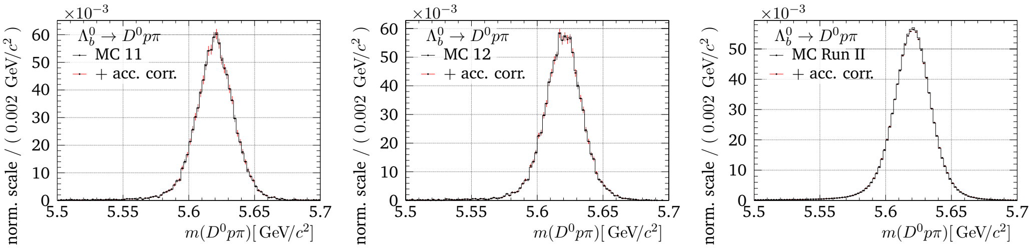

(a) 2011 (b) 2012 (c) Run II

Fig. I.5.: Test of the acceptance correction for $\Lambda_b^0 \to D^0 p\pi$ signal MC in $m(D^0 p\pi)$.

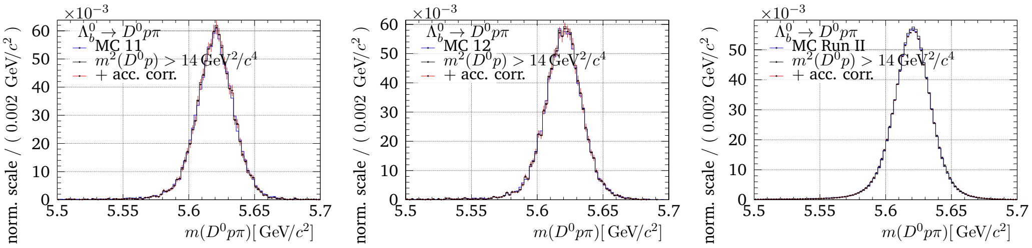

(a) 2011 (b) 2012 (c) Run II

Fig. I.6.: Test of selecting only the Λ^* Dalitz subregion and additional acceptance correction for $\Lambda_b^0 \to D^0 p\pi$ signal MC in $m(D^0 p\pi)$.

Tab. I.2.: Fitted shape parameters for $\Lambda_b^0 \to D^0 p\pi$ signal in $m(D^0 p\pi)$.

	2011	2012	Run II
N	17893 ± 134	24663 ± 157	2601277 ± 1613
f	0.32 ± 0.11	0.357 ± 0.063	0.482 ± 0.010
$\mu/\,\mathrm{MeV}/c^2$	5620.07 ± 0.12	5620.072 ± 0.097	5620.446 ± 0.012
$\sigma_1/\,\mathrm{MeV}/c^2$	19.5 ± 1.4	17.99 ± 0.95	15.63 ± 0.15
$\sigma_2/\,\mathrm{MeV}/c^2$	12.26 ± 0.43	11.76 ± 0.29	11.858 ± 0.050
α_1	-2.80 ± 0.29	-1.98 ± 0.20	-1.4651 ± 0.014
α_2	2.36 ± 0.14	2.25 ± 0.12	1.600 ± 0.029
n_1	0.08 ± 0.27	157 ± 657	33.8 ± 2.6
n_2	0.93 ± 0.22	0.99 ± 0.17	1.877 ± 0.055

I.2 $\mathit{\Lambda}_b^0 \to D^0 p\pi$ Mis-ID Shapes

The $\mathit{\Lambda}_b^0 \to D^0 p\pi$ mis-ID shape varies between 2011, 2012 and Run II. In 2011 it is described by a single Crystal-Ball function. In 2012 it is described by a sum of a Crystal-Ball function and a Gaussian and in Run II by a sum of two Crystal-Ball functions. The fitted shapes are visualised in table I.3 and their parameters listed in table I.3.

We find no distortion of the MC distributions by applying the acceptance correction, as it is shown in fig. I.8. This is not true for selecting only the $\mathit{\Lambda}^*$ resonance region in the Dalitz plot, as it can be seen in fig. I.9. We find a Novosibirsk (sum of Gaussian and Crystal-Ball) function in case of Run I (Run II) to describe the $\mathit{\Lambda}_b^0 \to D^0 p\pi$ mis-ID shape in the selected $\mathit{\Lambda}^*$ resonance region of the Dalitz plot. The fitted parameters are listed in table I.4 and the fit is shown in fig. I.10.

Tab. I.3.: Fitted shape parameters for $\mathit{\Lambda}_b^0 \to D^0 p\pi$ mis-ID in $m(D^0 pK)$.

	2011	2012	Run II
N	95.2 ± 9.8	247 ± 16	24409 ± 156
f		0.101 ± 0.074	0.484 ± 0.020
$\mu/\,\mathrm{MeV}/c^2$	5658.4 ± 4.1	5665.4 ± 2.0	5664.25 ± 0.43
$\sigma_1/\,\mathrm{MeV}/c^2$		161 ± 112	20.90 ± 0.31
$\sigma_2/\,\mathrm{MeV}/c^2$	13.6 ± 2.7	17.9 ± 1.8	12.4 ± 1.0
α_1			1.98 ± 0.13
α_2	-0.39 ± 0.18	-0.873 ± 0.18	-0.200 ± 0.027
n_1			1.91 ± 0.54
n_2	3.4 ± 2.7	1.63 ± 0.59	3.68 ± 0.66

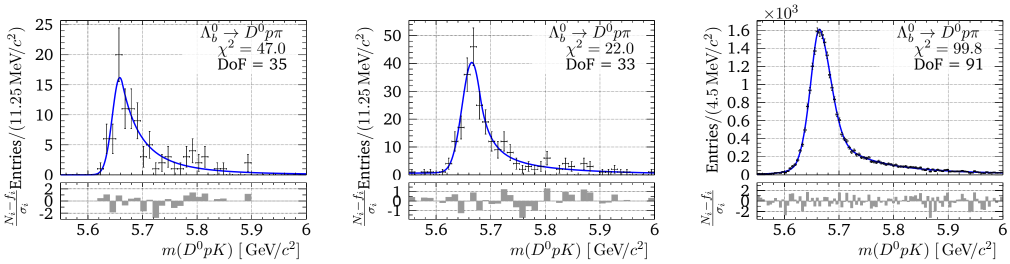

(a) 2011

(b) 2012

(c) Run II

Fig. I.7.: Fit to $\mathit{\Lambda}_b^0 \to D^0 p\pi$ mis-ID MC in $m(D^0 pK)$

Tab. I.4.: Fitted shape parameters for $\mathit{\Lambda}_b^0 \to D^0 p\pi$ mis-ID in $m(D^0 pK)$ of the $\mathit{\Lambda}^*$ Dalitz subregion.

	2011	2012	Run II
N	38.0 ± 6.1	73.0 ± 8.4	7906.91 ± 88.92
f			0.965 ± 0.007
$\mu/\,\mathrm{MeV}/c^2$	5657.4 ± 8.6	5662.5 ± 4.8	5675.72 ± 0.91
$\sigma_1/\,\mathrm{MeV}/c^2$	9.7 ± 5.4	4.5 ± 2.7	17.33 ± 0.66
$\sigma_2/\,\mathrm{MeV}/c^2$			110.41 ± 32.90
α_1	-0.10 ± 0.07	-0.09 ± 0.14	-0.34 ± 0.03
n_1	99.6 ± 0.9	1.5 ± 1.9	2.06 ± 0.21

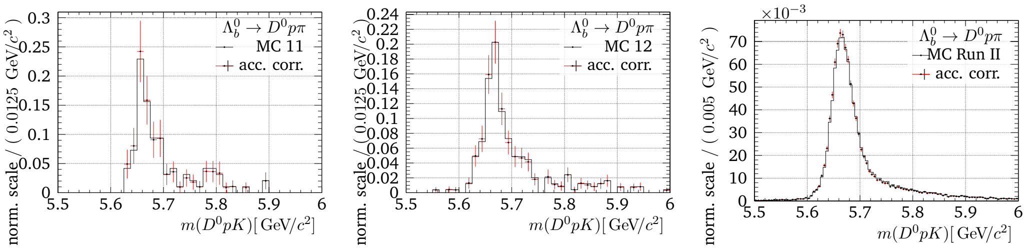

(a) 2011 (b) 2012 (c) Run II

Fig. I.8.: Test of the acceptance correction for $\Lambda_b^0 \to D^0 p\pi$ mis-ID MC in $m(D^0pK)$

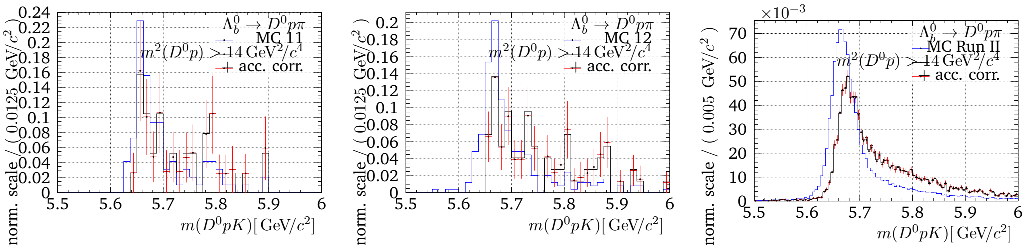

(a) 2011 (b) 2012 (c) Run II

Fig. I.9.: Test of selecting only the Λ^* Dalitz subregion and additional acceptance correction for $\Lambda_b^0 \to D^0 p\pi$ mis-ID MC in $m(D^0pK)$

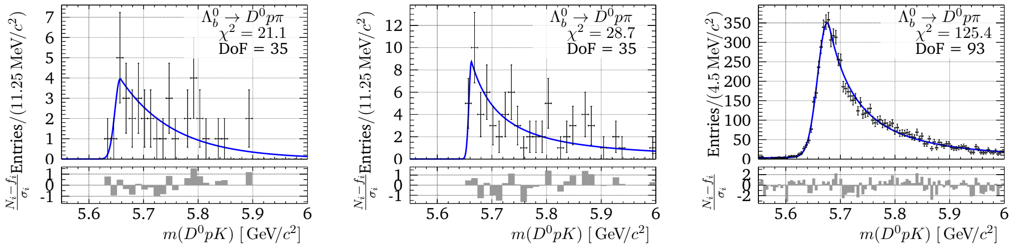

(a) 2011 (b) 2012 (c) Run II

Fig. I.10.: Fit to $\Lambda_b^0 \to D^0 p\pi$ mis-ID MC in $m(D^0pK)$ of the Λ^* Dalitz subregion.

I.3 $\Lambda_b^0 \to pKKK$ Shapes

Due to the low number of Λ_b^0 candidates the 2011 and 2012 samples are combined. Further we only have simulation with 2016 tuning available to determine the Run II shape. Both shapes are described by a single Gaussian, as shown in fig. I.11. The fitted parameters are listed in table I.5.

We find no distortion of the MC distributions by applying the acceptance correction, as it is shown in fig. I.12. The same is true for selecting only the Λ^* resonance region in the Dalitz plot, as it can be seen in fig. I.13.

Tab. I.5.: Fitted shape parameters for $\Lambda_b^0 \to pKKK$ in $m([KK]_{D^0}pK)$.

	Run I (2011 & 2012)	Run II (2016)
N	499 ± 23	1068 ± 34
$\mu/\,\mathrm{MeV}/c^2$	5629.48 ± 0.89	5632.06 ± 0.66
$\sigma/\,\mathrm{MeV}/c^2$	19.23 ± 0.63	20.93 ± 0.46

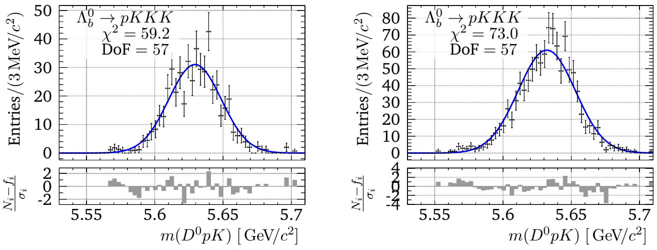

(a) Run I (2011 & 2012) (b) Run II (2016)

Fig. I.11.: Fit to $\Lambda_b^0 \to pKKK$ MC in $m(D^0pK)$

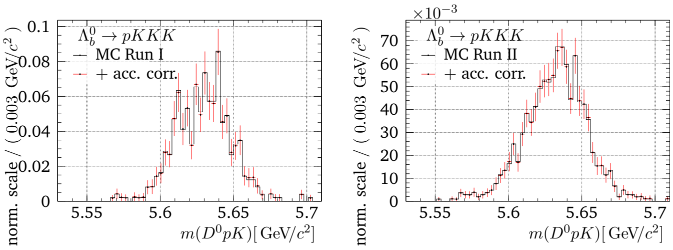

(a) Run I (2011 & 2012) (b) Run II (2016)

Fig. I.12.: Test of the acceptance correction for $\Lambda_b^0 \to pKKK$ MC in $m(D^0pK)$

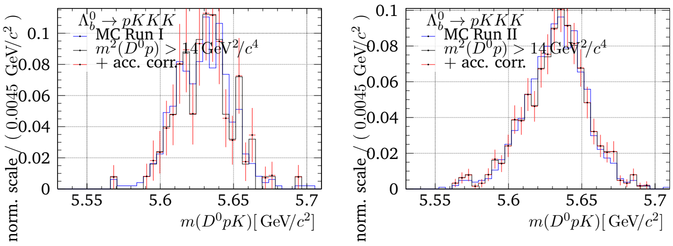

(a) Run I (2011 & 2012) (b) Run II (2016)

Fig. I.13.: Test of selecting only the Λ^* Dalitz subregion and additional acceptance correction for $\Lambda_b^0 \to pKKK$ MC in $m(D^0pK)$

I.4 $\Lambda_b^0 \to D^*ph$ Shapes

We only have MC with 2017 and 2018 tuning available for the partially reconstructed D^* modes. The shapes for the combined sets is used across all years. The mis-ID of $\Lambda_b^0 \to D^*p\pi$

in $m(D^0pK)$ is described by the sum of a Gaussian and a Crystal-Ball function. The fit is shown in fig. I.14 (c) and the shape parameters are listed in table I.6.

The best description of the $\Lambda_b^0 \to D^*ph$ shapes (no mis-ID) is found by a spline function. The reconstructed Λ_b^0 mass distribution is therefore plotted in a histogram of forty equidistant bins in the mass window $m(\Lambda_b^0) \in [5.25, 5.65]\,\mathrm{GeV}/c^2$. The histogram is smoothed and used as forty-one sampling points for the cubic spline class `TSpline3` of ROOT. The spline is nested as `C++` function in the `TF1` function wrapper of ROOT, which can be bound as PDF to RooFit. A test of this spline-PDF is performed via a fit to the unbinned MC, which is plot in fig. I.14 (a,b), showing, as expected, a sufficient agreement.

Tab. I.6.: Fitted shape parameters for $\Lambda_b^0 \to D^0p\pi$ mis-ID in $m(D^0pK)$.

N	8865 ± 94	$\sigma_1/\,\mathrm{MeV}/c^2$	96.7 ± 5.2
f	0.212 ± 0.027	$\sigma_2/\,\mathrm{MeV}/c^2$	40.1 ± 1.2
$\mu/\,\mathrm{MeV}/c^2$	5506.81 ± 0.81	α_2	-1.2017 ± 0.066
		n_2	1.87 ± 0.19

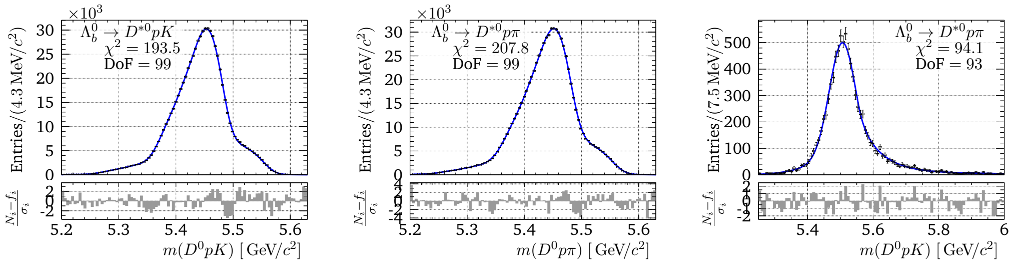

(a) $\Lambda_b^0 \to D^*pK$ in $m(D^0pK)$ (b) $\Lambda_b^0 \to D^*p\pi$ in $m(D^0p\pi)$ (c) $\Lambda_b^0 \to D^*p\pi$ in $m(D^0pK)$

Fig. I.14.: Fit to $\Lambda_b^0 \to D^*ph$ in $m(D^0ph)$ - Run II

The fit in chapter 5 will have the lower mass limit of $5.24\,\mathrm{GeV}/c^2$ and $\Lambda_b^0 \to D^*p\pi$ in $m(D^0p\pi)$ is sufficiently distanced from the $\Lambda_b^0 \to D^0p\pi$ signal. Therefore we will describe this contribution by the sum of a bifurcated Gaussian with a broad Gaussian. A bifurcated Gaussian has got two different widths left and right from its mean value and describes the peak of the D^* contribution in $m(D^0p\pi)$. The broad Gaussian helps to model the higher mass tail form the $D^* \to D^0\gamma$ channel. These parameters will be determined in the preliminary fits to DATA and then fixed for the fits split for Λ_b^0 and $\overline{\Lambda}_b^0$ type.

There is no distortion of the MC distributions in $m(D^0pK)$ by applying the acceptance correction, but a minor one of $\Lambda_b^0 \to D^*p\pi$ in $m(D^0p\pi)$, as it is shown in fig. I.15. Figure I.16 shows a clear distortion of the MC shapes, when selecting only the Λ^* resonance region in the Dalitz plot. We determine and fit another spline-PDF to the $m(D^0ph)$ distributions of the Λ^* Dalitz subregion. The fit can be found in fig. I.17.

We further use the spline-PDF ansatz to describe $\Lambda_b^0 \to D^*pK$ split for $D^* \to D^0\gamma$ and $D^* \to D^0\pi^0$. This is shown for the full phase space region in fig. I.18 and for the Λ^* Dalitz subregion in fig. I.19. The $D^* \to D^0\pi^0$ channel is further split for the different D^* polarisations, which are simulated, as proposed in section 4.5.2. $D^* \to D^0\pi^0$ shows an enhanced polarisation effect for $J_{m,D^{*0}} = 0$ in the Λ^* Dalitz subregion.

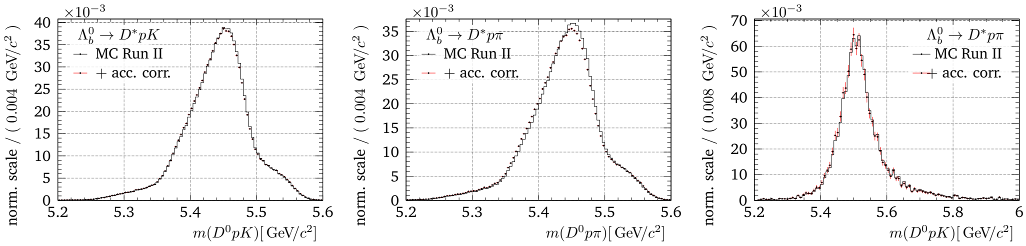

(a) $\Lambda_b^0 \to D^*pK$ in $m(D^0pK)$ (b) $\Lambda_b^0 \to D^*p\pi$ in $m(D^0p\pi)$ (c) $\Lambda_b^0 \to D^*p\pi$ in $m(D^0pK)$

Fig. I.15.: Test of the acceptance correction for $\Lambda_b^0 \to D^*ph$ in $m(D^0ph)$ - Run II

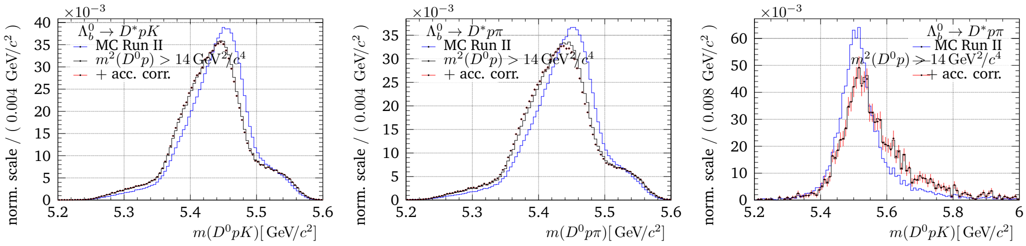

(a) $\Lambda_b^0 \to D^*pK$ in $m(D^0pK)$ (b) $\Lambda_b^0 \to D^*p\pi$ in $m(D^0p\pi)$ (c) $\Lambda_b^0 \to D^*p\pi$ in $m(D^0pK)$

Fig. I.16.: Test of selecting only the Λ^* Dalitz subregion and additional acceptance correction for $\Lambda_b^0 \to D^*ph$ in $m(D^0ph)$ - Run II

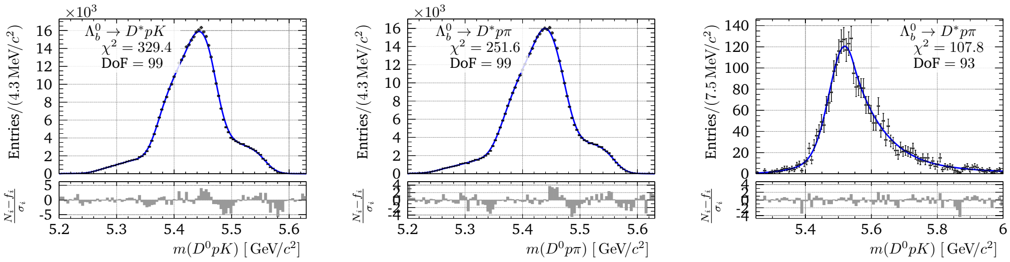

(a) $\Lambda_b^0 \to D^*pK$ in $m(D^0pK)$ (b) $\Lambda_b^0 \to D^*p\pi$ in $m(D^0p\pi)$ (c) $\Lambda_b^0 \to D^*p\pi$ in $m(D^0pK)$

Fig. I.17.: Fit to $\Lambda_b^0 \to D^*ph$ in $m(D^0ph)$ of the Λ^* Dalitz subregion - Run II

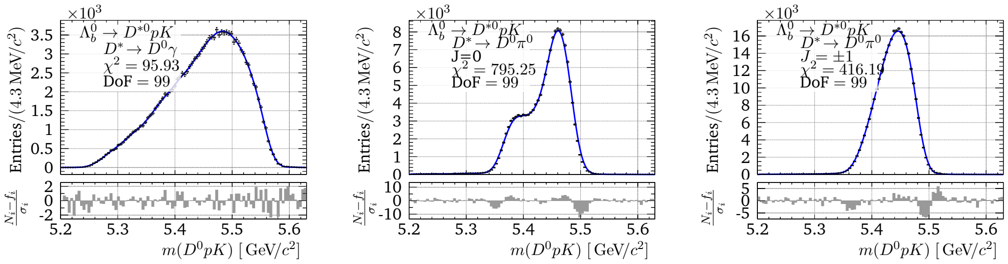

(a) $D^* \to D^0\gamma$ (b) $D^* \to D^0\pi^0$- $J_{D^*} = 0$ (c) $D^* \to D^0\pi^0$- $J_{D^*} = \pm1$

Fig. I.18.: Fit of $\Lambda_b^0 \to D^*pK$ MC in $m(D^0pK)$. The samples are split for the D^* modes and $D^* \to D^0\pi^0$ has different D^* polarisations simulated. - Run II

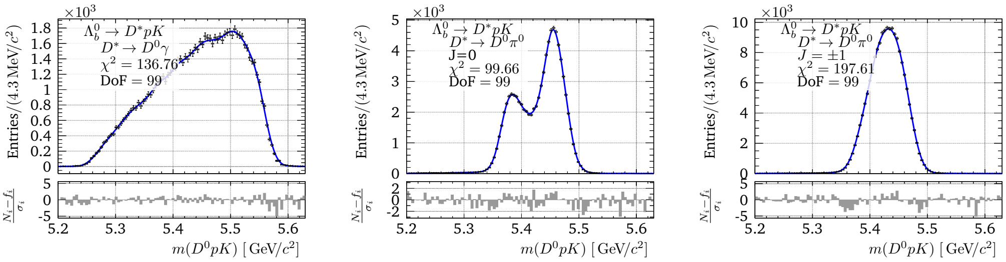

(a) $D^* \to D^0\gamma$

(b) $D^* \to D^0\pi^0$- $J_{D^*} = 0$

(c) $D^* \to D^0\pi^0$- $J_{D^*} = \pm1$

Fig. I.19.: Fit of $\Lambda_b^0 \to D^*pK$ MC in $m(D^0pK)$ of the Λ^* Dalitz subregion. The samples are split for the D^* modes and $D^* \to D^0\pi^0$ has different D^* polarisations simulated. - Run II

Fit to $m(D^0ph)$ - Parameters & Plots

J

J.1 Unweighted Dataset

J.1.1 Preliminary Fit to $m(D^0ph)$

Figures J.1 and J.2 show the preliminary fit to $m(D^0pK)$ and $m(D^0p\pi)$, as described in section 5.1.1. A list of all fit parameters is shown in listing J.1.

Listing J.1: Parameters of preliminary fit to $m(D^0pK)$ and $m(D^0p\pi)$.

```
/--------------------------------------------------------\
| RooFit Result - Preliminary SimFit to Full m(Dph) DATA |
\--------------------------------------------------------/

Constant Parameter            Value
--------------------------   ------------
effR_{11,Lb,D0pK2D0ppi,KK}    1.2302e+00
effR_{11,Lb,D0pK2D0ppi,Kpi}   1.2133e+00
effR_{11,Lb,pKKK2D0ppi,KK}    2.9570e-02
effR_{12,Lb,D0pK2D0ppi,KK}    1.1548e+00
effR_{12,Lb,D0pK2D0ppi,Kpi}   1.0115e+00
effR_{12,Lb,pKKK2D0ppi,KK}    2.1733e-02
effR_{r2,Lb,D0pK2D0ppi,KK}    1.0457e+00
effR_{r2,Lb,D0pK2D0ppi,Kpi}   1.0415e+00
effR_{r2,Lb,pKKK2D0ppi,KK}    1.7829e-02
B_{D02KK}                     4.0800e-03
B_{Lb2D0ppi}                  6.3000e-04

Floating Parameter            FinalValue +/- Error     GblCorr.
--------------------------   ------------------------  --------
#lambda_{11,D0pK,KK}         -2.4724e-03 +/-  1.37e-03  <none>
#lambda_{11,D0pK,Kmpip}      -3.2122e-02 +/-  3.13e-02  <none>
#lambda_{11,D0ppi,KK}        -4.7738e-03 +/-  6.83e-04  <none>
#lambda_{11,D0ppi,Kmpip}     -6.5773e-03 +/-  5.01e-04  <none>
#lambda_{12,D0pK,KK}         -3.2414e-03 +/-  1.00e-03  <none>
#lambda_{12,D0pK,Kmpip}      -4.6810e-03 +/-  1.44e-03  <none>
#lambda_{12,D0ppi,KK}        -3.2547e-03 +/-  4.49e-04  <none>
#lambda_{12,D0ppi,Kmpip}     -4.1532e-03 +/-  3.08e-04  <none>
#lambda_{r2,D0pK,KK}         -2.7921e-03 +/-  7.21e-04  <none>
#lambda_{r2,D0pK,Kmpip}      -3.6732e-03 +/-  8.45e-04  <none>
#lambda_{r2,D0ppi,KK}        -3.0620e-03 +/-  2.54e-04  <none>
#lambda_{r2,D0ppi,Kmpip}     -3.6364e-03 +/-  2.13e-04  <none>
B_{Lb2pKKK}                   1.1816e-05 +/-  1.09e-06  <none>
N_{11,Bkg,mD0pK,KK}           4.4620e+01 +/-  1.37e+01  <none>
N_{11,Bkg,mD0pK,Kmpip}        1.7886e+01 +/-  2.42e+01  <none>
N_{11,Bkg,mD0ppi,KK}          1.7260e+02 +/-  1.86e+01  <none>
N_{11,Bkg,mD0ppi,Kmpip}       8.4288e+02 +/-  7.11e+01  <none>
N_{11,Lb2D0ppi,KK}            2.1671e+02 +/-  5.64e+00  <none>
N_{11,Lb2D0ppi,Kmpip}         2.1248e+03 +/-  4.57e+01  <none>
N_{11,Lb2D0ppi,mD0pK,KK}      1.3324e+01 +/-  3.33e+00  <none>
N_{11,Lb2D0ppi,mD0pK,Kmpip}   1.2670e+02 +/-  1.44e+01  <none>
N_{11,Lb2Dst0ppi,mD0pK,KK}    1.4725e+01 +/-  6.65e+00  <none>
N_{11,Lb2Dst0ppi,mD0pK,Kmpip} 1.4810e+02 +/-  1.90e+01  <none>
N_{12,Bkg,mD0pK,KK}           1.2650e+02 +/-  2.94e+01  <none>
```

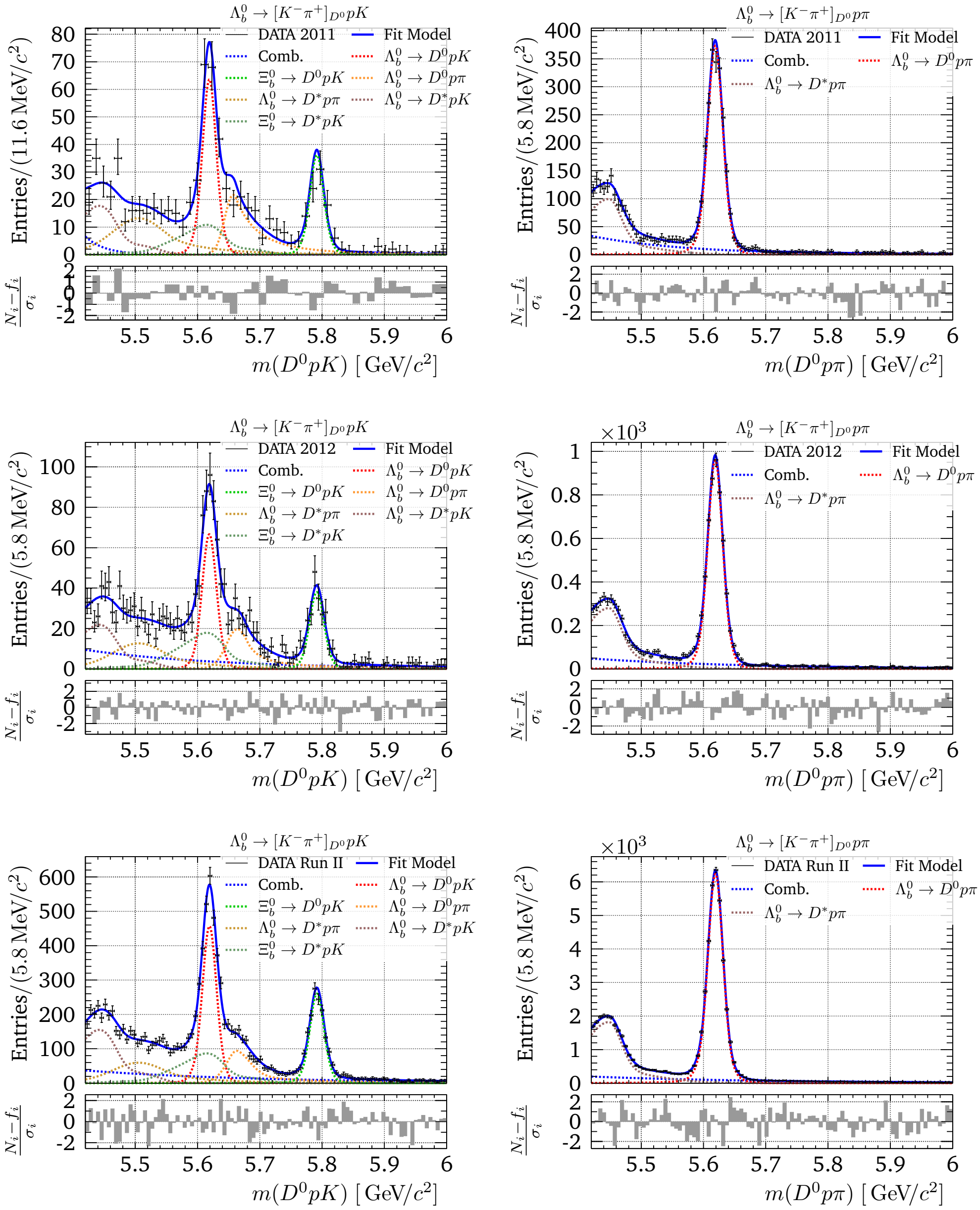

Fig. J.1.: Fitted distributions of $m([K^-\pi^+]_{D^0}ph)$ for the preliminary fit to $m(D^0pK)$ and $m(D^0p\pi)$.

```
    N_{12,Bkg,mD0pK,Kmpip}          3.2075e+02 +/-   1.49e+02   <none>
    N_{12,Bkg,mD0ppi,KK}            3.7518e+02 +/-   2.89e+01   <none>
    N_{12,Bkg,mD0ppi,Kmpip}         1.7965e+03 +/-   1.09e+02   <none>
    N_{r2,Bkg,mD0pK,KK}             5.7774e+02 +/-   1.09e+02   <none>
    N_{r2,Bkg,mD0pK,Kmpip}          1.5201e+03 +/-   3.96e+02   <none>
    N_{r2,Bkg,mD0ppi,KK}            1.6238e+03 +/-   7.80e+01   <none>
    N_{r2,Bkg,mD0ppi,Kmpip}         8.1798e+03 +/-   3.71e+02   <none>
    R_{Lb,Dst2D,K}                  1.6747e+00 +/-   3.42e-01   <none>
    R_{Lb,Dst2D,pi}                 1.9970e+00 +/-   1.05e-01   <none>
    R_{Lb,KK}                       9.5116e-02 +/-   8.38e-03   <none>
    R_{Lb,Kpi}                      6.4964e-02 +/-   2.08e-03   <none>
    R_{Xib,Dst2D,K}                 9.7642e-01 +/-   1.95e-01   <none>
    R_{Xib,KK}                      3.1737e-02 +/-   3.16e-03   <none>
```

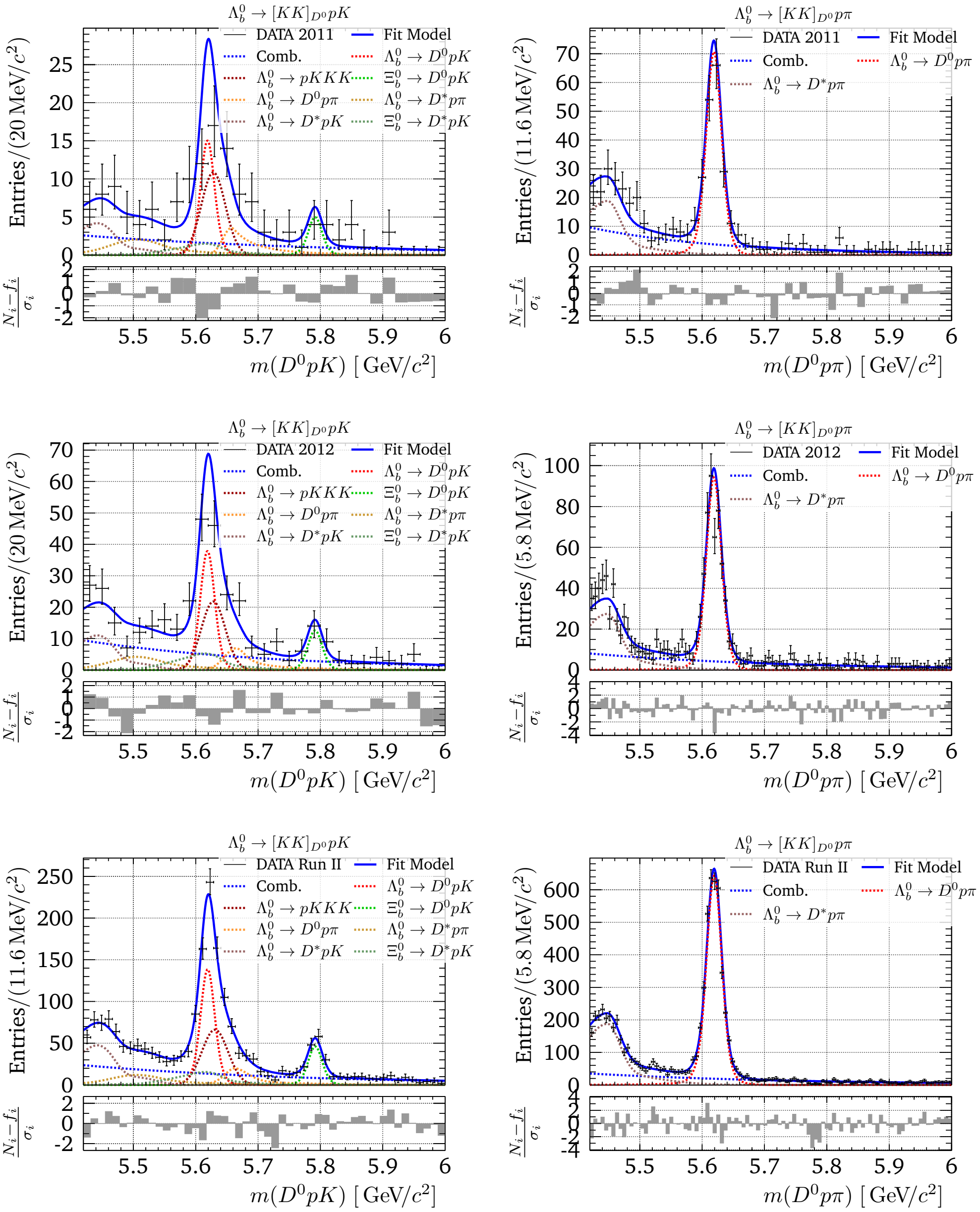

Fig. J.2.: Fitted distributions of $m([KK]_{D^0}ph)$ for the preliminary fit to $m(D^0pK)$ and $m(D^0p\pi)$.

```
    R_{Xib,Kpi}                    3.7191e-02 +/-  1.04e-03  <none>
    addGauss_f                     8.3062e-01 +/-  2.44e-02  <none>
    addGauss_sigma                 9.6345e+00 +/-  4.98e-01  <none>
    dM_{MC,shift,Dst}             -1.0921e+01 +/-  1.63e+00  <none>
    dM_{MC,shift}                 -1.1835e+00 +/-  6.74e-02  <none>
    dM_{Xib,Lb}                    1.7252e+02 +/-  3.61e-01  <none>
    m_pRecLb_mD0ppi_f              6.4082e-01 +/-  1.46e-02  <none>
    m_pRecLb_mD0ppi_mean           5.4483e+03 +/-  1.05e+00  <none>
    m_pRecLb_mD0ppi_sigma11        3.7965e+01 +/-  3.87e+00  <none>
    m_pRecLb_mD0ppi_sigma12        1.9277e+01 +/-  7.85e-01  <none>
    m_pRecLb_mD0ppi_sigma2         7.1506e+01 +/-  3.51e+00  <none>
    s_{S,r2,Lb2D0ppi,mD0pK}        8.8529e+00 +/-  1.22e+00  <none>
    s_{S,12,Lb2D0ppi,mD0pK}        1.8724e+00 +/-  3.39e-01  <none>
```

```
s_{S,12,Lb2D0ppi}             2.5004e+00 +/-  6.29e-02  <none>
s_{S,12,pRecLb,mD0pK}         2.4115e+00 +/-  7.87e-01  <none>
s_{S,12,pRecLb,mD0ppi}        2.8433e+00 +/-  1.68e-01  <none>
s_{S,12,pRecXib}              3.2225e+00 +/-  8.13e-01  <none>
s_{S,r2,Lb2D0ppi}             1.6666e+01 +/-  3.64e-01  <none>
s_{S,r2,pRecLb,mD0pK}         1.7190e+01 +/-  3.67e+00  <none>
s_{S,r2,pRecLb,mD0ppi}        1.8611e+01 +/-  9.80e-01  <none>
s_{S,r2,pRecXib}              1.5716e+01 +/-  3.29e+00  <none>


Goodness of Fit:
-> #chi^{2}/DoF = 0.92588
->     #chi^{2} = 786.998
->          DoF = 850
->        p-val = 0.939575
Sum of Fitted Norms:
->  Lb  -> D0pK  , D0 -> Kmpip =  2912.73  +/-  77.0049
->               , D0 -> KK    =   444.106 +/-  31.3718
->  Xib -> D0pK  , D0 -> Kmpip =  1667.49  +/-  38.444
->               , D0 -> KK    =   148.183 +/-  11.9651
->  Lb  -> D0ppi , D0 -> Kmpip = 42850.5   +/- 230.906
->               , D0 -> KK    =  4370.37  +/-  58.6258
->  Lb  -> pKKK  = 379.59 +/- 35.2372
```

J.1.2 Fit to Separate D^0 and $\Lambda_b^0/\overline{\Lambda}_b^0$ Samples

This appendix shows the fits to $m(D^0pK)$ and $m(D^0p\pi)$ for the split dataset, as described in section 5.1.2.

Fit to $m([K^-\pi^+]_{D^0}ph^-)$

Listing J.2: Parameters of Λ_b^0-type fit to $m(D^0pK)$ with $D^0 \to K^-\pi^+$.

```
/--------------------------------------------------\
| RooFit Result - SimFit to m(Dp+h-) with D->K-pi+ |
\--------------------------------------------------/

Constant Parameter            Value
--------------------------   ------------
R_{Lb,Dst2D,pi}               1.9970e+00
addGauss_f                    8.3062e-01
addGauss_sigma                9.6345e+00
dM_{MC,shift,Dst}            -1.0921e+01
dM_{MC,shift}                -1.1835e+00
dM_{Xib,Lb}                   1.7252e+02
effR_{11,Lb,D0pK2D0ppi,Kpi}   1.2133e+00
effR_{12,Lb,D0pK2D0ppi,Kpi}   1.0115e+00
effR_{r2,Lb,D0pK2D0ppi,Kpi}   1.0415e+00
m_pRecLb_mD0ppi_f             6.4082e-01
m_pRecLb_mD0ppi_mean          5.4483e+03
m_pRecLb_mD0ppi_sigma11       3.7965e+01
m_pRecLb_mD0ppi_sigma12       1.9277e+01
m_pRecLb_mD0ppi_sigma2        7.1505e+01
s_{S,12,Lb2D0ppi,mD0pK}       1.8724e+00
s_{S,12,Lb2D0ppi}             2.5004e+00
s_{S,12,pRecLb,mD0pK}         2.4114e+00
s_{S,12,pRecLb,mD0ppi}        2.8433e+00
s_{S,12,pRecXib}              3.2225e+00
s_{S,r2,Lb2D0ppi,mD0pK}       8.8529e+00
s_{S,r2,Lb2D0ppi}             1.6666e+01
s_{S,r2,pRecLb,mD0pK}         1.7190e+01
s_{S,r2,pRecLb,mD0ppi}        1.8611e+01
s_{S,r2,pRecXib}              1.5716e+01

```

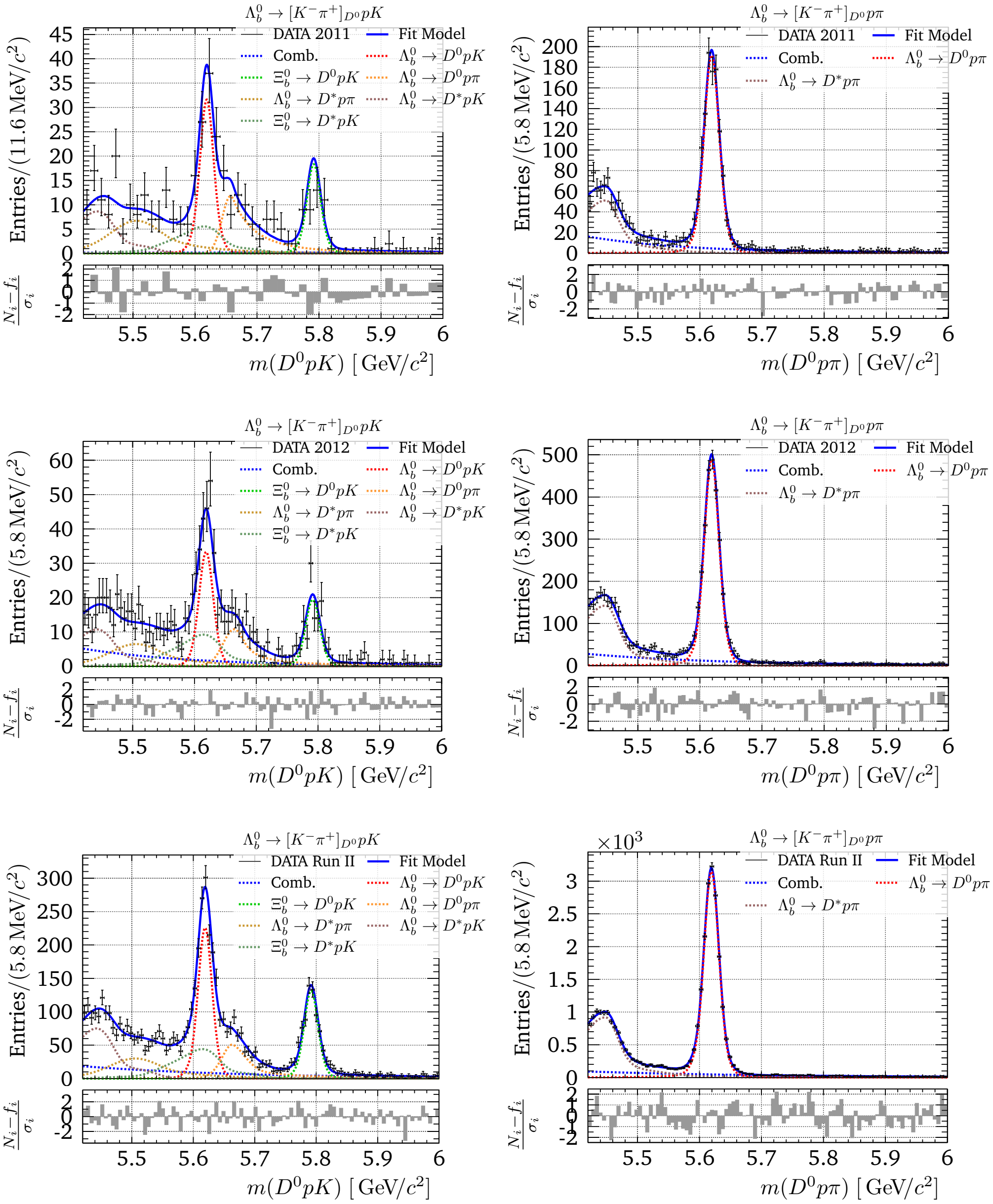

Fig. J.3.: Λ_b^0-type fit to $m(D^0pK)$ and $m(D^0p\pi)$ with $D^0 \to K^-\pi^+$.

```
    Floating Parameter              FinalValue +/-  Error      GblCorr.
    --------------------------   --------------------------  --------
    #lambda_{11,D0pK,Kmpip}       -8.7213e-07 +/-   2.94e-04   <none>
    #lambda_{11,D0ppi,Kmpip}      -6.2654e-03 +/-   5.53e-04   <none>
    #lambda_{12,D0pK,Kmpip}       -5.7132e-03 +/-   1.37e-03   <none>
    #lambda_{12,D0ppi,Kmpip}      -4.6531e-03 +/-   3.10e-04   <none>
    #lambda_{r2,D0pK,Kmpip}       -3.8867e-03 +/-   1.17e-03   <none>
    #lambda_{r2,D0ppi,Kmpip}      -3.4321e-03 +/-   1.71e-04   <none>
    N_{11,Lb2D0ppi,Kmpip}          1.0746e+03 +/-   7.24e+00   <none>
    N_{Bkg,D0pK,Kmpip}             8.9498e+02 +/-   2.88e+02   <none>
    N_{Bkg,D0ppi,Kmpip}            5.3640e+03 +/-   1.52e+02   <none>
    N_{Lb2D0ppi,mD0pK,Kmpip}       8.0382e+02 +/-   5.04e+01   <none>
    N_{Lb2Dst0ppi,mD0pK,Kmpip}     8.7895e+02 +/-   1.22e+02   <none>
```

```
R_{Lb,Dst2D,K}                 1.7109e+00 +/-  2.37e-01  <none>
R_{Lb,Kpi}                     6.3594e-02 +/-  2.76e-03  <none>
R_{Xib,Dst2D,K}                9.6738e-01 +/-  1.17e-01  <none>
R_{Xib,Kpi}                    3.7159e-02 +/-  1.46e-03  <none>
s_{B,12,D0pK,Kmpip}            1.7319e+01 +/-  5.90e+00  <none>
s_{B,12,D0ppi,Kmpip}           2.2634e+00 +/-  2.16e-01  <none>
s_{B,r2,D0pK,Kmpip}            8.7036e+01 +/-  2.66e+01  <none>
s_{B,r2,D0ppi,Kmpip}           9.5716e+00 +/-  8.00e-01  <none>


Goodness of Fit:
-> #chi^{2}/DoF = 0.836594
->     #chi^{2} = 444.231
->          DoF = 531
->        p-val = 0.997464
Sum of Fitted Norms:
->  Lb  -> D0pK  , D0 -> Kmpip =  1442.04  +/-  51.488
->  Xib -> D0pK  , D0 -> Kmpip =   842.612 +/-  27.1399
->  Lb  -> D0ppi , D0 -> Kmpip = 21671.8   +/- 122.223
```

Fit to $m([K^+\pi^-]_{D^0}\bar{p}h^+)$

Listing J.3: Parameters of $\overline{\Lambda}{}_b^0$-type fit to $m(D^0pK)$ with $D^0 \to K^-\pi^+$. Constant parameter are the same as for the Λ_b^0-type fit in listing J.2.

```
/---------------------------- ---------------------\
| RooFit Result - SimFit to m(Dp-h+) with D->K+pi- |
\--------------------------------------------------/

Constant Parameter            Value
--------------------------   ------------
>> same as Lb-type fit of D0 -> Kpi

Floating Parameter            FinalValue +/- Error     GblCorr.
--------------------------   ------------------------  --------
#lambda_{11,D0pK,Kmpip}      -3.5057e-02 +/-  2.67e-02  <none>
#lambda_{11,D0ppi,Kmpip}     -6.8758e-03 +/-  5.51e-04  <none>
#lambda_{12,D0pK,Kmpip}      -4.1205e-03 +/-  9.62e-04  <none>
#lambda_{12,D0ppi,Kmpip}     -3.6560e-03 +/-  3.17e-04  <none>
#lambda_{r2,D0pK,Kmpip}      -3.7475e-03 +/-  8.42e-04  <none>
#lambda_{r2,D0ppi,Kmpip}     -3.8455e-03 +/-  1.66e-04  <none>
N_{11,Lb2D0ppi,Kmpip}         1.0499e+03 +/-  7.16e+00  <none>
N_{Bkg,D0pK,Kmpip}            1.0462e+03 +/-  2.40e+02  <none>
N_{Bkg,D0ppi,Kmpip}           5.4628e+03 +/-  1.52e+02  <none>
N_{Lb2D0ppi,mD0pK,Kmpip}      6.6735e+02 +/-  4.78e+01  <none>
N_{Lb2Dst0ppi,mD0pK,Kmpip}    8.3405e+02 +/-  1.12e+02  <none>
R_{Lb,Dst2D,K}                1.7186e+00 +/-  2.02e-01  <none>
R_{Lb,Kpi}                    6.6924e-02 +/-  2.89e-03  <none>
R_{Xib,Dst2D,K}               9.9054e-01 +/-  1.21e-01  <none>
R_{Xib,Kpi}                   3.6992e-02 +/-  1.46e-03  <none>
s_{B,12,D0pK,Kmpip}           1.5339e+01 +/-  1.30e+01  <none>
s_{B,12,D0ppi,Kmpip}          2.0106e+00 +/-  1.90e-01  <none>
s_{B,r2,D0pK,Kmpip}           7.0496e+01 +/-  5.83e+01  <none>
s_{B,r2,D0ppi,Kmpip}          9.8616e+00 +/-  7.99e-01  <none>


Goodness of Fit:
-> #chi^{2}/DoF = 0.798241
->     #chi^{2} = 423.866
->          DoF = 531
->        p-val = 0.999783
Sum of Fitted Norms:
->  Lb  -> D0pK  , D0 -> Kmpip (cc) = 1482.69  +/-  52.6057
->  Xib -> D0pK  , D0 -> Kmpip (cc) =  819.541 +/-  26.5954
->  Lb  -> D0ppi , D0 -> Kmpip (cc) = 21173.9  +/- 120.945
```

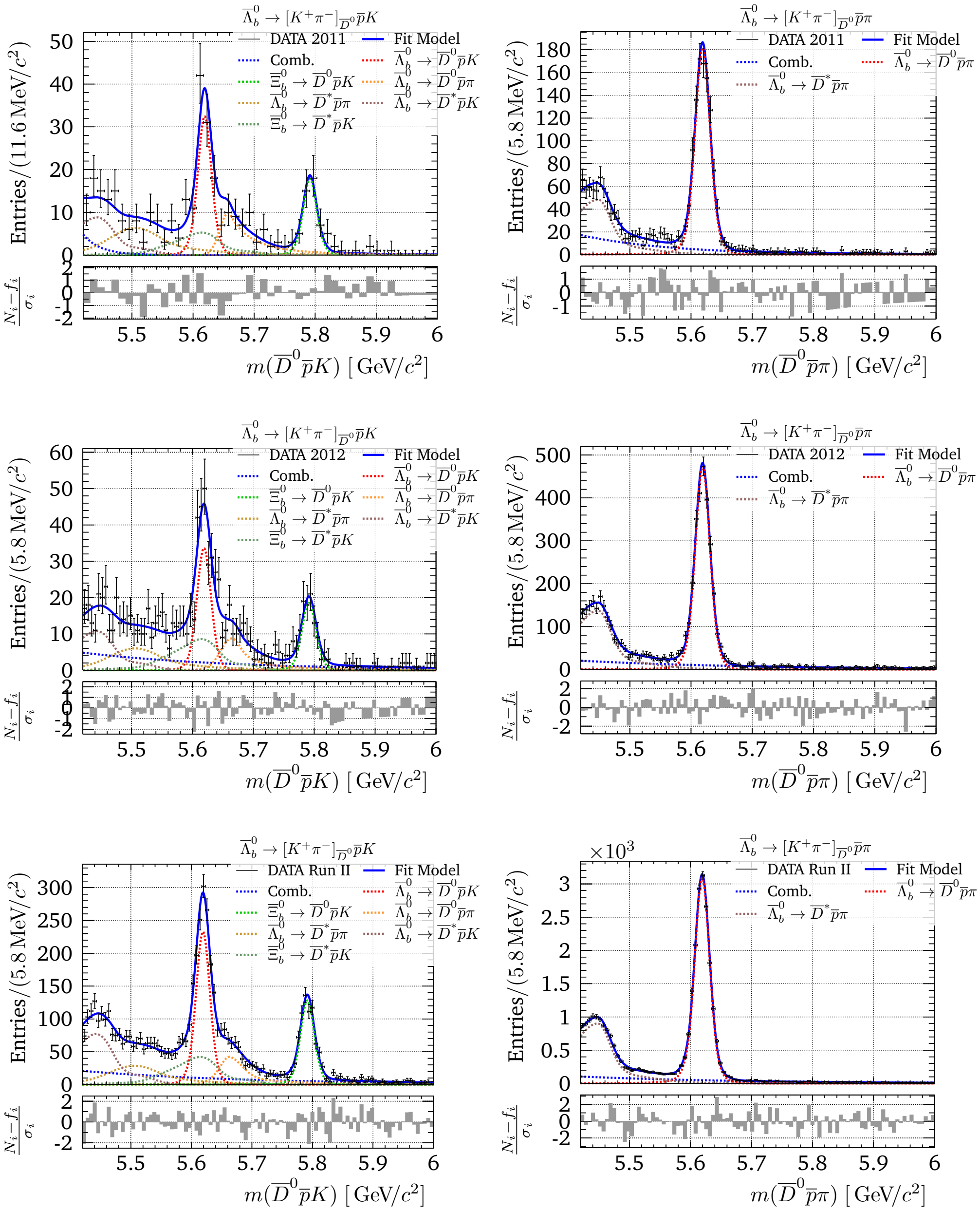

Fig. J.4.: $\overline{\Lambda}_b^0$-type fit to $m(D^0pK)$ and $m(D^0p\pi)$ with $D^0 \to K^-\pi^+$.

Fit to $m([KK]_{D^0}ph^-)$

Listing J.4: Parameters of Λ_b^0-type fit to $m(D^0pK)$ with $D^0 \to KK$.

```
/-----------------------------------------------\
| RooFit Result - SimFit to m(Dp+h-) with D->KK |
\-----------------------------------------------/

Constant Parameter            Value
--------------------------  ------------
B_{D02KK}                     4.0800e-03
B_{Lb2D0ppi}                  6.3000e-04
```

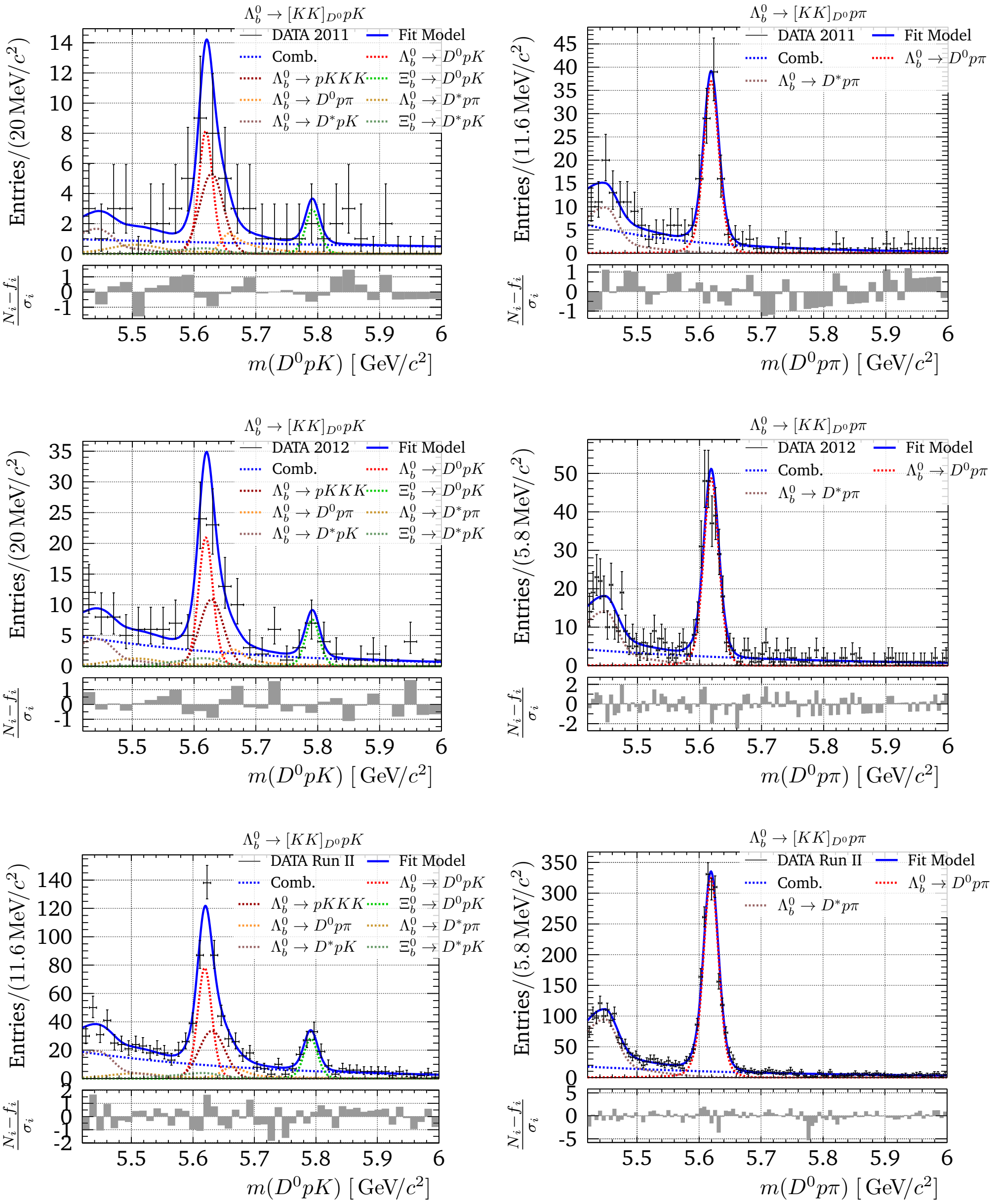

Fig. J.5.: Λ_b^0-type fit to $m(D^0pK)$ and $m(D^0p\pi)$ with $D^0 \to KK$.

```
    B_{Lb2pKKK}                    1.1816e-05
    R_{Lb,Dst2D,pi}                1.9970e+00
    addGauss_f                     8.3062e-01
    addGauss_sigma                 9.6345e+00
    dM_{MC,shift,Dst}             -1.0921e+01
    dM_{MC,shift}                 -1.1835e+00
    dM_{Xib,Lb}                    1.7252e+02
    effR_{11,Lb,D0pK2D0ppi,KK}     1.2302e+00
    effR_{11,Lb,pKKK2D0ppi,KK}     2.9570e-02
    effR_{12,Lb,D0pK2D0ppi,KK}     1.1548e+00
    effR_{12,Lb,pKKK2D0ppi,KK}     2.1733e-02
    effR_{r2,Lb,D0pK2D0ppi,KK}     1.0457e+00
    effR_{r2,Lb,pKKK2D0ppi,KK}     1.7829e-02
```

```
m_pRecLb_mD0ppi_f             6.4082e-01
m_pRecLb_mD0ppi_mean          5.4483e+03
m_pRecLb_mD0ppi_sigma11       3.7965e+01
m_pRecLb_mD0ppi_sigma12       1.9277e+01
m_pRecLb_mD0ppi_sigma2        7.1505e+01
s_{S,12,Lb2D0ppi,mD0pK}       1.8724e+00
s_{S,12,Lb2D0ppi}             2.5004e+00
s_{S,12,pRecLb,mD0pK}         2.4114e+00
s_{S,12,pRecLb,mD0ppi}        2.8433e+00
s_{S,12,pRecXib}              3.2225e+00
s_{S,r2,Lb2D0ppi,mD0pK}       8.8529e+00
s_{S,r2,Lb2D0ppi}             1.6666e+01
s_{S,r2,pRecLb,mD0pK}         1.7190e+01
s_{S,r2,pRecLb,mD0ppi}        1.8611e+01
s_{S,r2,pRecXib}              1.5716e+01

Floating Parameter            FinalValue +/- Error      GblCorr.
--------------------------   ------------------------  --------
#lambda_{11,D0pK,KK}         -1.2059e-03 +/-  2.11e-03  <none>
#lambda_{11,D0ppi,KK}        -5.3091e-03 +/-  9.13e-04  <none>
#lambda_{12,D0pK,KK}         -3.4162e-03 +/-  1.43e-03  <none>
#lambda_{12,D0ppi,KK}        -3.0174e-03 +/-  5.76e-04  <none>
#lambda_{r2,D0pK,KK}         -3.4173e-03 +/-  1.04e-03  <none>
#lambda_{r2,D0ppi,KK}        -3.0031e-03 +/-  3.20e-04  <none>
N_{11,Lb2D0ppi,KK}            1.0983e+02 +/-  2.36e+00  <none>
N_{Bkg,D0pK,KK}               4.9092e+02 +/-  1.42e+02  <none>
N_{Bkg,D0ppi,KK}              1.1294e+03 +/-  5.66e+01  <none>
N_{Lb2D0ppi,mD0pK,KK}         6.2229e+01 +/-  2.27e+01  <none>
N_{Lb2Dst0ppi,mD0pK,KK}       5.2395e+01 +/-  6.05e+01  <none>
R_{Lb,Dst2D,K}                2.2972e+00 +/-  1.00e+00  <none>
R_{Lb,KK}                     1.0550e-01 +/-  1.21e-02  <none>
R_{Xib,Dst2D,K}               2.3635e+00 +/-  2.82e+00  <none>
R_{Xib,KK}                    3.8270e-02 +/-  5.12e-03  <none>
s_{B,12,D0pK,KK}              2.7234e+00 +/-  9.26e-01  <none>
s_{B,12,D0ppi,KK}             2.0854e+00 +/-  3.45e-01  <none>
s_{B,r2,D0pK,KK}              1.7376e+01 +/-  5.42e+00  <none>
s_{B,r2,D0ppi,KK}             8.6376e+00 +/-  1.25e+00  <none>


Goodness of Fit:
-> #chi^{2}/DoF = 0.673902
->     #chi^{2} = 228.453
->          DoF = 339
->        p-val = 0.999999
Sum of Fitted Norms:
->  Lb   -> D0pK  , D0 -> KK =   249.641  +/- 22.8393
->  Xib  -> D0pK  , D0 -> KK =    90.5608 +/-  9.8305
->  Lb   -> D0ppi , D0 -> KK = 2214.98    +/- 39.8009
->  Lb   -> pKKK   = 192.391 +/- 4.12956
```

Fit to $m([KK]_{D^0}\overline{p}h^+)$

Listing J.5: Parameters of $\overline{\Lambda}{}_b^0$-type fit to $m(D^0pK)$ with $D^0 \to KK$. Constant parameter are the same as for the Λ_b^0-type fit in listing J.4.

```
/-----------------------------------------------\
| RooFit Result - SimFit to m(Dp-h+) with D->KK |
\-----------------------------------------------/

Constant Parameter            Value
--------------------------   ------------
>> same as Lb-type fit of D0 -> KK

Floating Parameter            FinalValue +/- Error      GblCorr.
--------------------------   ------------------------  --------
#lambda_{11,D0pK,KK}         -3.9688e-03 +/-  2.28e-03  <none>
#lambda_{11,D0ppi,KK}        -4.1498e-03 +/-  9.78e-04  <none>
#lambda_{12,D0pK,KK}         -2.9205e-03 +/-  1.24e-03  <none>
```

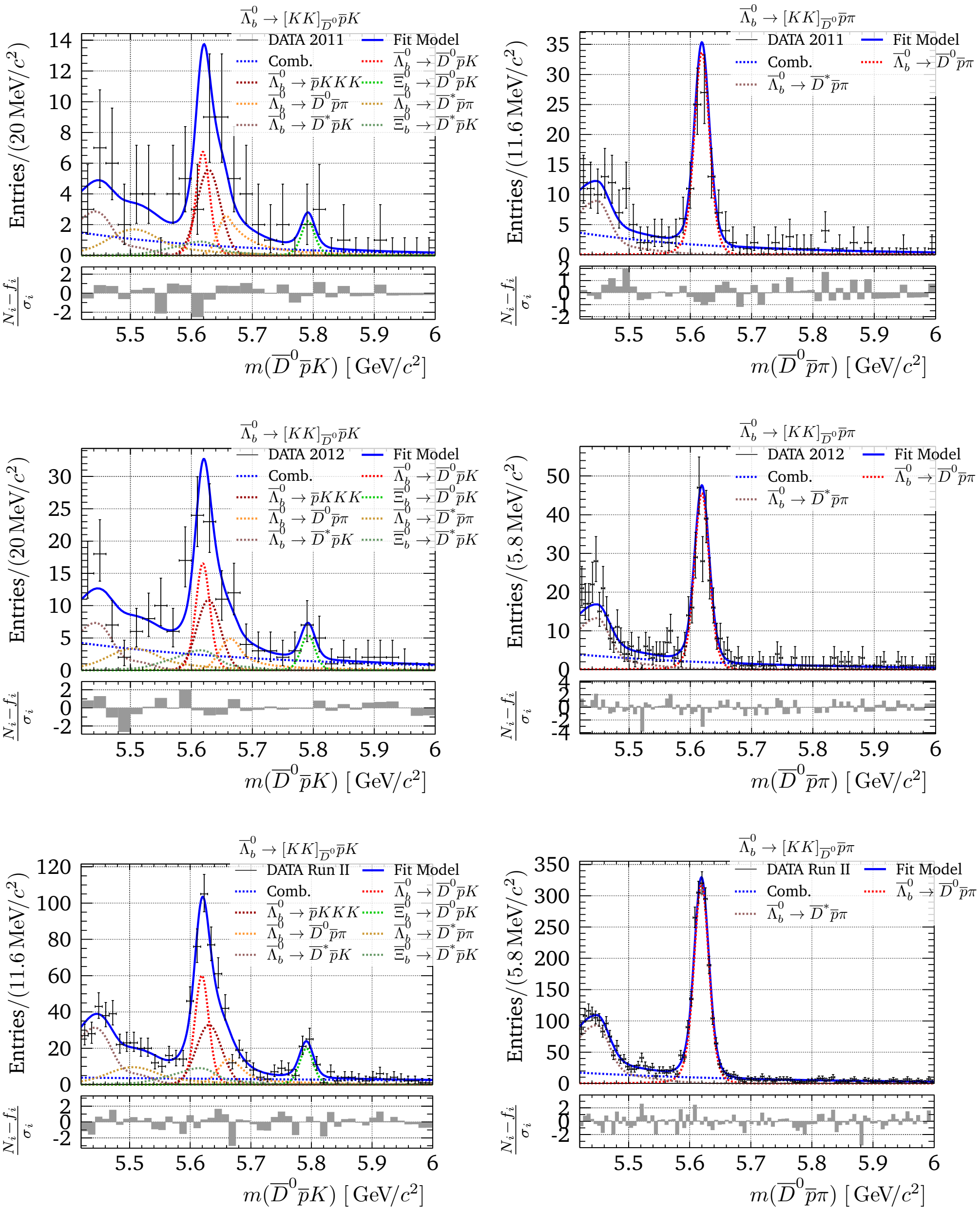

Fig. J.6.: $\overline{\Lambda}_b^0$-type fit to $m(D^0pK)$ and $m(D^0p\pi)$ with $D^0 \to KK$.

```
    #lambda_{12,D0ppi,KK}          -3.5303e-03 +/-   6.50e-04   <none>
    #lambda_{r2,D0pK,KK}           -8.6185e-04 +/-   1.73e-03   <none>
    #lambda_{r2,D0ppi,KK}          -3.1121e-03 +/-   3.42e-04   <none>
    N_{11,Lb2D0ppi,KK}              1.0712e+02 +/-   2.37e+00   <none>
    N_{Bkg,D0pK,KK}                 2.2507e+02 +/-   7.39e+01   <none>
    N_{Bkg,D0ppi,KK}                1.0396e+03 +/-   5.69e+01   <none>
    N_{Lb2D0ppi,mD0pK,KK}           1.0902e+02 +/-   2.36e+01   <none>
    N_{Lb2Dst0ppi,mD0pK,KK}         1.3736e+02 +/-   4.29e+01   <none>
    R_{Lb,Dst2D,K}                  1.1023e+00 +/-   2.26e-01   <none>
    R_{Lb,KK}                       8.3096e-02 +/-   1.16e-02   <none>
    R_{Xib,Dst2D,K}                 7.2249e-01 +/-   3.07e-01   <none>
    R_{Xib,KK}                      2.7624e-02 +/-   4.36e-03   <none>
```

```
s_{B,12,D0pK,KK}              3.2852e+00 +/-  1.59e+00  <none>
s_{B,12,D0ppi,KK}             2.2873e+00 +/-  4.33e-01  <none>
s_{B,r2,D0pK,KK}              8.0496e+00 +/-  3.61e+00  <none>
s_{B,r2,D0ppi,KK}             1.0383e+01 +/-  1.72e+00  <none>


Goodness of Fit:
-> #chi^{2}/DoF = 0.778048
->     #chi^{2} = 263.758
->          DoF = 339
->        p-val = 0.999065
Sum of Fitted Norms:
->  Lb  -> D0pK  , D0 -> KK (cc) =  191.776  +/- 21.498
->  Xib -> D0pK  , D0 -> KK (cc) =   63.7521 +/-  8.19053
->  Lb  -> D0ppi , D0 -> KK (cc) = 2160.23   +/- 39.9929
->  Lb  -> pKKK   = 187.635 +/- 4.14951
```

J.1.3 Fits for *sWeight* Calculation

A common approach to perform an amplitude analysis in the Dalitz plane would be to select only reconstructed candidates in the signal region. However, there are still various background contributions polluting the signal region. These would have to be described in the Dalitz plane as well. We make use of the *sPlot* formalism [95], as it is also done in section 4.3.3. With the calculation of *sWeights* requiring uncorrelated contributions in the fitted probability density function, we have to rephrase the PDF of section 5.1.2 without ratios or other correlations. Therefore we exclude the $m(D^0p\pi)$ samples from the fit and calculate additional scaling factors s^a for yields that previously had been linked by ratios. The signal yields are redefined to $N_{\text{sum}} = N^{(11)}(1 + s^{(12)} + s^{(\text{RunII})})$. All parameters except the yields are fixed and set to the results of the fits in section 5.1.2. Prior to calling the `RooStats::SPlot` implementation [134] in RooFit we perform a fit as it is defined in the module to ensure a correct *sWeight* calculation. In the following listings J.6 to J.9 summarise all parameters of the fitted models and figs. J.7 and J.8 visualise the fitresult. We find a good agreement of the modified model with the DATA.

Listing J.6: Parameters of Λ_b^0-type fit to $m(D^0pK)$ with $D^0 \to K^-\pi^+$ and no normalisation to $\Lambda_b^0 \to D^0p\pi$.

```
/-----------------------------------------------------------\
| RooFit Result - SimFit to m(Dp+K-) with D->K-pi+ (sPlot) |
\----------------------------------------------------------/

Constant Parameter            Value
--------------------------   ------------
#lambda_{11,D0pK,Kmpip}      -8.7213e-07
#lambda_{12,D0pK,Kmpip}      -5.7132e-03
#lambda_{r2,D0pK,Kmpip}      -3.8867e-03
addGauss_f                    8.3062e-01
addGauss_sigma                9.6345e+00
dM_{MC,shift,Dst}            -1.0921e+01
dM_{MC,shift}                -1.1835e+00
dM_{Xib,Lb}                   1.7252e+02
s_{B,12,D0pK,Kmpip}           1.7319e+01
s_{B,r2,D0pK,Kmpip}           8.7036e+01
s_{S,12,Lb2D0pK,Kpi}          2.0844e+00
s_{S,12,Lb2D0ppi,mD0pK}       1.8724e+00
s_{S,12,Xib2D0pK,Kpi}         2.0844e+00
s_{S,12,pRecLb,mD0pK}         2.4114e+00
s_{S,12,pRecXib}              3.2225e+00
s_{S,r2,Lb2D0pK,Kpi}          1.4306e+01
s_{S,r2,Lb2D0ppi,mD0pK}       8.8529e+00
```

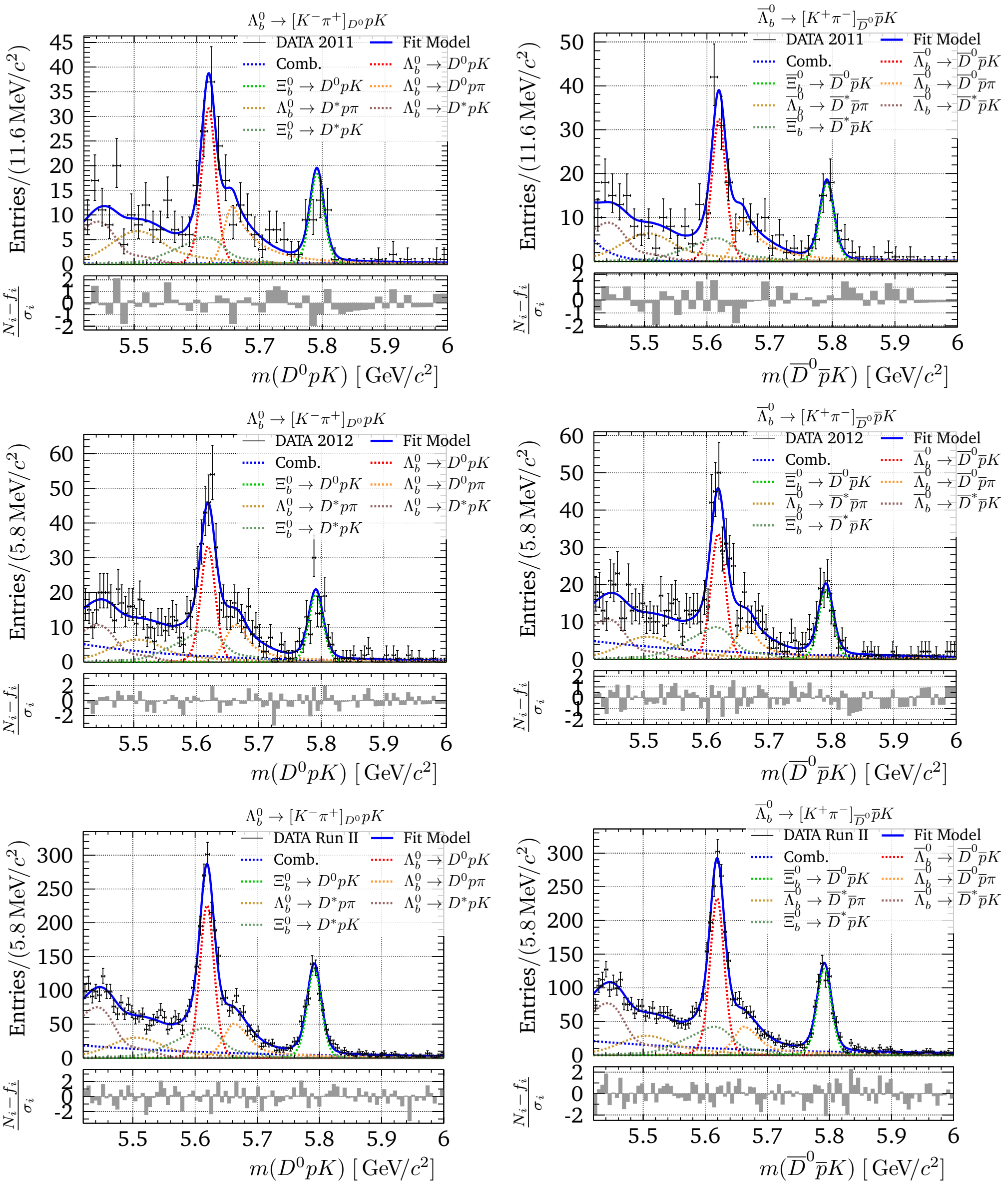

Fig. J.7.: $\mathit{\Lambda}_b^0$-type ($\overline{\mathit{\Lambda}}_b^0$-type) fit to $m(D^0pK)$ with $D^0 \to K^-\pi^+$ and no normalisation on the left (right).

```
    s_{S,r2,Xib2D0pK,Kpi}         1.4306e+01
    s_{S,r2,pRecLb,mD0pK}         1.7190e+01
    s_{S,r2,pRecXib}              1.5716e+01

    Floating Parameter            FinalValue +/- Error     GblCorr.
    --------------------------   ----------------------    --------
    N_{Bkg,D0pK,Kmpip}            8.9464e+02 +/-  1.14e+02  <none>
    N_{Lb2D0pK,Kpi}               1.4416e+03 +/-  6.21e+01  <none>
    N_{Lb2D0ppi,mD0pK,Kmpip}      8.0344e+02 +/-  4.94e+01  <none>
    N_{Lb2Dst0ppi,mD0pK,Kmpip}    8.7914e+02 +/-  8.57e+01  <none>
    N_{Lb2DstpK,mD0pK,Kpi}        9.9903e+02 +/-  5.63e+01  <none>
    N_{Xi2DstpK,mD0pK,Kpi}        9.9878e+02 +/-  9.72e+01  <none>
    N_{Xib2D0pK,Kpi}              8.4213e+02 +/-  3.24e+01  <none>

```

```

Goodness of Fit:
-> #chi^{2}/DoF = 0.922841
->     #chi^{2} = 213.176
->          DoF = 231
->        p-val = 0.793992
```

Listing J.7: Parameters of $\overline{\Lambda}_b^0$-type fit to $m(D^0pK)$ with $D^0 \to K^-\pi^+$ and no normalisation to $\Lambda_b^0 \to D^0p\pi$. Constant parameter are the same as for the Λ_b^0-type fit in listing J.6.

```
/----------------------------------------------------------\
| RooFit Result - SimFit to m(Dp-K+) with D->K+pi- (sPlot) |
\----------------------------------------------------------/

Constant Parameter            Value
--------------------------   ------------
>> same as Lb-type fit of D0 -> Kpi

Floating Parameter            FinalValue +/- Error     GblCorr.
--------------------------   ------------------------   --------
N_{Bkg,D0pK,Kmpip}            1.0462e+03 +/-  1.10e+02  <none>
N_{Lb2D0pK,Kpi}               1.4824e+03 +/-  6.20e+01  <none>
N_{Lb2D0ppi,mD0pK,Kmpip}      6.6692e+02 +/-  4.73e+01  <none>
N_{Lb2Dst0ppi,mD0pK,Kmpip}    8.3417e+02 +/-  8.55e+01  <none>
N_{Lb2DstpK,mD0pK,Kpi}        1.0220e+03 +/-  5.65e+01  <none>
N_{Xi2DstpK,mD0pK,Kpi}        9.4941e+02 +/-  9.65e+01  <none>
N_{Xib2D0pK,Kpi}              8.1901e+02 +/-  3.18e+01  <none>


Goodness of Fit:
-> #chi^{2}/DoF = 0.81486
->     #chi^{2} = 188.233
->          DoF = 231
->        p-val = 0.981969
```

Listing J.8: Parameters of Λ_b^0-type fit to $m(D^0pK)$ with $D^0 \to KK$ and no normalisation to $\Lambda_b^0 \to D^0p\pi$.

```
/-------------------------------------------------------\
| RooFit Result - SimFit to m(Dp+K-) with D->KK (sPlot) |
\-------------------------------------------------------/

Constant Parameter            Value
--------------------------   ------------
#lambda_{11,D0pK,KK}         -1.2059e-03
#lambda_{12,D0pK,KK}         -3.4162e-03
#lambda_{r2,D0pK,KK}         -3.4173e-03
addGauss_f                    8.3062e-01
addGauss_sigma                9.6345e+00
dM_{MC,shift,Dst}            -1.0921e+01
dM_{MC,shift}                -1.1835e+00
dM_{Xib,Lb}                   1.7252e+02
s_{B,12,D0pK,KK}              2.7234e+00
s_{B,r2,D0pK,KK}              1.7376e+01
s_{S,12,Lb2D0pK,KK}           2.3471e+00
s_{S,12,Lb2D0ppi,mD0pK}       1.8724e+00
s_{S,12,Lb2pKKK}              1.8378e+00
s_{S,12,Xib2D0pK,KK}          2.3471e+00
s_{S,12,pRecLb,mD0pK}         2.4114e+00
s_{S,12,pRecXib}              3.2225e+00
s_{S,r2,Lb2D0pK,KK}           1.4166e+01
s_{S,r2,Lb2D0ppi,mD0pK}       8.8529e+00
s_{S,r2,Lb2pKKK}              1.0049e+01
s_{S,r2,Xib2D0pK,KK}          1.4166e+01
s_{S,r2,pRecLb,mD0pK}         1.7190e+01
s_{S,r2,pRecXib}              1.5716e+01

Floating Parameter            FinalValue +/- Error     GblCorr.
--------------------------   ------------------------   --------
N_{Bkg,D0pK,KK}               4.7572e+02 +/-  5.95e+01  <none>
```

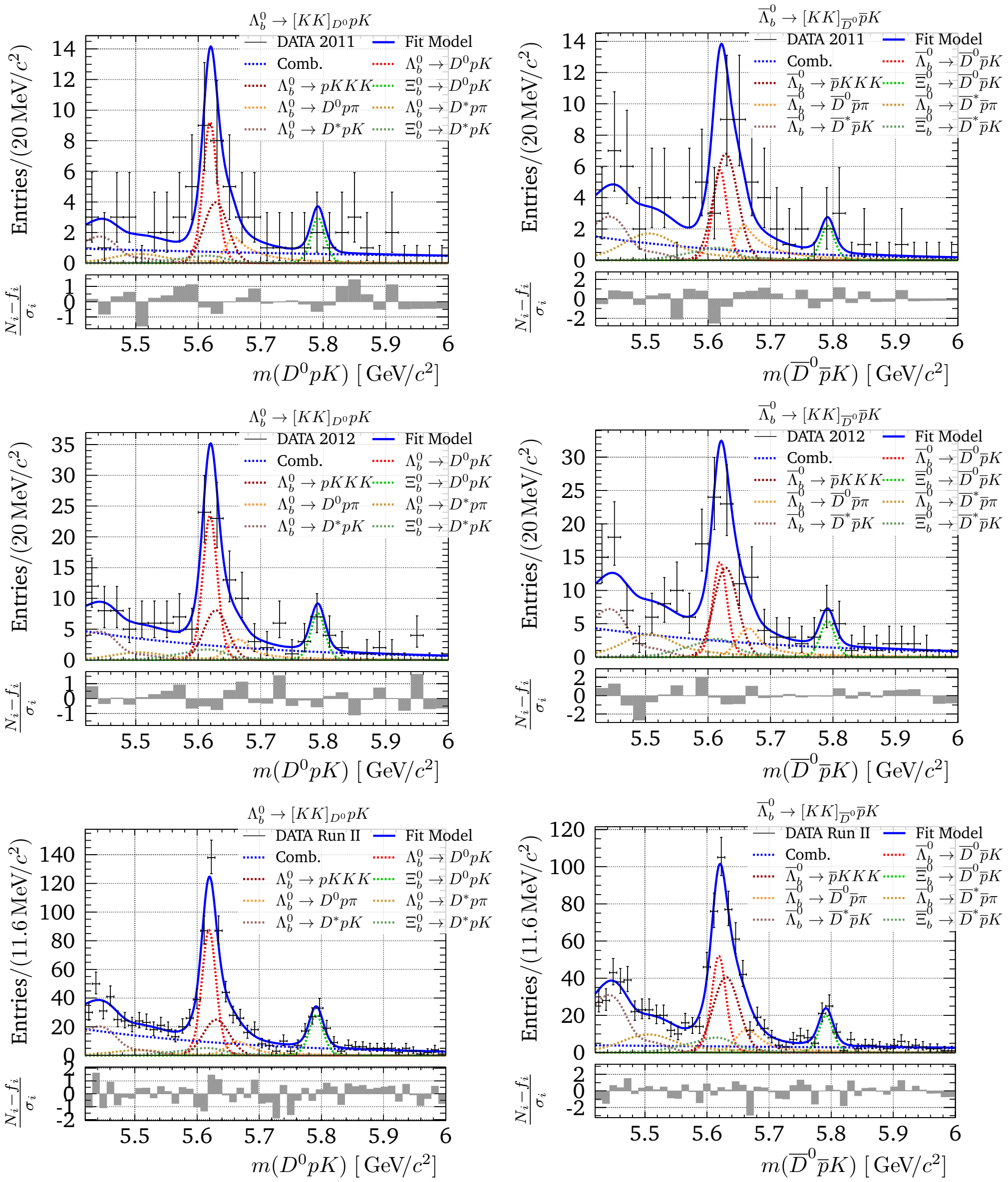

Fig. J.8.: Λ_b^0-type ($\overline{\Lambda}_b^0$-type) fit to $m(D^0pK)$ with $D^0 \to KK$ and no normalisation on the left (right).

```
    N_{Lb2D0pK,KK}                2.7913e+02 +/-  3.84e+01  <none>
    N_{Lb2D0ppi,mD0pK,KK}         7.6434e+01 +/-  2.52e+01  <none>
    N_{Lb2Dst0ppi,mD0pK,KK}       5.1735e+01 +/-  3.61e+01  <none>
    N_{Lb2DstpK,mD0pK,KK}         1.3205e+02 +/-  2.43e+01  <none>
    N_{Lb2pKKK}                   1.4222e+02 +/-  4.56e+01  <none>
    N_{Xi2DstpK,mD0pK,KK}         5.7255e+01 +/-  4.26e+01  <none>
    N_{Xib2D0pK,KK}               9.0581e+01 +/-  1.18e+01  <none>


    Goodness of Fit:
    -> #chi^{2}/DoF = 0.65027
    ->     #chi^{2} = 57.8741
    ->          DoF = 89
    ->        p-val = 0.995697
```

Listing J.9: Parameters of $\overline{\Lambda}{}_b^0$-type fit to $m(D^0pK)$ with $D^0 \to KK$ and no normalisation to $\Lambda_b^0 \to D^0p\pi$. Constant parameter are the same as for the Λ_b^0-type fit in listing J.8.

```
/-------------------------------------------------------\
| RooFit Result - SimFit to m(Dp-K+) with D->KK (sPlot) |
\-------------------------------------------------------/

Constant Parameter              Value
--------------------------    ------------
>> same as Lb-type fit of D0 -> KK

Floating Parameter              FinalValue +/- Error     GblCorr.
--------------------------    ------------------------  --------
N_{Bkg,D0pK,KK}                 2.3230e+02 +/-  3.44e+01  <none>
N_{Lb2D0pK,KK}                  1.6627e+02 +/-  3.62e+01  <none>
N_{Lb2D0ppi,mD0pK,KK}           9.6966e+01 +/-  2.40e+01  <none>
N_{Lb2Dst0ppi,mD0pK,KK}         1.4001e+02 +/-  3.46e+01  <none>
N_{Lb2DstpK,mD0pK,KK}           2.0268e+02 +/-  2.28e+01  <none>
N_{Lb2pKKK}                     2.3242e+02 +/-  4.47e+01  <none>
N_{Xi2DstpK,mD0pK,KK}           8.9472e+01 +/-  3.98e+01  <none>
N_{Xib2D0pK,KK}                 6.3894e+01 +/-  9.79e+00  <none>


Goodness of Fit:
-> #chi^{2}/DoF = 0.968125
->      #chi^{2} = 86.1632
->           DoF = 89
->         p-val = 0.565451
```

J.2 Acceptance Weighted

J.2.1 Preliminary Fit to $m(D^0ph)$

Figure J.9 shows the preliminary fit to $m(D^0pK)$ and $m(D^0p\pi)$ with acceptance weights, as described in section 5.2. A list of all fit parameters is shown in listing J.10.

Listing J.10: Parameters of preliminary fit to $m(D^0pK)$ and $m(D^0p\pi)$ with acceptance weights.

```
/---------------------------------------------------------\
| RooFit Result - Preliminary SimFit to Full m(Dph) DATA |
| DATA with acceptance weights                            |
\---------------------------------------------------------/

Constant Parameter              Value
--------------------------    ------------
B_{D02KK}                       4.0800e-03
B_{Lb2D0ppi}                    6.3000e-04
effR_{11,Lb,D0pK2D0ppi,KK}      1.2417e+00
effR_{11,Lb,D0pK2D0ppi,Kpi}     1.2417e+00
effR_{11,Lb,pKKK2D0ppi,KK}      2.9570e-02
effR_{11,Xib,D0pK2D0ppi,KK}     1.2718e+00
effR_{11,Xib,D0pK2D0ppi,Kpi}    1.2718e+00
effR_{12,Lb,D0pK2D0ppi,KK}      1.0427e+00
effR_{12,Lb,D0pK2D0ppi,Kpi}     1.0427e+00
effR_{12,Lb,pKKK2D0ppi,KK}      2.1733e-02
effR_{12,Xib,D0pK2D0ppi,KK}     8.3910e-01
effR_{12,Xib,D0pK2D0ppi,Kpi}    8.3910e-01
effR_{r2,Lb,D0pK2D0ppi,KK}      1.0583e+00
effR_{r2,Lb,D0pK2D0ppi,Kpi}     1.0583e+00
effR_{r2,Lb,pKKK2D0ppi,KK}      1.7829e-02
effR_{r2,Xib,D0pK2D0ppi,KK}     1.0168e+00
effR_{r2,Xib,D0pK2D0ppi,Kpi}    1.0168e+00

Floating Parameter              FinalValue +/- Error     GblCorr.
```

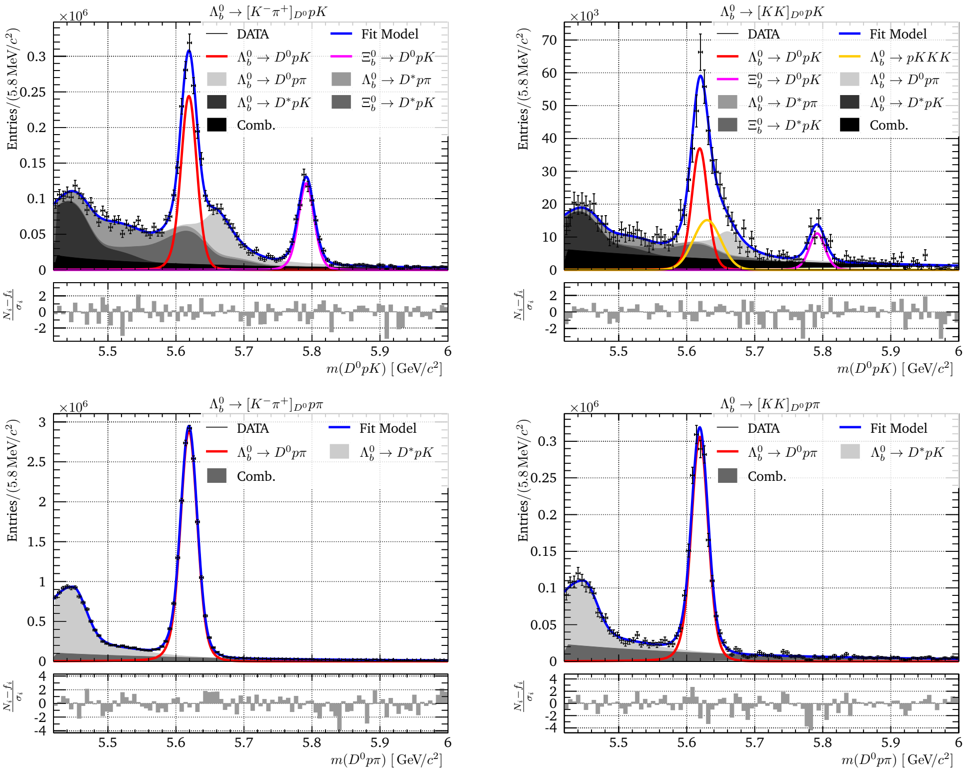

Fig. J.9.: Preliminary fit to $m(D^0pK)$ and $m(D^0p\pi)$ with acceptance weights. The models for 2011, 2012 and Run II are summed together and background models are stacked and visualised as shaded area.

```
--------------------------   ------------------------  --------
#lambda_{11,D0pK,KK}         -2.5790e-03 +/-  2.16e-03  <none>
#lambda_{11,D0pK,Kmpip}      -2.8852e-02 +/-  4.41e-02  <none>
#lambda_{11,D0ppi,KK}        -4.7785e-03 +/-  8.21e-04  <none>
#lambda_{11,D0ppi,Kmpip}     -6.2520e-03 +/-  9.76e-04  <none>
#lambda_{12,D0pK,KK}         -3.2475e-03 +/-  1.45e-03  <none>
#lambda_{12,D0pK,Kmpip}      -4.7921e-03 +/-  2.00e-03  <none>
#lambda_{12,D0ppi,KK}        -3.9720e-03 +/-  4.37e-04  <none>
#lambda_{12,D0ppi,Kmpip}     -3.8448e-03 +/-  4.43e-04  <none>
#lambda_{r2,D0pK,KK}         -2.7652e-03 +/-  1.22e-03  <none>
#lambda_{r2,D0pK,Kmpip}      -3.4834e-03 +/-  1.57e-03  <none>
#lambda_{r2,D0ppi,KK}        -2.7977e-03 +/-  3.40e-04  <none>
#lambda_{r2,D0ppi,Kmpip}     -3.3365e-03 +/-  3.92e-04  <none>
F_{Lb2pKKK}                   9.9719e-06 +/-  2.25e-06  <none>
N_{11,Bkg,mD0pK,KK}           3.1814e+04 +/-  1.60e+04  <none>
N_{11,Bkg,mD0pK,Kmpip}        1.8542e+04 +/-  6.45e+04  <none>
N_{11,Bkg,mD0ppi,KK}          1.1724e+05 +/-  1.60e+04  <none>
N_{11,Bkg,mD0ppi,Kmpip}       5.3988e+05 +/-  9.89e+04  <none>
N_{11,Lb2D0ppi,KK}            1.5538e+05 +/-  5.31e+03  <none>
N_{11,Lb2D0ppi,Kmpip}         1.4655e+06 +/-  4.39e+04  <none>
N_{11,Lb2D0ppi,mD0pK,KK}      1.1502e+04 +/-  3.34e+03  <none>
N_{11,Lb2D0ppi,mD0pK,Kmpip}   9.5152e+04 +/-  1.19e+04  <none>
N_{11,Lb2Dst0ppi,mD0pK,KK}    9.1891e+03 +/-  7.31e+03  <none>
N_{11,Lb2Dst0ppi,mD0pK,Kmpip} 1.0469e+05 +/-  1.87e+04  <none>
N_{12,Bkg,mD0pK,KK}           8.2323e+04 +/-  3.16e+04  <none>
N_{12,Bkg,mD0pK,Kmpip}        2.4438e+05 +/-  1.65e+05  <none>
N_{12,Bkg,mD0ppi,KK}          3.7080e+05 +/-  2.77e+04  <none>
N_{12,Bkg,mD0ppi,Kmpip}       1.1190e+06 +/-  1.07e+05  <none>
N_{r2,Bkg,mD0pK,KK}           1.9003e+05 +/-  6.62e+04  <none>
N_{r2,Bkg,mD0pK,Kmpip}        4.5539e+05 +/-  2.27e+05  <none>
```

```
N_{r2,Bkg,mD0ppi,KK}          5.0860e+05 +/-  3.40e+04  <none>
N_{r2,Bkg,mD0ppi,Kmpip}       2.5561e+06 +/-  2.23e+05  <none>
R_{Lb,Dst2D,K}                1.8927e+00 +/-  1.67e+00  <none>
R_{Lb,Dst2D,pi}               1.9602e+00 +/-  3.05e-01  <none>
R_{Lb,KK}                     1.0458e-01 +/-  1.42e-02  <none>
R_{Lb,Kpi}                    7.3315e-02 +/-  2.53e-03  <none>
R_{Xib,Dst2D,K}               1.0463e+00 +/-  3.52e-01  <none>
R_{Xib,KK}                    3.3741e-02 +/-  3.93e-03  <none>
R_{Xib,Kpi}                   3.9236e-02 +/-  1.29e-03  <none>
addGauss_f                    8.1292e-01 +/-  5.45e-02  <none>
addGauss_sigma                1.0294e+01 +/-  6.83e-01  <none>
dM_{MC,shift,Dst}            -1.0233e+01 +/-  1.92e+00  <none>
dM_{MC,shift}                -1.1510e+00 +/-  7.80e-02  <none>
dM_{Xib,Lb}                   1.7259e+02 +/-  3.97e-01  <none>
m_pRecLb_mD0ppi_f             6.3977e-01 +/-  1.93e-02  <none>
m_pRecLb_mD0ppi_mean          5.4482e+03 +/-  1.84e+00  <none>
m_pRecLb_mD0ppi_sigma11       3.9142e+01 +/-  6.19e+00  <none>
m_pRecLb_mD0ppi_sigma12       1.9364e+01 +/-  1.64e+00  <none>
m_pRecLb_mD0ppi_sigma2        7.8908e+01 +/-  1.32e+01  <none>
s_{S,12,Lb2D0ppi,mD0pK}       1.8436e+00 +/-  3.94e-01  <none>
s_{S,12,Lb2D0ppi}             2.4450e+00 +/-  7.65e-02  <none>
s_{S,12,pRecLb,mD0pK}         2.2840e+00 +/-  2.24e+00  <none>
s_{S,12,pRecLb,mD0ppi}        2.7607e+00 +/-  3.36e-01  <none>
s_{S,12,pRecXib}              2.7342e+00 +/-  1.18e+00  <none>
s_{S,r2,Lb2D0ppi,mD0pK}       4.4459e+00 +/-  7.24e-01  <none>
s_{S,r2,Lb2D0ppi}             7.7916e+00 +/-  2.19e-01  <none>
s_{S,r2,pRecLb,mD0pK}         9.0554e+00 +/-  8.00e+00  <none>
s_{S,r2,pRecLb,mD0ppi}        8.6361e+00 +/-  1.04e+00  <none>
s_{S,r2,pRecXib}              8.0566e+00 +/-  2.90e+00  <none>


Goodness of Fit:
-> #chi^{2}/DoF = 1.37437
->     #chi^{2} = 1168.22
->          DoF = 850
->        p-val = 1.9874e-12
Fitted Norms (sum):
->  Lb  -> D0pK  , D0 -> Kmpip = 1.29324e+06+/-31857.9
->               , D0 -> KK    = 195591+/-19071.2
->  Xib -> D0pK  , D0 -> Kmpip = 646660+/-15464.2
->               , D0 -> KK    = 58959.6+/-5005.66
->  Lb  -> D0ppi , D0 -> Kmpip = 1.64671e+07+/-136902
->               , D0 -> KK    = 1.74592e+06+/-25752.6
->  Lb  -> pKKK  = 133592+/-30033.6
Resulting B-Fractions:
->  B   (Lb->D0pK,Kpi) = 4.61884e-05 +/- 1.59297e-06
->  B_s(Lb->D0pK,KK)  = 6.58867e-05 +/- 8.94407e-06
```

J.2.2 Fit to Separate D^0 and $\Lambda_b^0/\overline{\Lambda}_b^0$ Samples

Figure J.10 shows the preliminary fit to $m(D^0pK)$ and $m(D^0p\pi)$ with acceptance weights, as described in section 5.2. A list of all fit parameters is shown in listing J.11.

Listing J.11: Parameters of Λ_b^0-type fit to $m(D^0pK)$ with $D^0 \to K^-\pi^+$ and acceptance weights.

```
/--------------------------------------------------\
| RooFit Result - SimFit to m(Dp+h-) with D->K-pi+ |
| DATA with acceptance weights                     |
\--------------------------------------------------/

Constant Parameter            Value
--------------------------   ------------
R_{Lb,Dst2D,pi}               1.9602e+00
addGauss_f                    8.1292e-01
addGauss_sigma                1.0294e+01
dM_{MC,shift,Dst}            -1.0233e+01
```

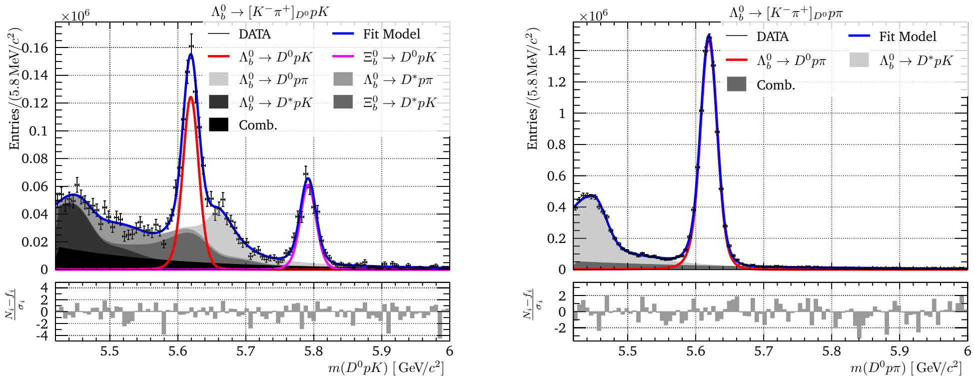

(a) $\mathit{\Lambda}_b^0$-type - $m(D^0ph^-)$, with $D^0 \to K^-\pi^+$

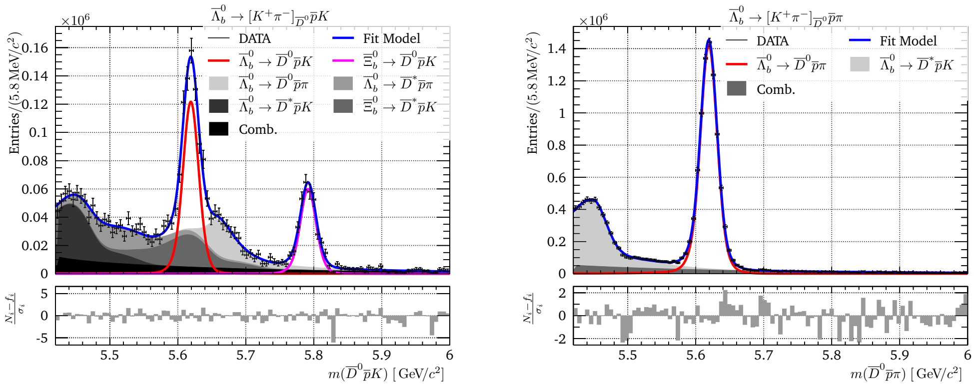

(b) $\overline{\mathit{\Lambda}}_b^0$-type - $m(D^0\overline{p}h^+)$, with $D^0 \to K^-\pi^+$

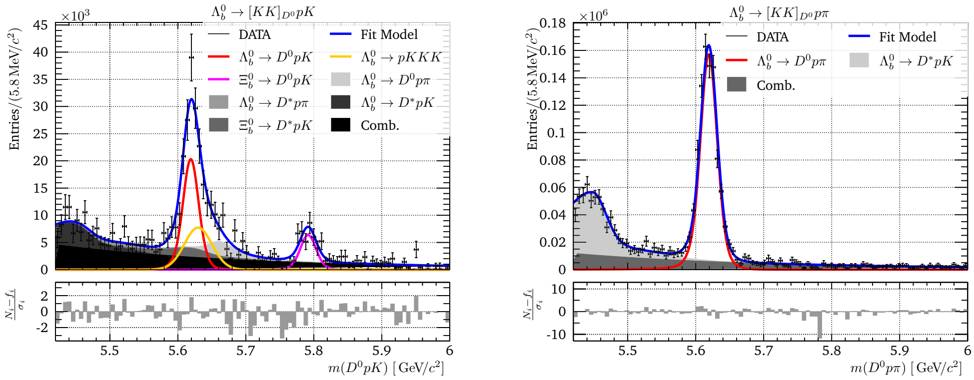

(c) $\mathit{\Lambda}_b^0$-type - $m(D^0ph^-)$, with $D^0 \to KK$

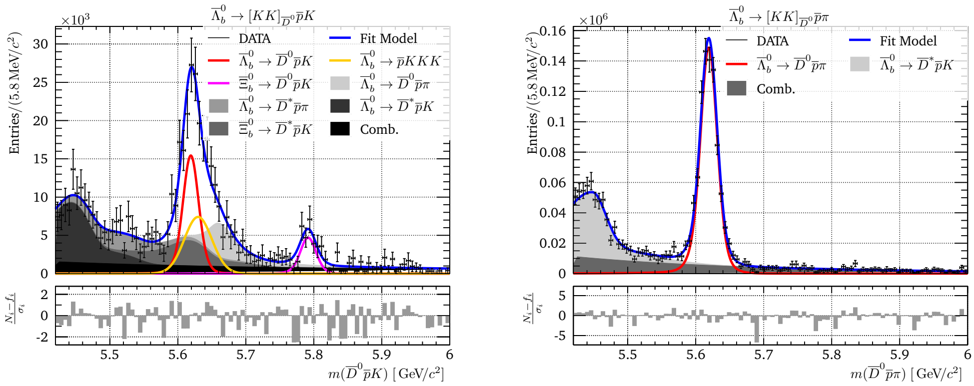

(d) $\overline{\mathit{\Lambda}}_b^0$-type - $m(D^0\overline{p}h^+)$, with $D^0 \to KK$

Fig. J.10.: Fits to $m(D^0pK)$ and $m(D^0p\pi)$ with acceptance weights and split for the D^0 modes and $\mathit{\Lambda}_b^0$-types.

```
dM_{MC,shift}               -1.1510e+00
dM_{Xib,Lb}                  1.7259e+02
effR_{11,Lb,D0pK2D0ppi,Kpi}  1.2417e+00
effR_{11,Xib,D0pK2D0ppi,Kpi} 1.2718e+00
effR_{12,Lb,D0pK2D0ppi,Kpi}  1.0427e+00
effR_{12,Xib,D0pK2D0ppi,Kpi} 8.3910e-01
effR_{r2,Lb,D0pK2D0ppi,Kpi}  1.0583e+00
effR_{r2,Xib,D0pK2D0ppi,Kpi} 1.0168e+00
m_pRecLb_mD0ppi_f            6.3977e-01
m_pRecLb_mD0ppi_mean         5.4482e+03
m_pRecLb_mD0ppi_sigma11      3.9142e+01
m_pRecLb_mD0ppi_sigma12      1.9364e+01
m_pRecLb_mD0ppi_sigma2       7.8908e+01
s_{S,12,Lb2D0ppi,mD0pK}      1.8436e+00
s_{S,12,Lb2D0ppi}            2.4450e+00
s_{S,12,pRecLb,mD0pK}        2.2840e+00
s_{S,12,pRecLb,mD0ppi}       2.7607e+00
s_{S,12,pRecXib}             2.7342e+00
s_{S,r2,Lb2D0ppi,mD0pK}      4.4459e+00
s_{S,r2,Lb2D0ppi}            7.7916e+00
s_{S,r2,pRecLb,mD0pK}        9.0554e+00
s_{S,r2,pRecLb,mD0ppi}       8.6361e+00
s_{S,r2,pRecXib}             8.0566e+00

Floating Parameter           FinalValue +/- Error     GblCorr.
--------------------------   ------------------------  --------
#lambda_{11,D0pK,Kmpip}     -8.3341e-03 +/-  4.92e-03  <none>
#lambda_{11,D0ppi,Kmpip}    -5.9062e-03 +/-  5.78e-04  <none>
#lambda_{12,D0pK,Kmpip}     -6.1369e-03 +/-  1.16e-03  <none>
#lambda_{12,D0ppi,Kmpip}    -4.3373e-03 +/-  3.30e-04  <none>
#lambda_{r2,D0pK,Kmpip}     -4.9846e-03 +/-  1.46e-03  <none>
#lambda_{r2,D0ppi,Kmpip}    -3.1215e-03 +/-  1.90e-04  <none>
N_{11,Lb2D0ppi,Kmpip}        7.4341e+05 +/-  5.02e+03  <none>
N_{Bkg,D0pK,Kmpip}           4.9513e+05 +/-  2.35e+05  <none>
N_{Bkg,D0ppi,Kmpip}          2.0997e+06 +/-  6.32e+04  <none>
N_{Lb2D0ppi,mD0pK,Kmpip}     3.6888e+05 +/-  2.83e+04  <none>
N_{Lb2Dst0ppi,mD0pK,Kmpip}   3.3043e+05 +/-  9.45e+04  <none>
R_{Lb,Dst2D,K}               2.2727e+00 +/-  6.07e-01  <none>
R_{Lb,Kpi}                   7.3679e-02 +/-  3.41e-03  <none>
R_{Xib,Dst2D,K}              1.1692e+00 +/-  1.91e-01  <none>
R_{Xib,Kpi}                  3.8906e-02 +/-  1.73e-03  <none>
s_{B,12,D0pK,Kmpip}          4.3489e+00 +/-  2.77e+00  <none>
s_{B,12,D0ppi,Kmpip}         2.2083e+00 +/-  2.38e-01  <none>
s_{B,r2,D0pK,Kmpip}          9.6480e+00 +/-  5.09e+00  <none>
s_{B,r2,D0ppi,Kmpip}         4.7075e+00 +/-  4.53e-01  <none>


Goodness of Fit:
-> #chi^{2}/DoF = 1.20946
->     #chi^{2} = 642.224
->          DoF = 531
->        p-val = 0.000640307
Fitted Norms (sum):
->  Lb  -> D0pK  , D0 -> Kmpip = 659282+/-21437.6
->  Xib -> D0pK  , D0 -> Kmpip = 325274+/-10499.2
->  Lb  -> D0ppi , D0 -> Kmpip = 8.35338e+06+/-41291.6
```

Listing J.12: Parameters of $\overline{\Lambda}{}_b^0$-type fit to $m(D^0pK)$ with $D^0 \to K^-\pi^+$ and acceptance weights. Constant parameter are the same as for the Λ_b^0-type fit in listing J.11.

```
/--------------------------- ----------------------\
| RooFit Result - SimFit to m(Dp-h+) with D->K+pi- |
| DATA with acceptance weights                     |
\--------------------------------------------------/

Constant Parameter           Value
--------------------------   ------------
>> same as Lb-type fit of D0 -> Kpi

Floating Parameter           FinalValue +/- Error     GblCorr.
--------------------------   ------------------------  --------
```

```
    #lambda_{11,D0pK,Kmpip}      -3.2930e-02 +/-  2.61e-02  <none>
    #lambda_{11,D0ppi,Kmpip}     -6.5798e-03 +/-  5.69e-04  <none>
    #lambda_{12,D0pK,Kmpip}      -4.3856e-03 +/-  9.72e-04  <none>
    #lambda_{12,D0ppi,Kmpip}     -3.3615e-03 +/-  3.36e-04  <none>
    #lambda_{r2,D0pK,Kmpip}      -3.6284e-03 +/-  1.30e-03  <none>
    #lambda_{r2,D0ppi,Kmpip}     -3.5541e-03 +/-  1.78e-04  <none>
    N_{11,Lb2D0ppi,Kmpip}         7.2190e+05 +/-  4.50e+03  <none>
    N_{Bkg,D0pK,Kmpip}            4.2158e+05 +/-  1.39e+05  <none>
    N_{Bkg,D0ppi,Kmpip}           2.1186e+06 +/-  5.84e+04  <none>
    N_{Lb2D0ppi,mD0pK,Kmpip}      3.1195e+05 +/-  2.35e+04  <none>
    N_{Lb2Dst0ppi,mD0pK,Kmpip}    3.5586e+05 +/-  6.04e+04  <none>
    R_{Lb,Dst2D,K}                1.9025e+00 +/-  2.86e-01  <none>
    R_{Lb,Kpi}                    7.4198e-02 +/-  3.27e-03  <none>
    R_{Xib,Dst2D,K}               1.0482e+00 +/-  1.30e-01  <none>
    R_{Xib,Kpi}                   3.9255e-02 +/-  1.66e-03  <none>
    s_{B,12,D0pK,Kmpip}           1.3954e+01 +/-  1.44e+01  <none>
    s_{B,12,D0ppi,Kmpip}          1.9522e+00 +/-  2.00e-01  <none>
    s_{B,r2,D0pK,Kmpip}           2.6143e+01 +/-  2.42e+01  <none>
    s_{B,r2,D0ppi,Kmpip}          4.7756e+00 +/-  4.14e-01  <none>


    Goodness of Fit:
    -> #chi^{2}/DoF = 1.17305
    ->     #chi^{2} = 622.888
    ->          DoF = 531
    ->        p-val = 0.00355279
    Fitted Norms (sum):
    ->  Lb  -> D0pK  , D0 -> Kmpip (cc) = 644718+/-20198.5
    ->  Xib -> D0pK  , D0 -> Kmpip (cc) = 318697+/-9849.35
    ->  Lb  -> D0ppi , D0 -> Kmpip (cc) = 8.11166e+06+/-37050.1
```

Listing J.13: Parameters of Λ_b^0-type fit to $m(D^0pK)$ with $D^0 \to KK$ and acceptance weights.

```
    /-----------------------------------------------\
    | RooFit Result - SimFit to m(Dp+h-) with D->KK |
    | DATA with acceptance weights                  |
    \-----------------------------------------------/

    Constant Parameter             Value
    --------------------------   ------------
    B_{D02KK}                      4.0800e-03
    B_{Lb2D0ppi}                   6.3000e-04
    F_{Lb2pKKK}                    9.9719e-06
    R_{Lb,Dst2D,pi}                1.9602e+00
    addGauss_f                     8.1292e-01
    addGauss_sigma                 1.0294e+01
    dM_{MC,shift,Dst}             -1.0233e+01
    dM_{MC,shift}                 -1.1510e+00
    dM_{Xib,Lb}                    1.7259e+02
    effR_{11,Lb,D0pK2D0ppi,KK}     1.2417e+00
    effR_{11,Lb,pKKK2D0ppi,KK}     2.9570e-02
    effR_{11,Xib,D0pK2D0ppi,KK}    1.2718e+00
    effR_{12,Lb,D0pK2D0ppi,KK}     1.0427e+00
    effR_{12,Lb,pKKK2D0ppi,KK}     2.1733e-02
    effR_{12,Xib,D0pK2D0ppi,KK}    8.3910e-01
    effR_{r2,Lb,D0pK2D0ppi,KK}     1.0583e+00
    effR_{r2,Lb,pKKK2D0ppi,KK}     1.7829e-02
    effR_{r2,Xib,D0pK2D0ppi,KK}    1.0168e+00
    m_pRecLb_mD0ppi_f              6.3977e-01
    m_pRecLb_mD0ppi_mean           5.4482e+03
    m_pRecLb_mD0ppi_sigma11        3.9142e+01
    m_pRecLb_mD0ppi_sigma12        1.9364e+01
    m_pRecLb_mD0ppi_sigma2         7.8908e+01
    s_{S,12,Lb2D0ppi,mD0pK}        1.8436e+00
    s_{S,12,Lb2D0ppi}              2.4450e+00
    s_{S,12,pRecLb,mD0pK}          2.2840e+00
    s_{S,12,pRecLb,mD0ppi}         2.7607e+00
    s_{S,12,pRecXib}               2.7342e+00
    s_{S,r2,Lb2D0ppi,mD0pK}        4.4459e+00
    s_{S,r2,Lb2D0ppi}              7.7916e+00
    s_{S,r2,pRecLb,mD0pK}          9.0554e+00
```

```
s_{S,r2,pRecLb,mD0ppi}        8.6361e+00
s_{S,r2,pRecXib}              8.0566e+00

Floating Parameter            FinalValue +/- Error     GblCorr.
--------------------------   ------------------------  --------
#lambda_{11,D0pK,KK}         -1.3926e-03 +/-  3.31e-03  <none>
#lambda_{11,D0ppi,KK}        -5.2705e-03 +/-  9.48e-04  <none>
#lambda_{12,D0pK,KK}         -3.6021e-03 +/-  2.40e-03  <none>
#lambda_{12,D0ppi,KK}        -3.6344e-03 +/-  5.44e-04  <none>
#lambda_{r2,D0pK,KK}         -3.5729e-03 +/-  2.16e-03  <none>
#lambda_{r2,D0ppi,KK}        -2.7088e-03 +/-  3.59e-04  <none>
N_{11,Lb2D0ppi,KK}            7.9738e+04 +/-  1.87e+03  <none>
N_{Bkg,D0pK,KK}               2.0081e+05 +/-  1.25e+05  <none>
N_{Bkg,D0ppi,KK}              5.2014e+05 +/-  2.79e+04  <none>
N_{Lb2D0ppi,mD0pK,KK}         3.2244e+04 +/-  1.30e+04  <none>
N_{Lb2Dst0ppi,mD0pK,KK}       1.5243e+04 +/-  4.96e+04  <none>
R_{Lb,Dst2D,K}                2.8713e+00 +/-  2.84e+00  <none>
R_{Lb,KK}                     1.1243e-01 +/-  1.21e-02  <none>
R_{Xib,Dst2D,K}               1.5627e+00 +/-  1.40e+00  <none>
R_{Xib,KK}                    3.7908e-02 +/-  5.88e-03  <none>
s_{B,12,D0pK,KK}              2.3541e+00 +/-  7.66e-01  <none>
s_{B,12,D0ppi,KK}             3.0057e+00 +/-  5.13e-01  <none>
s_{B,r2,D0pK,KK}              7.8726e+00 +/-  2.44e+00  <none>
s_{B,r2,D0ppi,KK}             3.9683e+00 +/-  6.14e-01  <none>


Goodness of Fit:
-> #chi^{2}/DoF = 1.12927
->     #chi^{2} = 382.824
->          DoF = 339
->        p-val = 0.0504099
Fitted Norms (sum):
->  Lb  -> D0pK  , D0 -> KK = 107904+/-8101.26
->  Xib -> D0pK  , D0 -> KK = 33993.2+/-3843.19
->  Lb  -> D0ppi , D0 -> KK = 895977+/-15408.6
->  Lb  -> pKKK  = 68557.1+/-1610.28
```

Listing J.14: Parameters of $\overline{\Lambda}_b^0$-type fit to $m(D^0pK)$ with $D^0 \to KK$ and acceptance weights. Constant parameter are the same as for the Λ_b^0-type fit in listing J.13.

```
/-----------------------------------------------\
| RooFit Result - SimFit to m(Dp-h+) with D->KK |
| DATA with acceptance weights                  |
\-----------------------------------------------/

Constant Parameter            Value
--------------------------   ------------
>> same as Lb-type fit of D0 -> KK

Floating Parameter            FinalValue +/- Error     GblCorr.
--------------------------   ------------------------  --------
#lambda_{11,D0pK,KK}         -4.3322e-03 +/-  2.39e-03  <none>
#lambda_{11,D0ppi,KK}        -4.2284e-03 +/-  1.00e-03  <none>
#lambda_{12,D0pK,KK}         -2.7903e-03 +/-  1.27e-03  <none>
#lambda_{12,D0ppi,KK}        -4.3854e-03 +/-  5.99e-04  <none>
#lambda_{r2,D0pK,KK}         -3.1323e-04 +/-  1.22e-03  <none>
#lambda_{r2,D0ppi,KK}        -2.9012e-03 +/-  3.80e-04  <none>
N_{11,Lb2D0ppi,KK}            7.5580e+04 +/-  1.84e+03  <none>
N_{Bkg,D0pK,KK}               9.4557e+04 +/-  2.44e+04  <none>
N_{Bkg,D0ppi,KK}              4.7745e+05 +/-  2.74e+04  <none>
N_{Lb2D0ppi,mD0pK,KK}         5.3206e+04 +/-  1.07e+04  <none>
N_{Lb2Dst0ppi,mD0pK,KK}       5.1034e+04 +/-  1.83e+04  <none>
R_{Lb,Dst2D,K}                1.2019e+00 +/-  2.31e-01  <none>
R_{Lb,KK}                     8.9328e-02 +/-  1.23e-02  <none>
R_{Xib,Dst2D,K}               5.6648e-01 +/-  1.63e-01  <none>
R_{Xib,KK}                    2.9185e-02 +/-  4.88e-03  <none>
s_{B,12,D0pK,KK}              3.0881e+00 +/-  1.54e+00  <none>
s_{B,12,D0ppi,KK}             3.3610e+00 +/-  6.31e-01  <none>
s_{B,r2,D0pK,KK}              3.4739e+00 +/-  1.61e+00  <none>
s_{B,r2,D0ppi,KK}             4.8027e+00 +/-  8.22e-01  <none>

```

```

Goodness of Fit:
-> #chi^{2}/DoF = 1.35111
->     #chi^{2} = 458.027
->          DoF = 339
->        p-val = 1.66582e-05
Fitted Norms (sum):
->  Lb   -> D0pK   , D0 -> KK (cc) = 81264.2+/-7924.6
->  Xib  -> D0pK   , D0 -> KK (cc) = 24806.6+/-3022.42
->  Lb   -> D0ppi  , D0 -> KK (cc) = 849263+/-15106.4
->  Lb   -> pKKK   (cc) = 64982.7+/-1578.7
```

J.3 Unweighted Dataset - Λ^* Resonances

J.3.1 Preliminary Fit to $m(D^0ph)$

Figure J.11 shows the preliminary fit to $m(D^0pK)$ and $m(D^0p\pi)$ in the Λ^* Dalitz subregion ($m^2(D^0p) > 14\,\mathrm{GeV}^2/c^4$), as described in section 5.3. A list of all fit parameters is shown in listing J.15.

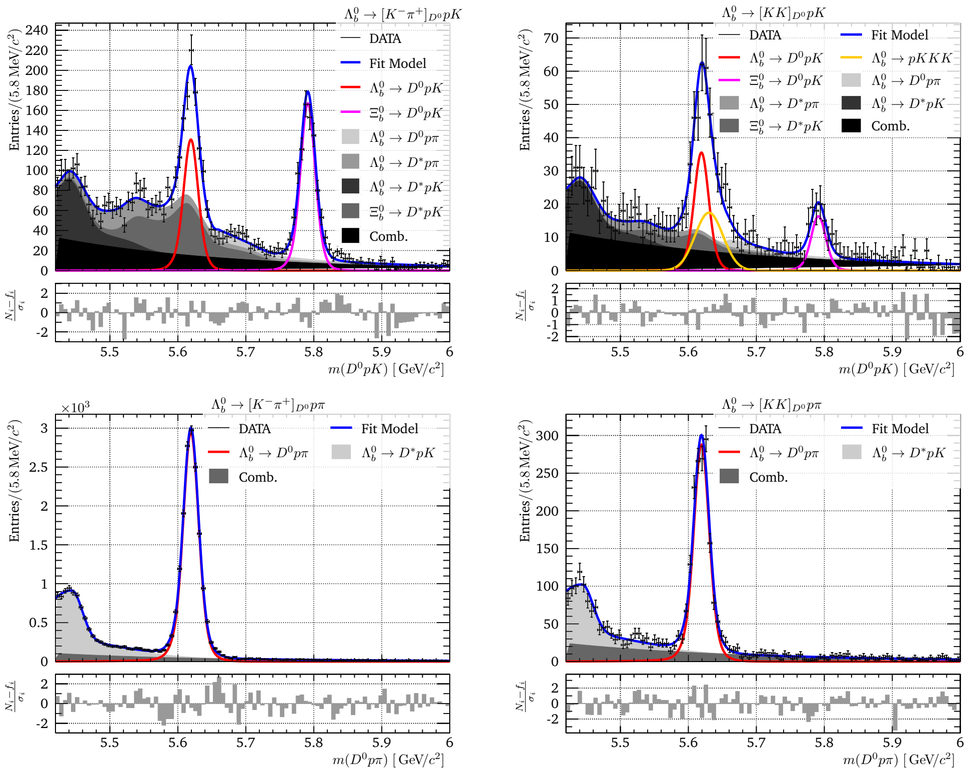

Fig. J.11.: Preliminary fit to $m(D^0pK)$ and $m(D^0p\pi)$ in the Λ^* Dalitz subregion ($m^2(D^0p) > 14\,\mathrm{GeV}^2/c^4$).

Listing J.15: Parameters of preliminary fit to $m(D^0pK)$ and $m(D^0p\pi)$ in the Λ^* Dalitz subregion ($m^2(D^0p) > 14\,\mathrm{GeV}^2/c^4$).

```
/--------------------------------------------------------\
| RooFit Result - Preliminary SimFit to Full m(Dph) DATA |
| DATA in L*-resonance region                             |
\--------------------------------------------------------/

Constant Parameter            Value
--------------------------   ------------
B_{D02KK}                     4.0800e-03
B_{Lb2D0ppi}                  6.3000e-04
effR_{11,Lb,D0pK2D0ppi,KK}    1.2302e+00
effR_{11,Lb,D0pK2D0ppi,Kpi}   1.2133e+00
effR_{11,Lb,pKKK2D0ppi,KK}    2.9570e-02
effR_{12,Lb,D0pK2D0ppi,KK}    1.1548e+00
effR_{12,Lb,D0pK2D0ppi,Kpi}   1.0115e+00
effR_{12,Lb,pKKK2D0ppi,KK}    2.1733e-02
effR_{r2,Lb,D0pK2D0ppi,KK}    1.0457e+00
effR_{r2,Lb,D0pK2D0ppi,Kpi}   1.0415e+00
effR_{r2,Lb,pKKK2D0ppi,KK}    1.7829e-02
m_pRecLb_mD0pK_GammaPion_f    3.5300e-01

Floating Parameter            FinalValue +/- Error     GblCorr.
--------------------------   ------------------------  --------
#lambda_{11,D0pK,KK}         -4.1402e-03 +/-  2.55e-03  <none>
#lambda_{11,D0pK,Kmpip}      -5.0824e-03 +/-  4.48e-03  <none>
#lambda_{11,D0ppi,KK}        -4.4039e-03 +/-  1.03e-03  <none>
#lambda_{11,D0ppi,Kmpip}     -6.7284e-03 +/-  9.62e-04  <none>
#lambda_{12,D0pK,KK}         -3.5630e-03 +/-  2.65e-03  <none>
#lambda_{12,D0pK,Kmpip}      -8.7962e-03 +/-  1.91e-02  <none>
#lambda_{12,D0ppi,KK}        -3.6265e-03 +/-  6.43e-04  <none>
#lambda_{12,D0ppi,Kmpip}     -5.0451e-03 +/-  5.32e-04  <none>
#lambda_{r2,D0pK,KK}         -3.1717e-03 +/-  7.12e-04  <none>
#lambda_{r2,D0pK,Kmpip}      -3.8682e-03 +/-  6.60e-04  <none>
#lambda_{r2,D0ppi,KK}        -3.7451e-03 +/-  3.57e-04  <none>
#lambda_{r2,D0ppi,Kmpip}     -3.7725e-03 +/-  4.24e-04  <none>
F_{Lb2pKKK}                   1.3599e-05 +/-  1.24e-06  <none>
N_{11,Bkg,mD0pK,KK}           3.1876e+01 +/-  3.72e+01  <none>
N_{11,Bkg,mD0pK,Kmpip}        4.6082e+01 +/-  1.83e+02  <none>
N_{11,Bkg,mD0ppi,KK}          7.2663e+01 +/-  1.21e+01  <none>
N_{11,Bkg,mD0ppi,Kmpip}       3.0831e+02 +/-  5.69e+01  <none>
N_{11,Lb2D0ppi,KK}            7.5635e+01 +/-  4.00e+00  <none>
N_{11,Lb2D0ppi,Kmpip}         7.7295e+02 +/-  3.63e+01  <none>
N_{11,Lb2D0ppi,mD0pK,KK}      3.2377e+00 +/-  7.98e+00  <none>
N_{11,Lb2D0ppi,mD0pK,Kmpip}   1.3220e+01 +/-  2.88e+01  <none>
N_{11,Lb2Dst0ppi,mD0pK,KK}    6.1173e+00 +/-  1.29e+01  <none>
N_{11,Lb2Dst0ppi,mD0pK,Kmpip} 4.4855e+01 +/-  9.13e+01  <none>
N_{12,Bkg,mD0pK,KK}           5.3223e+01 +/-  5.19e+01  <none>
N_{12,Bkg,mD0pK,Kmpip}        6.4802e+00 +/-  1.19e+02  <none>
N_{12,Bkg,mD0ppi,KK}          1.7145e+02 +/-  1.88e+01  <none>
N_{12,Bkg,mD0ppi,Kmpip}       6.8594e+02 +/-  7.43e+01  <none>
N_{r2,Bkg,mD0pK,KK}           4.2764e+02 +/-  9.94e+01  <none>
N_{r2,Bkg,mD0pK,Kmpip}        1.2533e+03 +/-  3.69e+02  <none>
N_{r2,Bkg,mD0ppi,KK}          7.4883e+02 +/-  5.10e+01  <none>
N_{r2,Bkg,mD0ppi,Kmpip}       2.9589e+03 +/-  2.76e+02  <none>
R_{Lb,Dst2D,K}                1.2633e+00 +/-  2.46e+00  <none>
R_{Lb,Dst2D,pi}               1.9664e+00 +/-  2.50e-01  <none>
R_{Lb,KK}                     1.0751e-01 +/-  1.49e-02  <none>
R_{Lb,Kpi}                    3.9802e-02 +/-  3.56e-03  <none>
R_{Xib,Dst2D,K}               1.1772e+00 +/-  7.47e-01  <none>
R_{Xib,KK}                    4.9628e-02 +/-  6.95e-03  <none>
R_{Xib,Kpi}                   5.0999e-02 +/-  2.02e-03  <none>
addGauss_f                    7.4234e-01 +/-  4.23e-02  <none>
addGauss_sigma                9.1460e+00 +/-  5.85e-01  <none>
dM_{MC,shift,Dst}            -1.2326e+01 +/-  2.14e+00  <none>
dM_{MC,shift}                -1.0819e+00 +/-  1.08e-01  <none>
dM_{Xib,Lb}                   1.7209e+02 +/-  4.99e-01  <none>
m_pRecLb_mD0pK_Pion_fPol      1.2783e-01 +/-  8.33e-02  <none>
m_pRecLb_mD0ppi_f             5.7301e-01 +/-  2.19e-02  <none>
m_pRecLb_mD0ppi_mean          5.4441e+03 +/-  1.81e+00  <none>
m_pRecLb_mD0ppi_sigma11       4.0912e+01 +/-  1.08e+01  <none>
m_pRecLb_mD0ppi_sigma12       1.5371e+01 +/-  1.37e+00  <none>
m_pRecLb_mD0ppi_sigma2        7.6861e+01 +/-  6.12e+00  <none>
```

```
s_{S,12,Lb2D0ppi,mD0pK}       4.7693e+00 +/-  1.05e+01  <none>
s_{S,12,Lb2D0ppi}             2.5759e+00 +/-  1.33e-01  <none>
s_{S,12,pRecLb,mD0pK}         3.7139e+00 +/-  7.76e+00  <none>
s_{S,12,pRecLb,mD0ppi}        2.5463e+00 +/-  3.56e-01  <none>
s_{S,12,pRecXib}              4.0182e+00 +/-  2.54e+00  <none>
s_{S,r2,Lb2D0ppi,mD0pK}       7.4660e+00 +/-  1.67e+01  <none>
s_{S,r2,Lb2D0ppi}             1.6838e+01 +/-  7.95e-01  <none>
s_{S,r2,pRecLb,mD0pK}         1.5468e+01 +/-  3.05e+01  <none>
s_{S,r2,pRecLb,mD0ppi}        1.7287e+01 +/-  2.18e+00  <none>
s_{S,r2,pRecXib}              1.8373e+01 +/-  1.14e+01  <none>


Goodness of Fit:
-> #chi^{2}/DoF = 0.829506
->     #chi^{2} = 645.356
->          DoF = 778
->        p-val = 0.999813
Sum of Fitted Norms:
->  Lb  -> D0pK  , D0 -> Kmpip = 657.024+/-48.7735
->               , D0 -> KK    = 177.363+/-19.5021
->  Xib -> D0pK  , D0 -> Kmpip = 841.851+/-27.4651
->               , D0 -> KK    = 81.8723+/-9.2324
->  Lb  -> D0ppi , D0 -> Kmpip = 15778.9+/-146.192
->               , D0 -> KK    = 1543.99+/-35.6347
```

J.3.2 Fit to Separate D^0 and $\Lambda_b^0/\overline{\Lambda}_b^0$ Samples

Figure J.12 shows the preliminary fit to $m(D^0pK)$ and $m(D^0p\pi)$ with acceptance weights, as described in section 5.3. A list of all fit parameters is shown in listings J.16 to J.19.

Listing J.16: Parameters of Λ_b^0-type fit to $m(D^0pK)$ with $D^0 \to K^-\pi^+$ in the Λ^* Dalitz subregion ($m^2(D^0p) > 14\,\mathrm{GeV}^2/c^4$).

```
/--------------------------------------------------\
| RooFit Result - SimFit to m(Dp+h-) with D->K-pi+ |
| DATA in L*-resonance region                      |
\--------------------------------------------------/

Constant Parameter            Value
--------------------------   ------------
R_{Lb,Dst2D,pi}               1.9785e+00
addGauss_f                    7.4282e-01
addGauss_sigma                9.1391e+00
dM_{MC,shift,Dst}            -1.2270e+01
dM_{MC,shift}                -1.0826e+00
dM_{Xib,Lb}                   1.7209e+02
effR_{11,Lb,D0pK2D0ppi,Kpi}   1.2133e+00
effR_{12,Lb,D0pK2D0ppi,Kpi}   1.0115e+00
effR_{r2,Lb,D0pK2D0ppi,Kpi}   1.0415e+00
m_pRecLb_mD0ppi_f             5.7321e-01
m_pRecLb_mD0ppi_mean          5.4441e+03
m_pRecLb_mD0ppi_sigma11       4.0896e+01
m_pRecLb_mD0ppi_sigma12       1.5367e+01
m_pRecLb_mD0ppi_sigma2        7.6765e+01
s_{S,12,Lb2D0ppi,mD0pK}       4.7240e+00
s_{S,12,Lb2D0ppi}             2.5760e+00
s_{S,12,pRecLb,mD0pK}         3.6081e+00
s_{S,12,pRecLb,mD0ppi}        2.5600e+00
s_{S,12,pRecXib}              3.8390e+00
s_{S,r2,Lb2D0ppi,mD0pK}       7.0578e+00
s_{S,r2,Lb2D0ppi}             1.6837e+01
s_{S,r2,pRecLb,mD0pK}         1.4486e+01
s_{S,r2,pRecLb,mD0ppi}        1.7382e+01
s_{S,r2,pRecXib}              1.7511e+01

Floating Parameter            FinalValue +/- Error     GblCorr.
```

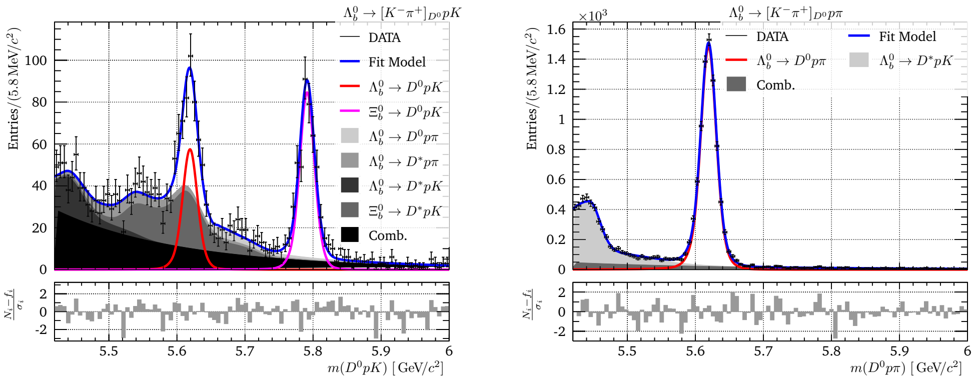

(a) $\mathit{\Lambda}_b^0$-type - $m(D^0ph^-)$, with $D^0 \to K^-\pi^+$

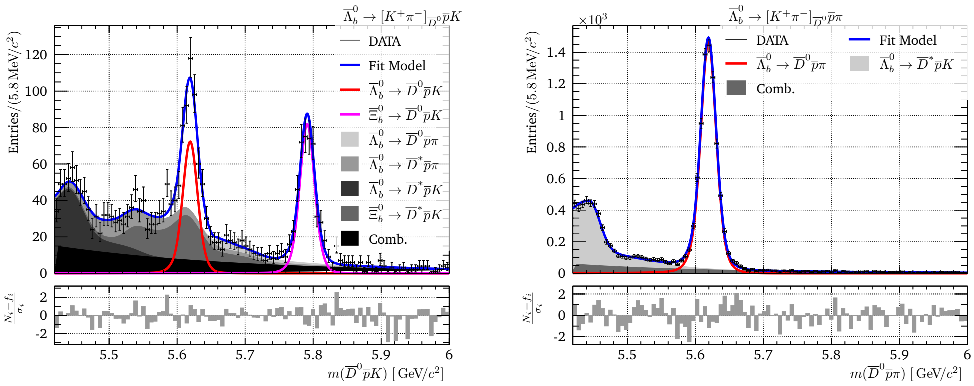

(b) $\overline{\mathit{\Lambda}}_b^0$-type - $m(D^0\overline{p}h^+)$, with $D^0 \to K^-\pi^+$

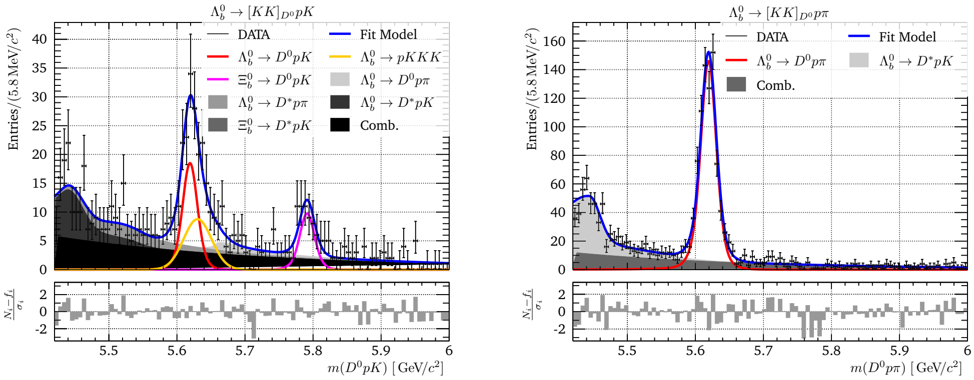

(c) $\mathit{\Lambda}_b^0$-type - $m(D^0ph^-)$, with $D^0 \to KK$

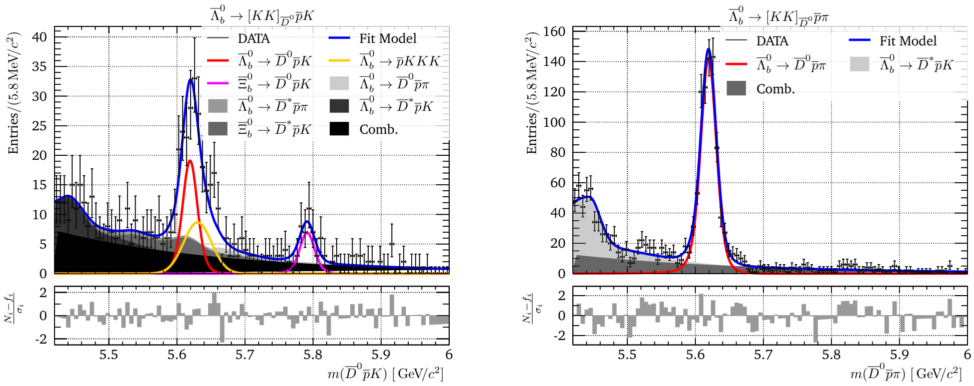

(d) $\overline{\mathit{\Lambda}}_b^0$-type - $m(D^0\overline{p}h^+)$, with $D^0 \to KK$

Fig. J.12.: Fits to $m(D^0pK)$ and $m(D^0p\pi)$ in the $\mathit{\Lambda}^*$ Dalitz subregion ($m^2(D^0p) > 14\,\mathrm{GeV}^2/c^4$) and split for the D^0 modes and $\mathit{\Lambda}_b^0$-types.

```
--------------------------   ------------------------  --------
#lambda_{11,D0pK,Kmpip}      -6.1206e-03 +/-  1.85e-03  <none>
#lambda_{11,D0ppi,Kmpip}     -5.6512e-03 +/-  8.28e-04  <none>
#lambda_{12,D0pK,Kmpip}      -1.0551e-02 +/-  5.08e-03  <none>
#lambda_{12,D0ppi,Kmpip}     -5.3700e-03 +/-  5.21e-04  <none>
#lambda_{r2,D0pK,Kmpip}      -4.7413e-03 +/-  5.14e-04  <none>
#lambda_{r2,D0ppi,Kmpip}     -3.2895e-03 +/-  2.84e-04  <none>
N_{11,Lb2D0ppi,Kmpip}         3.8893e+02 +/-  4.31e+00  <none>
N_{Bkg,D0pK,Kmpip}            9.1199e+02 +/-  1.51e+02  <none>
N_{Bkg,D0ppi,Kmpip}           1.8959e+03 +/-  8.78e+01  <none>
N_{Lb2D0ppi,mD0pK,Kmpip}      8.3009e+01 +/-  2.38e+01  <none>
N_{Lb2Dst0ppi,mD0pK,Kmpip}    1.8085e+02 +/-  9.02e+01  <none>
R_{Lb,Dst2D,K}                1.7222e+00 +/-  6.71e-01  <none>
R_{Lb,Kpi}                    3.4739e-02 +/-  3.91e-03  <none>
R_{Xib,Dst2D,K}               1.0854e+00 +/-  1.61e-01  <none>
R_{Xib,Kpi}                   5.1310e-02 +/-  2.82e-03  <none>
s_{B,12,D0pK,Kmpip}           1.4219e+00 +/-  8.10e-01  <none>
s_{B,12,D0ppi,Kmpip}          2.2045e+00 +/-  3.35e-01  <none>
s_{B,r2,D0pK,Kmpip}           2.0579e+01 +/-  5.72e+00  <none>
s_{B,r2,D0ppi,Kmpip}          8.9628e+00 +/-  1.20e+00  <none>


Goodness of Fit:
-> #chi^{2}/DoF = 0.734733
->     #chi^{2} = 301.241
->          DoF = 410
->        p-val = 0.999985
Sum of Fitted Norms:
->  Lb   -> D0pK  , D0 -> Kmpip = 288.528+/-26.8864
->  Xib  -> D0pK  , D0 -> Kmpip = 426.158+/-19.0526
->  Lb   -> D0ppi , D0 -> Kmpip = 7939.07+/-73.5668
```

Listing J.17: Parameters of $\overline{\Lambda}{}_b^0$-type fit to $m(D^0pK)$ with $D^0 \to K^-\pi^+$ in the Λ^* Dalitz subregion ($m^2(D^0p) > 14\,\mathrm{GeV}^2/c^4$). Constant parameter are the same as for the Λ_b^0-type fit in listing J.16.

```
/--------------------------- -----------------------\
| RooFit Result - SimFit to m(Dp-h+) with D->K+pi- |
| DATA in L*-resonance region                       |
\---------------------------------------------------/

Constant Parameter            Value
--------------------------   ------------
>> same as Lb-type fit of D0 -> Kpi

Floating Parameter            FinalValue +/- Error     GblCorr.
--------------------------   ------------------------  --------
#lambda_{11,D0pK,Kmpip}      -4.2145e-03 +/-  2.88e-03  <none>
#lambda_{11,D0ppi,Kmpip}     -8.0824e-03 +/-  1.01e-03  <none>
#lambda_{12,D0pK,Kmpip}      -2.5827e-08 +/-  4.06e-05  <none>
#lambda_{12,D0ppi,Kmpip}     -4.7587e-03 +/-  4.95e-04  <none>
#lambda_{r2,D0pK,Kmpip}      -3.6505e-03 +/-  4.87e-04  <none>
#lambda_{r2,D0ppi,Kmpip}     -4.2662e-03 +/-  2.67e-04  <none>
N_{11,Lb2D0ppi,Kmpip}         3.8386e+02 +/-  4.36e+00  <none>
N_{Bkg,D0pK,Kmpip}            6.3259e+02 +/-  7.94e+01  <none>
N_{Bkg,D0ppi,Kmpip}           2.0710e+03 +/-  9.19e+01  <none>
N_{Lb2D0ppi,mD0pK,Kmpip}      7.8006e+01 +/-  2.80e+01  <none>
N_{Lb2Dst0ppi,mD0pK,Kmpip}    2.9630e+02 +/-  5.87e+01  <none>
R_{Lb,Dst2D,K}                1.2341e+00 +/-  2.19e-01  <none>
R_{Lb,Kpi}                    4.4265e-02 +/-  4.18e-03  <none>
R_{Xib,Dst2D,K}               1.1693e+00 +/-  2.00e-01  <none>
R_{Xib,Kpi}                   5.0302e-02 +/-  2.82e-03  <none>
s_{B,12,D0pK,Kmpip}           4.7727e-01 +/-  8.53e-01  <none>
s_{B,12,D0ppi,Kmpip}          2.2429e+00 +/-  3.42e-01  <none>
s_{B,r2,D0pK,Kmpip}           3.6731e+01 +/-  2.26e+01  <none>
s_{B,r2,D0ppi,Kmpip}          1.0251e+01 +/-  1.38e+00  <none>


Goodness of Fit:
-> #chi^{2}/DoF = 0.750027
->     #chi^{2} = 307.511
```

```
->          DoF = 410
->        p-val = 0.999953
Sum of Fitted Norms:
->  Lb  -> D0pK  , D0 -> Kmpip (cc) = 362.855+/-28.2772
->  Xib -> D0pK  , D0 -> Kmpip (cc) = 412.339+/-18.8442
->  Lb  -> D0ppi , D0 -> Kmpip (cc) = 7835.63+/-74.3931
```

Listing J.18: Parameters of Λ_b^0-type fit to $m(D^0pK)$ with $D^0 \to KK$ in the Λ^* Dalitz subregion ($m^2(D^0p) > 14\,\mathrm{GeV}^2/c^4$).

```
/-----------------------------------------------\
| RooFit Result - SimFit to m(Dp+h-) with D->KK |
| DATA in L*-resonance region                   |
\-----------------------------------------------/

Constant Parameter            Value
--------------------------    ------------
B_{D02KK}                     4.0800e-03
B_{Lb2D0ppi}                  6.3000e-04
B_{Lb2pKKK}                   1.3607e-05
R_{Lb,Dst2D,pi}               1.9785e+00
addGauss_f                    7.4282e-01
addGauss_sigma                9.1391e+00
dM_{MC,shift,Dst}            -1.2270e+01
dM_{MC,shift}                -1.0826e+00
dM_{Xib,Lb}                   1.7209e+02
effR_{11,Lb,D0pK2D0ppi,KK}    1.2302e+00
effR_{11,Lb,pKKK2D0ppi,KK}    2.9570e-02
effR_{12,Lb,D0pK2D0ppi,KK}    1.1548e+00
effR_{12,Lb,pKKK2D0ppi,KK}    2.1733e-02
effR_{r2,Lb,D0pK2D0ppi,KK}    1.0457e+00
effR_{r2,Lb,pKKK2D0ppi,KK}    1.7829e-02
m_pRecLb_mD0ppi_f             5.7321e-01
m_pRecLb_mD0ppi_mean          5.4441e+03
m_pRecLb_mD0ppi_sigma11       4.0896e+01
m_pRecLb_mD0ppi_sigma12       1.5367e+01
m_pRecLb_mD0ppi_sigma2        7.6765e+01
s_{S,12,Lb2D0ppi,mD0pK}       4.7240e+00
s_{S,12,Lb2D0ppi}             2.5760e+00
s_{S,12,pRecLb,mD0pK}         3.6081e+00
s_{S,12,pRecLb,mD0ppi}        2.5600e+00
s_{S,12,pRecXib}              3.8390e+00
s_{S,r2,Lb2D0ppi,mD0pK}       7.0578e+00
s_{S,r2,Lb2D0ppi}             1.6837e+01
s_{S,r2,pRecLb,mD0pK}         1.4486e+01
s_{S,r2,pRecLb,mD0ppi}        1.7382e+01
s_{S,r2,pRecXib}              1.7511e+01

Floating Parameter            FinalValue +/- Error     GblCorr.
--------------------------   ------------------------  --------
#lambda_{11,D0pK,KK}         -1.1981e-03 +/-   3.35e-03  <none>
#lambda_{11,D0ppi,KK}        -5.4305e-03 +/-   1.40e-03  <none>
#lambda_{12,D0pK,KK}         -2.9932e-03 +/-   1.10e-02  <none>
#lambda_{12,D0ppi,KK}        -3.0545e-03 +/-   7.99e-04  <none>
#lambda_{r2,D0pK,KK}         -3.1454e-03 +/-   8.92e-04  <none>
#lambda_{r2,D0ppi,KK}        -3.6251e-03 +/-   4.58e-04  <none>
N_{11,Lb2D0ppi,KK}            3.8307e+01 +/-   1.41e+00  <none>
N_{Bkg,D0pK,KK}               2.6917e+02 +/-   9.98e+01  <none>
N_{Bkg,D0ppi,KK}              5.0301e+02 +/-   3.54e+01  <none>
N_{Lb2D0ppi,mD0pK,KK}         2.6782e+01 +/-   1.80e+01  <none>
N_{Lb2Dst0ppi,mD0pK,KK}       7.0406e+01 +/-   5.77e+01  <none>
R_{Lb,Dst2D,K}                1.1986e+00 +/-   4.44e-01  <none>
R_{Lb,KK}                     1.1102e-01 +/-   1.84e-02  <none>
R_{Xib,Dst2D,K}               3.8781e+02 +/-   7.83e+03  <none>
R_{Xib,KK}                    5.8629e-02 +/-   1.08e-02  <none>
s_{B,12,D0pK,KK}              7.6902e-01 +/-   2.71e+00  <none>
s_{B,12,D0ppi,KK}             2.3177e+00 +/-   5.57e-01  <none>
s_{B,r2,D0pK,KK}              2.4293e+01 +/-   1.43e+01  <none>
s_{B,r2,D0ppi,KK}             9.1268e+00 +/-   1.95e+00  <none>


```

```
Goodness of Fit:
-> #chi^{2}/DoF = 0.64956
->     #chi^{2} = 174.082
->          DoF = 268
->        p-val = 0.999998
Sum of Fitted Norms:
->  Lb  -> D0pK  , D0 -> KK = 92.7548+/-11.9563
->  Xib -> D0pK  , D0 -> KK = 48.9838+/-7.2844
->  Lb  -> D0ppi , D0 -> KK = 781.941+/-24.112
```

Listing J.19: Parameters of $\overline{\Lambda}{}_b^0$-type fit to $m(D^0pK)$ with $D^0 \to KK$ in the Λ^* Dalitz subregion ($m^2(D^0p) > 14\,\mathrm{GeV}^2/c^4$). Constant parameter are the same as for the Λ_b^0-type fit in listing J.18.

```
/-----------------------------------------------\
| RooFit Result - SimFit to m(Dp-h+) with D->KK |
| DATA in L*-resonance region                   |
\-----------------------------------------------/

Constant Parameter            Value
--------------------------   ------------
>> same as Lb-type fit of D0 -> KK

Floating Parameter            FinalValue +/- Error     GblCorr.
--------------------------   ------------------------  --------
#lambda_{11,D0pK,KK}         -6.1380e-03 +/-  2.15e-03  <none>
#lambda_{11,D0ppi,KK}        -3.4520e-03 +/-  1.36e-03  <none>
#lambda_{12,D0pK,KK}         -3.9520e-03 +/-  1.85e-03  <none>
#lambda_{12,D0ppi,KK}        -4.4039e-03 +/-  9.54e-04  <none>
#lambda_{r2,D0pK,KK}         -3.8218e-03 +/-  1.17e-03  <none>
#lambda_{r2,D0ppi,KK}        -3.8628e-03 +/-  4.50e-04  <none>
N_{11,Lb2D0ppi,KK}            3.7375e+01 +/-  1.41e+00  <none>
N_{Bkg,D0pK,KK}               2.7921e+02 +/-  1.20e+02  <none>
N_{Bkg,D0ppi,KK}              4.9067e+02 +/-  3.53e+01  <none>
N_{Lb2D0ppi,mD0pK,KK}         1.5621e+01 +/-  2.02e+01  <none>
N_{Lb2Dst0ppi,mD0pK,KK}       2.1204e+01 +/-  6.40e+01  <none>
R_{Lb,Dst2D,K}                1.7124e+00 +/-  1.25e+00  <none>
R_{Lb,KK}                     1.1643e-01 +/-  2.39e-02  <none>
R_{Xib,Dst2D,K}               8.7982e-01 +/-  7.04e-01  <none>
R_{Xib,KK}                    4.2273e-02 +/-  9.32e-03  <none>
s_{B,12,D0pK,KK}              2.1570e+00 +/-  1.07e+00  <none>
s_{B,12,D0ppi,KK}             2.3781e+00 +/-  6.43e-01  <none>
s_{B,r2,D0pK,KK}              9.4916e+00 +/-  2.80e+00  <none>
s_{B,r2,D0ppi,KK}             1.1583e+01 +/-  2.72e+00  <none>


Goodness of Fit:
-> #chi^{2}/DoF = 0.771036
->     #chi^{2} = 206.638
->          DoF = 268
->        p-val = 0.997852
Sum of Fitted Norms:
->  Lb  -> D0pK  , D0 -> KK (cc) = 94.9093+/-15.4655
->  Xib -> D0pK  , D0 -> KK (cc) = 34.459+/-6.14716
->  Lb  -> D0ppi , D0 -> KK (cc) = 762.91+/-24.0015
```

J.4 Acceptance Weighted - $\mathit{\Lambda}^*$ Resonances

J.4.1 Preliminary Fit to $m(D^0ph)$

Figure J.13 shows the preliminary fit to $m(D^0pK)$ and $m(D^0p\pi)$ in the $\mathit{\Lambda}^*$ Dalitz subregion ($m^2(D^0p) > 14\,\mathrm{GeV}^2/c^4$) with acceptance weights, as described in section 5.3. A list of all fit parameters is shown in listing J.20.

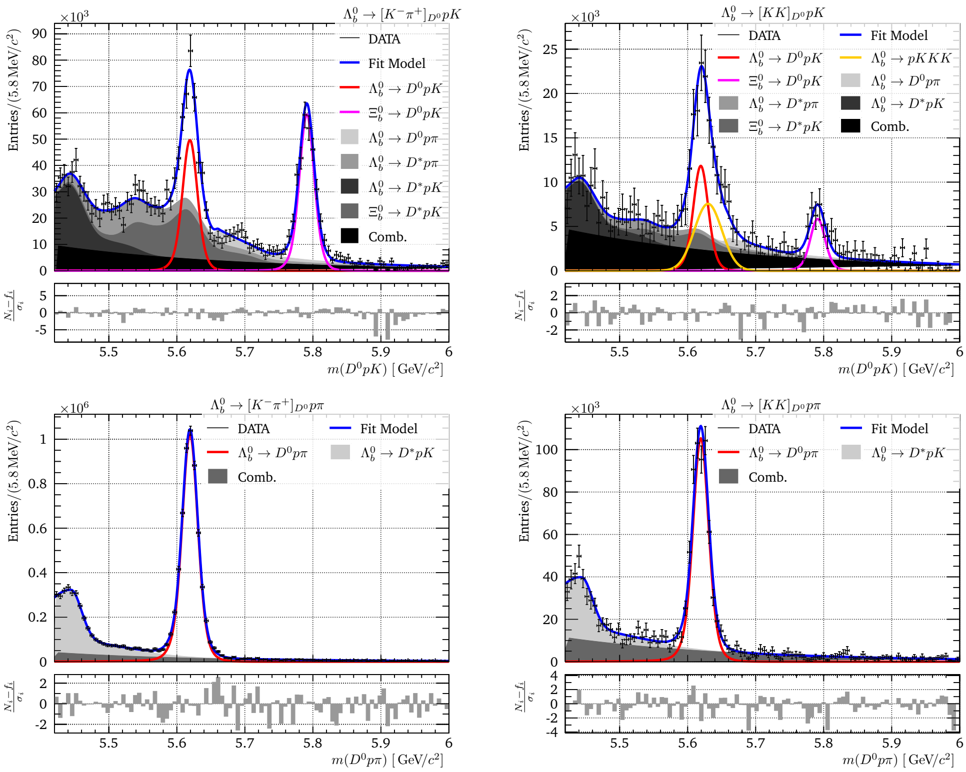

Fig. J.13.: Preliminary fit to $m(D^0pK)$ and $m(D^0p\pi)$ in the $\mathit{\Lambda}^*$ Dalitz subregion ($m^2(D^0p) > 14\,\mathrm{GeV}^2/c^4$) and acceptance weights.

Listing J.20: Parameters of preliminary fit to $m(D^0pK)$ and $m(D^0p\pi)$ in the $\mathit{\Lambda}^*$ Dalitz subregion ($m^2(D^0p) > 14\,\mathrm{GeV}^2/c^4$) and acceptance weights.

```
/--------------------------------------------------------\
| RooFit Result - Preliminary SimFit to Full m(Dph) DATA |
| DATA with acceptance weights in L*-resonance region    |
\--------------------------------------------------------/

Constant Parameter            Value
--------------------------   ------------
B_{D02KK}                     4.0800e-03
B_{Lb2D0ppi}                  6.3000e-04
effR_{11,Lb,D0pK2D0ppi,KK}    1.1679e+00
effR_{11,Lb,D0pK2D0ppi,Kpi}   1.1679e+00
effR_{11,Lb,pKKK2D0ppi,KK}    2.7813e-02
effR_{11,Xib,D0pK2D0ppi,KK}   1.3254e+00
effR_{11,Xib,D0pK2D0ppi,Kpi}  1.3254e+00
effR_{12,Lb,D0pK2D0ppi,KK}    9.9667e-01
effR_{12,Lb,D0pK2D0ppi,Kpi}   9.9667e-01
```

```
effR_{12,Lb,pKKK2D0ppi,KK}    2.0775e-02
effR_{12,Xib,D0pK2D0ppi,KK}   9.6292e-01
effR_{12,Xib,D0pK2D0ppi,Kpi}  9.6292e-01
effR_{r2,Lb,D0pK2D0ppi,KK}    1.0127e+00
effR_{r2,Lb,D0pK2D0ppi,Kpi}   1.0127e+00
effR_{r2,Lb,pKKK2D0ppi,KK}    1.6973e-02
effR_{r2,Xib,D0pK2D0ppi,KK}   1.0425e+00
effR_{r2,Xib,D0pK2D0ppi,Kpi}  1.0425e+00
m_pRecLb_mD0pK_GammaPion_f    3.5300e-01

Floating Parameter            FinalValue +/- Error     GblCorr.
--------------------------   ------------------------  --------
#lambda_{11,D0pK,KK}         -3.7099e-03 +/-  1.85e-03  <none>
#lambda_{11,D0pK,Kmpip}      -3.0669e-02 +/-  8.83e-03  <none>
#lambda_{11,D0ppi,KK}        -4.5371e-03 +/-  9.80e-04  <none>
#lambda_{11,D0ppi,Kmpip}     -6.8087e-03 +/-  6.66e-04  <none>
#lambda_{12,D0pK,KK}         -3.6810e-03 +/-  1.58e-03  <none>
#lambda_{12,D0pK,Kmpip}      -8.7611e-03 +/-  1.65e-01  <none>
#lambda_{12,D0ppi,KK}        -4.2166e-03 +/-  5.98e-04  <none>
#lambda_{12,D0ppi,Kmpip}     -5.0851e-03 +/-  4.46e-04  <none>
#lambda_{r2,D0pK,KK}         -3.3558e-03 +/-  1.27e-03  <none>
#lambda_{r2,D0pK,Kmpip}      -3.8160e-03 +/-  2.99e-03  <none>
#lambda_{r2,D0ppi,KK}        -3.5928e-03 +/-  3.69e-04  <none>
#lambda_{r2,D0ppi,Kmpip}     -3.6612e-03 +/-  2.96e-04  <none>
F_{Lb2pKKK}                   1.5998e-05 +/-  6.09e-06  <none>
N_{11,Bkg,mD0pK,KK}           1.8777e+04 +/-  1.18e+04  <none>
N_{11,Bkg,mD0pK,Kmpip}        4.3862e-07 +/-  8.91e-01  <none>
N_{11,Bkg,mD0ppi,KK}          4.8917e+04 +/-  7.52e+03  <none>
N_{11,Bkg,mD0ppi,Kmpip}       1.9327e+05 +/-  1.85e+04  <none>
N_{11,Lb2D0ppi,KK}            4.8210e+04 +/-  3.11e+03  <none>
N_{11,Lb2D0ppi,Kmpip}         4.6735e+05 +/-  9.15e+03  <none>
N_{11,Lb2D0ppi,mD0pK,KK}      2.5487e+03 +/-  4.14e+03  <none>
N_{11,Lb2D0ppi,mD0pK,Kmpip}   1.1995e+04 +/-  6.97e+03  <none>
N_{11,Lb2Dst0ppi,mD0pK,KK}    4.7142e+03 +/-  4.78e+03  <none>
N_{11,Lb2Dst0ppi,mD0pK,Kmpip} 4.3641e+04 +/-  1.88e+04  <none>
N_{12,Bkg,mD0pK,KK}           3.9431e+04 +/-  3.64e+04  <none>
N_{12,Bkg,mD0pK,Kmpip}        7.2266e-06 +/-  2.03e+00  <none>
N_{12,Bkg,mD0ppi,KK}          1.6437e+05 +/-  1.63e+04  <none>
N_{12,Bkg,mD0ppi,Kmpip}       4.2688e+05 +/-  3.46e+04  <none>
N_{r2,Bkg,mD0pK,KK}           1.4499e+05 +/-  1.38e+05  <none>
N_{r2,Bkg,mD0pK,Kmpip}        3.8767e+05 +/-  1.21e+06  <none>
N_{r2,Bkg,mD0ppi,KK}          2.3652e+05 +/-  1.57e+04  <none>
N_{r2,Bkg,mD0ppi,Kmpip}       8.8072e+05 +/-  5.49e+04  <none>
R_{Lb,Dst2D,K}                9.5843e-01 +/-  1.10e+00  <none>
R_{Lb,Dst2D,pi}               1.9343e+00 +/-  6.07e-02  <none>
R_{Lb,KK}                     1.0267e-01 +/-  5.83e-02  <none>
R_{Lb,Kpi}                    4.4513e-02 +/-  3.34e-02  <none>
R_{Xib,Dst2D,K}               1.2342e+00 +/-  2.73e+00  <none>
R_{Xib,KK}                    4.9695e-02 +/-  1.96e-02  <none>
R_{Xib,Kpi}                   5.2077e-02 +/-  9.44e-03  <none>
addGauss_f                    7.5688e-01 +/-  4.08e-02  <none>
addGauss_sigma                9.2283e+00 +/-  4.13e-01  <none>
dM_{MC,shift,Dst}            -1.1626e+01 +/-  3.66e+00  <none>
dM_{MC,shift}                -1.0194e+00 +/-  1.31e-01  <none>
dM_{Xib,Lb}                   1.7188e+02 +/-  2.18e+00  <none>
m_pRecLb_mD0pK_Pion_fPol      1.3746e-01 +/-  5.01e-01  <none>
m_pRecLb_mD0ppi_f             5.7433e-01 +/-  1.78e-02  <none>
m_pRecLb_mD0ppi_mean          5.4443e+03 +/-  1.28e+00  <none>
m_pRecLb_mD0ppi_sigma11       4.0893e+01 +/-  9.73e+00  <none>
m_pRecLb_mD0ppi_sigma12       1.5428e+01 +/-  9.80e-01  <none>
m_pRecLb_mD0ppi_sigma2        8.0061e+01 +/-  7.14e+00  <none>
s_{S,12,Lb2D0ppi,mD0pK}       3.3618e+00 +/-  5.11e-01  <none>
s_{S,12,Lb2D0ppi}             2.6875e+00 +/-  7.96e-02  <none>
s_{S,12,pRecLb,mD0pK}         2.7940e+00 +/-  6.63e-01  <none>
s_{S,12,pRecLb,mD0ppi}        2.6090e+00 +/-  1.43e-01  <none>
s_{S,12,pRecXib}              3.6577e+00 +/-  3.51e+00  <none>
s_{S,r2,Lb2D0ppi,mD0pK}       2.4630e+00 +/-  1.93e+01  <none>
s_{S,r2,Lb2D0ppi}             8.1328e+00 +/-  3.45e-01  <none>
s_{S,r2,pRecLb,mD0pK}         5.6842e+00 +/-  9.72e+00  <none>
s_{S,r2,pRecLb,mD0ppi}        8.3324e+00 +/-  2.90e-01  <none>
s_{S,r2,pRecXib}              8.5089e+00 +/-  5.96e+00  <none>
```

```


Goodness of Fit:
-> #chi^{2}/DoF = 1.3432
->     #chi^{2} = 1045.01
->          DoF = 778
->        p-val = 4.21173e-10
Fitted Norms (sum):
->  Lb   -> D0pK  , D0 -> Kmpip = 251349+/-140563
->                , D0 -> KK    = 59805.6+/-23691.2
->  Xib -> D0pK  , D0 -> Kmpip = 301582+/-44640.7
->                , D0 -> KK    = 29686.8+/-8057.21
->  Lb   -> D0ppi , D0 -> Kmpip = 5.52422e+06+/-112602
->                , D0 -> KK    = 569852+/-15181.8
```

J.4.2 Fit to Separate D^0 and $\Lambda_b^0/\overline{\Lambda}_b^0$ Samples

Figure J.14 shows the preliminary fit to $m(D^0pK)$ and $m(D^0p\pi)$ with acceptance weights, as described in section 5.3. A list of all fit parameters is shown in listings J.21 to J.24.

Listing J.21: Parameters of Λ_b^0-type fit to $m(D^0pK)$ with $D^0 \to K^-\pi^+$ in the Λ^* Dalitz subregion ($m^2(D^0p) > 14\,\mathrm{GeV}^2/c^4$) and acceptance weights.

```
/------------------------------------------------------\
| RooFit Result - SimFit to m(Dp+h-) with D->K-pi+    |
| DATA with acceptance weights in L*-resonance region |
\------------------------------------------------------/

Constant Parameter              Value
--------------------------    ------------
R_{Lb,Dst2D,pi}                1.9343e+00
addGauss_f                     7.5688e-01
addGauss_sigma                 9.2283e+00
dM_{MC,shift,Dst}             -1.1626e+01
dM_{MC,shift}                 -1.0193e+00
dM_{Xib,Lb}                    1.7188e+02
effR_{11,Lb,D0pK2D0ppi,Kpi}    1.1679e+00
effR_{11,Xib,D0pK2D0ppi,Kpi}   1.3254e+00
effR_{12,Lb,D0pK2D0ppi,Kpi}    9.9667e-01
effR_{12,Xib,D0pK2D0ppi,Kpi}   9.6292e-01
effR_{r2,Lb,D0pK2D0ppi,Kpi}    1.0127e+00
effR_{r2,Xib,D0pK2D0ppi,Kpi}   1.0425e+00
m_pRecLb_mD0ppi_f              5.7433e-01
m_pRecLb_mD0ppi_mean           5.4443e+03
m_pRecLb_mD0ppi_sigma11        4.0893e+01
m_pRecLb_mD0ppi_sigma12        1.5428e+01
m_pRecLb_mD0ppi_sigma2         8.0061e+01
s_{S,12,Lb2D0ppi,mD0pK}        3.3618e+00
s_{S,12,Lb2D0ppi}              2.6875e+00
s_{S,12,pRecLb,mD0pK}          2.7940e+00
s_{S,12,pRecLb,mD0ppi}         2.6090e+00
s_{S,12,pRecXib}               3.6577e+00
s_{S,r2,Lb2D0ppi,mD0pK}        2.4630e+00
s_{S,r2,Lb2D0ppi}              8.1328e+00
s_{S,r2,pRecLb,mD0pK}          5.6842e+00
s_{S,r2,pRecLb,mD0ppi}         8.3324e+00
s_{S,r2,pRecXib}               8.5089e+00

Floating Parameter              FinalValue +/-  Error     GblCorr.
--------------------------    ------------------------  --------
#lambda_{11,D0pK,Kmpip}       -7.1859e-03 +/-  3.12e-03   <none>
#lambda_{11,D0ppi,Kmpip}      -5.6455e-03 +/-  8.39e-04   <none>
#lambda_{12,D0pK,Kmpip}       -1.0056e-02 +/-  4.52e-03   <none>
#lambda_{12,D0ppi,Kmpip}      -5.3059e-03 +/-  5.41e-04   <none>
#lambda_{r2,D0pK,Kmpip}       -4.9578e-03 +/-  6.23e-04   <none>
#lambda_{r2,D0ppi,Kmpip}      -3.1406e-03 +/-  3.09e-04   <none>
```

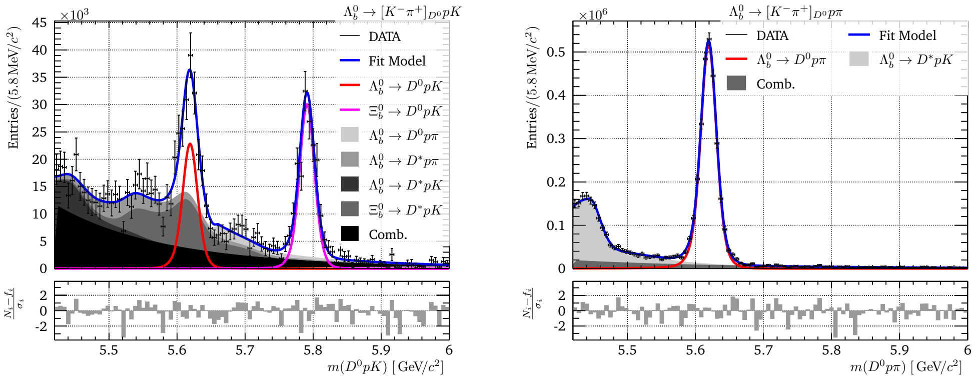

(a) Λ_b^0-type - $m(D^0ph^-)$, with $D^0 \to K^-\pi^+$

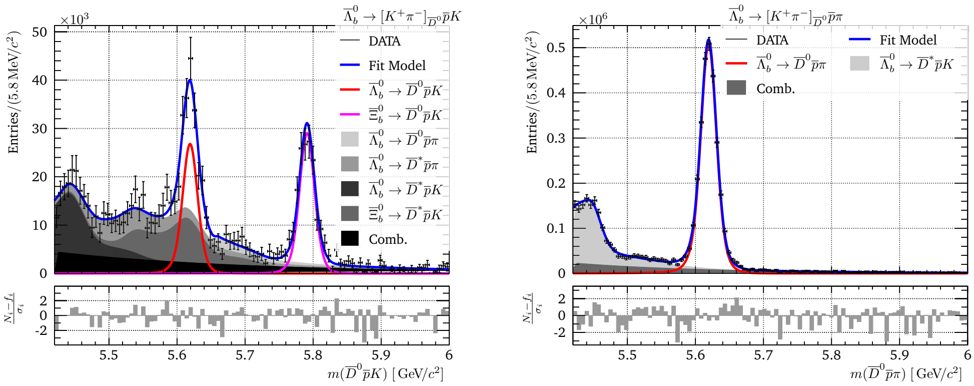

(b) $\overline{\Lambda}_b^0$-type - $m(D^0\overline{p}h^+)$, with $D^0 \to K^-\pi^+$

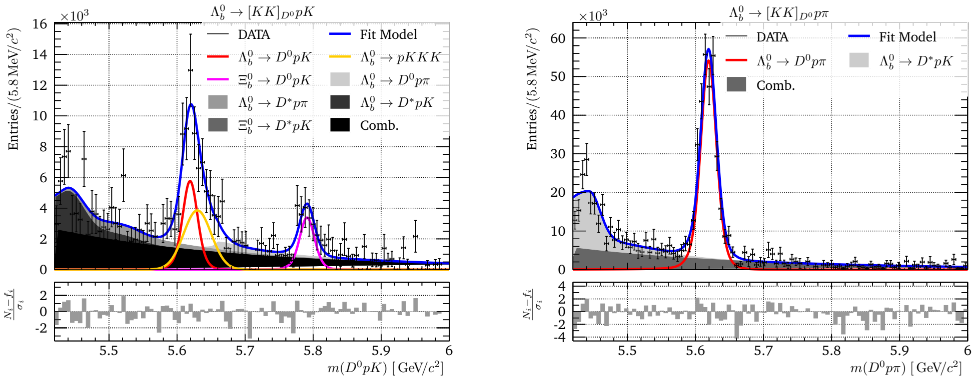

(c) Λ_b^0-type - $m(D^0ph^-)$, with $D^0 \to KK$

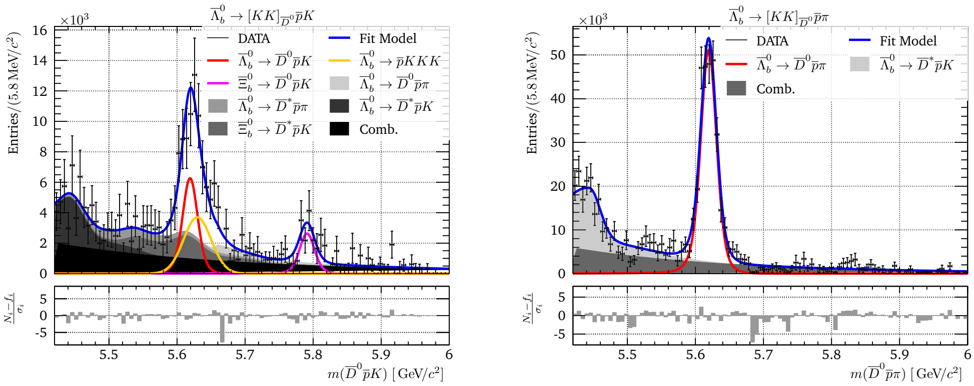

(d) $\overline{\Lambda}_b^0$-type - $m(D^0\overline{p}h^+)$, with $D^0 \to KK$

Fig. J.14.: Fits to $m(D^0pK)$ and $m(D^0p\pi)$ in the Λ^* Dalitz subregion ($m^2(D^0p) > 14\,\text{GeV}^2/c^4$) and acceptance weights, split for the D^0 modes and Λ_b^0-types.

```
N_{11,Lb2D0ppi,Kmpip}         2.3552e+05 +/-  2.84e+03  <none>
N_{Bkg,D0pK,Kmpip}            3.3665e+05 +/-  8.94e+04  <none>
N_{Bkg,D0ppi,Kmpip}           7.2251e+05 +/-  3.57e+04  <none>
N_{Lb2D0ppi,mD0pK,Kmpip}      3.7554e+04 +/-  1.23e+04  <none>
N_{Lb2Dst0ppi,mD0pK,Kmpip}    9.1517e+04 +/-  4.82e+04  <none>
R_{Lb,Dst2D,K}                1.8938e+00 +/-  1.38e+00  <none>
R_{Lb,Kpi}                    4.0637e-02 +/-  4.85e-03  <none>
R_{Xib,Dst2D,K}               1.3117e+00 +/-  2.72e-01  <none>
R_{Xib,Kpi}                   5.2338e-02 +/-  3.06e-03  <none>
s_{B,12,D0pK,Kmpip}           2.3414e+00 +/-  9.82e-01  <none>
s_{B,12,D0ppi,Kmpip}          2.2115e+00 +/-  3.51e-01  <none>
s_{B,r2,D0pK,Kmpip}           1.3895e+01 +/-  7.16e+00  <none>
s_{B,r2,D0ppi,Kmpip}          4.3307e+00 +/-  6.05e-01  <none>


Goodness of Fit:
-> #chi^{2}/DoF = 1.11944
->     #chi^{2} = 458.972
->          DoF = 410
->        p-val = 0.0475049
Fitted Norms (sum):
->  Lb  -> D0pK  , D0 -> Kmpip = 115637+/-9918.93
->  Xib -> D0pK  , D0 -> Kmpip = 152746+/-6343.19
->  Lb  -> D0ppi , D0 -> Kmpip = 2.78392e+06+/-24463.9
```

Listing J.22: Parameters of $\overline{\Lambda}_b^0$-type fit to $m(D^0pK)$ with $D^0 \to K^-\pi^+$ in the Λ^* Dalitz subregion ($m^2(D^0p) > 14\,\mathrm{GeV}^2/c^4$) and acceptance weights. Constant parameter are the same as for the Λ_b^0-type fit in listing J.21.

```
/--------------------------- -------------------------\
| RooFit Result - SimFit to m(Dp-h+) with D->K+pi-    |
| DATA with acceptance weights in L*-resonance region |
\-----------------------------------------------------/

Constant Parameter            Value
--------------------------   ------------
>> same as Lb-type fit of D0 -> Kpi

Floating Parameter            FinalValue +/- Error     GblCorr.
--------------------------   ------------------------  --------
#lambda_{11,D0pK,Kmpip}      -1.3902e-03 +/-  1.83e-02  <none>
#lambda_{11,D0ppi,Kmpip}     -8.1785e-03 +/-  1.02e-03  <none>
#lambda_{12,D0pK,Kmpip}       0.0000e+00 +/-  9.98e-13  <none>
#lambda_{12,D0ppi,Kmpip}     -4.8815e-03 +/-  5.08e-04  <none>
#lambda_{r2,D0pK,Kmpip}      -3.5992e-03 +/-  9.62e-04  <none>
#lambda_{r2,D0ppi,Kmpip}     -4.1771e-03 +/-  2.92e-04  <none>
N_{11,Lb2D0ppi,Kmpip}         2.3174e+05 +/-  3.07e+03  <none>
N_{Bkg,D0pK,Kmpip}            1.9306e+05 +/-  2.28e+04  <none>
N_{Bkg,D0ppi,Kmpip}           7.8007e+05 +/-  3.74e+04  <none>
N_{Lb2D0ppi,mD0pK,Kmpip}      3.6097e+04 +/-  2.51e+04  <none>
N_{Lb2Dst0ppi,mD0pK,Kmpip}    1.4406e+05 +/-  6.78e+04  <none>
R_{Lb,Dst2D,K}                1.0023e+00 +/-  5.25e-01  <none>
R_{Lb,Kpi}                    4.8492e-02 +/-  1.44e-02  <none>
R_{Xib,Dst2D,K}               1.2222e+00 +/-  7.38e-01  <none>
R_{Xib,Kpi}                   5.1382e-02 +/-  4.86e-03  <none>
s_{B,12,D0pK,Kmpip}           1.7855e+01 +/-  4.73e+02  <none>
s_{B,12,D0ppi,Kmpip}          2.2142e+00 +/-  2.98e-01  <none>
s_{B,r2,D0pK,Kmpip}           5.0283e+02 +/-  1.43e+04  <none>
s_{B,r2,D0ppi,Kmpip}          4.8078e+00 +/-  6.22e-01  <none>


Goodness of Fit:
-> #chi^{2}/DoF = 1.14886
->     #chi^{2} = 471.032
->          DoF = 410
->        p-val = 0.0198477
Fitted Norms (sum):
->  Lb  -> D0pK  , D0 -> Kmpip (cc) = 135774+/-29387.6
->  Xib -> D0pK  , D0 -> Kmpip (cc) = 147543+/-10270.4
->  Lb  -> D0ppi , D0 -> Kmpip (cc) = 2.73917e+06+/-26498.8
```

Listing J.23: Parameters of Λ_b^0-type fit to $m(D^0pK)$ with $D^0 \to KK$ in the Λ^* Dalitz subregion ($m^2(D^0p) > 14\,\mathrm{GeV}^2/c^4$) and acceptance weights.

```
/-----------------------------------------------------\
| RooFit Result - SimFit to m(Dp+h-) with D->KK       |
| DATA with acceptance weights in L*-resonance region |
\-----------------------------------------------------/

Constant Parameter              Value
--------------------------   ------------
B_{D02KK}                     4.0800e-03
B_{Lb2D0ppi}                  6.3000e-04
F_{Lb2pKKK}                   1.5998e-05
R_{Lb,Dst2D,pi}               1.9343e+00
addGauss_f                    7.5688e-01
addGauss_sigma                9.2283e+00
dM_{MC,shift,Dst}            -1.1626e+01
dM_{MC,shift}                -1.0193e+00
dM_{Xib,Lb}                   1.7188e+02
effR_{11,Lb,D0pK2D0ppi,KK}    1.1679e+00
effR_{11,Lb,pKKK2D0ppi,KK}    2.7813e-02
effR_{11,Xib,D0pK2D0ppi,KK}   1.3254e+00
effR_{12,Lb,D0pK2D0ppi,KK}    9.9667e-01
effR_{12,Lb,pKKK2D0ppi,KK}    2.0775e-02
effR_{12,Xib,D0pK2D0ppi,KK}   9.6292e-01
effR_{r2,Lb,D0pK2D0ppi,KK}    1.0127e+00
effR_{r2,Lb,pKKK2D0ppi,KK}    1.6973e-02
effR_{r2,Xib,D0pK2D0ppi,KK}   1.0425e+00
m_pRecLb_mD0ppi_f             5.7433e-01
m_pRecLb_mD0ppi_mean          5.4443e+03
m_pRecLb_mD0ppi_sigma11       4.0893e+01
m_pRecLb_mD0ppi_sigma12       1.5428e+01
m_pRecLb_mD0ppi_sigma2        8.0061e+01
s_{S,12,Lb2D0ppi,mD0pK}       3.3618e+00
s_{S,12,Lb2D0ppi}             2.6875e+00
s_{S,12,pRecLb,mD0pK}         2.7940e+00
s_{S,12,pRecLb,mD0ppi}        2.6090e+00
s_{S,12,pRecXib}              3.6577e+00
s_{S,r2,Lb2D0ppi,mD0pK}       2.4630e+00
s_{S,r2,Lb2D0ppi}             8.1328e+00
s_{S,r2,pRecLb,mD0pK}         5.6842e+00
s_{S,r2,pRecLb,mD0ppi}        8.3324e+00
s_{S,r2,pRecXib}              8.5089e+00

Floating Parameter              FinalValue +/-  Error     GblCorr.
--------------------------   ------------------------  --------
#lambda_{11,D0pK,KK}         -1.1466e-03 +/-  5.08e-03  <none>
#lambda_{11,D0ppi,KK}        -5.7312e-03 +/-  1.42e-03  <none>
#lambda_{12,D0pK,KK}         -4.5752e-03 +/-  3.73e-03  <none>
#lambda_{12,D0ppi,KK}        -3.4331e-03 +/-  7.76e-04  <none>
#lambda_{r2,D0pK,KK}         -3.4446e-03 +/-  1.07e-03  <none>
#lambda_{r2,D0ppi,KK}        -3.4404e-03 +/-  4.96e-04  <none>
N_{11,Lb2D0ppi,KK}            2.4784e+04 +/-  1.01e+03  <none>
N_{Bkg,D0pK,KK}               1.1245e+05 +/-  6.10e+04  <none>
N_{Bkg,D0ppi,KK}              2.3188e+05 +/-  1.72e+04  <none>
N_{Lb2D0ppi,mD0pK,KK}         9.7414e+03 +/-  9.64e+03  <none>
N_{Lb2Dst0ppi,mD0pK,KK}       2.0290e+04 +/-  3.44e+04  <none>
R_{Lb,Dst2D,K}                9.9682e-01 +/-  6.92e-01  <none>
R_{Lb,KK}                     9.7733e-02 +/-  1.95e-02  <none>
R_{Xib,Dst2D,K}               1.6200e+05 +/-  6.11e+07  <none>
R_{Xib,KK}                    5.6241e-02 +/-  1.13e-02  <none>
s_{B,12,D0pK,KK}              1.9561e+00 +/-  1.87e+00  <none>
s_{B,12,D0ppi,KK}             3.1230e+00 +/-  7.57e-01  <none>
s_{B,r2,D0pK,KK}              1.1956e+01 +/-  9.88e+00  <none>
s_{B,r2,D0ppi,KK}             4.1958e+00 +/-  8.89e-01  <none>


Goodness of Fit:
-> #chi^{2}/DoF = 0.999306
->     #chi^{2} = 267.814
->          DoF = 268
->        p-val = 0.491717
```

```
Fitted Norms (sum):
->  Lb  -> D0pK  , D0 -> KK = 29265.9+/-4034.33
->  Xib -> D0pK  , D0 -> KK = 17271.9+/-2466.07
->  Lb  -> D0ppi , D0 -> KK = 292952+/-8740.49
```

Listing J.24: Parameters of $\overline{\Lambda}_b^0$-type fit to $m(D^0pK)$ with $D^0 \to KK$ in the Λ^* Dalitz subregion ($m^2(D^0p) > 14\,\mathrm{GeV}^2/c^4$) and acceptance weights. Constant parameter are the same as for the Λ_b^0-type fit in listing J.23.

```
/-----------------------------------------------------\
| RooFit Result - SimFit to m(Dp-h+) with D->KK       |
| DATA with acceptance weights in L*-resonance region |
\-----------------------------------------------------/

Constant Parameter            Value
--------------------------   ------------
>> same as Lb-type fit of D0 -> KK

Floating Parameter            FinalValue +/-  Error     GblCorr.
--------------------------   ------------------------  --------
#lambda_{11,D0pK,KK}         -6.4003e-03 +/-  3.17e-03  <none>
#lambda_{11,D0ppi,KK}        -3.3764e-03 +/-  1.41e-03  <none>
#lambda_{12,D0pK,KK}         -3.0559e-03 +/-  3.33e-03  <none>
#lambda_{12,D0ppi,KK}        -5.2554e-03 +/-  9.02e-04  <none>
#lambda_{r2,D0pK,KK}         -3.2551e-03 +/-  1.73e-03  <none>
#lambda_{r2,D0ppi,KK}        -3.7495e-03 +/-  4.92e-04  <none>
N_{11,Lb2D0ppi,KK}            2.3409e+04 +/-  1.01e+03  <none>
N_{Bkg,D0pK,KK}               8.4634e+04 +/-  6.17e+04  <none>
N_{Bkg,D0ppi,KK}              2.1875e+05 +/-  1.69e+04  <none>
N_{Lb2D0ppi,mD0pK,KK}         9.5864e+03 +/-  1.01e+04  <none>
N_{Lb2Dst0ppi,mD0pK,KK}       1.8757e+04 +/-  3.09e+04  <none>
R_{Lb,Dst2D,K}                9.2158e-01 +/-  6.15e-01  <none>
R_{Lb,KK}                     1.1150e-01 +/-  2.31e-02  <none>
R_{Xib,Dst2D,K}               6.7719e-01 +/-  1.62e-01  <none>
R_{Xib,KK}                    4.5916e-02 +/-  1.09e-02  <none>
s_{B,12,D0pK,KK}              2.1044e+00 +/-  1.36e+00  <none>
s_{B,12,D0ppi,KK}             3.6346e+00 +/-  1.02e+00  <none>
s_{B,r2,D0pK,KK}              5.4803e+00 +/-  2.76e+00  <none>
s_{B,r2,D0ppi,KK}             5.6016e+00 +/-  1.38e+00  <none>


Goodness of Fit:
-> #chi^{2}/DoF = 1.56573
->     #chi^{2} = 419.617
->          DoF = 268
->        p-val = 8.68469e-09
Fitted Norms (sum):
->  Lb  -> D0pK  , D0 -> KK (cc) = 31536.2+/-4480.71
->  Xib -> D0pK  , D0 -> KK (cc) = 13318.9+/-2247.98
->  Lb  -> D0ppi , D0 -> KK (cc) = 276701+/-8704.59
```

K

Pull Distributions for $m(D^0ph)$ Likelihood Fit Validation

As described in section 5.4.1 we perform a set of one thousand pseudo experiments to calculate and fit parameter pull distributions. In this appendix we show the fitted pull distributions of the most relevant model parameters in figs. K.1 to K.3. All distributions show a sufficient Gaussian distributed behaviour. The resulting biases and variances are used to correct the measurements of the likelihood fits to $m(D^0ph)$ in chapter 5.

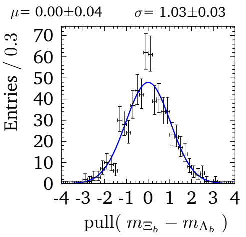

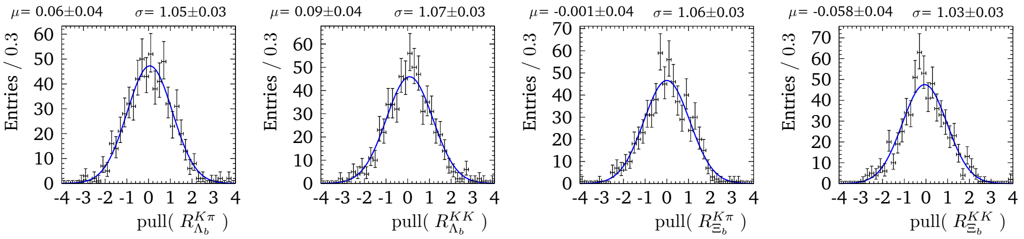

Fig. K.1.: Pull distributions of the measured values from pseudo experiments of the preliminary likelihood fit to $m(D^0ph)$.

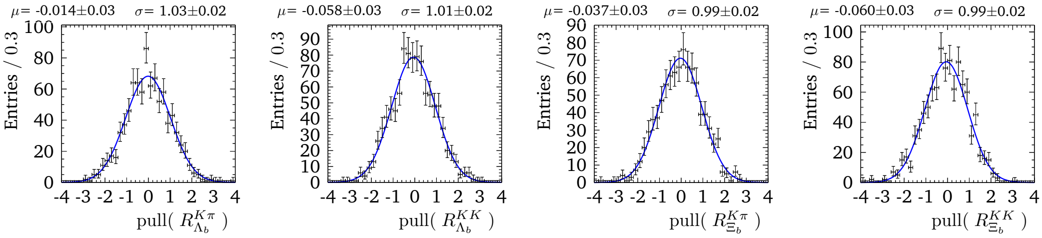

(a) Λ_b^0-type fits

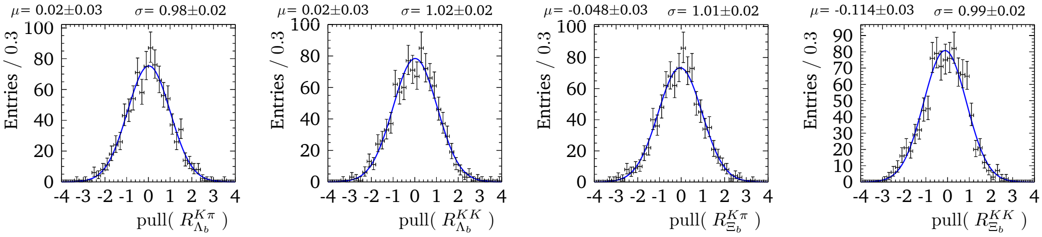

(b) $\overline{\Lambda}_b^0$-type fits

Fig. K.2.: Pull distributions of the measured values from pseudo experiments of the likelihood fits to $m(D^0ph)$ of the split datasets.

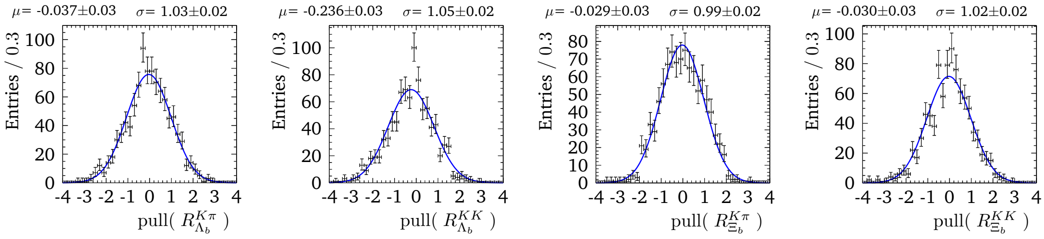

(a) $\mathit{\Lambda}_b^0$-type fits

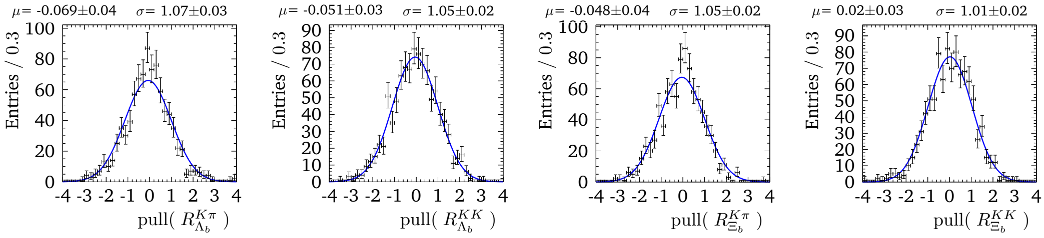

(b) $\overline{\mathit{\Lambda}}_b^0$-type fits

Fig. K.3.: Pull distributions of the measured values from pseudo experiments of the likelihood fits to $m(D^0ph)$ of the split datasets in the $\mathit{\Lambda}^*$ resonance region ($m^2(D^0p) > 14\,\mathrm{GeV}^2/c^4$).

L

Fits to $m(D^0ph)$ for Systematic Uncertainties

To determine the systematic uncertainties described in section 5.4, we perform several fits that are adopted from the nominal fit. As some measurements in section 5.5.1 show a systematically dominated uncertainty we study the visual discrepancy of these fit variations.

L.1 Charmless - Momentum Calibration

Due to the $m(D^0)$ constraint in the DTF, an insufficient momentum calibration is considered, by allowing a free shift $\Delta m_{\text{charmless}}$ for the peak value of the charmless $\Lambda_b^0 \to pKKK$ background. We measure a consistent shift to higher masses of

$$\begin{aligned} \Delta m_{\text{charmless}} &= 9.5 \pm 14.8\,\text{MeV}/c^2 && \text{full phase space} \\ &= 7.2 \pm 5.2\,\text{MeV}/c^2 && \Lambda^* \text{ resonance region} \end{aligned} \tag{L.1}$$

in the acceptance corrected fits, resulting into an enlarged Λ_b^0 signal peak. This behaviour is exemplarily shown for the preliminary fit to the full phase space in fig. L.1 and is consistent for all other fits involving the $D^0 \to KK$ mode.

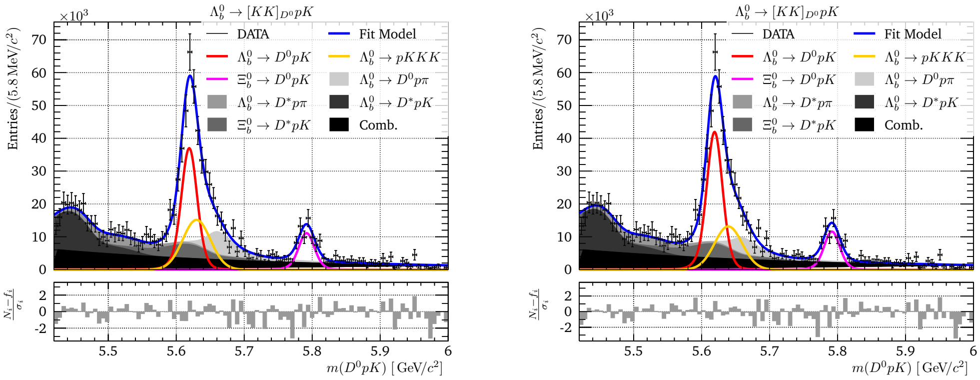

(a) Nominal Fit

(b) Charmless Systematic

Fig. L.1.: Comparison between the nominal fit and the charmless systematic fit with a free shift value $\Delta m_{\text{charmless}}$. Both plots show the preliminary fit for the acceptance corrected full phase space.

This systematic needs a more refined investigation in the true shift of the $\Lambda_b^0 \to pKKK$ peak value or a larger suppression of the charmless background. The latter could easily be achieved by a strengthened cut on the D^0 lifetime [109, 110]. In regard to the available number of events for the $D^0 \to KK$ mode, this would result into an unsustainable drop of the expected $\Lambda_b^0 \to D^0 pK$ signal. We have already shown the $\Lambda_b^0 \to pKKK$ suppression by a cut on the D^0 lifetime in comparison to the remaining $\Lambda_b^0 \to D^0 pK$ signal (fig. G.15), by fitting the D^0 lifetime in DATA.

L.2 D^{*0} Polarisation in $\Xi_b \to D^* pK$

We have already seen, that the deformation of the $\Lambda_b^0 \to D^* pK$ mass distribution[1] for the different D^{*0} modes increases from the full phase space (fig. I.18) to the Dalitz subregion of Λ^* resonances with $m^2(D^0 p) > 14\,\mathrm{GeV}^2/c^4$ (fig. I.19).

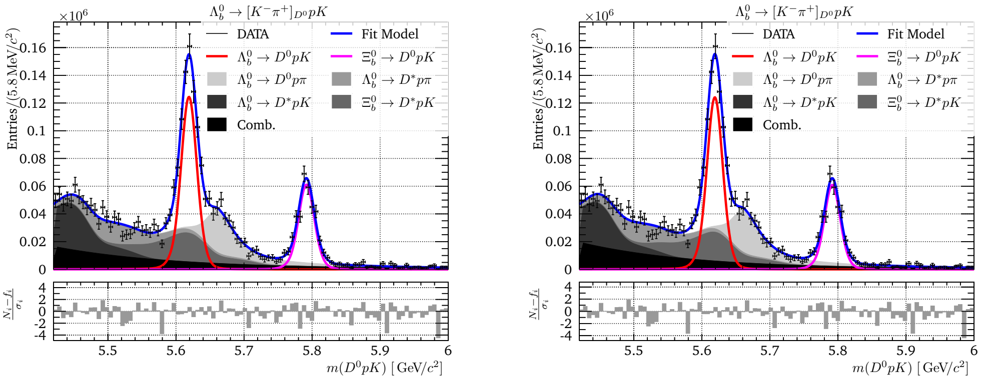

(a) Nominal Fit - Full Phase Space

(b) With D^{*0} Polarisation - Full Phase Space

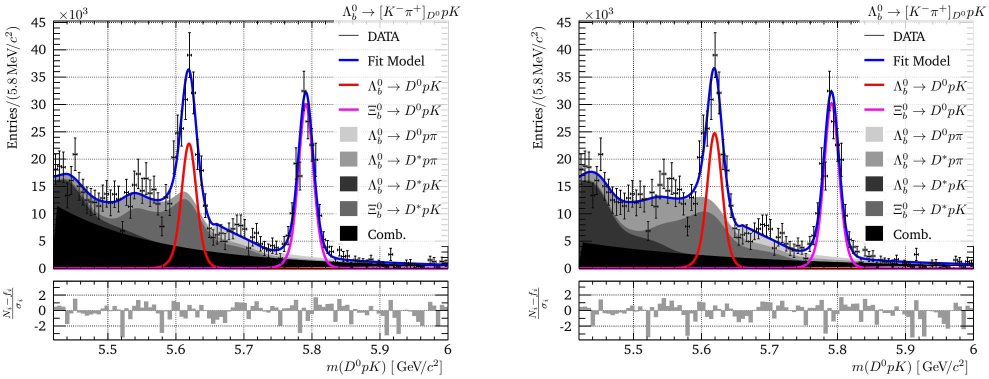

(c) Nominal Fit - Λ^* Resonance Region

(d) No D^{*0} Polarisation - Λ^* Resonance Region

Fig. L.2.: Comparison between the nominal fit and the systematic. The nominal fit in the full phase space assumes no D^{*0} polarisation and the one in the Λ^* resonance region allows polarisation. All plots show the Λ_b^0-type fit to the acceptance corrected $D^0 \to K\pi$ DATA.

This behaviour is also reflected in the Λ_b^0 candidate mass distribution in DATA. The D^{*0} polarisation has no effect on the overall background and signal shape for the full phase space, which can be seen in the comparison of the Λ_b^0-type fits in fig. L.2(a,b). The fits to

---

[1] We use the $\Lambda_b^0 \to D^* pK$ shape for $\Xi_b \to D^* pK$. Their shapes show a good agreement, as seen in fig. 4.16.

$m(D^0ph)$ in the Λ^* resonance region, which are shown in fig. L.2(c,d) visualise a strong background shape dependence on the D^{*0} polarisation and therefore on the Λ_b^0 signal peak size. As both fits show a sufficient pull distribution the unmeasured D^{*0} polarisation in $\Lambda_b^0 \to D^*pK$ is crucial for an exact signal determination in the Λ^* resonance region. A constraint on this polarisation could lessen the systematic error.

M

Dalitz Plot

M.1 Feynman Diagrams of Resonances

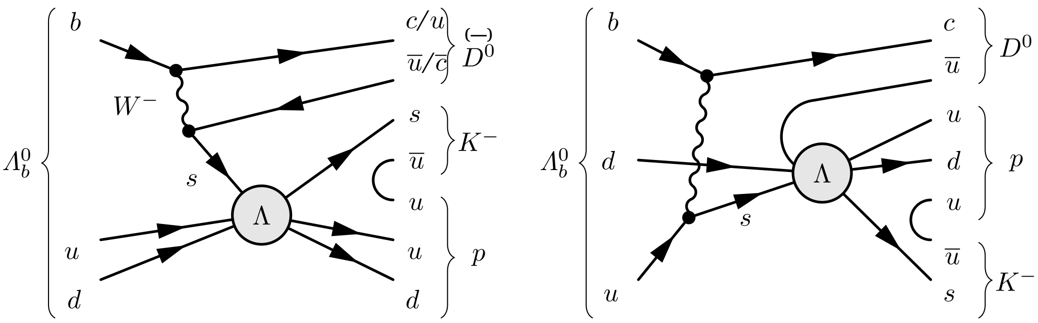

(a) Λ_b^0 tree-level (b) Λ_b^0 W-exchange

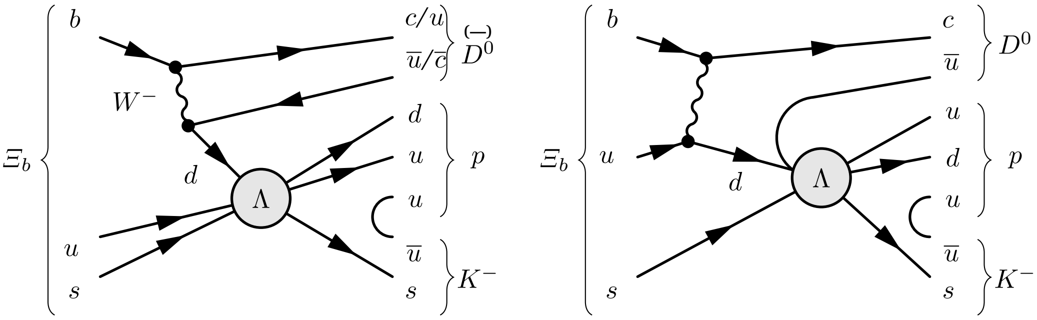

(c) Ξ_b tree-level (d) Ξ_b W-exchange

Fig. M.1.: $\{\Lambda_b^0, \Xi_b\} \to \{D^0, \overline{D}{}^0\}\Lambda$, $\Lambda \to pK^-$

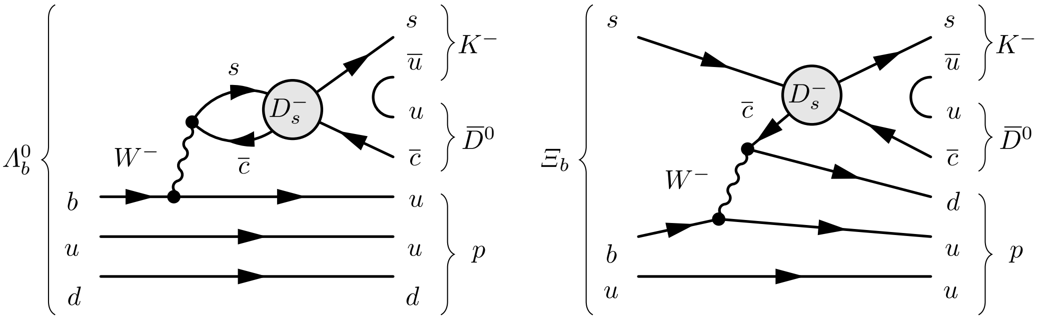

(a) Λ_b^0 tree-level (b) Ξ_b tree-level

Fig. M.2.: $\{\Lambda_b^0, \Xi_b\} \to D_s^- p$, $D_s^- \to \overline{D}{}^0 K^-$

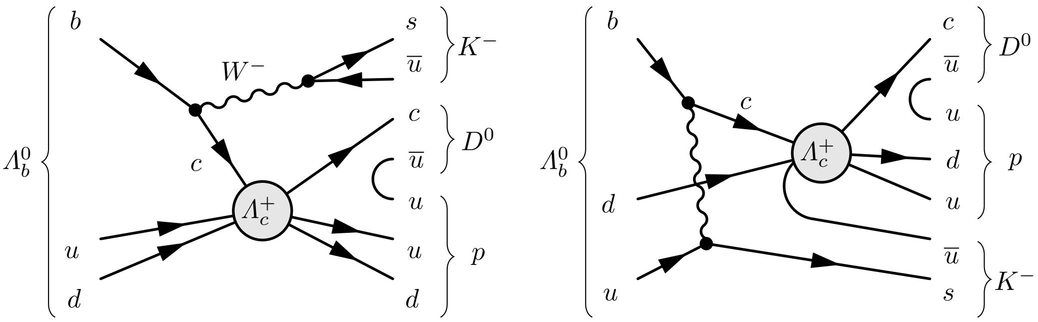

(a) Λ_b^0 tree-level (b) Λ_b^0 W-exchange

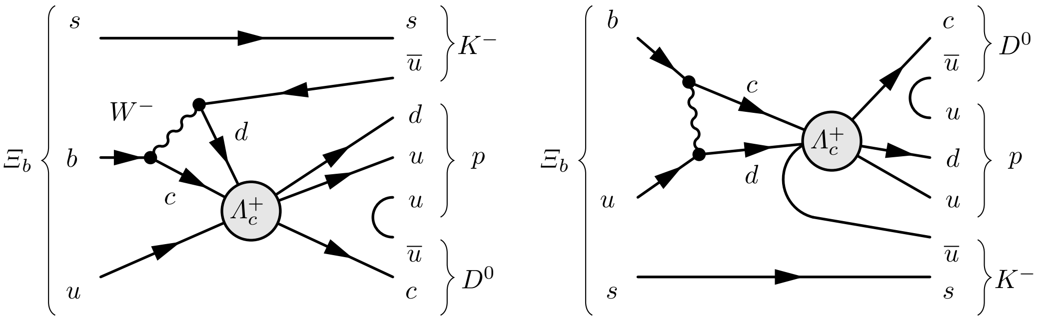

(c) Ξ_b tree-level (d) Ξ_b W-exchange

Fig. M.3.: $\{\Lambda_b^0, \Xi_b\} \to \Lambda_c^+ K^-$, $\Lambda_c^+ \to D^0 p$

M.2 Isospin States of Resonances

The decay $\Lambda_b^0 \to D^0 p K$ can form resonances of a particular quark state that do not have a distinct isospin state, like $|uds\rangle = \Lambda, \Sigma$. Isospin is only conserved in the presence of strong interaction, but the Λ_b^0 decays via weak interaction. As isospin is carried only by the light u and d quarks we approach this questioning at quark level. Λ_b^0 has got the quark state $|udb\rangle$, with isospin 0. Where the resonance D_s^- with $|s\overline{c}\rangle$ won't carry isospin the resonances $\Lambda = |uds\rangle$ and $\Lambda_c^+ = |udc\rangle$ could in principle have isospin 0 and 1. However if both light quarks of Λ and Λ_c^+ are spectators, the resonance will have the same isospin state as the Λ_b^0. This argumentation does not hold for the Ξ_b decay, as it only has one light u quark that can be a spectator. Under consideration of the Feynman diagrams found in appendix M.1, the possible isospin states of the different resonances can be evaluated. They are listed in table M.1.

Tab. M.1.: All possible isospin states of the different resonance channels are listed.

Channel	Λ_b^0		Ξ_b		Resonance
	tree	W ex.	tree	W ex.	
pK	0	$0,1$	$0,1$	$0,1$	Λ^*, Σ^*
D^0p	0	$0,1$	$0,1$	$0,1$	Λ_c^{+*}, Σ_c^*
$\overline{D}^0K^-$	0	0	0	0	D_s^{-*}

M.3 Calculation of the Helicity Angles

The calculation follows the general approach of section 2.5.1 within the two-dimensional representation presented in section 2.5.2.

Helicity Angles

decay	helicity angle θ
$\Lambda_b^0 \to D^0 \Lambda^*$	$\cos\theta_{\Lambda^*} = 1$
$\Lambda^* \to pK$	$\cos\theta_p = -\hat{p}_{D^0}^{(\Lambda^*)} \cdot \hat{p}_p^{(\Lambda^*)}$
$\Lambda_b^0 \to K \Lambda_c^{+*}$	$\cos\theta_{\Lambda_c^{+*}} = \hat{p}_{\Lambda^*}^{(\Lambda_b^0)} \cdot \hat{p}_{\Lambda_c^{+*}}^{(\Lambda_b^0)}$
$\Lambda_c^{+*} \to D^0 p$	$\cos\theta_{p'} = -\hat{p}_K^{(\Lambda_c^{+*})} \cdot \hat{p}_{p'}^{(\Lambda_c^{+*})}$
$\Lambda_b^0 \to p D_s^{-*}$	$\cos\theta_{D_s^{-*}} = \hat{p}_{\Lambda^*}^{(\Lambda_b^0)} \cdot \hat{p}_{D_s^{-*}}^{(\Lambda_b^0)}$
$D_s^{-*} \to D^0 K$	$\cos\theta_K = -\hat{p}_{p''}^{(D_s^{-*})} \cdot \hat{p}_K^{(D_s^{-*})}$

Proton Helicity Rotations

resonance	rotation θ_p^{rot}
Λ_c^{+*}	$\cos\theta_{p'}^{\text{rot}} = \hat{p}_K^{(p)} \cdot \hat{p}_{D^0}^{(p)}$
D_s^{-*}	$\cos\theta_{p''}^{\text{rot}} = \hat{p}_K^{(p)} \cdot \hat{p}_{D_s^{-*}}^{(p)}$

M.4 Width of the Modified Flaté

The $\Lambda(1405)$ resonance has got a mass below the kinetically allowed threshold. A special Flaté lineshape [51, 60] is used. A width for its decay to the dominant $\Lambda(1405) \to \Sigma\pi$ decay channel is added to the width of the pK channel yielding $\Gamma(m) = \Gamma_{pK}(m) + \Gamma_{\Sigma\pi}(m)$. Figure M.4 shows the modified width as a function of m_{pK} within the kinematically allowed limits.

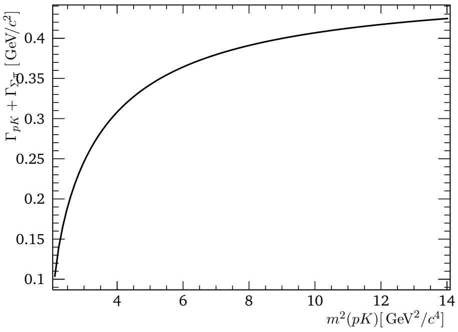

Fig. M.4.: Modified Flaté lineshape width for $\Lambda(1405)$ within the kinematically allowed limits.

M.5 Dalitz Plots of the Λ_b^0 and Ξ_b Candidates

In this appendix we present a summary of all Λ_b^0 and Ξ_b signal candidates in their Dalitz plot, that have not been fit in the amplitude fit in chapter 6. The phase space variables $m^2_{D^0p}$ and m^2_{pK} of the Ξ_b candidates are taken, in contrast to the Λ_b^0 candidates, from the DTF without the Λ_b^0 mass constraint. The contribution fractions in the selected 2σ mass window are listed in table M.2. We further use *sWeights* to show a signal like representation of the Λ_b^0 and Ξ_b candidates in their Dalitz plot. The *sWeights* are extracted from a fit to the $m(D^0pK)$ distribution in appendix J.1.3, which is a variation of the fit to the $m(D^0ph)$ distribution in section 5.1.2 without signal constraints.

Tab. M.2.: Fractions in % of all contributions in a 2σ window from the Λ_b^0 and Ξ_b mass peak value.

	D^0	Signal	$\Lambda_b^0 \to pKKK$	$\Xi_b \to D^*pK$	Comb.	$\Lambda_b^0 \to D^0p\pi$	$\Lambda_b^0 \to D^*p\pi$
Λ_b^0	$K\pi$	66		22	5	4	3
	KK	47	32	9	9	2	2
Ξ_b	$K\pi$	89			5	6	
	KK	88			6	6	

The $\Lambda_b^0 \to D^0pK$ candidates with *sWeights* show a similar distribution, as their scatter plot from the signal region in fig. 6.1. The $D^0 \to K\pi$ samples in fig. M.5 have a lessened contribution of Λ^* resonances compared to the Λ_c^{+*} resonances and continuum contributions in the low $m^2_{D^0p}$ region of the Dalitz plot. This is also reflected in the projections.

The $D^0 \to KK$ samples in fig. M.6 clearly show their lack of number of events coupled with the low signal expectation within the 2σ mass window of the signal peak. There are still Λ^* resonances visible, but the Λ^* region shows only a light enhancement for low m^2_{pK}. The projection of $m^2_{D^0K}$ also has a enhancement below $10\,\mathrm{GeV}^2/c^4$. When considering $m_{\min}(D^0K) = m_{D^0} + m_K \approx 2.359\,\mathrm{GeV}/c^2$ there are seven different excited D_s^{-*} possible, as listed in table M.3. One has to keep in mind, that each D_s^{-*} resonance adds up to the number of free parameters to be considered in the fit, which makes, besides the available low event count, an amplitude analysis of $\Lambda_b^0 \to D^0pK$ with $D^0 \to KK$ even more challenging.

Tab. M.3.: Potential D_s^{-*} resonances in the $D^0 \to KK$ samples of $\Lambda_b^0 \to D^0pK$. The mass and width are taken from the PDG [20]. Confidence levels are given for 90 %

	J^P	$m/\,\mathrm{MeV}/c^2$	$\Gamma/\,\mathrm{MeV}/c^2$	Note on $D_s^{-*} \to D^0K$
$D^*_{s1}(2460)^\pm$	1^+	2459.5 ± 0.6	< 3.5	not seen
$D^*_{s1}(2536)^\pm$	1^+	2535.11 ± 0.06	0.92 ± 0.09	$\Gamma_i/\Gamma < 0.12$
$D^*_{s2}(2573)$	2^+	2569.1 ± 0.8	16.9 ± 0.7	seen
$D^*_{s1}(2700)^\pm$	1^-	$2708.3^{+4.0}_{-3.4}$	120 ± 11	seen
$D^*_{s1}(2860)^\pm$	1^-	2859 ± 27	159 ± 80	seen
$D^*_{s3}(2860)^\pm$	3^-	2860 ± 7	53 ± 10	no decay seen
$D^*_{sJ}(3040)^\pm$	$?^?$	3044^{+31}_{-9}	238 ± 60	only $D^{*0}K^+$ seen

The $\Xi_b \to D^0pK$ Dalitz plots in fig. M.7 show both the same resonance regions as $\Lambda_b^0 \to D^0pK$, but no hint for D_s^{-*} resonances. As shown in appendix M.2 we have to expect the higher isospin states Σ_c^* and Σ^* in both resonance channels. The low m^2_{pK} region is significantly more structured as for the Λ_b^0 candidates and shows resonance lines. The

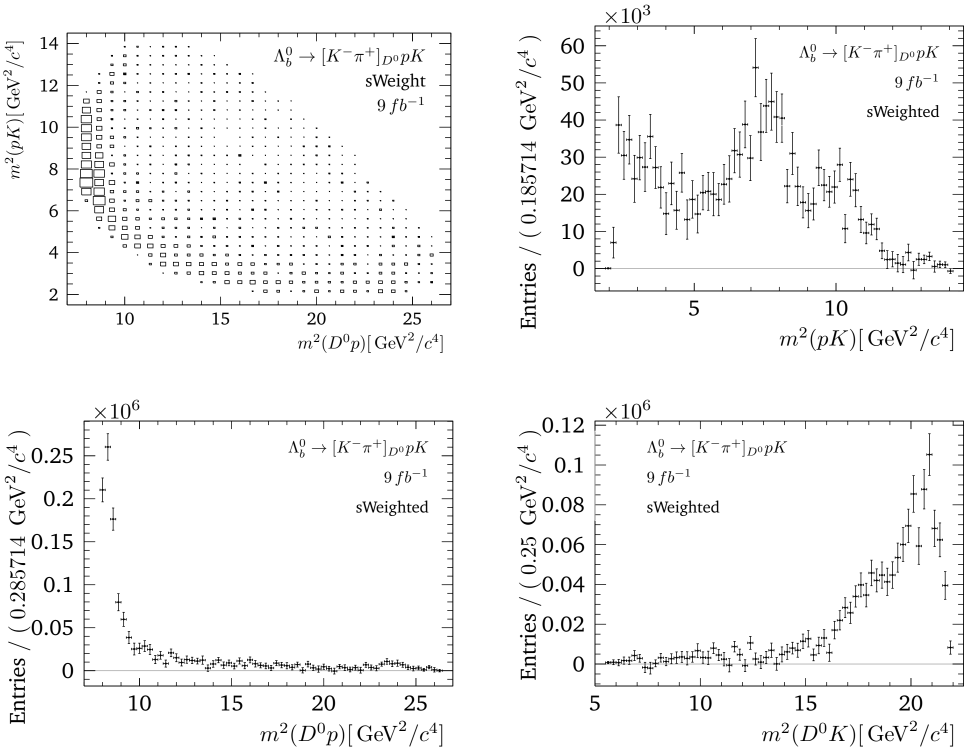

Fig. M.5.: *sWeight*'ed and acceptance corrected Dalitz plot of $\Lambda_b^0 \to D^0pK$ candidates from the $D^0 \to K^-\pi^+$ sample (a) and its projections (b-d).

sWeight'ed $D^0 \to K\pi$ sample in fig. M.8 shows a more distinct separation between the two resonance channels than the Λ_b^0 candidates. As we can expect resonances up to $\Lambda(2350)$ that then peak up to $m^2_{pK} < 5.6\,\mathrm{GeV}^2/c^4$ we probably see destructive interference effects in their overlap region. The projections on m^2_{pK} show a higher enhancement to lower masses than $m^2_{D^0p}$. From the likelihood fit of $m(D^0ph)$ for the low m^2_{pK} region in section 5.3 we have learned that there is a significant amount of $\Xi_b \to pKK\pi$ that tends to populate this region. The first impression of more resonances in the pK channel than in the D^0p channel is therefore not sustained. The Ξ_b Dalitz plot of the $D^0 \to KK$ samples in fig. M.9 shows, besides the lower number of events, similar resonance regions as the $D^0 \to K\pi$ samples. But there is a visible difference of the angular momentum structure from resonances of the pK channel in the $m^2_{D^0p}$ projection to the $D^0 \to K\pi$ samples.

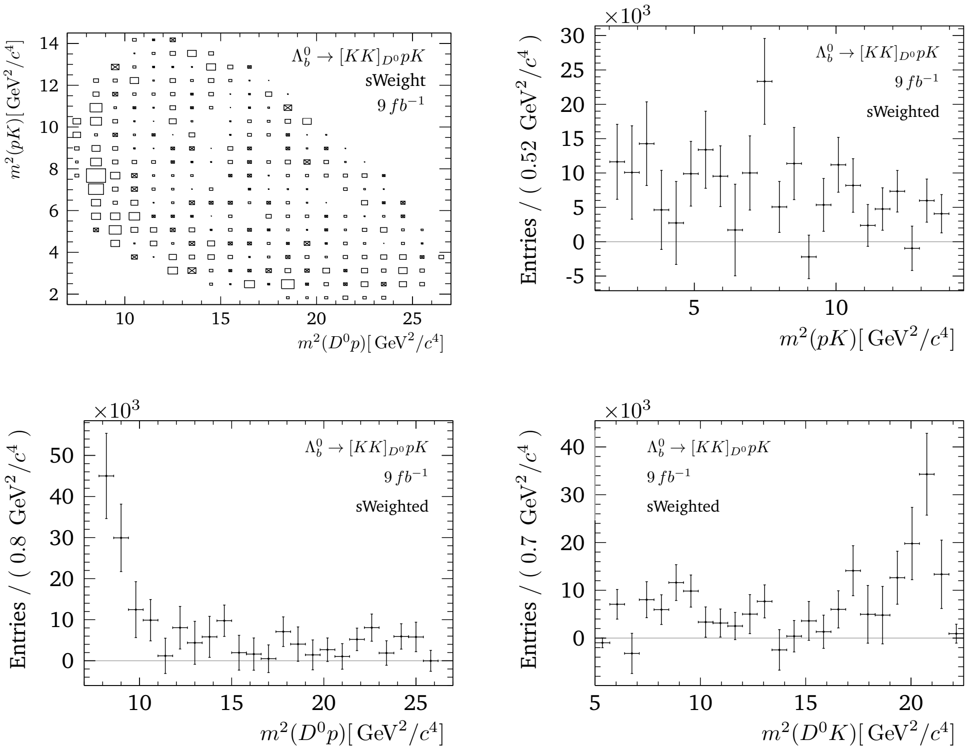

Fig. M.6.: *sWeight*'ed and acceptance corrected Dalitz plot of $\Lambda_b^0 \to D^0pK$ candidates from the $D^0 \to KK$ sample (a) and its projections (b-d).

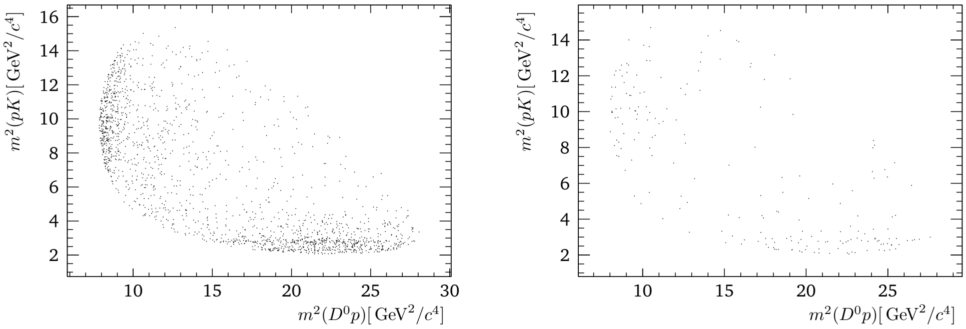

(a) $D^0 \to K\pi$

(b) $D^0 \to KK$

Fig. M.7.: Dalitz plot of the selected $\Xi_b \to D^0pK$ candidates within a 2σ mass window of $m(\Xi_b) \in [5764.42, 5819.05]\ \mathrm{MeV}/c^2$.

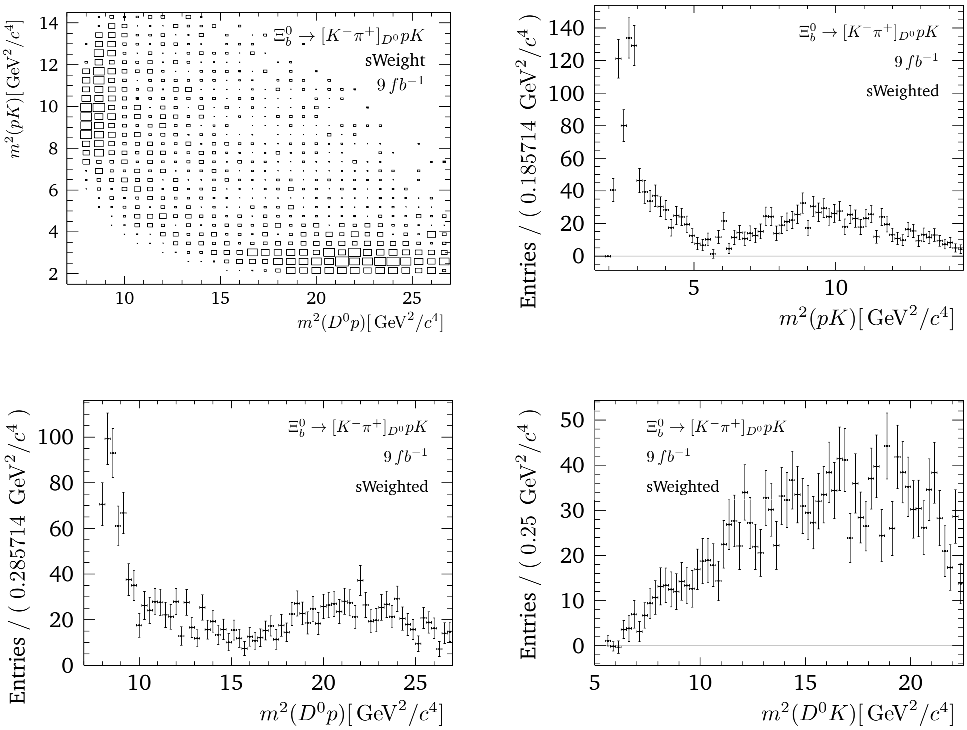

Fig. M.8.: sWeighted and acceptance corrected Dalitz plot of $\Xi_b \to D^0 pK$ candidates from the $D^0 \to K^-\pi^+$ sample (a) and its projections (b-d).

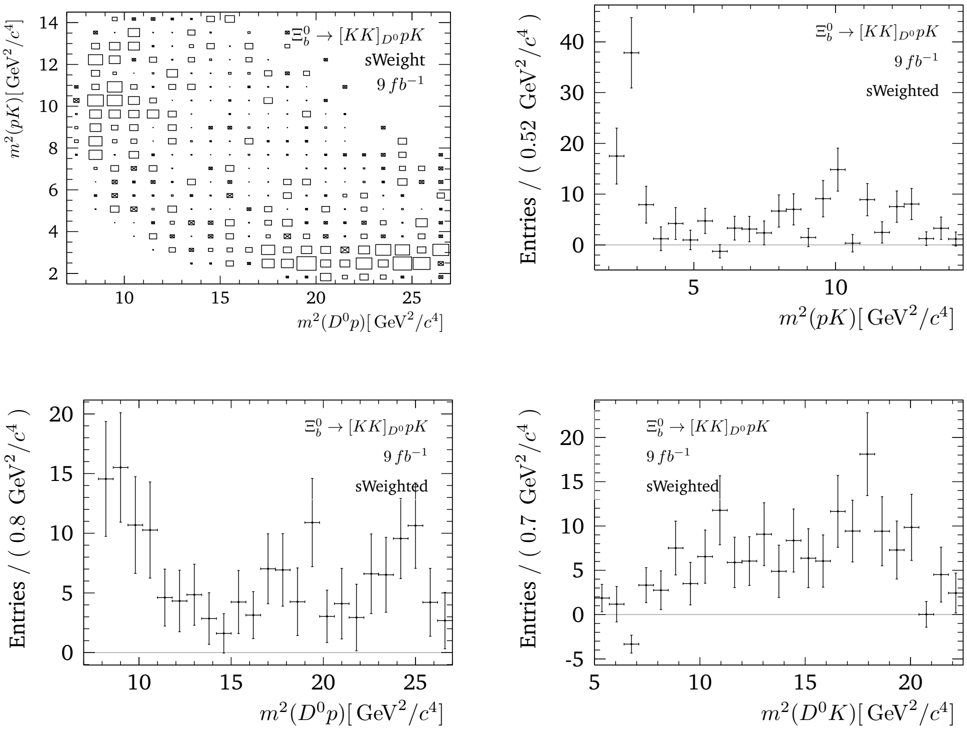

Fig. M.9.: sWeighted and acceptance corrected Dalitz plot of $\Xi_b \to D^0pK$ candidates from the $D^0 \to KK$ sample (a) and its projections (b-d).

N

Plots & Tables of the Amplitude Analysis

N.1 Helicity Couplings

In this appendix we show the fitted complex helicity couplings with their 1σ and 2σ covariance ellipse for

- fit to low $m^2_{D^0p}$ resonance region (appendix N.3.1) in fig. N.1.
- reduced fit to low $m^2_{D^0p}$ resonance region (appendix N.3.1) in fig. N.2.
- fit to low m^2_{pK} resonance region (appendix N.3.2) in fig. N.3.
- reduced fit to low m^2_{pK} resonance region (appendix N.3.2) in fig. N.4.
- reduced fit to full Dalitz plot (section 6.3.1) in fig. N.5.
- reduced *sFit* to full Dalitz plot (section 6.3.1) in fig. N.5.

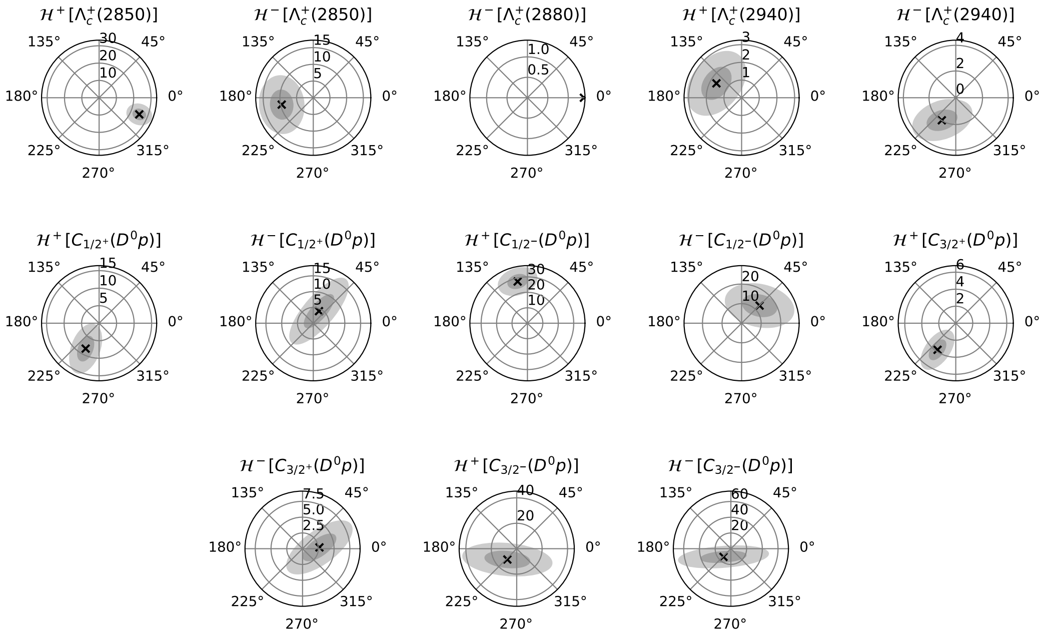

Fig. N.1.: Helicity couplings with their 1σ and 2σ covariance ellipse found in the fit to the low $m^2_{D^0p}$ region in appendix N.3.1.

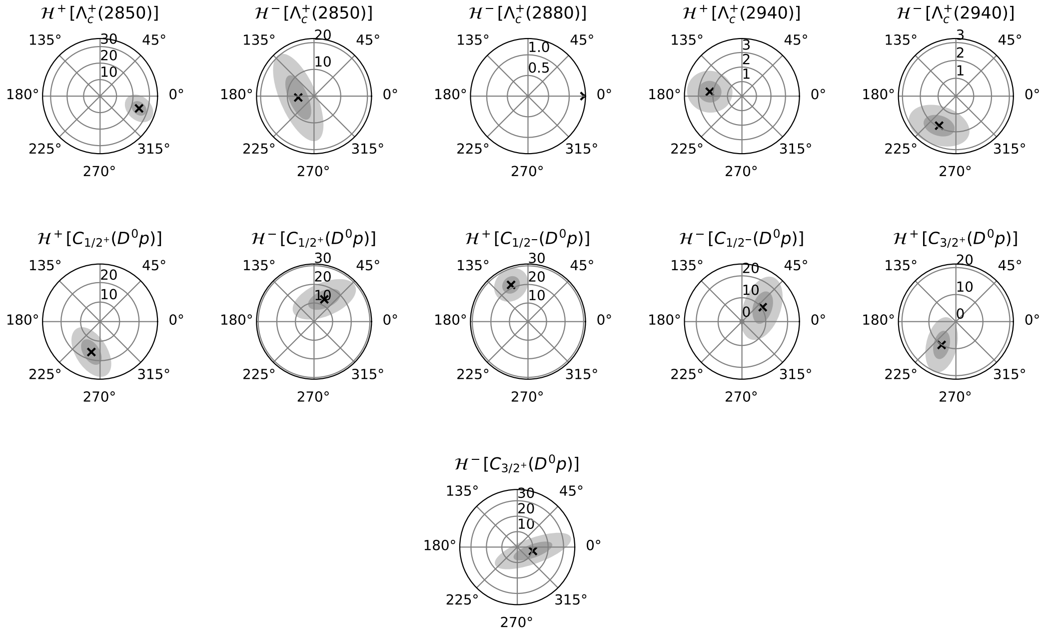

$\mathcal{H}^+[\Lambda_c^+(2850)]$ $\mathcal{H}^-[\Lambda_c^+(2850)]$ $\mathcal{H}^-[\Lambda_c^+(2880)]$ $\mathcal{H}^+[\Lambda_c^+(2940)]$ $\mathcal{H}^-[\Lambda_c^+(2940)]$

$\mathcal{H}^+[C_{1/2^+}(D^0p)]$ $\mathcal{H}^-[C_{1/2^+}(D^0p)]$ $\mathcal{H}^+[C_{1/2^-}(D^0p)]$ $\mathcal{H}^-[C_{1/2^-}(D^0p)]$ $\mathcal{H}^+[C_{3/2^+}(D^0p)]$

$\mathcal{H}^-[C_{3/2^+}(D^0p)]$

Fig. N.2.: Helicity couplings with their 1σ and 2σ covariance ellipse found in the reduced fit to the low $m^2_{D^0p}$ region in section 6.4.1.

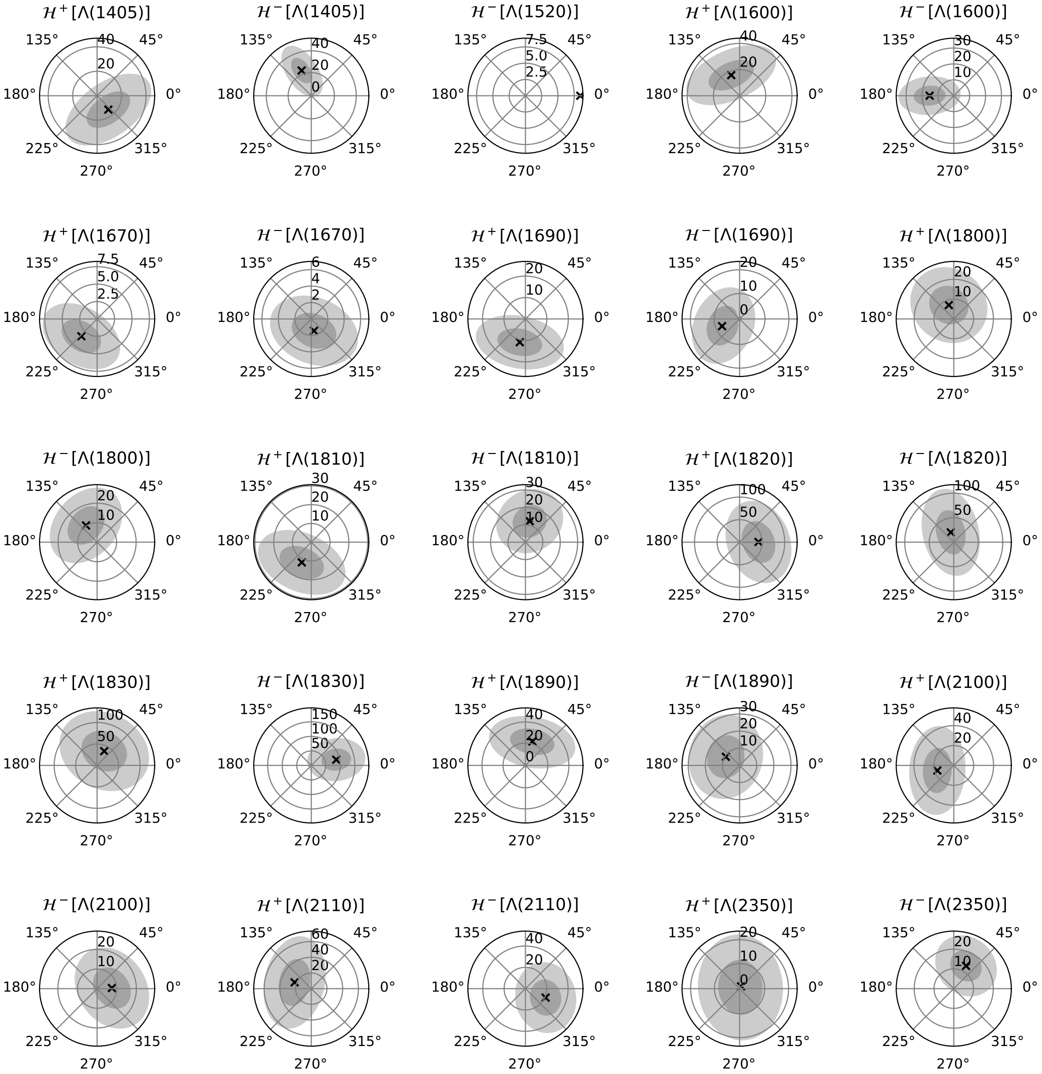

Fig. N.3.: Helicity couplings with their 1σ and 2σ covariance ellipse found in the fit to the low m_{pK}^2 region in appendix N.3.2.

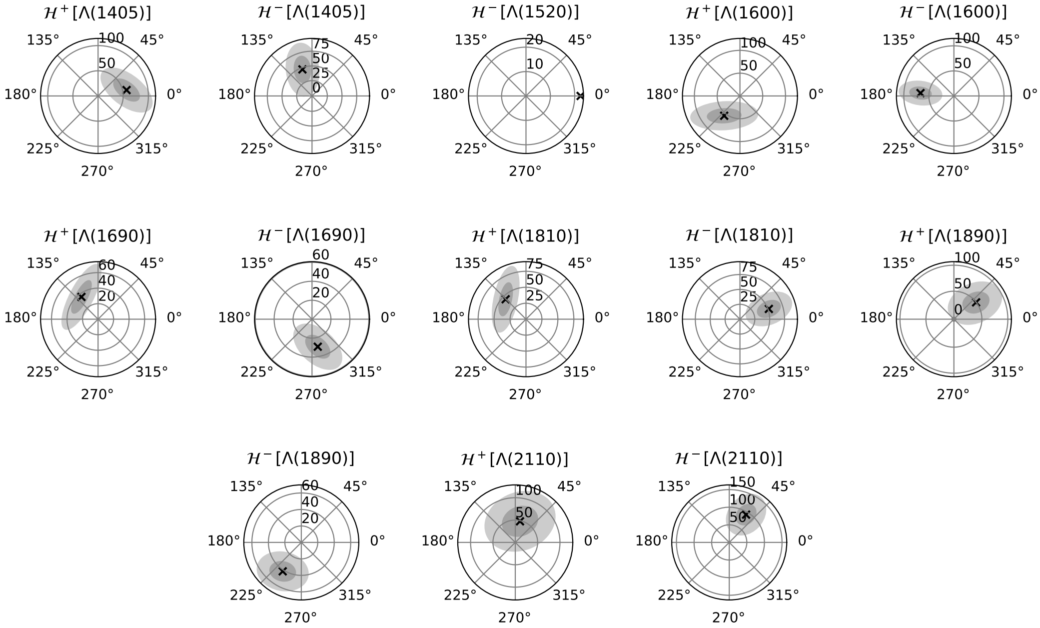

Fig. N.4.: Helicity couplings with their 1σ and 2σ covariance ellipse found in the reduced fit to the low m_{pK}^2 region in appendix N.3.2.

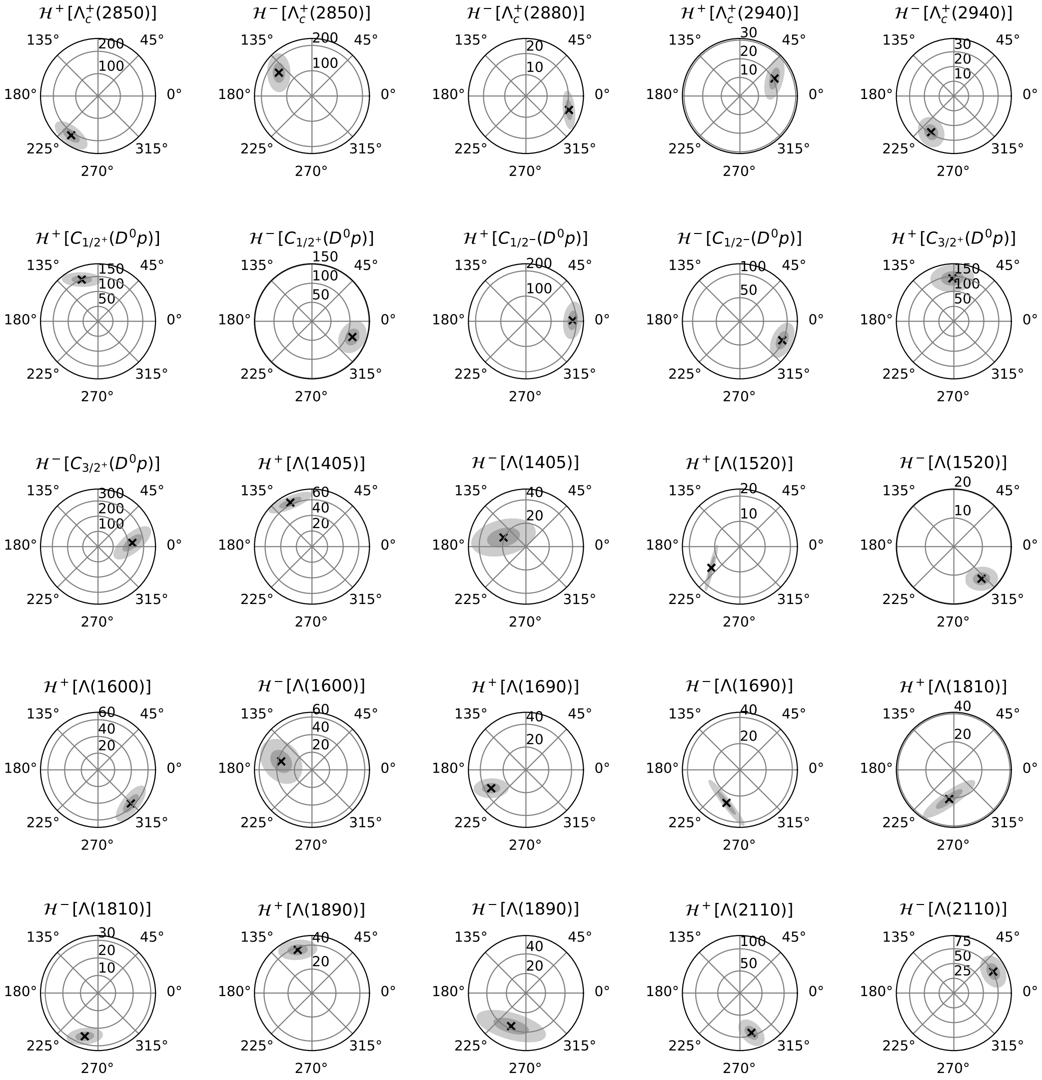

Fig. N.5.: Helicity couplings with their 1σ and 2σ covariance ellipse found in the reduced fit to the full Dalitz plot in section 6.3.1.

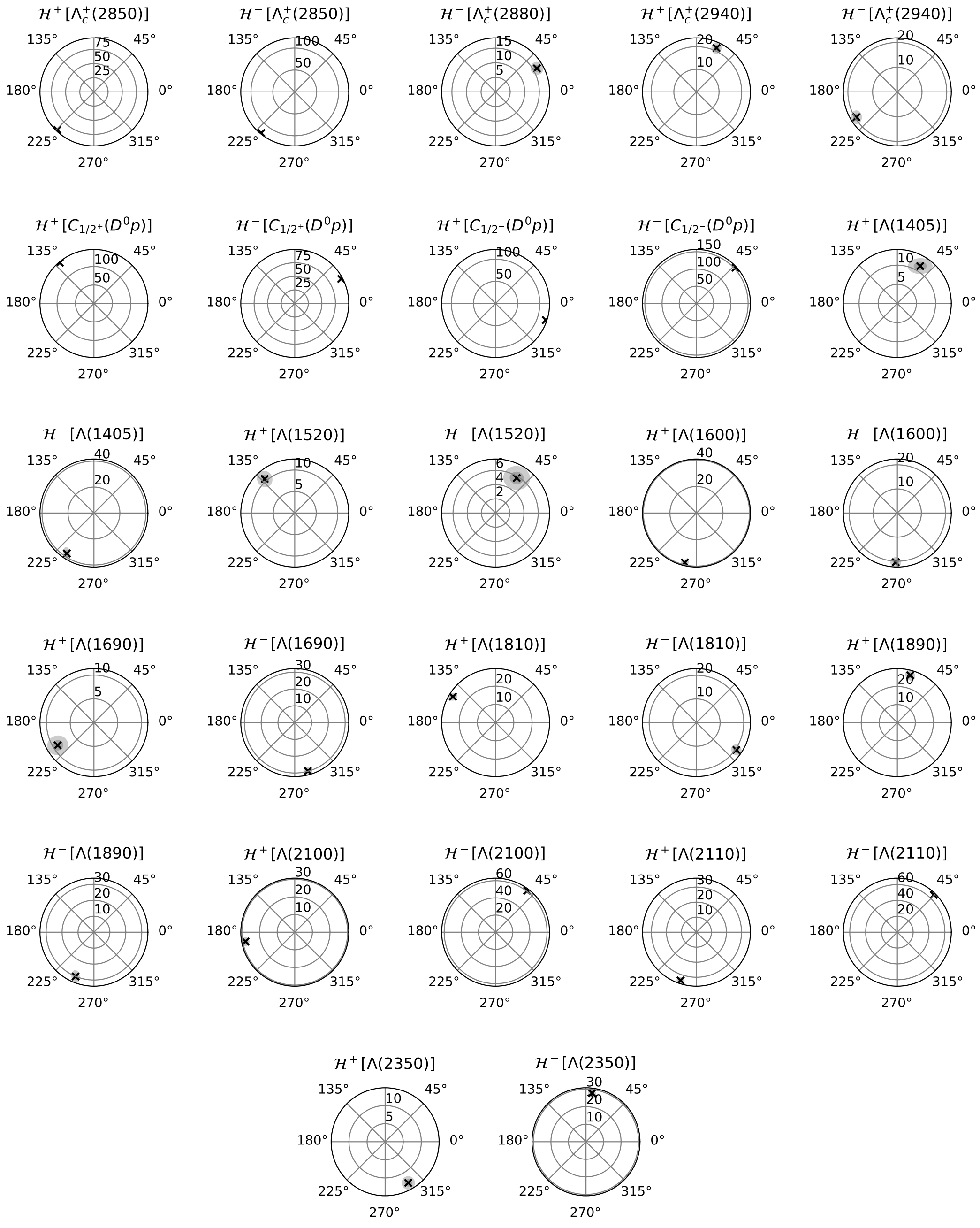

Fig. N.6.: Helicity couplings with their 1σ and 2σ covariance ellipse found in the reduced *sFit* to the full Dalitz plot in section 6.4.2.

N.2 $\mathcal{H}^{\pm}$ Interference

In the fits to the low $m^2_{D^0p}$ and m^2_{pK} regions of the Dalitz plot in appendices N.3.1 and N.3.2 helicity amplitudes of the same resonance add up incoherently. This is, however, only shown for resonances of the same decay channel [49]. To avoid lengthening algebraic calculations, that arise from a matrix element of the complexity, as presented in eq. (2.57), we approach this question numerically. In case of a similar incoherent sum in the presence of two decay channels, there should be no sensitivity to a generic phase shift between the helicity couplings $\mathcal{H}^+$ and $\mathcal{H}^-$. We use the model of all amplitudes from appendix N.3.3 and shift all phases of $\mathcal{H}^-$ by $\frac{1}{2}\pi$ increments. We then simulate 10^5 events from both models and calculate the difference in bins of the Dalitz plot. This difference is divided by its statistical uncertainty. The resulting differences for shifts up to 2π in fig. N.7 have an influence on the interference region of the two resonance channels. This clearly shows the necessity of the coherent sum for the helicity amplitudes of the same resonance.

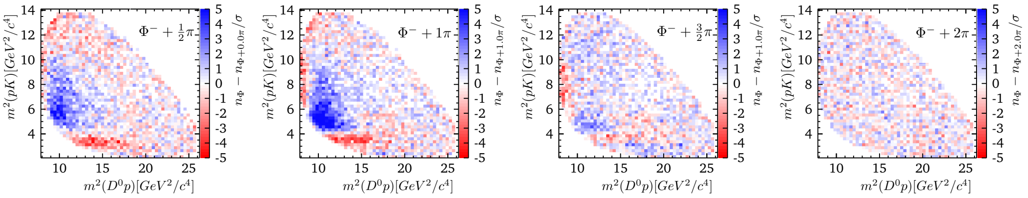

Fig. N.7.: Difference of $|M|^2$ in 50^2 bins for phase shifts on $\mathcal{H}^-$.

Shifting only the phase of the $\Lambda_c^+(2880)$ helicity coupling $\mathcal{H}^-$, there is a strong effect by the amplitude spin visible in fig. N.8. This ensures the ability to measure the phase difference between the $J_{m,R} = \pm{}^1/_2$ amplitudes of a resonance with the full amplitude model. We further test the previous statement for a model involving only one decay channel. In fig. N.9 we shift the phase of $\mathcal{H}^-$ for a model from the single resonance $\Lambda_c^+(2880)$. There is no interference effect present.

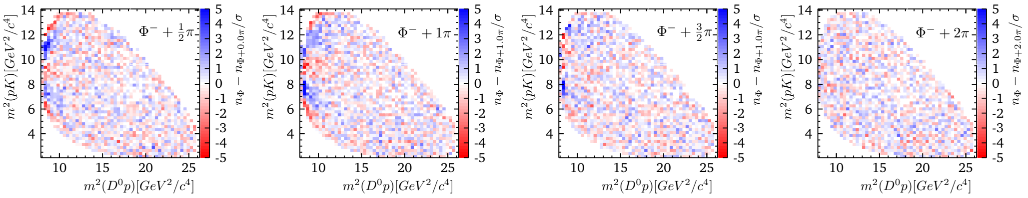

Fig. N.8.: Difference of $|M|^2$ in 50^2 bins for phase shifts only on $\mathcal{H}^-$ of $\Lambda_c^+(2880)$.

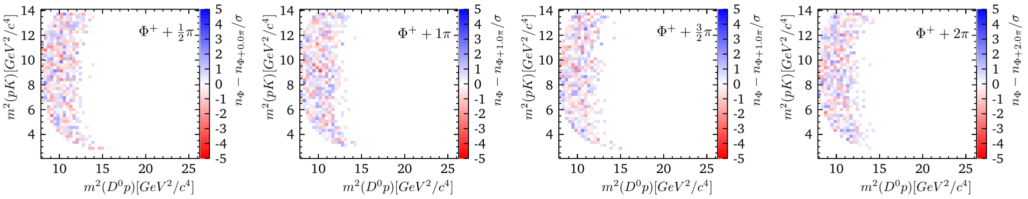

Fig. N.9.: Difference of $|M|^2$ of a single $\Lambda_c^+(2880)$ resonance in 50^2 bins for phase shifts on $\mathcal{H}^-$.

N.3 Amplitude Fit

N.3.1 Fit Λ_c^{+*} in Low $m^2_{D^0p}$ Region

We use the D^0p channel amplitudes of the LHCb analysis $\Lambda_b^0 \to D^0p\pi$ [49] as a starting point, as this decay is relatively similar to $\Lambda_b^0 \to D^0pK$. In addition to Λ_c^{+*} resonances, we consider four continuum contributions with an exponential lineshape, as introduced in eq. (2.55). In case of fitting only one resonance channel, the helicity amplitudes of the same resonance add up incoherently [49], which is tested numerically in appendix N.2. Thus, we can set the phase of $\mathcal{H}^-[\Lambda_c^+(2880)]$ to the arbitrary fixed value $\Phi^- = 0$. This constant phase is only valid for the amplitude fit with one resonance channel. All amplitudes considered for the D^0p channel in the low $m^2_{D^0p}$ region are listed in table N.1. With the additional exponential decay constants α there are 25 free parameters in the fit.

Tab. N.1.: Λ_c^{+*} resonances and continuum contributions considered in $m^2_{D^0p}$. The mass and width are taken from the PDG [20] except for $\Lambda_c^+(2850)$, which are taken from the $\Lambda_b^0 \to D^0p\pi$ amplitude analysis [49]. The number of helicity couplings for the full and reduced fit are listed.

	J^P	$m/\,\mathrm{MeV}/c^2$	$\Gamma/\,\mathrm{MeV}/c^2$	# full	# reduced
$\Lambda_c^+(2850)$	$3/2^+$	2856.07	67.61	2	2
$\Lambda_c^+(2880)$	$5/2^+$	2881.75	5.43	1	1
$\Lambda_c^+(2940)$	$3/2^-$	2944.81	27.69	2	2
$C_{1/2^+}(D^0p)$	$1/2^+$			2	2
$C_{1/2^-}(D^0p)$	$1/2^-$			2	2
$C_{3/2^+}(D^0p)$	$3/2^+$			2	2
$C_{3/2^-}(D^0p)$	$3/2^-$			2	0

The fitted matrix element and the overlayed Λ_b^0 candidates in fig. N.10 show a sufficient agreement, supported by their pull in the same figure. The matrix element describes the interference effects of the Λ_c^{+*} amplitudes well. There is an obvious enhancement visible towards lighter m^2_{pK}, which is reflected in its projection in fig. N.10. This asymmetry of the phase space can be explained with constructive (destructive) interference to lower (higher) pK masses. There is strong evidence for strong destructive and constructive interference of $\Lambda_c^+(2850)$ with the continuum contributions, when comparing both projections in fig. N.10. The amplitude squared of $\Lambda_c^+(2850)$ is higher than the complete $|M|^2$ in its peak region, where we only find exponential contributions in the $m^2_{D^0p}$ projections, and to higher pK masses. The final interference fit fractions from the fit to the full Dalitz plot in fig. 6.5 show the largest destructive interferences for $\Lambda_c^+(2850)$ to $C_{3/2^+}(D^0p)$ and $C_{1/2^-}(D^0p)$. This further supports the claim of the strong interferences. A summary of the fitted parameters and the resulting fit fractions is presented in table N.2. The helicity couplings are shown in their polar expression with covariance ellipses in fig. N.1.

To improve fit stability, we aim for a reduced parameter set by iteratively removing the most insignificant amplitudes or the ones with a fit fraction $\mathcal{F}_i < 4\%$. Still, we choose to keep the $\Lambda_c^+(2940)$ amplitude. Its necessity is visible from its enhancement of the Λ_b^0 candidates in the m_{D^0p} projection in fig. N.12. We find a reduced fit of 24 free parameters, that describes the fitted phase space as well as the previous fit with the full parameter set. This is apparent

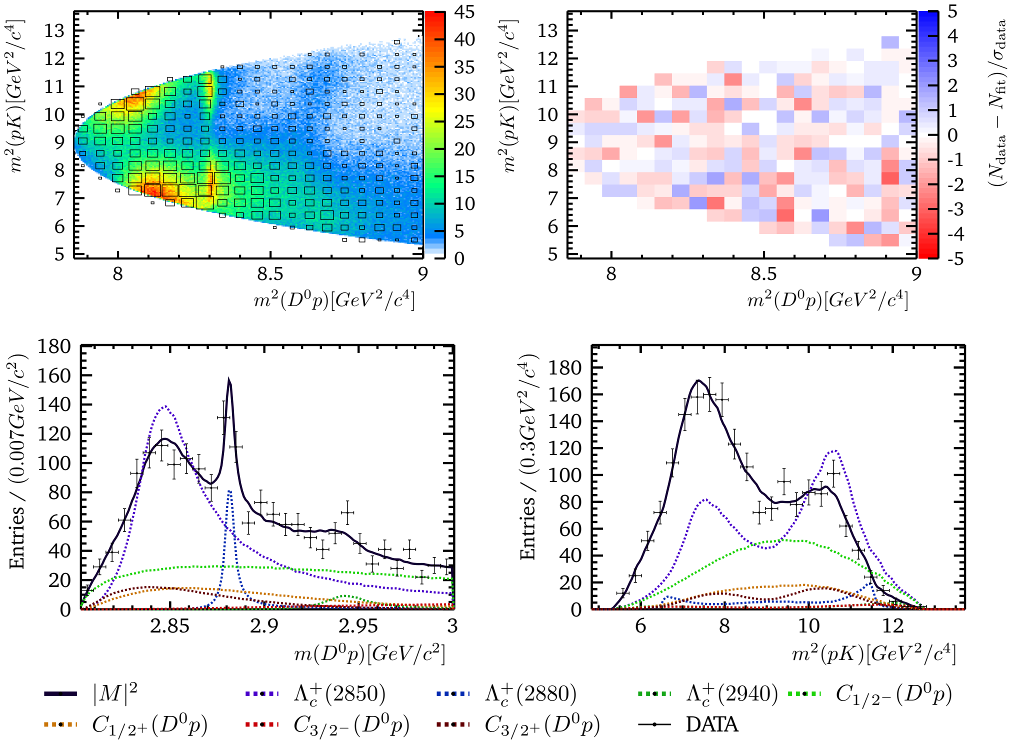

Fig. N.10.: Amplitude fit to the low $m^2_{D^0p}$ region, shown in the Dalitz plot with a resolution of 200×200 bins overlayed by DATA in a 20^2 bins box graph (top left) and their pull (top right). The projections on m_{D^0p} (bottom left) and on m^2_{pK} (bottom right) are shown. The partial amplitudes are shown as their amplitudes squared.

Tab. N.2.: Fit fractions and fitted parameters of the fit to the low $m^2_{D^0p}$ region.

	$\mathcal{F}_i$	$\mathrm{Re}\,\mathcal{H}^+$	$\mathrm{Im}\,\mathcal{H}^+$	$\mathrm{Re}\,\mathcal{H}^-$	$\mathrm{Im}\,\mathcal{H}^-$	α
$\Lambda_c^+(2850)$	67.66%	23.2 ± 3.5	-9.6 ± 3.0	-9.5 ± 3.3	-2 ± 4	
$\Lambda_c^+(2880)$	6.60%	1.0	0.0	1.4 ± 0.4	0.0	
$\Lambda_c^+(2940)$	2.71%	-1.4 ± 0.8	0.8 ± 0.9	-1.0 ± 1.1	-1.7 ± 0.8	
$C_{1/2^+}(D^0p)$	13.05%	-3.8 ± 2.3	-7.3 ± 3.5	2 ± 5	4 ± 5	2.35 ± 0.84
$C_{1/2^-}(D^0p)$	40.25%	-6 ± 6	27 ± 4	9 ± 9	9 ± 6	0.54 ± 0.17
$C_{3/2^+}(D^0p)$	9.61%	-2.1 ± 1.0	-3.1 ± 1.1	2.7 ± 2.6	0.2 ± 2.1	3.50 ± 0.70
$C_{3/2^-}(D^0p)$	2.51%	-7 ± 17	-9 ± 6	-9 ± 28	-10 ± 7	0.74 ± 1.50

from the Dalitz plot and pull distribution in fig. N.11. The projection on m_{D^0p} in fig. N.12 describes the DATA as well, but the previously mentioned interference of the $\Lambda_c^+(2850)$ is less prominent. Rather there is a general constructive interference of all amplitudes towards lower pK masses and destructive inferences with $\Lambda_c^+(2850)$ to higher pK masses. This is shown by the projections on m^2_{pK} for slices of the Λ_c^{+*} peak regions in table N.3. The fitted parameters and resulting fit fractions of the reduced fit are listed in table N.3. All helicity couplings are shown with their covariance ellipses in fig. N.2.

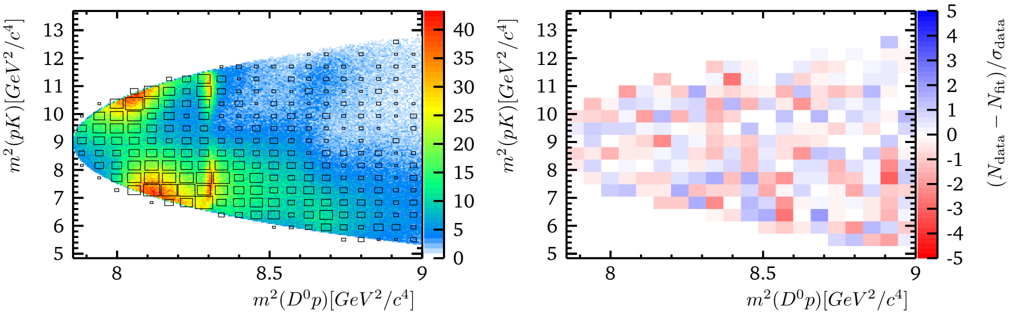

Fig. N.11.: Reduced amplitude fit to the low $m^2_{D^0p}$ region, shown in the Dalitz plot with a resolution of 200 × 200 bins overlayed by DATA in 20^2 bins (left) and the pull distribution (right).

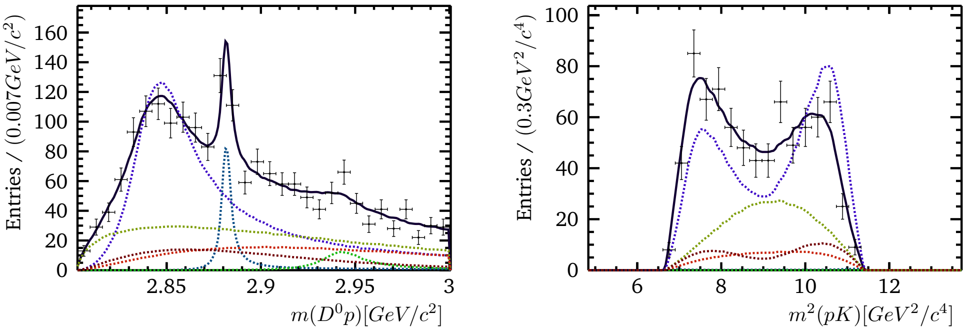

(a) Full Low $m^2_{D^0p}$ Region

(b) $\Lambda_c^+(2850)$-Slice

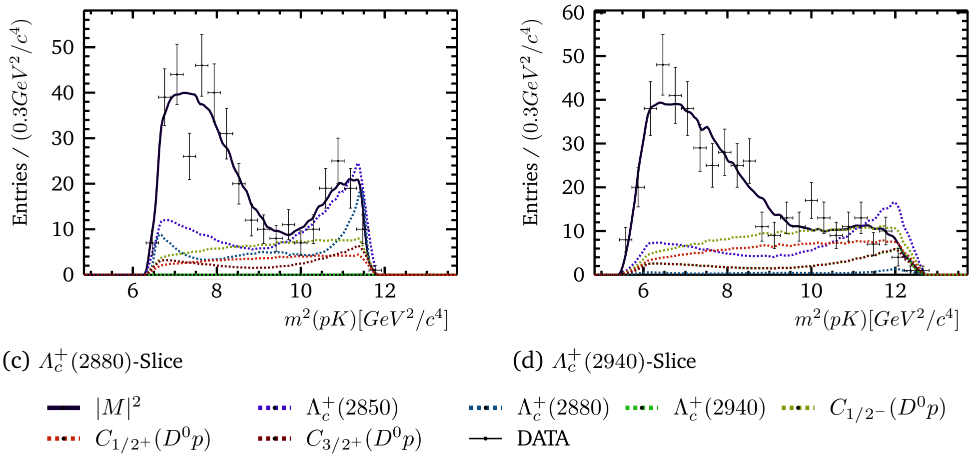

(c) $\Lambda_c^+(2880)$-Slice

(d) $\Lambda_c^+(2940)$-Slice

Fig. N.12.: Reduced amplitude fit to the low $m^2_{D^0p}$ region. Shown as projection on m_{D^0p} (a) and on m^2_{pK} in slices for $\Lambda_c^+(2850)$ with $m_{D^0p} < 2.87\,\mathrm{GeV}/c^2$ (b) , $\Lambda_c^+(2880)$ with $m^2_{D^0p} \in [2.87, 2.90]\,\mathrm{GeV}/c^2$ (c) and $\Lambda_c^+(2940)$ with $m^2_{D^0p} \in [2.92, 2.98]\,\mathrm{GeV}/c^2$ (d). The partial amplitudes are shown as their amplitudes squared.

Tab. N.3.: Fit fractions and fitted parameters of the reduced fit to the low $m^2_{D^0p}$ region.

	$\mathcal{F}_i$	$\mathrm{Re}\,\mathcal{H}^+$	$\mathrm{Im}\,\mathcal{H}^+$	$\mathrm{Re}\,\mathcal{H}^-$	$\mathrm{Im}\,\mathcal{H}^-$	α
$\Lambda_c^+(2850)$	61.72%	24 ± 4	-7 ± 4	-6 ± 5	-1 ± 8	
$\Lambda_c^+(2880)$	6.65%	1.0	0.0	1.4 ± 0.4	0.0	
$\Lambda_c^+(2940)$	3.60%	-2.2 ± 0.8	0.3 ± 0.7	-0.9 ± 0.8	-1.7 ± 0.6	
$C_{1/2^+}(D^0p)$	18.56%	-4 ± 5	-16 ± 6	6 ± 8	12 ± 5	1.27 ± 0.46
$C_{1/2^-}(D^0p)$	35.89%	-9 ± 4	20 ± 4	9 ± 4	6 ± 7	0.82 ± 0.23
$C_{3/2^+}(D^0p)$	13.10%	-5.3 ± 2.9	-9 ± 5	10 ± 12	-3 ± 6	2.15 ± 1.21

N.3.2 Fit Λ^* in Low m^2_{pK} Region

We proceed the study of the Dalitz plot in the low m^2_{pK} region. There are various possible Λ^* states which are listed by the PDG [20]. We select only states with known spin, mass and width parameters, as listed in table N.4. Resonances below the phase space limit are excluded, except for $\Lambda(1405)$. The latter contributes with a modified Flaté lineshape by factoring in its dominant $\Sigma\pi$ channel, as introduced in section 2.5.6. Similar to the fit to the low $m^2_{D^0p}$ region (appendix N.3.1), we consider contributions in one decay channel and therefore can apply the same rules for fixing magnitudes and phases. Being the most prominent amplitude contribution in the low m^2_{pK} region we fix $\mathcal{H}^+[\Lambda(1520)] = 1$ and the phase of $\mathcal{H}^-[\Lambda(1520)]$ to $\Phi^- = 0$. These values will not be fixed in the fit to the full Dalitz plot.

Tab. N.4.: Λ^* resonances and continuum contributions considered in m^2_{pK}. The mass and width are taken from the PDG [20]. The number of helicity couplings for the full and reduced fit are listed.

	J^P	$m/\,\text{MeV}/c^2$	$\Gamma/\,\text{MeV}/c^2$	# full	# reduced
$\Lambda(1405)$	$1/2^-$	1405.1	50.5	2	2
$\Lambda(1520)$	$3/2^-$	1519	16	1	1
$\Lambda(1600)$	$1/2^+$	1600	150	2	2
$\Lambda(1670)$	$1/2^-$	1674	30	2	0
$\Lambda(1690)$	$3/2^-$	1690	70	2	2
$\Lambda(1800)$	$1/2^-$	1800	200	2	0
$\Lambda(1810)$	$1/2^+$	1790	110	2	2
$\Lambda(1820)$	$5/2^+$	1820	80	2	0
$\Lambda(1830)$	$5/2^-$	1825	90	2	0
$\Lambda(1890)$	$3/2^+$	1890	120	2	2
$\Lambda(2100)$	$7/2^-$	2100	200	2	0
$\Lambda(2110)$	$5/2^+$	2090	250	2	2
$\Lambda(2350)$	$9/2^+$	2350	150	2	0

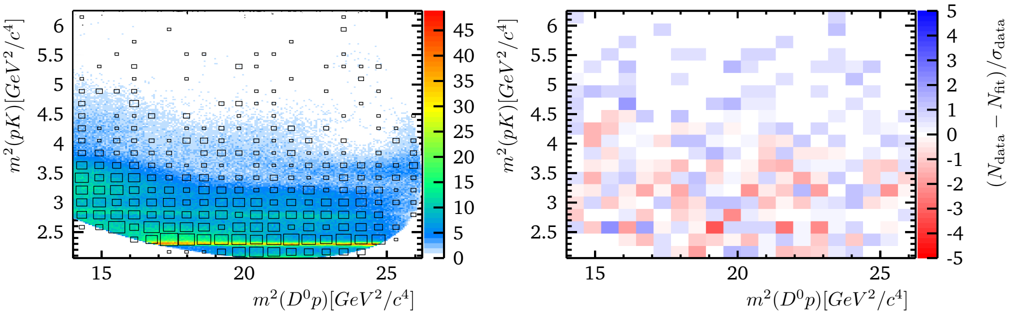

Fig. N.13.: Amplitude fit to the low m^2_{pK} region, shown in the Dalitz plot with a resolution of 200×200 bins overlayed by DATA in 20^2 bins (left) and the pull distribution (right).

The fit result in the low m^2_{pK} Dalitz region in fig. N.13 shows a sufficient agreement of the model and the data based on their pull. Again, we find the resonances to form an asymmetry with the constructive interference towards the lower mass in their helicity distribution, here $m^2_{D^0p}$. The effect however, is less prominent and thus not visible in the projections shown

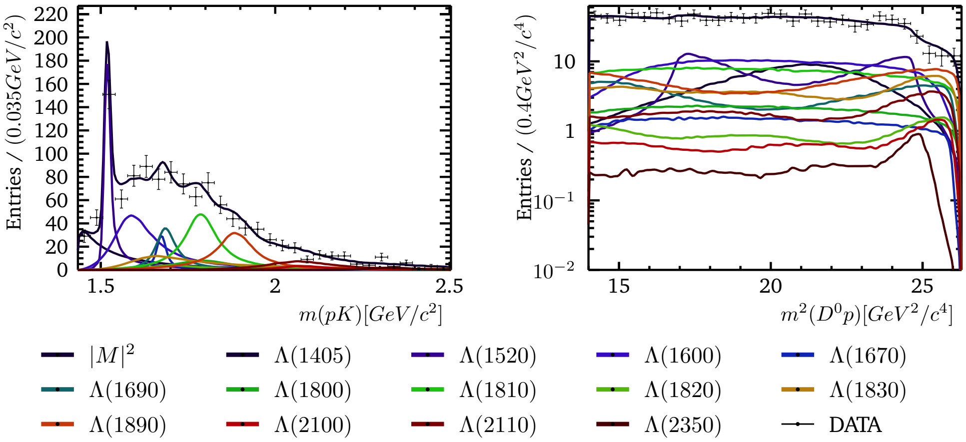

Fig. N.14.: Amplitude fit to the low m^2_{pK} region. Shown as projection on m_{pK} (left) and on $m^2_{D^0p}$ (right). The partial amplitudes are shown as their amplitudes squared.

in fig. N.14. There is a distinct peak of the $\Lambda(1520)$ resonance visible in the m_{pK} projection and is also observed in the two dimensional representation of the fitted Dalitz region. There are numerous other Λ^* resonances contributing to the unstructured parts of the projections, resulting into a faint structure in the Dalitz plot. These contributions are only distinguishable by their lineshape based on their spin. A summary of the fitted parameters and the resulting fit fractions is presented in table N.5. All helicity couplings are shown with their covariance ellipses in fig. N.3.

Tab. N.5.: Fit fractions and fitted parameters of the fit in the low m^2_{pK} region.

	$\mathcal{F}_i$	$\mathrm{Re}\,\mathcal{H}^+$	$\mathrm{Im}\,\mathcal{H}^+$	$\mathrm{Re}\,\mathcal{H}^-$	$\mathrm{Im}\,\mathcal{H}^-$
$\Lambda(1405)$	12.09%	9 ± 17	-11 ± 14	-8 ± 9	22 ± 11
$\Lambda(1520)$	15.15%	1.0	0.0	8 ± 4	0.0
$\Lambda(1600)$	21.19%	-6 ± 17	16 ± 11	-15 ± 10	0 ± 6
$\Lambda(1670)$	3.47%	-2.3 ± 2.7	-2.5 ± 2.3	0.3 ± 2.6	-1.4 ± 2.1
$\Lambda(1690)$	8.54%	-3 ± 10	-11 ± 6	-7 ± 6	-3 ± 8
$\Lambda(1800)$	5.18%	-2 ± 10	7 ± 9	-6 ± 9	9 ± 10
$\Lambda(1810)$	18.28%	-5 ± 11	-11 ± 8	2 ± 9	12 ± 9
$\Lambda(1820)$	2.37%	$(4 \pm 4) \times 10^1$	$(0 \pm 4) \times 10^1$	-6 ± 29	$(2 \pm 4) \times 10^1$
$\Lambda(1830)$	10.08%	$(2 \pm 5) \times 10^1$	$(3 \pm 5) \times 10^1$	$(9 \pm 5) \times 10^1$	$(2 \pm 4) \times 10^1$
$\Lambda(1890)$	13.47%	6 ± 20	22 ± 12	-8 ± 11	5 ± 12
$\Lambda(2100)$	1.76%	-16 ± 14	-5 ± 22	8 ± 9	0 ± 10
$\Lambda(2110)$	5.06%	-21 ± 19	8 ± 29	19 ± 14	-8 ± 16
$\Lambda(2350)$	0.78%	0 ± 9	1 ± 11	6 ± 8	12 ± 8

Similar to the Λ_c^{+*} model, we iteratively remove insignificant amplitude contributions. As to expect, resonances of high spin are removed. They contribute with a high angular momentum and therefore lessen in probability. We are able to reduce the fit from 49 free parameters to a set of 29 by maintaining the ability to describe the fitted Dalitz region. There is no difference visible for the fitted Dalitz region in fig. N.15. There is also an agreement of model and data in the projections on m_{pK} and $m^2_{D^0p}$ in fig. N.16. The latter is again shown for slices in the resonances mass distribution m_{pK}. The $m^2_{D^0p}$ projections in slices emphasise the mentioned separability by the different lineshapes of the resonances and show an increasing interference effect towards higher pK masses. The resulting fit fractions and parameters are listed in table N.6. Due to the missing number of events in the low m^2_{pK} region, the fitted parameters of the reduced model show high statistical uncertainties. These are reflected in the covariance ellipses of the helicity couplings in fig. N.4.

Tab. N.6.: Fit fractions and fitted parameters of the reduced fit in the low m^2_{pK} region.

	$\mathcal{F}_i$	$\mathrm{Re}\,\mathcal{H}^+$	$\mathrm{Im}\,\mathcal{H}^+$	$\mathrm{Re}\,\mathcal{H}^-$	$\mathrm{Im}\,\mathcal{H}^-$
$\Lambda(1405)$	12.11%	57 ± 25	12 ± 22	-16 ± 14	44 ± 22
$\Lambda(1520)$	14.39%	1.0	0.0	22 ± 7	0.0
$\Lambda(1600)$	42.75%	$(-3 \pm 4) \times 10^1$	-43 ± 15	-67 ± 21	6 ± 12
$\Lambda(1690)$	14.40%	-21 ± 12	29 ± 21	6 ± 13	-29 ± 12
$\Lambda(1810)$	40.24%	-32 ± 10	31 ± 26	49 ± 19	17 ± 14
$\Lambda(1890)$	13.29%	40 ± 24	30 ± 19	-23 ± 15	-35 ± 12
$\Lambda(2110)$	8.06%	$(1 \pm 4) \times 10^1$	47 ± 33	48 ± 28	79 ± 29

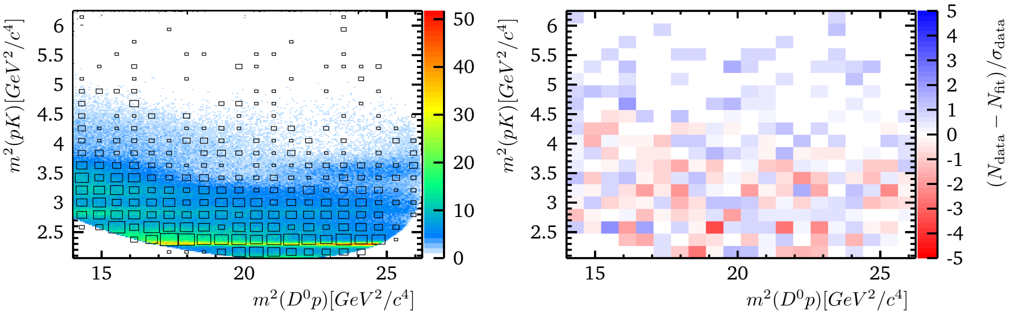

Fig. N.15.: Reduced amplitude fit to the low m^2_{pK} region, shown in the Dalitz plot with a resolution of 200×200 bins overlayed by DATA in 20^2 bins (left) and the pull distribution (right).

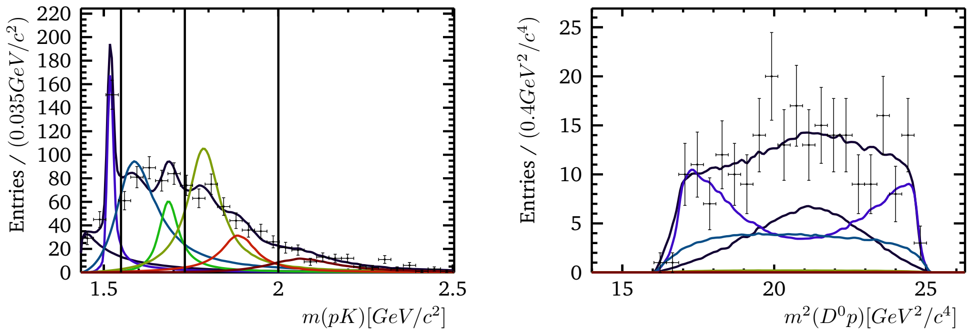

(a) Full Low m^2_{pK} Region

(b) Slice 1

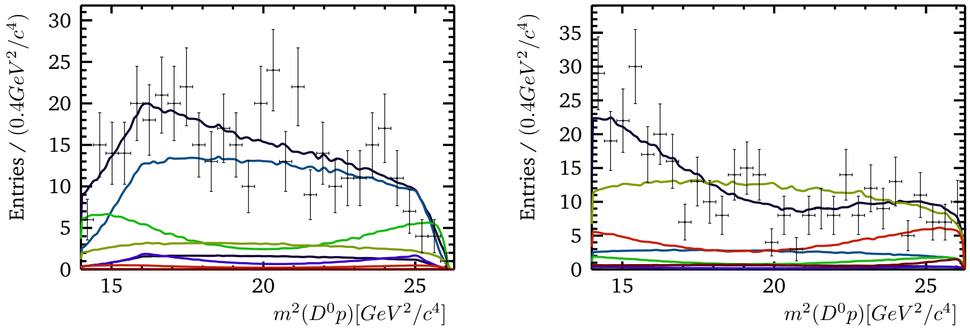

(c) Slice 2

(d) Slice 3

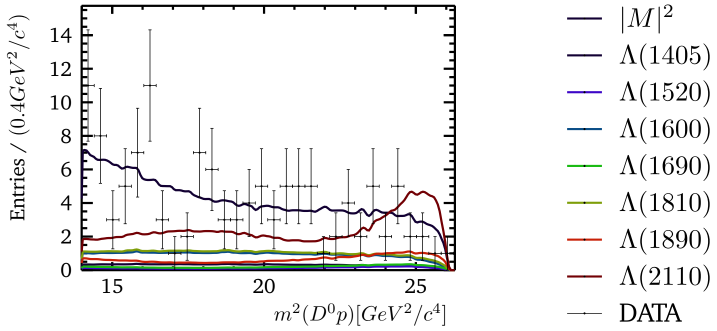

(e) Slice 4

Fig. N.16.: Reduced amplitude fit to the low m^2_{pK} region. Shown as projection on m_{pK} (a) and on $m^2_{D^0p}$ in slices of m_{pK} (b-e). The vertical lines in (a) indicate the slices 1-4 from left to right. The partial amplitudes are shown as their amplitudes squared.

N.3.3 Amplitude Fit to Full Dalitz Plot - Full Amplitude Set

In section 6.3.1 we present the fit of the reduced amplitude model to the full Dalitz plot. Here we show the fitted amplitude model with all considered Λ_c^{+*} and Λ^* resonances. It is shown in the full Dalitz plot in fig. N.17. The projections on the $m^2_{D^0p}$ and m^2pK are shown in fig. N.18. A summary of the fitted parameters and the resulting fit fractions is presented in table N.7.

Tab. N.7.: Fit fractions and fitted parameters of the fit in the full Dalitz plot region.

	$\mathcal{F}_i$	$\mathrm{Re}\,\mathcal{H}^+$	$\mathrm{Im}\,\mathcal{H}^+$	$\mathrm{Re}\,\mathcal{H}^-$	$\mathrm{Im}\,\mathcal{H}^-$
$\Lambda_c^+(2850)$	26.67%	-101 ± 14	-73 ± 14	-94 ± 9	-87 ± 13
$\Lambda_c^+(2880)$	3.28%	1.0	0.0	13.0 ± 1.1	11.2 ± 1.6
$\Lambda_c^+(2940)$	3.43%	12.7 ± 3.1	4.8 ± 3.4	-10.6 ± 3.3	-24.0 ± 2.4
$C_{1/2^+}(D^0p)$	9.16%	-49 ± 17	136 ± 11	34 ± 14	-15 ± 19
$C_{1/2^-}(D^0p)$	18.22%	128 ± 19	-29 ± 12	93 ± 14	22 ± 9
$C_{3/2^+}(D^0p)$	4.46%	$(5 \pm 4) \times 10^1$	$(1.4 \pm 0.4) \times 10^2$	$(1 \pm 4) \times 10^1$	-49 ± 20
$C_{3/2^-}(D^0p)$	1.68%	-35 ± 18	23 ± 22	-64 ± 15	-36 ± 15
$\Lambda(1405)$	5.16%	-15 ± 8	59.1 ± 2.9	-12.5 ± 3.4	9 ± 10
$\Lambda(1520)$	4.32%	-9.2 ± 0.7	-5.9 ± 1.5	12.0 ± 1.0	-0.1 ± 1.7
$\Lambda(1600)$	9.62%	30.7 ± 3.0	-28 ± 4	-18 ± 4	-29 ± 6
$\Lambda(1670)$	2.62%	-1.8 ± 1.0	8.8 ± 0.8	4.5 ± 0.9	5.2 ± 1.1
$\Lambda(1690)$	4.47%	-10.3 ± 1.5	8.4 ± 2.1	-2.3 ± 2.2	-30.0 ± 2.3
$\Lambda(1800)$	14.80%	62 ± 4	22 ± 6	7 ± 4	-27.7 ± 3.2
$\Lambda(1810)$	4.30%	-25.8 ± 1.8	6.0 ± 2.8	-8.9 ± 2.2	0.0 ± 3.3
$\Lambda(1820)$	1.04%	84 ± 18	-5 ± 9	1 ± 14	-51 ± 10
$\Lambda(1830)$	1.22%	-19 ± 9	-49 ± 10	81 ± 9	43 ± 8
$\Lambda(1890)$	3.80%	10 ± 5	36 ± 4	-15.3 ± 2.1	3.2 ± 2.1
$\Lambda(2100)$	2.75%	-8 ± 4	-19 ± 5	58 ± 4	35 ± 6
$\Lambda(2110)$	3.92%	-7 ± 8	-27 ± 4	74 ± 5	20 ± 6
$\Lambda(2350)$	0.81%	0.5 ± 2.0	-10 ± 4	-6.0 ± 2.0	36 ± 4

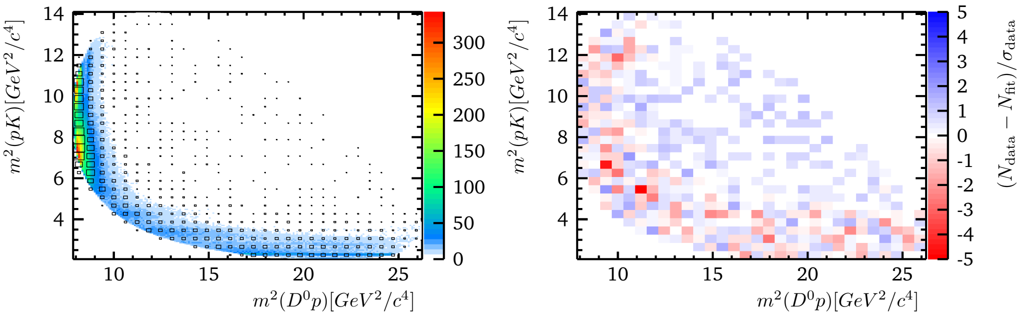

Fig. N.17.: Amplitude fit of all possible Λ_c^{+*} and Λ^* resonances to the full phase space, shown in the Dalitz plot with a resolution of 200 × 200 bins overlayed by DATA in 30 × 30 bins (left) and the pull distribution (right).

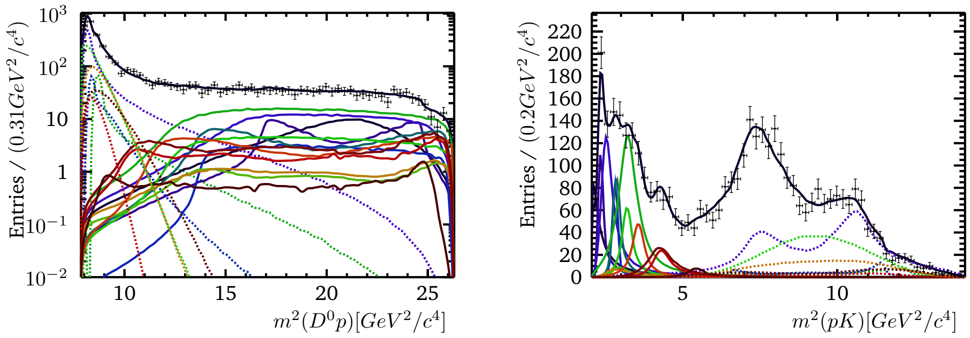

(a) Full Dalitz

(b) Full Dalitz

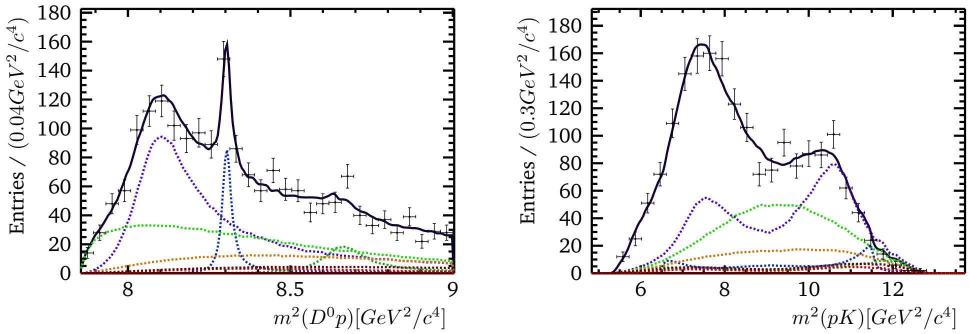

(c) Λ_c^{+*} Region Slice

(d) Λ_c^{+*} Region Slice

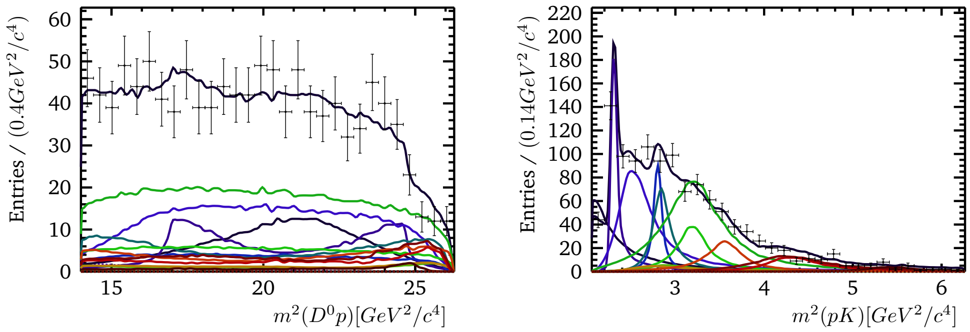

(e) Λ^* Region Slice

(f) Λ^* Region Slice

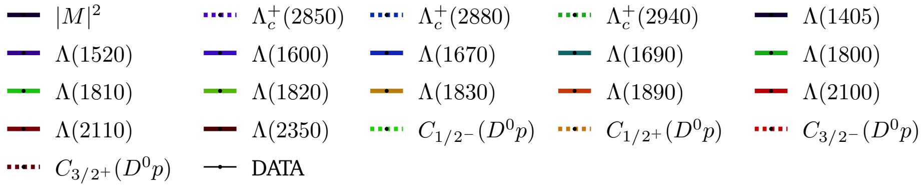

Fig. N.18.: Amplitude fit of all possible Λ_c^{+*} and Λ^* resonances to the full Dalitz plot. Shown as projection on $m^2_{D^0p}$ (left) and on m^2_{pK} (right). The partial components are shown as their amplitudes squared.

N.3.4 Partial Amplitudes Squared

The partial amplitudes squared of the reduced model in section 6.3.1 are only shown as projections. In fig. N.19 we show them in the two dimensional Dalitz plane.

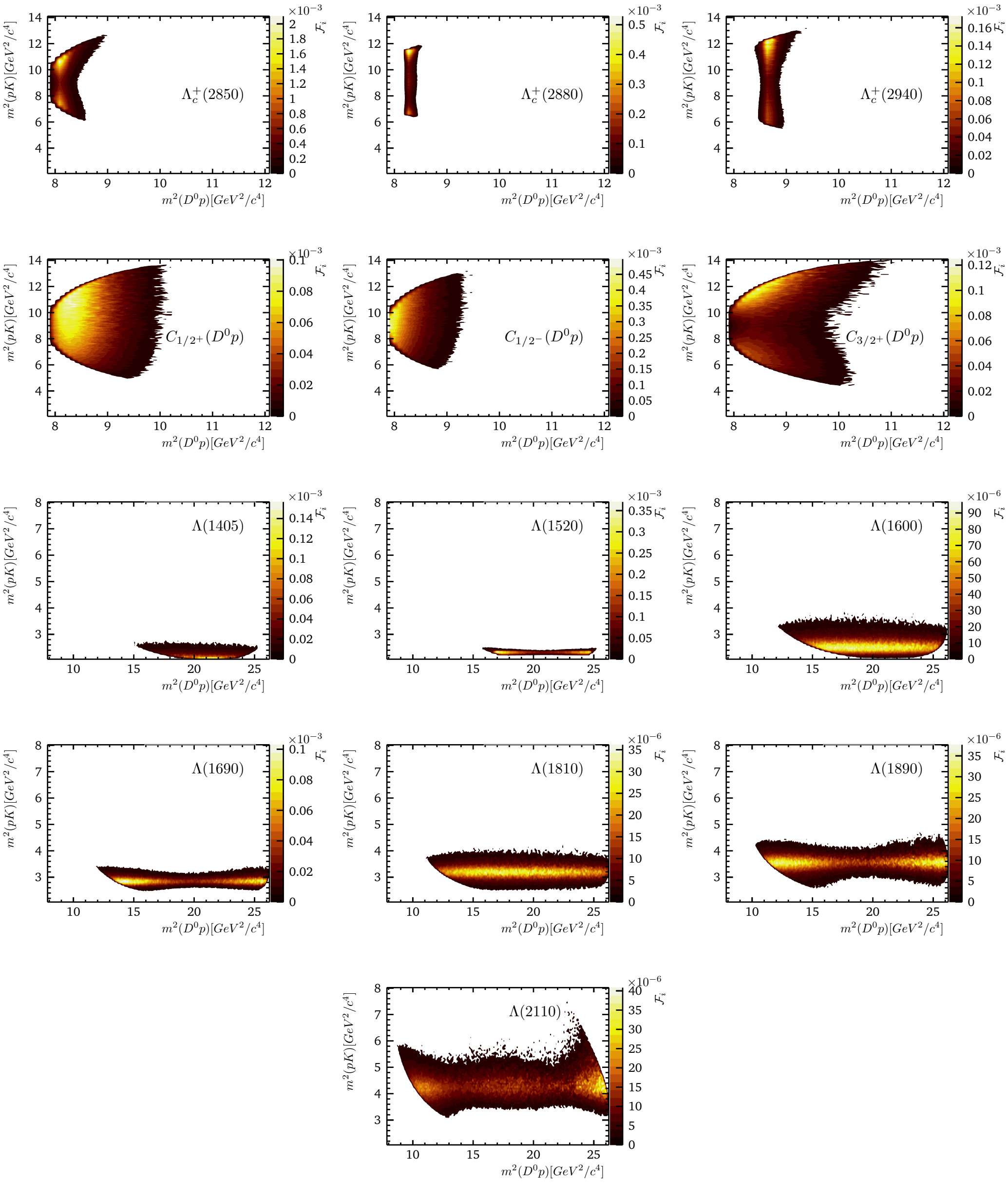

Fig. N.19.: Partial amplitudes squared of the reduced amplitude model, normalised and then scaled according to their fit fraction. They are visualised as contour plot from a resolution of 200 × 200 bins for full Dalitz plot.

N.3.5 Fit Validation & Corrected Values

In this appendix, we show the fitted distributions used to validate the amplitude model of $\Lambda_b^0 \to D^0 pK$ with $D^0 \to K\pi$ for the fit in a 2σ mass window from the Λ_b^0 mass peak value, as described in section 6.3.2. All distributions correspond to 1000 pseudo experiments. We do not show the 78 distributions of the interference fit fractions. In the following can be found the

- sum of the (interference) fit fractions in fig. N.20
- fit fraction correlations in fig. N.21
- fit fraction distributions in fig. N.22
- magnitude pull distributions of the helicity couplings in fig. N.23
- phase residual distributions of the helicity couplings in fig. N.24
- real part pull distributions of the helicity couplings in fig. N.25
- imaginary part pull distributions of the helicity couplings in fig. N.26
- correction table for the real and imaginary parts in table N.8
- interference fit fraction summary with uncertainties in table N.9

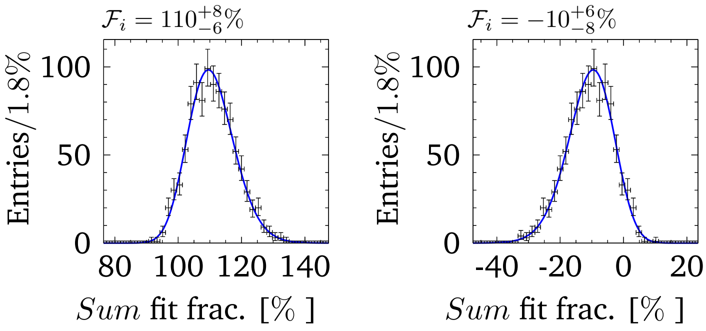

(a) fit fraction (b) interference fit fraction

Fig. N.20.: Sum of the (interference) fit fractions $\sum \mathcal{F}_{i(j)}$ from 1000 pseudo experiments of the reduced fit to the full Dalitz plot in section 6.3.1.

Tab. N.8.: Bias and scale of the systematic uncertainties for the helicity couplings real and imaginary part. The last row shows the corrected fit parameters significance in standard deviations.

		Fit value	Bias corr.	Error scale		Corrected	$n \cdot \sigma$
				lo	hi		
$\Lambda_c^+(2850)$	$\mathrm{Re}\,\mathcal{H}^+$	-120 ± 35	-15.4	-1.93	1.91	$(-1.4 \pm 0.7) \times 10^2$	$2.01 \cdot \sigma$
	$\mathrm{Im}\,\mathcal{H}^+$	-176 ± 30	-9.44	-1.94	2.33	$(-1.9^{+0.7}_{-0.6}) \times 10^2$	$2.87 \cdot \sigma$
	$\mathrm{Re}\,\mathcal{H}^-$	-131 ± 22	-1.63	-2.6	2.63	$(-1.3 \pm 0.6) \times 10^2$	$2.34 \cdot \sigma$
	$\mathrm{Im}\,\mathcal{H}^-$	$(9 \pm 4) \times 10^1$	-8.94	-1.78	1.78	83 ± 66	$1.26 \cdot \sigma$
$\Lambda_c^+(2880)$	$\mathrm{Re}\,\mathcal{H}^-$	20.3 ± 1.3	$+1.25$	-2.56	2.4	$21.5^{+3.2}_{-3.4}$	$6.44 \cdot \sigma$
	$\mathrm{Im}\,\mathcal{H}^-$	-7 ± 4	-1.97	-1.88	1.87	-9 ± 8	$1.04 \cdot \sigma$
$\Lambda_c^+(2940)$	$\mathrm{Re}\,\mathcal{H}^+$	18.6 ± 2.5	$+1.2$	-3.63	3.56	20 ± 9	$2.16 \cdot \sigma$
	$\mathrm{Im}\,\mathcal{H}^+$	9 ± 5	$+0.655$	-1.89	2.3	10^{+13}_{-10}	$0.87 \cdot \sigma$
	$\mathrm{Re}\,\mathcal{H}^-$	-15 ± 4	-0.854	-2.76	2.88	-16 ± 12	$1.35 \cdot \sigma$
	$\mathrm{Im}\,\mathcal{H}^-$	-25 ± 5	$+2.03$	-1.76	1.92	-22 ± 9	$2.48 \cdot \sigma$
$\Lambda(1405)$	$\mathrm{Re}\,\mathcal{H}^+$	-28 ± 13	$+0.237$	-1.57	1.75	-28^{+24}_{-21}	$1.23 \cdot \sigma$
	$\mathrm{Im}\,\mathcal{H}^+$	56 ± 6	$+4.27$	-2.33	1.84	61^{+12}_{-15}	$4.48 \cdot \sigma$
	$\mathrm{Re}\,\mathcal{H}^-$	-19 ± 14	$+9.32$	-1.96	1.76	-10^{+24}_{-27}	$0.39 \cdot \sigma$
	$\mathrm{Im}\,\mathcal{H}^-$	8 ± 8	-6.7	-3.11	3.1	1 ± 24	$0.05 \cdot \sigma$
$\Lambda(1520)$	$\mathrm{Re}\,\mathcal{H}^+$	-11.3 ± 1.2	-1.34	-4.3	4.97	-13^{+6}_{-5}	$2.30 \cdot \sigma$
	$\mathrm{Im}\,\mathcal{H}^+$	-8 ± 4	$+1.2$	-1.45	1.43	-7 ± 6	$1.13 \cdot \sigma$
	$\mathrm{Re}\,\mathcal{H}^-$	9.7 ± 2.8	$+1.67$	-2.99	2.01	11^{+6}_{-8}	$1.64 \cdot \sigma$
	$\mathrm{Im}\,\mathcal{H}^-$	-11.3 ± 2.0	-0.0757	-2.55	3.52	-11^{+7}_{-5}	$1.88 \cdot \sigma$
$\Lambda(1600)$	$\mathrm{Re}\,\mathcal{H}^+$	39 ± 9	$+1.78$	-2.12	2.44	41^{+21}_{-18}	$2.09 \cdot \sigma$
	$\mathrm{Im}\,\mathcal{H}^+$	-40 ± 10	-7.48	-1.19	2.03	-48^{+21}_{-12}	$2.87 \cdot \sigma$
	$\mathrm{Re}\,\mathcal{H}^-$	-35 ± 12	$+4.54$	-2.01	2.17	-30^{+25}_{-23}	$1.25 \cdot \sigma$
	$\mathrm{Im}\,\mathcal{H}^-$	10 ± 12	-5.71	-2.18	2.08	4^{+26}_{-27}	$0.15 \cdot \sigma$
$\Lambda(1690)$	$\mathrm{Re}\,\mathcal{H}^+$	-30 ± 7	$+1.48$	-2.2	2.2	-29 ± 16	$1.78 \cdot \sigma$
	$\mathrm{Im}\,\mathcal{H}^+$	-16 ± 4	-0.575	-3.09	3.25	-17^{+13}_{-12}	$1.31 \cdot \sigma$
	$\mathrm{Re}\,\mathcal{H}^-$	-10 ± 7	$+5.18$	-2.52	2.38	-5^{+16}_{-17}	$0.31 \cdot \sigma$
	$\mathrm{Im}\,\mathcal{H}^-$	-25 ± 9	-4.25	-1.43	1.61	-29^{+14}_{-12}	$2.27 \cdot \sigma$
$\Lambda(1810)$	$\mathrm{Re}\,\mathcal{H}^+$	-3 ± 9	$+1.11$	-2.36	1.34	-2^{+12}_{-21}	$0.13 \cdot \sigma$
	$\mathrm{Im}\,\mathcal{H}^+$	-21 ± 7	-1.99	-2.41	1.65	-23^{+11}_{-16}	$1.72 \cdot \sigma$
	$\mathrm{Re}\,\mathcal{H}^-$	-8 ± 5	$+4.17$	-3.57	3.97	-3^{+20}_{-18}	$0.18 \cdot \sigma$
	$\mathrm{Im}\,\mathcal{H}^-$	-24.6 ± 2.2	-0.158	-3.65	5.75	-25^{+13}_{-8}	$2.34 \cdot \sigma$
$\Lambda(1890)$	$\mathrm{Re}\,\mathcal{H}^+$	-12 ± 8	-2.58	-2.0	2.07	-14 ± 16	$0.90 \cdot \sigma$
	$\mathrm{Im}\,\mathcal{H}^+$	36 ± 4	$+0.211$	-3.33	3.33	36 ± 13	$2.74 \cdot \sigma$
	$\mathrm{Re}\,\mathcal{H}^-$	-15 ± 17	$+3.06$	-1.19	1.08	-12^{+19}_{-21}	$0.61 \cdot \sigma$
	$\mathrm{Im}\,\mathcal{H}^-$	-34 ± 8	-0.18	-1.34	2.17	-34^{+17}_{-11}	$2.44 \cdot \sigma$
$\Lambda(2110)$	$\mathrm{Re}\,\mathcal{H}^+$	26 ± 14	-13.4	-1.83	2.12	13^{+30}_{-26}	$0.46 \cdot \sigma$
	$\mathrm{Im}\,\mathcal{H}^+$	-90 ± 14	$+3.7$	-2.05	2.3	-86^{+33}_{-29}	$2.78 \cdot \sigma$
	$\mathrm{Re}\,\mathcal{H}^-$	67 ± 11	$+19.3$	-3.22	2.16	86^{+23}_{-34}	$3.04 \cdot \sigma$
	$\mathrm{Im}\,\mathcal{H}^-$	36 ± 13	$+5.87$	-2.89	2.89	42 ± 38	$1.12 \cdot \sigma$
$C_{1/2^-}(D^0p)$	$\mathrm{Re}\,\mathcal{H}^+$	186 ± 18	$+6.32$	-2.13	2.06	$(1.9 \pm 0.4) \times 10^2$	$5.13 \cdot \sigma$
	$\mathrm{Im}\,\mathcal{H}^+$	$(0 \pm 4) \times 10^1$	$+3.96$	-1.98	2.03	8^{+73}_{-71}	$0.10 \cdot \sigma$
	$\mathrm{Re}\,\mathcal{H}^-$	89 ± 12	$+4.01$	-3.37	3.37	94 ± 41	$2.27 \cdot \sigma$
	$\mathrm{Im}\,\mathcal{H}^-$	-40 ± 18	-19.8	-2.41	2.39	-60 ± 43	$1.40 \cdot \sigma$
$C_{1/2^+}(D^0p)$	$\mathrm{Re}\,\mathcal{H}^+$	-55 ± 32	-3.6	-1.8	1.83	-58^{+58}_{-57}	$1.00 \cdot \sigma$
	$\mathrm{Im}\,\mathcal{H}^+$	140 ± 11	-8.68	-3.59	3.41	$(1.3 \pm 0.4) \times 10^2$	$3.38 \cdot \sigma$
	$\mathrm{Re}\,\mathcal{H}^-$	106 ± 18	-3.54	-2.48	2.84	$(1.0^{+0.5}_{-0.4}) \times 10^2$	$2.18 \cdot \sigma$
	$\mathrm{Im}\,\mathcal{H}^-$	-41 ± 20	-0.443	-2.67	2.69	-42^{+55}_{-54}	$0.77 \cdot \sigma$
$C_{3/2^+}(D^0p)$	$\mathrm{Re}\,\mathcal{H}^+$	$(-0 \pm 4) \times 10^1$	-8.6	-2.27	2.74	$(-0.1^{+1.0}_{-0.8}) \times 10^2$	$0.15 \cdot \sigma$
	$\mathrm{Im}\,\mathcal{H}^+$	143 ± 22	$+10.9$	-2.99	3.43	$(1.5^{+0.7}_{-0.6}) \times 10^2$	$2.21 \cdot \sigma$
	$\mathrm{Re}\,\mathcal{H}^-$	$(2.3 \pm 0.6) \times 10^2$	$+2.15$	-1.79	1.23	$(2.3^{+0.7}_{-1.1}) \times 10^2$	$2.53 \cdot \sigma$
	$\mathrm{Im}\,\mathcal{H}^-$	$(2 \pm 5) \times 10^1$	-46.2	-2.19	2.2	$(-0.2^{+1.2}_{-1.1}) \times 10^2$	$0.19 \cdot \sigma$

Tab. N.9.: Summary of the evaluated (interference) fit fractions.

	$C_{3/2^+}(D^0p)$	$C_{1/2^+}(D^0p)$	$C_{1/2^-}(D^0p)$	$\Lambda(2110)$	$\Lambda(1890)$	$\Lambda(1810)$	$\Lambda(1690)$	$\Lambda(1600)$	$\Lambda(1520)$	$\Lambda(1405)$	$\Lambda_c^+(2940)$	$\Lambda_c^+(2880)$	$\Lambda_c^+(2850)$
$\Lambda_c^+(2850)$	-7^{+5}_{-6}	$-0.43^{+0.17}_{-0.18}$	$-4.0^{+0.5}_{-0.4}$	$0.20^{+0.32}_{-0.34}$	$0.67^{+0.15}_{-0.21}$	0.6 ± 0.4	$0.29^{+0.19}_{-0.23}$	$1.66^{+0.34}_{-0.54}$	$0.25^{+0.08}_{-0.13}$	$1.10^{+0.32}_{-0.46}$	-0.13 ± 0.05	$0.058^{+0.021}_{-0.023}$	$33.8^{+3.4}_{-3.5}$
$\Lambda_c^+(2880)$	$0.029^{+0.022}_{-0.025}$	$0.10^{+0.08}_{-0.07}$	0.021 ± 0.009	$0.05^{+0.05}_{-0.06}$	$0.057^{+0.019}_{-0.024}$	$0.043^{+0.023}_{-0.030}$	$0.008^{+0.028}_{-0.034}$	$0.095^{+0.020}_{-0.034}$	$0.015^{+0.017}_{-0.023}$	$0.050^{+0.010}_{-0.016}$	$0.15^{+0.06}_{-0.09}$	2.9 ± 0.5	
$\Lambda_c^+(2940)$	-0.08 ± 0.06	$-0.75^{+0.20}_{-0.18}$	$-0.22^{+0.05}_{-0.04}$	$0.21^{+0.06}_{-0.08}$	-0.06 ± 0.06	0.13 ± 0.19	$0.13^{+0.10}_{-0.13}$	$-0.24^{+0.24}_{-0.20}$	$0.20^{+0.06}_{-0.08}$	$-0.07^{+0.07}_{-0.05}$	$2.9^{+0.8}_{-0.7}$		
$\Lambda(1405)$	$0.04^{+0.09}_{-0.12}$	$-0.24^{+0.14}_{-0.13}$	$0.48^{+0.21}_{-0.29}$	$0.002^{+0.019}_{-0.016}$	$-0.067^{+0.035}_{-0.031}$	-0.06 ± 0.05	0.06 ± 0.06	$0.15^{+0.06}_{-0.07}$	$0.03^{+0.04}_{-0.05}$	$3.5^{+0.6}_{-0.5}$			
$\Lambda(1520)$	-0.03 ± 0.11	$0.42^{+0.10}_{-0.17}$	-0.01 ± 0.06	$-0.056^{+0.026}_{-0.020}$	$-0.010^{+0.009}_{-0.008}$	$-0.03^{+0.05}_{-0.04}$	$-0.0^{+0.7}_{-0.9}$	0.05 ± 0.09	3.9 ± 0.5				
$\Lambda(1600)$	$0.19^{+0.22}_{-0.24}$	$-0.66^{+0.32}_{-0.26}$	$0.47^{+0.16}_{-0.21}$	$0.23^{+0.10}_{-0.12}$	$-0.12^{+0.11}_{-0.08}$	$-0.1^{+2.5}_{-2.9}$	-0.14 ± 0.09	$9.0^{+2.2}_{-1.3}$					
$\Lambda(1690)$	$-0.03^{+0.13}_{-0.14}$	$0.40^{+0.15}_{-0.20}$	0.06 ± 0.07	$0.007^{+0.022}_{-0.021}$	$-0.026^{+0.010}_{-0.009}$	0.25 ± 0.11	$4.8^{+1.3}_{-1.0}$						
$\Lambda(1810)$	$0.09^{+0.11}_{-0.20}$	$0.17^{+0.18}_{-0.22}$	0.10 ± 0.18	$-0.25^{+0.13}_{-0.14}$	-0.35 ± 0.11	$4.0^{+3.1}_{-1.1}$							
$\Lambda(1890)$	$0.09^{+0.12}_{-0.15}$	$-0.052^{+0.038}_{-0.030}$	$0.40^{+0.16}_{-0.20}$	$-0.047^{+0.035}_{-0.033}$	$3.6^{+0.9}_{-0.8}$								
$\Lambda(2110)$	0.09 ± 0.14	0.2 ± 0.4	$0.20^{+0.07}_{-0.08}$	5.1 ± 0.7									
$C_{1/2^-}(D^0p)$	-1.2 ± 0.6	$-1.31^{+0.34}_{-0.43}$	$17.8^{+1.9}_{-1.5}$										
$C_{1/2^+}(D^0p)$	$-0.02^{+0.18}_{-0.17}$	$7.7^{+2.6}_{-2.1}$											
$C_{3/2^+}(D^0p)$	$7.7^{+3.4}_{-2.4}$												

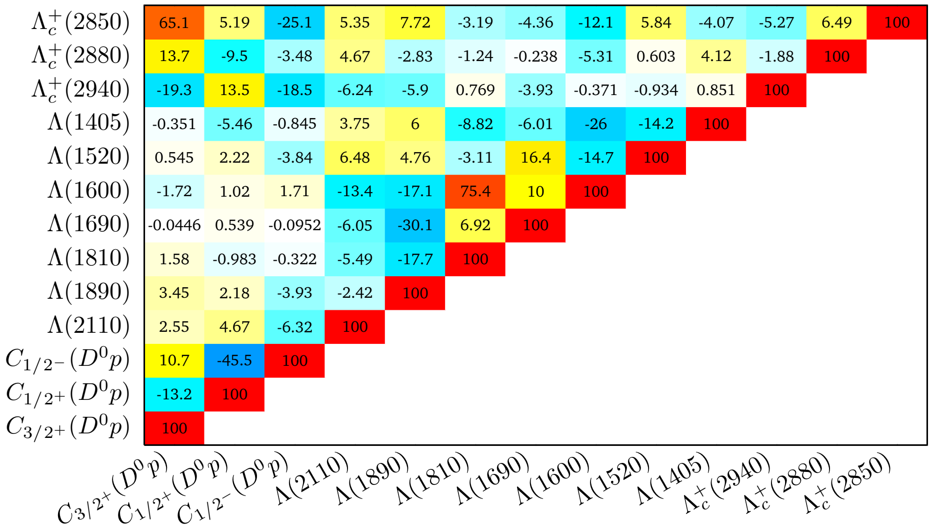

	$C_{3/2^+}(D^0p)$	$C_{1/2^+}(D^0p)$	$C_{1/2^-}(D^0p)$	$\Lambda(2110)$	$\Lambda(1890)$	$\Lambda(1810)$	$\Lambda(1690)$	$\Lambda(1600)$	$\Lambda(1520)$	$\Lambda(1405)$	$\Lambda_c^+(2940)$	$\Lambda_c^+(2880)$	$\Lambda_c^+(2850)$
$\Lambda_c^+(2850)$	65.1	5.19	-25.1	5.35	7.72	-3.19	-4.36	-12.1	5.84	-4.07	-5.27	6.49	100
$\Lambda_c^+(2880)$	13.7	-9.5	-3.48	4.67	-2.83	-1.24	-0.238	-5.31	0.603	4.12	-1.88	100	
$\Lambda_c^+(2940)$	-19.3	13.5	-18.5	-6.24	-5.9	0.769	-3.93	-0.371	-0.934	0.851	100		
$\Lambda(1405)$	-0.351	-5.46	-0.845	3.75	6	-8.82	-6.01	-26	-14.2	100			
$\Lambda(1520)$	0.545	2.22	-3.84	6.48	4.76	-3.11	16.4	-14.7	100				
$\Lambda(1600)$	-1.72	1.02	1.71	-13.4	-17.1	75.4	10	100					
$\Lambda(1690)$	-0.0446	0.539	-0.0952	-6.05	-30.1	6.92	100						
$\Lambda(1810)$	1.58	-0.983	-0.322	-5.49	-17.7	100							
$\Lambda(1890)$	3.45	2.18	-3.93	-2.42	100								
$\Lambda(2110)$	2.55	4.67	-6.32	100									
$C_{1/2^-}(D^0p)$	10.7	-45.5	100										
$C_{1/2^+}(D^0p)$	-13.2	100											
$C_{3/2^+}(D^0p)$	100												

Fig. N.21.: Correlation $\rho(\mathcal{F}_i, \mathcal{F}_j)$ of the fit fractions in %. Only the top half of the matrix is shown.

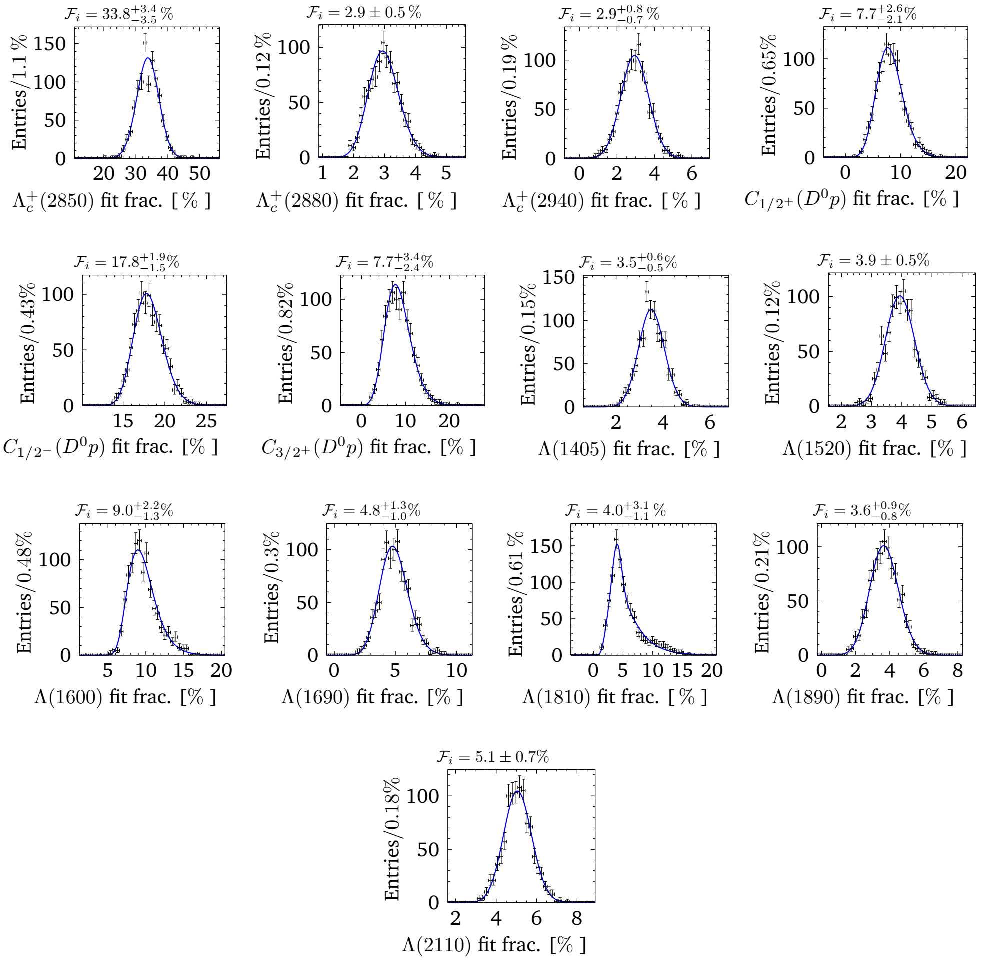

Fig. N.22.: Fit fractions $\mathcal{F}_i$ from 1000 pseudo experiments of the reduced fit to the full Dalitz plot in section 6.3.1.

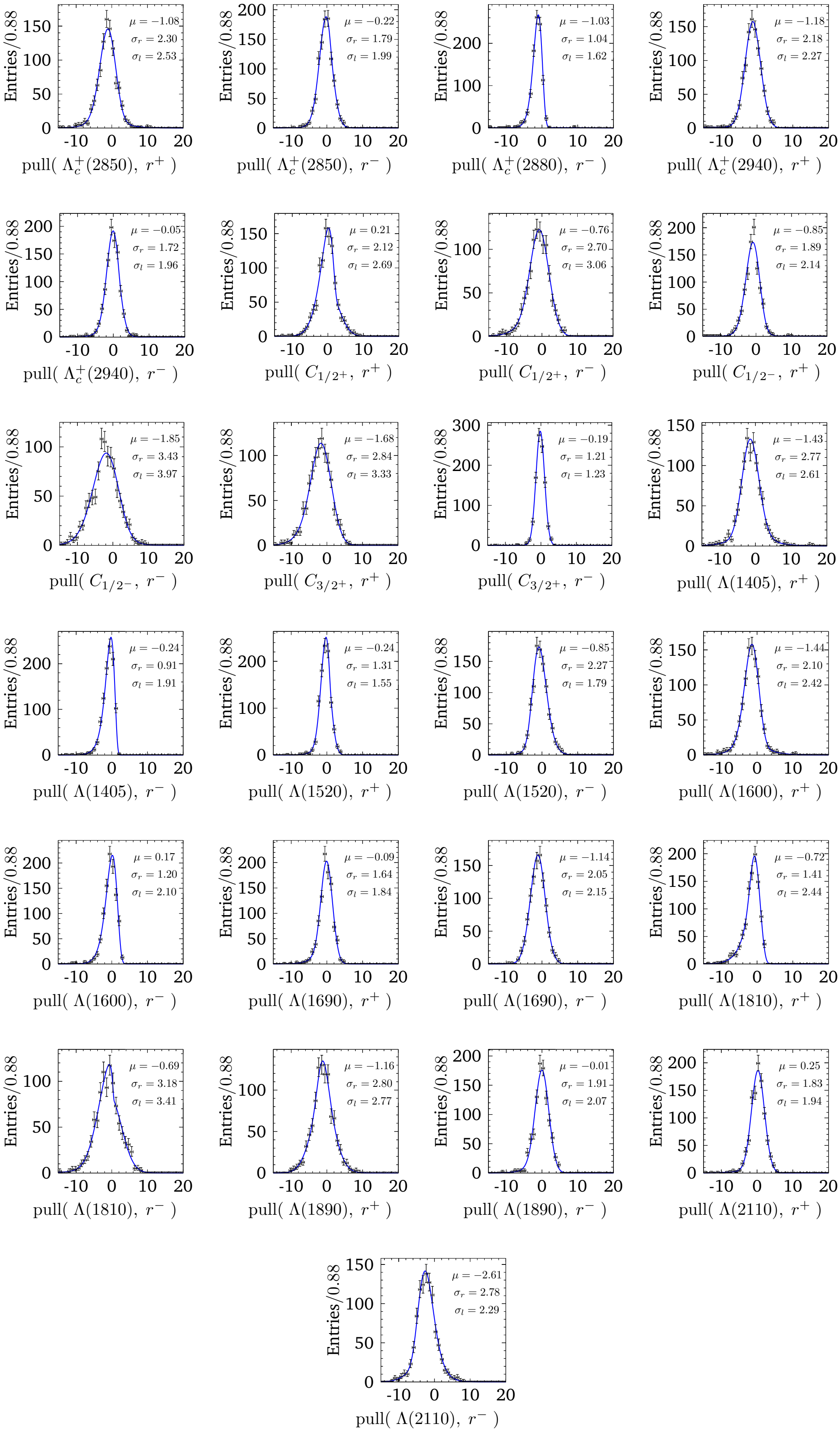

Fig. N.23.: Pull distribution of magnitude r of the helicity couplings from 1000 pseudo experiments of the reduced fit to the full Dalitz plot in section 6.3.1. C denotes the continuum contribution $C(D^0p)$.

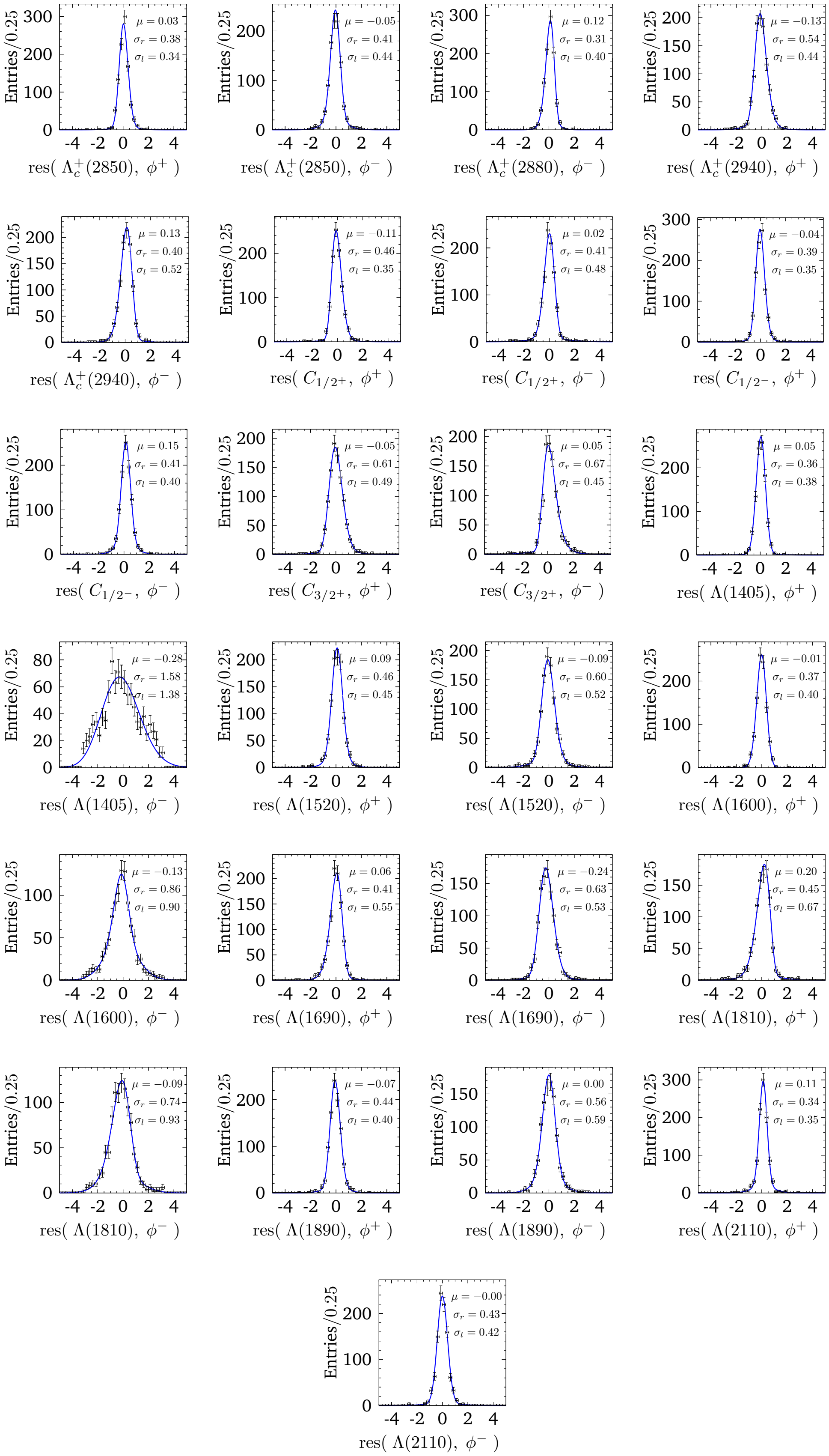

res($\Lambda_c^+(2850)$, ϕ^+) res($\Lambda_c^+(2850)$, ϕ^-) res($\Lambda_c^+(2880)$, ϕ^-) res($\Lambda_c^+(2940)$, ϕ^+)

res($\Lambda_c^+(2940)$, ϕ^-) res($C_{1/2^+}$, ϕ^+) res($C_{1/2^+}$, ϕ^-) res($C_{1/2^-}$, ϕ^+)

res($C_{1/2^-}$, ϕ^-) res($C_{3/2^+}$, ϕ^+) res($C_{3/2^+}$, ϕ^-) res($\Lambda(1405)$, ϕ^+)

res($\Lambda(1405)$, ϕ^-) res($\Lambda(1520)$, ϕ^+) res($\Lambda(1520)$, ϕ^-) res($\Lambda(1600)$, ϕ^+)

res($\Lambda(1600)$, ϕ^-) res($\Lambda(1690)$, ϕ^+) res($\Lambda(1690)$, ϕ^-) res($\Lambda(1810)$, ϕ^+)

res($\Lambda(1810)$, ϕ^-) res($\Lambda(1890)$, ϕ^+) res($\Lambda(1890)$, ϕ^-) res($\Lambda(2110)$, ϕ^+)

res($\Lambda(2110)$, ϕ^-)

Fig. N.24.: Residuum distribution of phase Φ of the helicity couplings from 1000 pseudo experiments of the reduced fit to the full Dalitz plot in section 6.3.1. C denotes the continuum contribution $C(D^0p)$.

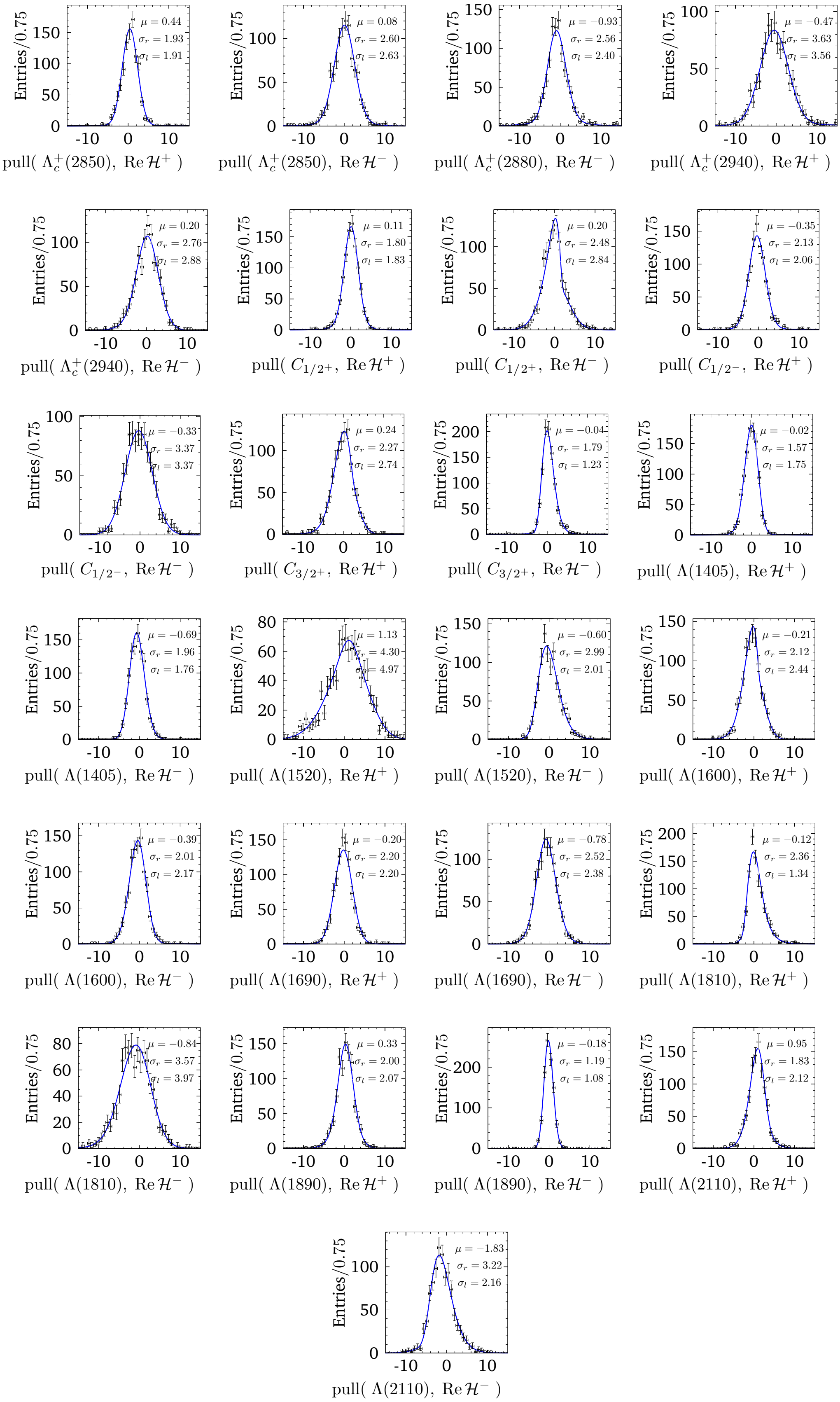

Fig. N.25.: Pull distribution of real part of the helicity couplings from 1000 pseudo experiments of the reduced fit to the full Dalitz plot in section 6.3.1. C denotes the continuum contribution $C(D^0p)$.

]

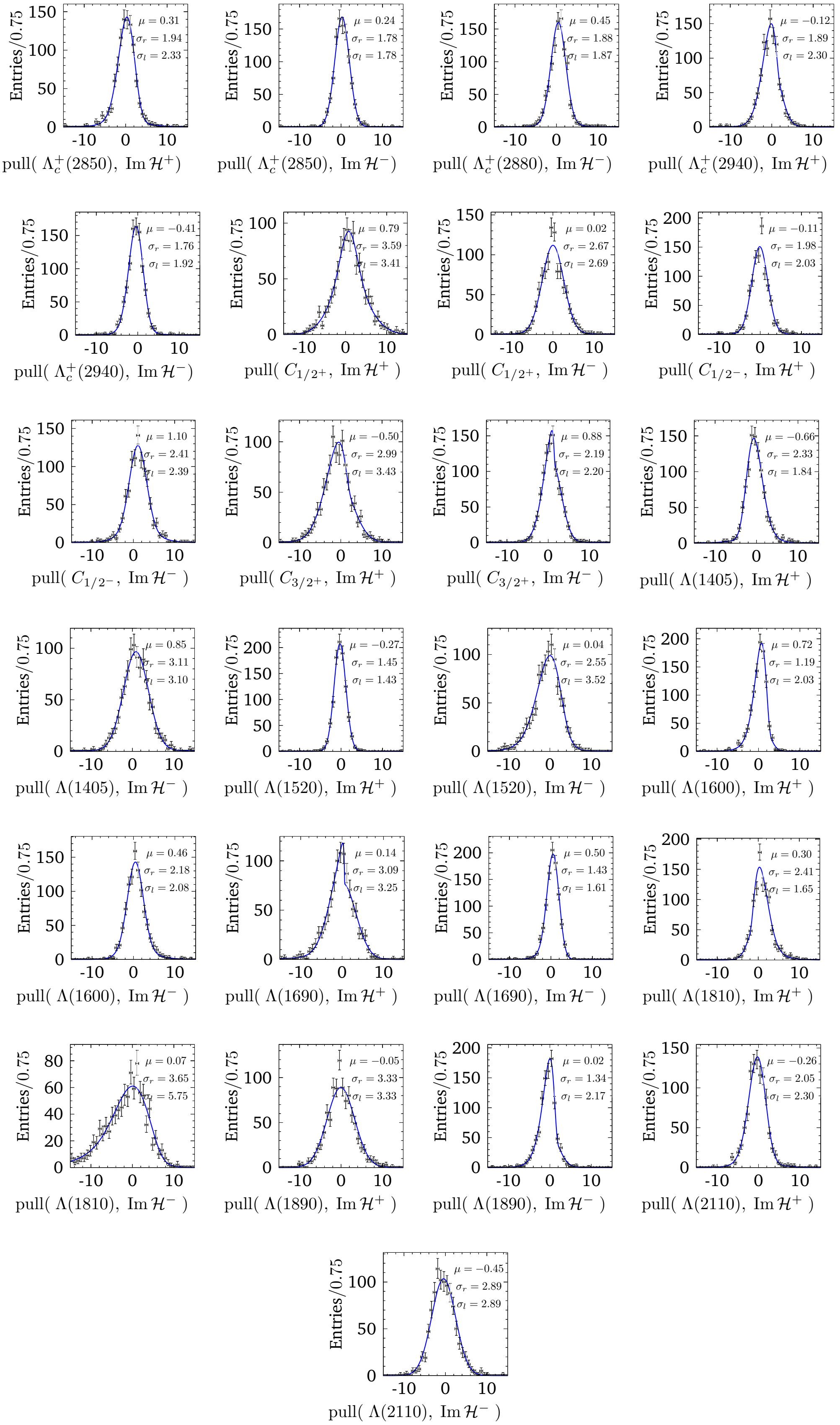

Fig. N.26.: Pull distribution of imaginary part of the helicity couplings from 1000 pseudo experiments of the reduced fit to the full Dalitz plot in section 6.3.1. C denotes the continuum contribution $C(D^0p)$.

N.4 Amplitude *sFit*

N.4.1 *sFit* Validation & Corrected Values

In this appendix, we show the fitted distributions used to validate the amplitude model of $\Lambda_b^0 \to D^0 pK$ with $D^0 \to K\pi$ for the *sFit*, as described in section 6.4.3. We do not show the 92 distributions of the interference fit fractions. All distributions correspond to 800 pseudo experiments. In the following can be found the

- sum of the (interference) fit fractions in fig. N.27
- fit fraction distributions in fig. N.28
- magnitude pull distributions of the helicity couplings in fig. N.29
- phase residual distributions of the helicity couplings in fig. N.30
- interference fit fraction summary with uncertainties in table N.10

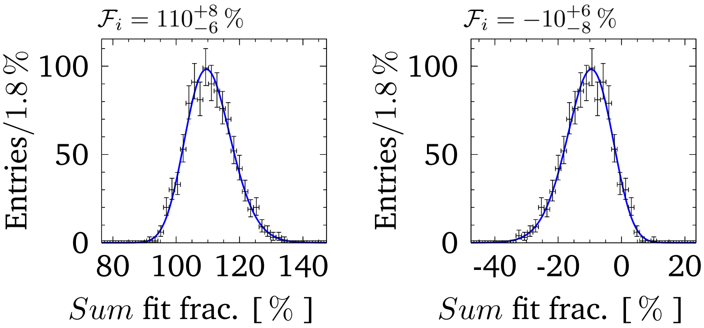

(a) fit fraction (b) interference fit fraction

Fig. N.27.: Sum of the (interference) fit fractions $\sum \mathcal{F}_{i(j)}$ from 800 pseudo experiments of the reduced fit to the full Dalitz plot in section 6.4.2.

Tab. N.10.: Summary of the evaluated *sFit* (interference) fit fractions.

	$C_{1/2^+}(D^0p)$	$C_{1/2^-}(D^0p)$	$\Lambda(2350)$	$\Lambda(2110)$	$\Lambda(2100)$	$\Lambda(1890)$	$\Lambda(1810)$	$\Lambda(1690)$	$\Lambda(1600)$	$\Lambda(1520)$	$\Lambda(1405)$	$\Lambda_c^+(2940)$	$\Lambda_c^+(2880)$	$\Lambda_c^+(2850)$
$\Lambda_c^+(2850)$	$-0.88^{+0.12}_{-0.11}$	-4.1 ± 0.4	$0.20^{+0.05}_{-0.06}$	$0.61^{+0.16}_{-0.20}$	$0.31^{+0.08}_{-0.11}$	0.05 ± 0.25	$-0.97^{+0.41}_{-0.27}$	$-0.15^{+0.20}_{-0.18}$	$-0.7^{+0.6}_{-0.4}$	$0.04^{+0.11}_{-0.12}$	$0.13^{+0.35}_{-0.43}$	$-0.217^{+0.037}_{-0.031}$	$0.073^{+0.015}_{-0.017}$	$22.9^{+2.0}_{-1.9}$
$\Lambda_c^+(2880)$	0.15 ± 0.08	$0.035^{+0.010}_{-0.012}$	-0.018 ± 0.018	-0.06 ± 0.05	-0.035 ± 0.035	$0.02^{+0.04}_{-0.06}$	$-0.070^{+0.052}_{-0.035}$	$-0.017^{+0.035}_{-0.032}$	$-0.03^{+0.06}_{-0.05}$	$-0.033^{+0.031}_{-0.014}$	$-0.008^{+0.023}_{-0.022}$	$0.13^{+0.08}_{-0.09}$	$3.4^{+0.7}_{-0.5}$	
$\Lambda_c^+(2940)$	-0.85 ± 0.23	$-0.26^{+0.07}_{-0.06}$	0.002 ± 0.004	$0.15^{+0.07}_{-0.08}$	$0.051^{+0.025}_{-0.027}$	$0.08^{+0.07}_{-0.09}$	$0.16^{+0.16}_{-0.21}$	$-0.01^{+0.14}_{-0.15}$	$0.07^{+0.24}_{-0.25}$	$0.12^{+0.08}_{-0.11}$	$-0.05^{+0.06}_{-0.05}$	$4.0^{+1.0}_{-0.8}$		
$\Lambda(1405)$	$0.08^{+0.14}_{-0.16}$	$-0.01^{+0.34}_{-0.36}$	0.0003 ± 0.0008	$-0.002^{+0.014}_{-0.015}$	$-0.003^{+0.006}_{-0.005}$	$-0.052^{+0.035}_{-0.030}$	$0.030^{+0.031}_{-0.047}$	$-0.145^{+0.052}_{-0.032}$	$0.11^{+0.05}_{-0.06}$	$0.074^{+0.028}_{-0.039}$	$2.3^{+0.6}_{-0.5}$			
$\Lambda(1520)$	$-0.04^{+0.24}_{-0.22}$	$0.06^{+0.07}_{-0.09}$	$-0.004^{+0.005}_{-0.004}$	$-0.019^{+0.024}_{-0.019}$	$-0.03^{+0.05}_{-0.04}$	$0.016^{+0.009}_{-0.013}$	$-0.04^{+0.06}_{-0.05}$	$-0.5^{+0.7}_{-0.6}$	$0.06^{+0.08}_{-0.07}$	2.8 ± 0.5				
$\Lambda(1600)$	$0.71^{+0.29}_{-0.44}$	$-0.55^{+0.32}_{-0.21}$	$-0.0022^{+0.0031}_{-0.0030}$	-0.10 ± 0.10	$-0.003^{+0.025}_{-0.028}$	$-0.09^{+0.15}_{-0.11}$	-3.0 ± 2.9	$0.15^{+0.07}_{-0.09}$	7.5 ± 1.6					
$\Lambda(1690)$	$0.55^{+0.15}_{-0.25}$	$-0.10^{+0.08}_{-0.06}$	$-0.011^{+0.007}_{-0.006}$	$0.007^{+0.024}_{-0.023}$	$-0.17^{+0.07}_{-0.06}$	$-0.019^{+0.015}_{-0.012}$	$0.18^{+0.10}_{-0.09}$	$4.7^{+1.0}_{-0.9}$						
$\Lambda(1810)$	$0.56^{+0.24}_{-0.31}$	$-0.25^{+0.22}_{-0.18}$	$-0.0068^{+0.0033}_{-0.0026}$	$-0.40^{+0.15}_{-0.11}$	$-0.070^{+0.035}_{-0.024}$	$-0.06^{+0.17}_{-0.21}$	$7.0^{+2.4}_{-2.1}$							
$\Lambda(1890)$	$-0.02^{+0.07}_{-0.05}$	$-0.21^{+0.35}_{-0.30}$	$-0.0004^{+0.0014}_{-0.0013}$	-0.02 ± 0.04	0.005 ± 0.009	4.2 ± 0.9								
$\Lambda(2100)$	$0.43^{+0.25}_{-0.27}$	$0.44^{+0.10}_{-0.12}$	$-0.080^{+0.023}_{-0.026}$	-0.27 ± 0.04	$2.8^{+0.8}_{-0.6}$									
$\Lambda(2110)$	$0.68^{+0.29}_{-0.39}$	$0.34^{+0.05}_{-0.07}$	-0.17 ± 0.05	$3.7^{+0.9}_{-0.8}$										
$\Lambda(2350)$	$0.09^{+0.13}_{-0.14}$	$0.27^{+0.10}_{-0.12}$	$0.64^{+0.29}_{-0.20}$											
$C_{1/2^-}(D^0p)$	$-3.6^{+0.5}_{-0.4}$	$30.7^{+2.3}_{-2.5}$												
$C_{1/2^+}(D^0p)$	$13.8^{+2.5}_{-2.3}$													

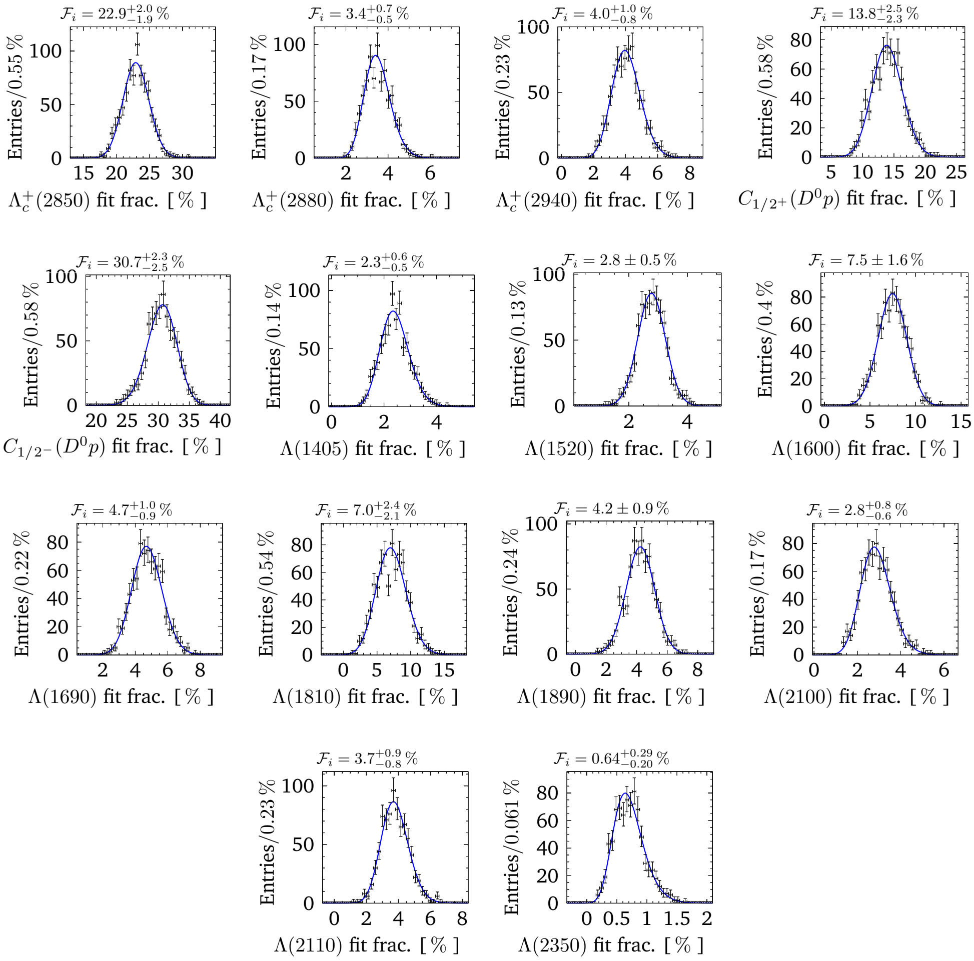

Fig. N.28.: Fit fractions $\mathcal{F}_i$ from 800 pseudo experiments of the reduced fit to the full Dalitz plot in section 6.4.2.

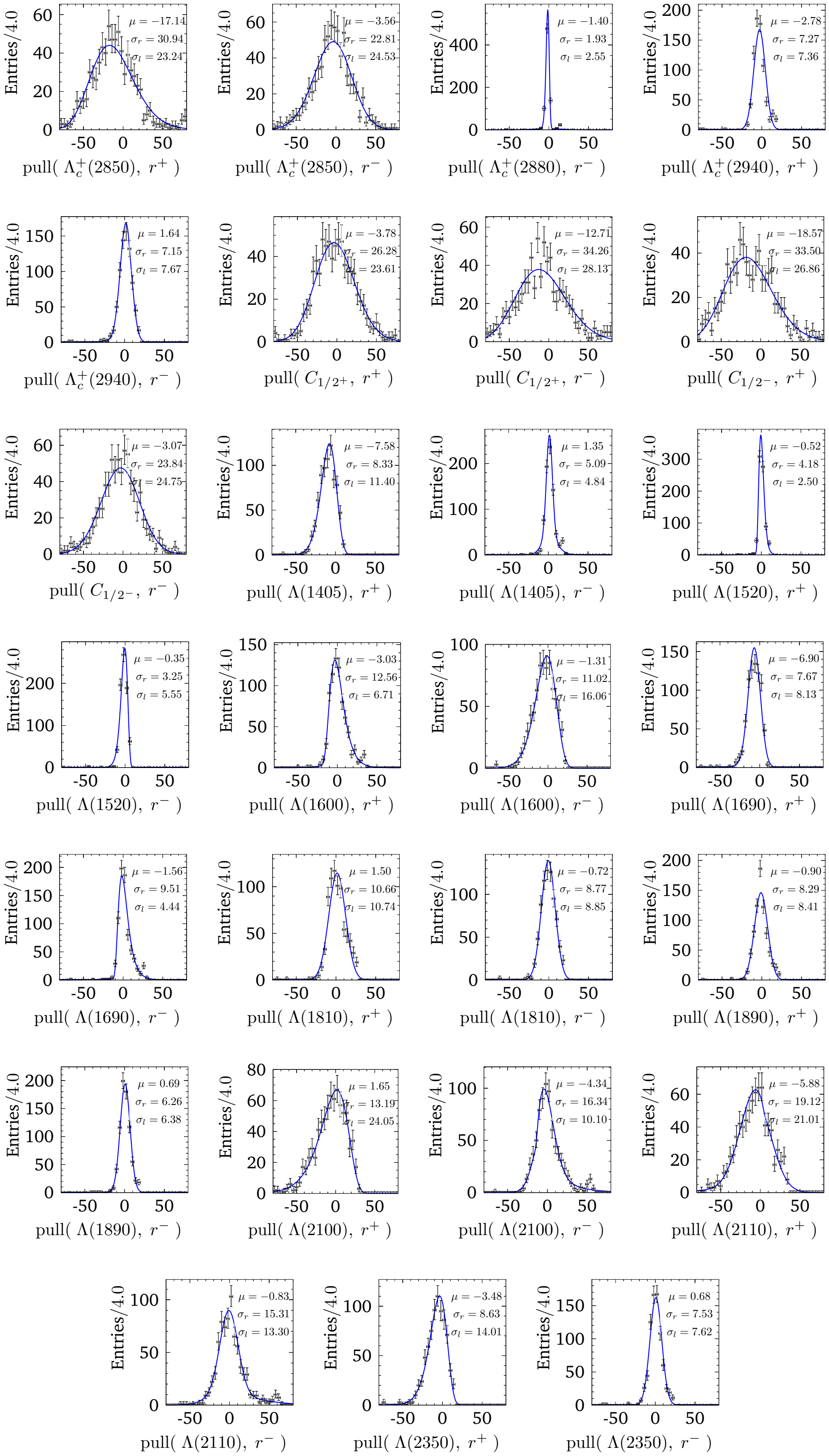

Fig. N.29.: Pull distribution of magnitude r of the helicity couplings from 800 pseudo experiments of the reduced fit to the full Dalitz plot in section 6.4.2. C denotes the continuum contribution $C(D^0p)$.

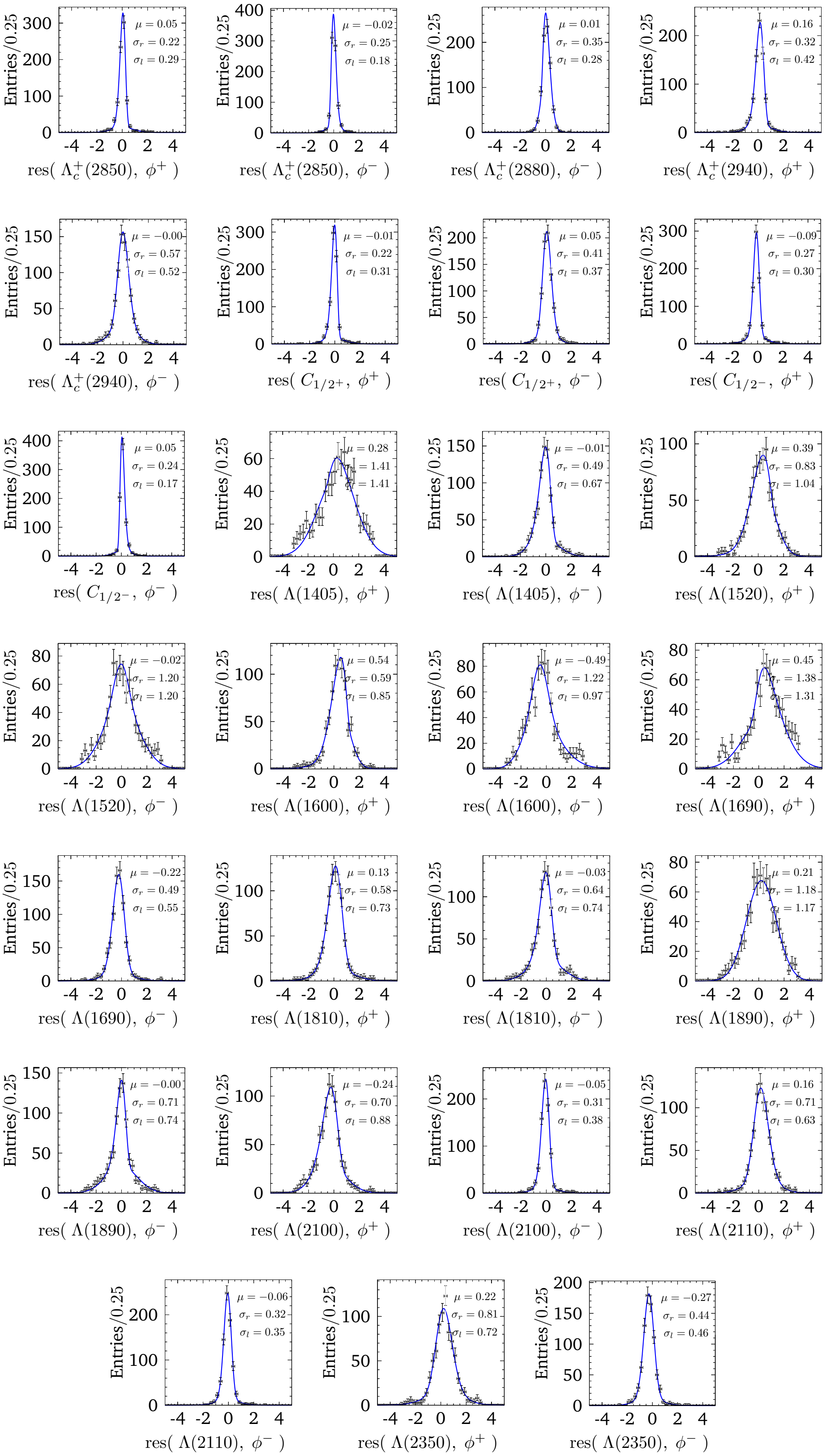

Fig. N.30.: Residuum distribution of phase Φ of the helicity couplings from 800 pseudo experiments of the reduced fit to the full Dalitz plot in section 6.4.2. C denotes the continuum contribution $C(D^0p)$.

N.4.2 Partial Amplitudes Squared

The partial amplitudes squared of the reduced model of the *sFit* in section 6.4.2 are only shown as projections. In fig. N.31 we show them in the two dimensional Dalitz plane.

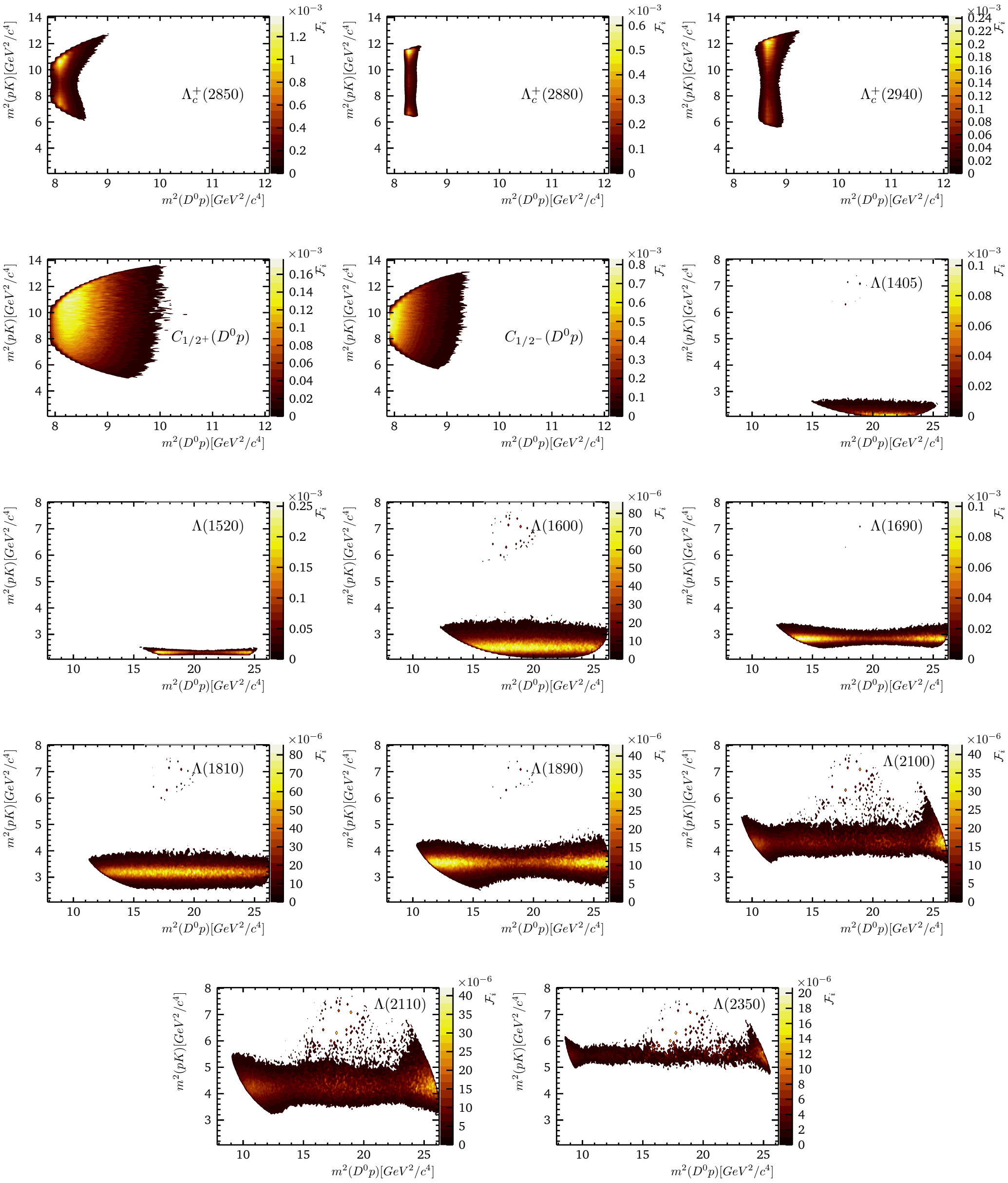

Fig. N.31.: Partial amplitudes squared of the reduced amplitude model of the *sFit*, normalised and then scaled according to their fit fraction. They are visualised as contour plot from a resolution of 200 × 200 bins for full Dalitz plot.

Abbreviations

ADS	Atwood-Dunietz-Soni	10
ALICE	A Large Ion Collider Experiment	28
ATLAS	A Toroidal LHC ApparatuS	28
BDT	boosted decision-tree	50
BDTG	gradient boosted decision-tree	49
CKM	Cabibbo-Kobayashi-Maskawa	2
CMB	cosmic microwave background	1
CMS	Compact Muon Solenoid	28
CP	charge-parity	1
CPT	charge-parity-time reversal	7
DTF	`DecayTreeFit`	41
FCNC	Flavour-Changing-Neutral-Current	6
GLW	Gronau-London-Wyler	10
HPD	Hybrid-Photo-Detectors	33
IT	Inner Tracker	31
LHC	Large-Hadron-Collider	27
LHCb	Large-Hadron-Collider beauty	2
LHCf	Large Hadron Collider forward	28
LL	logarithmic likelihood	39
mis-ID	mis-identification	39
MC	Monte Carlo	40
NC	Neutral Current	6
NLL	negative logarithmic likelihood	82
OT	Outer Tracker	32
PID	particle identification	38
PV	primary vertex	38
RICH	Ring Imaging Cherenkov Detector	29
ROC	receiver operating characteristic	51
ST	Silicon Tracker	31
SM	Standard Model	1
TOTEM	Total Elastic and Diffractive Cross Section Measurement	28
TT	Tracker Turicensis	31
VELO	Vertex Locator	29
PDG	particle data group	79
PDF	probability denstity function	71
TFA	TensorFlowAnalysis	82

List of Figures

List of Tables

Bibliography

[1] Paul A.M. Dirac. 'The quantum theory of the electron'. In: *Proc. Roy. Soc. Lond. A* A117 (1928), pp. 610–624.

[2] James M. Cline. 'Baryogenesis'. In: *Les Houches Summer School - Session 86: Particle Physics and Cosmology: The Fabric of Spacetime*. Sept. 2006. arXiv: `hep-ph/0609145`.

[3] Utpal Sarkar. *Particle and astroparticle physics*. Series in high energy physics, cosmology, and gravitation. New York, USA: Taylor & Francis, 2008.

[4] A.D. Sakharov. 'Violation of CP Invariance, C asymmetry, and baryon asymmetry of the universe'. In: *Sov. Phys. Usp.* 34.5 (1991), pp. 392–393.

[5] J. H. Christenson, J. W. Cronin, V. L. Fitch and R. Turlay. 'Evidence for the 2π Decay of the K_2^0 Meson'. In: *Phys. Rev. Lett.* 13 (1964), pp. 138–140.

[6] Nicola Cabibbo. 'Unitary Symmetry and Leptonic Decays'. In: *Phys. Rev. Lett.* 10 (12 June 1963), pp. 531–533.

[7] Makoto Kobayashi and Toshihide Maskawa. 'CP Violation in the Renormalizable Theory of Weak Interaction'. In: *Prog. Theor. Phys.* 49 (1973), pp. 652–657.

[8] Ashton B. Carter and A. I. Sanda. 'CP Violation in B Meson Decays'. In: *Phys. Rev.* D23 (1981), p. 1567.

[9] Bernard Aubert et al. 'The BaBar detector'. In: *Nucl. Instrum. Meth. A* 479 (2002), pp. 1–116. arXiv: `hep-ex/0105044`.

[10] A. Bondar. 'The BELLE detector'. In: *Nucl. Instrum. Meth. A* 408 (1998). Ed. by P. Schlein, pp. 64–76.

[11] M.B. Gavela, P. Hernandez, J. Orloff and O. Pene. 'Standard model CP violation and baryon asymmetry'. In: *Mod. Phys. Lett. A* 9 (1994), pp. 795–810. arXiv: `hep-ph/9312215`.

[12] Werner Bernreuther. 'CP violation and baryogenesis'. In: *Lect. Notes Phys.* 591 (2002), pp. 237–293. arXiv: `hep-ph/0205279`.

[13] Isard Dunietz. 'CP violation with beautiful baryons'. In: *Z. Phys. C* 56 (1992), pp. 129–144.

[14] A.K. Giri, R. Mohanta and M.P. Khanna. 'Possibility of extracting the weak phase gamma from $\Lambda_b \to \Lambda D^0$ decays'. In: *Phys. Rev. D* 65 (2002), p. 073029. arXiv: `hep-ph/0112220`.

[15] Isard Dunietz. 'CP violation with selftagging B(d) modes'. In: *Phys. Lett. B* 270 (1991), pp. 75–80.

[16] Roel Aaij et al. 'LHCb Detector Performance'. In: *Int. J. Mod. Phys.* A30.07 (2015), p. 1530022. arXiv: `1412.6352 [hep-ex]`.

[17] Roel Aaij et al. 'Studies of beauty baryon decays to D^0ph^- and $\Lambda_c^+h^-$ final states'. In: *Phys. Rev.* D89.3 (2014), p. 032001. arXiv: `1311.4823 [hep-ex]`.

[18] Tim Gershon and Mike Williams. 'Prospects for the Measurement of the Unitarity Triangle Angle gamma from $B^0 \to DK^+\pi^-$ Decays'. In: *Phys. Rev. D* 80 (2009), p. 092002. arXiv: `0909.1495 [hep-ph]`.

[19] Tim Gershon. 'On the Measurement of the Unitarity Triangle Angle γ from $B^0 \to$ DK*0 Decays'. In: *Phys. Rev. D* 79 (2009), p. 051301. arXiv: `0810.2706 [hep-ph]`.

[20] P.A. Zyla et al. 'Review of Particle Physics'. In: *PTEP* 2020.8 (2020), p. 083C01.

[21] Yorikiyo Nagashima. *Elementary particle physics. Vol. 1: Quantum field theory and particles*. 2010.

[22] S. L. Glashow. 'Partial Symmetries of Weak Interactions'. In: *Nucl. Phys.* 22 (1961), pp. 579–588.

[23] Abdus Salam. 'Weak and Electromagnetic Interactions'. In: *Conf. Proc.* C680519 (1968), pp. 367–377.

[24] Steven Weinberg. 'A Model of Leptons'. In: *Phys. Rev. Lett.* 19 (1967), pp. 1264–1266.

[25] Peter W. Higgs. 'Broken Symmetries and the Masses of Gauge Bosons'. In: *Phys. Rev. Lett.* 13 (1964). [,160(1964)], pp. 508–509.

[26] W. E. Burcham and M. Jobes. *Nuclear and particle physics*. 1995.

[27] O. Nachtmann. *Elementary Particle Physics: Concepts and Phenomena*. 1990.

[28] Emmy Noether. 'Invariant Variation Problems'. In: *Gott. Nachr.* 1918 (1918). [Transp. Theory Statist. Phys.1,186(1971)], pp. 235–257. arXiv: `physics/0503066 [physics]`.

[29] C. S. Wu, E. Ambler, R. W. Hayward, D. D. Hoppes and R. P. Hudson. 'Experimental Test of Parity Conservation in Beta Decay'. In: *Phys. Rev.* 105 (1957), pp. 1413–1414.

[30] Masud Chaichian, Alexander D. Dolgov, Victor A. Novikov and Anca Tureanu. 'CPT Violation Does Not Lead to Violation of Lorentz Invariance and Vice Versa'. In: *Phys. Lett.* B699 (2011), pp. 177–180. arXiv: `1103.0168 [hep-th]`.

[31] F. Englert and R. Brout. 'Broken Symmetry and the Mass of Gauge Vector Mesons'. In: *Phys. Rev. Lett.* 13 (1964), pp. 321–323.

[32] Lincoln Wolfenstein. 'Parametrization of the Kobayashi-Maskawa Matrix'. In: *Phys. Rev. Lett.* 51 (21 Nov. 1983), pp. 1945–1947.

[33] Ling-Lie Chau and Wai-Yee Keung. 'Comments on the Parametrization of the Kobayashi-Maskawa Matrix'. In: *Phys. Rev. Lett.* 53 (1984), p. 1802.

[34] Y. H. Ahn, Hai-Yang Cheng and Sechul Oh. 'Wolfenstein Parametrization at Higher Order: Seeming Discrepancies and Their Resolution'. In: *Phys. Lett.* B703 (2011), pp. 571–575. arXiv: `1106.0935 [hep-ph]`.

[35] CKMfitter. *The Global CKM Fit*. July 2019. URL: `http://ckmfitter.in2p3.fr/www/results/plots_summer19/ckm_res_summer19.html` (visited on 1st Mar. 2020).

[36] J. Charles et al. 'Current status of the Standard Model CKM fit and constraints on $\Delta F = 2$ New Physics'. In: *Phys. Rev.* D91.7 (2015), p. 073007. arXiv: `1501.05013 [hep-ph]`.

[37] Ashton B. Carter and A. I. Sanda. 'CP Violation in Cascade Decays of B Mesons'. In: *Phys. Rev. Lett.* 45 (1980), p. 952.

[38] Michael Gronau and Daniel Wyler. 'On determining a weak phase from CP asymmetries in charged B decays'. In: *Phys. Lett.* B265 (1991), pp. 172–176.

[39] David Atwood, Isard Dunietz and Amarjit Soni. 'Enhanced CP violation with $B \to KD^0$ (anti-D^0) modes and extraction of the CKM angle gamma'. In: *Phys. Rev. Lett.* 78 (1997), pp. 3257–3260. arXiv: `hep-ph/9612433 [hep-ph]`.

[40] Roel Aaij et al. 'Measurement of CP violation parameters in $B^0 \to DK^{*0}$ decays'. In: *Phys. Rev. D* 90.11 (2014), p. 112002. arXiv: `1407.8136 [hep-ex]`.

[41] R. H. Dalitz. 'On the analysis of τ-meson data and the nature of the τ-meson'. In: *Phil. Mag. Ser.7* 44 (1953), pp. 1068–1080.

[42] William Dunwoodie. *Suggestion for the Parametrization of Dalitz Plot Efficiency*. Rectangular Dalitz Plot. Nov. 2004. URL: `http://www.slac.stanford.edu/~wmd/bbkinematics/dalitz_efficiency.note` (visited on 24th Feb. 2020).

[43] Bernard Aubert et al. 'An amplitude analysis of the decay $B^{\pm} \to \pi^{\pm}\pi^{\pm}\pi^{\mp}$'. In: *Phys. Rev.* D72 (2005), p. 052002. arXiv: `hep-ex/0507025 [hep-ex]`.

[44] A. J. Bevan et al. 'The Physics of the B Factories'. In: *Eur. Phys. J.* C74 (2014), p. 3026. arXiv: `1406.6311 [hep-ex]`.

[45] Hong Chen and Rong-Gang Ping. 'Coherent helicity amplitude for sequential decays'. In: *Physical Review D* 95.7 (Apr. 2017).

[46] Klaus Peters. *A Primer on Partial Wave Analysis*. 2004. arXiv: `hep-ph/0412069 [hep-ph]`.

[47] Suh Urk Chung. *Spin formalisms; 1st updated version*. This report is an updated version of CERN-71-08. Upton, NY: Brookhaven Nat. Lab., 2008.

[48] J D Richman. *An experimenter's guide to the helicity formalism*. Tech. rep. CALT-68-1148. Pasadena, CA: Calif. Inst. Technol., June 1984.

[49] Roel Aaij et al. 'Study of the D^0p amplitude in $\Lambda_b^0 \to D^0p\pi^-$ decays'. In: *JHEP* 05 (2017), p. 030. arXiv: `1701.07873 [hep-ex]`.

[50] Anton Poluektov. 'Study of the D^0p amplitude in $\Lambda_b^0 \to D^0p\pi^-$ decays'. In: (Dec. 2015).

[51] Roel Aaij et al. 'Observation of $J/\psi p$ Resonances Consistent with Pentaquark States in $\Lambda_b^0 \to J/\psi K^-p$ Decays'. In: *Phys. Rev. Lett.* 115 (2015), p. 072001. arXiv: `1507.03414 [hep-ex]`.

[52] Yuanning Gao, Yang Zhenwei, Zhang Liming et al. 'Observation of pentaquark-charmonium states seen in $\Lambda_b^0 \to J/\psi pK^-$ decays'. In: (May 2015).

[53] Roel Aaij et al. 'Evidence for exotic hadron contributions to $\Lambda_b^0 \to J/\psi p\pi^-$ decays'. In: *Phys. Rev. Lett.* 117.8 (2016). [Addendum: Phys. Rev. Lett.117,no.10,109902(2016); Addendum: Phys. Rev. Lett.118,119901(2017)], p. 082003. arXiv: `1606.06999 [hep-ex]`.

[54] Yuanning Gao, Zhenwei Yang, Xuhao Yuan, Liming Zhang and Yanxi Zhang. 'Amplitude analysis of the $\Lambda_b^0 \to J/\psi p\pi^-$ decay and the $J/\psi p$ pentaquark candidates'. In: (June 2016).

[55] R Aaij et al. 'Measurements of the $\Lambda_b^0 \to J/\psi\Lambda$ decay amplitudes and the Λ_b^0 polarisation in pp collisions at $\sqrt{s} = 7$ TeV'. In: *Phys. Lett.* B724 (2013), pp. 27–35. arXiv: `1302.5578 [hep-ex]`.

[56] Roel Aaij et al. 'Measurement of the $\Lambda_b^0 \to J/\psi\Lambda$ angular distribution and the Λ_b^0 polarisation in pp collisions'. In: (Apr. 2020). arXiv: `2004.10563 [hep-ex]`.

[57] Alan Weinstein. 'Breit Wigners and Form Factors'. Sept. 1999.

[58] John Markus Blatt and Victor Frederick Weisskopf. *Theoretical nuclear physics*. New York: Springer, 1952.

[59] Ning Wu. 'Centrifugal-Barrier Effects and Determination of Interaction Radius'. In: *Commun. Theor. Phys.* 61.1 (2014), pp. 89–94. arXiv: `1305.5118 [physics.gen-ph]`.

[60] S.M. Flatté. 'Coupled-channel analysis of the $\pi\eta$ and $K\overline{K}$ systems near $K\overline{K}$ threshold'. In: *Physics Letters B* 63.2 (1976), pp. 224–227.

[61] A. Garmash et al. 'Dalitz analysis of the three-body charmless decays $B^+ \to K^+\pi^+\pi^-$ and $B^+ \to K^+K^+K^-$'. In: *Phys. Rev.* D71 (2005), p. 092003. arXiv: `hep-ex/0412066 [hep-ex]`.

[62] Julie Haffner. 'The CERN accelerator complex. Complexe des accélérateurs du CERN'. In: (Oct. 2013). General Photo.

[63] LHCb. *LHCb - Large Hadron Collider beauty experiment*. Feb. 2020. URL: `http://lhcb-public.web.cern.ch/lhcb-public/` (visited on 14th Feb. 2020).

[64] Michael Benedikt, Paul Collier, V Mertens, John Poole and Karlheinz Schindl. *LHC Design Report*. CERN Yellow Reports: Monographs. Geneva: CERN, 2004.

[65] A. Augusto Alves Jr. et al. 'The LHCb Detector at the LHC'. In: *JINST* 3 (2008), S08005.

[66] 'LHCb VELO TDR: Vertex locator. Technical design report'. In: (2001).

[67] Christian Lippmann. 'Particle identification'. In: *Nucl. Instrum. Meth.* A666 (2012), pp. 148–172. arXiv: `1101.3276 [hep-ex]`.

[68] 'LHCb calorimeters: Technical design report'. In: (2000).

[69] Maximilien Brice. 'The LHCb electromagnetic calorimeter. Le mur du calorimètre électromagnétique de LHCb a été entièrement monté en un petit mois seulement !' May 2005.

[70] 'LHCb trigger system technical design report'. In: (2003).

[71] R Hierk, M Merk, M Needham and R Van der Eijk. *Performance of the LHCb 00 track fitting software*. Tech. rep. LHCb-2000-086. Geneva: CERN, Aug. 2000.

[72] R Frühwirth. 'Application of Kalman filtering to track and vertex fitting'. In: *Nucl. Instrum. Methods Phys. Res., A* 262.HEPHY-PUB-503 (June 1987), 444. 19 p.

[73] P. Billoir, R. Frühwirth and M. Regler. 'Track element merging strategy and vertex fitting in complex modular detectors'. In: *Nuclear Instruments and Methods in Physics Research Section A: Accelerators, Spectrometers, Detectors and Associated Equipment* 241.1 (1985), pp. 115–131.

[74] University of Athens. *HY.P.A.T.I.A.* 2011. URL: `https://hypatia.iasa.gr/applet/en/help.html` (visited on 5th July 2020).

[75] A Powell. 'Particle Identification at LHCb. Particle ID in LHCb'. In: LHCb-PROC-2011-008. CERN-LHCb-PROC-2011-008 (Jan. 2011), 5 p.

[76] R. W. Forty and O. Schneider. 'RICH pattern recognition'. In: (1998).

[77] Nicholas Metropolis and S. Ulam. 'The Monte Carlo Method'. In: *Journal of the American Statistical Association* 44.247 (1949), pp. 335–341.

[78] Torbjorn Sjostrand, Stephen Mrenna and Peter Z. Skands. 'A Brief Introduction to PYTHIA 8.1'. In: *Comput. Phys. Commun.* 178 (2008), pp. 852–867. arXiv: `0710.3820 [hep-ph]`.

[79] I. Belyaev et al. 'Handling of the generation of primary events in Gauss, the LHCb simulation framework'. In: *J. Phys. Conf. Ser.* 331 (2011), p. 032047.

[80] D. J. Lange. 'The EvtGen particle decay simulation package'. In: *Nucl. Instrum. Meth.* A462 (2001), pp. 152–155.

[81] Piotr Golonka and Zbigniew Was. 'PHOTOS Monte Carlo: A Precision tool for QED corrections in Z and W decays'. In: *Eur. Phys. J.* C45 (2006), pp. 97–107. arXiv: `hep-ph/0506026 [hep-ph]`.

[82] M. Clemencic, G. Corti, S. Easo et al. 'The LHCb simulation application, Gauss: Design, evolution and experience'. In: *J. Phys. Conf. Ser.* 331 (2011), p. 032023.

[83] S. Agostinelli et al. 'GEANT4: A Simulation toolkit'. In: *Nucl. Instrum. Meth.* A506 (2003), pp. 250–303.

[84] John Allison et al. 'Geant4 developments and applications'. In: *IEEE Trans. Nucl. Sci.* 53 (2006), p. 270.

[85] LHCb. *The DECFILES Package*. URL: `http://lhcbdoc.web.cern.ch/lhcbdoc/decfiles/` (visited on 25th Mar. 2020).

[86] LHCb. *DecFiles Repository*. URL: `https://gitlab.cern.ch/lhcb-datapkg/Gen/DecFiles` (visited on 25th Mar. 2020).

[87] Wouter D. Hulsbergen. 'Decay chain fitting with a Kalman filter'. In: *Nucl. Instrum. Meth.* A552 (2005), pp. 566–575. arXiv: `physics/0503191 [physics]`.

[88] R. Brun and F. Rademakers. 'ROOT: An object oriented data analysis framework'. In: *Nucl. Instrum. Meth.* A389 (1997), pp. 81–86.

[89] I. Antcheva et al. 'ROOT: A C++ framework for petabyte data storage, statistical analysis and visualization'. In: *Comput. Phys. Commun.* 182 (2011), pp. 1384–1385.

[90] *The STRIPPING Project*. Mar. 2020. URL: `http://lhcbdoc.web.cern.ch/lhcbdoc/stripping/` (visited on 18th Mar. 2020).

[91] S Tolk, J Albrecht, F Dettori and A Pellegrino. *Data driven trigger efficiency determination at LHCb*. Tech. rep. LHCb-PUB-2014-039. CERN-LHCb-PUB-2014-039. Geneva: CERN, May 2014.

[92] Lucio Anderlini, Andrea Contu, Christopher Rob Jones et al. *The PIDCalib package*. Tech. rep. LHCb-INT-2016-028. CERN-LHCb-INT-2016-028. Geneva: CERN, June 2016.

[93] Anton Poluektov. *Correction of simulated particle identification response in LHCb using transformation of variables*. Tech. rep. LHCb-INT-2017-007. CERN-LHCb-INT-2017-007. Geneva: CERN, Apr. 2017.

[94] Vladimir Gligorov. *TupleToolMCBackgroundInfo*. May 2009. URL: `https://twiki.cern.ch/twiki/bin/view/LHCb/TupleToolMCBackgroundInfo` (visited on 21st Mar. 2020).

[95] Muriel Pivk and Francois R. Le Diberder. 'SPlot: A Statistical tool to unfold data distributions'. In: *Nucl. Instrum. Meth.* A555 (2005), pp. 356–369. arXiv: `physics/0402083 [physics.data-an]`.

[96] Roland Waldi. *Statistische Datenanalyse*. Springer Spektrum, Berlin, Heidelberg, 2019.

[97] Fred James and Matthias Winkler. 'MINUIT User's Guide'. In: (2004).

[98] Stuart Russell and Peter Norvig. *Artificial Intelligence: A Modern Approach*. 3rd. USA: Prentice Hall Press, 2009.

[99] Andreas Hocker et al. 'TMVA - Toolkit for Multivariate Data Analysis'. In: (2007). arXiv: `physics/0703039 [physics.data-an]`.

[100] Karl Pearson F.R.S. 'LIII. On lines and planes of closest fit to systems of points in space'. In: *The London, Edinburgh, and Dublin Philosophical Magazine and Journal of Science* 2.11 (1901), pp. 559–572. eprint: `https://doi.org/10.1080/14786440109462720`.

[101] Patrick T. Komiske, Eric M. Metodiev, Benjamin Nachman and Matthew D. Schwartz. 'Learning to classify from impure samples with high-dimensional data'. In: *Phys. Rev. D* 98 (1 July 2018), p. 011502.

[102] Leo Breiman. *Bias, Variance, and Arcing Classifiers*. Tech. rep. Statistics Department, University of California, 1996.

[103] Chapman and Hall. *Ensemble Methods: Foundations and Algorithms*. Taylor & Francis Inc, 2012.

[104] Sara van de Geer Peter Bühlmann. *Statistics for High-Dimensional Data*. Springer, Berlin, Heidelberg, 2011.

[105] Jerome Friedman. 'Greedy Function Approximation: A Gradient Boosting Machine'. In: *The Annals of Statistics* 29 (Nov. 2000).

[106] Yoav Freund and Robert E Schapire. 'A Decision-Theoretic Generalization of On-Line Learning and an Application to Boosting'. In: *Journal of Computer and System Sciences* 55.1 (1997), pp. 119–139.

[107] Leo Breiman. 'Random Forests'. In: *Machine Learning* 45.1 (2001), pp. 5–32.

[108] Tom Fawcett. 'ROC Graphs: Notes and Practical Considerations for Researchers'. In: *Machine Learning* 31 (Jan. 2004), pp. 1–38.

[109] Roel Aaij et al. 'Measurement of *CP* observables in $B^{\pm} \to D^{(*)}K^{\pm}$ and $B^{\pm} \to D^{(*)}\pi^{\pm}$ decays'. In: *Phys. Lett. B* 777 (2018), pp. 16–30. arXiv: `1708.06370 [hep-ex]`.

[110] Roel Aaij et al. 'Measurement of *CP* observables in the process $B^0 \to DK^{*0}$ with two- and four-body D decays'. In: *JHEP* 08 (2019), p. 041. arXiv: `1906.08297 [hep-ex]`.

[111] G. A. Cowan, D. C. Craik and M. D. Needham. 'RapidSim: an application for the fast simulation of heavy-quark hadron decays'. In: *Comput. Phys. Commun.* 214 (2017), pp. 239–246. arXiv: `1612.07489 [hep-ex]`.

[112] Wouter Verkerke and David P. Kirkby. 'The RooFit toolkit for data modeling'. In: *eConf* C0303241 (2003). [,186(2003)], MOLT007. arXiv: `physics/0306116 [physics]`.

[113] Albert Puig. *The LHCb trigger in 2011 and 2012*. Tech. rep. LHCb-PUB-2014-046. CERN-LHCb-PUB-2014-046. Geneva: CERN, Nov. 2014.

[114] Roel Aaij et al. 'Design and performance of the LHCb trigger and full real-time reconstruction in Run 2 of the LHC'. In: *JINST* 14.04 (2019), P04013. arXiv: `1812.10790 [hep-ex]`.

[115] LHCb. *L0 Trigger Configuration*. Nov. 2018. URL: `https://lbtwiki.cern.ch/bin/view/L0/L0TCK` (visited on 7th Apr. 2020).

[116] Roel Aaij et al. 'Measurements of *CP* asymmetries in charmless four-body Λ_b^0 and Ξ_b^0 decays'. In: *Eur. Phys. J.* C79.9 (2019), p. 745. arXiv: `1903.06792 [hep-ex]`.

[117] Roel Aaij et al. 'Precision measurement of the mass and lifetime of the Ξ_b^0 baryon'. In: *Phys. Rev. Lett.* 113 (2014), p. 032001. arXiv: `1405.7223 [hep-ex]`.

[118] Roel Aaij et al. 'Observation of the decays $\Lambda_b^0 \to \chi_{c1}pK^-$ and $\Lambda_b^0 \to \chi_{c2}pK^-$'. In: *Phys. Rev. Lett.* 119.6 (2017), p. 062001. arXiv: `1704.07900 [hep-ex]`.

[119] Yuehong Xie. 'sFit: a method for background subtraction in maximum likelihood fit'. In: (2009). arXiv: `0905.0724 [physics.data-an]`.

[120] Anton Poluektov. *TensorFlowAnalysis*. URL: `https://gitlab.cern.ch/poluekt/TensorFlowAnalysis` (visited on 14th May 2020).

[121] Martn Abadi et al. 'TensorFlow: Large-Scale Machine Learning on Heterogeneous Distributed Systems'. In: (Mar. 2016). arXiv: `1603.04467 [cs.DC]`.

[122] Anton Poluektov. 'Issue with ProbNNp in $\Lambda^0 \to p\pi$'. PID&CO meeting, CERN. Sept. 2017.

[123] Christoph Langenbruch. 'Parameter uncertainties in weighted unbinned maximum likelihood fits'. In: (Nov. 2019). arXiv: `1911.01303 [physics.data-an]`.

[124] Lars Eklund. 'The LHCb Upgrade'. In: *11th Conference on the Intersections of Particle and Nuclear Physics*. Sept. 2017. arXiv: `1709.04709 [physics.ins-det]`.

[125] Nicola Neri. 'The LHCb Upgrade II'. In: *PoS* BEAUTY2018 (2018). Ed. by Robert Fleischer, Neville Harnew, Guy Wilkinson, Fabrizio Palla and Giovanni Punzi, p. 057.

[126] Roel Aaij et al. 'Measurement of b hadron fractions in 13 TeV pp collisions'. In: *Phys. Rev.* D100.3 (2019), p. 031102. arXiv: `1902.06794 [hep-ex]`.

[127] R Aaij et al. 'Measurement of the fragmentation fraction ratio f_s/f_d and its dependence on B meson kinematics'. In: *JHEP* 04 (2013), p. 001. arXiv: `1301.5286 [hep-ex]`.

[128] Roel Aaij et al. 'Observation of the decay $B_s^0 \to \overline{D}^0 K^+ K^-$'. In: *Phys. Rev.* D98.7 (2018), p. 072006. arXiv: `1807.01891 [hep-ex]`.

[129] Gloria Corti, Luiz Fernández, Tomas Pilar, Patrick Robbe and Olivier Schneider. *Monte Carlo Event Type Definition Rules*. Tech. rep. LHCb-2005-034. CERN-LHCb-2005-034. latest revision submitted on 2014-02-13. Geneva: CERN, Feb. 2014.

[130] D. Müller, M. Clemencic, G. Corti and M. Gersabeck. 'ReDecay: A novel approach to speed up the simulation at LHCb'. In: *Eur. Phys. J.* C78.12 (2018), p. 1009. arXiv: `1810.10362 [hep-ex]`.

[131] ROOT. *ROOT - Bilinear Interpolation*. URL: `https://root.cern.ch/doc/v618/TH2_8cxx_source.html#l01194` (visited on 17th Apr. 2020).

[132] M. Oreglia. 'A Study of the Reactions $\psi' \to \gamma\gamma\psi$'. PhD thesis. SLAC, Dec. 1980.

[133] Tomasz Skwarnicki. 'A study of the radiative CASCADE transitions between the Upsilon-Prime and Upsilon resonances'. PhD thesis. Cracow, INP, 1986.

[134] sPlot- *`RooStats` Implementation*. Apr. 2020. URL: `https://root.cern.ch/doc/v612/classRooStats_1_1SPlot.html` (visited on 22nd Apr. 2020).